Project No. 12-3494

Accurate Holdup Calculations with Predictive Modeling & Data Integration

Fuel Cycle Research and Development

Yousry Azmy
North Carolina State University

In collaboration with:
University of South Carolina

Dan Vega, Federal POC
Mike Miller, Technical POC

NEUP Nuclear Energy University Programs
U.S. Department of Energy

Final Report NEUP Project 12-3494

Accurate Holdup Calculations with Predictive Modeling & Data Integration

Submitted by Project Principal Investigator

Yousry Y. Azmy
Department of Nuclear Engineering
North Carolina State University

Collaborators

Dan Cacuci
Department of Mechanical Engineering
University of South Carolina

Louise Worrall
Safeguards & Security Technology Group
Nuclear Security & Isotope Technology Division
Oak Ridge National Laboratory

Contents

Note: Page numbers in this *Table of Contents* refers to the PDF page numbers, not to the printed page numbers in each page's footer.

1. Abstract

In facilities that process special nuclear material (SNM) it is important to account accurately for the fissile material that enters and leaves the plant. Although there are many stages and processes through which materials must be traced and measured, the focus of this project is material that is "held-up" in equipment, pipes, and ducts during normal operation and that can accumulate over time into significant quantities. Accurately estimating the holdup is essential for proper SNM accounting (vis-à-vis nuclear non-proliferation), criticality and radiation safety, waste management, and efficient plant operation.

Usually it is not possible to directly measure the holdup quantity and location, so these must be inferred from measured radiation fields, primarily gamma and less frequently neutrons. Current methods to quantify holdup, i.e. Generalized Geometry Holdup (GGH), primarily rely on simple source configurations and crude radiation transport models aided by *ad hoc* correction factors. This project seeks an alternate method of performing measurement-based holdup calculations using a predictive model that employs state-of-the-art radiation transport codes capable of accurately simulating such situations. Inverse and data assimilation methods use the forward transport model to search for a source configuration that best matches the measured data and simultaneously provide an estimate of the level of confidence in the correctness of such configuration.

In this work the holdup problem is re-interpreted as an inverse problem that is under-determined, hence may permit multiple solutions. A probabilistic approach is applied to solving the resulting inverse problem. This approach rates possible solutions according to their plausibility given the measurements and initial information. This is accomplished through the use of Bayes' Theorem that resolves the issue of multiple solutions by giving an estimate of the probability of observing each possible solution. To use Bayes' Theorem, one must have a model $y(x)$ that maps the state variables x (the solution in this case) to the measurements y. In this case, the unknown state variables are the configuration and composition of the heldup SNM. The measurements are the detector readings. Thus, the natural model is neutral-particle radiation transport where a wealth of computational tools exists for performing these simulations accurately and efficiently. The combination of predictive model and Bayesian inference forms the Data Integration with Modeled Predictions (DIMP) method that serves as foundation for this project. The cost functional describing the model-to-data misfit is computed via a norm created by the inverse of the covariance matrix of the model parameters and responses. Since the model $y(x)$ for the holdup problem is nonlinear, a nonlinear optimization on Q is conducted via Newton-type iterative methods to find the optimal values of the model parameters x.

This project comprised a collaboration between NC State University (NCSU), the University of South Carolina (USC), and Oak Ridge National Laboratory (ORNL). The project was originally proposed in seven main tasks with an eighth contingency task to be performed if time and funding permitted; in fact time did not permit commencement of the contingency task and it was not performed. The remaining tasks involved holdup analysis with gamma detection strategies and separately with neutrons based on coincidence counting. Early in the project, and upon consultation with experts in coincidence counting it became evident that this approach is not viable for holdup applications and this task was replaced with an alternative, but valuable investigation that was carried out by the USC partner. Nevertheless, the experimental

measurements at ORNL of both gamma and neutron sources for the purpose of constructing Detector Response Functions (DRFs) with the associated uncertainties were indeed completed.

This report captures the final status of this project by detailing the work performed on each of the proposed tasks and highlighting its accomplishments. A brief summary of these tasks follows:

Task A: *Verify radiation transport packages & data for computing fluxes at a detector*

This task was successfully completed in the second quarter of the third budget period. The graduate student assigned to this task composed a manual for the DIMP code system, and the Postdoctoral Fellow who assisted with this task composed an installation guide for Denovo since it underlies DIMP.

Task B: *Equip transport packages with capability to compute neutron multiplicities & sensitivities*

Expert colleagues at ORNL advised that the original objective of this task is not viable for holdup applications because of the low multiplicity signal. Hence this task, as assigned to USC, was redefined at no additional cost to establish a broader theoretical foundation of DIMP using a paradigm problem configuration. The modified task entitled "Analyze DIMP in the Context of a Paradigm Inverse Source Determination Problem" was completed via transmission of a final report composed by the USC PI in the first quarter of the third budget period.

Task C: *Validate gamma detector response functions and their uncertainties*

This task was successfully completed in the fourth quarter of the second budget period. The graduate student who worked on this task defended and published his MS thesis on the measurements, construction of the gamma DRF and computation of its uncertainties.

Task D: *Develop & validate neutron detector response functions and their uncertainties*

This task was successfully completed in the third quarter of the second budget period. The postdoctoral fellow who worked on this task composed a report on the measurements, construction of the neutron DRF and computation of its uncertainties.

Task E: *Implement data integration and inverse methods*

This task was successfully completed by the USC collaborators in the fourth quarter of the one-year No-Cost-Extension Period. They published the report "MULTI-PRED: A Software Module for Reducing Uncertainties in Predicted Results through Data Assimilation, Model Calibration and Validation MULTI-PRED User's Manual Version 1" authored by Dan G. Cacuci and Madalina C. Badea.

Task F: *Perform high-quality holdup measurements*

This task was successfully completed in the fourth quarter of the third budget period. The graduate student who worked on this task in collaboration with the ORNL PI reported these results in the student's doctoral proposal that he successfully defended in December 2016. That document includes more than just the report on this task.

Task G: *Validate DIMP method against measured and manufactured data*

Progress was made on this Task that continued into a No-Cost-Extension Period until December 31, 2016, to permit the main graduate student assigned to this project to defend his proposal, a goal that has been achieved. However, several unforeseen difficulties in the progress of his research delayed full accomplishment of this task. Due to his investment of time and effort in this work, the graduate student, supported by the NCSU PI, are committed to completion of this task under separate funding. The current status of this task comprises a paper that has been accepted for publication and will be presented at the American Nuclear Society's Mathematics and Computation Topical Meeting, April 16-20, 2017, in Jeju, South Korea.

2. Introduction

In a nuclear materials processing facility, it is important to account accurately for the fissile material that enters and leaves the plant. Incorrect accounting could lead to issues with radiological safety, criticality safety, and nuclear security and safeguards. Although there are many stages and processes through which materials must be traced and measured, the focus of this project is the material that is left behind in equipment, pipes, and ducts. During normal operation, small amounts of material stick to pipe walls or get trapped in processing equipment. Over time, these small material "holdups" accumulate into significant quantities, sometimes several kilograms.[1] Thus, accurately estimating the holdup is an important component of material accounting. Although preventing the diversion of special nuclear material (SNM) is a key motivation for performing holdup calculations, it is not the only reason. Reilly lists a number of reasons that plant operators need to know the location and quantity of holdup:[1] criticality safety, radiation safety, waste management, and efficient plant operation.

Without accurate knowledge of the heldup material, it is possible that the processing plant will eventually evolve into an unsafe and/or insecure operating regime. While a criticality accident could be deadly, additional exposure to workers through unknown holdup deposits must also be avoided. Additionally, inaccurate accounting for SNM, and accumulated amounts of such materials pose serious proliferation risks. Therefore, facilities that process nuclear materials in general depend on accurate and precise estimates of the holdup to assure the public and the international community at large that their operations are safe and secure. Directly measuring the quantity of holdup is usually not possible, as it would require thoroughly cleaning out every piece of equipment. Thus, the quantities and locations of holdup must be measured indirectly. Since the nuclides of interest are radioactive, it is possible to infer their presence through the detection of their natural decay radiation. Gamma ray spectra are typically measured and this is facilitated, at least in part, by the availability and portability of detectors that can be held at pre-specified locations likely for holdup accumulation. Neutron measurements are also used, but less frequently.

The energies of photopeaks in the gamma spectrum indicate the identity of nuclides present, while the magnitude of the count rate provides clues to the amount of accumulated radioactive material. Current methods to compute the quantity of holdup material, i.e., Generalized

[1] T. D. Reilly, "Nondestructive assay of holdup," in *Passive Nondestructive Assay of Nuclear Material*: *2007 Addendum*, LA-UR-07-5149, 2007.

Geometry Holdup (GGH), primarily rely on a calculation of the geometric attenuation across the distance between the source and detector, assuming that the geometric shape of the source can be represented as a point, line, or plane.[1] With this basic estimate, the analysts apply corrections to compensate for various effects, such as attenuation in equipment or deviations from the simple source shapes. This project seeks an alternate method of performing these holdup calculations that are based on measured radiation fields using a predictive model that would naturally account for effects currently treated with simplified, hence potentially inaccurate, correction factors. Radiation transport codes can accurately simulate such situations. Inverse and data assimilation methods can then use a forward transport model to search for a source configuration that best matches the measured data and simultaneously provide an estimate of the level of confidence in the correctness of such configuration. This Data Integration with Modeled Predictions (DIMP) method comprises the backbone of this project.

3. Approach and Objectives

To be specific, the holdup problem is defined in terms of information that is known and information that is unknown. First, the configuration of the modeled space and equipment around the holdup measurement is considered known. There are two aspects comprising this information: the geometric configuration, i.e. shapes and dimensions, and the elemental/isotopic composition of each item occupying the volume. Engineering drawings or a CAD model should provide a complete description of the geometric configuration. Each distinct material, except the holdup material, in the room should have a known density and elemental composition, either natural abundance or isotopically enriched. These details could be estimated for most standard materials (such as concrete block walls). Small components in complex equipment should be included in the computational model of the configuration space if they could significantly affect the radiation fields around the detector or SNM.

Of course, in the specification of the room's geometry and material composition, the detailed distribution of the SNM, and potentially its nuclear composition, is fully or partly unspecified. In the problems considered here, the SNM geometric configuration is unknown. However, the SNM should be contained in only a few small (relative to the space volume) geometric bodies. Although theoretically possible, allowing the SNM to be anywhere in the room would make the problem significantly more difficult and would require many more detector measurements to achieve a sufficient level of confidence in the determined solution. Confining the nuclear materials to small volumes such as pipes or boxes makes the problem more tractable. Although the exact configuration of the held-up radiation sources is unknown, there may be certain patterns which it typically follows. For instance, the holdup in a pipe must be connected to the pipe wall, and material in a box may tend to accumulate in corners. These physically deductible patterns may be helpful in constraining the possible solutions.

The nuclides present in the SNM may or may not be known from the start. If the plant consistently processes one type of material, then it should be possible to estimate the nuclide composition in each component. However, in most plants, the type of input material varies widely, making it difficult to estimate a composition without first detecting gamma radiation and identifying the source nuclides from the measured peaks. In this project, the isotopic composition of the radioactive SNM is considered unknown.

The density of the held-up SNM is likely unknown also, although this value could be estimated with some certainty. A related unknown is the mass in the held-up SNM of each nuclide of interest. However, this is solely dependent on the geometric configuration of the holdup, the density of the holdup, and the isotopic composition of the holdup.

The amount of holdup is measured indirectly using radiation detectors. As stated above, both gamma and neutron detectors are used for this purpose, but gamma detectors are more common. Sodium iodide detectors are favored for their portability, but their energy resolution is poor.[2] Semiconductor detectors are increasingly available; they feature better peak resolution than NaI scintillation detectors. The resolution of the detector will certainly influence the ability to discern peaks in the spectrum that, in turn, identify the source nuclides in the SNM. The gamma detectors deployed in holdup measurements are typically collimated in order to cut down on the background radiation and radiation coming from other components at the expense of attaining lower count rates with larger statistical errors.

The use of neutron detectors is more difficult because they are larger, heavier, and due to the necessary moderating material, but they can provide useful and complementary data. They are also more difficult to collimate due to neutrons' typically lower interaction probabilities. While collimated neutron detectors are possible, they are large and must be transported on carts.[1] Neutron detectors are useful to peer into larger and heavier equipment, for which gamma rays are strongly attenuated and have limited penetration.

The quality of the counting statistics of the detector measurements is limited by the available time that the technicians are able to spend measuring each component. Most SNM processing plants contain many components, so any one part can only consume a brief length of time to measure. In the case of Y-12 HEU plant, several hundred spectra are acquired and saved in an hour.[3] Likewise, the time available for the processing of the detector data and computing the holdup amount and spatial distribution is limited as well. Although completing the calculation in a few minutes would be ideal, the longest acceptable run time is overnight, where the analyst would start the calculation during the workday and it would be complete by the next morning. For these calculations, it is assumed that the analyst has available a desktop workstation computer, and that generally there is no access to a high-performance computing cluster.

Our new approach that was attempted in this project is distinct from current approaches for estimating the holdup in that it casts it as an inverse problem. Although the precise definition of an "inverse problem" is difficult to pin down, the closely related ill-posed label is clearly defined. A well-posed problem has a unique solution that is stable and continuous.[4] An ill-posed problem lacks one or more characteristics of the well-posed problem. In a typical holdup situation, there are significantly more unknowns (mostly in the spatial location of the nuclides) than there are measurements. This means that the problem is under-determined, which implies that there will

[2] G. Knoll, *Radiation Detection and Measurement*, Wiley, 2010.
[3] P. Russo, H. Smith, J. J.K. Sprinkle, C. Bjork, G. Sheppard and S. Smith, "Evaluation of an integrated holdup measurement system using the GGH formalism with the M3CA," in *Transactions of the ANS*, Jackson Hole, WY, 1996.
[4] J. Idier, *Bayesian approach to inverse problems*, Wiley, 2008.

be many permissible solutions. Thus, the problem is ill-posed and can be thought of as an inverse problem.

Based on this viewpoint of the holdup problem we adapt the Data Integration with Modeled Predictions (DIMP) method for this application.

Solving the holdup problem using the DIMP approach has several benefits. One of the strongest advantages of DIMP is the consistent integration of all available measurements and prior information. This is especially relevant for holdup problems where both gamma and neutron measurements are conducted. In addition, there would likely be prior information about the holdup distribution based on past experience, which can be included in the method through the prior PDF.

The Bayesian inference component of DIMP is designed to estimate the confidence level in a particular solution, or solutions. The method can account for various uncertainties, whether from detector measurements, nuclear data, or geometric uncertainties. The method will provide a best-estimate of the mass and location of materials remaining, as well as the variance (or confidence level) of these quantities. Additionally, the width of the confidence interval of the solution could be used as a figure-of-merit to optimally select and locate subsequent confirmatory measurements.

One more advantage of the DIMP approach is the modularity of its requirements. Each of the functions can be performed by a dedicated module. In most cases, much time and effort has already been poured into implementing and verifying each module in its own right and for a broad variety of applications. Most of the computational tools necessary for this work, or at least parts thereof, are readily and publicly available and have been utilized in this project at no cost to the sponsor.

The combination of these tools makes a solution to the holdup problem tractable. However, the robustness and accuracy of the solution depends on the information content of the measurements. In the case of information-poor measurements, a high variance in the final estimate will indicate that the computed estimate of the held-up mass and spatial distribution is unreliable.

4. Detailed Report on Project Tasks

In this section we provide a detailed description of the accomplishment of each task using the same numbering sequence as in the awarded proposal. The responsible party for delivery of each task is stated together with a brief description of the task as envisioned in the original proposal. This is followed for each task by the corresponding final report on that task as composed by the responsible party.

4.1. Task A: Verify radiation transport packages & data for computing fluxes at a detector

These are the primary predictive models needed for the holdup problem. The model is the time-independent neutral-particle linear Boltzmann transport equation, valid for both gamma rays and neutrons with the appropriate cross section data. These simulators are part of the kernel of the inverse calculation. They will be called many times during the course of one holdup calculation. Thus, they must be both accurate and efficient. Deterministic methods for solving these problems are favored due to their computational efficiency. Here code packages like SCALE are useful, providing the benefit of decades of research and years of software engineering effort invested in the simulation tools. Specifically, we use Denovo, that is distributed as part of the SCALE package. The fine multigroup shielding cross section library from SCALE will suffice for the multigroup calculations, while ENDF/B-VII pointwise cross sections is employed for continuous or uncollided calculations. For accurate uncollided flux calculations we use the semi-analytical ray tracing technique, while for computing the fully-collided flux we employ the discrete ordinates approximation. In addition, all utilized transport codes must be equipped to compute the adjoint flux, as this is necessary to efficiently compute the sensitivity of the response to various model parameters. NC State University was responsible for completing this task.

The accomplishment of this task was reported in: Noel Nelson and Yousry Y. Azmy, *Data Integration with Modeled Predictions (DIMP) Code User Manual*, Department of Nuclear Engineering, NC State University, July 20, 2015. Additionally, a manual for the installation of the Denovo code that underlies the radiation transport functionality of DIMP was composed: Cyrus Proctor, *Denovo Installation Guide Mined from MediaWiki Installation Guide*, NC State University, 2015. These two documents are replicated on the following pages.

Data Integration with Modeled Predictions (DIMP) Code User Manual

Noel Nelson*and Yousry Y. Azmy†
Department of Nuclear Engineering
NC State University
Version 1

July 20, 2015

*Address: Box 7909, NCSU Campus, Raleigh, NC 27695. Email: nnelson@ncsu.edu
†Address: Box 7909, NCSU Campus, Raleigh, NC 27695. Email: yyazmy@ncsu.edu

Acknowledgements

Thanks to the Nuclear Energy University Programs (NEUP) for their generous funding of the project and helping to make the radiation source mapping concept a reality. Thanks also to Dr. Joshua Hykes for his private consultation and for sharing the earlier version of the code system.

Contents

1 DIMP Model and Theory

The Data Integration with Modeled Predictions (DIMP) model employs several steps to predict a photon radiation source model and solve the inverse transport problem. Unlike a forward transport problem (using source information to predict responses at some set of points) the inverse problem uses a priori information (known parameters) and adjoint sensitivities to predict the most probable value of the unknown parameters (posterior information). In the first section we will discuss the known model parameters (geometry, cross-sections, etc.) and the unknown parameters in this model. Next, we explain how responses are processed (whether these responses are generated synthetically or experimentally) and used in the DIMP model. Then, adjoint calculations performed with the discrete ordinates code, DENOVO [1], and their use in optimization of the source distribution will be discussed. Finally, an outline of the nonlinear Newton algorithm employed in the optimization procedure will be given to allow for a basic understanding of its function.

1.1 Parameters

1.1.1 Known Parameters

The known parameters of the DIMP model are extensive and often case dependent. Such parameter sets include but are not limited to: objects and structures (local geometry and nuclide composition), detector responses, source emission particle types and energies (from response spectra). These sets may be broken down further into useful parameter subsets.

The local geometry of a facility (pipe structures, ducts, and equipment) are generally well characterized in space and material composition. This information is usually known from factory specifications and measurements, but can be substituted for a 3-D image taken by a precision imaging system such as LIDAR. The spatial information and material cross-sections are processed by MAVRIC [1] (Monaco with Automated Variance Reduction using Importance Calculations) and Python to generate meshes for the adjoint transport and source mapping algorithms.

Detector response information comes directly from processed measured spectra. Specifically, response peak information is extracted by a combination of peak fitting and combined with detector efficiency to produce required uncollided flux information. In the absence of a measurement (e.g. for the purpose of verification and testing of the methods and code), this information may also be artificially synthesized with MCNP [2] (Monte Carlo N-Particle Transport code) flux tallies.

The final set of information (source energy and ID) will generally be known in certain applications (such as holdup). In cases where it is not, spectral peak identification may be used from detection measurements to identify the source material of interest and peak energies to be used by DIMP.

1.1.2 Unknown Parameters

The unknown parameters are the unknown quantities of interest. Such parameters include the source strength and distribution in energy and space (also called the source map, $\vec{q}(\vec{x}, E)$). Together with the known parameters, the inverse problem can be posed as follows

$$\vec{r} = S\vec{q} \tag{1}$$

where S is the adjoint flux solution of the uncollided transport equation and $\vec{r}$ is the vector containing the corresponding detector responses. Frequently, the number of unknown parameters exceeds the number of response measurements, and the solution is not unique. Instead of using an inversion operator a more stable Bayesian probabilistic method is used to find the most probable source map [3] (described further in Section 1.4).

1.2 Response Processing

Detector response information is spectral information collected by a detector at a known location. However, in its raw form a detector response is not very useful. For the Bayesian solution, response spectra must be processed into scalar fluxes at the detector locations. In general, a typical NaI detector response appears as follows (Figure 1)

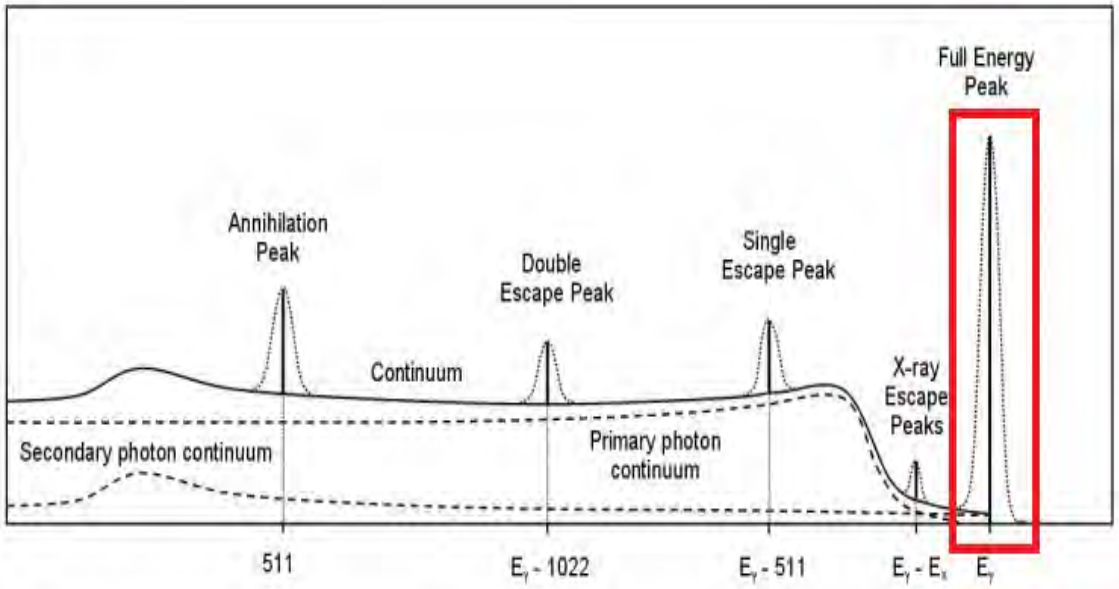

Figure 1: Example of a typical detector response and response peak. [4]

A typical response spectrum can be quite complex, and radiation interaction physics allows for many features in the continuum region of the spectrum. Because those continuum features can be difficult to predict and model, DIMP uses only the full energy peak of a detector response spectrum. A full energy peak represents photons that have deposited their full energy within the detector, and therefore can be used to estimate the uncollided photon flux.

DIMP code handles raw detector spectra according to the following procedure. First, all of the responses for a given case (listed by number of channels, location of detector, and potentially collimation angle) are compiled into a database. Then the user would manually identify peak channel ranges for source and background peaks from previous knowledge and observation. Next, an energy calibration is performed for the given detector by the user via the method of least-squares. Peak centroids are fit quadratically to known peak energies. [3] The background and measured spectra are rebinned according to energy, and background is subtracted from measured spectra. The net spectra are then fit via least squares according to the standard Gaussian model. Finally, the area under each gaussian peak (A_p) is determined and used to calculate the scalar flux ($\phi(E)$) effective locally within the detector's volume according to the following equations. [3]

$$J_- = \frac{A_p}{\epsilon_{ip}}, \tag{2}$$

$$\phi(E) = \frac{\langle l \rangle J_-(E}{V}), \tag{3}$$

where ϵ_{ip} is the intrinsic peak detector efficiency, $\langle l \rangle$ the average chord length of the detector crystal, $J_{-}(E)$ the uncollided partial current on the detector face, and V the detector volume. The detector efficiencies and the average chord length can be calculated by MCNP [2] simulation of the detector of interest. The chord length comes from tracing particle trajectories through the detector crystal using PTRAC. For the intrinsic peak efficiency, the given detector is simulated with 1E9 particle histories and tallies are taken of the number of particles that cross the detector crystal face and the number that terminate in the crystal without leaving its volume. These numbers are divided to estimate the detector peak efficiency. [5]

1.3 DENOVO and Sensitivities

Sensitivity is often only thought of for the calculation of uncertainty for measurement and model parameters. However, in inverse problems model uncertainties are highly useful for in determining the most probable solution of the unknown parameters. In the case of inhomogeneous transport, the sensitivities are the scalar flux solutions to the adjoint transport equations. The details of the inhomogeneous transport equations and adjoint formulation can be found in Ref. [5]. Consider the detector response

$$R = \langle \phi, \sigma_d \rangle, \tag{4}$$

where $\langle\rangle$ is the inner product, and ϕ is the scalar flux. Where ϕ is the solution to the forward transport problem

$$L\phi = q. \tag{5}$$

L is the transport operator, and q is the source. Vacuum boundary conditions are assumed. The adjoint transport problem can be defined as

$$L^{\dagger}\phi^{\dagger} = q^{\dagger}, \tag{6}$$

and choose $q^{\dagger} = \sigma_d$ where $q^{\dagger}$ is the adjoint source and σ_d the detector response function. This makes $L^{\dagger}$ is the adjoint transport operator and $\phi^{\dagger}$ the adjoint scalar flux or the importance. Next, take the inner product of Equation 5 with $\phi^{\dagger}$ (7)

$$\langle L\phi, \phi^{\dagger} \rangle = \langle q, \phi^{\dagger} \rangle, \tag{7}$$

and use the adjoint property

$$\langle \phi, L^{\dagger}\phi^{\dagger} \rangle = \langle q, \phi^{\dagger} \rangle. \tag{8}$$

Substitute the adjoint source condition (Equation 6)

$$\langle \phi, \sigma_d \rangle = \langle q, \phi^{\dagger} \rangle, \tag{9}$$

and finally, substitute the definition for detector response (Equation 4)

$$R = \langle q, \phi^{\dagger} \rangle \tag{10}$$

where R is the continuous representation of the detector response vector ($\vec{r}$) defined earlier. Hence, Equation (1) has been derived from an adjoint transport formulation under vacuum boundary conditions. This also means that the forward flux when folded with the detector response function should produce the same response as the adjoint flux folded with a given source. However, in practice this is not quite true as transport codes introduce discretization error and truncation errors into solutions. Therefore, DENOVO was chosen (over TORT) for calculation of the adjoint flux, as it minimized the relative error between forward calculated and adjoint calculated responses.

1.4 Optimization

The general inverse problem has been posed (Equation 1) and the known parameters (geometry, cross-sections, and detector responses) and adjoint sensitivities considered. In order to determine the most probable values of the unknown (source) parameters, a nonlinear Newton optimization method [**?**] has been implemented in the DIMP code. The Newton optimization method maximizes the posterior. Assuming "quadratic loss," the posterior is

$$p(\vec{z}|C) = \frac{1}{\sqrt{|2\pi C|}} \exp\Big[-\frac{1}{2} Q(\vec{z}) \Big], \tag{11}$$

where

$$\vec{z} \equiv \begin{bmatrix} \vec{\alpha} - \vec{\alpha}^0 \\ \vec{r} - \vec{r}_m \end{bmatrix} = \begin{bmatrix} \vec{z}_\alpha \\ \vec{z}_r \end{bmatrix}, \; Q(\vec{z}) \equiv \vec{z}^T C^{-1} \vec{z},$$

$\vec{\alpha}^0$ are the means of the prior on $\vec{\alpha}$, $\vec{r}_m$ are the measured responses, and C is the combined covariance matrix defined by

$$C \equiv \begin{bmatrix} C_\alpha & C_{\alpha r} \\ C_{\alpha r}^T & C_m \end{bmatrix} \tag{12}$$

where C_α is the covariance matrix for $\vec{\alpha}$, C_m is the $\vec{r}$ covariance matrix, and $C_{\alpha r}$ is the $\vec{\alpha}$-to-$\vec{r}$ covariance matrix.

Newton's method uses the first- and second-derivative information of the functional, more specifically the gradient $\vec{\nabla}_\alpha Q(\vec{z}_k)$ and Hessian $\nabla^2_\alpha Q(\vec{z}_k)$ in the update step

$$\vec{\alpha}_{k+1} = \vec{\alpha}_k - \lambda_k (\nabla^2_\alpha Q(\vec{z}_k))^{-1} \vec{\nabla}_\alpha Q(\vec{z}_k). \tag{13}$$

The line search parameter $\lambda_k \in [0, 1]$ adjusts the Newton step length for improved stability. At each iteration ($\vec{\alpha}_k$) the parameter sensitivities are recomputed. This update procedure continues until the convergence criterion is met, and ideally, the most probable source distribution has been converged. This approach is described in more detail in Ref. [3]

2 System and Program Requirements

System: 64-bit linux operating system with Ubuntu 12.04 LTS or 14.04 LTS. List of all required dependent codes and scripting languages required for running DIMP.

List of Codes

1. Python 2.7
2. Many Python Modules including:
   (a) Numpy
   (b) Scipy
   (c) Tables
   (d) unumpy
   (e) matplotlib
3. DENOVO
   (a) DENOVO Constituent Programs (described in Cyrus's installation manual) [8]
4. SCALE
5. MCNP

3 User Manual

3.1 Installation

3.1.1 Python Modules

Many of the control scripts for DIMP are written in Python language. First make sure the intended version of Python and the editor are installed. All work has been done with Python 2.7 which should be installed by default as part of the core code underlying the Ubuntu O.S. If using an alternate version of Python (like

Anaconda), then make sure all of the Python modules are installed there and the bash paths point to it.

Next, install the Python modules listed in Section 2. This can be done directly by downloading the .egg and setup.py files from PYPI (Python Package Index) at https://pypi.python.org/pypi, and then configuring them. The easier method of installation is to use an auto-installer such as pip. pip can be installed using the Ubuntu software databases using either the Ubuntu Software center or Synaptic.

3.1.2 DENOVO

DENOVO is a powerful discrete ordinates transport solver developed by and maintained by ORNL. [1] It is usually included in the SCALE package, however, DIMP was made using an older developer's version. The original DENOVO tarball is included with the DIMP software package.

The developer's version of the code can be tricky to install and is a lengthy process. Please refer Proctor's installation guide for further details. [8]

3.1.3 SCALE and MCNP

SCALE (Standardized Computer Analyses for Licensing Evaluation) [1] is a mass collection of government radiation physics codes distributed and controlled by the Radiation Safety Information Computational Center (RSICC). To gain permission to use SCALE, one may register and file requests for codes at https://rsicc.ornl.gov. Upon obtaining the SCALE package discs from RSICC, simply follow the installation directions included on the discs.

MCNP [2] is used for generating synthetic detector responses. This is useful to generate data for use as test synthetic cases. MCNP can be obtained from RSICC in the same manner as with SCALE.

3.2 Input/Output

This section is designed to guide the user in the creation of new case geometries. For the problem of interest, each input script that requires modification will be named and described. Finally, the resulting output results and format will be discussed.

3.2.1 Designing a New Case

First, the user should create a copy of the base case in the templates folder, and rename it according to the new case. Remove the master Python control scripts

"pmaster.py" and "inputs.py" from the new case folder and move them to the desired working directory ($\$Path\ to\ work\ directory\$/Case\_name$"). Open both files in the new case folder of the working directory to make the following changes.

pmaster
Update the first group of lines (12-21) to reflect the correct directory paths (i.e. change "$\$working\ directory\$/Case\_name$" and "$\$Path\ to\ DIMP\$$" to their true values). No other lines need to be changed in the master Python script. Other changes should only be made for debugging purposes if the user is sufficiently experienced with programming.

inputs
This file controls many options available to the user. Some are system dependent and will require system knowledge, while others are merely dependent on case data.

There are seven options. The first is merely a switch that allows the incorporation of experimental response data. If any experimental spectra are to be used then make sure the flag is set to False. Otherwise, set it to True to use purely synthetic responses from MCNP. The next two switches govern the number of computing processors DENOVO will run in parallel. The number of processors chosen depends on system resources available (e.g. 4,8,16,32.. CPU).

The next three options control which energy groups DENOVO will use. The first switch is the net total number of energy groups DENOVO will use. The second switch depicts the number available from the MAVRIC gip (cross-section file). The third switch informs DENOVO which energy group to start from in the MAVRIC gip file. Adjust to include the range of emission energies produced by the expected source material. Note: the MAVRIC file (local.mavrici) energy groups will have to be adjusted to match these groups. The final option controls whether or not to include the compton continua of the detector response spectra used in the source search. The default is False (peak response only). The algorithm for the inclusion of continua creates inconsistent results and is not recommended in the present version of DIMP.

In future versions, a consistent switch for eliminating cells containing only empty space is in development. This will decrease convergence times required by the Newton optimizerand enhance source location accuracy.

3.2.2 Local Geometry

Several files control the geometry simulated by DIMP. The three branches of code that require consistent source-detector geometric description include: MAVRIC, MCNP, and the DIMP source mapper. Each branch has a set of Python parsing/tool files that also need subsequent adjustment.

MAVRIC
Return to the new case directory of the templates folder in DIMP and navigate to the following file: "*inputs/mavric/local.mavric*". Edit the file to update the source geometry. Materials, object shapes and positions, and mesh dimensions for DENOVO adjoint transport calculations should be specified by the user. More detailed guidelines on correct MAVRIC programming may be found in the SCALE software manual. [1]

MCNP
Navigate to the mcnp folder in the inputs folder of the base case template and update the following files: *inputs/mcnp/bare/*2144.*inp*
inputs/mcnp/bare/parse_bare.py
*inputs/mcnp/shielded/*2144.*inp*
inputs/mcnp/shielded/parse_shielded.py
2144.inp is the MCNP5 input file for the detector configuration. The file in the shielded directory is designed for a collimated detector, and the one in the bare directory for a bare (unshielded) detector. Currently, both are set to generate synthetic responses, but a future update will allow the use of pure directional (collimated detectors). However, use of only an uncollimated detector is not recommended. Without directional detector responses, DIMP's capabilities are severely limited.

Input the new geometry and material cards along with the detector and (relative) source positions according to MCNP format [2]. In the case of an unknown source, just use a rough estimate of source position and strength. Also, be sure to match the detector flux tally bin edges with those of the actual detector after energy calibration.

Currently, the appropriate line corresponding to the peak (uncollided) fluxes in the flux tallies need to be selected in the parsing files (*parse_bare.pyorparse_shielded.py*). It is intended that an automatic way to choose these values from the MCNP mctal files be created to remove this step in the future.

DIMP Scripts
Navigate to the following file to update the mapping algorithm's internal geometry (*outputs/(eors)mapper/directional/bu*2144*_geometry.py*). Choose emapper for the experimental case or smapper for the synthetic. Note: this geometry can be left empty and only changed to match the mesh outer dimensions to purely plot the source characteristics. Inputing the local geometry in this script only puts it on the source map for reference, not calculation.

3.2.3 Detector Model and Responses

A one time calibration of the detector model must be performed based off of the detector specifications for the holdup measurement field detector. The base model that comes with DIMP is a 2x2" bare detector where collimation was added using a lead brick enclosure around the sides of the detector (creating a 2π detection window). Also, experimental detector response processing scripts must be adjusted based on the desired source of interest. The base setting is for U-235.

Detector Model
This section details the process to calculate the detector efficiency database (det-eff.npz). This database is needed for all experimental cases. In the detspecs folder there is a script called volume-averaged-eff.py. Simply edit the detector volume by adjusting the radius and height entries (lines 55 and 56). Also, input the number of peak energies of interest (line 99).

Next, navigate to the shielded and bare folders separately. Open each *det_peak_n.inp* file for the number of energy peaks desired and edit. Update the three tally energy bins to fit the user's detector and choose the peak energy of interest by updating the source card. Then run detbatch.sh. This will usually take quite some time as several groups of tallies must be run for each peak of interest. After detbatch.sh finishes, the file det-eff.npz will be produced containing all of the necessary detector peak effciencies. Move this file to $*path to DIMP*$/*templates/Case_name/inputs/exp_resp/*.
Note: this section of the code is still under construction and will be updated in future versions of DIMP.

Experimental Response Processing
Experimental processing has yet to be standardized, so as of now, the following scripts will need significant modification to fit the user's case.
inputs/exp_resp/measured_responses.py (choose which measurements to use from processed hdf5 database)
inputs/exp_resp/processdata/create_raw_table.py (organize measurements)
inputs/exp$_r$esp/processdata/process$_r$aw$_s$pectra.py (choose peaks to fit)

A more generalized processing procedure is in developement for this purpose.

3.2.4 Execution and Outputs

After setup of a new case has been concluded (make sure all changes were made to files in the desired case folder in the templates directory), navigate back to the case folder in the working directory. To execute DIMP run *pmaster.py* with the command "python pmaster.py." Be patient. The code usually take several hours to several days to run depending on the complexity of the case geometry and the capabilities of the computing platform. Several run messages will show in the terminal starting with MAVRIC details and ending with execution of the DIMP mapping and plotting subroutines.

The resulting output will be produced in the following path of the case directory: $\$Path\ to\ working\ directory\$/Case\_name/outputs/mapper/directional/figures/frames/$. In this file, colormap cross-sections of the source and room geometry will be displayed as well as a colormap of the resulting uncertainty for each peak energy group selected. Cross-sections will lie along the z-axis mesh gridlines. An example of such a source map cross-section is shown in Figure 2.

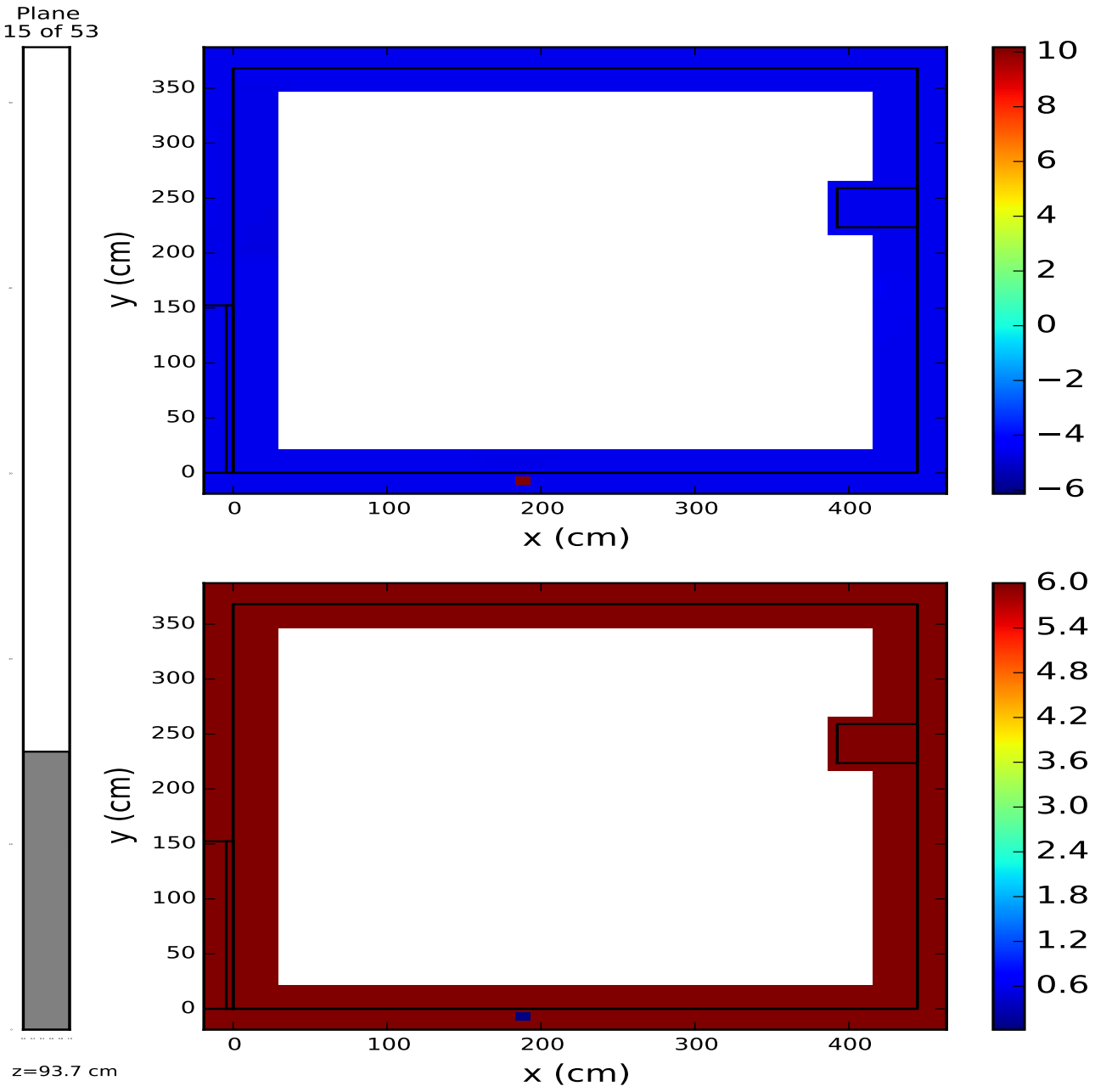

Figure 2: Example of a source map. Source is a Co-60 line source along the front wall. This is a reproduction of a case run in Ref. [5].

The white space in the center of the graphs is just a feature of excluding empty air space cells for this case where a radiation source is neither possible or permitted. The technique has been mentioned in Section 3.2.1 to be included in future versions of DIMP as an optional switch. As of now, it requires manual modification of cell choices in the mapping algorithm, which isn't recommended for beginning users.

The line source is mapped close to its true location, but only as a point. The source was fairly weak in this case and only the ends of the line source appeared in the source map. More consistent results are expected with stronger sources (over 3 μCi). The color scales are logarithmic (uncertainty is not relative). For more details consult Ref. [5].

References

[1] *Scale: A Comprehensive Modeling and Simulation Suite for Nuclear Safety Analysis and Design*, ORNL/TM-2005/39, Version 6.1, June 2011. Available from Radiation Safety Information Computational Center at Oak Ridge National Laboratory as CCC-785.

[2] X.-5. M. C. Team, "MCNP-A General Monte Carlo N-Particle Transport Code, Version 5," Los Alamos National Laboratory, Los Alamos, NM, 2003.

[3] J. M. Hykes and Y. Azmy, "Radiation Source Mapping with Bayesian Inverse Methods," *Nuclear Science and Engineering*, vol. 179, pp. 1-17, 2015.

[4] A. Berlizov, "Help: Gamma Spectrum Generator," 10 April 2008. [Online]. Available: `http://www.nucleonica.net/wiki/index.php/Help:Gamma_Spectrum_Generator`. [Accessed 11 April 2014].

[5] J. M. Hykes, "Radiation Source Mapping with Bayesian Inverse Methods," PhD Thesis, North Carolina State University, 2012.

[6] A. TARANTOLA, *Inverse Problem Theory and Methods for Model Parameter Estimation*, Society for Industrial and Applied Mathematics (2005).

[7] D. G. CACUCI and M. IONESCU-BUJOR. "Sensitivity and Uncertainty Analysis, Data Assimilation, and Predictive Best-Estimate Model Calibration," *Handbook of Nuclear Engineering*, D. G. CACUCI, Ed., Springer (2010).

[8] C. Proctor, "Denovo Installation Guide," Cyrus Proctor, 2015.

Denovo Installation Guide

Mined From MediaWiki Installation Guide

Cyrus Proctor © 2015

Contents

1 Installation Guide

Denovo requires several third-party dependencies in order to be properly compiled. This guide is one of many possible ways that configuration and installation may take place. This guide assumes the user is on a 64-bit Linux-based machine with a gcc-based compiler version >4.6. For this particular guide, the focus will be on installation for Ubuntu 12.04. Each of the dependencies should be installed in the order given below as some depend on each other. The user will need to know a couple of things before getting started. The line */path/to/install* or *</path/to/install>* will need to be replaced by the installation location for Denovo and friends. Generally, this would be system-wide at, say, */opt/simplex*. Or it could be locally for a single user, such as */home/user/simplex*. The other thing to know is the name of the host computer. This will be useful for designation of configuration files in the case of multiple computer installs. The user may find out the hostname by typing *echo $HOSTNAME* on the command line.

1.1 Third-Party Dependencies

- MPI[1]
- CMake[2]
- zlib[3]
- HDF[4]
- Silo[5]
- LAPACK[6]
- ATLAS[7]
- Python Modules[8]
- Trilinos[9]
- SCALE[10]

1 http://10.72.10.4/wiki/index.php/MPI
2 http://10.72.10.4/wiki/index.php/CMake
3 http://10.72.10.4/wiki/index.php/Zlib
4 http://10.72.10.4/wiki/index.php/HDF
5 http://10.72.10.4/wiki/index.php/Silo
6 http://10.72.10.4/wiki/index.php/LAPACK
7 http://10.72.10.4/wiki/index.php/ATLAS
8 http://10.72.10.4/wiki/index.php/Python_Modules
9 http://10.72.10.4/wiki/index.php/Trilinos
10 http://10.72.10.4/wiki/index.php/SCALE

1.2 Denovo Installation

A fixed source version of Denovo is available via the release version of SCALE. A development version circa summer 2012 has been passed down which has the capability for eigenvalue solves as well as inhomogeneous adjoint sensitivity analysis. The difference in installation is only one flag which will be pointed out below. When running on Ubuntu-based systems there is also an extra flag to add. This writeup will assume a development version of Denovo is being installed be default.

- Obtain a Denovo tarball (or potentially a git repository)
- *cd /path/to/install*
- *mkdir denovo*
- *cd denovo*
- *mv /path/to/tarball/denovo_tarball.tar.gz /path/to/install/denovo*
- *tar xvfz denovo_tarball.tar.gz*
- *cd denovo*
- *./denovo_config*
- Assuming nemesis is contained within the directory /path/to/install/denovo/denovo/nemesis and the user is located at /path/to/install/denovo/denovo we need to add four symbolic links
- *ln -s nemesis/config .*
- *ln -s nemesis/tools .*
- *cd src*
- *ln -s ../nemesis/src/harness .*
- *ln -s ../nemesis/src/comm .*
- *cd /path/to/install/denovo*
- *mkdir build*
- *cd build*
- *vim <hostname>_configure* add/update with the following/save/quit

```
#!/bin/bash

LDFLAGS=-L/usr/lib64
LIBS=-lgfortran
F90=gfortran

CFLAGS=
CXXFLAGS=
F90FLAGS=

/path/to/install/denovo/denovo/configure \
--prefix=/path/to/install/denovo/install \
--enable-shared \
--enable-python \
--enable-pykba \
--enable-mpi-compilers \
--without-superlu \
--without-brlcad \
--without-metis \
--with-trilinos-dir=/path/to/install/trilinos/install \
--with-silo-dir=/path/to/install/silo/install \
--with-hdf5-dir=/path/to/install/hdf5/install \
--with-lapack=atlas \
--with-lapack-dir=/path/to/install/atlas/install \
```

```
--with-opt=3 \
--with-dbc=0 -C
```

- This installs a release version of the code with optimization turned on and design by contract turned off. To install a debug version, change the --with-opt flag to 0 and the --with-dbc to 7.
- If development version, add flag *--enable-suq*
- If on Ubuntu-based systems, add flag *--with-ldflags="-Xlinker --no-as-needed"*
- *chmod +x <hostname>_configure*
- *./<hostname>_configure*
- Thoroughly check configuration logs for errors or problems
- *make*
- Edit <hostname>_configure and remove the flag *--enable-shared*. Save.
- *./<hostname>_configure*
- *make*
- This sequence allows for the shared and static versions of the Denovo library to built.
- Open ~/.bashrc and add

```
PATH=/path/to/install/denovo/install/bin:$PATH
export PATH

LD_LIBRARY_PATH=/path/to/install/denovo/install/lib:$LD_LIBRARY_PATH
export LD_LIBRARY_PATH
```

Note: You may need to install aclocal and automake via *apt-get install autotools-dev* and *apt-get install automake*, swig via *apt-get install swig*, graphviz via *apt-get install graphviz* and install doxygen via *apt-get install doxygen*.

2 MPI

MPICH Download[1]

- Download the mpich-3.0.4 stable release as a tar.gz file.
- *cd /path/to/install*
- *mkdir mpich*
- *cd mpich*
- *mv /path/to/download/mpich-3.0.4.tar.gz /path/to/install/mpich*
- *tar xvfz mpich-3.0.4.tar.gz*
- *mkdir build*
- *cd build*
- *vim <hostname>_gcc_configure* add/update with the following/save/quit

```
#!/bin/bash

CFLAGS=-fPIC
CXXFLAGS=-fPIC
FC=gfortran
F77=gfortran
/path/to/install/mpich/mpich-3.0.4/configure  \
--prefix=/path/to/install/mpich/install/gcc \
--enable-fc \
--enable-cxx \
--enable-shared \
--enable-sharedlibs=gcc \
2>&1 | tee config_gcc_hostname.log
```

- *chmod +x <hostname>_gcc_configure*
- *./<hostname_gcc_configure*
- Thoroughly check configuration logs for errors or problems
- *make*
- *make install*
- Open ~/.bashrc and add

```
PATH=/path/to/install/mpich/install/gcc/bin:$PATH
export PATH

LD_LIBRARY_PATH=/path/to/install/mpich/install/gcc/lib:$LD_LIBRARY_PATH
export LD_LIBRARY_PATH
```

1 http://www.mpich.org/downloads

3 CMake

CMake Download[1] Check to see if CMake is already available on your system with *which cmake* If your system does not automatically come with CMake, check with your distribution repository. For Debian/Unbuntu-based systems use: *sudo apt-get install cmake* The version should be greater than 2.8. The above link will provide a download for a manual source install which hopefully is unnecessary but provided nonetheless.

1 `http://www.cmake.org/cmake/resources/software.html`

4 Zlib

zlib Download[1]

- Download version 1.2.8 or greater as a tar.gz file
- *cd /path/to/install*
- *mkdir zlib*
- *cd zlib*
- *mv /path/to/download/zlib-1.2.8.tar.gz /path/to/install/zlib*
- *tar xvfz zlib-1.2.8.tar.gz*
- *mkdir build*
- *cd build*
- *vim <hostname>_configure* add/update with the following/save/quit

```
#!/bin/bash

cmake \
-D CMAKE_INSTALL_PREFIX:PATH=/path/to/install/zlib/install \
-D BUILD_SHARED_LIBS:BOOL=ON \
$*
```

- *chmod +x <hostname>_configure*
- *./<hostname>_configure ../zlib-1.2.8*
- Thoroughly check configuration logs for errors or problems
- *make*
- *make install*
- *make test*

1 http://www.zlib.net

5 HDF

HDF Download[1]

- Download HDF5 version 1.8.9 as a tar.gz file

Code Rot Notice: Most likely must stay below 1.8.10 to maintain compatibility.

- *cd /path/to/install*
- *mkdir hdf5*
- *cd hdf5*
- *mv /path/to/download/hdf5-1.8.9.tar.gz /path/to/install/hdf5*
- *tar xvfz hdf5-1.8.9.tar.gz*
- *mkdir build*
- *cd build*
- *vim <hostname>_configure* add/update with the following/save/quit

```
#!/bin/bash

CFLAGS=$CFLAGS -fPIC
CC=mpicc
CXX=mpicxx
FC=mpif90

/path/to/install/hdf5/hdf5-1.8.9/configure \
--prefix=/path/to/install/hdf5/install \
--w
ith-zlib=/path/to/install/zlib/install/include,/path/to/install/zlib/install/lib
 \
--enable-parallel \
--enable-shared \
--enable-fortran
```

- *chmod +x <hostname>_configure*
- *./<hostname>_configure*
- Thoroughly check configuration logs for errors or problems
- *make*
- *make install*
- *cd /path/to/install/hdf5/install/include*
- *ln -s /path/to/install/mpich/install/gcc/include/mpi.h*
- *ln -s /path/to/install/mpich/install/gcc/include/mpio.h*

1 http://www.hdfgroup.org

6 Silo

SILO Download[1]

- Download version 4.9.1 or greater as a tar.gz file
- *cd /path/to/install*
- *mkdir silo*
- *cd silo*
- *mv /path/to/download/silo-4.9.1.tar.gz /path/to/install/silo*
- *tar xvfz silo-4.9.1.tar.gz*
- *mkdir build*
- *cd build*
- *vim <hostname>_configure* add/update with the following/save/quit

```
#!/bin/bash

F77=mpif77
FC=mpif90
CC=mpicc
CXX=mpicxx
CFLAGS=-fPIC
CXXFLAGS=-fPIC
LDFLAGS=-L/usr/lib64
LIBS=-lstdc++


/path/to/install/silo/silo-4.9.1/configure \
--prefix=/path/to/install/silo/install \
--w
ith-hdf5=/path/to/install/hdf5/install/include,/path/to/install/hdf5/install/lib
 \
--w
ith-zlib=/path/to/install/zlib/install/include,/path/to/install/zlib/install/lib
 \
--disable-silex \
--without-qt \
--with-readline \
--enable-pythonmodule \
--with-gnu-ld
```

- *chmod +x <hostname>_configure*
- *./<hostname>_configure*
- Thoroughly check configuration logs for errors or problems
- *make*
- *make install*
- Open ~/.bashrc and add

```
PATH=/path/to/install/silo/install/bin:$PATH
```

1 https://wci.llnl.gov/codes/silo

```
export PATH

LD_LIBRARY_PATH=/path/to/install/silo/install/lib:$LD_LIBRARY_PATH
export LD_LIBRARY_PATH
```

Note: You may need to install the development version of Python with *sudo apt-get install python-dev*

7 LAPACK

LAPACK Download[1]

- Download version 3.5.0 or greater as a .tgz file
- *cd /path/to/install*
- *mkdir lapack*
- *cd lapack*
- *mv /path/to/download/lapack-3.5.0 /path/to/install/lapack*
- *tar xvfz lapack-3.5.0.tgz*
- *mkdir build*
- *cd build*
- *vim <hostname>_configure* add/update with the following/save/quit

```
#!/bin/bash

cmake \
-D CMAKE_INSTALL_PREFIX:PATH=/path/to/install/lapack/install \
-D CMAKE_Fortran_COMPILER:PATH=/usr/bin/gfortran \
$*
```

- *chmod +x <hostname>_configure*
- *./<hostname>_configure ../lapack-3.5.0*
- Thoroughly check configuration logs for errors or problems
- *make*
- *make install*

1 http://www.netlib.org/lapack

8 ATLAS

ATLAS Download[1]

- Download version 3.10.1 or greater as a tar.bz2 file
- *cd /path/to/install*
- *mkdir atlas*
- *cd atlas*
- *mv /path/to/download/atlas3.10.1.tar.bz2 /path/to/install/atlas*
- *tar xvfj atlas3.10.1.tar.bz2*
- *mv ATLAS atlas-3.10.1*
- *mkdir build*
- *cd build*
- *vim <hostname>_configure* add/update with the following/save/quit
- Note: CPU Throttling must be disabled. For GUI Ubuntu and sudo permissions, see here[2]. For command-line, with sudo rights, use *sudo indicator-cpufreq* and set to performance. This may also be set in the BIOS. And it may also be set by: *sudo apt-get install cpufrequtils; sudo /usr/bin/cpufreq-set -g performance*

```
#!/bin/bash

/path/to/install/atlas/atlas-3.10.1/configure \
--prefix=/path/to/install/atlas/install \
--shared \
-Fa alg -fPIC \
--with-netlib-lapack-tarfile=/path/to/install/lapack/lapack-3.5.0.tgz \
-D c \
-DPentiumCPS=CPU-Frequency in Mhz \
-b 64
```

- Note: You may find CPU-Frequency in Ubuntu with the command *lscpu | grep "MHz"*
- *chmod +x <hostname>_configure*
- *./<hostname>_configure*
- Thoroughly check configuration logs for errors or problems
- *make build*
- *make check*
- *make ptcheck*
- *make time*
- *make install*
- Open ~/.bashrc and add

```
LD_LIBRARY_PATH=/path/to/install/atlas/install/lib:$LD_LIBRARY_PATH
export LD_LIBRARY_PATH
```

1 http://math-atlas.sourceforge.net
2 http://askubuntu.com/questions/142688/cpu-frequency-scaling-for-12-04

9 Python Modules

NumPy and SciPy Downloads[1] There are numerous ways to install NumPy and SciPy including cloud repositories and with the help of pip. With that mentioned, the seemingly most universal and reliable way has been via source build. Plus, one can specify the proper locally tuned BLAS library to use for the most efficient computations.

9.1 Numpy

- Download version 1.7.2 or greater as a tar.gz file
- *cd /path/to/install*
- *mkdir python*
- *cd python*
- *mv /path/to/download/numpy-1.7.2.tar.gz /path/to/install/python*
- *tar xvfz numpy-1.7.2.tar.gz*
- *mkdir build*
- *cd build*
- *vim <hostname>_numpy_configure* add/update with the following/save/quit

```
#!/bin/bash

export BLAS=/path/to/install/atlas/install/lib/libtatlas.so
export LAPACK=/path/to/install/atlas/install/lib/libtatlas.so
export ATLAS=/path/to/install/atlas/install/lib/libtatlas.so

python /path/to/install/python/numpy-1.7.2/setup.py build
python /path/to/install/python/numpy-1.7.2/setup.py install
```

- *chmod +x <hostname>_numpy_configure*
- *./<hostname>_numpy_configure*
- Thoroughly check configuration logs for errors or problems

9.2 SciPy

- Download version 0.13.3 or greater as a tar.gz file
- *cd /path/to/install/python*
- *mv /path/to/download/scipy-0.13.3.tar.gz /path/to/install/python*
- *tar xvfz scipy-0.13.3.tar.gz*
- *cd build*
- *vim <hostname>_scipy_configure* add/update with the following/save/quit

1 http://www.scipy.org/scipylib/download.html

```
#!/bin/bash

#
# Run in source directory!
#

export BLAS=/path/to/install/atlas/install/lib/libtatlas.so
export LAPACK=/path/to/install/atlas/install/lib/libtatlas.so
export ATLAS=/path/to/install/atlas/install/lib/libtatlas.so

python /path/to/install/python/scipy-0.13.3/setup.py build
python /path/to/install/python/scipy-0.13.3/setup.py install
```

- *chmod +x <hostname>_scipy_configure*
- *cd /path/to/install/python/scipy-0.13.3*
- *../build/<hostname>_scipy_configure*
- Thoroughly check configuration logs for errors or problems

10 Trilinos

Trilinos Download[1]

10.1 Code Rot Notice

The version of Denovo that is being used for compilation is a version circa June 2012. This was the last point in which access to the git repository server angmar (Tom Evan's box in his office) was available. As a result, this version of Denovo requires a version of Trilinos that is also of this time period since both are working codes. Be sure to download version no later than 10.10.1. At some point soon after this release, there was a restructuring and splitting of libraries that Denovo expects under one static library. The options are to manually repackage the split libraries together using gcc (not tested) or to use an older version of Trilinos. Next, as a result of choosing an older version of Trilinos, compilation errors can arise using a gcc compiler version $>$ 4.6.3. A preprocessor directive in a particular file will be accepted using a version of gcc $<$ 4.6.3 and an error thrown for versions $>$ 4.6.3 (I've only tried 4.6.3 and 4.8.2 so it's an assumption). To check your version of gcc, go to the command line and type *gcc -v*. Adapt the instructions below based on your version number.

10.2 Installation

- Download version 10.10.1 or LESS as a tar.gz file
- *cd /path/to/install*
- *mkdir trilinos*
- *cd trilinos*
- *mv /path/to/download/trilinos-10.10.1.tar.gx /path/to/install/trilinos*
- *tar xvfz trilinos-10.10.1-Source.tar.gz*
- *mkdir build*
- *cd build*
- *vim <hostname>_configure* add/update with the following/save/quit

```
#!/bin/bash

EXTRA_ARGS=$@

cmake \
-D CMAKE_INSTALL_PREFIX:PATH=/path/to/install/trilinos/install \
-D CMAKE_BUILD_TYPE:STRING=RELEASE \
-D Trilinos_ENABLE_TESTS:BOOL=OFF \
```

1 http://trilinos.sandia.gov

```
-D Trilinos_ENABLE_Amesos:BOOL=ON \
-D Trilinos_ENABLE_Anasazi:BOOL=ON \
-D Trilinos_ENABLE_AztecOO:BOOL=ON \
-D Trilinos_ENABLE_EpetraExt:BOOL=ON \
-D Trilinos_ENABLE_Ifpack:BOOL=ON \
-D Trilinos_ENABLE_ML:BOOL=ON \
-D Trilinos_ENABLE_NOX:BOOL=ON \
-D BUILD_SHARED_LIBS:BOOL=ON \
-D CMAKE_C_FLAGS:STRING=-fPIC \
-D CMAKE_CXX_FLAGS:STRING=-fPIC \
-D CMAKE_Fortran_FLAGS:STRING=-fPIC \
-D TPL_ENABLE_MPI:BOOL=ON \
-D MPI_INCLUDE_DIRS:PATH=/path/to/install/mpich/install/gcc/include \
-D MPI_LIBRARY_DIRS:PATH=/path/to/install/mpich/install/gcc/lib \
-D TPL_ENABLE_BLAS:BOOL=ON \
-D BLAS_LIBRARY_NAMES:STRING=tatlas \
-D BLAS_INCLUDE_DIRS:PATH=/path/to/install/atlas/install/include \
-D BLAS_LIBRARY_DIRS:PATH=/path/to/install/atlas/install/lib \
-D Trilinos_EXTRA_LINK_FLAGS:STRING=-lgfortran \
-D TPL_ENABLE_LAPACK:BOOL=ON \
-D LAPACK_LIBRARY_NAMES:STRING=tatlas \
-D LAPACK_LIBRARY_DIRS:PATH=/path/to/install/atlas/install/lib \
$EXTRA_ARGS \
/path/to/install/trilinos/trilinos-10.10.1-Source/
```

- *chmod +x <hostname>_ configure*
- *./<hostname>_ configure ../trilinos-10.10.1-Source*
- Thoroughly check configuration logs for errors or problems
- **If gcc version > 4.6.3**
  - *vim </path/to/install>/trilinos/trilinos-10.10.1-Source/packages/zoltan/src/zz/murmur3.c*
  - edit line 15 from

```
#define FORCE_INLINE __attribute__((always_inline))
```

to

```
#define FORCE_INLINE inline __attribute__((always_inline))
```

- *make*
- *make install*
- Open ~/.bashrc and add

```
LD_LIBRARY_PATH=/path/to/install/trilinos/install/lib:$LD_LIBRARY_PATH
export LD_LIBRARY_PATH
```

11 SCALE

SCALE Registration[1] SCALE is released by ORNL's RSICC. Each user must register and request a DVD pack to be mailed to them. Different versions of SCALE will produce varying formats of Denovo xkba input generated via MAVRIC. The release version allows for ascii versions of xkba input while the development version (circa summer 2012) allows for binary xkba input. Follow the installation instructions that come with the DVD's. For reference, install to /path/to/install/scale6.1. SCALE will be used to process cross section information for use with Denovo.

1 http://scale.ornl.gov/index.shtml

4.2. Task B: Analyze DIMP in the Context of a Paradigm Inverse Source Determination Problem

This task was modified from its original intent based on advice from holdup experts at ORNL. The University of South Carolina was responsible for completing this task.

The accomplishment of this task was reported in: Dan G. Cacuci, *Comparative Analysis of Methods for Inverse Problems with Applications to Radiation Transport*, University of South Carolina, December 30, 2014. This document is replicated on the following pages.

COMPARATIVE ANALYSIS OF METHODS FOR INVERSE PROBLEMS WITH APPLICATIONS TO RADIATION TRANSPORT

Dan G. Cacuci
December 30, 2014

ABSTRACT

The assessment of material "held-up" in equipment, pipes, and ducts in a plant that processes nuclear materials must be inferred from measured radiation fields, primarily gamma and less frequently neutrons. Thus, the "holdup problem" falls under the category of "source identification problem". Such "inverse problems" are computationally unstable, so a naïve solution will be overcome by round-off errors or noise in the data, which can amplify to a degree that renders the computed solution useless.

This work presents the most popular methods for addressing inverse problems, starting with the Levenberg (1944)-Marquardt (1963) method, which is possibly the easiest to apply but also the least sophisticated. Tichonov's (1963) method, discussed next, subsumes elements of the LM-method, but has an additional term that controls the solution's smoothness. When implemented correctly, Tichonov's method provides convexity and compactness in the problem. However, even when done correctly, Tichonov's method actually changes the original problem into new ones (depending on the value of the parameter λ^2), and solutions to the new problems may not be close to those of original problem. Moreover, because of the discretionary user-parameter λ^2, it is not possible to compute quantitatively the error between the true, but actually unknown solution and the "regularized" solution.

The more modern method use Bayes' theorem to combine all of the available information to construct a posterior distribution for solving the inverse problem in a probabilistic sense, providing a range of possible "outcomes." The method presented Tarantola's book (2005) is also reviewed briefly, and shown to not only comprise Tichonov's, but to eliminate the appearance of Tichonov's discretionary user-parameter λ^2 my replacing it with a functional that contains the actual covariance matrices for modeling the respective uncertainties. The most recent and comprehensive method, which unifies both the forward and the inverse problems in the presence of computational and experimental uncertainties, is Cacuci's method (2014) for "*predictive modeling of coupled multi-physics systems*", which is also compared to the older methods.

Cacuci's (2014) method treats efficiently and explicitly coupled multi-physics systems in the presence of computational and experimental uncertainties. When reduced to a single multi-physics system, Cacuci's method is shown to comprise the Levenberg-Marquardt,

Tichonov, and Tarantola methods as particular cases, even. Cacuci's methodology (2014) uses the maximum entropy principle to construct an optimal approximation of the unknown a priori distribution for the a priori known mean values and covariances characterizing the parameters and responses for both multi-physics models. This approximate a priori distribution is combined using Bayes' theorem with the "likelihood" provided by the two multi-physics simulation models. Subsequently, the posterior distribution is evaluated using the saddle-point method to obtain analytical expressions for the optimally predicted values for the parameters and responses of both multi-physics models, along with corresponding reduced uncertainties for both the model parameters and responses. This methodology enables predictive modeling for coupled multi-physics systems, taking fully into account the coupling terms between the systems but using only the computational resources that would be needed to perform predictive modeling on each system separately.

The comparative analysis presented in this work highlights the following important conclusions:

(i) Cacuci's method (2014) calibrates simultaneously all of the model parameters as well as the model responses. In contradistinction, the other methods calibrate only the model responses. Therefore, even for a single model, Cacuci's method yields additional results by comparison to all of the other methods currently available.

(ii) Cacuci's method (2014) takes into account correlations between model parameters and model responses. No other method has this capability. Importantly, the predicted responses and parameters will become correlated, even if they were uncorrelated initially.

Noteworthy, Cacuci's (2014) methodology for coupled systems is constructed such that the systems can be considered sequentially rather than simultaneously, while preserving exactly the same results as if the systems were treated simultaneously. Consequently, very large coupled multi-physics systems, which could perhaps exceed the available computational resources if treated simultaneously, can be treated with Cacuci's (2014) methodology sequentially and without any loss of generality or information, requiring just the resources that would be needed if the systems were treated sequentially. This feature enables the treatment of very large systems which would currently exceed the computational resources available if treated with conventional data assimilation procedures. In particular, Cacuci's (2014) methodology would be ideally suited for performing large-scale coupled neutron-gamma inverse transport problems, in which the neutron and, respectively, the gamma transport computations would be performed using distinct computational tools.

1. INTRODUCTION

As is well known, the particle and/or radiation transport equation strives to describe all possible interactions of particles within the host medium while taking into account the medium's detailed material properties and geometry. One can distinguish between two fundamental types of problems in the mathematical description of the transport of particles through the host medium. The most common type are the *direct problems*, in which one is given the composition and geometry of the medium, as well as the location and magnitude of all sources of particles, and asked to determine the distribution of particles in the medium. *Thus, the "direct problem" solves the "parameter-to-output" mapping that describes the "cause-to-effect" relationship in the particle transport process.* The second, and far more difficult type of problems are the *inverse problems*, in which one is given (usually just partially) the particle distribution and is asked to determine the characteristics of the host medium or characteristics of the sources that have generated the respective particles. In general, two problems are called *inverses* of one another if the formulation of each involves all or part of the solution of the other. In particular, "measurement problems" are "inverse" to the direct problem in that they seek to determine (from measurements) the properties of the host medium (e.g., composition, geometry, including internal interfaces), or the properties of the source (e.g., strength, location, direction), and/or the size of the medium on its boundaries. Some authors further group such inverse problems into "invasive", when the interior particle distribution is accessible for measurements, as opposed to "non-invasive" ones, in which only particle distributions on the boundaries of (or exterior to) the medium can be measured. Such inverse problems are encountered in fields as diverse as astrophysics (in which one measures the intensity and spectral distribution of light in order to infer properties of starts), nuclear medicine (where radioisotopes are injected into patients and the radiation emitted is used in diagnostics to reconstruct body properties, e.g. tumors), non-destructive fault detection in materials, underground (oil, water) logging, and detection of sensitive materials. The "holdup problem" also falls under the category of "source identification problem". Recall that this problem arises because special nuclear (fissile) material (SNM) is "held-up" over time in plant equipment (e.g., pipes, ducts). Since it is not possible to measure directly the holdup quantity and location, these must be inferred from measured radiation fields, primarily gamma and less frequently neutrons.

The existence of a solution for an inverse problem is in most cases secured by defining the data space to be the set of solutions to the direct problem. This approach may fail if the data is incomplete, perturbed or noisy. Furthermore, problems involving differential operators are notoriously ill-posed, because the differentiation operator is not continuous with respect to any physically meaningful observation topology. If the uniqueness of a solution cannot de secured from the given data, additional data and/or a priori knowledge about the solution need to be used to further restrict the set of admissible solutions. In particular, stability of the solution is the most difficult to ensure and verify. If an inverse problem fails to be stable, then small round-off errors or noise in the data will amplify to a degree that renders a computed solution useless.

The historically older methods used for solving approximately an ill-posed problem were called *regularization procedures*. These procedures attempted to manipulate explicitly the direct (forward) equation in conjunction with measurements in order to estimate explicitly the unknown source and/or other unknown characteristics of the medium. On the other hand, the more modern "implicit" methods combine measurements with repeated solutions of the direct problem obtained with different values of the unknowns, iterating until an a priori selected functional, usually representing a user-defined "goodness of fit" between measurements and direct computations, is reduced to a value deemed to be "acceptable" by the user. The fundamental characteristics of inverse problems (namely that they are ill-posed and/or ill-conditioned, unstable to errors in the transport model parameters and the experimental measurements) have increasingly inclined the balance towards the development of implicit methods, which allow, to various degrees, the inclusion of the effects of such errors in the "inverse problem" algorithms.

This work is organized as follows: Section 2 presents a new methodology for *predictive modeling of coupled multi-physics* systems, which was recently conceived by Cacuci (2014), extending the predictive modeling methodology of Cacuci and Ionescu-Bujor (2010) from a single multi-physics system to two or more coupled multi-physics systems. Noteworthy, Cacuci's methodology enables coupled systems to be treated sequentially rather than simultaneously, while preserving exactly the same results as if the systems had been treated simultaneously, thus requiring just the resources that would be needed if the systems were treated simultaneously. Cacuci's methodology (2014) uses the maximum entropy principle to construct an optimal approximation of the unknown a priori distribution for the a priori known mean values and uncertainties characterizing the parameters and responses for both multi-physics models. This approximate a priori distribution is subsequently combined using Bayes' theorem with the "likelihood" provided by the multi-physics computational models. Finally, the posterior distribution is evaluated using the saddle-point method to obtain analytical expressions for the optimally predicted values for the parameters and responses of both multi-physics models, along with corresponding reduced uncertainties.

Section 3 reviews the previous methods for solving inverse problems with uncertain data, in chronological order of their appearance. Section 3.1 reviews the Levenberg (1944) - Marquard (1963) method. This method was used by Bledsoe et al (2011) to solve several inverse transport problems by minimizing an "a priori" chosen chi-square-type functional to estimate the "differences between measured and computed quantities of interest". Section 3.2 reviews Tichonov's method (1963), which takes into account not only the "misfits" between measurements and computations, but also takes into account the solution's smoothness, albeit at the expense of introducing an arbitrary parameter ("tunable" by the user). Section 3.3 reviews the so-called "Bayesian least squares methods", noting that all of the more recent methods use Bayes theorem in some form to deduce the posterior distribution of interest, and then further noting that, if the distributions are Gaussian, the evaluation of the posterior amounts to solving a least-squares problem. The most sophisticated of these is Tarantola's (2005) "functional inverse least-squares" (FILS-T) method, which replaces Tichonov's arbitrary parameter λ^2 by an expressions that contains uncertainties in the form of a priori parameter covariances. In addition, the FILS-T

method provides a "goodness of fit" metric, χ^2_{FILS-T}, which no other method, except for Cacuci's method, provides. The capabilities, advantages and disadvantages of these methods are discussed in Section 4. Appendix A provides the mathematical details of Cacuci's method, while Appendix B summarizes the salient equations underlying the transport of neutrons and gamma radiation underlying the modeling of hold-up problems.

2. CACUCI' S (2014) METHODOLOGY FOR PREDICTIVE MODELING OF DIRECT AND INVERSE PROBLEMS IN THE PRESENCE OF EXPERIMENTAL AND COMPUTATIONAL ERRORS

This Section presents the "predictive modeling" methodology developed by Cacuci (2014), which encompasses the concepts of "data assimilation", "model calibration", and "inverse problems" into a unifying conceptual and mathematical framework; this methodology yields best estimate predictions, with reduced predicted uncertainties. Cacuci (2014) considers two coupled computational models, called henceforth "*Model A*" and "*Model B,*" where each model represents a large-scale multi-physics system; furthermore, experimentally measured responses are available for both models, so that the ultimate goal is to perform *predictive modeling* for the coupled models. Cacuci's methodology is particularly useful when the number of computed and measured responses, as well as the number of parameters, are very large, since it takes fully into account the coupling terms between the systems but uses only the computational resources that would be needed to perform predictive modeling on each system separately.

2.1 *A Priori Information for the Two Multi-Physics Models: Mathematical Description*

Consider a multi-physics model, henceforth called "*Model A*" comprising N_α system (model) parameters α_n; *Model A* is used to compute results, henceforth called *responses*, which can also be measured experimentally. Consider now a second physical system, henceforth called "*Model B,*" comprising N_β system (model) parameters β_m, and which is also used to compute *responses* that can be measured experimentally. *Model A* and *Model B* are considered to be coupled. In reactor analysis and design, for example, *Model A* may comprise the neutron transport and depletion equations which are coupled to *Model B* computing the thermal-hydraulics conservation (mass, momentum, energy) equations. *For*

hold-up problems, Model A may be a code that simulates the transport of neutrons to neutron detectors, while Model B could simulate the transport of gamma-radiation to gamma detectors.

Consider next that there are N_r experimentally measured responses r_i associated mostly, but not necessarily exclusively, with *Model A*. Furthermore, consider also that there are N_q experimentally measured responses q_j associated mostly, but not necessarily exclusively, with *Model B*. For example, measurement of reaction rates and power (or flux) distributions could be considered to be responses of type r_i, while measurements of flow rates and temperature distributions could be considered responses of type q_j. In the same spirit, cross sections can be considered to be model parameters of type α_n, while heat transfer correlations can be considered model parameters of type β_m. Parameters modeling the geometry of the system, for example, could be considered to belong to either type of model parameters (i.e., either α_n or β_m), since they affect both the neutron transport equation and the thermal-hydraulics conservation equations.

In practice, the values of the parameters α_n and β_m are determined experimentally. Therefore, these parameters cannot be known exactly, but can be considered to behave stochastically, obeying some probability distribution function which-for large-scale systems, as customarily encountered in practice-is unknown. Such stochastic quantities will be called *variates* in this work; thus, the parameters α_n and β_m, as well as the measured responses r_i and q_j are variates. To simplify the mathematical derivations to follow in this section, the model parameters α_n will be considered to constitute the components of the (column) vector $\boldsymbol{\alpha}$ of, defined as

$$\boldsymbol{\alpha} = \left\{ \alpha_n \,|\, n = 1, \ldots, N_\alpha \right\} , \tag{2.1}$$

while the model parameters β_m will be considered to constitute the components of the (column) vector $\boldsymbol{\beta}$ defined as

$$\boldsymbol{\beta} = \left\{ \beta_m \mid m = 1, \ldots, N_\beta \right\} . \tag{2.2}$$

By convention, all of the vectors considered in this work (e.g., $\boldsymbol{\alpha}$ and $\boldsymbol{\beta}$) are column vectors; (e.g., $\boldsymbol{\alpha}^\dagger$ and $\boldsymbol{\beta}^\dagger$) are row vectors; a dagger ($\dagger$) will be used to denote "transposition." Similarly, the N_r experimentally measured responses r_i will be considered to be components of the column vector

$$\mathbf{r} = \left\{ r_i \,|\, i = 1, \ldots, N_r \right\} , \tag{2.3}$$

while the N_q experimentally measured responses q_j will be considered to be components of the column vector

$$\mathbf{q} = \left\{ q_j \mid j = 1, \ldots, N_q \right\}. \tag{2.4}$$

Most generally, the parameters α_n and β_m, as well as the responses r_i and q_j can be considered to obey some *a priori probability distribution function* $P(\boldsymbol{\alpha}, \boldsymbol{\beta}, \mathbf{r}, \mathbf{q})$. For large-scale systems, as customarily encountered in practice, the probability distribution $P(\boldsymbol{\alpha}, \boldsymbol{\beta}, \mathbf{r}, \mathbf{q})$ cannot possibly be known. The information usually available in practice comprises the mean values of the model parameters and responses together with the corresponding uncertainties (standard deviations and, occasionally, correlations) computed about the respective mean values. For notational simplicity, we will use angular brackets, $\langle f \rangle$, to denote the integral of the quantity $f(\boldsymbol{\alpha}, \boldsymbol{\beta}, \mathbf{r}, \mathbf{q})$ over the joint probability distribution $P(\boldsymbol{\alpha}, \boldsymbol{\beta}, \mathbf{r}, \mathbf{q})$, i.e.,

$$\langle f \rangle \equiv \int f(\boldsymbol{\alpha}, \boldsymbol{\beta}, \mathbf{r}, \mathbf{q}) P(\boldsymbol{\alpha}, \boldsymbol{\beta}, \mathbf{r}, \mathbf{q}) d\boldsymbol{\alpha} d\boldsymbol{\beta} d\mathbf{r} d\mathbf{q}. \tag{2.5}$$

Using the above convention, we will denote the mean values of the model parameters α_n as $\alpha_n^0 \equiv \langle \alpha_n \rangle$, and will consider them to constitute the components of the vector $\boldsymbol{\alpha}^0$ defined as

$$\boldsymbol{\alpha}^0 = \left\{ \alpha_n^0 \mid n = 1, \ldots, N_\alpha \right\}. \tag{2.6}$$

Similarly, the mean values of the parameters β_n are considered to be known, and will be denoted as $\beta_n^0 \equiv \langle \beta_n \rangle$. These mean values are considered to be the components of the vector $\boldsymbol{\beta}^0$ defined as

$$\boldsymbol{\beta}^0 = \left\{ \beta_n^0 \mid n = 1, \ldots, N_\beta \right\}. \tag{2.7}$$

We also consider that the parameters' second-order central moments, namely the standard deviations and correlations, are known. For the parameters α_n, the second-order central moments are the components of covariance matrices $\mathbf{C}_{\alpha\alpha}^{(N_\alpha \times N_\alpha)}$ defined as

$$\mathbf{C}_{\alpha\alpha}^{(N_\alpha \times N_\alpha)} \equiv \left[\operatorname{cov}(\alpha_i, \alpha_j) \right]_{N_\alpha \times N_\alpha} \equiv \left\langle \left(\alpha_i - \alpha_i^0 \right) \left(\alpha_j - \alpha_j^0 \right) \right\rangle_{N_\alpha \times N_\alpha} ; \quad i, j = 1, \ldots, N_\alpha, \tag{2.8}$$

while the second-order central moments (i.e., the standard deviations and correlations) for the parameters β_m form covariance matrices $\mathbf{C}_{\beta\beta}^{(N_\beta \times N_\beta)}$ defined as

$$\mathbf{C}_{\beta\beta}^{(N_\beta \times N_\beta)} \equiv \left[\mathrm{cov}\left(\beta_i, \beta_j\right) \right]_{N_\beta \times N_\beta} \equiv \left\langle \left(\beta_i - \beta_i^0\right)\left(\beta_j - \beta_j^0\right) \right\rangle_{N_\beta \times N_\beta} ; \;\; i, j = 1, \ldots, N_\beta . \tag{2.9}$$

In general, the components of the vectors $\boldsymbol{\alpha}$ and $\boldsymbol{\beta}$ may be correlated. The correlations among the parameters $\boldsymbol{\alpha}$ and $\boldsymbol{\beta}$ are quantified by correlation matrices $\mathbf{C}_{\alpha\beta}^{(N_\alpha \times N_\beta)}$ defined as

$$\mathbf{C}_{\alpha\beta}^{(N_\alpha \times N_\beta)} \equiv \left\langle \left(\boldsymbol{\alpha} - \boldsymbol{\alpha}^0\right)\left(\boldsymbol{\beta} - \boldsymbol{\beta}^0\right)^\dagger \right\rangle = \left[\mathbf{C}_{\beta\alpha}^{(N_\beta \times N_\alpha)} \right]^\dagger . \tag{2.10}$$

These experimentally measured responses are also considered to be characterized by known mean measured values and measured variances and covariances. Thus, for the N_r experimentally measured responses r_i, the *mean measured values* will be denoted as r_i^m, and will be considered to constitute the components of the vector $\mathbf{r}^m$ defined as

$$\mathbf{r}^m = \left\{ r_i^m \,|\, i = 1, \ldots, N_r \right\}, \quad r_i^m \equiv \left\langle r_i \right\rangle, \; i = 1, \ldots, N_r , \tag{2.11}$$

while the corresponding measured covariance matrix, denoted as $\mathbf{C}_{rr}^{(N_r \times N_r)}$, is defined as

$$\mathbf{C}_{rr}^{(N_r \times N_r)} \equiv \left\langle \left(r_i - r_i^m\right)\left(r_j - r_j^m\right) \right\rangle_{N_r \times N_r} , \;\; i, j = 1, \ldots, N_r . \tag{2.12}$$

Similarly, the N_q experimentally measured responses q_j are characterized by mean measured values, denoted as q_j^m, and constituting the components of the vector $\mathbf{q}^m$ defined as

$$\mathbf{q}^m = \left\{ q_j^m \,|\; j = 1, \ldots, N_q \right\}, \;\; q_j^m \equiv \left\langle q_j \right\rangle, \; j = 1, \ldots, N_q , \tag{2.13}$$

and by the measured covariance matrix $\mathbf{C}_{qq}^{(N_q \times N_q)}$ defined as

$$\mathbf{C}_{qq}^{(N_q \times N_q)} \equiv \left\langle \left(q_i - q_i^m\right)\left(q_j - q_j^m\right) \right\rangle_{N_q \times N_q} , \quad i, j = 1, \ldots, N_q . \tag{2.14}$$

Furthermore, the responses $\mathbf{r}$ and $\mathbf{q}$ may also be correlated; such correlations would be quantified by correlation matrices defined as

$$\mathbf{C}_{rq}^{(N_r \times N_q)} \equiv \left\langle \left(\mathbf{r} - \mathbf{r}^m\right)\left(\mathbf{q} - \mathbf{q}^m\right)^\dagger \right\rangle = \left[\mathbf{C}_{qr}^{(N_q \times N_r)} \right]^\dagger . \tag{2.15}$$

In the most general case, correlations my also exist among all parameters and responses. Such correlations would be quantified through matrices defined as follows:

$$\mathbf{C}_{\alpha r}^{(N_\alpha \times N_r)} \equiv \left\langle \left(\boldsymbol{\alpha} - \boldsymbol{\alpha}^0\right)\left(\mathbf{r} - \mathbf{r}^m\right)^\dagger \right\rangle = \left[\mathbf{C}_{r\alpha}^{(N_r \times N_\alpha)}\right]^\dagger, \tag{2.16}$$

$$\mathbf{C}_{\alpha q}^{(N_\alpha \times N_q)} \equiv \left\langle \left(\boldsymbol{\alpha} - \boldsymbol{\alpha}^0\right)\left(\mathbf{q} - \mathbf{q}^m\right)^\dagger \right\rangle = \left[\mathbf{C}_{q\alpha}^{(N_q \times N_\alpha)}\right]^\dagger, \tag{2.17}$$

$$\mathbf{C}_{\beta r}^{(N_\beta \times N_r)} \equiv \left\langle \left(\boldsymbol{\beta} - \boldsymbol{\beta}^0\right)\left(\mathbf{r} - \mathbf{r}^m\right)^\dagger \right\rangle = \left[\mathbf{C}_{r\beta}^{(N_r \times N_\beta)}\right]^\dagger, \tag{2.18}$$

$$\mathbf{C}_{\beta q}^{(N_\beta \times N_q)} \equiv \left\langle \left(\boldsymbol{\beta} - \boldsymbol{\beta}^0\right)\left(\mathbf{q} - \mathbf{q}^m\right)^\dagger \right\rangle = \left[\mathbf{C}_{q\beta}^{(N_q \times N_\beta)}\right]^\dagger. \tag{2.19}$$

2.2 *Construction of the A Priori Distribution Function* $p(\boldsymbol{\alpha},\boldsymbol{\beta},\mathbf{r},\mathbf{q})$ *as the Maximum Entropy Principle Approximation of the True but Unknown A Priori Distribution Function* $P(\boldsymbol{\alpha},\boldsymbol{\beta},\mathbf{r},\mathbf{q})$

The quantities defined in Eqs. (2.1) through (2.19) constitute the *prior information* regarding the uncertain parameters and measured responses in the two-model multi-physics system considered in the previous Section. As discussed, this prior information prescribes the means (i.e., the first-order moments) and covariances (i.e., the second-order moments) of an otherwise unknown distribution function $p(\boldsymbol{\alpha},\boldsymbol{\beta},\mathbf{r},\mathbf{q})$. Mathematically, these means and covariances are functionals of $p(\boldsymbol{\alpha},\boldsymbol{\beta},\mathbf{r},\mathbf{q})$, having the generic form

$$\left\langle F_k \right\rangle = \int p(\mathbf{x}) F_k(\mathbf{x}) d\mathbf{x}, \quad \mathbf{x} \equiv (\boldsymbol{\alpha},\boldsymbol{\beta},\mathbf{r},\mathbf{q}), \quad d\mathbf{x} \equiv d\boldsymbol{\alpha} d\boldsymbol{\beta} d\mathbf{r} d\mathbf{q}, \quad k = 1,2,\ldots,K, \tag{2.20}$$

with $F_k(\mathbf{x})$ representing, in turn, the quantities: $\left(\alpha_n - \alpha_n^0\right)$, $\left(\beta_n - \beta_n^0\right)$, $\left(r_n - r_n^m\right)$, $\left(q_n - q_n^m\right)$ $\left(\alpha_i - \alpha_i^0\right)\left(\alpha_j - \alpha_j^0\right)$, $\left(\beta_i - \beta_i^0\right)\left(\beta_j - \beta_j^0\right)$, $\left(r_i - r_i^m\right)\left(r_j - r_j^m\right)$, $\left(q_i - q_i^m\right)\left(q_j - q_j^m\right)$, $\left(\alpha_i - \alpha_i^0\right)\left(\beta_j - \beta_j^0\right)$, $\left(\alpha_i - \alpha_i^0\right)\left(r_j - r_j^m\right)$, $\left(\alpha_i - \alpha_i^0\right)\left(q_j - q_j^m\right)$, $\left(\beta_i - \beta_i^0\right)\left(r_j - r_j^m\right)$, $\left(\beta_i - \beta_i^0\right)\left(q_j - q_j^m\right)$, and $\left(r_i - r_i^m\right)\left(q_j - q_j^m\right)$.

The total number of first- and second-order moments is

$$\begin{aligned} K \equiv\ & N_\alpha + N_\beta + N_r + N_q + N_\alpha^2 + N_\beta^2 + N_r^2 + N_q^2 \\ & + \left(N_\alpha \times N_\beta\right) + \left(N_\alpha \times N_r\right) + \left(N_\alpha \times N_q\right) + \left(N_\beta \times N_r\right) + \left(N_\beta \times N_q\right) + \left(N_r \times N_q\right). \end{aligned} \tag{2.21}$$

An optimal way to approximate the true but unknown probability distribution function $P(\mathbf{x})$ using the information given in Eq. (2.20) is to apply the *maximum entropy formalism* (Jaynes, 1983). The maximum entropy formalism enables the determination of an *approximate probability distribution function, denoted here as* $p(\mathbf{x})$, which approximates the unknown distribution $P(\mathbf{x})$ by maximizing over $p(\mathbf{x})$ the Shannon information entropy (Shannon, 1948), defined as

$$S = -\int d\mathbf{x}\, p(\mathbf{x}) \ln \frac{p(\mathbf{x})}{m(\mathbf{x})}, \tag{2.22}$$

where $m(\mathbf{x})$ is a prior density that ensures form invariance under change of variable, while satisfying the constraints given in Eq. (2.20). This maximum entropy principle insures that the approximate distribution function $p(\mathbf{x})$ maximizes the optimal compatibility with the available information, namely the constraints given in Eq. (2.20), while simultaneously ensuring minimal spurious information content.

Maximizing the information entropy S over $p(\mathbf{x})$ subject to the constraints expressed by Eq. (2.20) constitutes a variational problem that can be solved by using the method of Lagrange multipliers to obtain a member of the exponential family, namely

$$p(\mathbf{x}) = \frac{1}{Z} m(\mathbf{x}) \exp\left[-\sum_k \lambda_k F_k(\mathbf{x}) \right], \tag{2.23}$$

where the quantities λ_k are the Lagrange multipliers. The normalization constant Z in Eq. (2.23) is defined as

$$Z \equiv \int d\mathbf{x}\, m(\mathbf{x}) \exp\left[-\sum_k \lambda_k F_k(\mathbf{x}) \right]. \tag{2.24}$$

The Lagrange multipliers λ_k must be found directly from the constraints [i.e., using Eqs. (2.20) and (2.23)] or from the equivalent equations

$$\langle F_k \rangle = -\frac{\partial}{\partial \lambda_k} \ln Z \quad , \qquad k = 1, 2, \ldots, K \,, \tag{2.25}$$

which are more convenient if Z can be expressed as an analytic function of the Lagrange parameters.

In the case of discrete distributions, if only the alternatives can be enumerated but the macroscopic data $\langle F_k \rangle$ are not known, then $m(\mathbf{x}) = 1$, and the maximum entropy algorithm

described in the foregoing yields the uniform distribution, as would be required by the principle of insufficient reason. Therefore, the maximum entropy principle can be considered as a far-reaching generalization of the principle of insufficient reason, ranging from discrete alternatives with no other information given, to cases with given global or macroscopic information, and also encompassing continuous distributions. Physicists will recognize the maximum entropy algorithm described above as the essence of the Gibbs-formalism for statistical mechanics, where Z is the partition function (or sum over states), carrying all information about the possible states of the system, from which the expected macroscopic parameters can be obtained by differentiation with respect to the Lagrange multipliers. If only the possible energies of a system and the average energy (i.e., the temperature) are given, one finds Gibbs' canonical ensemble, with probabilities proportional to the Boltzmann factors $\exp\left(-\lambda E_j\right)$, the Lagrange multiplier λ being essentially the inverse temperature. If, in addition, the average particle number is given, one finds the grand-canonical ensemble, with a second Lagrange multiplier equal to the chemical potential, etc.

Performing the respective (lengthy but straightforward) computations indicated in Eq. (2.25), solving the resulting system of equation for the Lagrange multipliers λ_k, and replacing the resulting expressions in Eq. (2.23) leads to the following expression for $p\left(\mathbf{x}\right)$

$$p\left(\mathbf{x}\,|\,\langle\mathbf{x}\rangle,\mathbf{C}\right)d\mathbf{x}=\frac{\exp\left[-\frac{1}{2}\left(\mathbf{x}-\langle\mathbf{x}\rangle\right)^{\dagger}\mathbf{C}^{-1}\left(\mathbf{x}-\langle\mathbf{x}\rangle\right)\right]d\mathbf{x},}{\sqrt{\det\left(2\pi\mathbf{C}\right)}},\ -\infty<x_j<\infty, \qquad (2.26)$$

where the dagger (†) denotes transposition (Hermitean conjugation of real vectors and matrices), and the matrix $\mathbf{C}$ is defined as

$$\mathbf{C}\equiv\begin{pmatrix}\mathbf{C}_{\alpha\alpha} & \mathbf{C}_{\alpha\beta} & \mathbf{C}_{\alpha r} & \mathbf{C}_{\alpha q}\\ \mathbf{C}_{\beta\alpha} & \mathbf{C}_{\beta\beta} & \mathbf{C}_{\beta r} & \mathbf{C}_{\beta q}\\ \mathbf{C}_{r\alpha} & \mathbf{C}_{r\beta} & \mathbf{C}_{rr} & \mathbf{C}_{rq}\\ \mathbf{C}_{q\alpha} & \mathbf{C}_{q\beta} & \mathbf{C}_{qr} & \mathbf{C}_{qq}\end{pmatrix},\ \textit{with}\ \ \mathbf{x}\equiv\begin{pmatrix}\boldsymbol{\alpha}\\ \boldsymbol{\beta}\\ \mathbf{r}\\ \mathbf{q}\end{pmatrix},\ \langle\mathbf{x}\rangle\equiv\begin{pmatrix}\boldsymbol{\alpha}^0\\ \boldsymbol{\beta}^0\\ \mathbf{r}^m\\ \mathbf{q}^m\end{pmatrix}. \qquad (2.27)$$

Thus, the foregoing considerations show that, when only mean values and covariances are known, the maximum entropy algorithm yields the Gaussian probability distribution shown in Eq. (2.27) as the most objective probability distribution consistent with the available information. Although all of the above results are valid for $-\infty<x_j<\infty$, these results can also be used for $0<x_j<\infty$ after introduction of a logarithmic scale (which leads to lognormal distributions on the original scale).

Gaussian distributions are often considered appropriate only if many independent random deviations act together so that the central limit theorem is applicable. At other times, Gaussian distributions are invoked for mere convenience, with accompanying warnings

about consequences if the true distribution is not Gaussian. The maximum entropy principle cannot eliminate these consequences, but it reassures the data user who is given only mean values and their (co)variances that the corresponding Gaussian is the best choice for all further inferences, whatever the unknown true distribution may happen to be. In contrast to the central limit theorem, the maximum entropy principle is also valid for correlated data.

2.3 *Construction of the A Posteriori Predicted Mean Values and Covariances for the Given Models (Likelihood Function) and Maximum Entropy Prior Distribution*

Consider next that the coupled *Models A* and *B* are used to compute the $\left(N_r + N_q\right)$ experimentally measured responses. These computed responses will be denoted as $\mathbf{r}^c\left(\boldsymbol{\alpha},\boldsymbol{\beta}\right) = \left\{r_i^c \mid i = 1,\ldots,N_r\right\}$ and $\mathbf{q}^c\left(\boldsymbol{\alpha},\boldsymbol{\beta}\right) = \left\{q_i^c \mid i = 1,\ldots,N_q\right\}$, respectively, where the superscript "c" indicates "computed." In principle, the computed responses may depend on some or all of the components of $\boldsymbol{\alpha}$ and $\boldsymbol{\beta}$. Consequently, $\mathbf{r}^c\left(\boldsymbol{\alpha},\boldsymbol{\beta}\right)$ and $\mathbf{q}^c\left(\boldsymbol{\alpha},\boldsymbol{\beta}\right)$ are also variates, characterized by probability distribution functions, which cannot, in general, be obtained in explicitly closed forms.

The next step is to combine the experimental and computational information in order to obtain the posterior distribution of $\mathbf{x} \equiv \left(\boldsymbol{\alpha},\boldsymbol{\beta},\mathbf{r},\mathbf{q}\right)$. This combination is rigorously performed by using Bayes' theorem, in which the (maximum entropy) prior is the Gaussian distribution computed in Eq. (2.26), while the likelihood is provided by the computational models $\mathbf{r}^c\left(\boldsymbol{\alpha},\boldsymbol{\beta}\right)$ and $\mathbf{q}^c\left(\boldsymbol{\alpha},\boldsymbol{\beta}\right)$. When the numerical and/or modeling errors are not explicitly taken into account, but are considered to be amenable to treatment via uncertain model parameters that are included among the components of $\boldsymbol{\alpha}$, the computational models are considered to be "hard constraints" of the form

$$\mathbf{r} = \mathbf{r}^c\left(\boldsymbol{\alpha},\boldsymbol{\beta}\right),\ \mathbf{q} = \mathbf{q}^c\left(\boldsymbol{\alpha},\boldsymbol{\beta}\right)\ . \tag{2.28}$$

It is clear *the posterior distribution, which consists of the prior given in Eq. (2.26) together with the likelihood expressed by Eq. (2.28)*, cannot be computed exactly. Nevertheless, the main contribution to the posterior distribution, and, in particular, the main contributions to the posterior distribution's means and covariances, can be obtained by applying the saddle-point method to evaluate the Gaussian prior in Eq. (2.26) subject to the constraints expressed by Eq. (2.28). As is well known, the saddle-point is the point where the gradient of exponent of the Gaussian prior in Eq. (2.26) vanishes subject to the constraints in Eq. (2.28). The method of Lagrange multipliers can be used to determine this saddle-point, by setting to zero the (partial) gradients with respect to $\boldsymbol{\alpha},\boldsymbol{\beta},\mathbf{r},\mathbf{q}$ of the following functional:

$$P\left(\boldsymbol{\alpha},\boldsymbol{\beta},\mathbf{r},\mathbf{q}\right)\equiv-\frac{1}{2}\left(\mathbf{x}-\left\langle\mathbf{x}\right\rangle\right)^{\dagger}\mathbf{C}^{-1}\left(\mathbf{x}-\left\langle\mathbf{x}\right\rangle\right)+\boldsymbol{\lambda}_r^{\dagger}\left[\mathbf{r}-\mathbf{r}^{c}\left(\boldsymbol{\alpha},\boldsymbol{\beta}\right)\right]+\boldsymbol{\lambda}_q^{\dagger}\left[\mathbf{q}-\mathbf{q}^{c}\left(\boldsymbol{\alpha},\boldsymbol{\beta}\right)\right],\quad(2.29)$$

where $\boldsymbol{\lambda}_r$ and $\boldsymbol{\lambda}_q$ are vectors of (yet undetermined) Lagrange multipliers of sizes N_r and N_q, respectively. Thus, the saddle point of $P\left(\boldsymbol{\alpha},\boldsymbol{\beta},\mathbf{r},\mathbf{q}\right)$ is attained at $\mathbf{x}^{pred}\equiv\left(\boldsymbol{\alpha}^{pred},\boldsymbol{\beta}^{pred},\mathbf{r}^{pred},\mathbf{q}^{pred}\right)$ where the following conditions are simultaneously fulfilled:

$$\nabla_{\lambda_r}P=\mathbf{r}-\mathbf{r}^{c}\left(\boldsymbol{\alpha},\boldsymbol{\beta}\right)=\mathbf{0};\quad\nabla_{\lambda_q}P=\mathbf{q}-\mathbf{q}^{c}\left(\boldsymbol{\alpha},\boldsymbol{\beta}\right)=\mathbf{0};\qquad(2.30)$$

$$\nabla_{\alpha}P=\mathbf{0};\ \nabla_{\beta}P=\mathbf{0};\ \nabla_{r}P=\mathbf{0};\ \nabla_{q}P=\mathbf{0}.\qquad(2.31)$$

The conditions expressed in Eq. (2.30) simply ensure that the saddle-point will satisfy the constraints imposed by the numerical simulation *Models A and B*. On the other hand, the conditions imposed in Eq. (2.31) can be written in block-matrix form as

$$\begin{pmatrix}\boldsymbol{\alpha}^{pred}-\boldsymbol{\alpha}^{0}\\ \boldsymbol{\beta}^{pred}-\boldsymbol{\beta}^{0}\\ \mathbf{r}^{pred}-\mathbf{r}^{m}\\ \mathbf{q}^{pred}-\mathbf{q}^{m}\end{pmatrix}=\begin{pmatrix}\mathbf{C}_{\alpha\alpha}&\mathbf{C}_{\alpha\beta}&\mathbf{C}_{\alpha r}&\mathbf{C}_{\alpha q}\\ \mathbf{C}_{\alpha\beta}^{\dagger}&\mathbf{C}_{\beta\beta}&\mathbf{C}_{\beta r}&\mathbf{C}_{\beta q}\\ \mathbf{C}_{\alpha r}^{\dagger}&\mathbf{C}_{\beta r}^{\dagger}&\mathbf{C}_{rr}&\mathbf{C}_{rq}\\ \mathbf{C}_{\alpha q}^{\dagger}&\mathbf{C}_{\beta q}^{\dagger}&\mathbf{C}_{rq}^{\dagger}&\mathbf{C}_{qq}\end{pmatrix}\begin{pmatrix}-\mathbf{S}_{r\alpha}^{\dagger}\boldsymbol{\lambda}_r-\mathbf{S}_{q\alpha}^{\dagger}\boldsymbol{\lambda}_q\\ -\mathbf{S}_{r\beta}^{\dagger}\boldsymbol{\lambda}_r-\mathbf{S}_{q\beta}^{\dagger}\boldsymbol{\lambda}_q\\ \boldsymbol{\lambda}_r\\ \boldsymbol{\lambda}_q\end{pmatrix}\qquad(2.32)$$

where the matrices $\mathbf{S}_{r\alpha}\left(\boldsymbol{\alpha}^{0},\boldsymbol{\beta}^{0}\right)$, $\mathbf{S}_{r\beta}\left(\boldsymbol{\alpha}^{0},\boldsymbol{\beta}^{0}\right)$, $\mathbf{S}_{q\alpha}\left(\boldsymbol{\alpha}^{0},\boldsymbol{\beta}^{0}\right)$, and $\mathbf{S}_{q\beta}\left(\boldsymbol{\alpha}^{0},\boldsymbol{\beta}^{0}\right)$ comprise first-order response-derivatives with respect to the model parameters, computed at the nominal parameter values $\left(\boldsymbol{\alpha}^{0},\boldsymbol{\beta}^{0}\right)$, and are defined as follows:

$$\mathbf{S}_{r\alpha}^{N_r\times N_\alpha}\equiv\begin{bmatrix}\frac{\partial r_1}{\partial\alpha_1}&\cdots&\frac{\partial r_1}{\partial\alpha_{N_\alpha}}\\ \vdots&\ddots&\vdots\\ \frac{\partial r_{N_r}}{\partial\alpha_1}&\cdots&\frac{\partial r_{N_r}}{\partial\alpha_{N_\alpha}}\end{bmatrix},\quad\mathbf{S}_{r\beta}^{N_r\times N_\beta}\equiv\begin{bmatrix}\frac{\partial r_1}{\partial\beta_1}&\cdots&\frac{\partial r_1}{\partial\beta_{N_\beta}}\\ \vdots&\ddots&\vdots\\ \frac{\partial r_{N_r}}{\partial\beta_1}&\cdots&\frac{\partial r_{N_r}}{\partial\beta_{N_\beta}}\end{bmatrix},\qquad(2.33)$$

$$\mathbf{S}_{q\alpha}^{N_q\times N_\alpha}\equiv\begin{bmatrix}\frac{\partial q_1}{\partial\alpha_1}&\cdots&\frac{\partial q_1}{\partial\alpha_{N_\alpha}}\\ \vdots&\ddots&\vdots\\ \frac{\partial q_{N_q}}{\partial\alpha_1}&\cdots&\frac{\partial q_{N_q}}{\partial\alpha_{N_\alpha}}\end{bmatrix},\quad\mathbf{S}_{q\beta}^{N_q\times N_\beta}\equiv\begin{bmatrix}\frac{\partial q_1}{\partial\beta_1}&\cdots&\frac{\partial q_1}{\partial\beta_{N_\beta}}\\ \vdots&\ddots&\vdots\\ \frac{\partial q_{N_q}}{\partial\beta_1}&\cdots&\frac{\partial q_{N_q}}{\partial\beta_{N_\beta}}\end{bmatrix}.\qquad(2.34)$$

Note that no approximations have been introduced thus far, i.e., Eq. (2.32) is exact for the a priori information considered to be known (i.e., known means and covariance matrices for the parameters and measured responses).

The results obtained by evaluating Eq. (2.32) to *first-order in response sensitivities* are presented in Appendix A, and are also summarized below.

1. The predicted optimal values for the model parameters:

$$\boldsymbol{\alpha}^{pred} = \boldsymbol{\alpha}^0 - \left[\mathbf{X}_\alpha \mathbf{D}_{11} + \mathbf{Y}_\alpha \mathbf{D}_{12}^\dagger\right]\mathbf{r}^d\left(\boldsymbol{\alpha}^0, \boldsymbol{\beta}^0\right) - \left[\mathbf{X}_\alpha \mathbf{D}_{12} + \mathbf{Y}_\alpha \mathbf{D}_{22}\right]\mathbf{q}^d\left(\boldsymbol{\alpha}^0, \boldsymbol{\beta}^0\right); \quad \text{(C.1)}$$

$$\boldsymbol{\beta}^{pred} = \boldsymbol{\beta}^0 - \left[\mathbf{X}_\beta \mathbf{D}_{11} + \mathbf{Y}_\beta \mathbf{D}_{12}^\dagger\right]\mathbf{r}^d\left(\boldsymbol{\alpha}^0, \boldsymbol{\beta}^0\right) - \left[\mathbf{X}_\beta \mathbf{D}_{12} + \mathbf{Y}_\beta \mathbf{D}_{22}\right]\mathbf{q}^d\left(\boldsymbol{\alpha}^0, \boldsymbol{\beta}^0\right); \quad \text{(C.2)}$$

2. The predicted optimal values for the model responses:

$$\mathbf{r}^{pred} = \mathbf{r}^m - \left[\mathbf{X}_r \mathbf{D}_{11} + \mathbf{Y}_r \mathbf{D}_{12}^\dagger\right]\mathbf{r}^d\left(\boldsymbol{\alpha}^0, \boldsymbol{\beta}^0\right) - \left[\mathbf{X}_r \mathbf{D}_{12} + \mathbf{Y}_r \mathbf{D}_{22}\right]\mathbf{q}^d\left(\boldsymbol{\alpha}^0, \boldsymbol{\beta}^0\right); \quad \text{(C.3)}$$

$$\mathbf{q}^{pred} = \mathbf{q}^m - \left[\mathbf{X}_q \mathbf{D}_{11} + \mathbf{Y}_q \mathbf{D}_{12}^\dagger\right]\mathbf{r}^d\left(\boldsymbol{\alpha}^0, \boldsymbol{\beta}^0\right) - \left[\mathbf{X}_q \mathbf{D}_{12} + \mathbf{Y}_q \mathbf{D}_{22}\right]\mathbf{q}^d\left(\boldsymbol{\alpha}^0, \boldsymbol{\beta}^0\right); \quad \text{(C.4)}$$

3. The predicted optimal covariance matrix $\mathbf{C}_{\alpha\alpha}^{pred}$ for the parameters $\boldsymbol{\alpha}$ of *Model A*:

$$\begin{aligned}\mathbf{C}_{\alpha\alpha}^{pred} &\equiv \left\langle \left(\boldsymbol{\alpha} - \boldsymbol{\alpha}^{pred}\right)\left(\boldsymbol{\alpha} - \boldsymbol{\alpha}^{pred}\right)^\dagger \right\rangle \\ &= \mathbf{C}_{\alpha\alpha} - \left[\mathbf{X}_\alpha\left(\mathbf{D}_{11}\mathbf{X}_\alpha^\dagger + \mathbf{D}_{12}\mathbf{Y}_\alpha^\dagger\right) + \mathbf{Y}_\alpha\left(\mathbf{D}_{21}\mathbf{X}_\alpha^\dagger + \mathbf{D}_{22}\mathbf{Y}_\alpha^\dagger\right)\right];\end{aligned} \quad \text{(C.5)}$$

4. The predicted covariance matrix $\mathbf{C}_{rr}^{pred}$ for the responses $\mathbf{r}$ of *Model A*:

$$\begin{aligned}\mathbf{C}_{rr}^{pred} &\equiv \left\langle \left(\mathbf{r} - \mathbf{r}^{pred}\right)\left(\mathbf{r} - \mathbf{r}^{pred}\right)^\dagger \right\rangle \\ &= \mathbf{C}_{rr} - \left[\mathbf{X}_r\left(\mathbf{D}_{11}\mathbf{X}_r^\dagger + \mathbf{D}_{12}\mathbf{Y}_r^\dagger\right) + \mathbf{Y}_r\left(\mathbf{D}_{21}\mathbf{X}_r^\dagger + \mathbf{D}_{22}\mathbf{Y}_r^\dagger\right)\right];\end{aligned} \quad \text{(C.6)}$$

5. The predicted correlation matrix $\mathbf{C}_{\alpha r}^{pred}$ for the parameters $\boldsymbol{\alpha}$ and $\mathbf{r}$ responses of *Model A*:

$$\begin{aligned}\mathbf{C}_{\alpha r}^{pred} &\equiv \left\langle \left(\boldsymbol{\alpha} - \boldsymbol{\alpha}^{pred}\right)\left(\mathbf{r} - \mathbf{r}^{pred}\right)^\dagger \right\rangle \\ &= \mathbf{C}_{\alpha r} - \left[\mathbf{X}_\alpha\left(\mathbf{D}_{11}\mathbf{X}_r^\dagger + \mathbf{D}_{12}\mathbf{Y}_r^\dagger\right) + \mathbf{Y}_\alpha\left(\mathbf{D}_{21}\mathbf{X}_r^\dagger + \mathbf{D}_{22}\mathbf{Y}_r^\dagger\right)\right];\end{aligned} \quad \text{(C.7)}$$

6. The predicted covariance matrix $\mathbf{C}_{\beta\beta}^{pred}$ for the parameters $\boldsymbol{\beta}$ of *Model B*:

$$\begin{aligned}\mathbf{C}_{\beta\beta}^{pred} &\equiv \left\langle \left(\boldsymbol{\beta}-\boldsymbol{\beta}^{pred}\right)\left(\boldsymbol{\beta}-\boldsymbol{\beta}^{pred}\right)^{\dagger}\right\rangle \\ &= \mathbf{C}_{\beta\beta}-\left[\mathbf{X}_{\beta}\left(\mathbf{D}_{11}\mathbf{X}_{\beta}^{\dagger}+\mathbf{D}_{12}\mathbf{Y}_{\beta}^{\dagger}\right)+\mathbf{Y}_{\beta}\left(\mathbf{D}_{21}\mathbf{X}_{\beta}^{\dagger}+\mathbf{D}_{22}\mathbf{Y}_{\beta}^{\dagger}\right)\right];\end{aligned} \tag{C.8}$$

7. The predicted covariance matrix $\mathbf{C}_{qq}^{pred}$ for the responses $\mathbf{q}$ of *Model B*:

$$\begin{aligned}\mathbf{C}_{qq}^{pred} &\equiv \left\langle \left(\mathbf{q}-\mathbf{q}^{pred}\right)\left(\mathbf{q}-\mathbf{q}^{pred}\right)^{\dagger}\right\rangle \\ &= \mathbf{C}_{qq}-\left[\mathbf{X}_{q}\left(\mathbf{D}_{11}\mathbf{X}_{q}^{\dagger}+\mathbf{D}_{12}\mathbf{Y}_{q}^{\dagger}\right)+\mathbf{Y}_{q}\left(\mathbf{D}_{21}\mathbf{X}_{q}^{\dagger}+\mathbf{D}_{22}\mathbf{Y}_{q}^{\dagger}\right)\right];\end{aligned} \tag{C.9}$$

8. The predicted correlation matrix $\mathbf{C}_{\beta q}^{pred}$ for the parameters $\boldsymbol{\beta}$ and the responses $\mathbf{q}$ of *Model B*:

$$\begin{aligned}\mathbf{C}_{\beta q}^{opt} &\equiv \left\langle \left(\boldsymbol{\beta}-\boldsymbol{\beta}^{pred}\right)\left(\mathbf{q}-\mathbf{q}^{pred}\right)^{\dagger}\right\rangle \\ &= \mathbf{C}_{\beta q}-\left[\mathbf{X}_{\beta}\left(\mathbf{D}_{11}\mathbf{X}_{q}^{\dagger}+\mathbf{D}_{12}\mathbf{Y}_{q}^{\dagger}\right)+\mathbf{Y}_{\beta}\left(\mathbf{D}_{21}\mathbf{X}_{q}^{\dagger}+\mathbf{D}_{22}\mathbf{Y}_{q}^{\dagger}\right)\right];\end{aligned} \tag{C.10}$$

9. The predicted correlation matrix $\mathbf{C}_{\alpha\beta}^{pred}$ for the parameters $\boldsymbol{\alpha}$ of *Model A* and the parameters $\boldsymbol{\beta}$ of *Model B:*

$$\begin{aligned}\mathbf{C}_{\alpha\beta}^{pred} &\equiv \left\langle \left(\boldsymbol{\alpha}-\boldsymbol{\alpha}^{pred}\right)\left(\boldsymbol{\beta}-\boldsymbol{\beta}^{pred}\right)^{\dagger}\right\rangle \\ &= \mathbf{C}_{\alpha\beta}-\left[\mathbf{X}_{\alpha}\left(\mathbf{D}_{11}\mathbf{X}_{\beta}^{\dagger}+\mathbf{D}_{12}\mathbf{Y}_{\beta}^{\dagger}\right)+\mathbf{Y}_{\alpha}\left(\mathbf{D}_{21}\mathbf{X}_{\beta}^{\dagger}+\mathbf{D}_{22}\mathbf{Y}_{\beta}^{\dagger}\right)\right];\end{aligned} \tag{C.11}$$

10. The predicted correlation matrix $\mathbf{C}_{\alpha q}^{pred}$ for the parameters $\boldsymbol{\alpha}$ of *Model A* and the responses $\mathbf{q}$ of *Model B:*

$$\begin{aligned}\mathbf{C}_{\alpha q}^{pred} &\equiv \left\langle \left(\boldsymbol{\alpha}-\boldsymbol{\alpha}^{pred}\right)\left(\mathbf{q}-\mathbf{q}^{pred}\right)^{\dagger}\right\rangle \\ &= \mathbf{C}_{\alpha q}-\left[\mathbf{X}_{\alpha}\left(\mathbf{D}_{11}\mathbf{X}_{q}^{\dagger}+\mathbf{D}_{12}\mathbf{Y}_{q}^{\dagger}\right)+\mathbf{Y}_{\alpha}\left(\mathbf{D}_{21}\mathbf{X}_{q}^{\dagger}+\mathbf{D}_{22}\mathbf{Y}_{q}^{\dagger}\right)\right];\end{aligned} \tag{C.12}$$

11. The predicted correlation matrix $\mathbf{C}_{\beta r}^{pred}$ for the parameters $\boldsymbol{\beta}$ of *Model B* and the responses $\mathbf{r}$ of *Model A:*

$$\begin{aligned}\mathbf{C}_{\beta r}^{pred} &\equiv \left\langle \left(\boldsymbol{\beta}-\boldsymbol{\beta}^{pred}\right)\left(\mathbf{r}-\mathbf{r}^{pred}\right)^{\dagger}\right\rangle \\ &= \mathbf{C}_{\beta r}-\left[\mathbf{X}_{\beta}\left(\mathbf{D}_{11}\mathbf{X}_{r}^{\dagger}+\mathbf{D}_{12}\mathbf{Y}_{r}^{\dagger}\right)+\mathbf{Y}_{\beta}\left(\mathbf{D}_{21}\mathbf{X}_{r}^{\dagger}+\mathbf{D}_{22}\mathbf{Y}_{r}^{\dagger}\right)\right];\end{aligned} \tag{C.13}$$

12. The predicted correlation matrix $\mathbf{C}_{rq}^{pred}$ for the responses $\mathbf{r}$ of *Model A* and the responses $\mathbf{q}$ of *Model B:*

$$\begin{aligned}\mathbf{C}_{rq}^{pred} &\equiv \left\langle \left(\mathbf{r}-\mathbf{r}^{pred}\right)\left(\mathbf{q}-\mathbf{q}^{pred}\right)^{\dagger} \right\rangle \\ &= \mathbf{C}_{rq} - \left[\mathbf{X}_r\left(\mathbf{D}_{11}\mathbf{X}_q^{\dagger}+\mathbf{D}_{12}\mathbf{Y}_q^{\dagger}\right)+\mathbf{Y}_r\left(\mathbf{D}_{21}\mathbf{X}_q^{\dagger}+\mathbf{D}_{22}\mathbf{Y}_q^{\dagger}\right)\right].\end{aligned} \tag{C.14}$$

Note also that, to first-order in response sensitivities, the covariance matrices of the computed responses arising from the uncertainties in the model parameters can be computed from Eqs. (2.39) and (2.40), respectively, to obtain:

$$\begin{aligned}\mathbf{C}_{rr}^{comp} &\equiv \left\langle \left[\mathbf{r}-\mathbf{r}^{c}\left(\boldsymbol{\alpha}^{0},\boldsymbol{\beta}^{0}\right)\right]\left[\mathbf{r}-\mathbf{r}^{c}\left(\boldsymbol{\alpha}^{0},\boldsymbol{\beta}^{0}\right)\right]^{\dagger} \right\rangle \\ &= \mathbf{S}_{r\alpha}\mathbf{C}_{\alpha\alpha}\mathbf{S}_{r\alpha}^{\dagger}+2\mathbf{S}_{r\alpha}\mathbf{C}_{\alpha\beta}\mathbf{S}_{r\beta}^{\dagger}+\mathbf{S}_{r\beta}\mathbf{C}_{\beta\beta}\mathbf{S}_{r\beta}^{\dagger},\end{aligned} \tag{C.15}$$

$$\begin{aligned}\mathbf{C}_{qq}^{comp} &\equiv \left\langle \left[\mathbf{q}-\mathbf{q}^{c}\left(\boldsymbol{\alpha}^{0},\boldsymbol{\beta}^{0}\right)\right]\left[\mathbf{q}-\mathbf{q}^{c}\left(\boldsymbol{\alpha}^{0},\boldsymbol{\beta}^{0}\right)\right]^{\dagger} \right\rangle \\ &= \mathbf{S}_{q\alpha}\mathbf{C}_{\alpha\alpha}\mathbf{S}_{q\alpha}^{\dagger}+2\mathbf{S}_{q\alpha}\mathbf{C}_{\alpha\beta}\mathbf{S}_{q\beta}^{\dagger}+\mathbf{S}_{q\beta}\mathbf{C}_{\beta\beta}\mathbf{S}_{q\beta}^{\dagger},\end{aligned} \tag{C.16}$$

$$\begin{aligned}\mathbf{C}_{rq}^{comp} &\equiv \left\langle \left[\mathbf{r}-\mathbf{r}^{c}\left(\boldsymbol{\alpha}^{0},\boldsymbol{\beta}^{0}\right)\right]\left[\mathbf{q}-\mathbf{q}^{c}\left(\boldsymbol{\alpha}^{0},\boldsymbol{\beta}^{0}\right)\right]^{\dagger} \right\rangle \\ &= \mathbf{S}_{r\alpha}\mathbf{C}_{\alpha\alpha}\mathbf{S}_{q\alpha}^{\dagger}+\mathbf{S}_{r\alpha}\mathbf{C}_{\alpha\beta}\mathbf{S}_{q\alpha}^{\dagger}+\mathbf{S}_{r\beta}\mathbf{C}_{\alpha\beta}^{\dagger}\mathbf{S}_{q\alpha}^{\dagger}+\mathbf{S}_{r\beta}\mathbf{C}_{\beta\beta}\mathbf{S}_{q\beta}^{\dagger}.\end{aligned} \tag{C.17}$$

13. The χ^2-distribution is a measure of the deviation of a "true distribution" (in this case – the distribution of experimental responses) from the hypothetic one (in this case – a Gaussian). Recall that the mean and variance of x are $\langle x \rangle = n$ and $\mathrm{var}(x) = 2n$. The value of χ^2 is computed using Eq. (2.86) to obtain

$$V_C \equiv \chi_C^2 = \left(\mathbf{r}^c-\mathbf{r}^m\right)^{\dagger}\mathbf{D}_{11}\left(\mathbf{r}^c-\mathbf{r}^m\right)+2\left(\mathbf{r}^c-\mathbf{r}^m\right)^{\dagger}\mathbf{D}_{12}\left(\mathbf{q}^c-\mathbf{q}^m\right)+\left(\mathbf{q}^c-\mathbf{q}^m\right)^{\dagger}\mathbf{D}_{22}\left(\mathbf{q}^c-\mathbf{q}^m\right). \tag{C.18}$$

The value of V_C computed using Eq. (C.18) provides a very valuable quantitative indicator for investigating the agreement between the computed and experimental responses, measuring essentially the consistency of the experimental responses with the model parameters. For example, if V_C is much larger than the number of "degrees of freedom" in the inverse problem, then some violation of the "first-order, Gaussian" hypotheses underlying the derivation of Eqs. (C.1)-(C.17) may have occurred. On the other hand, an improbably small value of V_C would indicated that some uncertainties (in the parameters or measured responses) may have been overestimated. The value of V_C can thus be used as a

validation metric for measuring the consistency between the computed and experimentally measured responses.

The following definitions were used in the above expressions:

$$\mathbf{X}_\alpha \equiv \mathbf{C}_{\alpha\alpha}\mathbf{S}^\dagger_{r\alpha} + \mathbf{C}_{\alpha\beta}\mathbf{S}^\dagger_{r\beta} - \mathbf{C}_{\alpha r}, \qquad \mathbf{Y}_\alpha \equiv \mathbf{C}_{\alpha\alpha}\mathbf{S}^\dagger_{q\alpha} + \mathbf{C}_{\alpha\beta}\mathbf{S}^\dagger_{q\beta} - \mathbf{C}_{\alpha q},$$
$$\mathbf{X}_\beta \equiv \mathbf{C}^\dagger_{\alpha\beta}\mathbf{S}^\dagger_{r\alpha} + \mathbf{C}_{\beta\beta}\mathbf{S}^\dagger_{r\beta} - \mathbf{C}_{\beta r}, \qquad \mathbf{Y}_\beta \equiv \mathbf{C}_{\beta\alpha}\mathbf{S}^\dagger_{q\alpha} + \mathbf{C}_{\beta\beta}\mathbf{S}^\dagger_{q\beta} - \mathbf{C}_{\beta q},$$
$$\mathbf{X}_r \equiv \mathbf{C}^\dagger_{\alpha r}\mathbf{S}^\dagger_{r\alpha} + \mathbf{C}^\dagger_{\beta r}\mathbf{S}^\dagger_{r\beta} - \mathbf{C}_{rr}, \qquad \mathbf{Y}_r \equiv \mathbf{C}^\dagger_{\alpha r}\mathbf{S}^\dagger_{q\alpha} + \mathbf{C}^\dagger_{\beta r}\mathbf{S}^\dagger_{q\beta} - \mathbf{C}^\dagger_{rq}$$
$$\mathbf{X}_q \equiv \mathbf{C}^\dagger_{\alpha q}\mathbf{S}^\dagger_{r\alpha} + \mathbf{C}^\dagger_{\beta q}\mathbf{S}^\dagger_{r\beta} - \mathbf{C}^\dagger_{rq}, \qquad \mathbf{Y}_q \equiv \mathbf{C}^\dagger_{\alpha q}\mathbf{S}^\dagger_{q\alpha} + \mathbf{C}^\dagger_{\beta q}\mathbf{S}^\dagger_{q\beta} - \mathbf{C}_{qq}.$$

$$\mathbf{D}_{11} \equiv \mathbf{D}^{-1}_{rr} + \mathbf{D}^{-1}_{rr}\mathbf{D}_{rq}\mathbf{D}_{22}\mathbf{D}^\dagger_{rq}\mathbf{D}^{-1}_{rr}, \qquad \mathbf{D}_{12} \equiv -\mathbf{D}^{-1}_{rr}\mathbf{D}_{rq}\mathbf{D}_{22},$$
$$\mathbf{D}^\dagger_{12} \equiv -\mathbf{D}_{22}\mathbf{D}^\dagger_{rq}\mathbf{D}^{-1}_{rr}, \qquad \mathbf{D}_{22} \equiv \left(\mathbf{D}_{qq} - \mathbf{D}^\dagger_{rq}\mathbf{D}^{-1}_{rr}\mathbf{D}_{rq}\right)^{-1},$$

$$\mathbf{D}_{rr} \equiv \mathbf{S}_{r\alpha}\left(\mathbf{C}_{\alpha\alpha}\mathbf{S}^\dagger_{r\alpha} + \mathbf{C}_{\alpha\beta}\mathbf{S}^\dagger_{r\beta} - \mathbf{C}_{\alpha r}\right) + \mathbf{S}_{r\beta}\left(\mathbf{C}^\dagger_{\alpha\beta}\mathbf{S}^\dagger_{r\alpha} + \mathbf{C}_{\beta\beta}\mathbf{S}^\dagger_{r\beta} - \mathbf{C}_{\beta r}\right) - \mathbf{C}^\dagger_{\alpha r}\mathbf{S}^\dagger_{r\alpha} - \mathbf{C}^\dagger_{\beta r}\mathbf{S}^\dagger_{r\beta} + \mathbf{C}_{rr},$$
$$\mathbf{D}_{rq} \equiv \mathbf{S}_{r\alpha}\left(\mathbf{C}_{\alpha\alpha}\mathbf{S}^\dagger_{q\alpha} + \mathbf{C}_{\alpha\beta}\mathbf{S}^\dagger_{q\beta} - \mathbf{C}_{\alpha q}\right) + \mathbf{S}_{r\beta}\left(\mathbf{C}^\dagger_{\alpha\beta}\mathbf{S}^\dagger_{q\alpha} + \mathbf{C}_{\beta\beta}\mathbf{S}^\dagger_{q\beta} - \mathbf{C}_{\beta q}\right) - \mathbf{C}^\dagger_{\alpha r}\mathbf{S}^\dagger_{q\alpha} - \mathbf{C}^\dagger_{\beta r}\mathbf{S}^\dagger_{q\beta} + \mathbf{C}_{rq},$$
$$\mathbf{D}_{qr} \equiv \mathbf{S}_{q\alpha}\left(\mathbf{C}_{\alpha\alpha}\mathbf{S}^\dagger_{r\alpha} + \mathbf{C}_{\alpha\beta}\mathbf{S}^\dagger_{r\beta} - \mathbf{C}_{\alpha r}\right) + \mathbf{S}_{q\beta}\left(\mathbf{C}^\dagger_{\alpha\beta}\mathbf{S}^\dagger_{r\alpha} + \mathbf{C}_{\beta\beta}\mathbf{S}^\dagger_{r\beta} - \mathbf{C}_{\beta r}\right) - \mathbf{C}^\dagger_{\alpha q}\mathbf{S}^\dagger_{r\alpha} - \mathbf{C}^\dagger_{\beta q}\mathbf{S}^\dagger_{r\beta} + \mathbf{C}^\dagger_{rq} = \mathbf{D}^\dagger_{rq},$$
$$\mathbf{D}_{qq} \equiv \mathbf{S}_{q\alpha}\left(\mathbf{C}_{\alpha\alpha}\mathbf{S}^\dagger_{q\alpha} + \mathbf{C}_{\alpha\beta}\mathbf{S}^\dagger_{q\beta} - \mathbf{C}_{\alpha q}\right) + \mathbf{S}_{q\beta}\left(\mathbf{C}^\dagger_{\alpha\beta}\mathbf{S}^\dagger_{q\alpha} + \mathbf{C}_{\beta\beta}\mathbf{S}^\dagger_{q\beta} - \mathbf{C}_{\beta q}\right) - \mathbf{C}^\dagger_{\alpha q}\mathbf{S}^\dagger_{q\alpha} - \mathbf{C}^\dagger_{\beta q}\mathbf{S}^\dagger_{\beta q} + \mathbf{C}_{qq},$$

$$\mathbf{r}^d\left(\boldsymbol{\alpha}^0, \boldsymbol{\beta}^0\right) \equiv \mathbf{r}^c\left(\boldsymbol{\alpha}^0, \boldsymbol{\beta}^0\right) - \mathbf{r}^m; \qquad \mathbf{q}^d\left(\boldsymbol{\alpha}^0, \boldsymbol{\beta}^0\right) \equiv \mathbf{q}^c\left(\boldsymbol{\alpha}^0, \boldsymbol{\beta}^0\right) - \mathbf{q}^m.$$

3. PREVIOUS METHODS FOR SOLVING INVERSE PROLEMS

Section 3.1 through 3.4 will review the salient features of the most important methods that have been used in various application fields, including radiation transport, for "regularizing" inverse problems.

3.1 *The Levenberg-Marquardt (LM) Method*

The Levenberg-Marquardt method [] approximately solves inverse problems by minimizing the following functional:

$$\chi^2 \equiv \sum_{d=1}^{D} \left[\frac{M_{d,0} - M_d(\mathbf{u})}{\sigma_{d,0}} \right]^2, \qquad \text{(LM)}$$

where $M_{d,0}$ denotes a *measured quantity* for measurement d $(d = 1,...,D)$, $\sigma_{d,0}$ denotes the associated statistical standard deviation associated with measurement *d*, and $M_d(\mathbf{u})$ denotes the value of the *computed quantity*, using nominal ("postulated") values for the vector $\mathbf{u} = (u_1,...,u_N)$ of model parameters (sources, material densities, etc.). The minimum of Eq. (3.LM) is obtained by computing the "updated" parameter values $\mathbf{u}^{up} = (u_1^{up},...,u_N^{up})$ such that they satisfy the condition

$$\left(\nabla\chi^2\right)_{\mathbf{u}^{up}} = \mathbf{0} \rightarrow \left(\frac{\partial\chi^2}{\partial u_k} \right)_{\left(u_1^{up},...,u_N^{up}\right)} = 0,\ k = 1,...,N.$$

Bledsoe et al [] used the LM-method to identify shield materials, material density, and source compositions in one- and two-dimensional inverse radiation transport problems.

3.2 *Tichonov's Method*

The "Tichonov solution" to a problem of the form

$$\mathbf{Ax} = \mathbf{b}$$

with "noisy" (uncertain or unknown) parameters $\mathbf{b}$ is defined as the solution to the minimization problem of the following sum of "squared 2-norms":

$$\min_{\mathbf{x}} \left\{ \left\| \mathbf{Ax} - \mathbf{b} \right\|_2^2 + \lambda^2 \left\| \mathbf{x} \right\|_2^2 \right\}, \qquad \text{(T)}$$

where

(i) The term $\left\| \mathbf{Ax} - \mathbf{b} \right\|_2^2$ measures the "goodness of fit", i.e., how well the solution $\mathbf{x}$ predicts the given noisy data $\mathbf{b}$. If this term is too large, then $\mathbf{x}$ cannot be considered to be a „good" solution because it does not "solve the problem". Intuitively, on the other hand, if this term is smaller than the average size of the errors in the data $\mathbf{b}$, then $\mathbf{x}$ would be „fitting" the "noise" in the data.

(ii) The term $\left\| \mathbf{x} \right\|_2^2$ measures the regularity of the solution. The incorporation of this term is based on the intuitive knowledge that the "naïve" solution is dominated by high-frequency components with large amplitudes, and the hope is that most (if not all) of these components could be suppressed by controlling the 2-norm of $\mathbf{x}$.

(iii) The balance between the above terms is controlled in Eq. (T) by the parameter λ^2, with $\lambda > 0$. The larger the positive parameter λ, the more weight is given to the solution's smoothness. On the other hand, as $\lambda \to 0$, the more weight is given to fitting the noisy data, so the solution tends to the less regular (noisy) "naïve" solution.

3.3 *Bayesian and Functional Inverse Least-Squares Methods*

As has been discussed in the Introduction, inverse problems are mathematically ill-posed, so their solutions are afflicted by existence, uniqueness, and stability difficulties. Therefore, naïvely inverting an operator to solve an inverse problem is usually a poor strategy. Instead, inverse problems are casts into a probabilistic framework, as has been described in Section 2 while reviewing Cacuci's method (2014). Using Bayes' theorem

$$p\left(hypothesis \middle| data, I\right) \sim p\left(data \middle| hypothesis, I\right) p\left(hypothesis \middle| I\right), \tag{B}$$

probabilistic methods represent the input as a range of possible values and an accompanying probability of observing each of those values, and returning a range of possible values for the unknowns. In the above (un-normalized) relation, the "hypothesis" represents the unknowns of the system, the "data" represents measurements taken to resolve the values of the unknowns, and all additional prior knowledge is represented by the "information" *I*. As is well known, the three probability distributions in Eq. (B) are as follows:

(i) $p\left(hypothesis \middle| I\right)$ represents the *prior* information about the hypothesis based only on other information *I*, before considering the data;

(ii) $p\left(data \middle| hypothesis, I\right)$ denotes the likelihood, which quantifies how well the data agrees with a given hypothesis;

(iii) $p\left(hypothesis \middle| data, I\right)$ denotes the posterior distribution, representing the updated probability for the hypothesis after having assimilated the information in the data.

Jarman et al (2011) applied directly Bayes' theorem to localize radiation sources, using a parametrization of the radiation source distribution as the "hypothesis", and radiation and particle detector measurements as the "data".

The exact posterior distribution is not available except perhaps in trivially simple problems. Therefore, the posterior distribution is evaluated to obtain posterior ("predicted") means and covariances. If the distributions are Gaussian, the evaluation of the posterior amounts to solving a least-squares problem in which the predicted parameters are obtained as the solution that minimizes a "misfit" functional (also called the "cost" functional, "objective" functional, "least-squares" functional, "chi-squared" functional). For example, Tarantola (2005) minimizes the following least-squares functional

$$\min_{\mathbf{m}} \left\{ \left\| \mathbf{g}(\mathbf{m}) - \mathbf{d}_{obs} \right\|_D^2 + \left\| \mathbf{m} - \mathbf{m}_{prior} \right\|_M^2 \right\}$$
$$= \min_{\mathbf{m}} \left\{ \left[\mathbf{g}(\mathbf{m}) - \mathbf{d}_{obs} \right]^\dagger \mathbf{C}_D^{-1} \left[\mathbf{g}(\mathbf{m}) - \mathbf{d}_{obs} \right] + \left[\mathbf{m} - \mathbf{m}_{prior} \right]^\dagger \mathbf{C}_M^{-1} \left[\mathbf{m} - \mathbf{m}_{prior} \right] \right\}, \quad \text{(FILS-T)}$$

where

(i) The a priori information that the (unknown) model $\mathbf{m}$ is a sample of a known Gaussian probability density whose mean is $\mathbf{m}_{prior}$ and whose covariance matrix is $\mathbf{C}_M$. The probability density is assumed to be a priori in the sense that it is independent of the measurements on the observable parameters $\mathbf{d}$ (considered below).

(ii) A relation of the form $\mathbf{g}(\mathbf{m}) = \mathbf{d}$ that solves the „forward problem“ (i.e., that predicts the values of the observable parameters $\mathbf{d}$ which should correspond to the model $\mathbf{m}$). This theoretical prediction is assumed to be “perfect” (i.e., free of any errors).

(iii) Measurements of the observable parameters $\mathbf{d}$ that can be represented by a Gaussian probability density whose mean is $\mathbf{d}_{obs}$ and whose covariance matrix is $\mathbf{C}_D$.

The solution to the above minimization problem yields [Tarantola, 2005]:

1. The “best-estimate” parameter values, $\tilde{\mathbf{m}}$, in the form

$$\tilde{\mathbf{m}} = \mathbf{m}_{prior} + \mathbf{C}_M \mathbf{G}^\dagger \left(\mathbf{G}\mathbf{C}_M \mathbf{G}^\dagger + \mathbf{C}_D \right)^{-1} \left(\mathbf{d}_{obs} - \mathbf{G}\mathbf{m}_{prior} \right), \quad \text{(FILS-T.1)}$$

2. The corresponding “best-estimate” predicted covariance matrix

$$\tilde{\mathbf{C}}_M = \mathbf{C}_M - \mathbf{C}_M \mathbf{G}^\dagger \left(\mathbf{G}\mathbf{C}_M \mathbf{G}^\dagger + \mathbf{C}_D \right)^{-1} \mathbf{G}\mathbf{C}_M, \quad \text{(FILS-T.2)}$$

where $\mathbf{G}$ represents the matrix of first-order derivatives with elements $\left\{ \partial g_i / \partial m_j \right\}$.

3. The “goodness of fit” χ^2_{FILS-T}, which measures the degree of consistency between the model and the observations, of the form

$$\chi^2_{FILS-T} = \left(\mathbf{G}\mathbf{m}_{prior} - \mathbf{d}_{obs} \right)^\dagger \left(\mathbf{G}\mathbf{C}_M \mathbf{G}^\dagger + \mathbf{C}_D \right)^{-1} \left(\mathbf{G}\mathbf{m}_{prior} - \mathbf{d}_{obs} \right). \quad \text{(FILS-T.3)}$$

It is important to note that the method above has many similarities with the state-of-the-art methods for data assimilation in the earth and atmospheric sciences [see, e.g., Refs.]. The *FILS-T* method, as well as the considerably more sophisticated method of Cacuci and Ionescu-Bujor (2012), were used by Hykes and Azmy (2014) for several radiation source mapping problems.

4. COMPARATIVE DISCUSSION AND CONCLUSIONS

It is clear from the presentation in Sections 2 and 3 that the Levenberg-Marquardt method is not only the oldest (chronologically) but also the least sophisticated and possibly the easiest to apply. Tichonov's method represents the next level of complexity and sophistication. Comparing Eq. (LM) with Eq. (T), it becomes apparent that the first term in Eq. (T) subsumes elements of the LM-method, bur has an additional term that controls the solution's smoothness. When implemented correctly, Tichonov's method provides convexity and compactness in the problem. However, even when done correctly, Tichonov's method actually changes the original problem into new ones (depending on the value of the parameter λ^2), and solutions to the new problems may not be close to those of original problem. Moreover, because of the discretionary user-parameter λ^2, it is not possible to compute quantitatively the error between the true, but actually unknown solution and the "regularized" solution.

Comparing Eq. (FILS-T) to Eq. (T), indicates that both expressions have similar terms, but the FILS-T functional contains the actual covariance matrices for modeling the respective uncertainties, while Tichonov's method contains the arbitrary parameter λ^2 in their stead. In addition, the FILS-T method provides a "goodness of fit" metric, χ^2_{FILS-T}, which no other method, except for Cacuci's method, provides.

Cacuci's method can be compared to the FILS-T method by comparing Eq. (2.29) to Eq. (FILS-T). Clearly, Cacuci's method is considerably more comprehensive than the others, treating efficiently and explicitly coupled multi-physics systems. In fact, even when reduced to a single multi-physics system, Cacuci's method is more general than all of the other methods, comprising them as particular cases (see Appendix A), which are reproduced below, for convenience:

$$\boldsymbol{\alpha}^{pred} = \boldsymbol{\alpha}^0 - \left(\mathbf{C}_{\alpha\alpha}\mathbf{S}_{r\alpha}^{\dagger} - \mathbf{C}_{\alpha r}\right)\left[\mathbf{S}_{r\alpha}\mathbf{C}_{\alpha\alpha}\mathbf{S}_{r\alpha}^{\dagger} - \mathbf{S}_{r\alpha}\mathbf{C}_{\alpha r} - \mathbf{C}_{\alpha r}^{\dagger}\mathbf{S}_{r\alpha}^{\dagger} + \mathbf{C}_{rr}\right]^{-1}\left(\mathbf{r}^c - \mathbf{r}^m\right), \qquad \text{(C.1a)}$$

$$\mathbf{r}^{pred} = \mathbf{r}^m - \left(\mathbf{C}_{\alpha r}^{\dagger}\mathbf{S}_{r\alpha}^{\dagger} - \mathbf{C}_{rr}\right)\left[\mathbf{S}_{r\alpha}\mathbf{C}_{\alpha\alpha}\mathbf{S}_{r\alpha}^{\dagger} - \mathbf{S}_{r\alpha}\mathbf{C}_{\alpha r} - \mathbf{C}_{\alpha r}^{\dagger}\mathbf{S}_{r\alpha}^{\dagger} + \mathbf{C}_{rr}\right]^{-1}\left(\mathbf{r}^c - \mathbf{r}^m\right), \qquad \text{(C.3a)}$$

$$\mathbf{C}_{\alpha\alpha}^{pred} = \mathbf{C}_{\alpha\alpha} - \left(\mathbf{C}_{\alpha\alpha}\mathbf{S}_{r\alpha}^{\dagger} - \mathbf{C}_{\alpha r}\right)\left[\mathbf{S}_{r\alpha}\mathbf{C}_{\alpha\alpha}\mathbf{S}_{r\alpha}^{\dagger} - \mathbf{S}_{r\alpha}\mathbf{C}_{\alpha r} - \mathbf{C}_{\alpha r}^{\dagger}\mathbf{S}_{r\alpha}^{\dagger} + \mathbf{C}_{rr}\right]^{-1}\left(\mathbf{C}_{\alpha\alpha}\mathbf{S}_{r\alpha}^{\dagger} - \mathbf{C}_{\alpha r}\right)^{\dagger}, \qquad \text{(C.5a)}$$

$$\mathbf{C}_{rr}^{pred} = \mathbf{C}_{rr} - \left(\mathbf{C}_{\alpha r}^{\dagger}\mathbf{S}_{r\alpha}^{\dagger} - \mathbf{C}_{rr}\right)\left[\mathbf{S}_{r\alpha}\mathbf{C}_{\alpha\alpha}\mathbf{S}_{r\alpha}^{\dagger} - \mathbf{S}_{r\alpha}\mathbf{C}_{\alpha r} - \mathbf{C}_{\alpha r}^{\dagger}\mathbf{S}_{r\alpha}^{\dagger} + \mathbf{C}_{rr}\right]^{-1}\left(\mathbf{C}_{\alpha r}^{\dagger}\mathbf{S}_{r\alpha}^{\dagger} - \mathbf{C}_{rr}\right)^{\dagger}, \qquad \text{(C.6a)}$$

$$\mathbf{C}_{\alpha r}^{pred} = \mathbf{C}_{\alpha r} - \left(\mathbf{C}_{\alpha\alpha}\mathbf{S}_{r\alpha}^{\dagger} - \mathbf{C}_{\alpha r}\right)\left[\mathbf{S}_{r\alpha}\mathbf{C}_{\alpha\alpha}\mathbf{S}_{r\alpha}^{\dagger} - \mathbf{S}_{r\alpha}\mathbf{C}_{\alpha r} - \mathbf{C}_{\alpha r}^{\dagger}\mathbf{S}_{r\alpha}^{\dagger} + \mathbf{C}_{rr}\right]^{-1}\left(\mathbf{C}_{\alpha r}^{\dagger}\mathbf{S}_{r\alpha}^{\dagger} - \mathbf{C}_{rr}\right)^{\dagger}. \qquad \text{(C.7a)}$$

$$V_C \equiv \chi_C^2 = \left(\mathbf{r}^c - \mathbf{r}^m\right)^{\dagger}\mathbf{D}_{rr}\left(\mathbf{r}^c - \mathbf{r}^m\right). \qquad \text{(C.18a)}$$

The following features become apparent by comparing the above results with the results in Eqs. (FILS-T.1) -(FILS-T.3):

(iii) Cacuci's method calibrates simultaneously all of the model parameters as well as the model responses. In contradistinction, the FILS-T method (as well as all of the other methods used thus far) calibrates only the model responses. Therefore, even for a single model, Cacuci's method yields additional results [e.g., Eqs. (C.3a) and (C.6a), above] by comparison to all of the other methods currently available.

(iv) Cacuci's method takes into account correlations between model parameters and model responses. No other method has this capability. Therefore, Cacuci's method yields predicted covariance matrices between parameters and responses, cf. Eq. (C.7a), above, for a single model. Note that after having applied Cacuci's method to assimilate the experimentally available information, the responses and parameters will become correlated, even if they were uncorrelated initially; in other words, $\mathbf{C}_{\alpha r}^{pred} \neq 0$ even if $\mathbf{C}_{\alpha r} = 0$.

(v) Setting $\mathbf{C}_{\alpha r} = 0$ (i.e., assuming no prior correlations among the model's parameters and responses) in Cacuci's results for a single model reduce to those of the FILS-T method. Specifically, when $\mathbf{C}_{\alpha r} = 0$, we note that: Eq. (C.1a) = Eq. (FILS-T.1); Eq. (C.6a) = Eq. (FILS-T.2), Eq. (C.18a) = Eq. (FILS-T.3).

The discussion above highlights the fact that Cacuci's methodology (2012) for "*predictive modeling of coupled multi-physics systems*" provides the most comprehensive methodology to date for analyzing inverse problems in the presence of computational and experimental uncertainties. This methodology enables predictive modeling for coupled multi-physics systems, taking fully into account the coupling terms between the systems but using only the computational resources that would be needed to perform predictive modeling on each system separately. The methodology uses the maximum entropy principle to construct an optimal approximation of the unknown a priori distribution for the a priori known mean values and covariances characterizing the parameters and responses for both multi-physics models. This approximate a priori distribution is combined using Bayes' theorem with the "likelihood" provided by the two multi-physics simulation models. Subsequently, the posterior distribution is evaluated using the saddle-point method to obtain analytical expressions for the optimally predicted values for the parameters and responses of both multi-physics models, along with corresponding reduced uncertainties for both the model parameters and responses.

Noteworthy, Cacuci's methodology for coupled systems is constructed such that the systems can be considered sequentially rather than simultaneously, while preserving exactly the same results as if the systems were treated simultaneously. Consequently, very large coupled multi-physics systems, which could perhaps exceed the available computational resources if treated simultaneously, can be treated with Cacuci's methodology sequentially and without any loss of generality or information, requiring just the resources that would be needed if the systems were treated sequentially. This feature enables the treatment of very large systems which would currently exceed the computational resources available if treated with conventional data assimilation procedures.

In particular, Cacuci's methodology would be ideally suited for performing large-scale coupled neutron-gamma inverse transport problems, in which the neutron and, respectively, the gamma transport computations would be performed using distinct computational tools.

REFERENCES

Bledsoe, K.C., Favorite, J. A., and Aldemir, T., 2011, "Using the Levenberg-Marquardt Method for Solutions of Inverse Transport Problems in One- and Two-Dimensional Geometries", *Nucl. Techn.*, **176**, 106.

Cacuci, D.G., 1981a, "Sensitivity theory for nonlinear systems: I. Nonlinear functional analysis approach". *J., Math. Phys*. **22**, 2794–2802.

Cacuci, D.G., 1981b, "Sensitivity theory for nonlinear systems: II. Extensions to additional classes of responses"., *J. Math. Phys***. 22**, 2803–2812.

Cacuci, D.G., 2003, *Sensitivity and Uncertainty Analysis*: Theory, Vol. 1, Chapman & Hall/CRC, Boca Raton.

Cacuci, D.G., 2014, "Predictive modeling of coupled multi-physics systems: I. Theory", *Ann. Nucl. Energy*, **70**, 266–278.

Cacuci, D.G., Badea, M. C., 2014, "Predictive Modeling of Coupled Multi-Physics Systems: II. Illustrative Application to Reactor Physics," *Annals of Nuclear Energy*, **70**, 279 –291.

Cacuci, D.G., Ionescu-Bujor, M., 2010, "Model Calibration and Best-Estimate Prediction Through Experimental Data Assimilation: I. Mathematical Framework," *Nucl. Sci. Eng.*, **165**, 18-44.

Cacuci, D.G., Navon, M.I., Ionescu-Bujor, M., 2013, *Computational Methods for Data Evaluation and Assimilation*. Chapman & Hall/CRC, Boca Raton.

Faragó, I., Havasi, Á., and Zlatev, Z., (Editors), 2014, *Advanced Numerical Methods for Complex Environmental Models: Needs and Availability,* Bentham Science Publishers.

Hykes, J. M., and Azmy, Y. Y., 2014, "Radiation Source Mapping with Bayesian Inverse Methods," *Nucl. Sci. Eng.*,

Jarman, K.D., Miller, E.I, Wittman, R. S., and Gesh, C.J.,2011, "Bayesian Radiation Source Localization", *Nuclear Technology*, **175**, 326–334.

Levenberg, K., 1944, "A method for the solution of certain nonlinear problems in least squares", *Quart. Appl. Math.*, **2**, 164–168.

Marquardt, D.W., 1963, "An algorithm for least-squares estimation of nonlinear parameters," *J. Soc. Indust. Appl. Math.*, **11**, 431–441.

Tarantola, A., 2005, *Inverse problem theory and methods for model parameter estimation*, Society for Industrial & Applied Mathematics.

Tichonov, A. N., 1963, "Regularization of Non-Linear Ill-Posed Problems", *Doklady Akademii Nauk*, **49**(4). See also: A. N. Tichonov, "Solution of Incorrectly Formulated Problems and the Regularization Method", *Soviet Math. Doklady*, **4**, 1035 (1963).

APPENDIX A: EXPLICIT RESULTS FOR CACUCI'S INVERSE PREDICTIVE MODELING METHODOLOGY

Note: *The numbering of equations in this Appendix connects without interruption to the numbering of equations in Section 2, since the equations in this Appendix are the logical continuation of Cacuci's inverse modeling methodology presented in Section 2.*

To first-order in the parameter variations the model responses $\mathbf{r}$ (for *Model A*) and $\mathbf{q}$ (for *Model B*) would be linear functions of the parameter variations of the form

$$\mathbf{r} = \mathbf{r}^c\left(\boldsymbol{\alpha}^0, \boldsymbol{\beta}^0\right) + \mathbf{S}_{r\alpha}\left(\boldsymbol{\alpha} - \boldsymbol{\alpha}^0\right) + \mathbf{S}_{r\beta}\left(\boldsymbol{\beta} - \boldsymbol{\beta}^0\right) + \textit{higher order terms}, \tag{2.39}$$

$$\mathbf{q} = \mathbf{q}^c\left(\boldsymbol{\alpha}^0, \boldsymbol{\beta}^0\right) + \mathbf{S}_{q\alpha}\left(\boldsymbol{\alpha} - \boldsymbol{\alpha}^0\right) + \mathbf{S}_{q\beta}\left(\boldsymbol{\beta} - \boldsymbol{\beta}^0\right) + \textit{higher order terms}. \tag{2.40}$$

In particular, *for the predicted parameter values* $\boldsymbol{\alpha}^{pred}$ *and* $\boldsymbol{\beta}^{pred}$**,** *the responses predicted by the linearized models would be given the following expressions:*

$$\mathbf{r}^{pred} = \mathbf{r}^{c}\left(\boldsymbol{\alpha}^{0},\boldsymbol{\beta}^{0}\right) + \mathbf{S}_{r\alpha}\left(\boldsymbol{\alpha}^{pred} - \boldsymbol{\alpha}^{0}\right) + \mathbf{S}_{r\beta}\left(\boldsymbol{\beta}^{pred} - \boldsymbol{\beta}^{0}\right) + \textit{higher order terms}, \quad (2.41)$$

$$\mathbf{q}^{pred} = \mathbf{q}^{c}\left(\boldsymbol{\alpha}^{0},\boldsymbol{\beta}^{0}\right) + \mathbf{S}_{q\alpha}\left(\boldsymbol{\alpha}^{pred} - \boldsymbol{\alpha}^{0}\right) + \mathbf{S}_{q\beta}\left(\boldsymbol{\beta}^{pred} - \boldsymbol{\beta}^{0}\right) + \textit{higher order terms}. \quad (2.42)$$

The following intermediate steps are now performed in order to eliminate the Lagrange multipliers: (i) replace $\mathbf{r}^{pred}$ and $\mathbf{q}^{pred}$ from Eqs. (2.41) and (2.42) into Eqs. (2.35) through (2.38) to obtain a system of four equations for the four unknowns $\left(\boldsymbol{\alpha}^{pred},\boldsymbol{\beta}^{pred},\boldsymbol{\lambda}_{r},\boldsymbol{\lambda}_{q}\right)$; (ii) from this system, eliminate the quantities $\left(\boldsymbol{\alpha}^{pred} - \boldsymbol{\alpha}^{0}\right)$ and $\left(\boldsymbol{\beta}^{pred} - \boldsymbol{\beta}^{0}\right)$; and (iii) re-arrange the resulting equations to obtain the following coupled equations for the Lagrange multipliers:

$$\begin{bmatrix} \mathbf{D}_{rr} & \mathbf{D}_{rq} \\ \mathbf{D}_{qr} & \mathbf{D}_{qq} \end{bmatrix} \begin{bmatrix} \boldsymbol{\lambda}_{r} \\ \boldsymbol{\lambda}_{q} \end{bmatrix} = \begin{bmatrix} \mathbf{r}^{d}\left(\boldsymbol{\alpha}^{0},\boldsymbol{\beta}^{0}\right) \\ \mathbf{q}^{d}\left(\boldsymbol{\alpha}^{0},\boldsymbol{\beta}^{0}\right) \end{bmatrix}, \quad (2.43)$$

where the block-matrix of known quantities on the left-side, and the block-vector of known quantities on the right-side of the above equations are defined as follows:

$$\mathbf{D}_{rr} \equiv \mathbf{S}_{r\alpha}\left(\mathbf{C}_{\alpha\alpha}\mathbf{S}_{r\alpha}^{\dagger} + \mathbf{C}_{\alpha\beta}\mathbf{S}_{r\beta}^{\dagger} - \mathbf{C}_{\alpha r}\right) + \mathbf{S}_{r\beta}\left(\mathbf{C}_{\alpha\beta}^{\dagger}\mathbf{S}_{r\alpha}^{\dagger} + \mathbf{C}_{\beta\beta}\mathbf{S}_{r\beta}^{\dagger} - \mathbf{C}_{\beta r}\right) - \mathbf{C}_{\alpha r}^{\dagger}\mathbf{S}_{r\alpha}^{\dagger} - \mathbf{C}_{\beta r}^{\dagger}\mathbf{S}_{r\beta}^{\dagger} + \mathbf{C}_{rr}, \quad (2.44)$$

$$\mathbf{D}_{rq} \equiv \mathbf{S}_{r\alpha}\left(\mathbf{C}_{\alpha\alpha}\mathbf{S}_{q\alpha}^{\dagger} + \mathbf{C}_{\alpha\beta}\mathbf{S}_{q\beta}^{\dagger} - \mathbf{C}_{\alpha q}\right) + \mathbf{S}_{r\beta}\left(\mathbf{C}_{\alpha\beta}^{\dagger}\mathbf{S}_{q\alpha}^{\dagger} + \mathbf{C}_{\beta\beta}\mathbf{S}_{q\beta}^{\dagger} - \mathbf{C}_{\beta q}\right) - \mathbf{C}_{\alpha r}^{\dagger}\mathbf{S}_{q\alpha}^{\dagger} - \mathbf{C}_{\beta r}^{\dagger}\mathbf{S}_{q\beta}^{\dagger} + \mathbf{C}_{rq}, \quad (2.45)$$

$$\begin{aligned} \mathbf{D}_{qr} \equiv\ & \mathbf{S}_{q\alpha}\left(\mathbf{C}_{\alpha\alpha}\mathbf{S}_{r\alpha}^{\dagger} + \mathbf{C}_{\alpha\beta}\mathbf{S}_{r\beta}^{\dagger} - \mathbf{C}_{\alpha r}\right) + \mathbf{S}_{q\beta}\left(\mathbf{C}_{\alpha\beta}^{\dagger}\mathbf{S}_{r\alpha}^{\dagger} + \mathbf{C}_{\beta\beta}\mathbf{S}_{r\beta}^{\dagger} - \mathbf{C}_{\beta r}\right) \\ & - \mathbf{C}_{\alpha q}^{\dagger}\mathbf{S}_{r\alpha}^{\dagger} - \mathbf{C}_{\beta q}^{\dagger}\mathbf{S}_{r\beta}^{\dagger} + \mathbf{C}_{rq}^{\dagger} = \mathbf{D}_{rq}^{\dagger}, \end{aligned} \quad (2.46)$$

$$\mathbf{D}_{qq} \equiv \mathbf{S}_{q\alpha}\left(\mathbf{C}_{\alpha\alpha}\mathbf{S}_{q\alpha}^{\dagger} + \mathbf{C}_{\alpha\beta}\mathbf{S}_{q\beta}^{\dagger} - \mathbf{C}_{\alpha q}\right) + \mathbf{S}_{q\beta}\left(\mathbf{C}_{\alpha\beta}^{\dagger}\mathbf{S}_{q\alpha}^{\dagger} + \mathbf{C}_{\beta\beta}\mathbf{S}_{q\beta}^{\dagger} - \mathbf{C}_{\beta q}\right) - \mathbf{C}_{\alpha q}^{\dagger}\mathbf{S}_{q\alpha}^{\dagger} - \mathbf{C}_{\beta q}^{\dagger}\mathbf{S}_{\beta q}^{\dagger} + \mathbf{C}_{qq}, \quad (2.47)$$

$$\mathbf{r}^{d}\left(\boldsymbol{\alpha}^{0},\boldsymbol{\beta}^{0}\right) \equiv \mathbf{r}^{c}\left(\boldsymbol{\alpha}^{0},\boldsymbol{\beta}^{0}\right) - \mathbf{r}^{m}; \qquad \mathbf{q}^{d}\left(\boldsymbol{\alpha}^{0},\boldsymbol{\beta}^{0}\right) \equiv \mathbf{q}^{c}\left(\boldsymbol{\alpha}^{0},\boldsymbol{\beta}^{0}\right) - \mathbf{q}^{m}. \quad (2.48)$$

Note that *the vectors* $\mathbf{r}^{d}\left(\boldsymbol{\alpha}^{0},\boldsymbol{\beta}^{0}\right)$ *and* $\mathbf{q}^{d}\left(\boldsymbol{\alpha}^{0},\boldsymbol{\beta}^{0}\right)$ *measure the differences ("deviations") between the computed and measured responses.* Note also that the matrices defined in Eqs.

(2.44) through (2.47) have the following dimensions: $\dim \mathbf{D}_{rr} = \left(N_r \times N_r\right)$; $\dim \mathbf{D}_{rq} = \left(N_r \times N_q\right)$; $\dim \mathbf{D}_{qr} = \mathbf{D}_{rq}^{\dagger} = \left(N_q \times N_r\right)$; and $\dim \mathbf{D}_{qq} = \left(N_q \times N_q\right)$.

(i) The matrix $\mathbf{D}_{rr}$ is actually the covariance matrix of the vector of response "deviations" for *Model A*, i.e.,

$$\mathbf{D}_{rr} = \left\langle \mathbf{r}^d\left(\boldsymbol{\alpha}^0, \boldsymbol{\beta}^0\right)\left[\mathbf{r}^d\left(\boldsymbol{\alpha}^0, \boldsymbol{\beta}^0\right)\right]^{\dagger}\right\rangle; \tag{2.49}$$

(ii) The matrix $\mathbf{D}_{qq}$ is actually the covariance matrix of the vector of response "deviations" for *Model B*, i.e.,

$$\mathbf{D}_{qq} = \left\langle \mathbf{q}^d\left(\boldsymbol{\alpha}^0, \boldsymbol{\beta}^0\right)\left[\mathbf{q}^d\left(\boldsymbol{\alpha}^0, \boldsymbol{\beta}^0\right)\right]^{\dagger}\right\rangle; \tag{2.50}$$

(iii) The matrix $\mathbf{D}_{rq} = \mathbf{D}_{rq}^{\dagger}$ is actually the correlation matrix between the vector of response "deviations" for *Model A and Model B*, i.e.,

$$\mathbf{D}_{rq} = \left\langle \mathbf{q}^d\left(\boldsymbol{\alpha}^0, \boldsymbol{\beta}^0\right)\left[\mathbf{r}^d\left(\boldsymbol{\alpha}^0, \boldsymbol{\beta}^0\right)\right]^{\dagger}\right\rangle; \qquad \mathbf{D}_{qr} = \left\langle \mathbf{r}^d\left(\boldsymbol{\alpha}^0, \boldsymbol{\beta}^0\right)\left[\mathbf{q}^d\left(\boldsymbol{\alpha}^0, \boldsymbol{\beta}^0\right)\right]^{\dagger}\right\rangle. \tag{2.51}$$

The Lagrange multipliers $\boldsymbol{\lambda}_r$ and $\boldsymbol{\lambda}_q$ are obtained by solving Eq. (2.41), which requires the inverse of the matrix

$$\mathbf{D} \equiv \begin{bmatrix} \mathbf{D}_{rr} & \mathbf{D}_{rq} \\ \mathbf{D}_{rq}^{\dagger} & \mathbf{D}_{qq} \end{bmatrix} \tag{2.52}$$

The above matrix can be inverted by partitioning it to obtain

$$\mathbf{D}^{-1} \equiv \begin{bmatrix} \mathbf{D}_{11} & \mathbf{D}_{12} \\ \mathbf{D}_{12}^{\dagger} & \mathbf{D}_{22} \end{bmatrix}, \tag{2.53}$$

where

$$\mathbf{D}_{11} \equiv \mathbf{D}_{rr}^{-1} + \mathbf{D}_{rr}^{-1}\mathbf{D}_{rq}\mathbf{D}_{22}\mathbf{D}_{rq}^{\dagger}\mathbf{D}_{rr}^{-1}, \tag{2.54}$$

$$\mathbf{D}_{12} \equiv -\mathbf{D}_{rr}^{-1}\mathbf{D}_{rq}\mathbf{D}_{22}, \tag{2.55}$$

$$\mathbf{D}_{12}^{\dagger} \equiv -\mathbf{D}_{22}\mathbf{D}_{rq}^{\dagger}\mathbf{D}_{rr}^{-1}, \tag{2.56}$$

$$\mathbf{D}_{22} \equiv \left(\mathbf{D}_{qq} - \mathbf{D}_{rq}^{\dagger}\mathbf{D}_{rr}^{-1}\mathbf{D}_{rq}\right)^{-1}. \tag{2.57}$$

After obtaining the expressions of $\boldsymbol{\lambda}_r$ and $\boldsymbol{\lambda}_q$ by solving Eq. (2.43), they are replaced in Eqs. (2.35)-(2.38) to obtain the following expressions for the optimally predicted values of model parameters and responses:

$$\boldsymbol{\alpha}^{pred} = \boldsymbol{\alpha}^0 - \left[\mathbf{X}_\alpha \mathbf{D}_{11} + \mathbf{Y}_\alpha \mathbf{D}_{12}^\dagger\right]\mathbf{r}^d\left(\boldsymbol{\alpha}^0, \boldsymbol{\beta}^0\right) - \left[\mathbf{X}_\alpha \mathbf{D}_{12} + \mathbf{Y}_\alpha \mathbf{D}_{22}\right]\mathbf{q}^d\left(\boldsymbol{\alpha}^0, \boldsymbol{\beta}^0\right), \quad (2.58)$$

$$\boldsymbol{\beta}^{pred} = \boldsymbol{\beta}^0 - \left[\mathbf{X}_\beta \mathbf{D}_{11} + \mathbf{Y}_\beta \mathbf{D}_{12}^\dagger\right]\mathbf{r}^d\left(\boldsymbol{\alpha}^0, \boldsymbol{\beta}^0\right) - \left[\mathbf{X}_\beta \mathbf{D}_{12} + \mathbf{Y}_\beta \mathbf{D}_{22}\right]\mathbf{q}^d\left(\boldsymbol{\alpha}^0, \boldsymbol{\beta}^0\right), \quad (2.59)$$

$$\mathbf{r}^{pred} = \mathbf{r}^m - \left[\mathbf{X}_r \mathbf{D}_{11} + \mathbf{Y}_r \mathbf{D}_{12}^\dagger\right]\mathbf{r}^d\left(\boldsymbol{\alpha}^0, \boldsymbol{\beta}^0\right) - \left[\mathbf{X}_r \mathbf{D}_{12} + \mathbf{Y}_r \mathbf{D}_{22}\right]\mathbf{q}^d\left(\boldsymbol{\alpha}^0, \boldsymbol{\beta}^0\right), \quad (2.60)$$

$$\mathbf{q}^{pred} = \mathbf{q}^m - \left[\mathbf{X}_q \mathbf{D}_{11} + \mathbf{Y}_q \mathbf{D}_{12}^\dagger\right]\mathbf{r}^d\left(\boldsymbol{\alpha}^0, \boldsymbol{\beta}^0\right) - \left[\mathbf{X}_q \mathbf{D}_{12} + \mathbf{Y}_q \mathbf{D}_{22}\right]\mathbf{q}^d\left(\boldsymbol{\alpha}^0, \boldsymbol{\beta}^0\right), \quad (2.61)$$

where

$$\mathbf{X}_\alpha \equiv \mathbf{C}_{\alpha\alpha}\mathbf{S}_{r\alpha}^\dagger + \mathbf{C}_{\alpha\beta}\mathbf{S}_{r\beta}^\dagger - \mathbf{C}_{\alpha r}, \quad (2.62)$$

$$\mathbf{Y}_\alpha \equiv \mathbf{C}_{\alpha\alpha}\mathbf{S}_{q\alpha}^\dagger + \mathbf{C}_{\alpha\beta}\mathbf{S}_{q\beta}^\dagger - \mathbf{C}_{\alpha q}, \quad (2.63)$$

$$\mathbf{X}_\beta \equiv \mathbf{C}_{\alpha\beta}^\dagger\mathbf{S}_{r\alpha}^\dagger + \mathbf{C}_{\beta\beta}\mathbf{S}_{r\beta}^\dagger - \mathbf{C}_{\beta r}, \quad (2.64)$$

$$\mathbf{Y}_\beta \equiv \mathbf{C}_{\beta\alpha}\mathbf{S}_{q\alpha}^\dagger + \mathbf{C}_{\beta\beta}\mathbf{S}_{q\beta}^\dagger - \mathbf{C}_{\beta q}, \quad (2.65)$$

$$\mathbf{X}_r \equiv \mathbf{C}_{\alpha r}^\dagger\mathbf{S}_{r\alpha}^\dagger + \mathbf{C}_{\beta r}^\dagger\mathbf{S}_{r\beta}^\dagger - \mathbf{C}_{rr}, \quad (2.66)$$

$$\mathbf{Y}_r \equiv \mathbf{C}_{\alpha r}^\dagger\mathbf{S}_{q\alpha}^\dagger + \mathbf{C}_{\beta r}^\dagger\mathbf{S}_{q\beta}^\dagger - \mathbf{C}_{rq}^\dagger, \quad (2.67)$$

$$\mathbf{X}_q \equiv \mathbf{C}_{\alpha q}^\dagger\mathbf{S}_{r\alpha}^\dagger + \mathbf{C}_{\beta q}^\dagger\mathbf{S}_{r\beta}^\dagger - \mathbf{C}_{rq}^\dagger, \quad (2.68)$$

$$\mathbf{Y}_q \equiv \mathbf{C}_{\alpha q}^\dagger\mathbf{S}_{q\alpha}^\dagger + \mathbf{C}_{\beta q}^\dagger\mathbf{S}_{q\beta}^\dagger - \mathbf{C}_{qq}. \quad (2.69)$$

The computations of the optimal predicted covariance matrices for the responses and parameters involve tedious. We present below just the final results:

14. The predicted optimal covariance matrix $\mathbf{C}_{\alpha\alpha}^{pred}$ for the parameters $\boldsymbol{\alpha}$ of *Model A*:

$$\begin{aligned}\mathbf{C}_{\alpha\alpha}^{pred} &\equiv \left\langle \left(\boldsymbol{\alpha} - \boldsymbol{\alpha}^{pred}\right)\left(\boldsymbol{\alpha} - \boldsymbol{\alpha}^{pred}\right)^\dagger \right\rangle \\ &= \mathbf{C}_{\alpha\alpha} - \left[\mathbf{X}_\alpha\left(\mathbf{D}_{11}\mathbf{X}_\alpha^\dagger + \mathbf{D}_{12}\mathbf{Y}_\alpha^\dagger\right) + \mathbf{Y}_\alpha\left(\mathbf{D}_{21}\mathbf{X}_\alpha^\dagger + \mathbf{D}_{22}\mathbf{Y}_\alpha^\dagger\right)\right];\end{aligned} \quad (2.70)$$

15. The predicted covariance matrix $\mathbf{C}_{rr}^{pred}$ for the responses $\mathbf{r}$ of *Model A*:

$$\begin{aligned}\mathbf{C}_{rr}^{pred} &\equiv \left\langle \left(\mathbf{r} - \mathbf{r}^{pred}\right)\left(\mathbf{r} - \mathbf{r}^{pred}\right)^\dagger \right\rangle \\ &= \mathbf{C}_{rr} - \left[\mathbf{X}_r\left(\mathbf{D}_{11}\mathbf{X}_r^\dagger + \mathbf{D}_{12}\mathbf{Y}_r^\dagger\right) + \mathbf{Y}_r\left(\mathbf{D}_{21}\mathbf{X}_r^\dagger + \mathbf{D}_{22}\mathbf{Y}_r^\dagger\right)\right];\end{aligned} \quad (2.71)$$

16. The predicted correlation matrix $\mathbf{C}_{\alpha r}^{pred}$ for the parameters $\boldsymbol{\alpha}$ and $\mathbf{r}$ responses of *Model A*:

$$\begin{aligned}\mathbf{C}_{\alpha r}^{pred} &\equiv \left\langle \left(\boldsymbol{\alpha}-\boldsymbol{\alpha}^{pred}\right)\left(\mathbf{r}-\mathbf{r}^{pred}\right)^{\dagger}\right\rangle \\ &= \mathbf{C}_{\alpha r}-\left[\mathbf{X}_{\alpha}\left(\mathbf{D}_{11}\mathbf{X}_{r}^{\dagger}+\mathbf{D}_{12}\mathbf{Y}_{r}^{\dagger}\right)+\mathbf{Y}_{\alpha}\left(\mathbf{D}_{21}\mathbf{X}_{r}^{\dagger}+\mathbf{D}_{22}\mathbf{Y}_{r}^{\dagger}\right)\right];\end{aligned} \tag{2.72}$$

17. The predicted covariance matrix $\mathbf{C}_{\beta\beta}^{pred}$ for the parameters $\boldsymbol{\beta}$ of *Model B*:

$$\begin{aligned}\mathbf{C}_{\beta\beta}^{pred} &\equiv \left\langle \left(\boldsymbol{\beta}-\boldsymbol{\beta}^{pred}\right)\left(\boldsymbol{\beta}-\boldsymbol{\beta}^{pred}\right)^{\dagger}\right\rangle \\ &= \mathbf{C}_{\beta\beta}-\left[\mathbf{X}_{\beta}\left(\mathbf{D}_{11}\mathbf{X}_{\beta}^{\dagger}+\mathbf{D}_{12}\mathbf{Y}_{\beta}^{\dagger}\right)+\mathbf{Y}_{\beta}\left(\mathbf{D}_{21}\mathbf{X}_{\beta}^{\dagger}+\mathbf{D}_{22}\mathbf{Y}_{\beta}^{\dagger}\right)\right];\end{aligned} \tag{2.73}$$

18. The predicted covariance matrix $\mathbf{C}_{qq}^{pred}$ for the responses $\mathbf{q}$ of *Model B*:

$$\begin{aligned}\mathbf{C}_{qq}^{pred} &\equiv \left\langle \left(\mathbf{q}-\mathbf{q}^{pred}\right)\left(\mathbf{q}-\mathbf{q}^{pred}\right)^{\dagger}\right\rangle \\ &= \mathbf{C}_{qq}-\left[\mathbf{X}_{q}\left(\mathbf{D}_{11}\mathbf{X}_{q}^{\dagger}+\mathbf{D}_{12}\mathbf{Y}_{q}^{\dagger}\right)+\mathbf{Y}_{q}\left(\mathbf{D}_{21}\mathbf{X}_{q}^{\dagger}+\mathbf{D}_{22}\mathbf{Y}_{q}^{\dagger}\right)\right];\end{aligned} \tag{2.74}$$

19. The predicted correlation matrix $\mathbf{C}_{\beta q}^{pred}$ for the parameters $\boldsymbol{\beta}$ and the responses $\mathbf{q}$ of *Model B*:

$$\begin{aligned}\mathbf{C}_{\beta q}^{opt} &\equiv \left\langle \left(\boldsymbol{\beta}-\boldsymbol{\beta}^{pred}\right)\left(\mathbf{q}-\mathbf{q}^{pred}\right)^{\dagger}\right\rangle \\ &= \mathbf{C}_{\beta q}-\left[\mathbf{X}_{\beta}\left(\mathbf{D}_{11}\mathbf{X}_{q}^{\dagger}+\mathbf{D}_{12}\mathbf{Y}_{q}^{\dagger}\right)+\mathbf{Y}_{\beta}\left(\mathbf{D}_{21}\mathbf{X}_{q}^{\dagger}+\mathbf{D}_{22}\mathbf{Y}_{q}^{\dagger}\right)\right];\end{aligned} \tag{2.75}$$

20. The predicted correlation matrix $\mathbf{C}_{\alpha\beta}^{pred}$ for the parameters $\boldsymbol{\alpha}$ of *Model A* and the parameters $\boldsymbol{\beta}$ of *Model B:*

$$\begin{aligned}\mathbf{C}_{\alpha\beta}^{pred} &\equiv \left\langle \left(\boldsymbol{\alpha}-\boldsymbol{\alpha}^{pred}\right)\left(\boldsymbol{\beta}-\boldsymbol{\beta}^{pred}\right)^{\dagger}\right\rangle \\ &= \mathbf{C}_{\alpha\beta}-\left[\mathbf{X}_{\alpha}\left(\mathbf{D}_{11}\mathbf{X}_{\beta}^{\dagger}+\mathbf{D}_{12}\mathbf{Y}_{\beta}^{\dagger}\right)+\mathbf{Y}_{\alpha}\left(\mathbf{D}_{21}\mathbf{X}_{\beta}^{\dagger}+\mathbf{D}_{22}\mathbf{Y}_{\beta}^{\dagger}\right)\right];\end{aligned} \tag{2.76}$$

21. The predicted correlation matrix $\mathbf{C}_{\alpha q}^{pred}$ for the parameters $\boldsymbol{\alpha}$ of *Model A* and the responses $\mathbf{q}$ of *Model B:*

$$\begin{aligned}\mathbf{C}_{\alpha q}^{pred} &\equiv \left\langle \left(\boldsymbol{\alpha}-\boldsymbol{\alpha}^{pred}\right)\left(\mathbf{q}-\mathbf{q}^{pred}\right)^{\dagger}\right\rangle \\ &= \mathbf{C}_{\alpha q}-\left[\mathbf{X}_{\alpha}\left(\mathbf{D}_{11}\mathbf{X}_{q}^{\dagger}+\mathbf{D}_{12}\mathbf{Y}_{q}^{\dagger}\right)+\mathbf{Y}_{\alpha}\left(\mathbf{D}_{21}\mathbf{X}_{q}^{\dagger}+\mathbf{D}_{22}\mathbf{Y}_{q}^{\dagger}\right)\right];\end{aligned} \tag{2.77}$$

22. The predicted correlation matrix $\mathbf{C}_{\beta r}^{pred}$ for the parameters $\boldsymbol{\beta}$ of *Model B* and the responses $\mathbf{r}$ of *Model A:*

$$\begin{aligned}\mathbf{C}_{\beta r}^{pred} &\equiv \left\langle \left(\boldsymbol{\beta}-\boldsymbol{\beta}^{pred}\right)\left(\mathbf{r}-\mathbf{r}^{pred}\right)^{\dagger}\right\rangle \\ &= \mathbf{C}_{\beta r}-\left[\mathbf{X}_{\beta}\left(\mathbf{D}_{11}\mathbf{X}_{r}^{\dagger}+\mathbf{D}_{12}\mathbf{Y}_{r}^{\dagger}\right)+\mathbf{Y}_{\beta}\left(\mathbf{D}_{21}\mathbf{X}_{r}^{\dagger}+\mathbf{D}_{22}\mathbf{Y}_{r}^{\dagger}\right)\right];\end{aligned} \tag{2.78}$$

23. The predicted correlation matrix $\mathbf{C}_{rq}^{pred}$ for the responses $\mathbf{r}$ of *Model A* and the responses $\mathbf{q}$ of *Model B:*

$$\begin{aligned}\mathbf{C}_{rq}^{pred} &\equiv \left\langle \left(\mathbf{r}-\mathbf{r}^{pred}\right)\left(\mathbf{q}-\mathbf{q}^{pred}\right)^{\dagger}\right\rangle \\ &= \mathbf{C}_{rq}-\left[\mathbf{X}_{r}\left(\mathbf{D}_{11}\mathbf{X}_{q}^{\dagger}+\mathbf{D}_{12}\mathbf{Y}_{q}^{\dagger}\right)+\mathbf{Y}_{r}\left(\mathbf{D}_{21}\mathbf{X}_{q}^{\dagger}+\mathbf{D}_{22}\mathbf{Y}_{q}^{\dagger}\right)\right].\end{aligned} \tag{2.79}$$

Note also that, to first-order in response sensitivities, the covariance matrices of the computed responses arising from the uncertainties in the model parameters can be computed from Eqs. (2.39) and (2.40), respectively, to obtain:

$$\begin{aligned}\mathbf{C}_{rr}^{comp} &\equiv \left\langle \left[\mathbf{r}-\mathbf{r}^{c}\left(\boldsymbol{\alpha}^{0},\boldsymbol{\beta}^{0}\right)\right]\left[\mathbf{r}-\mathbf{r}^{c}\left(\boldsymbol{\alpha}^{0},\boldsymbol{\beta}^{0}\right)\right]^{\dagger}\right\rangle \\ &= \mathbf{S}_{r\alpha}\mathbf{C}_{\alpha\alpha}\mathbf{S}_{r\alpha}^{\dagger}+2\mathbf{S}_{r\alpha}\mathbf{C}_{\alpha\beta}\mathbf{S}_{r\beta}^{\dagger}+\mathbf{S}_{r\beta}\mathbf{C}_{\beta\beta}\mathbf{S}_{r\beta}^{\dagger},\end{aligned} \tag{2.80}$$

$$\begin{aligned}\mathbf{C}_{qq}^{comp} &\equiv \left\langle \left[\mathbf{q}-\mathbf{q}^{c}\left(\boldsymbol{\alpha}^{0},\boldsymbol{\beta}^{0}\right)\right]\left[\mathbf{q}-\mathbf{q}^{c}\left(\boldsymbol{\alpha}^{0},\boldsymbol{\beta}^{0}\right)\right]^{\dagger}\right\rangle \\ &= \mathbf{S}_{q\alpha}\mathbf{C}_{\alpha\alpha}\mathbf{S}_{q\alpha}^{\dagger}+2\mathbf{S}_{q\alpha}\mathbf{C}_{\alpha\beta}\mathbf{S}_{q\beta}^{\dagger}+\mathbf{S}_{q\beta}\mathbf{C}_{\beta\beta}\mathbf{S}_{q\beta}^{\dagger},\end{aligned} \tag{2.81}$$

$$\begin{aligned}\mathbf{C}_{rq}^{comp} &\equiv \left\langle \left[\mathbf{r}-\mathbf{r}^{c}\left(\boldsymbol{\alpha}^{0},\boldsymbol{\beta}^{0}\right)\right]\left[\mathbf{q}-\mathbf{q}^{c}\left(\boldsymbol{\alpha}^{0},\boldsymbol{\beta}^{0}\right)\right]^{\dagger}\right\rangle \\ &= \mathbf{S}_{r\alpha}\mathbf{C}_{\alpha\alpha}\mathbf{S}_{q\alpha}^{\dagger}+\mathbf{S}_{r\alpha}\mathbf{C}_{\alpha\beta}\mathbf{S}_{q\alpha}^{\dagger}+\mathbf{S}_{r\beta}\mathbf{C}_{\alpha\beta}^{\dagger}\mathbf{S}_{q\alpha}^{\dagger}+\mathbf{S}_{r\beta}\mathbf{C}_{\beta\beta}\mathbf{S}_{q\beta}^{\dagger}.\end{aligned} \tag{2.82}$$

Construction of the A Posteriori Predicted Consistency Metrics for Model Validation

At the saddle-point $\left(\boldsymbol{\alpha}^{pred},\boldsymbol{\beta}^{pred},\mathbf{r}^{pred},\mathbf{q}^{pred}\right)$, the functional $P\left(\boldsymbol{\alpha},\boldsymbol{\beta},\mathbf{r},\mathbf{q}\right)$ defined in Eq.(2.29), and the first-order computational model equations become

$$P^{\min} = \begin{pmatrix} \boldsymbol{\alpha}^{pred} - \boldsymbol{\alpha}^{0} \\ \boldsymbol{\beta}^{pred} - \boldsymbol{\beta}^{0} \\ \mathbf{r}^{pred} - \mathbf{r}^{m} \\ \mathbf{q}^{pred} - \mathbf{q}^{m} \end{pmatrix}^{\dagger} \mathbf{C}^{-1} \begin{pmatrix} \boldsymbol{\alpha}^{pred} - \boldsymbol{\alpha}^{0} \\ \boldsymbol{\beta}^{pred} - \boldsymbol{\beta}^{0} \\ \mathbf{r}^{pred} - \mathbf{r}^{m} \\ \mathbf{q}^{pred} - \mathbf{q}^{m} \end{pmatrix} \tag{2.83}$$

$$\mathbf{r}^{pred} = \mathbf{r}^{c}\left(\boldsymbol{\alpha}^{0}, \boldsymbol{\beta}^{0}\right) + \mathbf{S}_{r\alpha}\left(\boldsymbol{\alpha}^{pred} - \boldsymbol{\alpha}^{0}\right) + \mathbf{S}_{r\beta}\left(\boldsymbol{\beta}^{pred} - \boldsymbol{\beta}^{0}\right) = \mathbf{r}^{c}\left(\boldsymbol{\alpha}^{pred}, \boldsymbol{\beta}^{pred}\right) \tag{2.84}$$

$$\mathbf{q}^{pred} = \mathbf{q}^{c}\left(\boldsymbol{\alpha}^{0}, \boldsymbol{\beta}^{0}\right) + \mathbf{S}_{q\alpha}\left(\boldsymbol{\alpha}^{pred} - \boldsymbol{\alpha}^{0}\right) + \mathbf{S}_{q\beta}\left(\boldsymbol{\beta}^{pred} - \boldsymbol{\beta}^{0}\right) = \mathbf{q}^{c}\left(\boldsymbol{\alpha}^{opt}, \boldsymbol{\beta}^{opt}\right) \tag{2.85}$$

The values $\left(\boldsymbol{\alpha}^{pred}, \boldsymbol{\beta}^{pred}, \mathbf{r}^{pred}, \mathbf{q}^{pred}\right)$ can be eliminated from the expression of by using Eqs. (2.84) and (2.85) together with Eq. (2.32) to obtain

$$P^{\min} \equiv V = \left[\left(\mathbf{r}^{d}\right)^{\dagger}, \left(\mathbf{q}^{d}\right)^{\dagger}\right] \begin{bmatrix} \mathbf{D}_{11} & \mathbf{D}_{12} \\ \mathbf{D}_{12}^{\dagger} & \mathbf{D}_{22} \end{bmatrix} \begin{bmatrix} \mathbf{r}^{d}\left(\boldsymbol{\alpha}^{0}, \boldsymbol{\beta}^{0}\right) \\ \mathbf{q}^{d}\left(\boldsymbol{\alpha}^{0}, \boldsymbol{\beta}^{0}\right) \end{bmatrix}. \tag{2.86}$$

Note that the quadratic form on the rightmost-side of Eq. (2.86) is distributed according to a χ^2 distribution with $\left(N_r + N_q\right)$ degrees of freedom. Note that V can be evaluated directly from the originally given data (i.e., from given parameters and responses, together with their original uncertainties), once the response sensitivities have been computed by either forward or adjoint methods (see, e.g., Cacuci 1981a, 1981b, 2003). Recall that the χ^2 (chi-square) distribution with n degrees of freedom of the continuous variable $x,\ 0 \le x < \infty,$ is defined as

$$P\left(x < \chi^2 < x + dx\right)dx = \frac{1}{2^{n/2}\Gamma\left(n/2\right)} x^{n/2-1} e^{-x/2} dx,\ x > 0,\ \left(n = 1, 2, \ldots\right). \tag{2.87}$$

The χ^2-distribution is a measure of the deviation of a "true distribution" (in this case – the distribution of experimental responses) from the hypothetic one (in this case – a Gaussian). Recall that the mean and variance of x are $\langle x \rangle = n$ and $\mathrm{var}\left(x\right) = 2n$. The value of χ^2 is computed using Eq. (2.86) to obtain

$$V \equiv \chi^2 = \left(\mathbf{r}^{c} - \mathbf{r}^{m}\right)^{\dagger} \mathbf{D}_{11} \left(\mathbf{r}^{c} - \mathbf{r}^{m}\right) + 2\left(\mathbf{r}^{c} - \mathbf{r}^{m}\right)^{\dagger} \mathbf{D}_{12} \left(\mathbf{q}^{c} - \mathbf{q}^{m}\right) + \left(\mathbf{q}^{c} - \mathbf{q}^{m}\right)^{\dagger} \mathbf{D}_{22} \left(\mathbf{q}^{c} - \mathbf{q}^{m}\right). \tag{2.88}$$

The value of χ^2 computed using Eq. (2.88) provides a very valuable quantitative indicator for investigating the agreement between the computed and experimental responses, measuring essentially the consistency of the experimental responses with the model

parameters. The value of V can be used as a validation metric for measuring the consistency between the computed and experimentally measured responses.

DISCUSSION AND PARTICULAR CASES

The derivations in the previous section were carried out in the response-space because in large-scale practical problems, the number of measured responses is smaller than the number of model parameters. The only matrix inversion required in the response space is the computation of $\mathbf{D}^{-1}$ in Eq. (2.53), which is of size $\left(N_r + N_q\right)^2$. If this matrix is too large to be inverted directly, as has been assumed in this work, its inversion can be performed by partitioning it as shown in Eqs. (2.54) – (2.57). The inversion of $\mathbf{D}$ by partitioning requires only the inversion of the matrix $\mathbf{D}_{rr}$ of size N_r, and the inversion of the matrix $\left(\mathbf{D}_{qq} - \mathbf{D}_{rq}^{\dagger}\mathbf{D}_{rr}^{-1}\mathbf{D}_{rq}\right)$, which is of size N_q.

Cacuci's predictive modeling methodology presented in Section 2 can also be used if one starts with the data assimilation and model calibration for one of the Models (either *Model A* or *Model B*), and subsequently couples the second model to the first one. Without the *PMCMPS* methodology, when the second Model (e.g., *Model B*) is coupled to the first one (e.g., *Model A*), both models would have to be calibrated anew, simultaneously, and the work performed initially for calibrating *Model A* alone would become useless. Using this methodology, however, the work initially performed for calibrating *Model A* would not become useless, but would simply be augmented by the specific additional terms arising from *Model B, thus performing predictive modeling of coupled multi-physics systems in a sequential and more efficient way.*

It is also important to note that the explicit separation, in Eqs. (2.85) through (2.88), of contributions from *Model A* and *Model B* to the overall validation metric V enables the explicit evaluation of adding or subtracting measured responses. As is well known, large contributions to V indicate that the respective responses may be inconsistent or discrepant, and such discrepancies warrant further investigations.

It often happens in practice that, *after one has already performed a model calibration, e.g., using Model A* (involving N_α model parameters α_n and N_r experimentally measured responses r_i), *additional measurements may become available and/or additional parameters* (which were not considered in the initial data assimilation/model calibration/predictive modeling procedure) *may need to be taken into account* (e.g., model parameters for which quantified uncertainties became available only after the initial data assimilation/model calibration/predictive modeling procedure was already performed), all *for the same Model A*. The *predictive modeling methodology presented in Section 2 can also be used as a most efficient procedure for systematically adding or subtracting responses and/or parameters for performing a subsequent data assimilation/model calibration/predictive modeling procedure on the same model*. In this interpretation/usage

of the predictive modeling methodology presented in Section 2, *Model B* is considered to be identical to *Model A* (i.e., *Model B* and *Model A* represent the same physical phenomena, described by identical mathematical equations). In this context, *"efficient" means "without wasting the information already obtained in previous predictive modeling computations involving a different (higher or lower) number of responses and/or model parameters."* As will be shown in the next Sub-section, the mathematical methodology for performing data assimilation/model calibration/predictive modeling by adding and/or subtracting measurements (responses) and/or model parameters to the same model-without needing to discard previous predictive modeling computations-actually amounts to considering particular cases of Cacuci's general predictive modeling methodology presented in Section 2.

Particular Cases

a) "One-Model" Case: Predictive modeling solely for Model A, involving N_α model parameters α_n and N_r experimentally measured responses r_i

In this case, Eq. (2.44) through (2.47) become

$$\mathbf{D}_{rq}=\mathbf{0},\ \mathbf{D}_{qr}=\mathbf{0},\ \mathbf{D}_{qq}=\mathbf{0},\ \mathbf{D}_{rr}=\mathbf{S}_{r\alpha}\mathbf{C}_{\alpha\alpha}\mathbf{S}_{r\alpha}^{\dagger}-\mathbf{S}_{r\alpha}\mathbf{C}_{\alpha r}-\mathbf{C}_{\alpha r}^{\dagger}\mathbf{S}_{r\alpha}^{\dagger}+\mathbf{C}_{rr}. \tag{A.1}$$

$$\mathbf{X}_\alpha\equiv\mathbf{C}_{\alpha\alpha}\mathbf{S}_{r\alpha}^{\dagger}-\mathbf{C}_{\alpha r},\ \ \mathbf{Y}_\alpha\equiv 0,\ \ \mathbf{X}_r\equiv\mathbf{C}_{\alpha r}^{\dagger}\mathbf{S}_{r\alpha}^{\dagger}-\mathbf{C}_{rr},\ \ \mathbf{Y}_r=\mathbf{0}. \tag{A.2}$$

Furthermore, the predictive modeling equations (2.58) through (2.79) reduce to the final results presented originally by Cacuci and Ionescu-Bujor (2010), namely:

$$\boldsymbol{\alpha}^{pred}=\boldsymbol{\alpha}^0-\left(\mathbf{C}_{\alpha\alpha}\mathbf{S}_{r\alpha}^{\dagger}-\mathbf{C}_{\alpha r}\right)\left[\mathbf{D}_{rr}\right]^{-1}\mathbf{r}^d\left(\boldsymbol{\alpha}^0\right), \tag{A.3}$$

$$\mathbf{r}^{pred}=\mathbf{r}^m-\left(\mathbf{C}_{\alpha r}^{\dagger}\mathbf{S}_{r\alpha}^{\dagger}-\mathbf{C}_{rr}\right)\left[\mathbf{D}_{rr}\right]^{-1}\mathbf{r}^d\left(\boldsymbol{\alpha}^0\right), \tag{A.4}$$

$$\mathbf{C}_{\alpha\alpha}^{pred}=\mathbf{C}_{\alpha\alpha}-\left(\mathbf{C}_{\alpha\alpha}\mathbf{S}_{r\alpha}^{\dagger}-\mathbf{C}_{\alpha r}\right)\left[\mathbf{D}_{rr}\right]^{-1}\left(\mathbf{C}_{\alpha\alpha}\mathbf{S}_{r\alpha}^{\dagger}-\mathbf{C}_{\alpha r}\right)^{\dagger}, \tag{A.5}$$

$$\mathbf{C}_{rr}^{pred}=\mathbf{C}_{rr}-\left(\mathbf{C}_{\alpha r}^{\dagger}\mathbf{S}_{r\alpha}^{\dagger}-\mathbf{C}_{rr}\right)\left[\mathbf{D}_{rr}\right]^{-1}\left(\mathbf{C}_{\alpha r}^{\dagger}\mathbf{S}_{r\alpha}^{\dagger}-\mathbf{C}_{rr}\right)^{\dagger}, \tag{A.6}$$

$$\mathbf{C}_{\alpha r}^{pred}=\mathbf{C}_{\alpha r}-\left(\mathbf{C}_{\alpha\alpha}\mathbf{S}_{r\alpha}^{\dagger}-\mathbf{C}_{\alpha r}\right)\left[\mathbf{D}_{rr}\right]^{-1}\left(\mathbf{C}_{\alpha r}^{\dagger}\mathbf{S}_{r\alpha}^{\dagger}-\mathbf{C}_{rr}\right)^{\dagger}. \tag{A.7}$$

Note that if the model is perfect (i.e., $\mathbf{C}_{\alpha\alpha}=\mathbf{0}$ and $\mathbf{C}_{\alpha r}=\mathbf{0}$), then Eqs. (A.3) through (A.7) would yield $\boldsymbol{\alpha}^{pred}=\boldsymbol{\alpha}^0$ and $\mathbf{r}^{pred}=\mathbf{r}^c\left(\boldsymbol{\alpha}^0,\boldsymbol{\beta}^0\right)$, predicted "perfectly," without any

accompanying uncertainties (i.e., $\mathbf{C}_{rr}^{pred}=\mathbf{0}$, $\mathbf{C}_{\alpha\alpha}^{pred}=\mathbf{0}$, $\mathbf{C}_{\alpha r}^{pred}=\mathbf{0}$). In other words, for a perfect model, Cacuci's methodology predicts values for the responses and the parameters that coincide with the model's values (assumed to be perfect), and the experimental measurements would have no effect on the predictions (as would be expected, since imperfect measurements could not possibly improve the "perfect" model's predictions).

On the other hand, if the measurements were perfect, (i.e., $\mathbf{C}_{rr}=\mathbf{0}$ and $\mathbf{C}_{\alpha r}=\mathbf{0}$), but the model were imperfect, then Eqs. (A.3) through (A.7) would yield $\boldsymbol{\alpha}^{pred}=\boldsymbol{\alpha}^{0}-\mathbf{C}_{\alpha\alpha}\mathbf{S}_{r\alpha}^{\dagger}\left[\mathbf{S}_{r\alpha}\mathbf{C}_{\alpha\alpha}\mathbf{S}_{r\alpha}^{\dagger}\right]^{-1}\mathbf{r}^{d}\left(\boldsymbol{\alpha}^{0}\right)$, $\mathbf{C}_{\alpha\alpha}^{pred}=\mathbf{C}_{\alpha\alpha}-\mathbf{C}_{\alpha\alpha}\mathbf{S}_{r\alpha}^{\dagger}\left[\mathbf{S}_{r\alpha}\mathbf{C}_{\alpha\alpha}\mathbf{S}_{r\alpha}^{\dagger}\right]^{-1}\mathbf{S}_{r\alpha}\mathbf{C}_{\alpha\alpha}$, $\mathbf{r}^{pred}=\mathbf{r}^{m}$, $\mathbf{C}_{rr}^{pred}=\mathbf{0}$, $\mathbf{C}_{\alpha r}^{pred}=\mathbf{0}$. In other words, in the case of perfect measurements, the predicted values for the responses would coincide with the measured values (assumed to be perfect), but the model's uncertain parameters would be calibrated by taking the measurements into account to yield improved nominal values and reduced parameters uncertainties.

b) Predictive modeling for Model A with β additional parameters, but no additional responses

In this case, Eq. (2.44) through (2.47) become

$$\mathbf{D}_{rq}=\mathbf{0},\ \mathbf{D}_{qr}=\mathbf{0},\ \mathbf{D}_{qq}=\mathbf{0}, \tag{A.8}$$

$$\begin{aligned}\mathbf{D}_{rr}=&\mathbf{S}_{r\alpha}\left(\mathbf{C}_{\alpha\alpha}\mathbf{S}_{r\alpha}^{\dagger}+\mathbf{C}_{\alpha\beta}\mathbf{S}_{r\beta}^{\dagger}-\mathbf{C}_{\alpha r}\right)+\mathbf{S}_{r\beta}\left(\mathbf{C}_{\alpha\beta}^{\dagger}\mathbf{S}_{r\alpha}^{\dagger}+\mathbf{C}_{\beta\beta}\mathbf{S}_{r\beta}^{\dagger}-\mathbf{C}_{\beta r}\right)\\&-\mathbf{C}_{\alpha r}^{\dagger}\mathbf{S}_{r\alpha}^{\dagger}-\mathbf{C}_{\beta r}^{\dagger}\mathbf{S}_{r\beta}^{\dagger}+\mathbf{C}_{rr}.\end{aligned} \tag{A.9}$$

$$\mathbf{X}_{\alpha}\equiv\mathbf{C}_{\alpha\alpha}\mathbf{S}_{r\alpha}^{\dagger}+\mathbf{C}_{\alpha\beta}\mathbf{S}_{r\beta}^{\dagger}-\mathbf{C}_{\alpha r}, \tag{A.10}$$

$$\mathbf{X}_{\beta}\equiv\mathbf{C}_{\alpha\beta}^{\dagger}\mathbf{S}_{r\alpha}^{\dagger}+\mathbf{C}_{\beta\beta}\mathbf{S}_{r\beta}^{\dagger}-\mathbf{C}_{\beta r}, \tag{A.11}$$

$$\mathbf{X}_{r}\equiv\mathbf{C}_{\alpha r}^{\dagger}\mathbf{S}_{r\alpha}^{\dagger}+\mathbf{C}_{\beta r}^{\dagger}\mathbf{S}_{r\beta}^{\dagger}-\mathbf{C}_{rr}, \tag{A.12}$$

$$\mathbf{X}_{q}\equiv\mathbf{0},\ \mathbf{Y}_{\alpha}\equiv\mathbf{0},\ \mathbf{Y}_{r}\equiv\mathbf{0},\ \mathbf{Y}_{\beta}\equiv\mathbf{0},\ \mathbf{Y}_{q}\equiv\mathbf{0}, \tag{A.13}$$

$$\mathbf{D}_{11}\equiv\mathbf{D}_{rr}^{-1},\ \mathbf{D}_{12}=\mathbf{0},\ \mathbf{D}_{12}^{\dagger}=\mathbf{0},\ \mathbf{D}_{12}^{\dagger}=\mathbf{0},\ \mathbf{D}_{22}=\mathbf{0}, \tag{A.14}$$

$$\boldsymbol{\alpha}^{pred}=\boldsymbol{\alpha}^{0}-\mathbf{X}_{\alpha}\mathbf{D}_{11}\mathbf{r}^{d}\left(\boldsymbol{\alpha}^{0},\boldsymbol{\beta}^{0}\right), \tag{A.15}$$

$$\boldsymbol{\beta}^{pred}=\boldsymbol{\beta}^{0}-\mathbf{X}_{\beta}\mathbf{D}_{11}\mathbf{r}^{d}\left(\boldsymbol{\alpha}^{0},\boldsymbol{\beta}^{0}\right), \tag{A.16}$$

$$\mathbf{r}^{pred} = \mathbf{r}^{m} - \mathbf{X}_r \mathbf{D}_{11} \mathbf{r}^{d}\left(\boldsymbol{\alpha}^{0}, \boldsymbol{\beta}^{0}\right), \tag{A.17}$$

$$\mathbf{C}_{\alpha\alpha}^{pred} = \mathbf{C}_{\alpha\alpha} - \mathbf{X}_{\alpha} \mathbf{D}_{11} \mathbf{X}_{\alpha}^{\dagger}, \tag{A.18}$$

$$\mathbf{C}_{rr}^{pred} = \mathbf{C}_{rr} - \mathbf{X}_{r} \mathbf{D}_{11} \mathbf{X}_{r}^{\dagger}, \tag{A.19}$$

$$\mathbf{C}_{\alpha r}^{pred} = \mathbf{C}_{\alpha r} - \mathbf{X}_{\alpha} \mathbf{D}_{11} \mathbf{X}_{r}^{\dagger}, \tag{A.20}$$

$$\mathbf{C}_{\beta\beta}^{opt} = \mathbf{C}_{\beta\beta} - \mathbf{X}_{\beta} \mathbf{D}_{11} \mathbf{X}_{\beta}^{\dagger}, \tag{A.21}$$

$$\mathbf{C}_{\alpha\beta}^{pred} = \mathbf{C}_{\alpha\beta} - \mathbf{X}_{\alpha} \mathbf{D}_{11} \mathbf{X}_{\beta}^{\dagger}, \tag{A.22}$$

$$\mathbf{C}_{\beta r}^{pred} = \mathbf{C}_{\beta r} - \mathbf{X}_{\beta} \mathbf{D}_{11} \mathbf{X}_{r}^{\dagger}. \tag{A.23}$$

As the above expressions clearly demonstrate, the predictive modeling formulation in the "response space" (as has been developed in Section 2) allows the consideration of additional parameters for a model without increasing the size of the matrix $\mathbf{D}_{rr}$ to be inverted.

c) Predictive modeling for Model A with *q* additional responses, but no additional parameters

In this case, Eq. (2.44) through (2.47) become

$$\mathbf{D}_{rr} = \mathbf{S}_{r\alpha} \mathbf{C}_{\alpha\alpha} \mathbf{S}_{r\alpha}^{\dagger} - \mathbf{S}_{r\alpha} \mathbf{C}_{\alpha r} - \mathbf{C}_{\alpha r}^{\dagger} \mathbf{S}_{r\alpha}^{\dagger} + \mathbf{C}_{rr} \equiv \mathbf{C}_{d},\ Dim\left(\mathbf{D}_{rr}\right) = \left(N_r \times N_r\right), \tag{A.24}$$

$$\mathbf{D}_{rq} = \mathbf{S}_{r\alpha} \mathbf{C}_{\alpha\alpha} \mathbf{S}_{q\alpha}^{\dagger} - \mathbf{S}_{r\alpha} \mathbf{C}_{\alpha q} - \mathbf{C}_{\alpha r}^{\dagger} \mathbf{S}_{q\alpha}^{\dagger} + \mathbf{C}_{rq},\ Dim\left(\mathbf{D}_{rq}\right) = \left(N_r \times N_q\right), \tag{A.25}$$

$$\mathbf{D}_{qr} = \mathbf{S}_{q\alpha} \mathbf{C}_{\alpha\alpha} \mathbf{S}_{r\alpha}^{\dagger} - \mathbf{C}_{\alpha q}^{\dagger} \mathbf{S}_{r\alpha}^{\dagger} - \mathbf{S}_{q\alpha} \mathbf{C}_{\alpha r} + \mathbf{C}_{rq}^{\dagger},\ Dim\left(\mathbf{D}_{qr}\right) = \left(N_q \times N_r\right), \tag{A.26}$$

$$\mathbf{D}_{qq} = \mathbf{S}_{q\alpha} \mathbf{C}_{\alpha\alpha} \mathbf{S}_{q\alpha}^{\dagger} - \mathbf{S}_{q\alpha} \mathbf{C}_{\alpha q} - \mathbf{C}_{\alpha q}^{\dagger} \mathbf{S}_{q\alpha}^{\dagger} + \mathbf{C}_{qq},\ Dim\left(\mathbf{D}_{qq}\right) = \left(N_q \times N_q\right). \tag{A.27}$$

$$\mathbf{X}_{\alpha} \equiv \mathbf{C}_{\alpha\alpha} \mathbf{S}_{r\alpha}^{\dagger} - \mathbf{C}_{\alpha r}, \tag{A.28}$$

$$\mathbf{Y}_{\alpha} \equiv \mathbf{C}_{\alpha\alpha} \mathbf{S}_{q\alpha}^{\dagger} - \mathbf{C}_{\alpha q}, \tag{A.29}$$

$$\mathbf{X}_{\beta} \equiv \mathbf{0},\ \mathbf{Y}_{\beta} \equiv \mathbf{0}, \tag{A.30}$$

$$\mathbf{X}_{r} \equiv \mathbf{C}_{\alpha r}^{\dagger} \mathbf{S}_{r\alpha}^{\dagger} - \mathbf{C}_{rr}, \tag{A.31}$$

$$\mathbf{Y}_{r} \equiv \mathbf{C}_{\alpha r}^{\dagger} \mathbf{S}_{q\alpha}^{\dagger} - \mathbf{C}_{rq}^{\dagger}, \tag{A.32}$$

$$\mathbf{X}_{q} \equiv \mathbf{C}_{\alpha q}^{\dagger} \mathbf{S}_{r\alpha}^{\dagger} - \mathbf{C}_{rq}^{\dagger}, \tag{A.33}$$

$$\mathbf{Y}_{q} \equiv \mathbf{C}_{\alpha q}^{\dagger} \mathbf{S}_{q\alpha}^{\dagger} - \mathbf{C}_{qq}, \tag{A.34}$$

$$\boldsymbol{\alpha}^{pred} = \boldsymbol{\alpha}^0 - \left[\mathbf{X}_\alpha \mathbf{D}_{11} + \mathbf{Y}_\alpha \mathbf{D}_{12}^\dagger\right]\mathbf{r}^d\left(\boldsymbol{\alpha}^0, \boldsymbol{\beta}^0\right) - \left[\mathbf{X}_\alpha \mathbf{D}_{12} + \mathbf{Y}_\alpha \mathbf{D}_{22}\right]\mathbf{q}^d\left(\boldsymbol{\alpha}^0, \boldsymbol{\beta}^0\right), \quad \text{(A.35)}$$

$$\mathbf{r}^{pred} = \mathbf{r}^m - \left[\mathbf{X}_r \mathbf{D}_{11} + \mathbf{Y}_r \mathbf{D}_{12}^\dagger\right]\mathbf{r}^d\left(\boldsymbol{\alpha}^0, \boldsymbol{\beta}^0\right) - \left[\mathbf{X}_r \mathbf{D}_{12} + \mathbf{Y}_r \mathbf{D}_{22}\right]\mathbf{q}^d\left(\boldsymbol{\alpha}^0, \boldsymbol{\beta}^0\right), \quad \text{(A.36)}$$

$$\mathbf{q}^{pred} = \mathbf{q}^m - \left[\mathbf{X}_q \mathbf{D}_{11} + \mathbf{Y}_q \mathbf{D}_{12}^\dagger\right]\mathbf{r}^d\left(\boldsymbol{\alpha}^0, \boldsymbol{\beta}^0\right) - \left[\mathbf{X}_q \mathbf{D}_{12} + \mathbf{Y}_q \mathbf{D}_{22}\right]\mathbf{q}^d\left(\boldsymbol{\alpha}^0, \boldsymbol{\beta}^0\right), \quad \text{(A.37)}$$

$$\mathbf{C}_{\alpha\alpha}^{pred} = \mathbf{C}_{\alpha\alpha} - \left[\mathbf{X}_\alpha\left(\mathbf{D}_{11}\mathbf{X}_\alpha^\dagger + \mathbf{D}_{12}\mathbf{Y}_\alpha^\dagger\right) + \mathbf{Y}_\alpha\left(\mathbf{D}_{21}\mathbf{X}_\alpha^\dagger + \mathbf{D}_{22}\mathbf{Y}_\alpha^\dagger\right)\right], \quad \text{(A.38)}$$

$$\mathbf{C}_{rr}^{pred} = \mathbf{C}_{rr} - \left[\mathbf{X}_r\left(\mathbf{D}_{11}\mathbf{X}_r^\dagger + \mathbf{D}_{12}\mathbf{Y}_r^\dagger\right) + \mathbf{Y}_r\left(\mathbf{D}_{21}\mathbf{X}_r^\dagger + \mathbf{D}_{22}\mathbf{Y}_r^\dagger\right)\right], \quad \text{(A.39)}$$

$$\mathbf{C}_{\alpha r}^{pred} = \mathbf{C}_{\alpha r} - \left[\mathbf{X}_\alpha\left(\mathbf{D}_{11}\mathbf{X}_r^\dagger + \mathbf{D}_{12}\mathbf{Y}_r^\dagger\right) + \mathbf{Y}_\alpha\left(\mathbf{D}_{21}\mathbf{X}_r^\dagger + \mathbf{D}_{22}\mathbf{Y}_r^\dagger\right)\right], \quad \text{(A.40)}$$

$$\mathbf{C}_{qq}^{pred} = \mathbf{C}_{qq} - \left[\mathbf{X}_q\left(\mathbf{D}_{11}\mathbf{X}_q^\dagger + \mathbf{D}_{12}\mathbf{Y}_q^\dagger\right) + \mathbf{Y}_q\left(\mathbf{D}_{21}\mathbf{X}_q^\dagger + \mathbf{D}_{22}\mathbf{Y}_q^\dagger\right)\right], \quad \text{(A.41)}$$

$$\mathbf{C}_{\alpha q}^{pred} = \mathbf{C}_{\alpha q} - \left[\mathbf{X}_\alpha\left(\mathbf{D}_{11}\mathbf{X}_q^\dagger + \mathbf{D}_{12}\mathbf{Y}_q^\dagger\right) + \mathbf{Y}_\alpha\left(\mathbf{D}_{21}\mathbf{X}_q^\dagger + \mathbf{D}_{22}\mathbf{Y}_q^\dagger\right)\right], \quad \text{(A.42)}$$

$$\mathbf{C}_{rq}^{pred} = \mathbf{C}_{rq} - \left[\mathbf{X}_r\left(\mathbf{D}_{11}\mathbf{X}_q^\dagger + \mathbf{D}_{12}\mathbf{Y}_q^\dagger\right) + \mathbf{Y}_r\left(\mathbf{D}_{21}\mathbf{X}_q^\dagger + \mathbf{D}_{22}\mathbf{Y}_q^\dagger\right)\right], \quad \text{(A.43)}$$

$$\mathbf{C}_{\alpha\beta}^{pred} = \mathbf{0},\ \mathbf{C}_{\beta\beta}^{opt} = \mathbf{0},\ \mathbf{C}_{\beta r}^{pred} = \mathbf{0},\ \mathbf{C}_{\beta q}^{opt} = \mathbf{0}. \quad \text{(A.44)}$$

Note also that (to first-order in response sensitivities) the covariance matrices of the computed responses arising from the uncertainties in the model parameters become:

$$\mathbf{C}_{rr}^{comp} \equiv \left\langle\left[\mathbf{r} - \mathbf{r}^c\left(\boldsymbol{\alpha}^0, \boldsymbol{\beta}^0\right)\right]\left[\mathbf{r} - \mathbf{r}^c\left(\boldsymbol{\alpha}^0, \boldsymbol{\beta}^0\right)\right]^\dagger\right\rangle = \mathbf{S}_{r\alpha}\mathbf{C}_{\alpha\alpha}\mathbf{S}_{r\alpha}^\dagger, \quad \text{(A.45)}$$

$$\mathbf{C}_{qq}^{comp} \equiv \left\langle\left[\mathbf{q} - \mathbf{q}^c\left(\boldsymbol{\alpha}^0, \boldsymbol{\beta}^0\right)\right]\left[\mathbf{q} - \mathbf{q}^c\left(\boldsymbol{\alpha}^0, \boldsymbol{\beta}^0\right)\right]^\dagger\right\rangle = \mathbf{S}_{q\alpha}\mathbf{C}_{\alpha\alpha}\mathbf{S}_{q\alpha}^\dagger, \quad \text{(A.46)}$$

$$\mathbf{C}_{rq}^{comp} \equiv \left\langle\left[\mathbf{r} - \mathbf{r}^c\left(\boldsymbol{\alpha}^0, \boldsymbol{\beta}^0\right)\right]\left[\mathbf{q} - \mathbf{q}^c\left(\boldsymbol{\alpha}^0, \boldsymbol{\beta}^0\right)\right]^\dagger\right\rangle = \mathbf{S}_{r\alpha}\mathbf{C}_{\alpha\alpha}\mathbf{S}_{q\alpha}^\dagger. \quad \text{(A.47)}$$

APPENDIX B: DIRECT AND INVERSE RADIATION TRANSPORT PROBLEMS

The processes which neutrons and/or photons undergo while propagating through a medium are modeled by the linear integro-differential equation bearing Boltzmann's name. The processes described by the Boltzmann equation include the scattering of neutrons and/or photons off nuclei, the capture of neutrons, the creation of neutrons through fission events, and the streaming of neutrons from one collision site to the next. The traditional mathematical formulation of the neutron transport equation is:

$$\begin{aligned}&\frac{1}{v}\frac{\partial\varphi}{\partial t}+\boldsymbol{\Omega}\cdot\nabla\varphi\left(\mathbf{r},\boldsymbol{\Omega},E,t\right)+\Sigma_t\left(\mathbf{r},E\right)\varphi\left(\mathbf{r},\boldsymbol{\Omega},E,t\right)=\\&\int_{4\pi}d\boldsymbol{\Omega}'\int_0^\infty dE'\,\Sigma_s\left(\mathbf{r},E'\to E,\boldsymbol{\Omega}'\to\boldsymbol{\Omega}\right)\varphi\left(\mathbf{r},\boldsymbol{\Omega}',E',t\right)\\&+\frac{\chi_p\left(E\right)}{4\pi}\int_{4\pi}d\boldsymbol{\Omega}'\int_0^\infty dE'\,\nu\left(E'\right)\Sigma_f\left(\mathbf{r},E'\right)\varphi\left(\mathbf{r},\boldsymbol{\Omega}',E',t\right)+Q\left(\mathbf{r},\boldsymbol{\Omega},E,t\right)\end{aligned}\qquad\text{(B.1)}$$

where $\varphi\left(\mathbf{r},\boldsymbol{\Omega},E,t\right)$ denotes the neutron flux at time t, position $\mathbf{r}$, direction $\boldsymbol{\Omega}$, and kinetic energy E. The notation and quantities in Eq. (B.1) have their usual meaning: on the left side of Eq. Eq. (B.1), first term represents the time rate of change of the flux, the second term represents the net leakage rate out of an incremental volume dV, while the third term represents the collision rate in dV. On the right side of Eq. (B.1), the first term represents the "in-scattering" rate, the second term represents the rate of production of prompt neutrons through fissions, while the third term represents the rate at which neutrons are produced by flux-independent sources. For investigating processes in which the delayed neutrons are important, Eq. (B.1) is augmented by a term (on the right side) to account for their production, and additional equations to describe their decay. Delayed neutrons will not be involved in the transport processes considered here. Also, we do not consider here the "criticality problem", for which Eq. (B.1) becomes an eigenvalue problem with a non-zero solution for the angular flux, in the absence of external sources. The integro-differential Eq. (B.1) becomes a well-posed problem by specifying an initial condition for the angular flux, i.e.,

$$\varphi\left(\mathbf{r},\boldsymbol{\Omega},E,0\right)=\varphi^i\left(\mathbf{r},\boldsymbol{\Omega},E\right),\ \mathbf{r}\in V,\ \boldsymbol{\Omega}\in 4\pi,\ 0<E<\infty,\qquad\text{(B.2)}$$

along with boundary conditions appropriate to the problem under consideration. The most frequently used boundary conditions for Eq. (B.1) are as follows:

i) Specification of a boundary source $\varphi^b\left(\mathbf{r}_s,\boldsymbol{\Omega},E,t\right)$, representing particle fluxes that enter the physical system V through its outer boundary ∂V. In this work, the volume V will be assumed to be convex, so that particles that leak out of V cannot reenter through ∂V. Thus, the boundary flux $\varphi^b\left(\mathbf{r}_s,\boldsymbol{\Omega},E,t\right)$ is an external source, independent of the flux within the system, which must be specified for: all points on the system's outer boundary $\mathbf{r}_s\in\partial V$; all (incoming) directions of flight pointing into the system $\boldsymbol{\Omega}\cdot\mathbf{n}<0,$ where $\mathbf{n}$ is the unit outer normal vector at $\mathbf{r}_s\in\partial V$); all energies and all times after the initial time. On the boundary, the angular flux is required to satisfy

$$\varphi\left(\mathbf{r}_s,\boldsymbol{\Omega},E,t\right)=\varphi^b\left(\mathbf{r}_s,\boldsymbol{\Omega},E,t\right),\ \mathbf{r}_s\in\partial V,\ \boldsymbol{\Omega}\cdot\mathbf{n}<0,\ 0<E<\infty,\ 0<t. \tag{B.3}$$

In particular, a "*vacuum boundary condition*" is specified by setting $\varphi^b=0$.

ii) The *albedo boundary condition* is used to relate the incoming flux with the known outgoing flux. This boundary condition is written as

$$\varphi\left(\mathbf{r}_s,\boldsymbol{\Omega},E,t\right)=\beta\varphi\left(\mathbf{r}_s,\boldsymbol{\Omega}',E,t\right),\ \mathbf{r}_s\in\partial V,\ \boldsymbol{\Omega}\cdot\mathbf{n}<0,\ 0<E<\infty,\ 0<t, \tag{B.4}$$

where $\boldsymbol{\Omega}'$ represents the direction of the outgoing particle. The scalar β takes the values $0\le\beta\le1$, with $\beta=0$ representing vacuum and $\beta=1$ representing total reflection. Specular reflection corresponds to the case when $\boldsymbol{\Omega}\cdot\mathbf{n}=-\boldsymbol{\Omega}'\cdot\mathbf{n}$ *and* $\left(\boldsymbol{\Omega}\cdot\boldsymbol{\Omega}'\right)\cdot\mathbf{n}=0$.

iii) The *white boundary condition* is a reflective condition where all particles striking the boundary turn back into V with an isotropic angular distribution. This boundary condition is written as

$$\varphi\left(\mathbf{r}_s,\boldsymbol{\Omega},E,t\right)=\frac{\beta}{\pi}\int\limits_{\boldsymbol{\Omega}'\cdot\mathbf{n}>0}\left(\boldsymbol{\Omega}'\cdot\mathbf{n}\right)\varphi\left(\mathbf{r}_s,\boldsymbol{\Omega}',E',t\right)d\boldsymbol{\Omega}',\ \boldsymbol{\Omega}\cdot\mathbf{n}<0,\ 0<E<\infty,\ 0<t. \tag{B.5}$$

iv) The *periodic boundary condition* describes a system in which the flux on one boundary is equal to the flux on another parallel boundary in a periodic lattice grid. In this case

$$\varphi\left(\mathbf{r}_s,\boldsymbol{\Omega},E,t\right)=\varphi\left(\mathbf{r}_s+\Delta\mathbf{r},\boldsymbol{\Omega},E,t\right),\ \ 0<E<\infty,0<t, \tag{B.6}$$

where $\Delta\mathbf{r}$ is the lattice pitch.

v) Boundary conditions describing system symmetries (planar, spherical, cylindrical) dependent on the flux and which can be generally denoted in the form

$$\mathbf{r}=\mathbf{r}\left[\varphi\left(\mathbf{r},\boldsymbol{\Omega},E,t\right),\boldsymbol{\alpha}\left(\mathbf{x}\right)\right]. \tag{B.8}$$

where $\boldsymbol{\alpha}\left(\mathbf{x}\right)$ is a vector representing parameters (cross sections, number densities, etc.) that appear in the model and in defining the detector. *Thus, the "direct problem" solves the "parameter-to-output" mapping that describes the "cause-to-effect" relationship in the particle transport process.*

The transport equation for photons (gamma rays) has the same form as the neutron transport equation. Its stationary (time-independent) form is presented below, for future reference:

$$\begin{aligned}&\boldsymbol{\Omega}\cdot\nabla I\left(\mathbf{r},\boldsymbol{\Omega},\lambda\right)+\mu\left(\mathbf{r},\lambda\right)I\left(\mathbf{r},\boldsymbol{\Omega},\lambda\right)=\\&\int_{4\pi}d\boldsymbol{\Omega}'\int_{0}^{\infty}d\lambda'\frac{\lambda}{\lambda'}\mu_s\left(\mathbf{r},\lambda'\to\lambda,\boldsymbol{\Omega}'\to\boldsymbol{\Omega}\right)I\left(\mathbf{r},\boldsymbol{\Omega}',\lambda'\right)+\lambda S\left(\mathbf{r},\boldsymbol{\Omega},E,t\right),\end{aligned}\tag{B.9}$$

where $I\left(\mathbf{r},\boldsymbol{\Omega},\lambda\right)$ denotes the radiation intensity (also called the doubly differential energy flux density) at position $\mathbf{r}$, direction $\boldsymbol{\Omega}$, and wave length λ. The quantity $\mu\left(\mathbf{r},\lambda\right)$ denotes the total interaction coefficient (or attenuation coefficient, or macroscopic cross section), while the secondary production coefficient $\mu_s\left(\mathbf{r},\lambda'\to\lambda,\boldsymbol{\Omega}'\to\boldsymbol{\Omega}\right)$ usually comprises only the three dominant photon-medium interactions, namely Compton scattering, pair production and photoelectric absorption, and is generally represented in the form

$$\begin{aligned}\mu_s\left(\mathbf{r},\lambda'\to\lambda,\boldsymbol{\Omega}'\to\boldsymbol{\Omega}\right)=N\left(\mathbf{r}\right)\sigma_c\left(\lambda',\lambda,\boldsymbol{\Omega}'\to\boldsymbol{\Omega}\right)+2\frac{N\left(\mathbf{r}\right)}{4\pi}\sigma_{pp}\left(\mathbf{r},\lambda'\right)\delta\left(\mu-1\right)\\+\frac{N\left(\mathbf{r}\right)}{4\pi}\sigma_{ph}\left(\mathbf{r},\lambda'\right)N_{ph}\left(\mathbf{r},\lambda',\lambda\right).\end{aligned}\tag{B.10}$$

In the above expression, $N\left(\mathbf{r}\right)$ denotes the atomic density of the medium at position $\mathbf{r}$, and the spatial dependence of σ_{pp} (the pair production cross section), σ_{ph} (the photoelectric absorption cross section), and $N_{ph}\left(\mathbf{r},\lambda',\lambda\right)$ (the number of photons in unit wave length emitted per photon at wave length absorbed in a photoelectric interaction at $\mathbf{r}$) is due only o atomic composition variations. The transport equation (B.1) comprises several approximations which are customarily made when one is interested in the "dose" arising from the deposition of photon energy in the medium. The most important approximations concern the treatment of fluorescence radiation, bremsstrahlung and pair production. Thus, since fluorescence radiation is generally small both in energy and intensity, it is generally assumed that the entire energy of the photoelectric event is carried away by the photoelectron. Also, the neglect of bremsstrahlung implies that all kinetic energy of the secondary electrons is transferred directly to the medium. *Such approximations ultimately imply that the energy is ultimately deposited in a different spatial location than would be predicted by a more rigorous computation. This observation is important in that it identifies a source of spatial error that would be present even if the transport equation were solved with perfect numerical accuracy.*

Many measurement problems are "inverse" to the direct problem in that they seek to determine (from measurements) the properties of the medium (i.e., various cross sections), or the properties of the source $Q\left(\mathbf{r},\boldsymbol{\Omega},E,t\right)$, and/or the size of the medium on its boundaries. Some authors further group such inverse problems into "invasive", when the

interior flux $\varphi(\mathbf{r},\mathbf{\Omega},E,t)$ is accessible for measurements, as opposed to "non-invasive" ones, in which only fluxes on the boundary of (or exterior to) the medium can be measured.

In general, two problems are called *inverses* of one another if the formulation of each involves all or part of the solution of the other. Several "inverse problems" that correspond to the setting of Eqs. (B.1)-(B.5) can be formulated, as follows:

(a) The classical "inverse problem": given the source $Q(\mathbf{r},\mathbf{\Omega},E,t)$, determine the fluxes $\varphi(\mathbf{r},\mathbf{\Omega},E,t)$;

(b) "Source identification problem": given the responses $\mathbf{r}=\mathbf{r}\left[\boldsymbol{\alpha}(\mathbf{x}),\mathbf{u}(\mathbf{x})\right]$ and the model parameters (cross sections, geometry, materials, etc.), denoted here as $\boldsymbol{\alpha}(\mathbf{x})$, determine the sources $Q(\mathbf{r},\mathbf{\Omega},E,t)$;

(c) "Parameter identification problem": given the responses $\mathbf{r}=\mathbf{r}\left[\boldsymbol{\alpha}(\mathbf{x}),\mathbf{u}(\mathbf{x})\right]$ and the sources $Q(\mathbf{r},\mathbf{\Omega},E,t)$, determine (some or all of) the model parameters;

(d) "Parameter and source identification problem": given the responses $\mathbf{r}=\mathbf{r}\left[\boldsymbol{\alpha}(\mathbf{x}),\mathbf{u}(\mathbf{x})\right]$, determine the sources and the model parameters;

(e) When the domain Ω_x contains inhomogeneous materials, and the responses $\mathbf{r}=\mathbf{r}\left[\boldsymbol{\alpha}(\mathbf{x}),\mathbf{u}(\mathbf{x})\right]$ are given, identify internal boundaries between the inhomogeneous materials, identify the description of the system's structure ("structural identification"), etc.

4.3. Task C: Validate gamma detector response functions and their uncertainties

In the past decade, significant research has been done on the calculation of DRFs. Many NaI DRFs were published in the literature. This data is essential for converting between the gamma flux/spectrum and the resulting multichannel detector response. Fully accounting for the uncertainties in the DRF was the main hurdle in this task. Without well-quantified DRF uncertainties, the predictive model was expected to be severely lacking, even if the radiation transport model is flawless. NC State University was responsible for completing this task.

The accomplishment of this task was reported in: Noel Benjamin Nelson, *Validation and Uncertainty Quantification of a* 1x2*" NaI Collimated Detector Using Detector Response Functions Created by g03*, Masters of Science Thesis, NC State University, 2014. This document is replicated on the following pages.

ABSTRACT

NELSON, NOEL BENJAMIN. Validation and Uncertainty Quantification of a 1x2" NaI Collimated Detector Using Detector Response Functions Created by g03. (Under the direction of Yousry Azmy.)

Detector response functions (DRFs) are relatively new theoretical constructs most useful for inverse analysis of radiation sources and elemental composition. A DRF is formally defined as a function that transforms the incident flux of radiation on a detector into a differential pulse height spectrum or detector response (as measured by a physical detector). Such functions have not yet been derived from first principles of physics, so semi-empirical and Monte Carlo based methods are generally used. One such method, based on semi-empirical modeling and Monte Carlo simulation of photon interactions with a sodium iodide (NaI) detector, is implemented by a code named g03 developed in the Center for Engineering Applications of Radioisotopes (CEAR). g03 has been validated for simple geometries (e.g. centered on-axis sources) with bare (i.e. uncollimated) detectors with 3x3" and 6x6" crystal dimensions. This work uses measurements from three radioactive sources with a 1x2" collimated NaI detector for complex geometries (e.g. off-axis and attenuated sources) to validate the DRF constructed with g03. Three measurement campaigns were performed: on-axis detection of calibration sources, off-axis measurements of a highly enriched uranium disc (HEU) at 41 cm, and on-axis measurements of the HEU disc at 11 cm with steel plates in between to provide attenuation. Simulated responses were created using MCNP computed fluxes folded with a DRF determined via g03. Furthermore, this work quantifies the uncertainty of the Monte Carlo (MC) simulations used in and with g03, as well as the uncertainties associated with each semi-empirical model employed in the full DRF representation. Most of the uncertainties associated with Monte Carlo simulations were controlled by the number of histories run. The uncertainties in the empirical model were determined by either Frequentist or Bayesian methods. In the case of many data points (degree of freedom, DOF, four or higher), direct Frequentist calculation of uncertainty by least squares and parameter derivatives proved more expedient than the Bayesian method (factor of 100 less computation time). However, in cases where fewer measurements were available (DOF less than four), a delayed rejection adaptive Metropolis (DRAM) algorithm was used instead. Overall, the response computed by the DRF for the prediction of the full energy peak region of responses was very good (well within two standard deviations of the experimental response), but tended to overestimate the Compton continuum by about 45-65 % due to physics associated with electron transport in the case of the calibration sources. For the HEU disc measurements, DRF responses tended to significantly underestimate (more than 20%) secondary full energy peaks due to scattering with the detector collimator and aluminum can which is not accounted for in the g03 model of the DRF. Though immediate outside detector scattering is thought to be the main reason for the underestimation, some contribution may also come from unsimulated geometry and uranium

daughter product decay radiation. All of the Monte Carlo uncertainties were constrained to the lowest experimental counting bin (peak channel) relative standard deviation by running a sufficient number of histories. The uncertainties associated with least squares fits to the experimental data tended to have parameter relative standard deviations lower than the peak channel relative standard deviation in most cases and good reduced chi-square values (close to one). However, two fits out of the sixty considered did not meet these criteria: the energy calibration and the Ba-133 Gaussian peak fits for the power law. Fortunately, the energy calibration still proved to be fairly accurate (within 1% of the true incident gamma ray energies) and had a negligible effect on the validation exercise. The other misfit had to be resolved by weighting the power law by the standard deviation of the Gaussian peak standard deviations.

© Copyright 2014 by Noel Benjamin Nelson

All Rights Reserved

Validation and Uncertainty Quantification of a 1x2" NaI Collimated Detector Using Detector Response Functions Created by g03

by
Noel Benjamin Nelson

A thesis submitted to the Graduate Faculty of
North Carolina State University
in partial fulfillment of the
requirements for the Degree of
Master of Science

Nuclear Engineering

Raleigh, North Carolina

2014

APPROVED BY:

Robin Gardner	John Mattingly
Ralph Smith	Louise Worrall

Yousry Azmy
Chair of Advisory Committee

DEDICATION

In memory of my dearest and loving mother, Deanna Nelson.

BIOGRAPHY

The author was [redacted] He graduated from Grant Union High School as the Valedictorian in 2008. He continued his studies at Oregon State University (OSU) for four years in Nuclear Engineering.

At OSU he worked diligently beside his studies as a cook for the university dormitory kitchens and as an undergraduate researcher for the chemistry department. In his chemistry research, he observed the effects of electric voltage, frequency, and amperage on the polymer brush growth of hemoglobin for use in the manufacture of prosthetics. He graduated Summa Cum Laude from Oregon State with an Honors B.S. in nuclear engineering in the summer of 2012.

He continued his graduate studies at North Carolina State University under the direction of Dr. Yousry Azmy. His research includes inverse holdup source characterization methods, and detector response validation and uncertainty quantification.

ACKNOWLEDGEMENTS

Infinite gratitude to my advisor, Dr. Yousry Azmy, for all of his guidance and assistance. All of my committee provided good support and assistance. Dr. Mattingly offered all of his knowledge and expertise in detection. Dr. Gardner and his students Wes Holmes and Adan Calderon were invaluable in learning the g03 software and understanding the intricacies of DRFs. Dr. Smith's assistance with and class on uncertainty quantification were greatly useful. Without his help I would still have no idea what Bayes theory was let alone how to use it.

Many thanks also goes to Dr. Louise Worrall, Steve Cleveland, and Dr. Shaheen Dewji of the Safeguards & Security Technology Group at Oak Ridge National Laboratory (ORNL) for all of their help. With them, I planned and executed this measurement campaign for the validation work. Whenever I needed an extra measurement, they took care of it for me. Also, I extend my gratitude to Alex Okowita of ORNL for providing the Monte Carlo N-Particle (MCNP) Transport model of the 1x2" NaI detector used for all of the measurements.

TABLE OF CONTENTS

LIST OF TABLES

LIST OF FIGURES

CHAPTER

1

INTRODUCTION

1.1 Research Motivation and Goals

Detector response functions (DRF) have become an area of increasing scientific interest for the last thirty years in several industrial detection applications. These applications include coal spectrometry for composition and location in the interest of mining, oil-well logging, radio-tracing in medicine, computerized tomography (CT) scans, and holdup source characterization. DRF uses could be extended to nuclear safeguards and security applications as well such as border monitoring for illegal transport of radioactive materials, cargo and package monitoring, and unknown source identification at source recovery sites. However, a rigorous mathematical formulation of the DRF has yet to be developed. Therefore, a few working empirical and stochastic approaches have been developed instead to create DRFs.

The concept of a DRF is defined in Section 2.3. For basic purposes a DRF can be considered a function that converts the energy-dependent flux of incoming source particles incident on a detector into a detector response spectrum similar to what is observed in experimental detector measurements. The DRF can also be used in the reverse sense in an inverse problem setting, as a step in the process of predicting the physical characteristics of an unknown source (e.g. holdup problem).

Much of the most recent work on DRFs has been performed by Dr. Robin Gardner and his research group at North Carolina State University. Gardner has developed a fairly accurate DRF model through empirical curve fitting and Monte Carlo analysis. The DRF has been validated against experimental measurements taken by Heath and was found to agree within two standard deviations of the experimental results from Heath. The measurements were taken with 3x3" and 6x6" NaI detectors and Cs-137 sources centered on the detector's front axis at a distance of 10 cm. There was agreement with the Heath benchmark detector measurements of the same sizes up to two standard deviations of the measured Poisson error. [16][4]

Some validation work has been carried out on the source positioned off-axis relative to the detector and with intervening material placed between the source and detector pair. This was done in the interest of developing spectrum analysis software specific to the Compton continuum in order to identify attenuators and account for off-axis geometries. The software that accomplishes this purpose is still under development, but once it reaches fruition it should be considered for incorporation into future works that employ DRFs.

The goal of this work was to use the NaI DRF model developed by Gardner to characterize a NaI 1x2" detector for on-axis geometries, off-axis geometries and attenuated configurations and to validate it against experimental measurements. Also, uncertainty in the model was calculated by Frequentist and Bayesian methods, and compared to measurement and Monte Carlo transport uncertainties. The overarching goal is to incorporate an accurate DRF model into an holdup problem approach to the holdup application to characterize special nuclear material (SNM) deposits at nuclear production and processing facilities.

1.2 Summary of Results and Conclusion

There were three major sets of measurements: on-axis detection of calibration sources, off-axis measurements with a highly enriched uranium (HEU) disc, and the HEU disc with steel plate attenuation between the source and detector. In terms of the calibration source spectra with one or two peaks and a Compton continuum, the computed spectrum predicted the peak well within two standard deviations of the experimental count rate, but overestimated the continuum and valley between the peak and Compton edge. This problem likely came from miscalibration of the electron range multiplier (Equation 2.4) used originally for an uncollimated 3x3" detector, as the same effect was observed in Gardner's original validation work when the multiplier was set too low.

However, this effect did not appear in the two major experimental campaigns involving the HEU disc, as the highest energy peak observed was of too low an energy to create a Compton continuum. The model reproduced the main peak (186 keV) and its shoulder peak (205 keV) well, again within

two standard deviations of the measured count rate, but underestimated the convolved peak at (150 keV) and did not reproduce the lead backscatter peak near 100 keV. This was due to scattering with the lead collimator that was unaccounted for by the DRF model, as the model currently only reproduces the effects of scattering within the detector crystal.

Finally, uncertainty quantification of the model took place on every calculated quantity from the flux calculation in MCNP to the Gaussian peak fits for shifting the program. Where the uncertainty was controllable by the number of particle histories chosen in Monte Carlo simulations, it was reduced below the lowest measured uncertainty. Where it was constrained to the accuracy of the model for least squares fitting, the reduced chi-square test was performed to check for goodness of fit.

Two mediocre least squares fits were encountered out of many: the energy calibration and the Ba-133 Gaussian peak fits used for the power law fit. The effects of the energy calibration were found to be inconsequential to the validation results. While the Ba-133 peaks effects on the power law were minimized through a special sum of the least squares weighted by the uncertainties in the Gaussian peak uncertainties (σ^{σ_T}).

CHAPTER

2

REVIEW OF THE LITERATURE

The purpose of this literature review is to lay the foundation for the development of the sodium iodide (NaI) detector response function and the corresponding uncertainty quantification based on the results and discoveries of previous scientists in the field of gamma radiation transport and detection. First, the history and development of the NaI detector and its supplementary equipment will be summarized. Then the major developments in Monte Carlo based transport theory relevant to the construction of DRFs will be discussed. The third section will detail the creation of detector response models. Finally, the last section will concern relevant Bayesian uncertainty quantification methods.

2.1 NaI Detection and Detector Response

Before detector response functions were even considered, detector responses and operation principles had to be developed. The detector of interest in our work is a sodium iodide scintillation detector. Scintillation is simply the emission of a visible photon from a material by dexcitation of an electron following its interaction with incident gamma. The favorable scintillation properties of NaI doped with trace amounts of Thallium (NaI(Tl))were first discovered by Robert Hofstadter in 1948 [20].

Hofstadter concluded that NaI(Tl) would be an efficent detector of ionizing radiation. He determined this based off of the duration of light emission, distribution of light pulses, particle energy discrimination (therefore radioactive source discrimination), and the proportionality of counting events to voltage and amplifier gain. He compared some of these characteristics with another detection material, anthracene, while merely verifying other materials to conclude that NaI(Tl) is a viable detector.

A NaI(Tl) crystal alone does not make a detector. Light emitted from the crystal after an interaction is captured via a photoelectric effect interaction with the photocathode of the detector. The freed electrons are multiplied and amplified into a detectable electronic signal pulse by the photomultiplier tube (PMT). The first photmultiplier tube was developed by Harley Iams and Bernard Salzberg much earlier than Hofstadter, in 1935. [6]

They observed the amplification of the primary photocurrent (a stream of electrons) through the effects of secondary emission and the photoelectric effect. Secondary emission is when an electron current strikes a charged plate and releases more electrons than were absorbed by the plate. Iams and Salzberg found that their photomultiplier tube was superior to gas phototubes as they had no interference at high audio frequencies from small fluctuations in its current supply, while still comparable to the vacuum phototubes (other detector PMT candidates). This model is the basis for modern PMT's.

The small electronic output signal from the PMT is then amplified and reshaped from a sharp edged pulse into a wider pulse (based on the difference between a rising and falling exponential) for easy processing. This wider pulse is passed to the multichannel analyzer (MCA), which outputs a differential pulse height spectrum (DPHS) also known as a detector response. A DPHS is created simply by setting a small pulse amplitude window to count pulses of varying heights within the window within a counting period between two energies called a channel. An MCA does this for hundreds of channels at once across the entire detector's energy range. The detector's energy range is determined partially by size and pulse amplitude gain settings. Low energy photons are resolved better by higher gain and the inverse is true for high energy photons. Also, large detectors have better interaction cross sections with higher energy gammas.

The first MCA was invented by George Kelly at Oak Ridge National Laboratories (ORNL) in 1953. Kelly prized his method as being much faster than older methods using single channel analyzers and more reliable with channel width and position errors meeting statistical standards set at the time. [7] Since then MCAs and pulse processing equipment have become more efficient and compact, such that they are often combined together into one machine that is controlled by local desktop software.

Figure 2.1 summarizes and illustrates the whole basic NaI detection process. For further details

of the detection process and pulse processing equipment, please refer to KNOLL's book on Radiation Detection and Measurement.

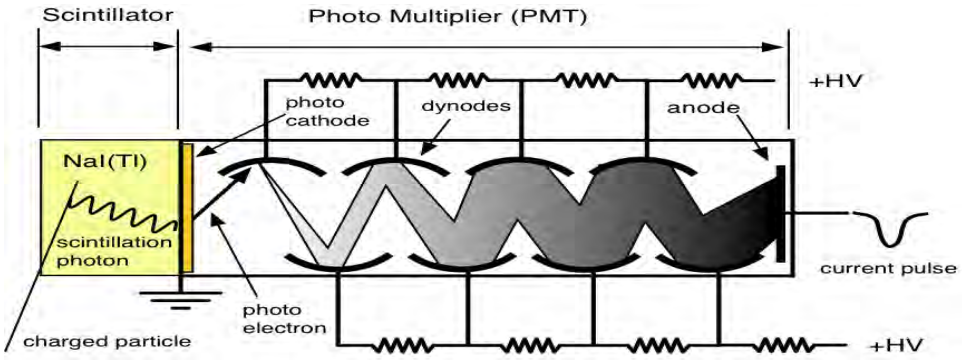

Figure 2.1 A basic NaI detector schematic. [14]

In most cases, the current pulse is sent to the pulse processing equipment and MCA to convert the small collection of electrons from the PMT into a response spectrum. Detector response spectra can be used to locate and identify sources of gamma radiation since the response peak channel is proportional to the incident energy of the incident radiation. It is proportional because the relationship between the energy deposited by radiation in the NaI crystal to the scintillation light yield is fairly linear for energies above 100 keV. A quadratic energy calibration using at least three known sources can account for the slight nonproportionality of detector channel to energy, and thereby be used to identify the energy of the incident radiation from other unknown sources.

In this case, detector response measurements of known sources will be validated against synthetic responses for attenuated and off-axis geometries. A typical detector response spectrum for a small detector is shown in Figure 2.2.

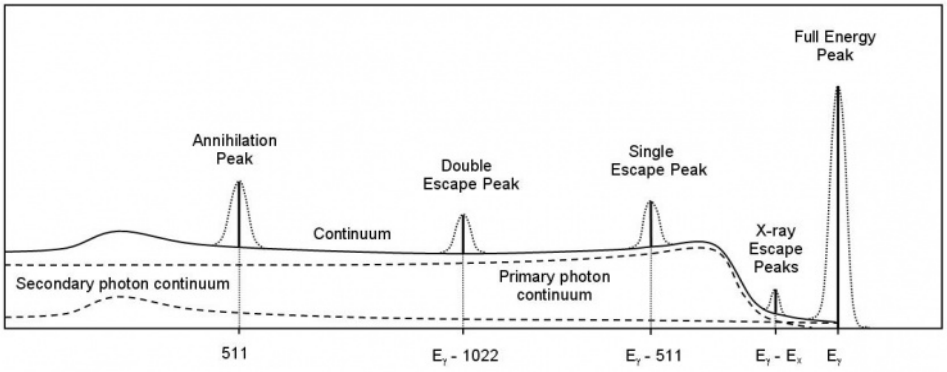

Figure 2.2 Predicted detector response spectrum of a medium sized detector with labeled regions of interest [15]

Every section of the response spectrum is the result of a combination of one or more photon interactions with the detector crystal or its casing material. The three major types of photon interactions with matter include: photoelectric effect, Compton scatter, and pair production. The photoelectric effect occurs when a photon is absorbed by an atom, and a bound electron is then expelled from that atom. Compton scatter occurs when a photon is merely deflected by an atom, and thereby loses a fraction of its energy and changes direction. The third interaction occurs when a high energy photon (greater than 1.022 MeV) interacts with the nuclear electromagnetic field and creates an electron-positron pair that are propelled in opposing directions. Further details of basic particle interactions can be found in Hubbell's report on Photon Cross Sections. [5]

Knoll's book mentions several spectral components that appear in a typical response spectrum as a result of the three basic particle interactions. These include the full energy peak, Compton continuum, and the several other types of peaks that appear in Figure 2.2.

The full energy peak of the spectrum is produced by a combination of all three basic gamma particle interactions with the detector crystal resulting in full energy deposition. Ideally, the full-energy peak would be a straight vertical line, but due to the finite energy resolution of a detector, the spectrum is blurred or spread to a Gaussian profile centered around the true peak channel, or energy. The sources of the spread can be usually attributed to statistical fluctuations in the total number of information carriers (scintillation photons for scintillators) created during a given detection event. Other reasons include electronic noise (radio signals, other electronic equipment, etc.), variations in the active detector volume (ie. defects, nonuniformity), and changes in operating parameters during measurements. In an investigation to validate a Monte Carlo calculated NaI detector response, a good representation for NaI energy resolution was measured to vary inversely (improve) with

increasing incident particle energy. For most measurements it varies from 8-15%. [17]

The continuum is created by the probable set of energy depositions from Compton scatter at various angles of deflection with incomplete energy deposition in the detector crystal. The continuum can also be affected by Compton scattering outside of the detector where the deflected photon is detected instead of the electron that is freed when the scatter occurs in the detector crystal. One example is a backscatter peak where the photon scatters at a 180^o angle from the rear detector wall into the detector crystal. [9] The shape of the continuum and backscatter peaks can also be significantly affected if an attenuator is in placed front of the source, or if the source is off-axis affecting the number of photons that scatter off of the detector casing into the crystal at a given energy. It is useful in many applications to be able to match different continuum shapes to their most probable cause.

Escape peaks arise when pair production occurs in the detector crystal, but one (single) or both (double) the photons that are created from the annihilation of the resulting positron escape. These events typically occur in small detectors near the edge of the crystal where it is easy for electrons to escape the crystal. When the positron-electron pair is created, the original photon loses the amount of energy required to create the mass of an electron and a positron. The rest mass of both an electron and a positron are approximately 511 keV. The electron created will not contribute much to the response, but the positron does once it annihilates with another electron. The annihilation event creates two photons equivalent to the lost rest mass of each particle, 511 keV, which travel in opposite directions. If both photons escape frequently without depositing energy in the detector crystal, then a double escape will appear in the spectrum at the energy of the incident gamma minus two times the electron rest mass ($E_o - 1.022 MeV$). If only one of the photons deposit their energy in the crystal frequently, then a single escape peak will appear in the spectrum at the original incident gamma energy minus one electron rest mass ($E_o - 0.511 MeV$).

An annihilation peak is observed when pair production occurs in the detector shielding, or alternatively in the source shielding, and one of the 0.511 MeV photons created in the following positron annihilation event is detected. Finally, characteristic X-rays (usually $E_{X-ray} < 100 keV$) are created from the de-excitation of atoms that were involved in a photoelectric event with an incident photon. Typically, the emitted X-rays is reabsorbed by the detector medium and contributes to the full energy peak. However, if the detector is fairly small and these X-rays escape, then an X-ray escape peak is observed in the response slightly below the full-energy peak ($E_o - E_{X-ray}$).

Any detector can produce a response, but NaI(Tl) scintillators are some of the most commonly used in practice. This is because they are cheap and fairly easy to manufacture in varying sizes, have fairly high light emission among scintillators, have high scintillation efficiency (heavy material Z=53) and fairly linear radiative energy deposited to light yield. The two major weaknesses of

NaI(Tl) detectors are their large decay times between pulses and fairly low energy resolution (wide full-energy peaks).

Decay time simply refers to the amount of time it takes for the ionized electrons from a detection event to decay from an excited state at the Thallium activator sites back to the ground state and produce scintillation photons for the detector pulse. Subsequent incident gamma rays cannot be detected during this decay time. For NaI(Tl), the decay time is 230 ns, which is much slower than an organic scintillator which have typial decay times around 2 ns. Therefore, organic scintillators are preferred for fast counting experiments where spectral information is less important than timing.

Knoll defines Energy resolution as $R = \frac{FWHM}{H_o}$ where $FWHM$ is the full width at half the maximum of the full energy peak and H_o is the height of the peak at its center. Therefore, a lower resolution means the peak is narrower compared to its height and requires fewer channels to define the peak (better for distinguishing peaks that are close together in energy). Because FWHM is energy dependent and dependent on the statistical fluctuation in a given measurement, for a given detector type the Poisson limit of the resolution is defined as $R|_{Poissonlimit} = 2.35/\sqrt{N}$, where N is the total number of information carriers. For NaI detectors, the theoretical limit would be about 1.2%, since it produces around N=38,000 information carriers (scintillation photons), whereas a semiconductor detector with $N = 10^5 - 10^6$ has a much lower limit of about 2.25%. NaI does not approach this limit closely though, as their is further loss of those scintillation photons from emission to absorption in the photocathode.

However, NaI(Tl) is the best scintillation detector for spectroscopy applications (not fast pulse timing experiments) because it has one of the highest photon absorption to light yield of 38,000 photons/MeV. Only CsI(Tl) and Cs(Na) are higher with 65,000 and 39,000 photons/MeV respectively. Cs(Na) has pretty equivalent properties to NaI, but has a much slower decay time between pulses. Additionally, CsI(Tl) has a bad emission wavelength (540 nm) that doesn't couple well with standard PMTs absorption spectrum (400-450 nm). Due to these weaknesses, generally NaI(Tl) is preferred among scintillators. [9]

For fine measurement applications in the lab, however, a semiconductor detector made of high purity Germanium (HPGe) is usually preferred. It has better resolution overall ranging from 0.13-1%. [21] So, the full-energy peaks of the HPGe would be at least ten times thinner than a NaI peak at the same energy. However, the major weaknesses of HPGe are that it requires cryogenic cooling, it is difficult to manufacture in large sizes, and it is generally expensive. Therefore, for field work (e.g. uranium holdup measurements), NaI(Tl) detectors are generally used due to their greater affordability and portability. Field application is the goal of this work, plus continuum effects are more important than peak resolution for determining source strength and location. Hence, a 1x2" NaI(Tl) scintillation detector was chosen to conduct the validation exercise reported here.

2.2 Monte Carlo Based Radiation Transport

Detector responses can be predicted mathematically by taking the product of the detector's response function (DRF) with the flux (particle speed per volume) of the radiation incident on the detector [9]. The particle flux can be predicted from the solution of the Boltzmann transport equation at the location of the detector crystal due to a given source. The equation was first derived by Ludwig Boltzmann in 1872. [8] Since then, many approximate methods have been developed for solving the Boltzmann equation under certain assumptions suitable for a variety of applications.

One of the more popular transport methods is the Monte Carlo method. The Monte Carlo method does not solve the transport equation itself, instead it simulates the particles and their trajectories through the modeled materials using sequences of pseudo-random numbers. Then it determines the average state of the physical system from the average behavior of the particles. [13] The software chosen for these calculations is the Monte Carlo Neutron-Particle (MCNP) transport code. It was created formally in 1977, though its roots extend back to the late 1940s, at the dawn of the nuclear age. This section outlines the basics of MC transport for calculating incident flux on the detector for the purpose of validating the DRF.

First, particles are simulated and transported according to Boltzmann physics within the volume of interest. Instead of solving the transport explicitly for the entire volume to obtain the flux, the fluence is calculated inside the detector volume only. The fluence, Φ, is defined as

$$\Phi = \lim_{\Delta V \to 0} [\frac{\sum_i s_i}{\Delta V}]. \tag{2.1}$$

If a large number of particles were simulated, this quantity could be calculated directly. [10] Simply by tracking particles through a cell of interest and summing up all of the particle tracks within the very small discrete spheres, the flux is approximated. For large volumes like nuclear power reactors this method becomes inefficient and less accurate. For small detector volumes, however, it works quite well. [2]

That is how Monte Carlo simulation works by simulating moving particles directly and tracking them through simulated media. Particle tracks from birth in a source to death (absorption or escape) from the system including all intervening scatters are called histories. The number of particle histories (N) executed in an MCNP run is chosen in order to obtain the desired level of uncertainty in the calculated quantities.

A typical particle history proceeds as follows. First, particles are initialized with random location, energy, and direction of motion according to a defined source distribution. Particles then interact or pass through the specified media according to well defined, material dependent, probability

distributions called cross sections. A photon microscopic cross section, $\sigma_{reactiontype}$ is defined as the probability of a photon-nuclear reaction with a nucleus. [1] It can also be thought of as the effective cross sectional area presented by the nucleus to the beam of incident photons, and cross sections have units of cm^2. Cross sections depend on energy, material, and interaction type.

Often microscopic cross sections are multiplied by the atom density of the medium to make a macroscopic cross section. Photon macroscopic cross sections, $\mu_{interaction}$, (also called attenuation coefficients) are simply the probability of a certain interaction with the medium occurring per unit path length traveled. [1] Summing the macroscopic cross sections of every interaction type yields the total attenuation cross section, μ. There are several minor interaction cross sections (Raleigh scattering, Thompson scattering, etc.), but the largest contributions for photons come from the three aforementioned interactions: photoelectric effect, Compton scatter, and pair production.

If these interactions produce secondary particles, they too are stored and tracked as new histories after the original particles terminate. Finally, after each particle history has been recorded, the particle track (s_i) through the detector volume is added to the running tally calculating the flux according to the average of Equation (1) piece by piece until all the histories are tallied.

The Monte Carlo transport method is very effective and simple, but can be inefficient and have high variances if variance reduction techniques are not applied. Variance in Monte Carlo is based on the number of histories run, so the simplest way to reduce variance in such a calculation is to run more particle histories. Sometimes this is not feasible (rare events), therefore variance reduction techniques are used instead. In Exploring Monte Carlo Methods by Dunn and Shultis the most common variance techniques are described, which include particle weighting, truncation, splitting, and Russian roulette.

The first method is called weighting. A biased multiplier (called a weight) may be applied to particles undergoing desired physical events in order to force rare interactions to occur more often without running as large numbers of histories. The biased particles' contribution to the tally (the score) is then renormalized by mulitplying by $1/weight$. This ensures that desired events are well sampled, but the tally still represents an unbiased system.

Further subtypes of this technique include importance sampling, and implicit absorption. In importance sampling a particle's contribution to the tally may be taken as the product of the particle's weight and the probability of the occurrence of the event of interest. The probability density function (PDF) that describes this event may be adjusted to an alternate simpler PDF, as long as a multiplicative correction factor is applied to the weight equivalent to the original PDF divided by the alternate PDF. When optimum adjoint transport solutions are applied, the variance can theoretically be reduced to zero. Similarly, alternate PDFs may also be used to force interactions or affect the distance between collisions.

For implicit absorption, particles are never allowed to be killed by absorption. Instead, every time an absorption event would occur, the particle's weight is reduced by multiplying its weight by the probability of survival $(1-\frac{\mu_a}{\mu})$. Then a particle interaction is chosen for the particle from the remaining non-absorption interaction probabilities. Therefore, in this scenario, a particle may only be killed by leaking out of the system. To prevent buildup of low weight particles in the system, this technique is usually paired with the Russian roulette technique.

Truncation methods set cutoff limits for when a particle should be terminated. For example, if a particle reaches a position outside of the system of interest (leakage), then tracking would be terminated. Other examples, include unfavorable directions, low energies, and low weights unlikely to contribute much to the tally of interest. Truncation helps to kill particles early that are only wasting computational resources.

Finally, splitting and Russian roulette schemes are almost always applied together. Splitting occurs when a particle enters a region designated of higher importance and interest (e.g. the cell where a tally is calculated, and it is split into m particles. Each particle weight is then given by a 1/m fraction of the weight of the original particle. Russian roulette is exactly the opposite of splitting. Particles that travel into regions of low interest may be killed by random selection. Some 1/m fraction of particles are killed, and the remainder increased in weight by a factor of m. [2]

All of the variance reduction techniques reduce variance without biasing the tallies, if used correctly. Often these techniques increase computational efficiency and decrease computation times. Many production Monte Carlo transport codes apply some of these techniques automatically, while allowing the others to be chosen as options.

In this work, the Los Alamos National Laboratories (LANL) code Monte Carlo Neutron Transport code (MCNP) was used to compute flux tallies incident on the 1x2" NaI detector model. The code was originally implemented for neutron transport, but can also be used for other particle transport, such as photon transport. Monte Carlo based calculation was also used in part to calculate the DRF.

2.3 Detector Response Functions

The DRF ($R(E,h)$) is defined as the probability that a photon incident on the detector with energy E will give rise to a pulse with height h. [18] DRFs are useful for converting flux to counting spectra, calculating detector efficiencies, and also for the reverse, transforming responses back into flux. The latter purpose will be explored more in future research, but in this work focus will remain on the former purpose.

At the present, no fully physical model exists to describe DRFs, but there are several stochastic (MC) and empirical models. Gardner's NaI DRF model is one that combines empirical relations with

Monte Carlo simulation. Gardner's original work with his colleague Avneet Sood validated 3x3 NaI synthetic detector responses to the Heath benchmark Cs-137 spectrum. Gardner's model was found to be more efficient (required far less particle histories for accurate calculation) and was shown to match better with the Heath experiments than MCNP's F8 response tally. [16] It was chosen for our work for these reasons and also because MCNP simulates responses according to direct energy deposition in the detector crystal. It generates no DRF, and a DRF will be needed for future holdup work.

The Heath experiments were performed on a 3x3" NaI detector in 1964 as a benchmark for a number of gamma sources. All measurements were very high fidelity. The measurements were performed in a lead shielded box to reduce background radiation and all spectra were counted well over 10,000 counts in the peak channel for less than 1% counting uncertainty. For further information, see Heath's Gamma Ray Spectrum Catalogue. [4]

Gardner's model generates a DRF for a desired detector size, source distance, and source energy (single peak), through the following set of steps. First, Gardner's model takes into account the non-linear dependence of NaI scintillation efficiency ($\frac{scintillation\,light\,yield}{energy\,deposited}$) on the energy deposited in the detector by the incident photon. As mentioned before (section 2.1), the nonlinearity in scintillation efficiency is an inherent property of NaI(Tl) crystals, and it is particularly pronounced at energies below 100 keV. However, this nonlinearity is still significant for all incident energies below 3 MeV. Gardner used the following nonlinear empirical relationship (from fits to experimental data) to calculate scintillation efficiency for his DRF

$$\begin{aligned} S(E_e) &= 1 + k_1 exp[-(ln\ E_e - k_2)^2/k_3], \\ E_e &\geq 10\,keV, \\ S(E_e) &= 1 + k_1 exp[-(ln\ E_e - k_2)^2/k_4], \\ E_e &\leq 10\,keV, \end{aligned} \tag{2.2}$$

where E_e is electron energy in keV. k_1 is 0.245, and k_2 is $ln\ 10 = 2.30258$. k_3 is 7.1635, and k_4 is 5.1946. The electrons are the very same electrons that are involved in interactions with photons incident on the detector crystal. The second step involves Monte Carlo particle transport simulation in which each scattered electron that deposits energy in the detector is multiplied by the scintillation efficiency (Equation 2.2) at the energy deposited. [16]

The Monte Carlo calculation is conducted with Peplow's code called DRFNCS. It simulates several hundred detector response spectra through Monte Carlo transport where photon interactions are forced in the detector, but leakage of secondary particles is allowed producing the continuum of

the spectra. Only about 100,000 particle histories are necessary to produce results with uncertainty under 1%, whereas MCNP F8 Gaussian energy broadened (GEB) spectra require on the order of billions of particles to produce the same precision. The difference typically saves about a day in computation time.

Next, the peaks were stripped from the response spectra so that each contiuum could be processed alone. Principle component analysis (PCA) was performed on the correlated response variables and the covariance matrix to produce a small set of uncorrelated variables (principal components). The principal components and the mean vector were stored as data and can reproduce accurate continuum easily when multiplied with the desired channels vector.Essentially, the continuum can be recalled quickly without the need to be regenerated by Monte Carlo simulation for each DRF generated.

So, when a new DRF needs to be generated, the algorithm need only to generate the full-energy peak of interest by Monte Carlo transport simulation and adds this contribution to the continuum to produce the desired DRF. [22] The modified version of Peplow's code (adjusted by the nonlinear scintillation efficiency) is called g03. The code is in the process of being updated and is proprietary to the Center for Engineering Applications of Radioisotopes (CEAR).

Finally, the Monte Carlo simulation of g03 is modified by several empirical equations to correct pieces of the spectra that are not simulated fully by the Monte Carlo calculation. The g03 DRF peak section is spread according to the following power law (Equation (2.3))

$$\sigma_T(E_I) = a E_I^b, \tag{2.3}$$

where a and b are empirical fit parameters, and E_I is the energy of the incident gamma ray. This law is simply an empirical relation that comes from a Least Squares fit of the standard deviations of experimentally measured full-energy peak responses produced by the detector of interest. [16]

The flat Compton continuum of the DRF is produced by various empirical fits of entire experimental responses (not only the peaks). This is necessary because there is as of yet, some undiscovered phenomena causing a higher magnitude of the continuum than predicted by current physics models and data. Simple Compton scatter and pair production physics and partial energy deposition due to electron or photon leakage through the detector walls can predict the shape of the Compton continuum but underestimates its magnitude. A normalization factor was developed to account for this effect called the electron range multiplier, since the effect causing the underestimation of the continuum was believed to be connected to the electron range. The empirical relation is given by Equation 2.4

$$R_e = 1 + A_1 exp(-A_2 E_I) + A_3 exp(-A_4 E_I) \tag{2.4}$$

$$A_1 = 39.662,\ A_2 = 3.4052,\ A_3 = 1.5434,\ A_4 = 0.1576,$$

where E_I is the energy of the incident photon, and $A_1 - A_4$ are parameters fit from experimental responses. This factor is a pseudo-electron range equation designed to correct the magnitude of the synthetic Compton continuum produced by the Gardner's DRF. It was fit through trial and error for 3x3" NaI detectors and may not apply to the detector of interest in this work (1x2" NaI detector). [23]

Responses, thus, may be measured or calculated. Validation of Gardner's model has already been completed on some levels, but almost no uncertainty quantification of the model has been performed. The primary goal of this work is to conduct a validation exercise of the DRF for a specific NaI detector of interest and account for its uncertainties.

2.4 Uncertainty Quantification

In the process of comparing measured to computational model results there are three types of uncertainty in practice. There is measurement uncertainty, model uncertainty, and numerical (simulation) uncertainty. Quantifying uncertainty is important in determining the precision of the model and the computed results. The more precise a result is, the more likely it can be reproduced, and the higher the level of confidence in the applicability of the computational model.

Measurement uncertainty for detection and counting was found to follow a Poisson distribution for a single measurement. This is because the decay of a nucleus is a binary process. It either decays or it does not. The chance of decay per unit time is constant and rather small for a large number of nuclei and a short measurement time (compared to the nuclide's half-life). A binomial distribution under these conditions (constant and small probability of success) will reduce to a Poisson distribution. [9]

In a Poisson distribution the variance is equal to the mean (the number of counts). Therefore, the variance of the measurement is equal to the mean number of counts. In a single measurement this would be the number of counts measured in a detector channel. The standard deviation is then simply the square root of this count, and the fractional standard deviation (relative to the total count) is one divided by the root of the count.

To then extend this measurement uncertainty to count rates and net counts (gross count - background count), one simply uses propagation of uncertainty. Anytime a basic operation (addition, subtraction, multiplication, or division) is performed on the measured count, likewise a transformation must be made to the variance of the counts. If the variables involved (e.g. counts and time) are

independent of one another, then a general formula exists for calculating total uncertainty of the final quantity (Equation 2.5)

$$\sigma_u^2 = (\frac{\partial u}{\partial x})^2\sigma_x^2 + (\frac{\partial u}{\partial y})^2\sigma_y^2 + (\frac{\partial u}{\partial z})^2\sigma_z^2 + /ldots, \tag{2.5}$$

where $u = u(x, y, z, \ldots)$ is the quantity derived from basic quantities $(x, y, z, \ldots)$ with known variances $(\sigma^2_{variable})$. The formula is useful for determining the associated uncertainties of many quantities (e.g. count rates and net counts) for various purposes, such as those used in the reduced chi-square test described near the end of this section. [9]

It turns out that simulation uncertainty for Monte Carlo transport calculation is very similar to that of measurement uncertainty. This is due to the fact that the particles themselves are being simulated and tracked as a psuedo-random process. Measurement standard deviation is equivalent to the square root of the number of counts (the mean) in a channel. So it makes sense that the Monte Carlo standard deviation is simply the square root of the number of particle histories in a tally bin. The fractional standard deviation is simply equivalent to the reciprical of the standard deviation. [2]

Determination of the model parameter uncertainty is a more difficult task. For this purpose, there are two major statistical methods to choose from: Bayesian and Frequentist Theory. Since the core of Frequentist Theory requires a large number of data points, a Bayesian method was naturally chosen for the power law Gaussian fits, power law, and the energy calibration fits. Whereas Freqentist methods were chosen for the normal Gaussian fits for shifting spectra and the Gaussian fits of the peaks of experimental spectra for the energy calibration due to the abundance of channels in the peaks of those spectra and for efficient calculation.

Smith's book, Uncertainty Quantification, describes Frequentist and Bayesian statistics quite well. In both methods, parameter means of each relationship were found via the method of nonlinear least squares. This method solves for the mean parameter values that produced the lowest value of the L_2 norm (sum of the squares) of the error. Frequentist methods treat these values as the parameter means and subsequently calculates a Chi squared and covariance matrix to determine the parameter uncertainties. Bayesian methods only use the means for an initial guess (priori information). Further details of least squares methods can typically be found in advanced linear algebra texts. With parameter derivatives and error variance, the Chi squared and covariance matrices can be calculated.

First, however, the error variance must be calculated from the residuals. The error variance is defined as follows

$$\sigma^2 = \frac{1}{n-p} R^T R \tag{2.6}$$

where R is the residual vector of the differences between the model evaluated at the means predicted

by least squares and the experimental data ($R = Y_{experimental} - f_{model}(q)$). Also, n is the number of parameters, and p is the number of model parameters. Next the χ matrix can be calculated as simply the derivative of the model with respect to each parameter, k at each data point i ($\chi_{ik}(q) = \frac{\partial f_i(q)}{\partial q_k}$). Using the square of the χ matrix and the error variance the covariance matrix can simply be defined as

$$V = \sigma^2[\chi^T(q)\chi(q)]^{-1}. \tag{2.7}$$

The covariance matrix contains each parameter variance along its diagonal. Simply take the square root of the diagonal values to find the parameter standard deviations. The Frequentist method is very accurate and quick to calculate for cases where there are many more experimental data points than the number of parameters. However, when confidence in a fit is lower due to fewer data points, Bayesian codes fair better. [11]

Bayes theorem expressed in words simply states that parameters are random variables with associated probabilistic densities that make use of known information or new information obtained from conducted measurements. This method picks the best posterior density that reflects the distribution of parameter values based on sampled observations. In other words it finds the probability density functions (pdfs) of model parameters that maximizes the likelihood function. Further details of the likelihood function and Bayesian theory are given in Smith's Book or his reference D. Calvetti and E. Somersalo, Introduction to Bayesian Scientific Computing.

DRAM was used to calculate Bayesian model parameter uncertainties. From Haario's article "DRAM: Efficient adaptive MCMC" one learns that DRAM stands for Delayed Rejection Adaptive Metropolis algorithm. In this work it is used to estimate the most likely means of the model of interests parameters to verify those determined by least squares fits by employing Monte Carlo random sampling of the parameter values, called chains. DRAM also determines the uncertainty in the parameters from the direct statistical variations in the parameter chains.

The basis of DRAM comes from the Random Walk Metropolis algorithm (RWM). RWM comes from Monte Carlo principles and is fairly easy to implement. First, the variance is obtained in the same way that the error variance is typically calculated: from the sum of the square of the residuals divided by the number of degrees of freedom (Equation 2.6). Second, the covariance is estimated from the inverse of the χ squared distribution which come from partial parameter derivatives of the model (as defined by Equation 2.7). A Choleski factorization of the covariance matrix is formed. Lastly, with the factored matrix, the parameters are varied in a semi-random way with psuedo-random numbers chosen from a set of different distributions. Based on likelihoods of randomly chosen parameter values the algorithm either chooses to accept (if the likelihood is increased) or possibly reject and the rejection probability increases every time the likelihood function decreases.

Using regular statistical methods, again the parameter standard deviations can be estimated from the chains of random parameter values.

DRAM works along the same principles, except that the rejection condition is augmented with a more advanced algorithm that increases the probability of acceptance (promoting mixing or broader exploration of the chains). Also, DRAM adapts by suggesting a Gaussian proposal distribution centered at each chain position and retrieves more information about the posterior using it to update the covariance matrix. Together these advancements make a much more efficient algorithm than basic RWM. [19]

Additionally, both Frequentist and Bayesian methods give estimates of the model parameters that best reproduce a curve along the measured data points. Sometimes, least squares fits and maximum likelihood estimates can produce poor curve fits. So, from Bevington and Robinson's Data Reduction and Error Analysis, one can obtain two useful tools for model examination: the reduced chi-square test and linear correlation coefficients.

The reduced chi-square test helps to provide a quantified measurement of the goodness of fit. The definition of the reduced chi-square is shown by Equation 2.8.

$$\chi^2 = \sum_{j=1}^{n} \frac{[h(x_j) - y(x_j)]^2}{\sigma_j(h)^2}$$
$$\chi^2_\nu = \chi^2/\nu, \tag{2.8}$$

where n is the total number of data points. $h(x_j)$ is the measurement, and $y(x_j)$ is the model solution at data point j. Also, $\sigma_j(h)^2$ is the variance in the measurement at data point j, and ν is the number of degrees of freedom ($\nu = n - p$) where p is the number of parameters. In our work, the variance will likely be the poisson variance for a simple count spectrum, or the propagated uncertainty for net counts and count rates. A reduced chi-square test will produce a value equal to one for an ideal case, however, it is generally considered to be still a good fit for values less than ten. Values less than one simply mean that the spectrum was overfit, and may have required a simpler model or fewer data points to produce a similar result.

Furthermore, in the event of a poor fit, the model can be examined more closely by examining the linear correlation coefficients. The linear correlation coefficient matrix can be calculated as follows (Equation 2.9):

$$\rho_{jk} = \frac{\sigma^2_{jk}}{\sigma_j \sigma_k} \tag{2.9}$$

where σ_{jk} is the covariance at row i and column j as calculated by Equation 2.7, and σ_j and σ_k

are the diagonal standard deviations of the parameters from the covariance matrix (σ_{jj} and σ_{kk}). The linear correlation coefficients of a model can reveal a weak parameter in the model that might not be contributing much to the model fit. Parameters with many correlation coefficients under 0.2 should be considered for removal or substitution. [3]

CHAPTER

3

EXPERIMENTAL SETUP AND COMPUTATIONAL MODEL

This section will detail the experimental setup and the Monte Carlo computational transport models used to simulate the experiment's geometric configuration and calculate the flux incident on the detector. A detector description will also be provided, as well as how the detector intrinsic efficiency was calculated. The Monte Carlo calculated quantities are necessary for calculating response spectra for comparison against those obtained via experimental measurements with the actual detector.

3.1 Experimental Setup

The entire experimental campaign was designed and performed at the Safeguards Laboratory at Oak Ridge National Laboratory. The initial campaign was completed over the course of a couple of weeks in June of 2013. Further measurements (such as those for the power law fit) were taken on various days over the course of the spring of 2014, courtesy of ORNL personnel. All sources and detection equipment were provided by ORNL. Each measurement was taken with the same detector, detection equipment, and settings.

The detector of interest for validation of Gardner's DRF model is a 1 inch diameter by 2 inches

height right cylinder EFC Model 1X2P collimated NaI detector. This small detector is one used in uranium holdup experiments at ORNL and is an example of a detector used for field measurements of holdup within the holdup measurement system, HMS. A schematic of the detector is shown in Figure 3.1.

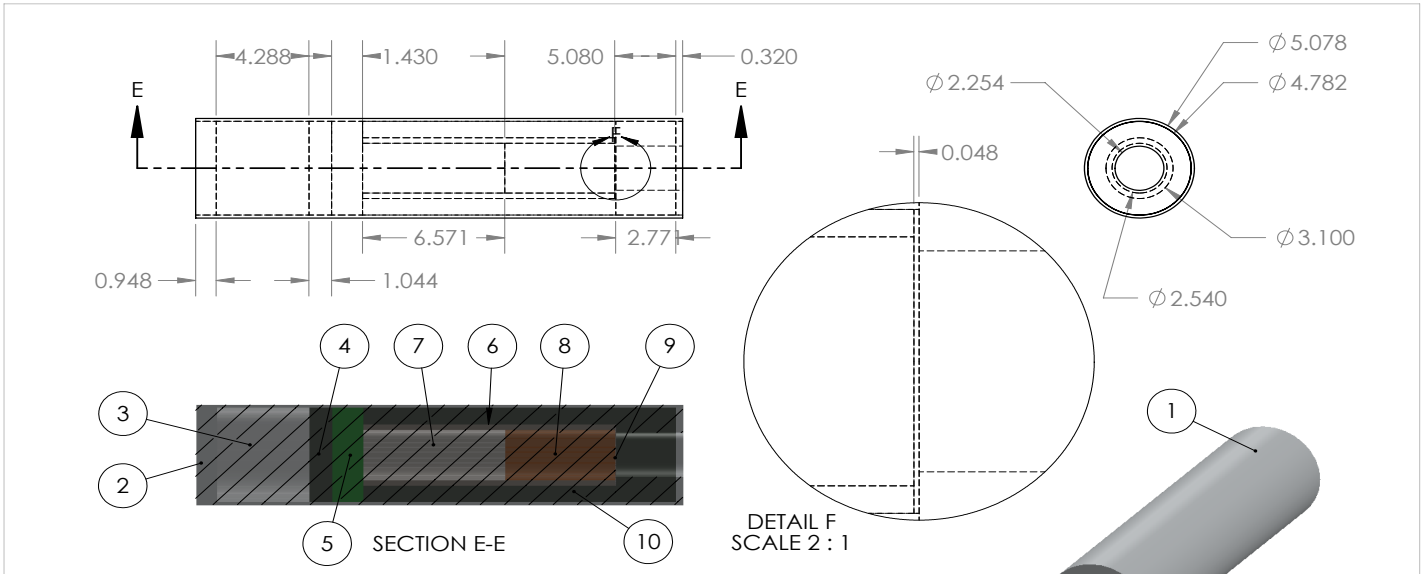

ITEM NO.	PART	Material
1	Case	Aluminum
2	Plug	Aluminum
3	Electronic Housing	Void
4	Rear Shield	Lead
5	Polymer plate	Plastic
6	Steel Enclosure	Stainless Steel
7	PMT	Void
8	Crystal	NaI
9	Tin Shield	Tin
10	Collimator	Lead
11	Collimator Front	Lead
12	Front Cap	Aluminum

UNLESS OTHERWISE SPECIFIED:
DIMENSIONS ARE IN CENTIMETERS
TOLERANCES: 0.001
FRACTIONAL ±
ANGULAR: MACH ± BEND ±
TWO PLACE DECIMAL ±
THREE PLACE DECIMAL ±
INTERPRET GEOMETRIC TOLERANCING PER:
MATERIAL
FINISH
DO NOT SCALE DRAWING

	NAME	DATE
DRAWN	NBN	8/22/14
CHECKED		
ENG APPR.		
MFG APPR.		
Q.A.		
COMMENTS:		

TITLE: ORNL 1x2" NaI Detector

SIZE A | DWG. NO. NAIDET | REV

SCALE: 1:2.5 | WEIGHT: | SHEET 1 OF 1

5 4 3 2 1

Figure 3.1 A schematic detailing the 1x2" NaI detector used at ORNL.

As can be seen, the detector is well shielded with lead except on the front face where the collimator aperture allows radiation into the detector from a limited extent of directions covering the corresponding fraction of the unit sphere. Hence, the detector has approximately a 45 degree in-axial-plane angle of vision from the center of its circular front. Contributions to the detector response from any source of radiation far enough off of the axis of the cylindrical detector will be significantly attenuated and radiation incident on the side or rear of the detector will not likely contribute to the measured response spectrum (except for very high energy photons that are not sufficiently attenuated by the detector's lead collimator). The rest of the detector components are fairly standard. It has a PMT, an aluminum sheath (container), etc., as shown in the detector schematic, Fig. 3.1.

Overall, measurements were taken far away from the walls on a table with at most a aluminum tee in the setup. Scattering off of the plastic table, walls, and floor were very unlikely since there is a high probability for interaction of gamma-ray photons with high Z materials. The tee included a small scattering possibility, but it was considered negligible. Therefore, the room geometry and the aluminum tee were not simulated. Only the source, detector, and the air in between were simulated.

In the first set of experiments, a source was placed at a set distance from the detector center (on-axis). The source was held in place on a ring stand, or taped to the front of the detector (for quick counts). The source was typically a button calibration source with known activity and dimensions. These measurements were performed for base validation, energy calibration of the detector, and power law fitting for the DRF.

The parameters of all of the calibration sources used for validation are listed in Table 3.1. Details of the sources used for the energy calibration and the power law fit are not reported here, as these measurements were only intended for determining detector properties.

Table 3.1 Dimensions and activities of calibration sources used for experimental measurements

Source	A.R. (cm)	Thick. (cm)	Act. (μCi)	Created	Measured	Act. Meas. (μCi)
Cs-137	0.25	0.318	5.01	9/28/2005	2/20/2014	4.13 ± 0.62
Co-60	0.25	0.318	0.8516	3/1/2002	6/21/2013	0.1927 ± 0.029

Note: All calibration sources used in this work were created by Eckert and Ziegler, and the active source dimensions (active radius, A.R., and thickness) used in the MCNP model were taken from the Type D disc model in the catalog. Furthermore, according to the supplier "Sources are manufactured with contained activity (Act.) values of ±15% of the requested activity value unless otherwise noted in the catalog." [27]

Note that only the active volume of these sources was simulated in MCNP and not the plastic

case surrounding them, since attenuation was assumed to be negligible. The emission energies and relative intensities of the gamma-rays of interest for each source used are tabulated in Table 3.2.

Table 3.2 Gamma ray energies and relative intensities of all sources measured were taken from Brookhaven National Laboratory's Nudat2.6 database. [28] Unlisted uncertainties were assumed to be one in the last digit.

Source	Peak No.	Energy (keV)	Relative Intensity (%)
Am-241	1	59.5409(1)	35.9(4)
U-235	1	105.0(1)	2.00(3)*
U-235	2	109.0(1)	2.16(13)*
U-235	3	143.76(2)	10.96(14)
U-235	4	163.356(3)	5.08(6)
U-235	5	185.715(5)	57.0(6)
U-235	6	202.12(1)	1.080(23)
U-235	7	205.316(10)	5.02(6)
Ba-133	1	80.9979(11)	35.6(3)*
Ba-133	2	356.0129(7)	62.05(1)
Cs-137	1	661.657(3)	85.10(20)
Mn-54	1	834.848(3)	99.9760(10)
Na-22	1	1274.537(7)	99.941(14)
Co-60	1	1173.228(3)	99.85(3)
Co-60	2	1332.492(4)	99.9825(6)

*Note: gamma-rays from the same source that were within 1 keV of each other were averaged and their intensities summed together.

The next set of experiments focused on the source of interest (uranium-235 or U-235) and were specifically conducted for the DRF validation exercise. Since it is very unlikely that a detector will be directly pointed at a holdup material deposit when the deposit has an unknown location, strength, and shape, off-axis detector spectra are of great interest in the holdup field. This is also necessary for holdup configurations where the source is distributed and thus contributes to the response of a stationary detector from broad angles of incidence. So, a source was affixed to an aluminum tee and prepared specifically for accurate off-axis measurements.

The detector was placed on the center steel bar while the source was put on the crossbar held by a vice and a steel ring holder at a distance of 38 cm from the detector face (41 cm from the front face of the detector crystal). The source was then moved laterally left and right of center, or the axially aligned position, in 5 cm intervals up to 20 cm. Measurements ceased at 20 cm because the source

started to become indistinguishable from background beyond that distance. For visual reference, a photograph of the lateral off-axis experimental setup is shown in Figure 3.2.

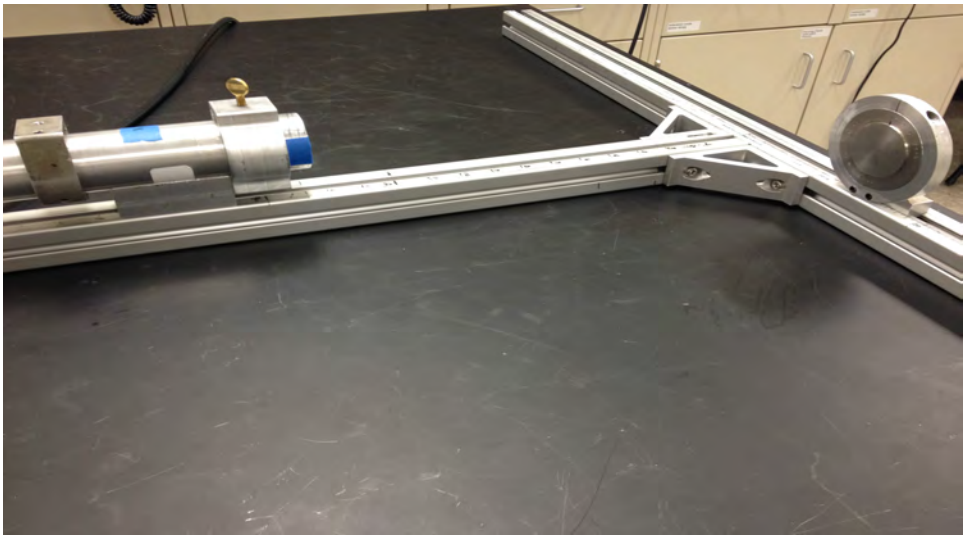

Figure 3.2 Photograph of the HEU disc off-axis experiment 41 cm from the detector and 15 cm to the right (x=+15cm).

The source was a highly enriched uranium (HEU) disc source of known activity, dimensions, and enrichment. The dimensions of the U-235 source are given in Figure 3.3.

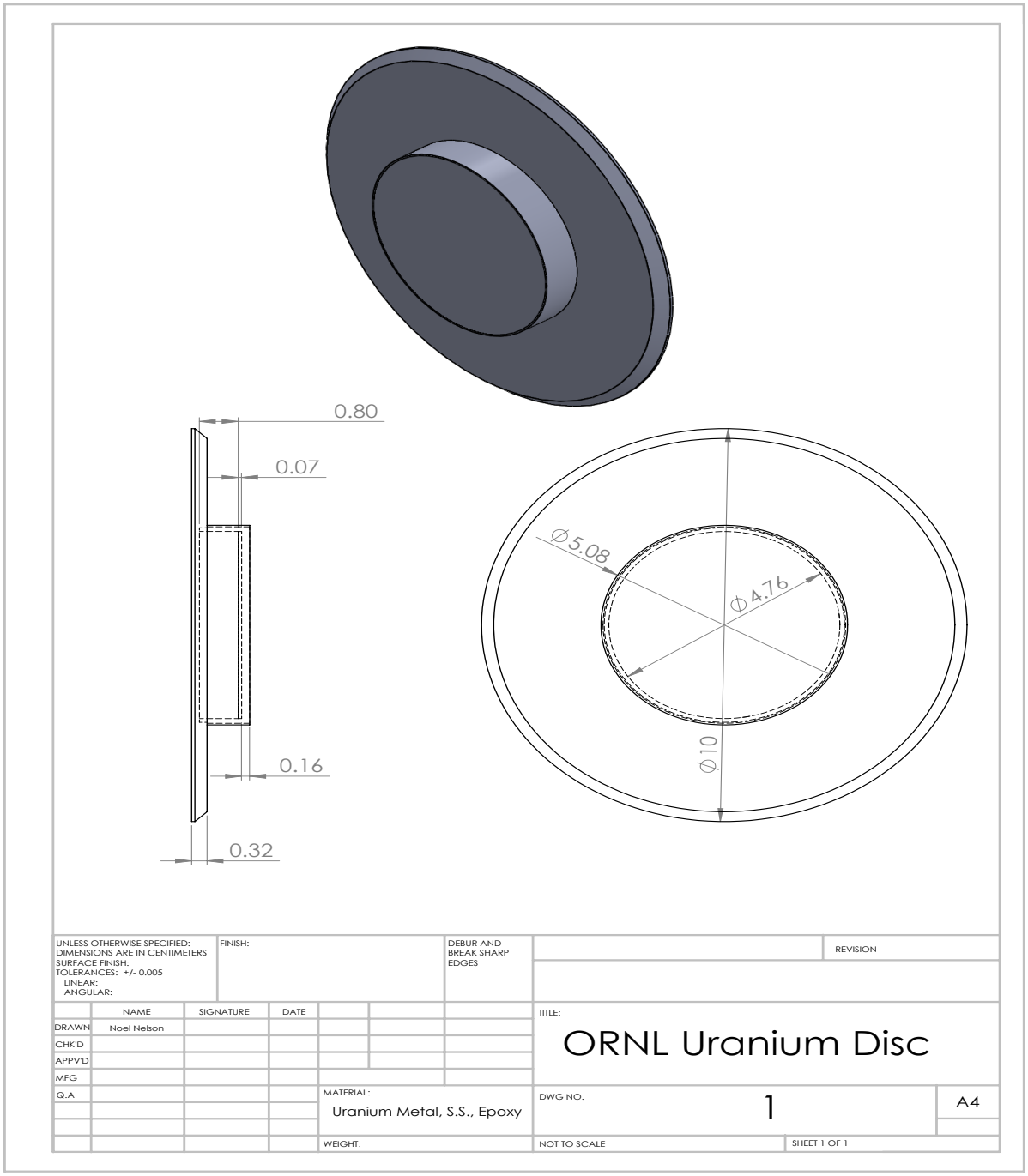

Figure 3.3 Dimensions of the HEU disc as prescribed from ORNL. The disc is made of stainless steel (shell), epoxy (adhesive), and HEU (4.76x0.07cm active source area).

The source in the disc is composed of U_3O_8, uranium's naturally occurring chemical form. The uranium compound is set on polyethylene epoxy and encased in stainless steel. The activity of the disc was 736 μ Ci on December 1, 2004. However, since uranium-235 has a very long half life (703.8 million years for U-235), the activity of the source at the time of the measurement was similar to its initial activity. The individual uranium nuclides that comprise the disc source employed in our experimental campaign are listed in Table 3.3.

Table 3.3 Enrichment of the uranium disc source

Nuclide	Weight %
U-234	1.016
U-235	93.162
U-236	0.400
U-238	5.421
C (natural)	1.009E-3

The disc is of a high enrichment of U-235. U-235 is a common target material for holdup problems in the nuclear fuel production industry because holdup material deposits present a proliferation risk and can become a criticality safety concern. The typical holdup measurement in this case will seek to detect the naturally emitted low energy gamma radiation. Hence, the focus of the validation experiments has been on the low energies of the detector spectrum where the highest intensity (most probable) gamma rays of U-235 are emitted (140-190 keV). This also explains the choice of the smaller NaI detector size, as high energy detection that would necessitate larger detectors to improve detection efficiency is of lower interest in the holdup field.

The last set of experiments were also performed on the highly enriched uranium disc but with a few modifications. First, one or two steel plates taped to the front of the NaI detector to provide attenuation. Second, the lateral distance between detector and source was reduced from 38 cm to 8 cm (11 cm from the crystal), and finally only on-axis measurements were taken. These measurements simulated the attenuation that would be provided by steel pipe and equipment walls that normally stand between the detector and a holdup material deposit. The dimensions of the first steel plate were 105.22mm x 157.75mm ($\pm 0.02mm$) with a thickness of 0.86 $\pm 0.04mm$. The second plate was 101.62mm x 152.66mm ($\pm 0.02mm$) and 0.90 $\pm 0.02mm$. For visual reference, a photograph of the HEU attenuation experiment at 11 cm is shown in Figure 3.4.

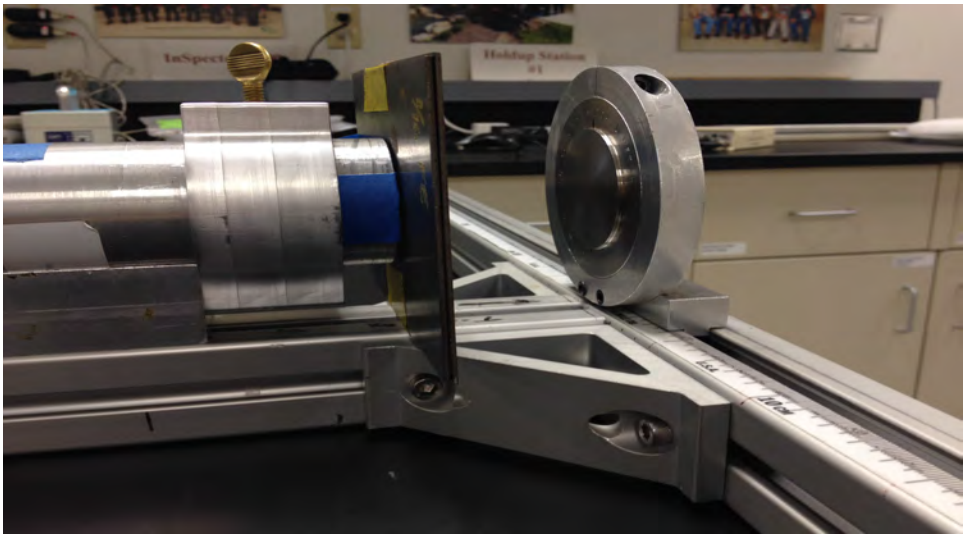

Figure 3.4 Photograph of the HEU disc attenuation experiment with two stainless steel plates attached to the detector (11 cm from the source).

For simplicity, in the MCNP simulation the isotopic compositions of the stainless steel plates were kept the same as the steel used to encase the detector and to encase the HEU source. The weight percent of each elemental isotope used in the steel alloy is listed in Table 3.4.

Table 3.4 Stainless steel alloy composition used in the MCNP simulations.

Nuclide	Weight %
Cr-50	0.800
Cr-52	16.2
Cr-53	0.200
Cr-54	0.400
Mn-55	2.00
Fe-54	4.20
Fe-56	64.8
Fe-57	1.50
Fe48	0.200
Ni-58	6.60
Ni-60	2.50
Ni-61	0.100
Ni-62	0.300
Ni-64	0.100

This composition of steel was taken directly from the MCNP model created by ORNL. The original model is available upon request from the Safeguards & Security Technology Group at ORNL.

3.2 Monte Carlo Transport Models

Version five of the Monte Carlo (MC) code MCNP (Monte Carlo N-Partical Transport Code) was used to calculate the incident gamma-ray photon flux on the 1x2 NaI detector crystal. MCNP is a radiation transport code developed by Los Alamos National Laboratory (LANL) that simulates a large number of random particle histories (particle tracks through a medium as well as collisions with its nuclei) in a user specified geometric configuration according to specified material cross sections (taken from the Evaluated Nuclear Data Files, ENDF). On the order of a few billion particle histories were run for each flux calculation to keep the MC statistical errors smaller than the measurement uncertainties.

The computational geometry specified for MCNP was simplified from the actual experimental geometric setups described in Sec. 3.1. Instead of including all details (i.e. objects) within the room, only the detector and all of its components and the source were simulated within a sphere of air. Only immediately adjacent objects like the table, the aluminum tee, and source holding

apparatuses would be likely to contribute in a small way to the collided fluence tally. There would be no contribution to the uncollided fluence tally as at least one Compton scatter with one of these objects would be required before the particle struck the detector. The detector collimator reduces the likelihood of these events further by reducing the detector solid angle by which particles can strike the detector crystal. So, the secondary geometry (table, tee, etc.) would only make a small contribution to the Compton continuum portion of detector spectra and hence was excluded from the MC models.

With the simplified geometry, an F4 (average fluence) tally was taken in the detector crystal cell by MCNP. MCNP calculates the fluence in a manner very similar to the fluence definition given by Equation 2.1, by summing the particle track lengths over the given cell volume for each discrete energy bin as specified by the user. In our case, 512 equal and discrete energy bins were chosen to match the energy range given by the DRF, and to match the 512 channels observed in the measured spectra. The average fluence tally over cell volume V was approximated discretely as follows,

$$\bar{\Phi}_V(E) \simeq \frac{1}{NV\Delta E} \sum_{i=1}^{N} \sum_{j=1}^{n_i} W_i^j s_i^j \, [\frac{1}{cm^2}], \tag{3.1}$$

where n_i is the number of times the ith particle enters V at energy E_k within energy bin k, s_i^j is that particle's jth track length in V, and W_i^j is the particle's weight when entering V for the jth time. Also, N is the total number of histories simulated by MCNP, and ΔE is the width of the tally's energy bin centered at energy E. This relation is only an approximation of the average fluence, but if a large number of particle histories pass through the cell volume, then it is a fairly accurate tally. [2]

However, as the MCNP fluence is based on the total number of particle histories, it can be converted to a flux as follows

$$\bar{\phi}(E) = \bar{\Phi}_V(E) \cdot A\gamma \, [\frac{photons}{cm^2 \cdot sec \cdot MeV}] \tag{3.2}$$

where A is the activity of the source in Becquerels (Bq) or decays/sec, and γ is the yield in particles/decay. So simply multiplying the F4 tally (fluence) by the source activity and yield converts the tally to the approximate scalar flux effective over the volume of the detector crystal.

Again, the detector response can be predicted by multiplying the DRF by the incident flux. However, Gardner's DRF does not fully include a direct property of specific NaI detectors, absolute efficiency, so it must be considered in the formal definition (Equation 3.3). [24] A differential pulse height spectrum (detector response), dN/dH is defined as

$$\frac{dN}{dH} = \int R(H,E)S(E)dE \approx \sum_{i=1}^{G} R_G(H,E_i)\bar{\phi}(E_i)\epsilon_{abs}(E_i). \tag{3.3}$$

The formal definition from Knoll is listed first and is approximated by the more directly applicable second definition. R(H,E) is the differential probability that a quanta of energy within dE about E leads to a pulse with amplitude within dH about H (DRF). S(E)dE is the differential number of incident radiation quanta with energy within dE about E. [9] $R_G(H,E_i)$ is Gardner's DRF, which is the differential probability that a flux of energy E_i leads to a pulse with amplitude within dH about H (DRF), and $\epsilon_{abs}(E_i)$ is the absolute efficiency. $\bar{\phi}(E_i)$ is the flux. To fully determine a detector response using Gardner's model, a new quantity must be defined and calculated: absolute efficiency.

Detector efficiency in general determines the percentage of radiation particles detected to the number emitted. There are two main classes of detector efficiency, absolute efficiency and intrinsic efficiency. Knoll defines absolute efficiency as simply the ratio of the number of detector pulses recorded to the number of particles with energy E emitted from the source. Absolute efficiency is dependent mainly on detector properties (cross-sections) and the counting geometry (source to detector position). Whereas the intrinsic efficiency is the ratio of the number of detector pulses recorded to the number of radiation quanta incident on the detector. The intrinsic efficiency is accounted for by the DRF, however, the absolute efficiency is not. Therefore it must be approximated as the energy deposited along the average path length through the detector crystal in MCNP simulation. [9]

In other words, the total absolute efficiency is the probability of particles incident on the detector interacting with the detector crystal over all energies (thereby creating a pulse at energy E). This probability is defined as

$$\epsilon^{j}_{abs}(E) = P_{interaction} = 1 - e^{-\mu_{tot}(E)\cdot s_j(E)} \tag{3.4}$$

where $\mu_{tot}(E \rightarrow E', \Omega \rightarrow \Omega')$ is the NaI photon macroscopic cross section and probability that an incident particle of energy E interacts per unit path length. $s_j(E)$ is the track length and an MCNP program called ptrac was used to record a large number of possible particle track lengths. This distribution was then averaged over all track lengths to produce an average absolute efficiency $\bar{\epsilon}_{abs}(E)$ as shown in Equation 3.5.

$$\bar{\epsilon}_{abs}(E) = \frac{1}{N_t}\sum_{j=1}^{N_t} \epsilon^{j}_{abs}(E) \tag{3.5}$$

N_t is the total number of track lengths recorded by ptrac. Again, the absolute efficiency is

multiplied by the DRF and the incident flux to produce a response spectrum (Equation 3.3). However, since Gardner's model typically underestimates the flat continuum under the response due to electron physics concerning channeling or possibly NaI impurities the resulting computed response must be normalized to the experimental response. [16] In our work, the normalization factors (the ratio of the areas under each curve) necessary to pull up the computed response to the experimental were found to be between two and eighteen. This is in good agreement with Gardner and Sood's results as they had experimental measurements that were up to around an order of magnitude greater than the responses predicted by g03.

CHAPTER

4

VALIDATION

Overall, the simulated detector responses predicted by Gardner's model predicted the highest intensity peak region of the experimental spectra fairly well, but had some difficulty in the continuum and secondary peak regions. In the highest intensity peak region of the response, most of the computed spectrum lay within two standard deviations of the experimental spectrum's centroid. The continuum discrepancies between the predicted and measured responses in the calibration sources appear to stem from miscalibration of the electron range multiplier (Equation 2.4) for the collimated 1x2" NaI detector. Gardner's current model was validated only for larger bare NaI detectors and not for collimated detectors and therefore some differences were expected. Whereas, significant underestimation of the secondary peaks occurred in the highly enriched uranium (HEU) disc spectra most likely due to outside crystal scattering with the detector collimator and other components.

4.1 Cs-137 Measurement

The first measurement was of a Cs-137 source. The Cs-137 source measurement was taken at a distance of 10 cm from the center of the detector face with the calibration source described by Table 3.1. The high source activity (4.13 μCi) allowed for for a precise measurement with less than one

percent uncertainty in the peak region in terms of counts (according to Poisson counting statistics), and it was counted for 4000 seconds. This source was used for validation and as one of the data points for the power law fit but not for the final energy calibration. The resulting spectra computed and measured are given in Figure 4.1a and compared with the computed response without the lead collimator and aluminum sheath simulated in the MCNP flux calculation (Figure 4.1b).

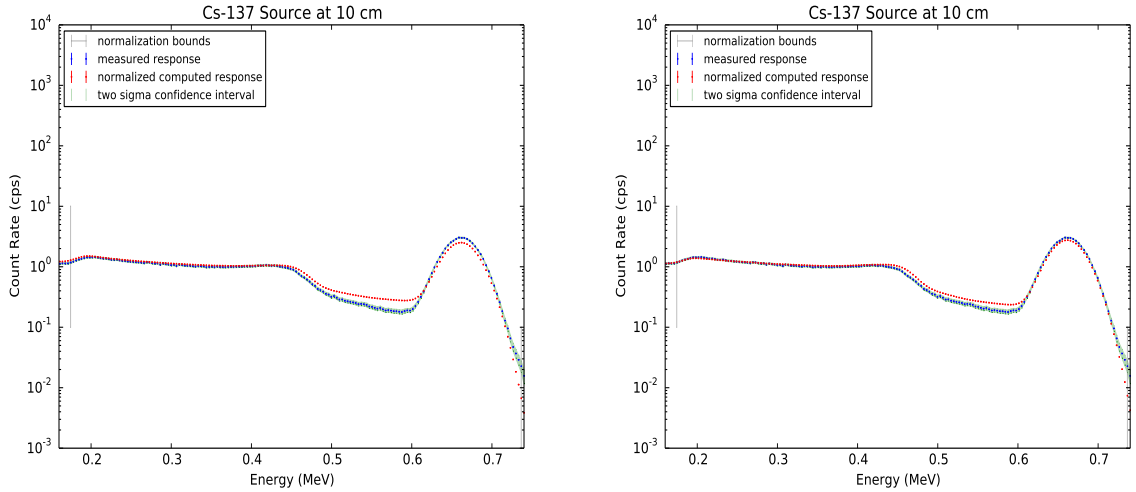

(a) **(b)**

Figure 4.1 Measured and normalized computed responses for the Cs-137 calibration source at 10 cm (normalized across bounds) with aluminum can (a) and without aluminum can and collimator (b).

It is apparent that the backscatter peak is overestimated and the peak underestimated. However, the greatest difference lies in the area between Compton edge and the peak, which will henceforth be referred to the valley of the response. At first this effect was thought to be just a product of the model being unable to account for the collimator geometry. In Sood's PhD thesis, a similar problem was occurring in the valley region of the response for their NaI 3x3" detector. However, the effect was reversed. For a bare NaI crystal simulation in MCNP for the flux calculation, the resulting response underestimated the valley. Simulating the detector aluminum sheath or can corrected this underestimation. [12]

In that manner, the same effect is observed here. Taking away the collimator and aluminum sheath from the MCNP geometry resulted in a response with a lower valley. This means that the collimator and can geometry were not the source of the shallow valley discrepancy.

Another difference between this validation exercise and Gardner and Sood's validation exercises, was how the computed spectrum was normalized to the measured response. Gardner and Sood chose to normalize to the peak channel only, whereas in this work, normalization to the area under the section of interest bounded by the normalization bounds was chosen instead. The normalization factor used to normalize the computed to the measured response spectrum is described mathematically by Equation 4.1

$$A_c = \sum_{n_{b1}}^{n_{b2}} R_i^c,$$

$$A_m = \sum_{n_{b1}}^{n_{b2}} R_i^m,$$

$$N_f = \frac{A_m}{A_c}, \tag{4.1}$$

where R_i^c is the computed count rate, and R_i^m is the measured count rate at channel i. n_{b1} and n_{b2} are the normalization bounds. Normalization bounds were chosen on a case by case basis. In this case the bounds were chosen to avoid bins artificially augmented by the rebinning process and unnecessary noise after the full energy peaks. Rebinning was accomplished by assuming the count rates within the old bins were uniformly distributed, and then collecting them into the new bins according to the fractions of the old bins determined by the uniform pdf. All contribution from the negative energy bins created from the energy calibration were lumped into the first two bins by the rebinning algorithm. Therefore those two bins were not included in the normalization.

The main reason for the normalization according to sections was chosen to minimize the effects of response error in parts of the spectrum. The other reason was to avoid choosing between multiple peaks in a spectrum. However, in this case normalizing to the peak channel revealed the true source of the valley problem as shown by the renormalized spectrum in Figure 4.2a and Gardner's responses resulting from various electron range multipliers: Figure 4.2b.

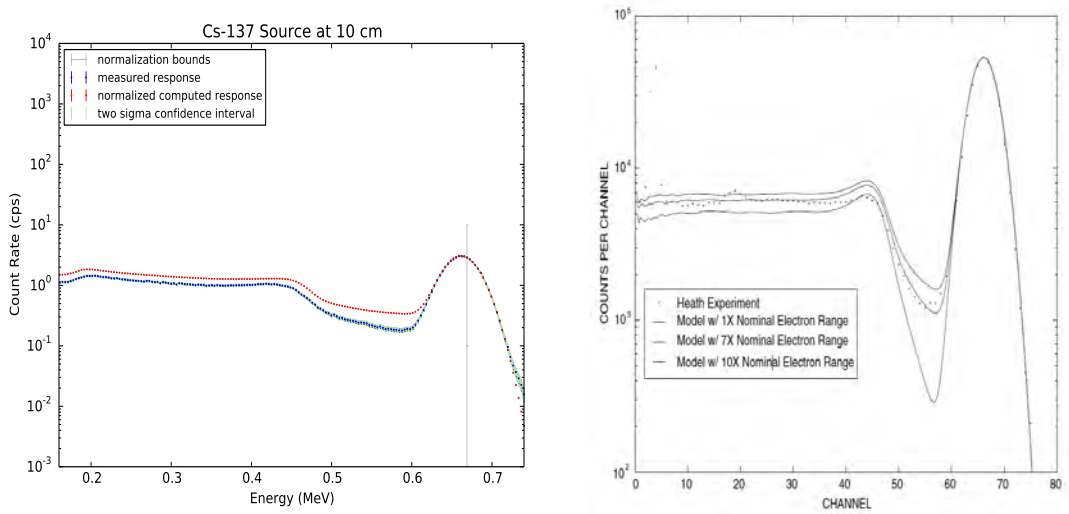

(a) **(b)**

Figure 4.2 (a) Measured and normalized computed responses for the Cs-137 calibration source at 10 cm (normalized to the peak). (b) 3x3" NaI detector computed responses over a varying electron range multiplier compared with the measured response from the Heath benchmark.

Now, as can be seen, the whole response spectrum is overestimated to the left of the peak for the figure on the left. A similar effect is observed by a spectrum with an electron range factor that is too low in Gardner's figure (right). [16] A range multiplier that is too high underestimates the continuum and a valley, while the reverse is true for one that is too low. Since the size of the detector and number of channels of the 1x2" ORNL detector is very different from Gardner's detector it is not surprising that the value of the electron range multiplier may no longer be optimal. Furthermore, the psuedo-electron range multiplier (Equation 2.4) was fit for Gardner's detector by trial and error. For this reason, and the fact that the HEU spectrum of interest contains far less contribution from Compton scatter, the correction of the factor is reserved for future work.

4.2 Co-60 Measurement

The next measurement concerned the Co-60 source described in Table 3.1 taped directly to the detector face. The low source activity (0.1927 μCi) required 1600 seconds for a reasonable number of counts (400 counts, 5% Poisson uncertainty) even on the detector face, so no further measurements were taken with this source. However, this source was only used for the detector energy calibration

and a simple baseline validation (shown in Figure 4.3a). The energy calibration and its parameter uncertainties are discussed further in Section 5.2.

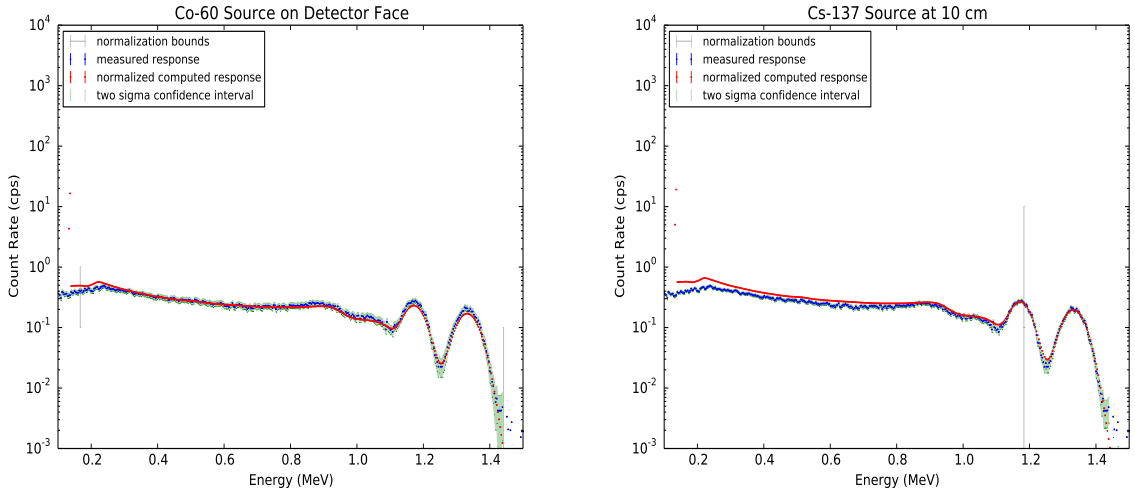

(a) **(b)**

Figure 4.3 (a) Measured and normalized computed responses for the Co-60 calibration source on the detector face using normalization across a range of channels (a) and normalized to the highest intensity peak (b).

As expected, the measured spectrum shows some significant fluctuation in the confidence interval along the response due to the low number of counts (higher uncertainty). The normalized computed response stays mostly well within the confidence interval of the measured response except at the backscatter peak around 2 MeV and the peaks are slightly underestimated. The two Compton edges and most of the continuum are predicted fairly well, however the backscatter peak region around 0.2 MeV is overestimated and the full energy peaks are slightly underestimated.

The overestimation may appear to be less significant in this case due to wider confidence bounds (from the lower fidelity of the measurement), but it is still apparent on closer inspection. The cause is most likely the same as the Cs-137 case, miscalibration of the electron range fit in the g03 source code. Normalization bounds were chosen for the same reasons as the Cs case.

4.3 Axial HEU Disc Measurement Set

The first set of HEU disc measurements were performed in order to test the performance of the DRF model for off-axis geometry. All measurements were carried out at a distance of 41 cm on-axis (y direction) from the crystal (38 cm from the face) and in set increments of 5 cm in the x direction. The central and first two positions used a 400 s background count, whereas the last two positions (x=15,20 cm) used background count times equivalent to the measurement count times. All background count times were chosen based on propagation of the net count uncertainty.

The HEU disc source at the central position (x=0 cm) was counted for four hundred seconds. The normalized computed and measured responses are given by Figure 4.4. The HEU disc specifications and composition can be found along with further details of the source geometry for the entire measurement set in Section 3.1.

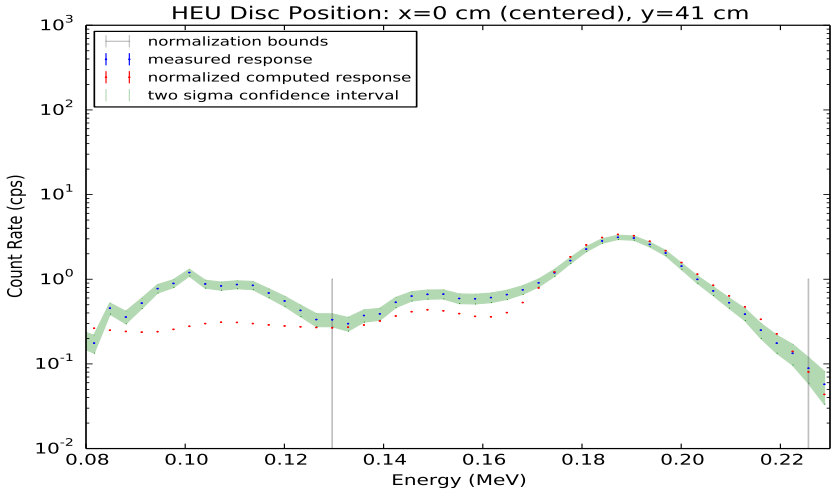

Figure 4.4 Measured and normalized computed responses for the HEU disc at the central position.

The normalized computed spectrum approximated the measured spectrum fairly well (within two standard deviations of the experimental response) for the main full energy peak at 186 keV and its shoulder peak at 205 keV with only a slight overestimation, however the secondary peaks at 163 and 144 keV are underestimated to compensate through normalization. The HEU gamma radiation energies are too low in this case to produce much of a Compton continuum, and any continuum that was produced is obscured by secondary peaks. So, it follows that absorption from the collimator

created a significant decrease in flux unaccounted for by the DRF. The cross sections from Table 4.1 verify this line of thought by demonstrating an absorption cross section that is about 10 times larger than the scattering cross section at 200 keV.

Table 4.1 Various photon cross sections ($c\,m^2/g$) from 60 keV to 2 MeV. [25]

Energy (MeV)	Coh. Scattering	Inc. Scattering	Absorp.	Total
6.000E-02	4.900E-01	9.734E-02	4.432E+00	5.020E+00
8.000E-02	3.078E-01	9.923E-02	2.012E+00	2.419E+00
8.800E-02	2.632E-01	9.928E-02	1.547E+00	1.910E+00
8.800E-02	2.632E-01	9.928E-02	7.321E+00	7.684E+00
1.000E-01	2.128E-01	9.894E-02	5.237E+00	5.549E+00
1.500E-01	1.049E-01	9.484E-02	1.815E+00	2.015E+00
2.000E-01	6.260E-02	8.966E-02	8.464E-01	9.986E-01
3.000E-01	2.988E-02	8.036E-02	2.930E-01	4.032E-01
4.000E-01	1.746E-02	7.310E-02	1.417E-01	2.323E-01
5.000E-01	1.143E-02	6.734E-02	8.257E-02	1.613E-01
6.000E-01	8.060E-03	6.263E-02	5.406E-02	1.248E-01
8.000E-01	4.621E-03	5.537E-02	2.871E-02	8.870E-02
1.000E+00	2.991E-03	4.993E-02	1.810E-02	7.102E-02
1.022E+00	2.865E-03	4.944E-02	1.732E-02	6.962E-02
1.250E+00	1.930E-03	4.476E-02	1.168E-02	5.875E-02
1.500E+00	1.347E-03	4.075E-02	8.321E-03	5.222E-02
2.000E+00	7.626E-04	3.482E-02	5.034E-03	4.607E-02

In terms of mean free paths (mfp), the 3 cm of lead provided by the collimator is approximately 29 mfp in terms of absorption and only three mfp in terms of incoherent scattering. The collimator is now optically thick in terms absorption but still thin in terms of scatter. While scattering will still only reduce the flux of the highest full energy peak of the spectrum, it would add to the flux of the lower energy peaks. This explains the overestimation of the high energy peak balanced with the underestimation of the lower peak. The scattering also distorted the shape of the two convolved peaks at 163 and 144 keV really only producing a peak at about 150 keV. Since simulation of the low fidelity results with the peaks combined and averaged in position and intensity yielded better results than the two simulated separately, they were kept together for all subsequent simulations. The comparison of the low fidelity runs with the peaks separated and combined can be found in the Appendix A.1.

The lowest energy peaks below the normalization bounds were originally thought to be a set of

four very low intensity peaks. However, upon further investigation it was found that the backscatter peaks from the three main full energy peaks were of the same energy. Using the Compton scattering equation in terms of energy, it was calculated that the backscatter peaks from the lead shielding would be centered at 114, 108, and 95 keV for the full energy peaks at 205, 186, and 150 keV, respectively. Backscattering that occurs inside the detector crystal is accounted for by the DRF, but that which occurs in the lead shielding is not. Therefore, the backscatter peaks are acknowledged, but excluded from the normalization region in order to avoid skewing the other validation regions.

It is worthy to note that two other factors could have also contributed to the underestimation of the two secondary peaks besides scattering in the collimator. Scattering within the table and aluminum tee that were not simulated in the MCNP fluence model, and gamma rays emitted by the decay products of U-234, U235, and U-238 could also have made some contribution. It was assumed that scattered photons from the table and tee would be negligible due to shielding provided by the collimator. Gamma radiation from uranium daughter products, however, were not simulated simply because there were too many low energy gamma rays with low relative yields (probability of emission per decay).

The HEU disc at the first position: 5 cm off-axis, was counted for a total of five hundred seconds. Measurements were taken in both the positive and negative x directions. The normalized computed and measured responses of both measurements are shown by Figure 4.5.

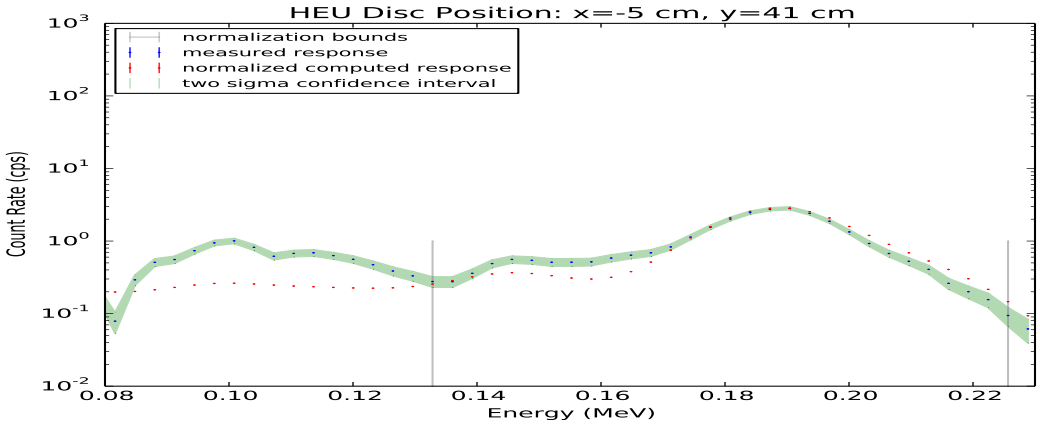

(a)

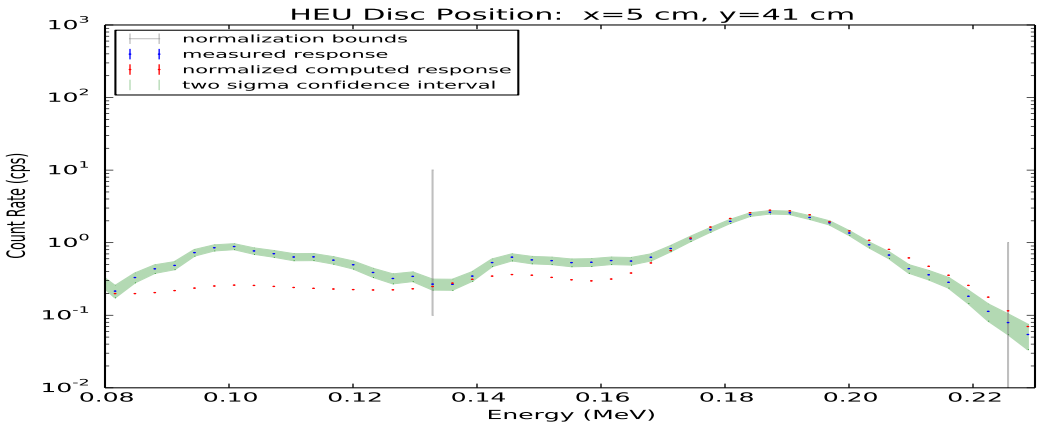

(b)

Figure 4.5 Measured and normalized computed responses for the HEU disc source at y=41 cm and (a) five centimeters left of center x=-5 cm and (b) five centimeters right of center x= 5 cm.

As expected, the entire count rate for both spectra have decreased slightly (about 25%) from the central position due to attenuation with the collimator and increased distance from the source. The lead backscatter peaks have also consolidated into a slightly different shape to accommodate a new more favorable set of scattering angles. The computed response again overestimates the main full energy peak and underestimates the secondary peaks due to the increased scatter from the collimator. Finally, normalization bounds remained the same as the central case.

The second position was 10 cm off-axis, and the HEU disc source was counted for 750 seconds.

The source at the third position (15 cm off-axis) was counted for 1600 seconds. The normalized computed and measured repsonses for the positive and negative axis positions at x=10 cm and x=15 cm are contained in Figure 4.6

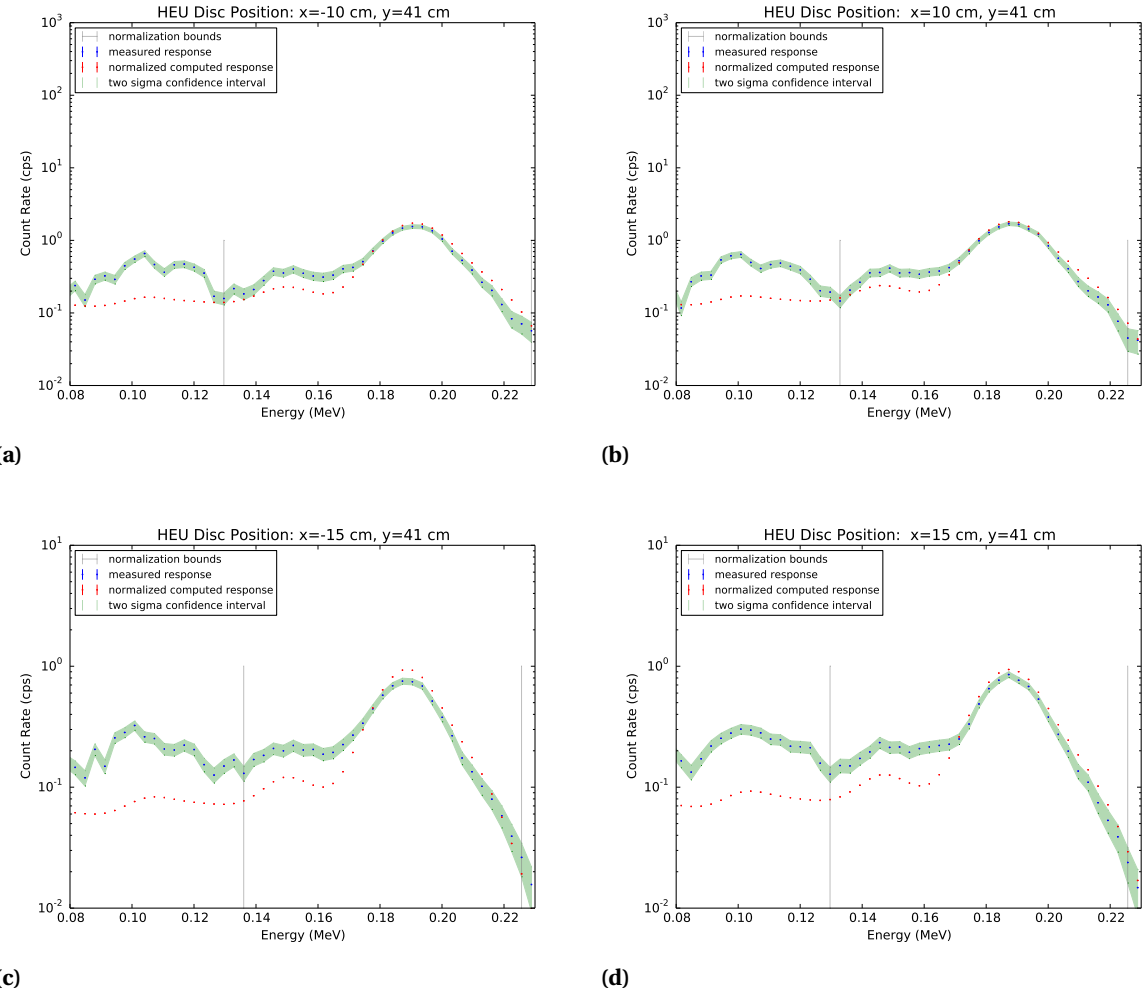

Figure 4.6 Measured and normalized computed responses for the HEU disc source at y=41 cm and (a) ten centimeters left of center x=-10 cm, (b) ten centimeters right of center x=10 cm, (c) fifteen centimeters left of center x=-15 cm, and (d) fifteen centimeters right of center x=15 cm.

The decreasing response trend continues for both positions (10,15 cm) with increased attenuation from the collimator and increased distance. At 15 cm, the secondary peak and the lead

backscatter peaks become nearly indistinguishable from background radiation. The reason for this high background is that the experiment was designed to ensure only the visibility of the main 186 keV peak. Even the least squares fit for the linear shifting process could not fit a Gaussian peak to the 150 keV peak for the x=-15 cm position in Figure 4.8c. So, only a one peak based shift was performed on this spectrum. Normalization bounds remained the same as previous cases for simplicity.

The final position (20 cm off-axis) was most influenced by background and required a long count time in order to overcome it. The HEU disc at 20 cm was counted for 4800 seconds. The normalized computed and measured responses are shown by Figure 4.7.

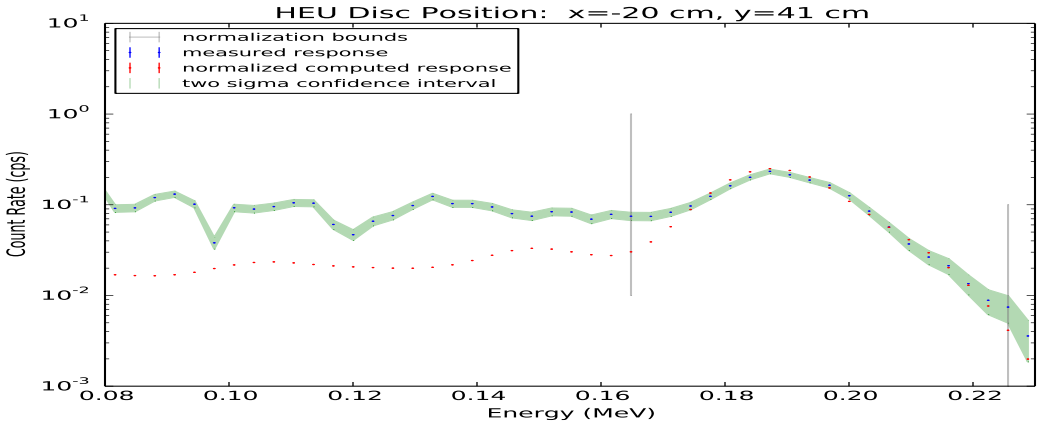

(a)

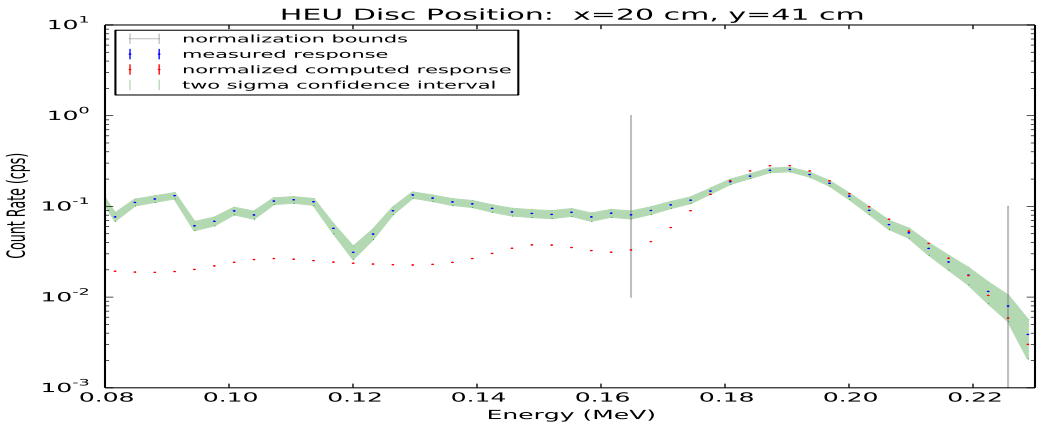

(b)

Figure 4.7 Measured and normalized computed responses for the HEU disc source at y=41 cm and (a) twenty centimeters left of center x=-20 cm and (b) twenty centimeters right of center x= 20 cm.

The count rate for this position was the lowest and most attenuated. Again, in order to focus on the main peak and maintain reasonable count times, only the main peak at 186 keV was resolved from background. Furthermore, the normalization was narrowed to only contain the main peak range. The normalized simulated response approximates peak behavior quite easily in spite of collimation and geometry when isolated from the rest of the spectrum.

4.4 HEU Disc Attenuation Measurement Set

The second set of HEU disc measurements were done in the interest of testing the DRF model's simulation of purely attenuated responses. Each measurement was performed centered on-axis at a distance of 11 cm from the crystal (only 8 cm from the face). The first measurement was counted without any attenuators. The second and third cases involved taping one and two stainless steel plates, respectively, to the face of the detector. The count time was kept constant at 300 s for all three measurements. The normalized computed and measured responses for all three cases are contained in Figure 4.8

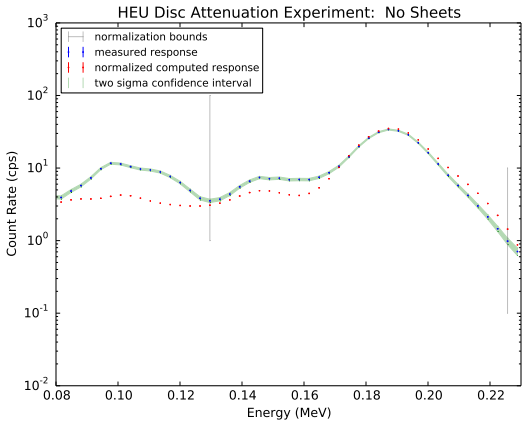

(a)

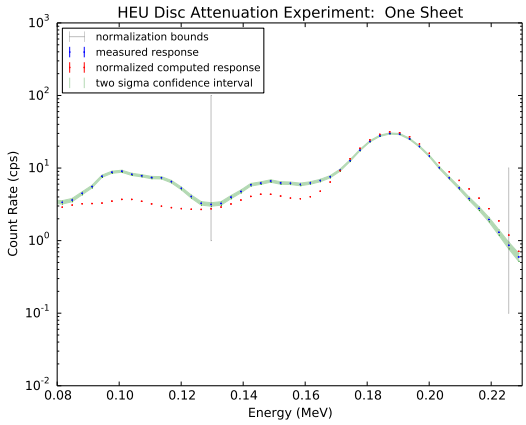

(b)

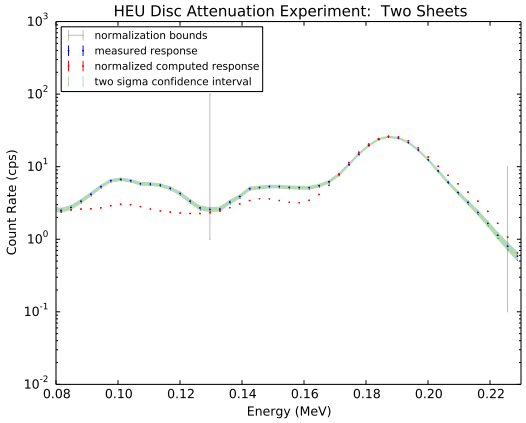

(c)

Figure 4.8 Measured and normalized computed responses for the HEU disc source with (a) no, (b) one, and (c) two stainless steel sheets taped to the detector face.

The same effects as observed before for the central position at 41 cm is observed for the unattenuated response: imbalance between the two full energy peaks and no prediction of the lead backscatter peak. However, the count rate is higher due to the closer proximity of the source. Naturally, the normalization bounds were kept the same as the inner axial HEU measurements. As stainless steel sheets are added to the face of the detector, a decrease in count rate across the entire spectrum is observed. The effect is very similar to that of the off-axis cases, except the background shape does not change since the angle of incident radiation is constant.

CHAPTER

5

UNCERTAINTY QUANTIFICATION

The other major goal is to quantify the uncertainties associated with the simulated responses that were used to validate the 1x2" NaI ORNL field detector. Validation reveals the accuracy of the model whereas uncertainty yields the expected precision of the simulated responses providing a level of confidence in the results. Each step in calculating the detector responses for each case has an associated uncertainty that has been calculated and compared to the experimental uncertainty where applicable.

Uncertainties that were easily reducible (e.g. MCNP uncertainties are based on the number of histories run), were always reduced below the peak channel uncertainty for each measurement case. Fitting uncertainties were based on the number of data points and the data uncertainty and therefore constrained to the quality of measurements performed. Even so, most of the fixed uncertainties tended to be under the respective measurement's experimental uncertainty.

5.1 Monte Carlo Based Uncertainties

The first quantity required to calculate a simulated response is the MCNP fluence calculated by particle track length tallies in MCNP. The fluence tally was divided into small energy bins according to the energy structure of the DRF calculated by g03. MCNP calculates the relative uncertainty of

each bin based on the number of particle track lengths that fall into that bin. Therefore, the number of total tallies were chosen in order to make the energy bin with the highest standard deviation have the same uncertainty as the lowest experimental uncertainty for each measurement excluding the Am-241 seed peak region. The number of histories required was then easily predicted, since again Monte Carlo standard deviation is equal to the inverse square root of the number of particle histories. In all cases, excluding Co-60, the number of histories required was on the order of billions. Similarly, in the Cs-137, Co-60, and HEU attenuation cases the highest computational uncertainties above 80 keV were ensured to be below the lowest uncertainty of the experimental results.

In certain cases of the HEU disc measurements at forty one centimeters, meeting the lowest experimental uncertainty for every tally energy bin was difficult to do in a reasonable amount of computational time. Certain MCNP modeling measures were taken to compensate and reduce computation times. First, the lowest energy bins below 80 keV were excluded for two reasons. These bins had the highest computational uncertainty, and they were overshadowed by leftover noise from the background subtraction of the Am-241 seed peak in the measured spectrum anyway.

The other change involved simply reducing the source definition from an isotropic source to only producing particle histories within the solid angle calculated to actually strike the detector whole, not just the face. All particles were then weighted using a form of importance sampling called forcing to prevent biasing the fluence tally, where the alternate pdf was uniform over the reduced angle and the original pdf was uniform in all directions. The modified pdf ($\tilde{f}(x)$) and the weighting factor (w) can be derived from Equations 5.1 and 5.2 respectively.

$$\tilde{f}(x) = \frac{f(x)}{\int_{x_1}^{x_2} f(x)dx} \; for \; x_{min} \leq x_1 \leq x \leq x_2 \leq x_{max}, \tag{5.1}$$

$$w = w_0 \frac{\int_{x_1}^{x_2} f(x)dx}{\int_{x_{min}}^{x_{max}} f(x)dx}, \tag{5.2}$$

where w is the forced weight of the particle and w_0 is the original weight of the particle. $f(x)$ is the original pdf, and x_1 and x_2 are the new bounds to be imposed on the pdf in order to only sample the important region contained by them. [26] In our work, the initial source distribution direction was modified from being isotropic in all directions to being contained within the angle cosine relative to a directional vector ($\vec{v}$) aligned with the center of the detector face but still isotropic in the other directions. A diagram of the detector to source geometry is shown for reference in Figure 5.1.

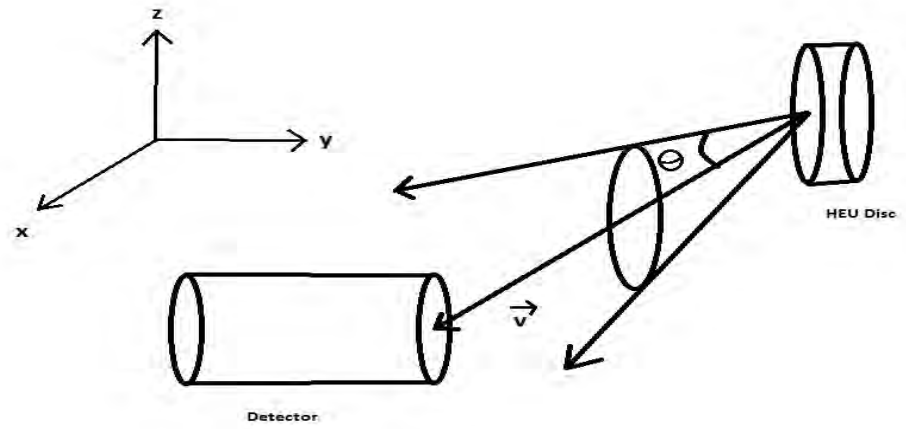

Figure 5.1 Diagram of the detector to source geometry and the solid angle chosen for the initial source distribution forcing pdf.

If μ_c is the cosine of angle θ (chosen to include the whole detector surface area), and the original pdf is $f(x) = d\mu/2$. The solid angle bounds are set to $x_1 = \mu_c$ and $x_2 = 1$ for a narrower forward direction. The modified pdf becomes

$$\tilde{f}(\mu) = \frac{\frac{d\mu}{2}}{\int_{\mu_c}^{1} \frac{d\mu}{2}} = \frac{d\mu}{1-\mu_c}, \tag{5.3}$$

which is sampled from instead of the full isotropic pdf. The corresponding weight can be derived as

$$w = w_0 \frac{\int_{\mu_c}^{1} \frac{d\mu}{2}}{\int_{-1}^{1} \frac{d\mu}{2}} = w_0 \frac{1-\mu_c}{2}, \tag{5.4}$$

which is multiplied by the original weight of each particle emitted from the source. This change reduced the variance significantly allowing a more reasonable amount of particles to be run for the $x = \pm 15$ cm and $x = \pm 20$ cm cases.

Since the table and room geometry are not simulated in the MCNP model anyway, it is a small approximation assuming that off direction photons would likely escape the system of interest.

Rather than show all of the bin uncertainties for each case, the case with the highest uncertainty (HEU disc at x=41 cm, y=-20 cm) excluding the Co-60 measurement will be given as an example. The fluence F4 tally is plotted with its uncertainty bounds in Figure 5.2.

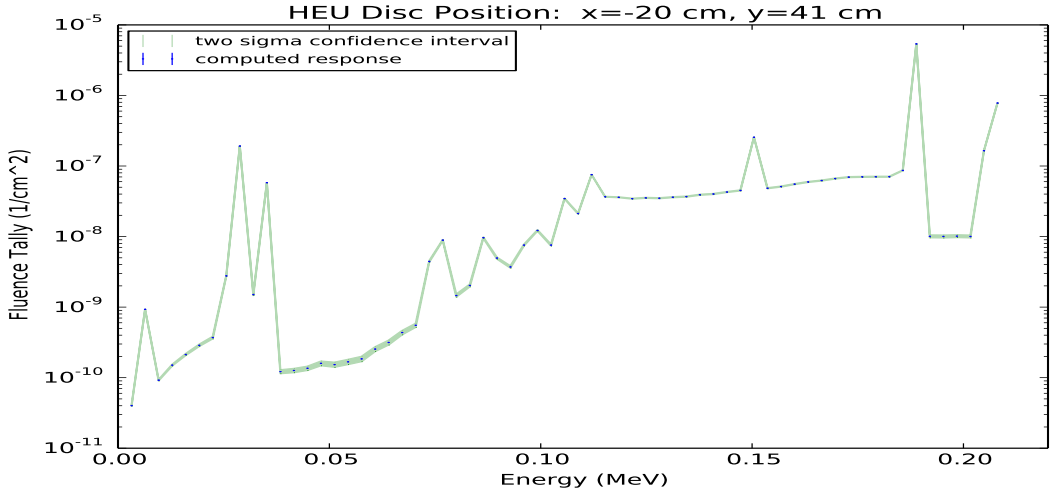

Figure 5.2 MCNP computed fluence and two sigma confidence interval

The bounds are fairly narrow beyond 80 keV. Each spike in the fluence corresponds to an incident gamma ray energy from the HEU disc starting from 105 keV and ending at 205 keV. The highest relative standard deviation greater than 80 keV was 2.44% at 195 keV. This was well below the lowest relative standard deviation of the HEU disc measurements at 41 cm which was 2.72%. As can be seen, the confidence bound between the 186 keV peak and the maximum energy peak at 205 keV is wider than anywhere else above 80 keV. Even the bins in under 80 keV did not exceed 5% relative standard deviations.

The DRF itself contains a Monte Carlo calculation that fully calculates the probabilities of a count in each channel based on contributions from all other channels using the fit parameters. Once again, the number of particle histories controls the relative uncertainty of the DRF, and the same threshold of the lowest experimental uncertainty for each case was selected for the highest DRF channel uncertainty. The order of particles required was much less than that of the flux calculations and only on the order of hundreds of thousands for all DRF Monte Carlo calculations.

Again, it is not feasible to show every uncertainty for each measurement, so only the highest uncertainty case (excluding Co-60) will be shown. As expected, this case would be the HEU disc at forty one centimeters for the off-axis experiments. Furthermore, six DRFs (one for each incident photon energy) are summed together to produce the total DRF, so the peak DRF with the highest uncertainty was chosen (105 keV peak). Because g03 did not have a second axis distance variable, only one total DRF was used for the off-axis HEU disc experiments. Now, since the full DRF depends

on two variables and would produce a three dimensional surface plot it will be easier to display the uncertainty bounded along the peak channel densities, as displayed in Figure 5.3.

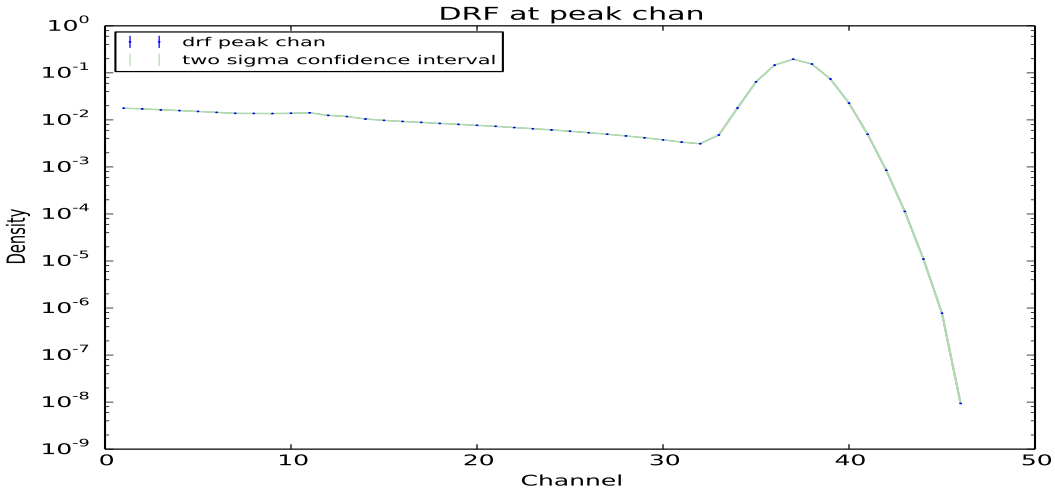

Figure 5.3 HEU disc at 41 cm with DRF densities for the 105 keV peak at channel 33 and the two sigma confidence interval

The highest probability density channel contributions for channel 33 are the immediate channels above that channel as expected from the spread of Gaussian uncertainty. However, the peak of the densities is actually about five to six channels over channel 33 which might explain the need to shift the computed spectra about the same number of channels. Channels above the spread have no contribution (density=zero), and the channels below are fairly constant. When the entire DRF is multiplied by the flux, the entire row of densities for each channel is multiplied by the flux vector and summed, so naturally the uncertainty is constant for each channel. The relative standard deviation for this channel was 0.420% and well under the 2.72% experimental uncertainty. Each channel row in the DRF possesses a similar density curve, so the highest flux channel will produce the highest response automatically. The highest relative standard deviation of all the DRF channels was for the last channel (512) and was only 1.80%.

The total absolute efficiency calculation was carried out through calculation with an XCOM NaI cross section and particle track lengths through the crystal volume in MCNP as described by Equation 3.5. The number of histories were increased accordingly until the proper number of path lengths were acquired to reduce the highest relative standard deviation to approximately that of

the lowest experimental uncertainties. The highest uncertainty case is shown for the HEU disc at forty one centimeters. The resulting density curve with a two sigma confidence interval is shown in Figure 5.4.

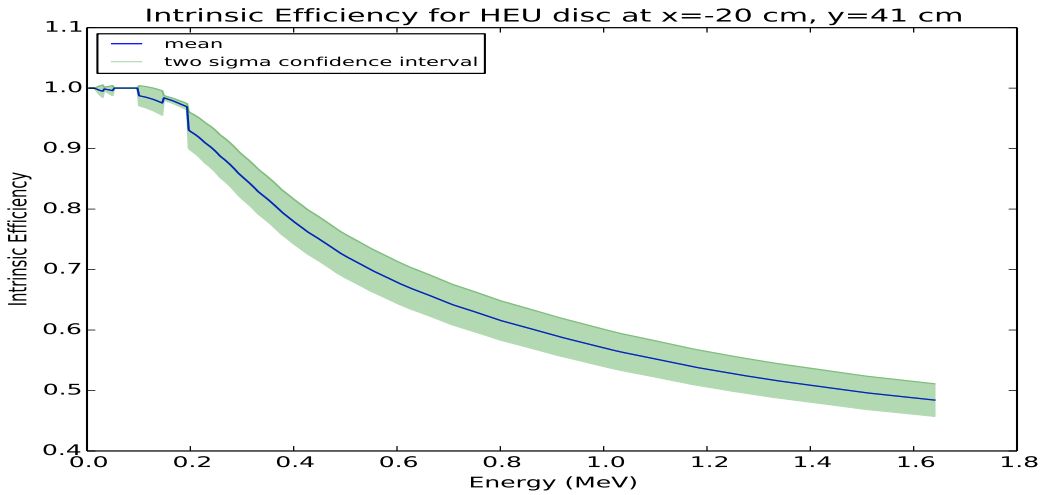

Figure 5.4 Absolute efficiency of the HEU disc at 41 and two standard deviation confidence interval

This curve is essentially the probability of an interaction of energy E, occurring within the crystal. So, low energies are almost certain to be absorbed and higher energies are more likely to escape. The relative uncertainty is fairly small at low energies, but grows as energy increases. The relative standard deviation was 2.78% at the highest energy which was close to the lowest experimental relative uncertainty of 2.72%. At 0.2 MeV or less where the majority of the HEU spectrum lies the relative uncertainty is much lower and well below 1%. The higher uncertainty at higher energies is purely a factor of lack of information or no particle tracks at those energies.

5.2 Parameter Uncertainties

The first set of parameters are associated with both the measured and computed results: the energy calibration. The energy calibration is simply a polynomial that converts channel data to energy data based off of the nonlinear scintillation behavior of NaI detectors. This is a necessary piece for verifying physical measurements and a required conversion for the empirical power law of the DRF. The energy polynomial is given by Equation 5.5

$$E(keV) = \alpha_2 x^2 + \alpha_1 x + \alpha_0, \tag{5.5}$$

where x is the channel, E is energy in keV, and α_0, α_1, and α_2 are the polynomial parameters. The energy calibration parameters were found by a least squares fit of measurements of known sources with known energies at the gain settings discussed in Section 3.1. Three sources were used to determine the energy calibration polynomial: the Am-241 seed source, and the Cs-137 and Co-60 sources detailed in Table 3.1. Each channel mean for the energy calibration was found by taking the peak section of the measured responses for each source and fitting them according to a simple Gaussian plus linear background empirical model. The linear Gaussian model is given by Equation 5.6

$$G_y = \frac{B}{\sqrt{2\pi}\sigma_T} e^{-\frac{1}{2}(\frac{x-\bar{x}}{\sigma_T})^2} + a_1(x-\bar{x}) + a_0. \tag{5.6}$$

where x is the detector channel and G_y is the resulting point in the Gaussian curve. B is the normalization constant, and σ is the standard deviation of the Gaussian. Finally, $\bar{x}$ is the mean of the Gaussian, and a_0 and a_1 form the linear background term. The Gaussian channel means and parameter standard deviations are shown in Table 5.1.

Table 5.1 Channel means and associated standard deviations (STD) of the Gaussian fits for the energy calibration.

Source	Pk. No.	Mean Chan., $\bar{x}$	STD, $\sigma^{\bar{x}}$	Rel. STD, $\sigma^{\bar{x}}_{rel}$ (%)	Red. Chi-Square, χ^2_v
Am-241	1	20.92	2.767E-3	1.323E-2	0.8973
Cs-137	1	195.79	1.804E-2	9.212E-3	2.569
Co-60	1	341.64	0.2214	6.479E-2	1.059
Co-60	2	386.38	0.1761	4.557E-2	0.7260

Each least squares fit was performed by a nonlinear least squares algorithm in MATLAB called lsqnonlin. The standard deviation was found through the simple Frequentist methods described in Section 2.5 from the parameter covariance matrix. Classical Frequentist methods were used in lieu of Bayesian for all Gaussian peak fitting except for the power law measurements because there were usually a larger number of points in each peak. Also, Frequentist calculations require less calculation time than DRAM (about 100 times less). The algorithm had no trouble fitting these peaks, as each relative standard deviation of the mean channel is well under 1%. Co-60, as expected, had the highest uncertainty because it had the lowest source strength and a low count time (low

fidelity measurement). However, all peaks were well approximated by the model producing reduced chi-squares well under ten.

A similar least squares fit was performed by lsqnonlin using the energy polynomial (Equation 5.5). The resulting parameter means and standard deviations are tabulated in Table 5.2.

Table 5.2 Energy calibration parameter means and standard deviations.

Parameter	Mean	STD., σ	Rel. STD, σ_{rel} (%)	χ^2_v
a_2	2.104E-4	4.352E-5	20.68	530.4
a_1	3.395	1.762E-2	0.5188	
a_0	-11.07	1.382	12.48	

Since there were a low number of data points for the energy calibration fit, the Bayesian code DRAM was used to calculate the standard deviations and optimize the parameter means from the least squares starting values. NaI is fairly linear in terms of scintillation to energy deposited ratio for low energies, so it is no surprise that the second order term is very small. Unfortunately, this also means that it has a larger relative standard deviation. The y-intercept term (a_0) has a little more effect but also has more uncertainty than the first order term (which holds the lowest uncertainty at about half of a percent).

In order to check DRAM for a possible error in the fit and uncertainty calculations, a standard linear regression fit with Frequentist calculations was calculated for comparison. A slightly better reduced chi-squared value of 430.5 was found, and the parameter values were modulated within 1% of the Bayesian values. The uncertainties were also halved. So, in this case, it may actually have been slightly better to use the standard linear regression, however, the improvement in the results would have been marginal.

Overall, the calibration still performed well in spite of the poor reduced chi-squared value, as each channel mean converted to energy was found to be within two keV (1% relative error) from its true value for all peaks that were not convolved with another peak (e.g. the 150 keV convolved HEU peak). This is acceptable because the same energy calibration is used for both computed spectra and measured spectra. So, any additional error would offset both spectra by the same amount.

The next set of parameters involves the power law of the DRF model itself. g03 not only uses Monte Carlo simulation to calculate DRFs, but requires an empirically fit power law based on Gaussian spread data from the detector of interest. The power law is the very same described in the DRF model section of the Literature review by Equation 2.3.

Again, linear Gaussian (Equation 5.6) least squares fits of several sources were required to obtain mean Gaussian standard deviations for the power law. Five sources were used: Am-241 (seed source), Ba-133, Cs-137 (same as in Table 3.1), Mn-54, and Na-22. Since Ba-133 has two full energy peaks, a total of six full energy peaks were fit.

Source geometry and activity were not required for the power law fit. However, each peak was counted until 10,000 counts were registered in the peak channel to keep the experimental uncertainty close to one percent in the peak region. Some weak sources needed multiple measurements added together to meet 10,000 counts due to the MCA timer limit. Furthermore, there should be no added uncertainty in the measurements because the spectra were checked for gain drift and perfomred immediately after one another. The mean Gaussian standard deviations ($\sigma_T(E_I)$) and their uncertainties are compiled in Table 5.3.

Table 5.3 Channel means and associated standard deviations of the Gaussian fits for the power law.

Source	Pk. No.	Energy (MeV)	Gauss. STD, σ_T	STD, σ^{σ_T}	Rel. STD, $\sigma_{rel}^{\sigma_T}$ (%)	χ_v^2
Am-241	1	5.954E-2	4.454E-3	2.128E-5	0.4778	0.9191
Ba-133	1	8.100E-2	4.879E-3	4.478E-4	9.177	56.51
Ba-133	2	3.560E-1	1.499E-2	2.106E-4	1.405	13.09
Cs-137	1	6.617E-1	2.137E-2	7.599E-5	0.3556	2.295
Mn-54	1	8.348E-1	2.468E-2	8.469E-5	0.3432	1.011
Na-22	1	1.275	3.207E-2	8.001E-5	0.2495	1.611

Some of the peaks involved in the Gaussian fits for the power law spread data were sparse in data points, so DRAM was used to optimize the Gaussian spread parameter means (σ_T) and determine their respective standard deviations (σ^{σ_T}). The first Ba-133 peak suffered quite a bit of background interference from convolution with the Am-241 peak, and had fewer points to fit the linear Gaussian curve to resulting in the highest uncertainty and a reduced chi-square well over ten ($\chi_{red}^2 \leq 10$ is considered a good fit). The first peak's data was almost thrown out for its poor Gaussian fit. The second Ba-133 peak was also over 1% in relative uncertainty and had a reduced chi-square over ten (to a much lesser extent than the first). This was probably due to some interference with a third lower intensity peak at 300 keV obscuring the left tail of the Gaussian.

As a follow up, examining the linear correlation coefficients of a model can reveal weak model parameters. If the correlation coefficients of a parameter are all under about 0.2, then that parameter shares no linear relationship to any of the other parameters. Sometimes, removing such parameters from the model can improve the fit. An example of this model will be provided using the worst fit

case to check for model weaknesses. The linear correlation coefficient matrix for the first Ba-133 peak (81 keV) is listed as Table 5.4.

Table 5.4 Linear correlation coefficients for the 81 keV Ba-133 linear Gaussian model fit.

Parameter	σ_T	$\bar{x}$	B	a_0	a_1
σ_T	1	-0.9594	0.9901	-0.9838	0.9737
$\bar{x}$	-0.9594	1	-0.9727	0.9664	-0.9801
B	0.9901	-0.9727	1	-0.9978	0.9922
a_0	-0.9838	0.9664	-0.9978	1	-0.9936
a_1	0.9737	-0.9801	0.9922	-0.9936	1

All of the coefficients are very highly correlated (>0.9), so there are no weak parameters. This does not mean that the model cannot be improved, just no terms should be removed. Maybe a few terms could be added to account for the nonlinear tail of the 60 keV Am-241 seed peak, however, a more practical alternative was found by weighting the power law fit by the x-data uncertainties at each point.

This alternative was developed in response to the higher uncertainty in the Ba-133 peaks and the distrust in the Am-241 seed peak due to lack of exact knowledge of the seed's position relative to the center of the crystal. Originally, only three sources were used to calibrate the DRF power law, but results showed some error in the peak widths of some of the validation measurements. To counter this issue, the power law fit was thought to be improved with extra measurements at energies between the three original points. However, rather than throw out less than ideal data points for the power law, the least squares fit was simply adjusted to weight each data point by its uncertainty. Instead of purely minimizing the sum of squares (classical least squares), the weighted sum of squares (Equation 5.7) was minimized.

$$WSS_q = \sum_{i=1}^{n} \left(\frac{\Upsilon_i - f(x_i, p_j)}{\sigma(x_i)}\right)^2 \tag{5.7}$$

Above, n is the total number of data points. Υ_i is the measured result at data point i, and $f(x_i, p_j)$ is the value of the function being fit to the data at i. p_j are the parameters, and $\sigma(x_i)$ is the standard deviation of Υ_i used as a weight. In this case the function fit was the power law, Equation 2.3, and Υ was simply $\sigma_T(E)$.

The rest of the least squares and uncertainty calculations remained the same. The resulting parameter means and standard deviations of the weighted power law fit are in Table 5.5.

Table 5.5 Power law parameter means and standard deviations.

Parameter	Mean	Standard Deviation, σ	Relative STD, σ_{rel} (%)	χ^2_ν
a	0.027608	1.684E-4	0.6100	8.500E-6
b	0.644237	5.719E-3	0.8877	

There were several data points for the power law, and it was uncertain if the weighted sum of squares would behave well with the Bayesian code. So, the classical Frequentist values were used in the DRF calculations for expedience. The Bayesian code was tested later and gave comparable results which are given in Appendix A.2. The parameter values are on the order of Peplow and Heath's power law coefficients, and the relative standard deviations are under 1%. The power law is a bit overfit, but that is somewhat expected as several extra measurements were taken when the three point fit proved insufficient.

The final process requiring uncertainty quantification is the linear energy shift required to allign the computed and measured spectra. g03 contains a small bug that tends to offset the entire spectrum by several channels to the right. A program called gshift (courtesy of Gardner's group) corrects this issue by linearly interpolating between the channels and shifting the pulse height spectrum to the desired channels according to Equation 5.8

$$x_{chan} = A \cdot E_p + B, \tag{5.8}$$

$$E_p = E \cdot f(E),$$

where x_{chan} is the channel number, and A is a normalization constant. B is the number of background channels, and E_p is the energy of the original pulse-height spectrum. Finally, E is the true energy of the gamma-ray (or desired energy to shift the peak to), and f(E) is the functional relationship of the ratio: Ep/E. A and B are adjusted accordingly to shift the peak(s) to the desired location, while f(E) is chosen by the user. Either f(E) is based off of the natural NaI nonlinearity (for two or more peaks), or directly proportional (for one peak).

In order to determine the linear shift required, the mean peak channels of both the measured and computed spectra had to be found. The means were found in the same manner as those for the energy calibration fit, by fitting the spectral peaks to the linear Gaussian model (Equation 5.6). The Gaussian peak channel means and the associated uncertainties for the computed spectra are given by Table 5.6 and those of the measured spectra by Table 5.7.

Table 5.6 Computed spectrum channel means and associated standard deviations of the Gaussian fits for the energy energy shift.

Source	Pk. No.	Mean Chan., $\bar{x}$	Stand. Dev., $\sigma^{\bar{x}}$	Rel. STD, $\sigma^{\bar{x}}_{rel}$ (%)	χ^2_v
Cs-137	1	204.67	9.799E-3	4.788E-3	1.528E-4
Co-60	1	354.68	1.310E-2	3.692E-3	3.867E-6
Co-60	2	397.71	7.363E-3	1.851E-3	1.985E-6
HEU Rad.					
Center	1	52.22	1.610E-2	3.084E-2	3.257E-3
Center	2	64.51	1.093E-2	1.695E-2	0.2371
L1	1	52.22	1.596E-2	3.056E-2	1.586E-3
L1	2	64.51	1.072E-2	1.661E-2	0.1116
L2	1	52.23	1.527E-2	2.924E-2	4.388E-4
L2	2	64.51	1.069E-2	1.656E-2	3.294E-2
L3	1	52.24	1.442E-2	2.760E-2	1.318E-4
L3	2	64.51	1.090E-2	1.689E-2	1.127E-2
L4	1	52.26	1.272E-2	2.433E-2	3.262E-5
L4	2	64.52	1.174E-2	1.819E-2	4.119E-3
R1	1	52.22	1.592E-2	3.049E-2	1.576E-3
R1	2	64.51	1.073E-2	1.663E-2	0.1122
R2	1	52.23	1.523E-2	2.916E-2	4.344E-4
R2	2	64.52	1.073E-2	1.663E-2	3.309E-2
R3	1	52.24	1.450E-2	2.775E-2	1.318E-4
R3	2	64.52	1.095E-2	1.698E-2	1.141E-2
R4	1	52.25	1.282E-2	2.453E-2	3.303E-5
R4	2	64.52	1.156E-2	1.791E-2	3.971E-3
HEU atten.					
0 sheets	1	52.15	2.380E-2	4.564E-2	2.151E-2
0 sheets	2	64.46	3.873E-3	6.008E-3	7.474E-2
1 sheet	1	52.13	2.600E-2	4.987E-2	2.249E-2
1 sheet	2	64.45	3.312E-3	5.139E-3	4.582E-2
2 sheets	1	52.12	2.818E-2	5.407E-2	2.286E-2
2 sheets	2	64.44	2.891E-3	4.487E-3	2.658E-2

Table 5.7 Experimental net spectrum channel means and associated standard deviations of the Gaussian fits for the energy shift.

Source	Pk. No.	Mean Chan., $\bar{x}$	Stand. Dev., $\sigma^{\bar{x}}$	Rel. STD, $\sigma^{\bar{x}}_{rel}$ (%)	χ^2_v
Cs-137	1	195.79	1.804E-2	9.212E-3	2.569
Co-60	1	341.64	0.2214	6.479E-2	1.059
Co-60	2	386.38	0.1761	4.557E-2	0.7260
HEU Rad.					
Center	1	46.90	0.8512	1.815	0.5671
Center	2	58.30	3.464E-2	5.942E-2	8.139E-2
L1	1	45.84	0.1005	0.2192	6.329E-2
L1	2	58.54	0.1584	0.2706	0.9686
L2	1	46.2	0.4500	0.9740	1.626
L2	2	58.55	0.2289	0.3910	1.060
L3	1	X	X	X	X
L3	2	58.51	0.1789	0.3057	0.8369
L4	1	X	X	X	X
L4	2	58.23	0.1407	0.2416	1.837
R1	1	45.94	0.1990	0.4332	0.8888
R1	2	58.34	0.1473	0.2525	1.168
R2	1	46.02	0.3772	0.8197	0.8361
R2	2	58.35	0.1200	0.2057	0.5307
R3	1	46.25	0.4760	1.029	0.9318
R3	2	58.20	0.2007	0.3449	2.701
R4	1	X	X	X	X
R4	2	58.54	0.2326	0.3973	1.716
HEU atten.					
0 sheets	1	46.02	0.2425	0.5269	3.488
0 sheets	2	58.37	6.708E-2	0.1149	1.298
1 sheet	1	46.12	0.3239	0.7023	4.015
1 sheet	2	58.32	7.000E-2	0.1200	1.248
2 sheets	1	45.99	0.3881	0.8438	5.661
2 sheets	2	58.33	5.568E-2	9.545E-2	1.104

All of the computational channel relative standard deviations were well under 1% (lowest Poisson uncertainty estimated from highest peak channels), but not all of the net (background subtracted) experimental ones were. However, the experimental channel uncertainties that were over 1% occurred only in the lower intensity 150 keV peak of forty one centimeter HEU disc measurements. Furthermore, those uncertainties were expected to be higher as the lowest peak channel poisson uncertainty of the forty one centimeter HEU measurements was 2.72%. Some of the reduced chi-

square values showed some overfitting (perhaps the linear background was unnecessary for the computed results), but none of the values were over ten.

All of the computational peak fits naturally had much lower uncertainties then the experimental peak fits. Some of the 150 keV experimental peaks of the far off-axis HEU disc measurements were not well developed, and could not be fit. In these cases, the shifting program employed the single peak shift algorithm (Equation reference if available here) instead using only the main 186 keV peak channel means to shift the computed spectrum in alignment with the measured.

CHAPTER

6

CONCLUSION AND FUTURE WORK

The goal of this work was to validate and quantify the uncertainty of Gardner's DRF model for several source types and geometric configurations of a 1x2" NaI detector. How these goals were met has already been detailed in the body of this thesis, but the implications of the results of this work and extensions to future work will be discussed in this section.

6.1 Conclusion

Validation of calibration sources The model aligned within two standard deviations of the measured spectrum of the full energy peaks of the Co-60 and Cs-137 button source spectra, but significantly overestimated the Compton continuum by about 45-60%. At first this discrepancy was thought to be simply an effect of the collimator being unaccounted for by the DRF model, but this hypothesis proved to be incorrect. More light was shed on the discrepancy when a peak normalization of the spectrum instead of the sectional normalization was performed in order to compare spectra with a previous one from Gardner's validation work.

Under peak normalization, the computed spectrum nearly matched with the peak of the measured response, but overestimated the rest of the spectrum. This effect was very similar to one of Gardner's spectra in which the electron range multiplier (Equation 2.4) was set too low. The electron

range multiplier is a semi-empirical model of the electron range that was fit by trial and error. Further details of the fit were not given.

Validation of HEU disc The HEU validation campaigns consisted of two sets of experiments: one concerning x-axis off-sets of the source from the origin at a y-axis distance of 41 cm, and another one involving attenuation using steel plates for the disc centered on the x-axis at a distance of 11 cm. Both campaigns showed predictable physics effects in terms of backscatter peak distortion and attenuation for each type of geometrical configuration change, but a markedly different effect occurred instead of the continuum overestimation witnessed in the calibration source validation.

Since the full energy peak of U-235 is too low for any sizable Compton scatter losses from the detector crystal, there is no visible Compton continuum in the HEU spectra. Without a continuum, there are only four main peaks observed in the measured spectrum: the main full energy peak (186 keV), the shoulder peak (205 keV), the convolved peak (150 keV), and a few backscatter peaks (around 100 keV). The model reproduced the main peak and its shoulder peak well, again within two standard deviations of the measured count rate, but underestimated the convolved peak and did not reproduce the backscatter peak. The backscatter peak is an artifact of the lead collimator around the detector. This collimator is not accounted for by the DRF model because the model currently only reproduces the effects of scattering within the detector crystal. It is also possible that not accounting for the local geometry of the table and aluminum tee and the daughter product decay photons of the uranium may also have contributed to the secondary peak underestimation.

Uncertainty quantification Finally, uncertainty quantification of the model was conducted on every calculated quantity from the flux calculation by MCNP to the Gaussian peak fits for the spectral shifting program. Where the uncertainty was controllable by the number of particle histories chosen in Monte Carlo simulations, it was reduced below the lowest measured uncertainty. Where it was constrained to the accuracy of the model for least squares fitting, it was compared to the experimental uncertainty and the reduced chi-square test was performed to check for goodness of fit.

Only two poor fits were observed, out of a total of sixty examined in this work, (in terms of parameter variance and chi-square): the energy calibration and the Ba-133 Gaussian peak fits used for the power law fit. The first was compared with other data points to verify a working accuracy, since the measurement of further known sources was impractical. The largest error between the calculated energy of a peak and its known value was approximately one percent for any non-convolved full energy peak. Because the energy calibration is applied to both the measured and computed spectrum (not affecting any differences between the spectra), it was deemed acceptable.

The poor Ba-133 peak fits were largely caused by the peak convolutions with other peaks. The fit was necessary to obtain the peak standard deviation for the power law fit. Rather than discard

the Ba-133 points, the problem was resolved by weighting the power law fit by the uncertainty in the Gaussian peak width data points using a weighted least squares technique (Equation 5.7). All other parameter uncertainties fell well under the lowest experimental uncertainty and passed the chi-square test, hence they are considered reliable for use in future work.

6.2 Future Work

There are many parameters that could affect the shape of the normalized computed responses produced by the DRF. In order to narrow down the parameters that contribute most to the secondary peaks and the Compton continuum of the spectrum, a parameterization study could be performed. Parameters such as the electron range multiplier, collimator thickness and density, source position and peak intensity, and input cross-sections would be incrementally changed to test the resulting sensitivity of the normalized computed response. The most sensitive parameters could then be prioritized for further study.

The electron range multiplier This factor was originally said to have been fit by trial and error. Details of experimental data used and how it was fit have not yet been found. Further investigation could be helpful for tuning the factor for new detector configurations. However, it is possible that the parameters were not fit but guessed until a favorable result was found. If so, then it is clear that future experiments should be performed not only to determine the electron range of the 1x2" detector in order to better fit this equation in the g03 source code, but to verify the original parameter choices for Gardner's detectors. A better fit could potentially correct the continuum overestimation problem observed in the calibration validation work reported in this thesis.

Outside detector crystal scattering g03 could eventually be modified to account for outside detector crystal scattering. Doing so would be highly valuable for a variety of reasons. For one thing, it might allow distinguishing of detector geometry from attenuation by the distortion versus decreased amplitude of the backscatter peak. Being able to do this would be very helpful in inverse problems focusing on unknown radiation source characterization. Some members of Gardner's research group are already addressing this problem.

Verify Assumptions Several assumptions were made throughout this work, such as modeling the detector PMT and the electronic housing as void, only modeling the photons emitted directly by U-235, and not using the table and aluminum tee in the MCNP model. Further work could be done to check the validity of these assumptions. For example, the detector PMT could be modeled as a homogeneous mixture of its constituent components to better model scattering within it. Simulation of the decay products of all of the uranium isotopes and the local geometry (table and tee) could improve the HEU computed response spectrum in the secondary peak regions.

REFERENCES

[1] J. J. Duderstadt and L. J. Hamilton, Nuclear Reactor Analysis, Ann Arbor, MI: John Wiley & Sons, 1976.

[2] W. L. Dunn and J. K. Shultis, Exploring Monte Carlo Methods, Burlington, MA: Academic Press, 2012.

[3] P. R. Bevington and K. D. Robinson, Data Reduction and Error Analysis, Boston: McGraw-Hill, 2003.

[4] R. L. Heath, "Scintillation Spectrometry Gamma-Ray Spectrum Catalogue," Idaho National Laboratories, Idaho Falls, ID, 1997.

[5] J. H. Hubbell, "Photon Cross Sections, Attenuation Coefficients, and Energy Absorption Coefficients From 10 keV to 100 GeV," National Bureau of Standards, Washington, D.C., 1969.

[6] H. Iams and B. Salzberg, "The Secondary Emission Phototube," in *Proceedings of the Institute of Radio Engineers*, New York City, 1935.

[7] G. Kelley, "Multichannel Analyzer". United States of America Patent 2642527, 16 June 1953.

[8] R. G. Lerner and G. L. Trigg, Encyclopaedia of Physics, Weinham, Germany: VCH, 1990.

[9] G. F. Knoll, Radiation Detection and Measurement, Hoboken, NJ: John Wiley & Sons, 2000.

[10] J. K. Shultis and R. E. Faw, Radiation Shielding, La Grange Park, IL: American Nuclear Society, Inc., 2000.

[11] R. C. Smith, Uncertainty Quantification, Philadelphia: Society for Industrial and Applied Mathematics, 2014.

[12] A. Sood, "A New Monte Carlo Assisted Approach to Detector Response Functions," North Carolina State University, Raleigh, NC, 2000.

[13] X.-5. M. C. Team, "MCNP-A General Monte Carlo N-Particle Transport Code, Version 5," Los Alamos National Laboratory, Los Alamos, NM, 2003.

[14] ”Scintillation Detection,” Florida International University, 2011. [Online]. Available: `http://wanda.fiu.edu/teaching/courses/Modern_lab_manual/scintillator.html#`. [Accessed 11 April 2014].

[15] A. Berlizov, "Help: Gamma Spectrum Generator," 10 April 2008. [Online]. Available: `http://www.nucleonica.net/wiki/index.php/Help:Gamma_Spectrum_Generator`. [Accessed 11 April 2014].

[16] R. P. Gardner and A. Sood, "A Monte Carlo simulation approach for generating NaI detector response functions (DRFs) that accounts for non-linearity and variable flat continua," *Nuclear Instruments and Methods in Physics Research B*, vol. 213, pp. 87-99, 2004.

[17] R. J. Beattie and J. Byrne, "A Monte Carlo Program for Evaluating the Response of a Scintillation Counter to Monoenergetic Gamma Rays," *Nuclear Instuments and Methods*, vol. 104, pp. 163-168, 1972.

[18] M. J. Berger and S. M. Seltzer, "Response Functions for Sodium Iodide Scintillation Detection," *Nuclear Instruments and Methods*, vol. 104, pp. 317-332, 1972.

[19] H. Haario, M. Laine and A. Mira, "DRAM: Efficient adaptive MCMC," *Stat Comput*, vol. 16, pp. 339-354, 2006.

[20] R. Hofstadter, "The Detection of Gamma-Rays with Thallium-Activated Sodium Iodide Crystals," *Physics Review*, vol. 75, p. 796, 1949.

[21] A. Owens, "Spectral Degredation Effects in an 86 $c\,m^3$ Ge(HP) Detector," *Nuclear Instruments and Methods in Physics Research A*, vol. 238, no. 2-3, pp. 473-478, 1985.

[22] D. E. Peplow, "Sodium Iodide Detector Response Functions Using Simplified Monte Carlo Simulation and Principal Components," *Nuclear Geophysics*, vol. 8, no. 3, pp. 243-259, 1994.

[23] J. Wang, Z. Wang, J. Peeples, H. Yu and R. P. Gardner, "Development of a Simple Detector Response Function Generation Program: The CEARDRFs Code," *Applied Radiation and Isotopes*, vol. 70, pp. 1166-1174, 2012.

[24] R. P. Gardner, Interviewee, *Absolute Efficiency Factor for g03*. [Interview]. 15 January 2014.

[25] M. J. Berger, J. H. Hubbell, S. M. Seltzer, J. Chang, J. S. Coursey, R. Sukumar, D. S. Zucker and K. Olsen, "XCOM: Photon Cross Sections Database," National Institute of Standards and Technology, 9 Dec. 2011. [Online]. Available: `http://www.nist.gov/pml/data/xcom/`. [Accessed 15 July 2014].

[26] R. P. Gardner, C. L. Barrett, W. Haq and D. E. Peplow, "Efficient Monte Carlo Simulation of O-16 Neutron Activation and N-16 Decay Gamma-Ray Detection in a Flowing Fluid for On-Line

Oxygen Analysis or Flow Rate Measurement," *Nuclear Science and Engineering*, vol. 122, pp. 326-343, 1996.

[27] Eckert & Ziegler Isotope Products, "Eckert & Ziegler Reference & Calibration Sources: Product Information," Valencia, CA, 2007.

[28] National Nuclear Data Center, "Nudat2.6: Decay Radiation Search," Brookhaven National Laboratory, 2013. [Online]. Available: `http://www.nndc.bnl.gov/nudat2/indx_dec.jsp`. [Accessed 14 June 2015].

APPENDIX

APPENDIX

A

ALTERNATIVE METHODS AND MODELS

This appendix contains a couple of alternative methods for parts of the validation and uncertainty quantification work, as well as an alternative model for the simulation of detector responses. The alternatives are compared with the chosen primary methods, and then the reasoning behind the method chosen is discussed briefly.

A.1 HEU Disc Response: Separate Versus Combined Peaks

At first, the number of full energy peaks chosen to be entered into g03 for simulation were only those that were over 1% in relative intensity. Seven peaks met this criteria, and so the seven peaks were matched with their relative channel locations and entered into g03. The resulting spectrum did not approximate the large lower intensity peak next to the main peak at 186 keV very well in early simulations. This peak was the result of the interaction between three full energy peaks: one at 144, 163, and the 186 keV peak.

It was thought that combining the two lower energy and intensity peaks may improve the result. So, their energies were averaged to 150 keV and their intensities summed before entering them into g03, leaving only six peaks. A comparison of the two responses for the HEU disc case centered at forty one centimeters from the detector is shown in Figure A.1.

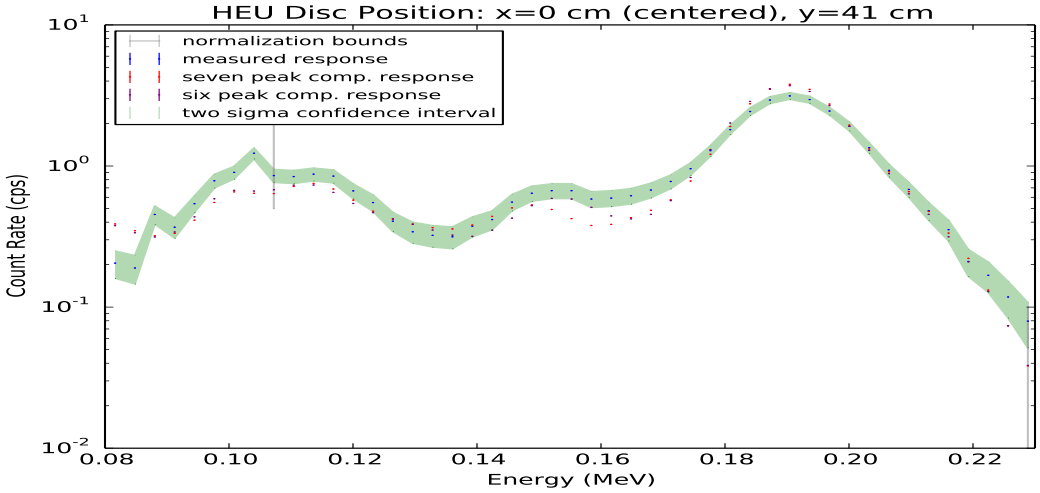

Figure A.1 Full simulation of seven peaks vs. six peaks with two combined at 150 keV.

Both responses underestimate the lower energy peaks while slightly overestimating the main full energy peak at 186 keV. Note: this was a low number of histories run, so the added uncertainty in the calculation made the 100 keV peaks appear closer to the lead backscatter peaks. In the high fidelity runs, the underestimation of the backscatter peaks is more apparent.

It is clear though that the combined peak aligns much better with the center of the peak around 150 keV and more closely approximates its amplitude. As a consequence of this result, the six peak scheme was chosen for the final results.

A.2 Freqentist and Bayesian Power Law Uncertainty

In the main body of this work, it was mentioned that Frequentist uncertainty analysis was performed on the power law model due to the lack of confidence in the Bayesian code's ability to analyze the weighted least squares scheme. Later, the Bayesian code was tested and compared with the Frequentist calculation. The results of both analyses for the power law parameters are contained in Table A.1.

Table A.1 Power law parameter means and standard deviations for Frequentist and Bayesian methods.

Frequentist				
Parameter	Mean	Standard Deviation, σ	Relative STD, σ_{rel} (%)	χ^2_v
a	0.027608	1.684E-4	0.6100	8.500E-6
b	0.644237	5.719E-3	0.8877	
Bayes				
a	0.027608	1.606E-4	5.818E-3	8.501E-6
b	0.64436	5.75E-3	8.923E-3	

The values of the parameters and their respective uncertainties are very similar for both methods. The Bayesian parameters gain a slightly less overfit reduced chi-squared value, and exchange slightly lower uncertainty in a for greater uncertainty in b. Again, the Frequentist method was chosen for expedience and direct application of the weighted least squares, however, the methods prove to be essentially equivalent in this case.

A.3 Alternative Response Calculation: MCNP F8 Tally

Gardner's DRF model proved to be able to simulate the full energy peaks of responses fairly well, but needs recalibration for some detectors to reproduce good Compton continua. Additionally it suffers under the strain of advanced geometries being unable to reproduce the effects of outside detector scattering events on the detector response. One alternative model was considered and compared to g03 responses: MCNP's F8 tally with Gaussian energy broadening (GEB).

MCNP can approximate a detector response to a fair degree with the correct geometry. The same detector and source model as was used for the the F4 flux tally was used for the F8 tally. Additionally the power law equation for MCNP (Equation A.1) was fit to the same sources used for Gardner's model

$$fwhm = a + b\sqrt{E + cE^2} \tag{A.1}$$

where E is the energy of the incident gamma ray, a,b and c the parameters, and fwhm is the full width at half maximum of the peak. This information was used in a special GEB input of the F8 tally in order to spread the peak to the appropriate width in the resulting response from MCNP. The response from MCNP is compared with the response created by g03 and the experimental response in Figure A.2

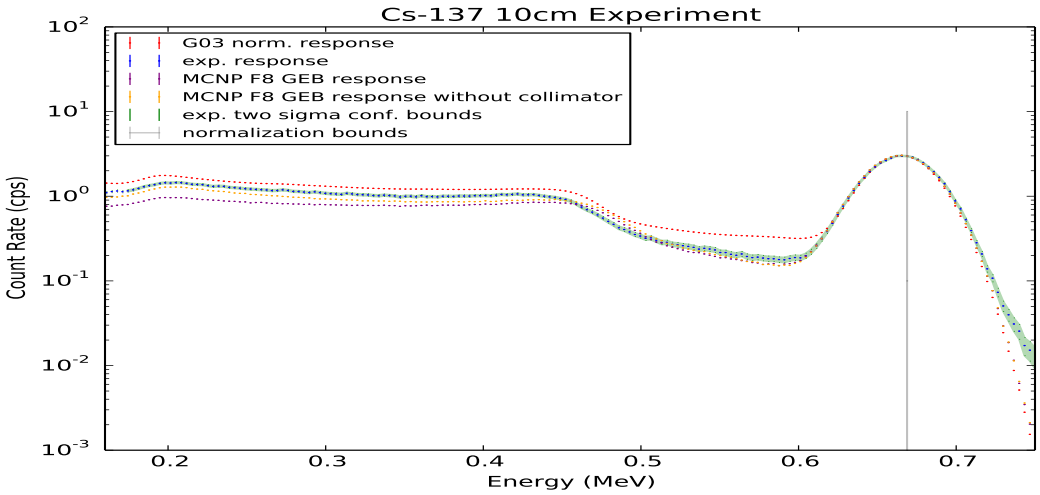

Figure A.2 Peak normalized computed responses from MCNP with and without the collimator simulated and g03 versus the measured response.

Both methods approximate the full-energy peak well, however, where g03 overestimates the continuum MCNP underestimates. MCNP predicts the electron physics of the valley region better than g03 (without recalibration of the range law), but underestimates the rest of the Compton continuum by a good margin. The response from MCNP without the collimator is shown to illustrate a possible cause of they underestimation. There is a great shift in the continuum without the lead, so it seems likely that some physics with the lead collimator and aluminum can of the detector are not well approximated by MCNP's F8 tally.

g03 was chosen as the main model mainly for two reasons. First, g03 calculates a DRF with far fewer histories (four orders of magnitude) with similar accuracy and thereby taking much less time for computation. Second, g03 produces a full DRF for the user which will be useful in further research with inverse problems, whereas MCNP produces a response directly without a DRF. However, it may still be useful to give the MCNP calculation a closer examination for its approximations of the physics in the valley region in order to improve future models.

4.4. Task D: Develop & validate neutron detector response functions and their uncertainties

In addition to the gamma DRFs, neutron DRFs are necessary to include neutron measurements in the DIMP procedure. Unlike gamma detectors, neutron detectors typically only measure an energy-integrated count rate. Gas-filled neutron detectors, commonly used for passive neutron assay, are relatively insensitive to the incident neutron energy. This is especially true when the detectors are encased with low-A moderator to increase the probability of neutron interaction. Thus, the neutron DRF is simpler than for the gamma detector. The main task here was estimating the detector efficiency as a function of incident neutron energy, as well as quantifying the associated errors in this estimate. While the efficiencies can be estimated with Monte Carlo simulations, comparisons with experimental data was expected to demonstrate the level of error in the simulation. The University of South Carolina was originally assigned to complete this task but in fact NC State University ended up completing it.

The accomplishment of this task was reported in: Cyrus Proctor, *Accurate Holdup Calculations with Predictive Modeling and Data Integration: Neutron Experimental and Computational Study*, NC State University, January 20, 2015. This document is replicated on the following pages.

Accurate Holdup Calculations with Predictive Modeling and Data Integration: Neutron Experimental and Computational Study

Cyrus Proctor

January 20, 2015

Contents

List of Figures

List of Tables

I Introdution

This work was completed under NEUP 2012 narrative 3494, "Accurate Calculations with Predictive Modeling and Data Integration". The overall objective was to develop and validate neutron detector response functions and their associated uncertainties for later use in data integration and inverse methodologies. These methodologies are being explored to more accurately locate, identify and quantify nuclear holdup using non-destructive passive assay techniques.

Neutron holdup was the focus for this work. Experiments were conducted at Oak Ridge National Lab with californium-252 sources and a moderated five helium-3 tube neutron detector manufactured by Canberra. Simulations of the experimental setups were created in both MCNP and SCALE/Denovo as a valdiation exercise. Overall detector response values and their associated uncertainties from stochastic, cross section data, source emission rate, and experimental measurement are quantified and addressed.

Section II covers the details of the experimental setup, calibration and results obtained from the experimental campagin. Section III addresses the setup and details related to MCNP and Denovo simulations that are created as a validation exercise. Lastly, Section IV compares the simulated and experimental results along with their associated uncertainties.

II Experiment

This section details work completed at the ORNL Safeguards Laboratory June 10th through June 21st, 2013. This write-up is meant to be a comprehensive guide to understand and reproduce the experiments conducted during this time period. The specific experiments documented were conducted by W. Cyrus Proctor and supervised by Louise Worrall, Steven Cleveland, and Tyler Guzzardo, with input from Stephen Croft

II.A Detector Components and Spatial Setups

All experimental work was conducted in Room D104 of Building 5800 located on the ORNL campus. Results were recorded on a Lenovo T60 laptop running Windows XP connected to a JSR-15 shift register provided by Canberra with the detector. The software to collect and store the data included two versions of International Neutron Coincidence Counting; INCC 5.0.4 and 5.1.2 [1]. The detector setup used throughout the measurement campaign is illustrated in Figure 1 and includes all relevant connections to the detector, shift register and laptop computer.

The detector itself, manufactured in January of 2013 by Canberra Industries Inc., includes five Reuter-Stokes helium-3 tubes, model RS-P4-0820-103, which are 1 inch in diameter and have a 20 inch active length. The five tubes are configured in a row to maximize efficiency and connected via JAB-01 board within the high voltage junction box. The entire length of the

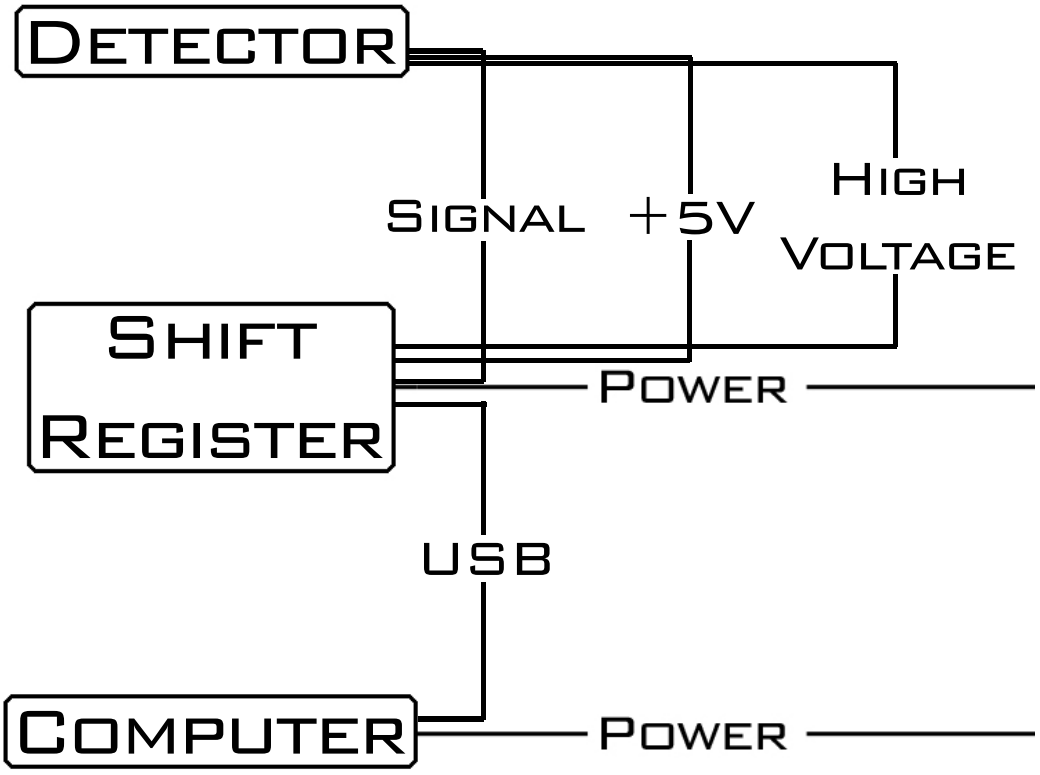

Figure 1: Detector setup used throughout the measurement campaign.

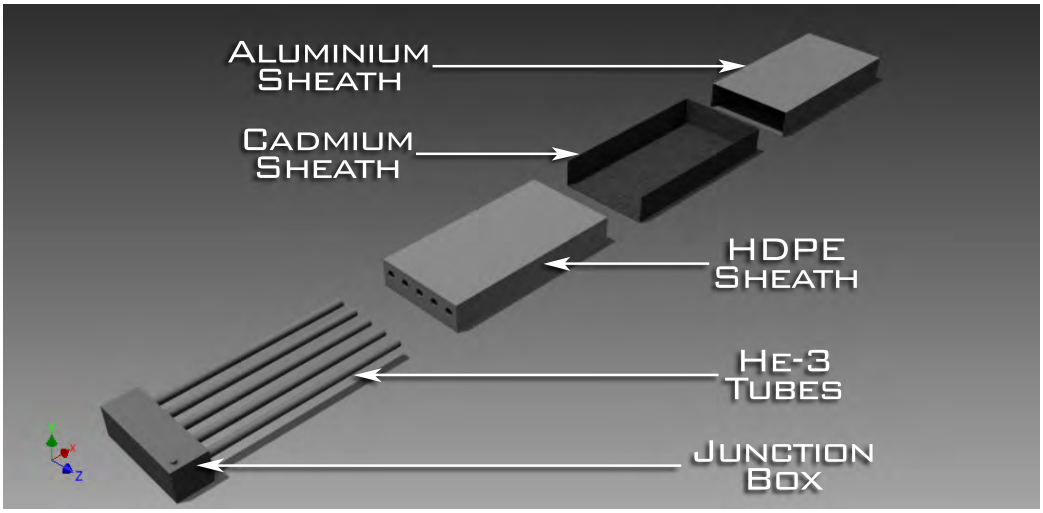

Figure 2: *Bare detector assembly* including five helium-3 tubes, junction box, high density polyethylene, cadmium and aluminum sheaths.

helium-3 tubes are encased in a removable sheath of high density polyethylene (HDPE) and surrounded first by a cadmium sheath on four sides (front and top excluded) which is then surrounded by an aluminum sheath on five sides (top excluded). The holes for the detector tubes in the HDPE sheath are drilled all the way through. Figure 2 illustrates what will be referred to as the *bare detector assembly* throughout the remainder of this document. While the helium-3 tubes are not technically bare within the assembly, this particular configuration does lack the other inner and outer housing and cadmium front face described in subsequent assemblies.

The *bare detector assembly* can then be housed within the *inner housing assembly*. This includes an aluminum inner cradle and inner HDPE housing illustrated in Figure 3. The *inner housing assembly* is held together by a set

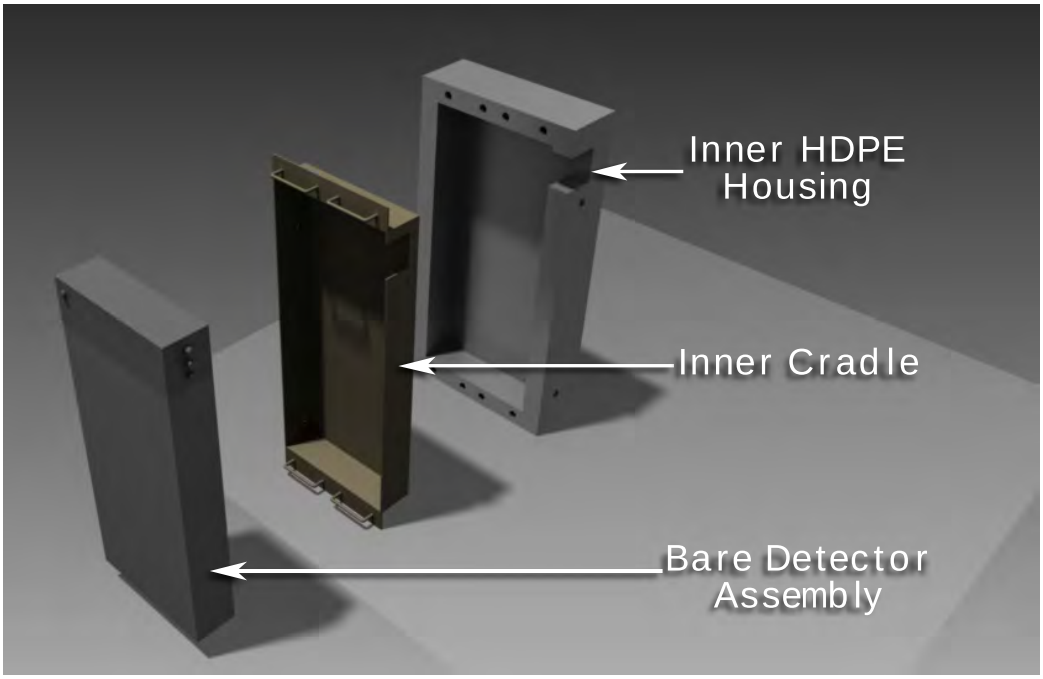

Figure 3: *Inner housing assembly* including bare detector assembly, aluminum inner cradle, and inner HDPE housing.

of four threaded bolts that penetrate from the outside of the HDPE housing and inner cradle to secure to matching threads of the bare detector assembly. Lastly, the *inner housing assembly* is contained within the *outer housing assembly* which includes the hand truck, the outer housing, the outer HDPE housing and the outer cradle. Four of the outer HDPE housing components are loosely held in the outer housing while the two side components are directly screwed. The outer cradle is then screwed directly to the outer housing which is then bolted to the hand truck to hold all outer components in place. The *inner housing assembly* is held in place by a metal tab at the lower end while a metal latch is used towards the top. Figure 4 shows the exploded components of the *outer housing assembly* while Figure 5 shows all components exploded in one view. Each component is shown in full detail in Appendix A.

Overall, twenty major components (including the front cadmium shield not shown) constitute relevant structures for use in neutron transport modeling. The entire detector assembly weighs approximately 282 pounds and is transported via a Magliner model 112-UA-1060 hand truck with 500 pound carrying capacity. The detector serial number is 13000001 and/or 7077236. The default settings for this particular detector were set as a high voltage of 1680 V, a gate width of 64 μs and a pre-delay of 4.5 μs.

Three distinct spatial setups were used during the experimental measurement campaign. One setup in particular, the *upright spatial setup*, shown in Figure 6, has been used in computation validation exercises. The detector,

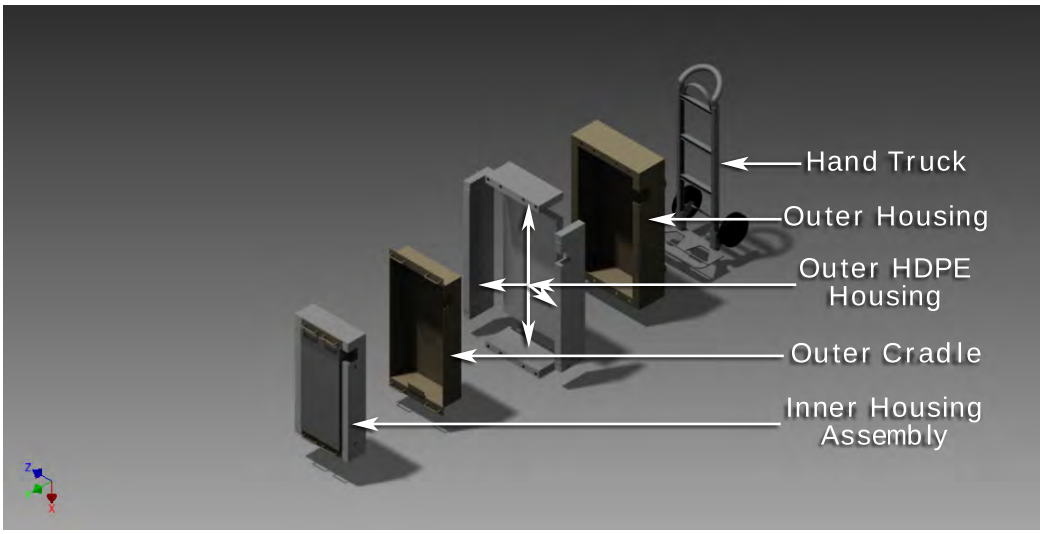

Figure 4: *Outer housing assembly* including inner housing assembly, aluminum outer cradle, outer HDPE housing, aluminum outer housing, and aluminum hand truck.

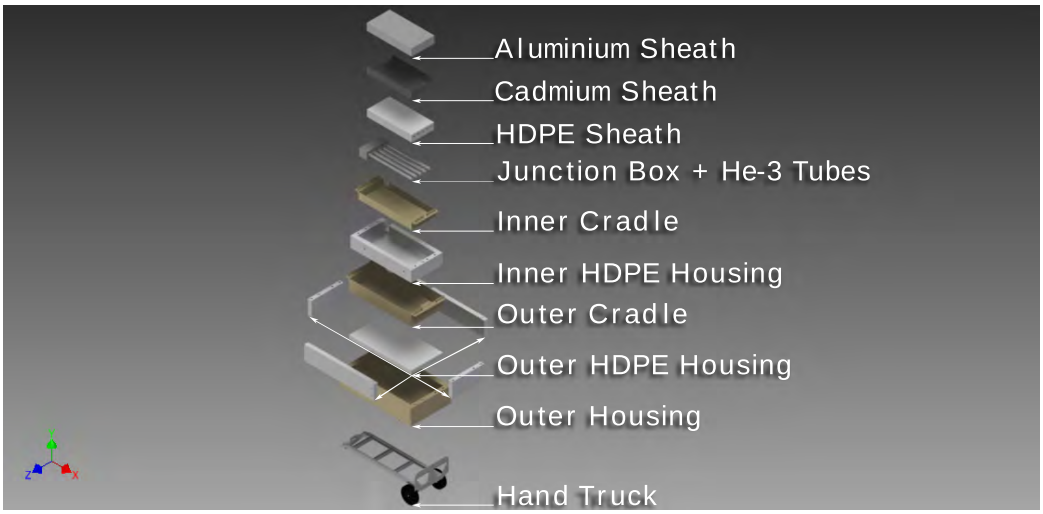

Figure 5: All detector components exploded in one view including the *outer housing assembly*, *inner housing assembly*, and *bare detector assembly*.

fully assembled, is stood upright on the floor, while a neutron source suspended from a laboratory ring stand is placed in front of the detector's face and is subsequently moved along the axis perpendicular.

The *horizontal spatial setup*, shown in Figure 7, tilts the detector's front face parallel to the floor facing upwards. Lastly, the *table-top spatial setup*, shown in Figure 8, utilizes only the *bare detector assembly* placed on an aluminum cart also with the detector face parallel with the floor facing upwards. In both of these setups, the ring stand's height is adjusted for varying distance measurements with a neutron source.

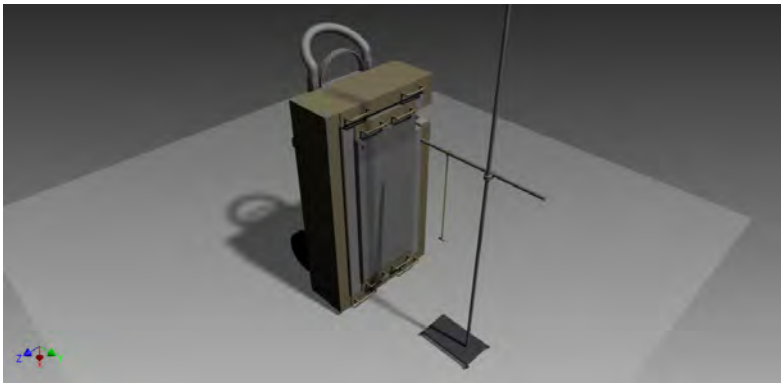

(a) Computer aided design (CAD) model.

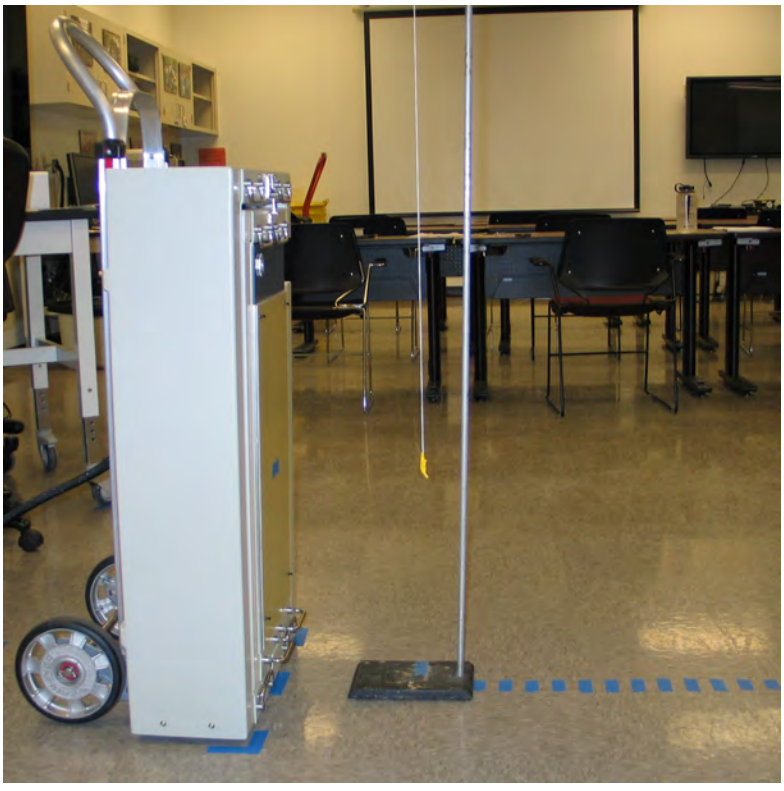

(b) Picture of experimental *upright spatial setup*.

Figure 6: This *upright spatial setup* includes the fully assembled detector stood perpendicular to the floor and a neutron source suspended from a ring stand which may be moved to different measurement locations.

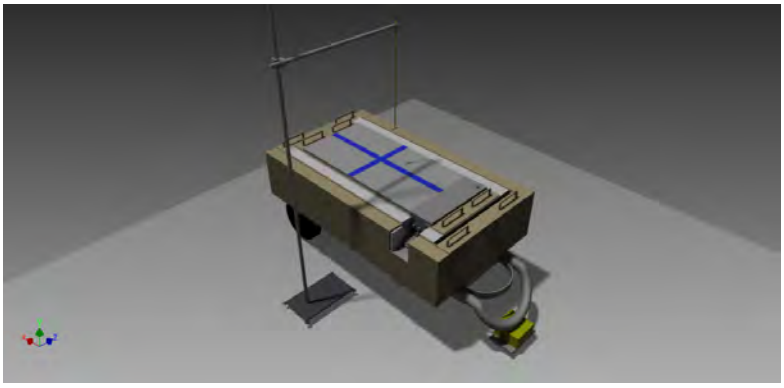

(a) Computer aided design (CAD) model.

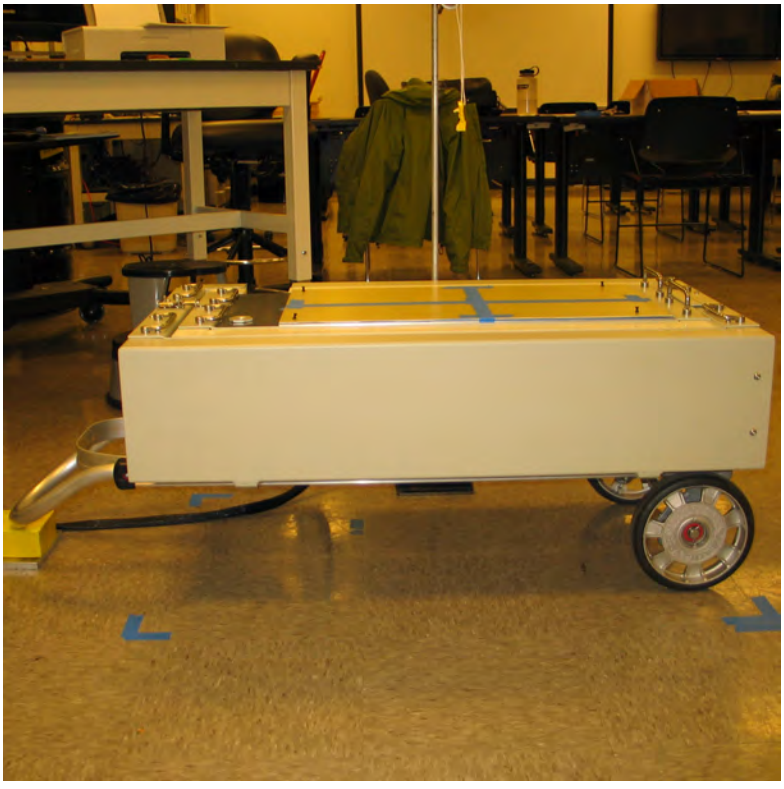

(b) Picture of experimental *horizontal spatial setup*.

Figure 7: This *horizontal spatial setup* includes the fully assembled detector resting parallel to the floor and a neutron source suspended from a ring stand which may be moved to different measurement heights.

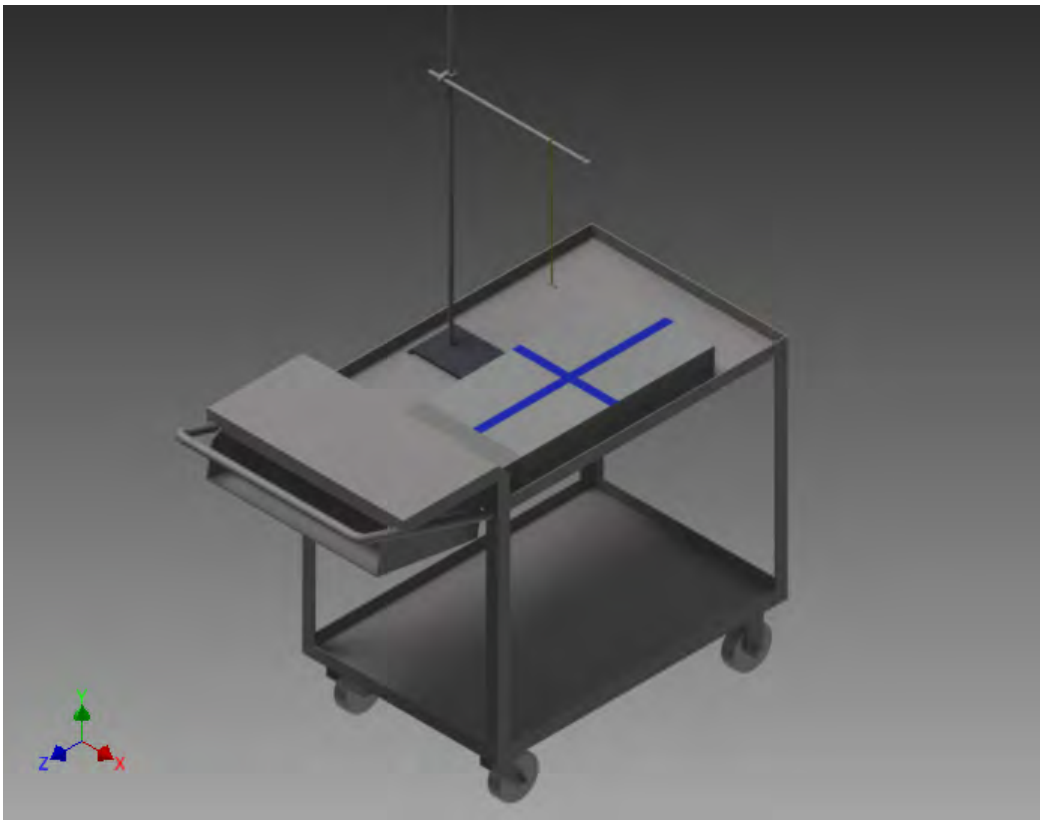

Figure 8: This *table-top spatial setup* includes only the *bare detector assembly* resting on an aluminum table parallel to the floor with a neutron source suspended from a ring stand which may be moved to different measurement heights. Laboratory picture not taken.

II.B Neutron Source Descriptions

Two neutron sources, manufactured by Frontier Technologies Inc., were used during the experimental campaign. The sources, identified by their serial numbers FTC-CF-053 and FTC-CF-004 are reported as models 10s and 10 respectively via Oak Ridge National Lab's (ORNL) radiation source inventory (RASIN). Each source consists of a 304L stainless steel capsule, see Figure 9 and Figure 10, which contains a small palladium wire in which californium has been deposited on [2]. The wire is packed inside of the capsule which is then tungsten-inert-gas (TIG) welded shut.

According to Frontier's records, FTC-CF-053 was calibrated on December 11, 1988 while FTC-CF-004 was calibrated on April 21, 1986. Through non-trivial comparison with ORNL's records and via computational simulation, it became necessary to perform a recalibration of the absolute source strength via a cross-calibration with another Frontier source, FTC-CF-1830, using passive neutron correlation counting outlined in [3]. This process was carried out for FTC-CF-004 using ORNL's californium shuffler to obtain an absolute source strength of $157755 \pm 2.4\%$ neutrons per second corrected to June 30, 2013 – just after the end of the experimental campaign. Experimental and computational results are compared for FTC-CF-004 in this work.

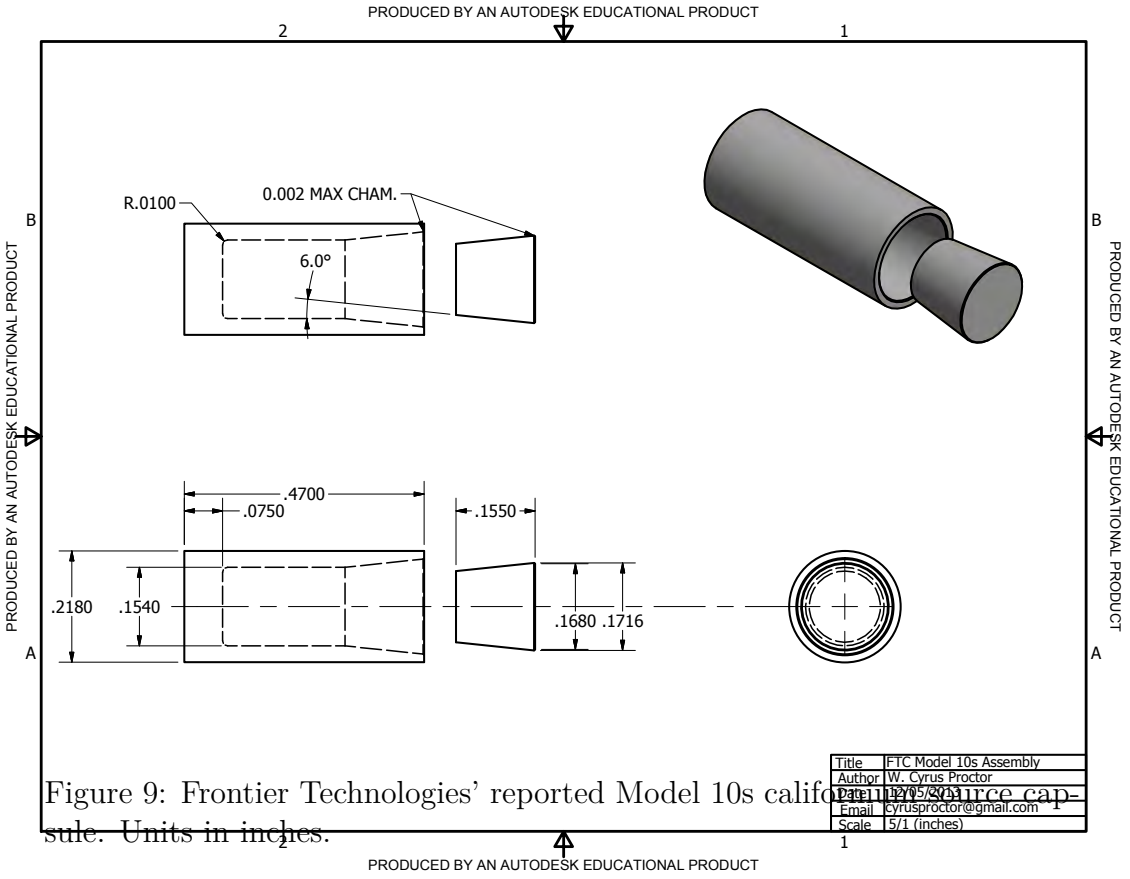

Figure 9: Frontier Technologies' reported Model 10s californium source capsule. Units in inches.

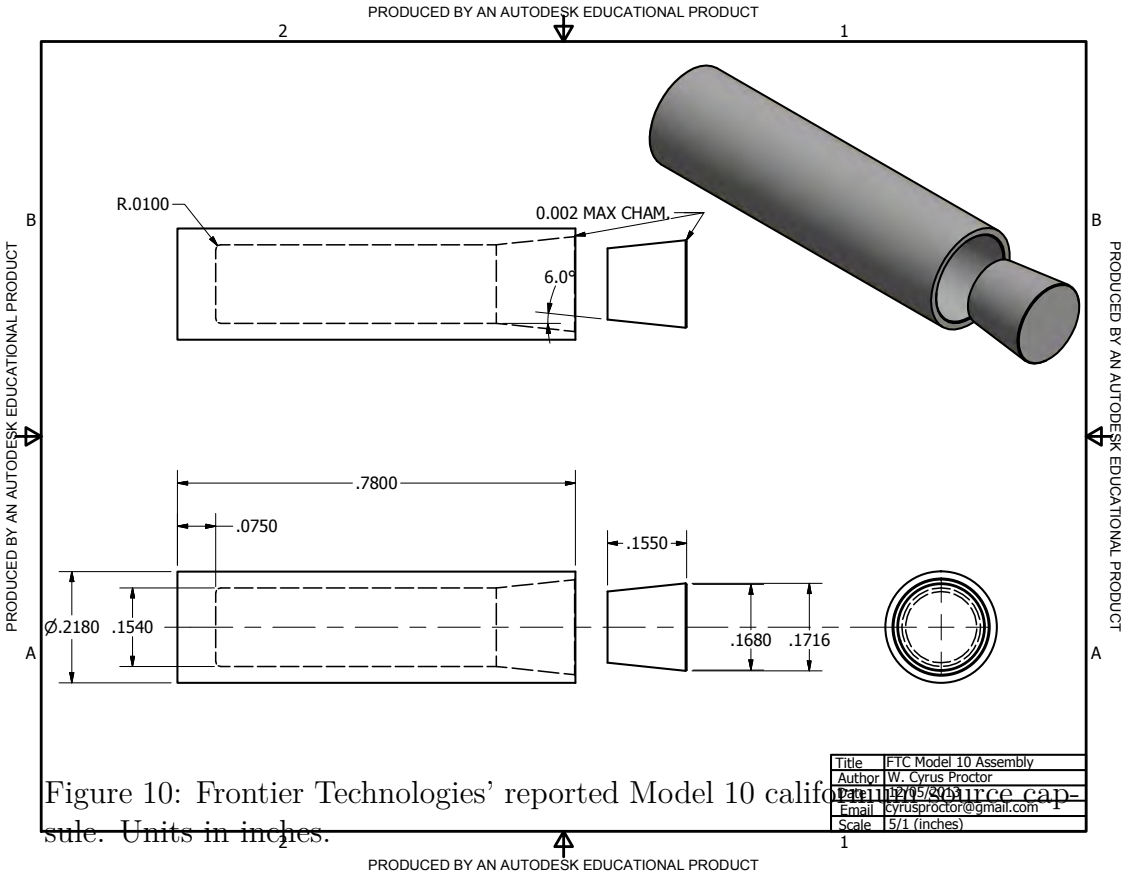

Figure 10: Frontier Technologies' reported Model 10 californium source capsule. Units in inches.

II.C Detector Calibration

To begin, a 15 minute background count was taken while the detector was in the *upright spatial setup*; as seen in Figure 6. INCC is able to repeat and record a "cycle" a certain number of times for a specific duration. For the preliminary background count, 15 cycles, each for a duration of 60 seconds, was performed. The measured background rate is reported as 2.058 ± 0.047 counts per second.

Following the background count, a preliminary count at the default detector settings mentioned above was conducted for each of the two californium sources that were available. Both sources were manufactured by Frontier Technology with the serial numbers FTC-CF-053 and FTC-CF-004 for the model 10s and model 10 sources respectively. To complete this set of counts, one source at a time was taped to the center of the detector's front face. Five and fifteen minute counts were conducted with 60 second cycle lengths. The overall count rate, absolute uncertainty and relative percent uncertainty are reported in both Table 1 and Table 2 for each of the californium sources.

It is clear that FTC-CF-004 is producing roughly an order of magnitude more counts directly on the detector face than its counterpart, FTC-CF-053. This close to the detector, both sources exhibit excellent singles rate counting statistics of well below 1% relative uncertainty for both the 5 minute and fifteen minute counts.

With confirmation that counting times could proceed in reasonable (and relatively short) lengths of time without having to be particularly mindful

Table 1: FTC-CF-053 preliminary count.

FTC-CF-053			
-	**Count Rate** (c/s)	**Count Rate Uncertainty** (c/s)	**Count Rate Uncertainty** $(Rel.\%)$
5 Minute Count			
Singles	873.126	0.534	0.06
Doubles	46.937	0.550	1.17
Triples	1.281	0.150	11.71
15 Minute Count			
Singles	872.494	1.129	0.13
Doubles	46.454	0.530	1.14
Triples	1.126	0.105	9.33

Table 2: FTC-CF-004 preliminary count.

FTC-CF-004			
-	**Count Rate** (c/s)	**Count Rate Uncertainty** (c/s)	**Count Rate Uncertainty** $(Rel.\%)$
5 Minute Count			
Singles	9610.822	5.836	0.06
Doubles	521.057	6.573	1.26
Triples	6.913	5.720	82.74
15 Minute Count			
Singles	9606.098	4.008	0.04
Doubles	509.716	2.852	0.56
Triples	3.208	1.803	56.20

about the magnitude of counting uncertainties, a series of high voltage (HV) plateau curves were acquired. Two separate setups were used in the collection of the HV plateau data.

Each plateau curve was completed using INCC version 5.1.2 because it had an automated function that allowed one to set necessary input parameters and be able leave overnight to come back to a completed data set over a particular voltage range. In all, four separate plateaus were gathered, each voltage point taken in one 1000 second cycle.

First, two plateaus were taken with only background present, i.e. no sources. One plateau was taken in the *horizontal spatial setup* (Figure 7) and the other was taken in the *table-top spatial setup* (Figure 8). These two are plotted together in Figure 11. They show that background count rates never exceed 4 counts per second in any typical voltage range to be considered in this work.

Next, while the detector was in the *horizontal spatial setup*, the FTC-CF-004 source was added. Later, a cesium source was added to the californium source to see the effects of having an appreciable gamma source present. Both of these plateau curves are plotted below in Figure 12.

With the 1000 second count times, a clean, well-rounded knee is visible for the high voltage plateau curves. It was decided based on the characteristics of the curves that the operating voltage of 1725 V was to be adopted over the default voltage of 1680 V due to the farther proximity to the knee of the curve.

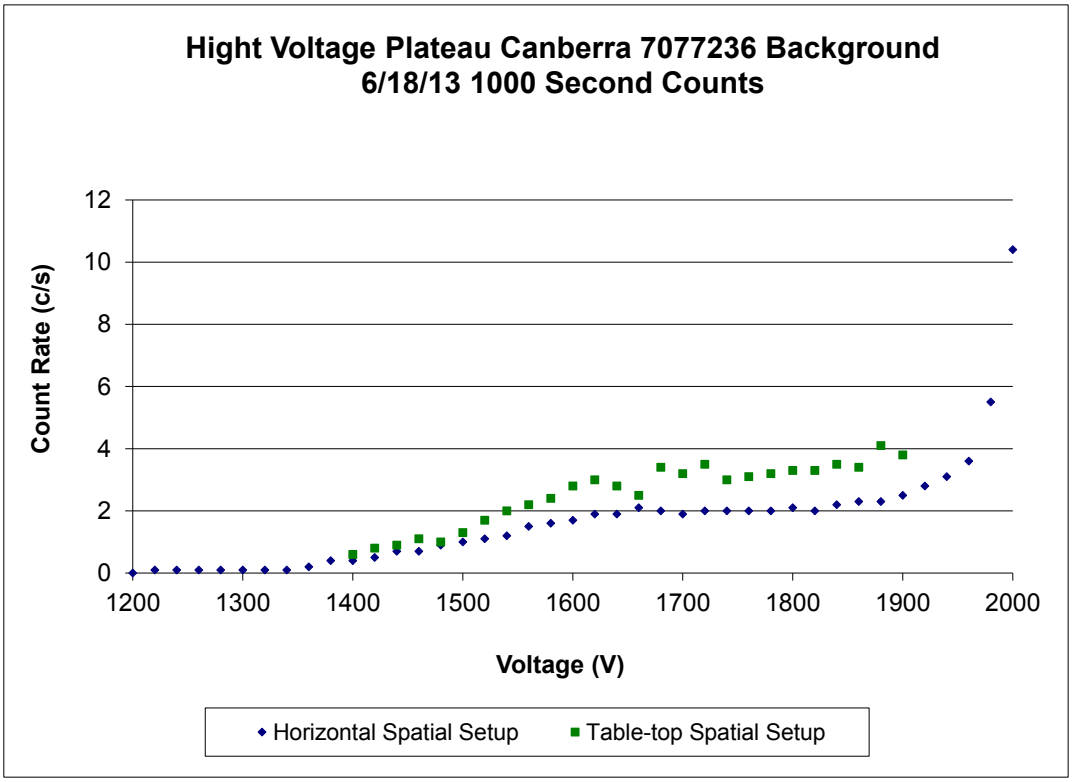

Figure 11: Two high voltage plateaus were established with no source present; one while in the *horizontal spatial setup* and the other while in the *table-top spatial setup*. Counts were taken for one 1000 second cycle at each voltage.

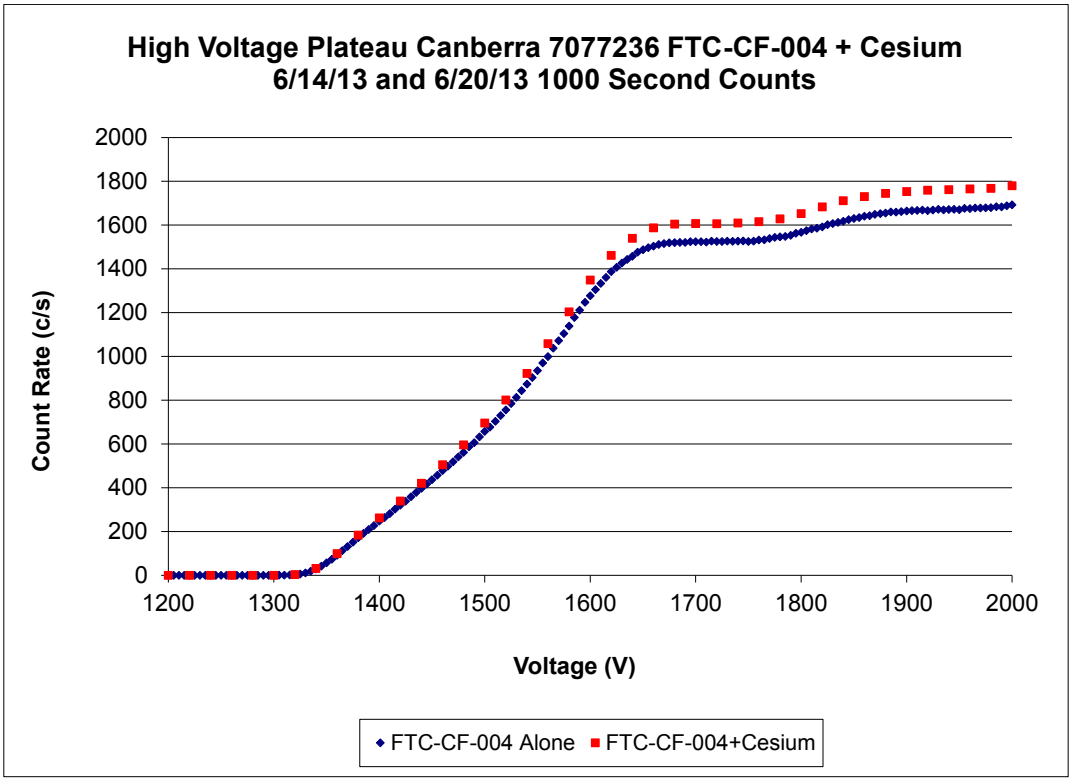

Figure 12: Two high voltage plateaus were established while in the *horizontal spatial setup*; one with only FTC-CF-004 present and the other with FTC-CF-004 and a gamma-emitting cesium source. Counts were taken for one 1000 second cycle at each voltage.

II.D Experimental Results

Next, at nominal operation settings and a high voltage setting of $1725\,V$, the detector was placed in the *upright spatial setup* with neutron source FTC-CF-004 attached to a ring stand and positioned collinear to the center of the detector's front face. The ring stand was moved along the axis orthogonal to the detector front face in increments of $5\,cm$ starting at distance of $16.1275\,cm$ and ranging to $61.1275\,cm$ between the centerpoint of the neutron source and the centerpoint of the central helium-3 tube within the detector.

Singles and doubles count rates and their uncertainties were measured via INCC and are displayed in Figure 13 and Table 3. The experimental uncertainties for both singles and doubles are also displayed in Figure 13 and in Table 4. Counts were taken in 10 cycles of 60 seconds each for a total count time of 600 seconds per data point.

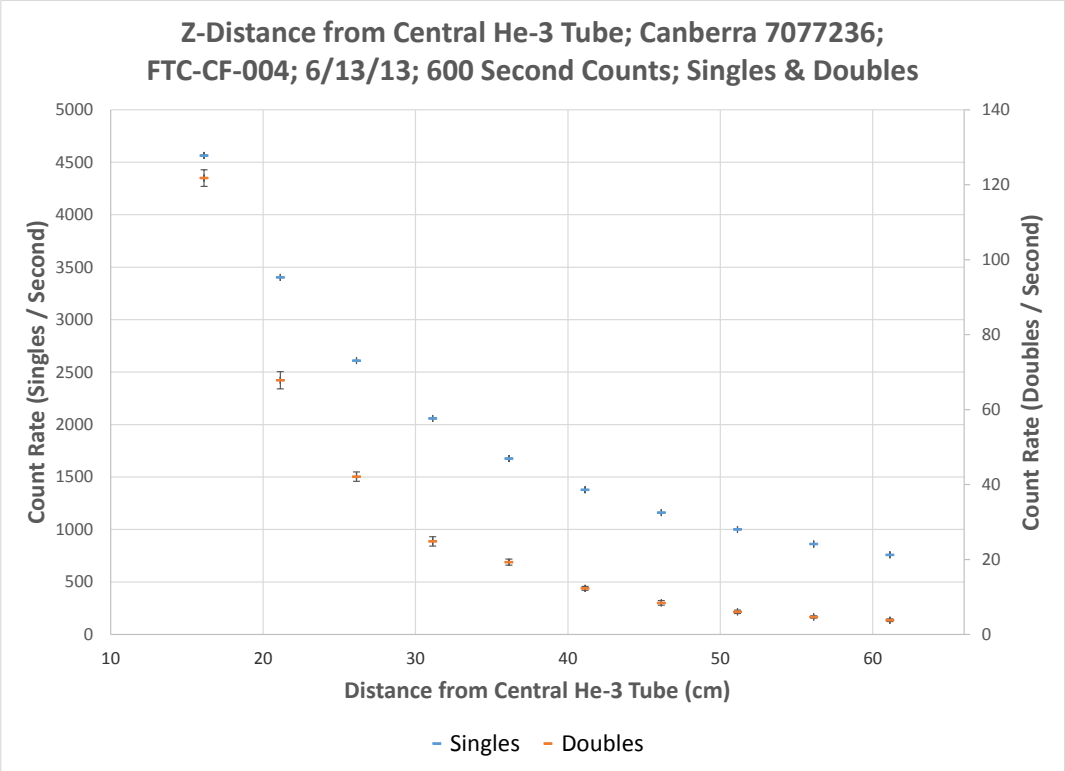

Figure 13: Source FTC-CF-004 is moved in 5 cm increments perpendicular to the detector face while it is in the *horizontal spatial setup*. Singles and doubles count rates from 600 second counts (60 second cycles; 10 cycles) are reported along their respective uncertainties.

Table 3: Detector response experimental measurements including singles and doubles count rates. Source distances are measured from the center of the central helium-3 tube to the center of the californium-252 source (FTC-CF-004) which is placed collinear with the centerpoint of the detector front face.

Distance from Detector (cm)	**Singles Count Rate (c/s)**	**Doubles Count Rate (c/s)**
16.1275	4565.001	121.780
21.1275	3402.641	67.828
26.1275	2610.021	42.117
31.1275	2058.254	24.832
36.1275	1676.399	19.292
41.1275	1378.492	12.302
46.1275	1161.146	8.423
51.1275	1000.609	6.038
56.1275	861.684	4.667
61.1275	758.584	3.800

Table 4: Detector response experimental measurement uncertainties including singles and doubles count rate uncertainties.

Distance from Detector (cm)	**Singles Uncertainty (c/s)**	**Doubles Uncertainty (c/s)**
16.1275	3.973	2.217
21.1275	2.025	2.295
26.1275	1.846	1.249
31.1275	2.419	1.250
36.1275	1.936	0.808
41.1275	1.151	0.517
46.1275	1.997	0.624
51.1275	1.780	0.451
56.1275	1.521	0.321
61.1275	1.372	0.362

III Simulation

This section details work completed from summer of 2013 until winter of 2014. Included in this write-up is all the information necessary to reproduce the simulated results from MCNP and Denovo. The specific computational work was conducted by W. Cyrus Proctor and supervised by Yousry Azmy and Dan Cacuci, with input from John Mattingly.

III.A Simulation Setup

The californium sources were spatially modeled based on the design given via the Frontier Technologies website described in Section II.B. For the modeling of the sources' energy spectrums, a Watt energy spectrum of the form

$$f(E) = e^{-E/a} sinh\left(\sqrt{bE}\right), \tag{1}$$

was assumed for the spontaneous fission neutron energy probability distribution where the parameters a and b are fit for a particular isotope. The discrepancies between spectrum parameters a and b in MCNP 5 and MCNP 6.1 manuals for californium-252 are of note [4, 5]. MCNP 5 gives $a = 1.025\,MeV$ and $b = 2.296\,MeV^{-1}$ while MCNP 6 gives $a = 1.18\,MeV$ and $b = 1.03419\,MeV^{-1}$. Further investigation led to the experimental work of Mannhart located and summarized within Valentine's MCNP-DSP manual [6, 7].

Mannhart used a corrected Maxwellian distribution of the form

$$f(E) = R(E)\sqrt{\frac{4E}{\pi T^3}}e^{-\frac{E}{T}}, \tag{2}$$

to fit his experimental results where the nuclear temperature, T, is typically $1.42\,MeV$ for californium-252. The Maxwellian does not agree precisely with the measured spectrum for californium-252; therefore, Mannhart developed an energy dependent correction factor, $R(E)$, which when multiplied by the Maxwellian spectrum would reproduce the measured spectrum. A least-squares polynomial regression model was used to obtain a functional form for Mannhart's correction factor. For energies less than $5\,MeV$, the correction factor is represented by

$$\begin{aligned} R(E) &= 0.955 + 0.0707E - 0.0444E^2 + 0.01998E^3 \\ &\quad -0.00457E^4 + 0.000368E^5. \end{aligned} \tag{3}$$

For energies greater than $5\,MeV$, the correction factor is represented as

$$R(E) = 1.16 - 0.0432E + 0.00185E^2 - 0.0000316E^3. \tag{4}$$

The energy ranges were chosen such that the functional representation adequately reproduces Mannhart's discrete points. Other fits could be applied to Mannhart's correction factor that when multiplied by the Maxwellian should adequately reproduce the measured spectra. The average neutron en-

ergy obtained from the corrected spectrum is $2.13\,MeV$, which agrees well with the measured value. The integral of the corrected spectrum as a function of energy was normalized to unity. The two Watt fission spectrum distributions recommended by MCNP and the modified Maxwellian spectrum distribution by Mannhart are normalized, subdivided into one thousand energy bins and compared in Figure 14. In Figure 15, the three corresponding cumulative distribution functions are plotted. In addition, the Mannhart spectrum was re-binned within the SCALE6.1 ENDF/B-VII.0 200 and 27 group energy boundaries for comparison.

It is evident that the MCNP 6 parameters match more closely to the experimental distribution staying within roughly 5% up to about $13\,MeV$. To determine the range of effect that the differences within the californium-252 spontaneous fission spectrum would have on the count rate response of the MCNP simulations as a function of distance, cases in which the source FTC-CF-004 was located at the closest and farthest experimentally measured distances (16 and 61 cm respectively) were configured using the *upright spatial setup*. A total of four preliminary runs were completed, two with MCNP 5 and two with MCNP 6, then compared in Table 5. Roughly, a change in response of 2.5% resulted from the shift in Watt spectrum parameters. From this point forward in this work, the MCNP 6 spectrum parameters will be used.

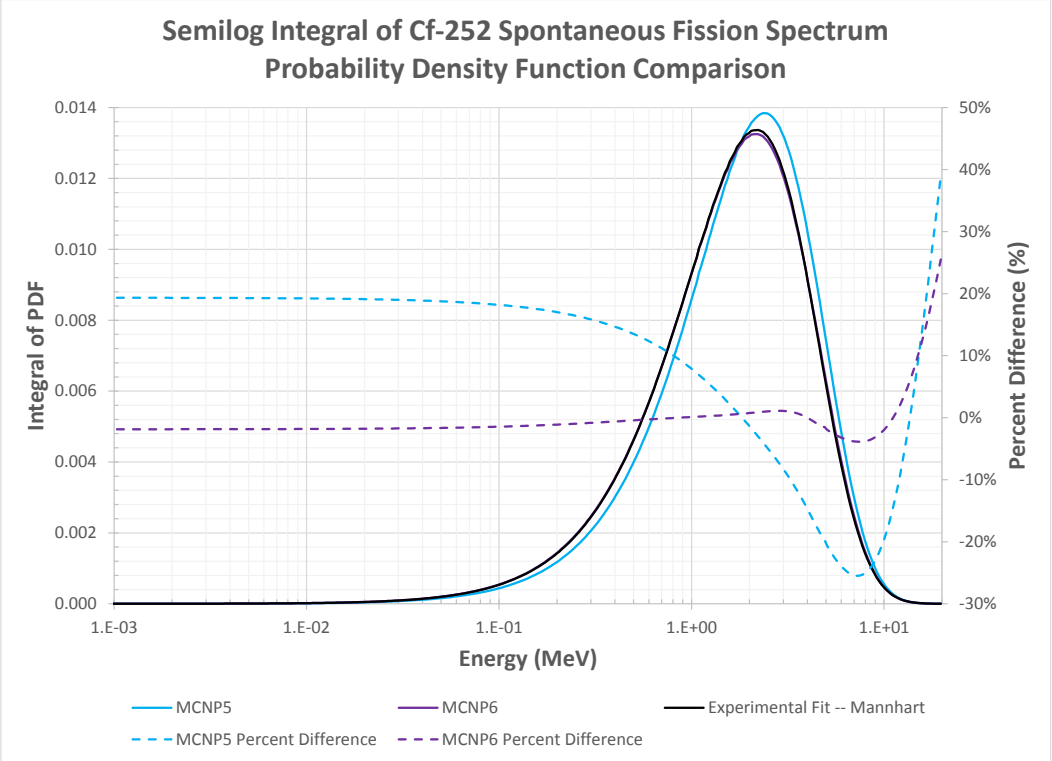

Figure 14: Californium-252 fission spectrum probability density function comparison per MeV. Mannhart's fitted experimental distribution is used as reference in comparison against MCNP 5 and MCNP 6 reported Watt fission spectrums.

Table 5: Preliminary californium-252 spontaneous fission spectrum comparison between MCNP 5 and MCNP 6 recommended Watt fission spectrum parameters using neutron source FTC-CF-004 within the *upright spatial setup* configuration. 10^7 histories were used for each run. Response count rates reported.

Spectrum	**(c/s) at 16 cm**	**(c/s) at 61 cm**
MCNP 5 Watt	4554.86	749.84
MCNP 6 Watt	4684.74	768.37
% Difference	-2.77%	-2.41%

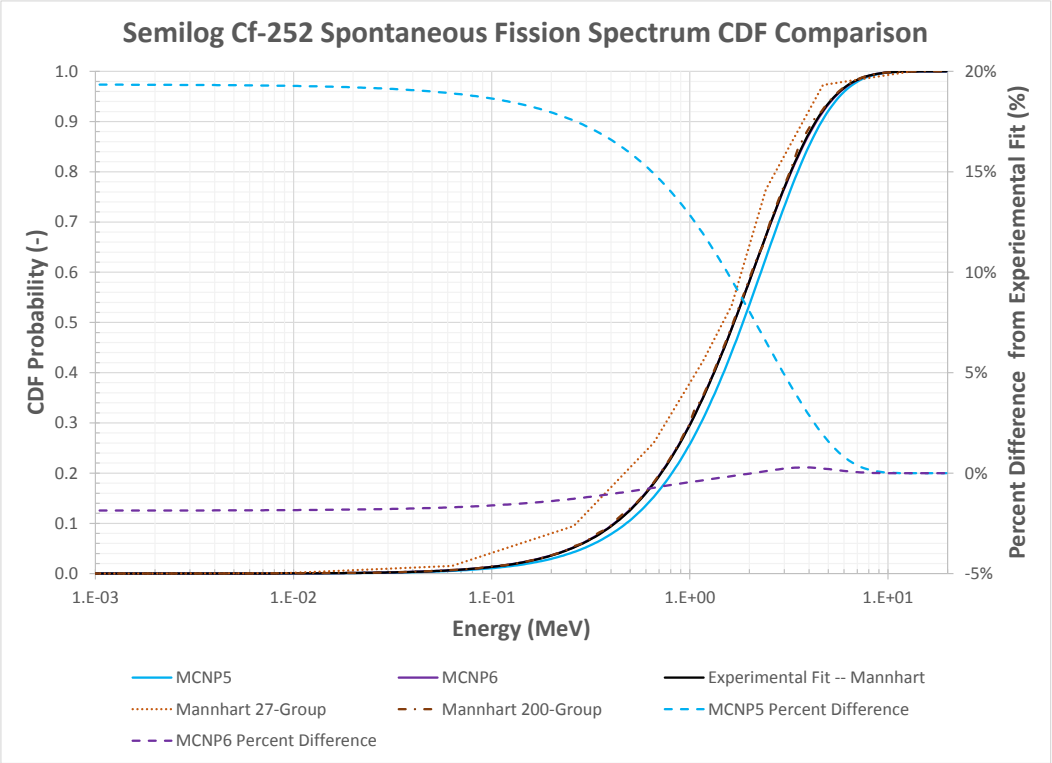

Figure 15: Californium-252 fission spectrum cumulative probability density function comparison per MeV. Mannhart's fitted experimental distribution is used as reference in comparison against MCNP 5 and MCNP 6 reported Watt fission spectrums. Also, Mannhart's fitted distribution is sampled within the SCALE6.1 ENDF/B-VII.0 200 and 27 group energy boundaries for reference.

III.B Material Specifications

Most Material compositions were based upon Pacific Northwest National Laboratory's "Compendium of Material Composition Data for Radiation Transport Modeling" [8] with one notable exception, the detector's fill gas described in the paragraphs below. The input specifications for MCNP and SCALE are summarized in Table 6. The constants used include the ideal gas constant $R = 0.08205746\,\frac{L\,atm}{K\,mol}$, a temperature $T = 293.15\,K$ and Avogadro's Number $N_a = 6.0220434469282E23\,\frac{atoms}{mol}$.

Detector Tubes are set at $4\,atm$ partial pressure of helium-3 and $1\,atm$ partial pressure of P-10 gas. The density of helium-3 may be found using the ideal gas law

$$P_{He3}V = n_{He3}RT, \tag{5}$$

where P_{He3} is the partial pressure of the helium-3, V is the volume, n_{He3} is the number of moles of helium-3, R is the ideal gas constant, and T is the temperature of the gas. This may be rearranged by multiplying through by the molecular mass of helium-3

$$\frac{m_{He3}}{V} = \rho_{He3} = \frac{M_{He3}P_{He3}}{RT}, \tag{6}$$

where ρ_{He3} is the density of the helium-3 gas, m is the mass, and M_{He3} is the molecular mass of helium-3. By substitution, the helium-3 gas density is $\rho_{He3} = 5.0151924e-4\,g/cm^3$. P-10 gas consists of 10% by volume methane

Table 6: Material specifications used in MCNP and Denovo simulations.

Constituent	**Molecular Weight** $\left(\frac{g}{mol}\right)$	**Weight Fraction (-)**	**Atomic Fraction (-)**	**Atomic Density** $\left(\frac{atoms}{barn\,cm}\right)$
Air (Dry, Near Sea Level); 0.001205 $\frac{g}{mol}$				
C	12.01070000	0.00012400	0.00015019	7.49176761E-09
N	14.00674000	0.75526800	0.78443022	3.91286576E-05
O	15.99940000	0.23178100	0.21074847	1.05124772E-05
Ar	39.94800000	0.01282700	0.00467111	2.33002717E-07
Aluminum; 2.6989 $\frac{g}{mol}$				
Al	26.98153800	1.00000000	1.00000000	6.02370890E-02
Cadmium; 8.65 $\frac{g}{mol}$				
Cd	112.4110000	1.00000000	1.00000000	4.63394826E-02
Californium-252; 15.1 $\frac{g}{mol}$				
Cf-252	252.0816196	1.00000000	1.00000000	3.60727832E-02
Concrete (NBS 03); 2.35 $\frac{g}{mol}$				
H-1	1.00782500	0.00848500	0.14985422	1.19145726E-02
C	12.01070000	0.05006400	0.07419241	5.89887201E-03
O-16	15.99491460	0.47348300	0.52689579	4.18923007E-02
Mg	24.30500000	0.02418300	0.01770993	1.40807665E-03
Al-27	26.98153860	0.03606300	0.02379016	1.89150236E-03
Si	28.08550000	0.14510000	0.09195758	7.31134032E-03
S	32.06500000	0.00297000	0.00164865	1.31080157E-04
K	39.09830000	0.00169700	0.00077255	6.14236633E-05
Ca	40.07800000	0.24692400	0.10966285	8.71904681E-03
Fe	55.84500000	0.01103100	0.00351587	2.79538954E-04
Fill Gas (He-3 + P-10 Quench); 0.0020628254 $\frac{g}{mol}$				
He-3	3.01602931	0.24312247	0.74074074	1.00137306E-04
C	12.01070000	0.02420460	0.01851852	2.50343266E-06
H	1.00794000	0.00812502	0.07407407	1.00137306E-05
Ar	39.94800000	0.72454791	0.16666667	2.25308939E-05
High Density Polyethylene; 0.95 $\frac{g}{mol}$				
C	12.01070000	0.85628143	0.33333333	4.07864303E-02
H	1.00794000	0.14371857	0.66666667	8.15728606E-02

Table 7: Material specifications used in MCNP and Denovo simulations (continued).

Constituent	**Molecular Weight** $\left(\frac{g}{mol}\right)$	**Weight Fraction** (-)	**Atomic Fraction** (-)	**Atomic Density** $\left(\frac{atoms}{barn\,cm}\right)$
Stainless Steel 304 L; 8.0 $\frac{g}{mol}$				
C	12.01070000	0.00030000	0.00137279	1.20333572E-04
Si-28	27.97692650	0.00459400	0.00902490	7.91088116E-04
Si-29	28.97649470	0.00024100	0.00045711	4.00686829E-05
Si-30	29.97377020	0.00016500	0.00030255	2.65201785E-05
P-31	30.97376150	0.00022500	0.00039925	3.49963249E-05
S-32	31.97207070	0.00014200	0.00024410	2.13969293E-05
S-33	32.97145850	0.00000100	0.00000167	1.46115306E-07
S-34	33.96786680	0.00000700	0.00001133	9.92804273E-07
Cr-50	49.94604960	0.00793000	0.00872616	7.64902208E-04
Cr-52	51.94051190	0.15903100	0.16827778	1.47505915E-02
Cr-53	52.94065380	0.01837800	0.01907920	1.67241024E-03
Cr-54	53.93888490	0.00466100	0.00474929	4.16304409E-04
Mn-55	54.93804960	0.01000000	0.01000410	8.76921331E-04
Fe-54	53.93961480	0.03999600	0.04075303	3.57225613E-03
Fe-56	55.93494210	0.64476400	0.63353234	5.55330414E-02
Fe-57	56.93539870	0.01502600	0.01450482	1.27143713E-03
Fe-58	57.93328050	0.00203900	0.00193437	1.69559831E-04
Ni-58	57.93534790	0.06234000	0.05913905	5.18390519E-03
Ni-60	59.93079060	0.02465400	0.02260938	1.98185217E-03
Ni-61	60.93106040	0.00108500	0.00097868	8.57876702E-05
Ni-62	61.92834880	0.00350400	0.00310975	2.72589089E-04
Ni-64	63.92796960	0.00091700	0.00078837	6.91054495E-05
Zircaloy-2; 6.56 $\frac{g}{mol}$				
O-16	15.99491460	0.00119700	0.00679928	2.95637791E-04
Cr	51.99610000	0.00099700	0.00174211	7.57481642E-05
Fe	55.84500000	0.00099700	0.00162204	7.05275158E-05
Ni	58.69340000	0.00049900	0.00077243	3.35860555E-05
Zr	91.22400000	0.98234800	0.97837825	4.25406359E-02
Sn	118.7100000	0.01396200	0.01068589	4.64630861E-04

Table 8: Calculated weight fractions for a $4\,atm$ helium-3, $1\,atm$ P-10 tube.

Species	Weight Fraction
$\frac{\rho_C}{\rho_{total}}$	0.02420459821
$\frac{\rho_H}{\rho_{total}}$	0.00812501610
$\frac{\rho_{Ar}}{\rho_{total}}$	0.72454791170
$\frac{\rho_{He3}}{\rho_{total}}$	0.24312247390

and 90% by volume Argon. The density of the P-10 gas may be calculated in a manner similar to helium-3

$$\frac{m_{P10}}{V} = \rho_{P10} = \frac{M_{P10}P_{P10}}{RT}. \tag{7}$$

For an ideal gas, the volume fractions of the gas mixtures equals the molar fractions. Therefore, the molecular mass of the P-10 gas is given by

$$M_{P10} = 0.10M_{CH_4} + 0.90M_{Ar} = 37.5574460\,g/mol, \tag{8}$$

which gives a P-10 density of $1.561306196\,g/mol$. To determine the individual species' densities, divide both sides of Equation 7 by M_{P10} and interchange the mass fraction of P-10 with the molar fractions of carbon, hydrogen and argon. Adding all densities together yields a total gas density of $\rho_{total} = 0.0020628254\,g/cm^3$ with partial gas weight fractions summarized in Table 8.

III.C MCNP Simulations

An MCNP model of the neutron detector was created to compute the detector response function (DRF) $\sigma_d(E)$. To compute the DRF, an isotropic point source with uniform intensity from $1E-11$ to $20\,MeV$, was placed at the same locations as in the experimental setup detailed in Section II.D. A bounding box was placed just around the volume of the detector to tally the surface current as a function of energy that was entering from the uniform source. The current entering the front surface of the detector is labeled as $T_{fsc}(E)$. Figure 16 is a summary of incoming F1 surface current tallies of the front face of the detector as a function of energy and distance away from the helium-3 proportional counter tubes embedded within the detector. Slight deviations from a uniform current are attributed to neutron interactions with materials outside the bounding box of the detector (i.e. floor, hand truck, and surrounding air)

Another tally was created to calculate the average number of (n,p) reactions occurring within the active region of the helium-3 tubes – which contains 4 atm partial pressure He-3 and 1 atm P-10 gas – labeled $T_{np}(E)$. To calculate $T_{np}(E)$, the average flux was multiplied by the energy dependent microscopic cross section, $\sigma^{^3He}_{(n,p)}$, and the number density, N, within the cell via an FM card, i.e. $N\sigma^{^3He}_{(n,p)}\bar{\phi}^{Active\,Reg.}$ This gives units of $interactions/cm^3$. The volume of the active regions of the helium-3 tubes was calculated based on a radius of $1.190625\,cm$ and an active length of $50.8\,cm$ to give $V = 1131.185\,cm$. Multiplying the volume gives the average number of (n,p)

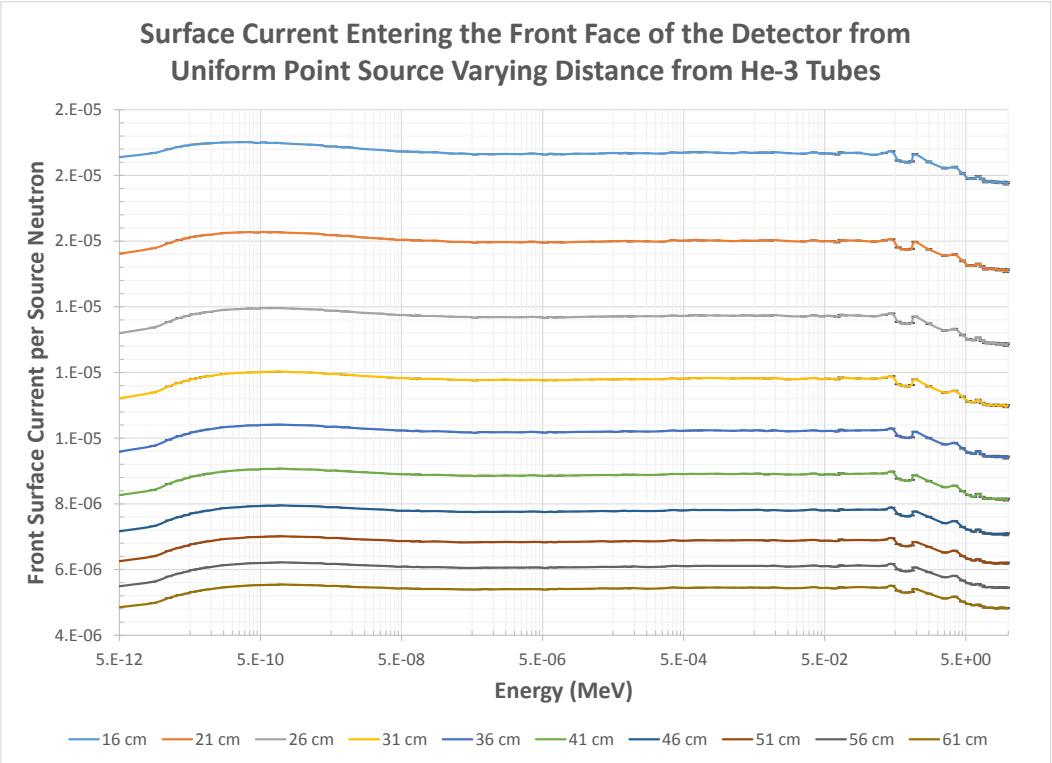

Figure 16: Surface current per source neutron entering the front face of the bounding box of the detector from a uniform isotropic point source as a function of energy and source distance away from the central helium-3 tube.

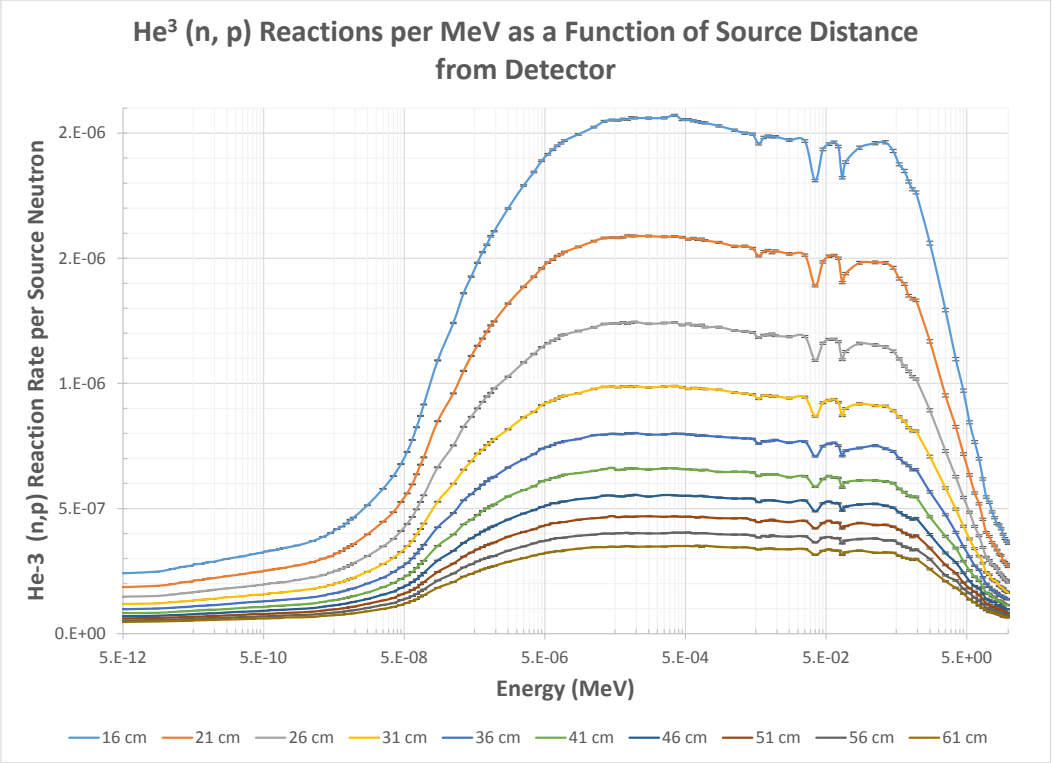

Figure 17: Average number of (n, p) reactions within the active regions of the helium-3 tubes per source neutron as a function of energy and source distance from helium-3 tubes.

reactions per source neutron as function of energy. Figure 17 gives these reactions, $T_{np}(E)$, and their statistical uncertainties as a function of source distance away from the helium-3 tubes.

To determine the detector response function, $\sigma_d(E)$, the average number of (n, p) reactions, $T_{np}(E)$, was divided by the incoming surface current on the front face of the detector, $T_{fsc(E)}$,

$$\sigma_d(E) = \frac{T_{np}(E)}{T_{fsc}(E)} = \frac{N\sigma_{(n,p)}^{^3He}\bar{\phi}^{Active\,Reg.}V}{T_{fsc}(E)}. \tag{9}$$

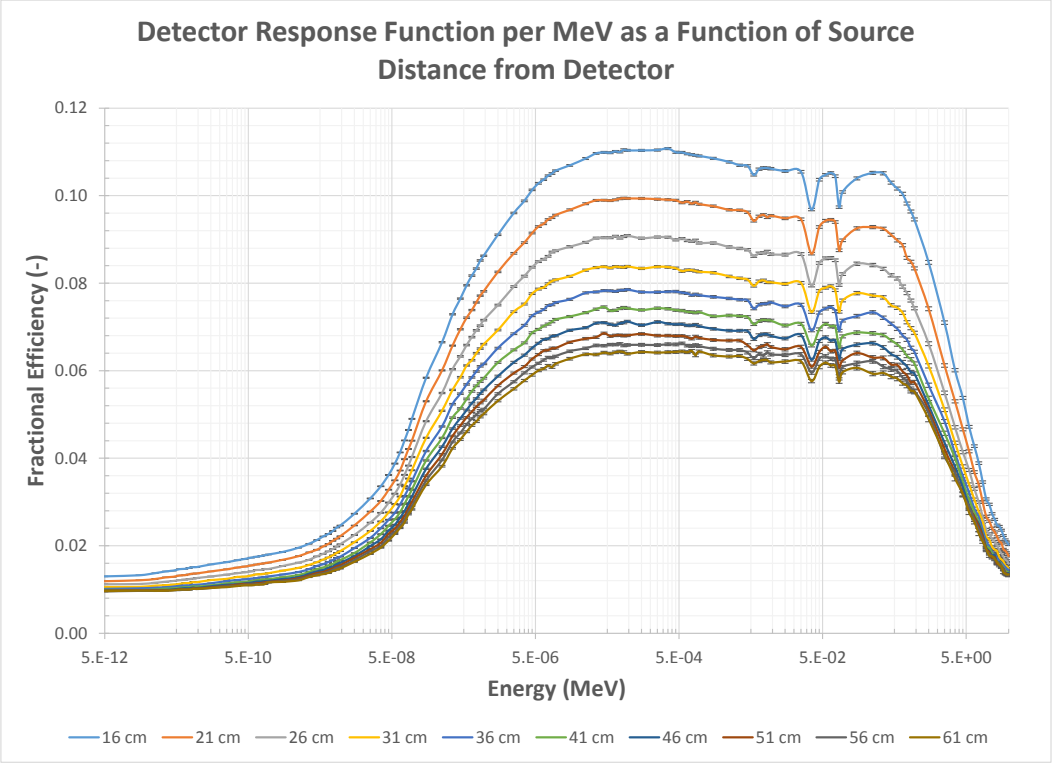

Figure 18: Detector efficiency as a function of energy and source distance away from the central He-3 tube.

The result for $\sigma_d(E)$ is provided via Figure 18 along with its statistical uncertainty for all experimentally measured source distances. The detector response function is also summarized in Table 9 through Table 12.

Next, given the available information about the FTC-CF-004 used in the lab, a MCNP input deck was constructed to serve as an accurate model of the source spectrum and geometry. This input deck contained the same detector bounding box as the previous input decks minus the detector itself; the goal being to accurately tally the incoming surface current impending on the front face of the detector bounding box as a function of energy – labeled $T_s(E)$. By

Table 9: Detector efficiency as a function of energy and source distance away from the central He-3 tube (Part 1).

Average Energy (MeV)	16 cm	21 cm	26 cm	31 cm	36 cm
5.0E-12	1.2998E-02	1.1890E-02	1.1195E-02	1.0564E-02	1.0149E-02
1.5E-11	1.3247E-02	1.2098E-02	1.1250E-02	1.0599E-02	1.0265E-02
2.5E-11	1.3723E-02	1.2387E-02	1.1529E-02	1.0865E-02	1.0394E-02
3.5E-11	1.4124E-02	1.2765E-02	1.1765E-02	1.0990E-02	1.0516E-02
4.5E-11	1.4311E-02	1.2903E-02	1.1947E-02	1.1108E-02	1.0647E-02
5.5E-11	1.4648E-02	1.3198E-02	1.2117E-02	1.1284E-02	1.0826E-02
6.5E-11	1.4712E-02	1.3269E-02	1.2252E-02	1.1445E-02	1.0910E-02
7.5E-11	1.4940E-02	1.3462E-02	1.2356E-02	1.1489E-02	1.0928E-02
8.5E-11	1.5113E-02	1.3637E-02	1.2489E-02	1.1694E-02	1.1041E-02
9.5E-11	1.5112E-02	1.3666E-02	1.2610E-02	1.1651E-02	1.1065E-02
1.5E-10	1.5727E-02	1.4130E-02	1.2969E-02	1.2147E-02	1.1409E-02
2.5E-10	1.6244E-02	1.4611E-02	1.3399E-02	1.2422E-02	1.1917E-02
3.5E-10	1.6686E-02	1.5015E-02	1.3718E-02	1.2875E-02	1.2163E-02
4.5E-10	1.6993E-02	1.5243E-02	1.3935E-02	1.2943E-02	1.2320E-02
5.5E-10	1.7284E-02	1.5493E-02	1.4142E-02	1.3197E-02	1.2476E-02
6.5E-10	1.7492E-02	1.5715E-02	1.4446E-02	1.3454E-02	1.2588E-02
7.5E-10	1.7633E-02	1.5876E-02	1.4463E-02	1.3481E-02	1.2755E-02
8.5E-10	1.7827E-02	1.5993E-02	1.4685E-02	1.3615E-02	1.2837E-02
9.5E-10	1.8001E-02	1.6145E-02	1.4667E-02	1.3721E-02	1.2968E-02
1.5E-09	1.8573E-02	1.6776E-02	1.5373E-02	1.4300E-02	1.3422E-02
2.5E-09	1.9539E-02	1.7614E-02	1.6130E-02	1.4939E-02	1.3987E-02
3.5E-09	2.0453E-02	1.8490E-02	1.6785E-02	1.5616E-02	1.4657E-02
4.5E-09	2.1284E-02	1.9072E-02	1.7577E-02	1.6234E-02	1.5378E-02
5.5E-09	2.2118E-02	1.9840E-02	1.8143E-02	1.6819E-02	1.5774E-02
6.5E-09	2.2675E-02	2.0403E-02	1.8703E-02	1.7327E-02	1.6271E-02
7.5E-09	2.3343E-02	2.1120E-02	1.9232E-02	1.7817E-02	1.6691E-02
8.5E-09	2.4145E-02	2.1640E-02	1.9813E-02	1.8352E-02	1.7227E-02
9.5E-09	2.4599E-02	2.2163E-02	2.0340E-02	1.8754E-02	1.7480E-02
1.5E-08	2.7293E-02	2.4630E-02	2.2443E-02	2.0801E-02	1.9455E-02
2.5E-08	3.0824E-02	2.7807E-02	2.5284E-02	2.3372E-02	2.1782E-02
3.5E-08	3.3581E-02	3.0223E-02	2.7519E-02	2.5555E-02	2.4002E-02
4.5E-08	3.6177E-02	3.2798E-02	2.9854E-02	2.7626E-02	2.5928E-02
5.5E-08	3.8768E-02	3.4937E-02	3.1892E-02	2.9505E-02	2.7521E-02
6.5E-08	4.1325E-02	3.7181E-02	3.3947E-02	3.1263E-02	2.9407E-02
7.5E-08	4.4063E-02	3.9776E-02	3.6182E-02	3.3596E-02	3.1352E-02
8.5E-08	4.6471E-02	4.2101E-02	3.8315E-02	3.5359E-02	3.3064E-02
9.5E-08	4.8970E-02	4.4007E-02	4.0292E-02	3.7246E-02	3.4734E-02
1.5E-07	5.8375E-02	5.3002E-02	4.8456E-02	4.4648E-02	4.1642E-02
2.5E-07	6.6508E-02	6.0069E-02	5.4912E-02	5.0860E-02	4.7262E-02
3.5E-07	7.2876E-02	6.5733E-02	6.0345E-02	5.5626E-02	5.2354E-02
4.5E-07	7.6478E-02	6.9460E-02	6.3286E-02	5.8509E-02	5.4762E-02
5.5E-07	7.9524E-02	7.2102E-02	6.5852E-02	6.1183E-02	5.6877E-02
6.5E-07	8.1727E-02	7.3844E-02	6.7682E-02	6.2392E-02	5.8476E-02
7.5E-07	8.3336E-02	7.5584E-02	6.9238E-02	6.3992E-02	5.9830E-02
8.5E-07	8.5184E-02	7.7153E-02	7.0286E-02	6.5071E-02	6.0987E-02
9.5E-07	8.6269E-02	7.8148E-02	7.1569E-02	6.6049E-02	6.1547E-02
1.5E-06	9.1067E-02	8.2567E-02	7.4997E-02	6.9281E-02	6.5170E-02
2.5E-06	9.6045E-02	8.6817E-02	7.9234E-02	7.3477E-02	6.8449E-02
3.5E-06	9.8798E-02	8.9253E-02	8.1607E-02	7.5231E-02	7.0373E-02
4.5E-06	1.0132E-01	9.1456E-02	8.3649E-02	7.7606E-02	7.2548E-02
5.5E-06	1.0281E-01	9.2932E-02	8.4911E-02	7.8642E-02	7.3380E-02
6.5E-06	1.0365E-01	9.3561E-02	8.5477E-02	7.9014E-02	7.3974E-02
7.5E-06	1.0457E-01	9.4561E-02	8.6156E-02	7.9867E-02	7.4887E-02
8.5E-06	1.0505E-01	9.4948E-02	8.7116E-02	8.0463E-02	7.5050E-02
9.5E-06	1.0571E-01	9.5574E-02	8.7399E-02	8.0765E-02	7.5575E-02
1.5E-05	1.0691E-01	9.6744E-02	8.8331E-02	8.1561E-02	7.6308E-02
2.5E-05	1.0849E-01	9.8142E-02	8.9341E-02	8.2988E-02	7.7772E-02
3.5E-05	1.0966E-01	9.8929E-02	9.0300E-02	8.3574E-02	7.7978E-02
4.5E-05	1.0988E-01	9.8955E-02	9.0372E-02	8.3754E-02	7.8272E-02

Table 10: Detector efficiency as a function of energy and source distance away from the central He-3 tube (Part 2).

Average Energy (MeV)	16 cm	21 cm	26 cm	31 cm	36 cm
5.5E-05	1.0981E-01	9.8884E-02	9.0381E-02	8.3477E-02	7.8253E-02
6.5E-05	1.1012E-01	9.9049E-02	9.0725E-02	8.3766E-02	7.8121E-02
7.5E-05	1.0997E-01	9.9302E-02	9.0323E-02	8.3686E-02	7.8367E-02
8.5E-05	1.1047E-01	9.9411E-02	9.0664E-02	8.3600E-02	7.8388E-02
9.5E-05	1.1034E-01	9.9359E-02	9.0868E-02	8.3829E-02	7.8552E-02
1.5E-04	1.1034E-01	9.9345E-02	9.0287E-02	8.3373E-02	7.7968E-02
2.5E-04	1.1043E-01	9.9200E-02	9.0527E-02	8.3744E-02	7.7956E-02
3.5E-04	1.1078E-01	9.9060E-02	9.0483E-02	8.3688E-02	7.8060E-02
4.5E-04	1.0991E-01	9.8941E-02	8.9902E-02	8.3414E-02	7.8080E-02
5.5E-04	1.0987E-01	9.8407E-02	9.0194E-02	8.2757E-02	7.7828E-02
6.5E-04	1.0955E-01	9.8633E-02	8.9756E-02	8.2982E-02	7.7684E-02
7.5E-04	1.0937E-01	9.8196E-02	8.9551E-02	8.2976E-02	7.7237E-02
8.5E-04	1.0921E-01	9.8465E-02	8.9792E-02	8.2776E-02	7.7450E-02
9.5E-04	1.0908E-01	9.8061E-02	8.9177E-02	8.2609E-02	7.7240E-02
1.5E-03	1.0852E-01	9.7588E-02	8.9164E-02	8.2386E-02	7.6872E-02
2.5E-03	1.0771E-01	9.6765E-02	8.8271E-02	8.1550E-02	7.6521E-02
3.5E-03	1.0694E-01	9.6687E-02	8.7928E-02	8.1119E-02	7.6227E-02
4.5E-03	1.0682E-01	9.6212E-02	8.7634E-02	8.0825E-02	7.6097E-02
5.5E-03	1.0473E-01	9.4250E-02	8.6170E-02	7.9385E-02	7.4189E-02
6.5E-03	1.0606E-01	9.5280E-02	8.6841E-02	8.0427E-02	7.5096E-02
7.5E-03	1.0632E-01	9.5617E-02	8.6934E-02	8.0636E-02	7.5301E-02
8.5E-03	1.0628E-01	9.5043E-02	8.7232E-02	8.0208E-02	7.5332E-02
9.5E-03	1.0616E-01	9.5413E-02	8.6612E-02	8.0206E-02	7.5616E-02
1.5E-02	1.0562E-01	9.4834E-02	8.6514E-02	7.9839E-02	7.4712E-02
2.5E-02	1.0546E-01	9.4605E-02	8.6657E-02	8.0047E-02	7.5051E-02
3.5E-02	9.6813E-02	8.6732E-02	7.9465E-02	7.3409E-02	6.9201E-02
4.5E-02	1.0365E-01	9.2841E-02	8.4607E-02	7.8226E-02	7.3287E-02
5.5E-02	1.0476E-01	9.4255E-02	8.5672E-02	7.8951E-02	7.4199E-02
6.5E-02	1.0519E-01	9.4480E-02	8.5765E-02	7.9306E-02	7.4565E-02
7.5E-02	1.0445E-01	9.3984E-02	8.5229E-02	7.8401E-02	7.3618E-02
8.5E-02	9.7385E-02	8.7510E-02	7.9570E-02	7.3469E-02	6.9146E-02
9.5E-02	1.0083E-01	8.9805E-02	8.2064E-02	7.6041E-02	7.1433E-02
1.5E-01	1.0395E-01	9.2526E-02	8.4440E-02	7.7724E-02	7.2457E-02
2.5E-01	1.0521E-01	9.2797E-02	8.4129E-02	7.7158E-02	7.3331E-02
3.5E-01	1.0509E-01	9.2452E-02	8.3258E-02	7.6759E-02	7.2100E-02
4.5E-01	1.0296E-01	9.1060E-02	8.1777E-02	7.4954E-02	7.0730E-02
5.5E-01	1.0162E-01	8.9762E-02	8.1084E-02	7.4375E-02	6.9562E-02
6.5E-01	1.0041E-01	8.8689E-02	7.9217E-02	7.3247E-02	6.8075E-02
7.5E-01	9.8216E-02	8.5787E-02	7.7748E-02	7.1087E-02	6.7064E-02
8.5E-01	9.6372E-02	8.4911E-02	7.6018E-02	6.9724E-02	6.5214E-02
9.5E-01	9.4549E-02	8.3389E-02	7.4274E-02	6.8663E-02	6.4317E-02
1.5E+00	8.4752E-02	7.4169E-02	6.6171E-02	6.1107E-02	5.6659E-02
2.5E+00	7.0967E-02	6.1177E-02	5.4948E-02	5.1079E-02	4.8394E-02
3.5E+00	6.0120E-02	5.3003E-02	4.7064E-02	4.3517E-02	4.1100E-02
4.5E+00	5.3772E-02	4.6605E-02	4.1400E-02	3.8111E-02	3.5915E-02
5.5E+00	4.7166E-02	4.1565E-02	3.7302E-02	3.4012E-02	3.2135E-02
6.5E+00	4.2757E-02	3.6812E-02	3.2997E-02	3.0568E-02	2.8494E-02
7.5E+00	3.8889E-02	3.3913E-02	2.9969E-02	2.7740E-02	2.6579E-02
8.5E+00	3.4561E-02	2.9990E-02	2.6569E-02	2.5425E-02	2.3630E-02
9.5E+00	3.0665E-02	2.6711E-02	2.3708E-02	2.2188E-02	2.1110E-02
1.1E+01	2.9440E-02	2.5624E-02	2.2699E-02	2.1397E-02	1.9805E-02
1.2E+01	2.7301E-02	2.3978E-02	2.1460E-02	1.9698E-02	1.8585E-02
1.3E+01	2.6007E-02	2.3133E-02	2.0991E-02	1.9135E-02	1.8021E-02
1.4E+01	2.4690E-02	2.2031E-02	2.0141E-02	1.8755E-02	1.7237E-02
1.5E+01	2.4419E-02	2.0981E-02	1.8951E-02	1.7363E-02	1.6393E-02
1.6E+01	2.3551E-02	2.0627E-02	1.8246E-02	1.6889E-02	1.6047E-02
1.7E+01	2.2311E-02	1.9178E-02	1.7535E-02	1.6432E-02	1.5594E-02
1.8E+01	2.1352E-02	1.8836E-02	1.6790E-02	1.5524E-02	1.5119E-02
1.9E+01	2.0836E-02	1.8382E-02	1.6587E-02	1.5285E-02	1.4721E-02
2.0E+01	2.0234E-02	1.7645E-02	1.5891E-02	1.4826E-02	1.4512E-02

Table 11: Detector efficiency as a function of energy and source distance away from the central He-3 tube (Part 3).

Average Energy (MeV)	41 cm	46 cm	51 cm	56 cm	61 cm
5.0E-12	9.9196E-03	9.7276E-03	9.7362E-03	9.5643E-03	9.6218E-03
1.5E-11	9.8670E-03	9.7492E-03	9.8005E-03	9.6869E-03	9.7522E-03
2.5E-11	1.0019E-02	9.8800E-03	9.7906E-03	9.6746E-03	9.7104E-03
3.5E-11	1.0209E-02	9.9009E-03	9.8405E-03	9.7187E-03	9.7217E-03
4.5E-11	1.0252E-02	1.0012E-02	9.8916E-03	9.8482E-03	9.8174E-03
5.5E-11	1.0410E-02	1.0169E-02	1.0026E-02	9.8592E-03	9.9726E-03
6.5E-11	1.0514E-02	1.0304E-02	9.9949E-03	9.9664E-03	9.9864E-03
7.5E-11	1.0520E-02	1.0274E-02	1.0056E-02	9.9736E-03	9.9783E-03
8.5E-11	1.0736E-02	1.0459E-02	1.0270E-02	1.0199E-02	1.0154E-02
9.5E-11	1.0661E-02	1.0344E-02	1.0218E-02	1.0100E-02	1.0129E-02
1.5E-10	1.0924E-02	1.0732E-02	1.0483E-02	1.0325E-02	1.0349E-02
2.5E-10	1.1392E-02	1.1085E-02	1.0828E-02	1.0753E-02	1.0547E-02
3.5E-10	1.1639E-02	1.1207E-02	1.1110E-02	1.0875E-02	1.0784E-02
4.5E-10	1.1735E-02	1.1420E-02	1.1289E-02	1.1119E-02	1.0969E-02
5.5E-10	1.1909E-02	1.1570E-02	1.1266E-02	1.1139E-02	1.0964E-02
6.5E-10	1.2109E-02	1.1815E-02	1.1429E-02	1.1233E-02	1.1109E-02
7.5E-10	1.2245E-02	1.1821E-02	1.1479E-02	1.1253E-02	1.1139E-02
8.5E-10	1.2304E-02	1.1922E-02	1.1655E-02	1.1451E-02	1.1236E-02
9.5E-10	1.2354E-02	1.1984E-02	1.1740E-02	1.1632E-02	1.1643E-02
1.5E-09	1.2792E-02	1.2387E-02	1.2037E-02	1.1886E-02	1.1743E-02
2.5E-09	1.3312E-02	1.2834E-02	1.2558E-02	1.2313E-02	1.2101E-02
3.5E-09	1.4026E-02	1.3596E-02	1.3195E-02	1.2954E-02	1.2845E-02
4.5E-09	1.4668E-02	1.4136E-02	1.3769E-02	1.3436E-02	1.3222E-02
5.5E-09	1.5004E-02	1.4434E-02	1.3978E-02	1.3708E-02	1.3523E-02
6.5E-09	1.5475E-02	1.4880E-02	1.4456E-02	1.4069E-02	1.3778E-02
7.5E-09	1.5844E-02	1.5239E-02	1.4805E-02	1.4507E-02	1.4213E-02
8.5E-09	1.6362E-02	1.5772E-02	1.5309E-02	1.4962E-02	1.4532E-02
9.5E-09	1.6722E-02	1.6103E-02	1.5521E-02	1.5147E-02	1.4790E-02
1.5E-08	1.8318E-02	1.7621E-02	1.7245E-02	1.6696E-02	1.6312E-02
2.5E-08	2.0741E-02	1.9922E-02	1.9199E-02	1.8762E-02	1.8147E-02
3.5E-08	2.2642E-02	2.1465E-02	2.0657E-02	1.9952E-02	1.9564E-02
4.5E-08	2.4561E-02	2.3465E-02	2.2727E-02	2.1985E-02	2.1196E-02
5.5E-08	2.6072E-02	2.4781E-02	2.3914E-02	2.3153E-02	2.2703E-02
6.5E-08	2.7637E-02	2.6417E-02	2.5432E-02	2.4650E-02	2.4049E-02
7.5E-08	2.9578E-02	2.7896E-02	2.6814E-02	2.6000E-02	2.5306E-02
8.5E-08	3.1283E-02	2.9669E-02	2.8539E-02	2.7770E-02	2.7194E-02
9.5E-08	3.2807E-02	3.1224E-02	3.0015E-02	2.9078E-02	2.8311E-02
1.5E-07	3.9503E-02	3.7572E-02	3.6011E-02	3.4891E-02	3.3935E-02
2.5E-07	4.4636E-02	4.2630E-02	4.0910E-02	3.9616E-02	3.8161E-02
3.5E-07	4.9275E-02	4.6784E-02	4.5085E-02	4.3727E-02	4.2262E-02
4.5E-07	5.1372E-02	4.9113E-02	4.7475E-02	4.5771E-02	4.4280E-02
5.5E-07	5.3543E-02	5.1010E-02	4.9339E-02	4.7740E-02	4.6064E-02
6.5E-07	5.5289E-02	5.2579E-02	5.0625E-02	4.9022E-02	4.7492E-02
7.5E-07	5.6545E-02	5.3649E-02	5.1758E-02	4.9929E-02	4.8387E-02
8.5E-07	5.7505E-02	5.4773E-02	5.2611E-02	5.0902E-02	4.9418E-02
9.5E-07	5.8281E-02	5.5611E-02	5.3281E-02	5.1186E-02	5.0141E-02
1.5E-06	6.1866E-02	5.8746E-02	5.6590E-02	5.4710E-02	5.3128E-02
2.5E-06	6.4750E-02	6.1907E-02	5.9443E-02	5.7487E-02	5.5843E-02
3.5E-06	6.6380E-02	6.3553E-02	6.0954E-02	5.9491E-02	5.7741E-02
4.5E-06	6.8681E-02	6.5209E-02	6.2687E-02	6.0852E-02	5.9036E-02
5.5E-06	6.9437E-02	6.6269E-02	6.3683E-02	6.1689E-02	6.0054E-02
6.5E-06	7.0197E-02	6.7141E-02	6.4563E-02	6.2446E-02	6.0451E-02
7.5E-06	7.0649E-02	6.7279E-02	6.4688E-02	6.3037E-02	6.1153E-02
8.5E-06	7.1198E-02	6.7908E-02	6.5133E-02	6.2975E-02	6.0795E-02
9.5E-06	7.1720E-02	6.7992E-02	6.5152E-02	6.3303E-02	6.1565E-02
1.5E-05	7.2374E-02	6.9216E-02	6.6501E-02	6.4445E-02	6.2738E-02
2.5E-05	7.3269E-02	6.9835E-02	6.7307E-02	6.5126E-02	6.3742E-02
3.5E-05	7.4052E-02	7.0875E-02	6.7652E-02	6.5767E-02	6.3693E-02
4.5E-05	7.4564E-02	7.0961E-02	6.8554E-02	6.5720E-02	6.4117E-02

Table 12: Detector efficiency as a function of energy and source distance away from the central He-3 tube (Part 4).

Average Energy (MeV)	41 cm	46 cm	51 cm	56 cm	61 cm
5.5E-05	7.3733E-02	7.0605E-02	6.7900E-02	6.5970E-02	6.3899E-02
6.5E-05	7.3782E-02	7.0411E-02	6.8077E-02	6.5976E-02	6.4223E-02
7.5E-05	7.4191E-02	7.0819E-02	6.8121E-02	6.6143E-02	6.4361E-02
8.5E-05	7.4415E-02	7.0979E-02	6.7991E-02	6.5765E-02	6.4234E-02
9.5E-05	7.4261E-02	7.1272E-02	6.8061E-02	6.5878E-02	6.3852E-02
1.5E-04	7.3873E-02	7.0416E-02	6.8398E-02	6.5914E-02	6.4263E-02
2.5E-04	7.4265E-02	7.1137E-02	6.8011E-02	6.5864E-02	6.4124E-02
3.5E-04	7.4148E-02	7.0746E-02	6.8017E-02	6.6041E-02	6.4236E-02
4.5E-04	7.3837E-02	7.0594E-02	6.7911E-02	6.5998E-02	6.4290E-02
5.5E-04	7.3736E-02	7.0631E-02	6.7947E-02	6.6229E-02	6.4405E-02
6.5E-04	7.3450E-02	7.0333E-02	6.7693E-02	6.5718E-02	6.4210E-02
7.5E-04	7.3399E-02	7.0333E-02	6.7307E-02	6.5643E-02	6.4532E-02
8.5E-04	7.3245E-02	7.0500E-02	6.7799E-02	6.5824E-02	6.3526E-02
9.5E-04	7.3415E-02	7.0168E-02	6.7512E-02	6.5621E-02	6.4382E-02
1.5E-03	7.2457E-02	6.9567E-02	6.7025E-02	6.5015E-02	6.3523E-02
2.5E-03	7.2626E-02	6.9149E-02	6.6895E-02	6.4737E-02	6.3237E-02
3.5E-03	7.2472E-02	6.9137E-02	6.6884E-02	6.4715E-02	6.3358E-02
4.5E-03	7.2264E-02	6.9063E-02	6.5811E-02	6.4142E-02	6.2678E-02
5.5E-03	7.0613E-02	6.7231E-02	6.4645E-02	6.2862E-02	6.1656E-02
6.5E-03	7.1347E-02	6.8107E-02	6.5383E-02	6.3855E-02	6.2207E-02
7.5E-03	7.1604E-02	6.8323E-02	6.5660E-02	6.3443E-02	6.2445E-02
8.5E-03	7.1517E-02	6.8330E-02	6.6069E-02	6.4221E-02	6.2427E-02
9.5E-03	7.1463E-02	6.7970E-02	6.5426E-02	6.3713E-02	6.1888E-02
1.5E-02	7.0321E-02	6.7377E-02	6.4886E-02	6.3612E-02	6.2090E-02
2.5E-02	7.0728E-02	6.8142E-02	6.5433E-02	6.3720E-02	6.2139E-02
3.5E-02	6.5749E-02	6.2508E-02	6.0928E-02	5.9555E-02	5.7634E-02
4.5E-02	6.9465E-02	6.6790E-02	6.4257E-02	6.2757E-02	6.0858E-02
5.5E-02	7.0707E-02	6.7610E-02	6.5483E-02	6.3269E-02	6.1836E-02
6.5E-02	7.0121E-02	6.6850E-02	6.4421E-02	6.2714E-02	6.1188E-02
7.5E-02	7.0066E-02	6.6852E-02	6.4521E-02	6.2613E-02	6.1109E-02
8.5E-02	6.5322E-02	6.2676E-02	6.0739E-02	5.8730E-02	5.7486E-02
9.5E-02	6.7831E-02	6.4902E-02	6.2326E-02	6.0824E-02	5.9640E-02
1.5E-01	6.8713E-02	6.5938E-02	6.4020E-02	6.1710E-02	6.0649E-02
2.5E-01	6.8525E-02	6.6281E-02	6.3005E-02	6.2183E-02	5.9304E-02
3.5E-01	6.8147E-02	6.5295E-02	6.2909E-02	6.0922E-02	5.9467E-02
4.5E-01	6.6951E-02	6.3814E-02	6.1423E-02	6.0308E-02	5.8648E-02
5.5E-01	6.5987E-02	6.3072E-02	6.1293E-02	5.9898E-02	5.8176E-02
6.5E-01	6.4825E-02	6.1933E-02	5.9850E-02	5.8413E-02	5.7147E-02
7.5E-01	6.3363E-02	6.0952E-02	5.8912E-02	5.7616E-02	5.6560E-02
8.5E-01	6.2609E-02	5.9648E-02	5.7256E-02	5.5818E-02	5.5385E-02
9.5E-01	6.1631E-02	5.9349E-02	5.7359E-02	5.5378E-02	5.5181E-02
1.5E+00	5.3677E-02	5.2105E-02	5.1019E-02	5.0251E-02	4.8966E-02
2.5E+00	4.5699E-02	4.3514E-02	4.2101E-02	4.0419E-02	4.0830E-02
3.5E+00	3.9968E-02	3.8050E-02	3.6739E-02	3.6587E-02	3.5357E-02
4.5E+00	3.4537E-02	3.3313E-02	3.1819E-02	3.1631E-02	3.1799E-02
5.5E+00	3.0552E-02	2.9090E-02	2.8661E-02	2.8996E-02	2.7598E-02
6.5E+00	2.7656E-02	2.6543E-02	2.6673E-02	2.5951E-02	2.5454E-02
7.5E+00	2.5405E-02	2.4999E-02	2.4369E-02	2.3650E-02	2.2747E-02
8.5E+00	2.2629E-02	2.2437E-02	2.2141E-02	2.1528E-02	2.0949E-02
9.5E+00	2.0037E-02	1.9591E-02	1.9310E-02	1.8998E-02	1.9316E-02
1.1E+01	1.9436E-02	1.8772E-02	1.8570E-02	1.8184E-02	1.7699E-02
1.2E+01	1.8255E-02	1.7730E-02	1.7282E-02	1.7570E-02	1.7631E-02
1.3E+01	1.7709E-02	1.7880E-02	1.7361E-02	1.7068E-02	1.6943E-02
1.4E+01	1.6219E-02	1.6036E-02	1.5901E-02	1.6387E-02	1.6234E-02
1.5E+01	1.6313E-02	1.6226E-02	1.5926E-02	1.5880E-02	1.5543E-02
1.6E+01	1.5726E-02	1.5097E-02	1.5380E-02	1.5295E-02	1.5131E-02
1.7E+01	1.4959E-02	1.4716E-02	1.4754E-02	1.4650E-02	1.3960E-02
1.8E+01	1.4331E-02	1.3861E-02	1.3923E-02	1.3696E-02	1.3642E-02
1.9E+01	1.4077E-02	1.3768E-02	1.3587E-02	1.3489E-02	1.3384E-02
2.0E+01	1.3932E-02	1.3776E-02	1.3264E-02	1.3206E-02	1.3487E-02

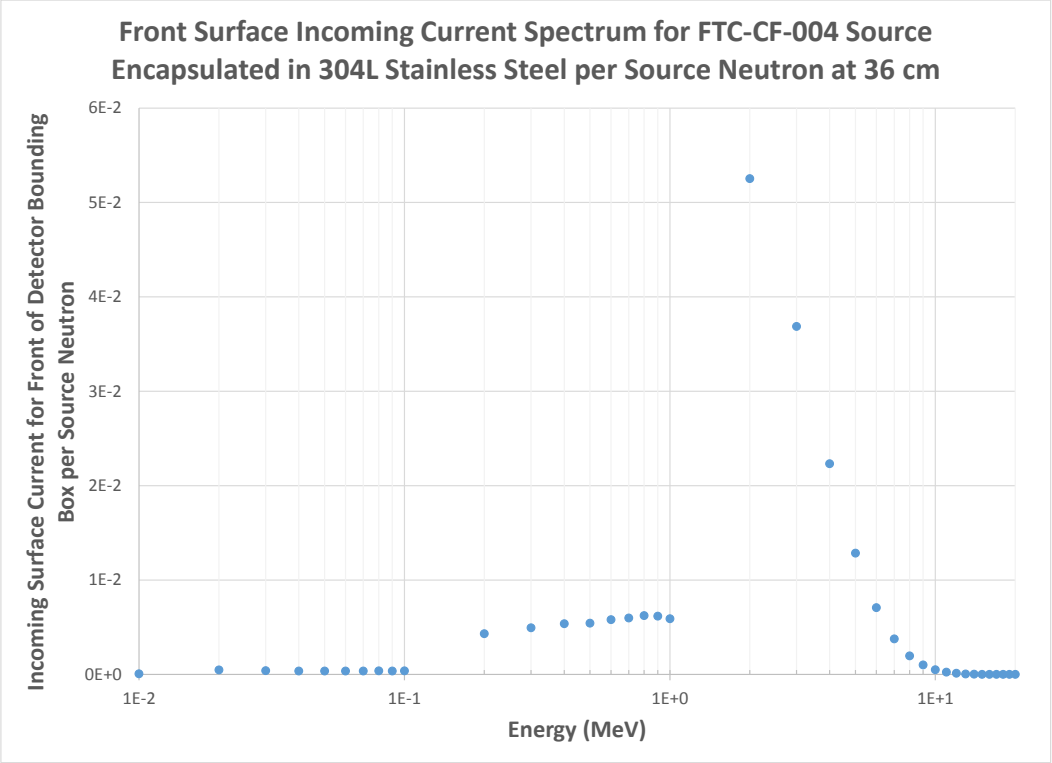

Figure 19: Representative detector bounding box front surface incoming neutron spectrum from FTC-CF-004.

removing the detector, this allows for far quicker simulation wall clock times. Figure 19 shows a representative incoming spectrum. The spectrum is very similar to the Watt spectrum that is used to characterize the californium-252 spontaneous fission neutron source. The particular energy binning structure, which is graduated in decades, creates the 'step' seen in Figure 19.

To calculate the detector response, and ultimately the expected counts per second from the MCNP simulations to compare with experiment, the sum product between the detector response function, $\sigma_d(E)$, and the source spectrum tally, $T_s(E)$, was computed. This quantity was then multiplied by

the source activity, S,

$$R^{DRF} \equiv S \int \sigma_d(E) T_s(E) dE \approx S \sum_i \sigma_d(E_i) T_s(E_i). \tag{10}$$

The associated uncertainty for the MCNP DRF response, ΔR^{DRF}, is due to a combination of stochastic uncertainties from MCNP Tallies, from the source emission strength uncertainty, and from estimated response uncertainty due to input cross section uncertainty calculated via Denovo. ΔR^{DRF} is given by

$$\Delta R^{DRF} \equiv \sqrt{\left(\frac{\sqrt{\boldsymbol{C_{rc}}}}{R}\right)^2 + \xi^2}, \tag{11}$$

where $\boldsymbol{C_{rc}}$ is defined in Equation 41 and ξ is given as

$$\xi \equiv |R| \sqrt{\left(\frac{\Delta S}{S}\right)^2 + \zeta^2}, \tag{12}$$

where ΔS is the source emission uncertainty, S is the source emission rate in counts per second, and ζ is given by

$$\zeta \equiv \frac{\sqrt{\sum_i \left(\sigma_d\left(E_i\right) T_s\left(E_i\right)\right)^2 \left[\left(\frac{\Delta \sigma_d(E_i)}{\sigma_d(E_i)}\right)^2 + \left(\frac{\Delta T_s(E_i)}{T_s(E_i)}\right)^2\right]}}{\sum_i \sigma_d\left(E_i\right) T_s\left(E_i\right)}, \tag{13}$$

where $\Delta T_s\left(E_i\right)$ is the absolute stochastic uncertainty for tally T_s at each

energy E_i and $\Delta\sigma_d(E_i)$ is given by

$$\Delta\sigma_d(E_i) \equiv |\sigma_d(E_i)| \sqrt{\left(\frac{\Delta T_{np}(E_i)}{T_{np}(E_i)}\right)^2 + \left(\frac{\Delta T_{fsc}(E_i)}{T_{fsc}(E_i)}\right)^2}, \tag{14}$$

where $\Delta T_{np}(E_i)$ and $\Delta T_{fsc}(E_i)$ are the absolue stochastic uncertainties for tallies T_{np} and T_{fsc} at each energy E_i respectively.

In addition to using the detector response function approximation to compare against experiment, MCNP input decks were created that contained both a detailed source and detector. These input decks were run to directly calculate the detector response via an F4 tally, $T_{rr}(E)$, that computed the helium-3 (n,p) reaction rate with an FM card. The full response, R^{full}, is given as

$$R^{full} \equiv SV \sum_i T_{rr}(E_i) = SVN \sum_i \sigma^{^3He}_{(n,p)}(E_i)\, \bar{\phi}^{ActiveReg.}(E_i) \tag{15}$$

where V is the total active helium-3 tube volume.The associated uncertainty for the MCNP full response, ΔR^{full}, is due to a combination of stochastic uncertainties from MCNP Tallies, from the source emission strength uncertainty, and from estimated response uncertainty due to input cross section uncertainty calculated via Denovo. ΔR^{full} is given by

$$\Delta R^{full} \equiv \sqrt{\left(\frac{\sqrt{\boldsymbol{C_{rc}}}}{R}\right)^2 + \theta^2}, \tag{16}$$

where $\boldsymbol{C_{rc}}$ is defined in Equation 41 and θ is given as

$$\theta \equiv |V| \left| S \sum_i T_{rr}\left(E_i\right) \right| \sqrt{\left(\frac{\Delta S}{S}\right)^2 + \omega^2}, \tag{17}$$

where ω is defined as

$$\omega \equiv \frac{\sqrt{\sum_i \left(\Delta T_{rr}\left(E_i\right)\right)^2}}{\sum_i T_{rr}\left(E_i\right)}, \tag{18}$$

where $\Delta T_{rr}\left(E_i\right)$ is the absolute stochastic uncertainty for tally T_{rr} at each energy E_i.

Results for both R^{DRF} and R^{full}, along with their associated uncertainties, ΔR^{DRF} and ΔR^{full} are compared against experiment in Section IV.

A sensitivity study was conducted to help bound the effects of uncertain quantities to the resulting count rates. The study was carried out for source FTC-CF-004 at 16, 36 and 61 cm away from the central helium-3 tube. For each of the 84 MCNP runs, there were a total of 1 billion neutron histories run. Results are summarized in Table 13.

For this particular source and setup combination, the source position and presence of the floor have the greatest effect on the response count rate. As the source moves farther away from the detector, the floor becomes increasingly important for reflecting neutrons that otherwise would not have reached the helium-3 tubes. Inversely, as the source moves closer to the detector, the detector occupies a larger solid angle with respect to the source. This proximity means a small change in source position has a larger effect on response count rates.

Table 13: Sensitivities of neutron source FTC-CF-004 at three collinear distances away from the center of the detector face computed via perturbed MCNP *upright spatial setup* models. Nominal conditions are given inside (parentheses).

Model 10 Source (FTC-CF-004) MCNP Simulations Percent Changes from Prescribed Nominals			
Distance From Detector	**16 cm**	**36 cm**	**61 cm**
Source Orientation (Upright 0°)			
-90°	-1.13% ± 0.0215%	-2.11% ± 0.0357%	-2.23% ± 0.0522%
90°	-1.68% ± 0.0214%	-3.72% ± 0.0354%	-5.40% ± 0.0523%
Source Capsule Material (304L Stainless Steel)			
Zircaloy	0.02% ± 0.0216%	0.08% ± 0.0360%	0.05% ± 0.0527%
No Capsule	-0.68% ± 0.0215%	-0.80% ± 0.0359%	-0.65% ± 0.0526%
Source Position $\mathbf{r}^0 + \mathbf{r}'$ ($r'_i = 0$ cm)			
r'_i =-5	-28.94% ± 0.0204%	-18.91% ± 0.0343%	-11.56% ± 0.0512%
r'_i =-1	-6.16% ± 0.0214%	-3.99% ± 0.0354%	-2.41% ± 0.0521%
r'_i =1	6.16% ± 0.0219%	4.00% ± 0.0364%	2.38% ± 0.0526%
r'_i =5	29.50% ± 0.0235%	19.56% ± 0.0376%	11.66% ± 0.0544%
Detector High Density Polyethylene Density (0.95 g/cc)			
Den. +1%	0.53% ± 0.0216%	0.51% ± 0.0361%	0.44% ± 0.0528%
Den. +10%	4.42% ± 0.0218%	4.31% ± 0.0361%	3.72% ± 0.0530%
Detector Fill Gas Density (2.0628E-3 g/cc; 4 atm He-3 and 1 atm P-10)			
Den. +1%	0.26% ± 0.0216%	0.26% ± 0.0361%	0.26% ± 0.0528%
Den. +10%	2.48% ± 0.0218%	2.48% ± 0.0364%	2.48% ± 0.0537%
Floor Presence (Concrete NBS 03)			
No Floor	-2.52% ± 0.0213%	-7.00% ± 0.0351%	-14.23% ± 0.0511%
Stochastic uncertainties represent a 1σ confidence interval in absolute percent. ($1E9$ Histories)			

III.D Denovo Simulations

III.D.1 Theory

An input model was created for Denovo to obtain response sensitivity and uncertainty information with regard to microscopic cross section uncertainties via capabilities implemented by R. T. Evans [9]. Denovo is a code development from ORNL that solves the three dimensional time-independent Boltzmann transport equation given as

$$\begin{aligned}\boldsymbol{\Omega}\cdot\vec{\nabla}\psi(\vec{r},\boldsymbol{\Omega},E)+\Sigma_t(\vec{r},E)\psi(\vec{r},\boldsymbol{\Omega},E)=\\ \int_{4\pi}d\boldsymbol{\Omega}'\int_0^{\infty}dE'\,\Sigma_s(\vec{r},\boldsymbol{\Omega}'\rightarrow\boldsymbol{\Omega},E'\rightarrow E)\psi(\vec{r},\boldsymbol{\Omega}',E')+Q(\vec{r},\boldsymbol{\Omega},E).\end{aligned}\quad(19)$$

With the adjoint, first-order sensitivities are obtained for responses such as nuclide density and reaction rates of the form

$$r_k\equiv\langle\sigma,\phi\rangle_w\quad(20)$$

where σ represents (usually but not necessarily) cross sections (microscopic or macroscopic), ϕ the scalar flux and $\langle\cdot,\cdot\rangle_w$ may denote a user-defined inner-product space. For convenience, the inner-product can be taken over the state space. To solve the fixed source problem, recast Equation 19 into an

equation of the form

$$\begin{aligned}\boldsymbol{\Omega}\cdot\vec{\nabla}\psi(\vec{r},\boldsymbol{\Omega},E)+\Sigma_t(\vec{r},E)\psi(\vec{r},\boldsymbol{\Omega},E) &= q(\vec{r},\boldsymbol{\Omega},E)+\\ \int_{4\pi}d\boldsymbol{\Omega}'\int_0^\infty dE'\,\Sigma_s(\vec{r},\boldsymbol{\Omega}'\to\boldsymbol{\Omega},E'\to E)\psi(\vec{r},\boldsymbol{\Omega}',E')&+\\ \frac{\chi\,(\vec{r},E)}{4\pi}\int_{4\pi}d\boldsymbol{\Omega}'\int_0^\infty dE'\,\nu_f(\vec{r},E')\Sigma_f(\vec{r},E')\psi(\vec{r},\boldsymbol{\Omega}',E'),&\quad(21)\end{aligned}$$

where the angular flux ψ is implicitly a function of the cross sections Σ_t, Σ_s and Σ_f, the fission spectrum χ and neutron multiplicity ν_f which are all considered input parameters $\boldsymbol{\alpha}$ and, in general, functions of space $\vec{r}$, energy E and neutron angle $\boldsymbol{\Omega}$. In this work, the external source, q, corresponds to the spontaneous fission occurring within the californium-252 sources.

For convenience, Equation 21 may be written in operator form as

$$\boldsymbol{M}\psi = q, \tag{22}$$

where

$$\boldsymbol{M} \equiv \boldsymbol{L} - \boldsymbol{S} - \boldsymbol{F},$$

and

$$\boldsymbol{L} \equiv \boldsymbol{\Omega}\cdot\vec{\nabla}\psi(\vec{r},\boldsymbol{\Omega},E)+\Sigma_t(\vec{r},E)\psi(\vec{r},\boldsymbol{\Omega},E),$$

$$\boldsymbol{S} \equiv \int_{4\pi}d\boldsymbol{\Omega}'\int_0^\infty dE'\,\Sigma_s(\vec{r},\boldsymbol{\Omega}'\to\boldsymbol{\Omega},E'\to E)\psi(\vec{r},\boldsymbol{\Omega}',E'),$$

$$\boldsymbol{F} \equiv \frac{\chi\,(\vec{r},E)}{4\pi}\int_{4\pi}d\boldsymbol{\Omega}'\int_0^\infty dE'\,\nu_f(\vec{r},E')\Sigma_f(\vec{r},E')\psi(\vec{r},\boldsymbol{\Omega}',E').$$

This forward system may be solved to obtain ψ. From this, the response r_k may then be computed.

Given the forward, nominal fixed source system in Equation 22

$$\boldsymbol{M}\left(\boldsymbol{\alpha}^0\right)\psi^0 = q^0, \tag{23}$$

with superscript "0" denoting the nominal state and with a slightly more general (but no less enlightening) response than in Equation 20

$$R\left(\boldsymbol{e}^0\right) = R\left(\psi^0, \boldsymbol{\alpha}^0\right) = R^0 = \left\langle \sigma^0, \psi^0 \right\rangle_w, \tag{24}$$

the sensitivity of the response with respect to a variation in parameters $\boldsymbol{\alpha}$ is represented as $\delta R\left(\boldsymbol{e}^0; \boldsymbol{h}\right)$; where $\boldsymbol{e}^0 \equiv \left(\boldsymbol{u}^0, \boldsymbol{\alpha}^0\right)$ denotes the nominal values of the state vector $\boldsymbol{u}$ and parameter vector $\boldsymbol{\alpha}$ while $\boldsymbol{h} \equiv \left(\boldsymbol{h}_{\boldsymbol{u}}, \boldsymbol{h}_{\boldsymbol{\alpha}}\right)$ represent arbitrary increment vectors in state $\left(\boldsymbol{h}_{\boldsymbol{u}}\right)$ and parameter $\left(\boldsymbol{h}_{\boldsymbol{\alpha}}\right)$ spaces. In this particular case, the state vector contains the angular flux while the parameter vector contains the cross sections mentioned in the previous section.

As will be shown shortly, because $\delta R\left(\boldsymbol{e}^0; \boldsymbol{h}\right)$ is linear in the state variable, the variation in R can consequently be written as

$$\delta R\left(\boldsymbol{e}^0; \boldsymbol{h}\right) = R'_{\boldsymbol{u}}\left(\boldsymbol{e}^0\right)\boldsymbol{h}_{\boldsymbol{u}} + R'_{\boldsymbol{\alpha}}\left(\boldsymbol{e}^0\right)\boldsymbol{h}_{\boldsymbol{\alpha}} \tag{25}$$

where $R'_{\boldsymbol{u}}\left(\boldsymbol{e}^0\right)$ and $R'_{\boldsymbol{\alpha}}\left(\boldsymbol{e}^0\right)$ denote, respectively, the partial Gâteaux deriva-

tives at $\boldsymbol{e}^0$ of $R(\boldsymbol{e})$ with respect to $\boldsymbol{u}$ and $\boldsymbol{\alpha}$. Taking the Gâteaux derivative

$$\frac{d}{d\epsilon}\left\{\left(R^0+\epsilon\delta R\right)=\left\langle\left(\sigma^0+\epsilon\delta\sigma\right),\left(\psi^0+\epsilon h_\psi\right)\right\rangle_w\right\}\Big|_{\epsilon=0}. \tag{26}$$

Expanding and noting that only the terms that are first-order in ϵ will survive, the variation is

$$\delta R\left(\boldsymbol{e}^0;\boldsymbol{h}\right)=\left\langle\sigma^0,h_\psi\right\rangle_w+\left\langle\delta\sigma,\psi^0\right\rangle_w. \tag{27}$$

The first term only contains variations (h_ψ) in the angular flux while the second term only contains variations ($\delta\sigma$) contained within the parameter vector. It is the variations in the state which, at this point, are unknown. To obtain h_ψ either the forward sensitivity analysis procedure (FSAP) or the adjoint sensitivity analysis procedure (ASAP) from [10] may be performed. In lieu of the fact that the typical number of input parameters far exceed the typical number of output parameters in a transport model calculation, the ASAP will prove computationally more efficient.

To utilize the ASAP and, thus, remove the dependence on h_ψ in the sensitivity of the response, first, the Gâteaux derivative of the system (Equation 23) is taken:

$$\frac{d}{d\epsilon}\left\{\left(\boldsymbol{M}^0+\epsilon\delta\boldsymbol{M}\right)-\left(\psi^0+\epsilon h_\psi\right)\right\}\Big|_{\epsilon=0}=\frac{d}{d\epsilon}\left\{\left(q^0+\epsilon\delta q\right)\right\}\Big|_{\epsilon=0} \tag{28}$$

Again, expanding, only terms first-order in ϵ will survive, yielding

$$\psi^0 \delta \boldsymbol{M} + \boldsymbol{M}^0 h_\psi = \delta q. \tag{29}$$

Equation 29 is termed the forward sensitivity analysis equation. The unknown is the variation in the flux, h_ψ. Given a variation(s) in an input parameter cross section(s), subsequent variations in $\boldsymbol{M}$ and q are readily available and the system may be solved for h_ψ. To continue towards elimination of the h_ψ dependency in both Equation 27 and Equation 29, multiply Equation 29 with an (as of yet) arbitrary function $\psi^\dagger$ and integrate over the same space utilized in the response

$$\left\langle \psi^\dagger, \delta \boldsymbol{M} \psi^0 \right\rangle_w + \left\langle \psi^\dagger, \boldsymbol{M}^0 h_\psi \right\rangle_w = \left\langle \psi^\dagger, \delta q \right\rangle_w \tag{30}$$

The term multiplying h_ψ may be transferred to $\psi^\dagger$ by taking the adjoint of the operator (denoted here as a "dagger" †)

$$\left\langle \psi^\dagger, \delta \boldsymbol{M} \psi^0 \right\rangle_w + \left\langle \boldsymbol{M}^\dagger \psi^\dagger, h_\psi \right\rangle_w = \left\langle \psi^\dagger, \delta q \right\rangle_w . \tag{31}$$

$\psi^\dagger$ may be chosen specifically such that

$$\boldsymbol{M}^\dagger \psi^\dagger = q^\dagger = \sigma^0 \tag{32}$$

This apropos choice is exercised by multiplying Equation 32 by h_ψ and inte-

grating over the appropriate space

$$\left\langle \boldsymbol{M}^{\dagger}\psi^{\dagger}, h_{\psi} \right\rangle_{w} = \left\langle \sigma^{0}, h_{\psi} \right\rangle_{w} \tag{33}$$

recalling Equation 27 and Equation 32, this leads to the following expression for the response variation

$$\delta R\left(\boldsymbol{e}^{0}; \boldsymbol{h}\right) = \left\langle \psi^{0}, \delta\sigma \right\rangle_{w} - \left\langle \psi^{\dagger}, \psi^{0}\delta\boldsymbol{M} \right\rangle_{w} + \left\langle \psi^{\dagger}, \delta q \right\rangle_{w} \tag{34}$$

To obtain the first order sensitivities for response R, a Taylor series expansion around a nominal point $\boldsymbol{e}^{0}$ is carried out

$$R\left(\boldsymbol{e}, \boldsymbol{h}\right) = R\left(\boldsymbol{e}^{0}, \boldsymbol{h}\right) + \sum_{i=1, \boldsymbol{N}_{\alpha}} \left.\frac{\partial R}{\partial \alpha_{i}}\right|_{\boldsymbol{e}^{0}} \delta\alpha_{i} + \ldots,$$

$$R\left(\boldsymbol{e}, \boldsymbol{h}\right) - R\left(\boldsymbol{e}^{0}, \boldsymbol{h}\right) \cong \sum_{i} \left.\frac{\partial R}{\partial \alpha_{i}}\right|_{\boldsymbol{e}^{0}} \delta\alpha_{i},$$

$$\delta R\left(\boldsymbol{e}, \boldsymbol{h}\right) \cong \sum_{i} \left.\frac{\partial R}{\partial \alpha_{i}}\right|_{\boldsymbol{e}^{0}} \delta\alpha_{i}. \tag{35}$$

Varying the i^{th} parameter while leaving the rest zero gives

$$\frac{\delta R_{i}}{\delta\alpha_{i}} \cong \frac{\partial R}{\partial \alpha_{i}} = S_{i}^{a} \equiv \left\langle \psi^{0}, \frac{\partial\sigma}{\partial\alpha_{i}} \right\rangle_{w} - \left\langle \psi^{\dagger}, \psi^{0}\frac{\partial \boldsymbol{M}}{\partial\alpha_{i}} \right\rangle_{w} + \left\langle \psi^{\dagger}, \frac{\partial q}{\partial\alpha_{i}} \right\rangle_{w}, \tag{36}$$

where S_{i}^{a} is referred to as the absolute sensitivity of response R with respect to input parameter α_{i}.

$$S_{i}^{r} = S_{i}^{a}\frac{\alpha_{i}}{R}, \tag{37}$$

is referred to as the relative sensitivity of response R with respect to input parameter α_i.

Thus, the sensitivity of response $R(\boldsymbol{e}^0)$ with respect to the input parameters $\boldsymbol{\alpha}$ can be computed via Equation 36 which only depends on the forward angular flux (ψ^0), the adjoint angular flux $\left(\psi^\dagger\right)$, and variations in the operators due to variations in the parameters. Given other responses, $\boldsymbol{r} = (r_k; k = 1, \ldots, \boldsymbol{N}_r)$, of the same form as Equation 24, only $\boldsymbol{N}_r$ adjoint runs need be completed to acquire sensitivities to every parameter in $\boldsymbol{\alpha} = (\alpha_i; i = 1, \ldots, \boldsymbol{N}_\alpha)$. This is opposed to $\boldsymbol{N}_\alpha$ homogeneous forward runs if one were to utilize just the forward sensitivity analysis equation.

III.D.2 Application

A SCALE input deck, shown in Appendix C, was created based on the *upright spatial setup* used in the MCNP validation exercise [11]. Simulations were completed with FTC-CF-004 at 16 and 61 cm away from the central helium-3 tube. A simulation at 16 cm with the cadmium front cover was also performed for comparison.

A three-dimensional, orthogonal mesh was generated with $124 \times 95 \times 56$ cells for the 16 cm simulations while a $92 \times 121 \times 56$ mesh was used for the 61 cm simulation. In all three runs, the detector was split down the center and a reflective boundary condition was used. While the detector is not perfectly symmetric due to the access port for high voltage and data acquisition cabling, a verification run on a coarser mesh showed a change

in response of 0.001327% due to reflection. Each simulation was completed using SCALE's 200 energy group shielding library "V7-200N47G". A Gauss-Legendre quadrature was used with 12 polar and 14 azimuthal angles per octant, a total of 1344 angles, while a P_1 expansion was utilized for the scattering kernel. A step characteristics discretization approximation was used throughout with an inner and outer iteration absolute solution tolerance of 1.0E-9.

These discretization choices were necessitated by the restriction of computational resources. The simulations were run in parallel via MPI on a dual machine cluster with a total of 64 cores and 256 GB of RAM. A finer spatial mesh would be necessary to obtain response values on the order of accuracy of the MCNP simulations. Nonetheless, the results presented here serve as a sound basis for estimates on the sensitivity of the response value with respect to changes in the cross section input parameters.

A discretization study, utilizing a coarser spatial mesh of $73 \times 71 \times 125$ cells and 27 group energy structure is presented in Table 14. The final run, using a P_5 expansion, Gauss-Legendre quadrature of 12×14 angles per octant, step-characteristics and tolerance of $1.0E-9$ serves as a reference point from which all other percent differences are based.

Figure 20 illustrates the spatial mesh for the $16\,cm$ simulations. The detector and californium-252 source are split and reflected on their vertical axis. The source is located collinear with the center of the detector's front face $16.1275\,cm$ away from the central point of the central helium-3 detector.

Table 14: Various combinations of spatial discretizations (weighted diamond differencing, step characteristics), angular discretizations (level symmetric, Gauss-Legendre product), Pn expansion orders (0 – 5), and solver tolerances (1E-3, 1E-6, 1E-9) were simulated with a fixed spatial and energy mesh to estimate the amount of discretization error incurred. Percent differences based on the simulation with the highest number of degrees of freedom.

Spa. Des.	**Ang. Des.**	**Sn**	**Pol.**	**Azi.**	**Pn**	**Tol.**	**% Diff.**
WDD	LS	4	-	-	0	1.00E-03	-97.1134
WDD	LS	8	-	-	3	1.00E-06	-33.7336
WDD	LS	16	-	-	5	1.00E-09	-3.5827
WDD	GL	-	6	8	3	1.00E-06	-63.4713
SC	GL	-	6	8	3	1.00E-06	-49.5191
SC	GL	-	8	10	3	1.00E-09	-0.0887
SC	GL	-	10	12	3	1.00E-09	-0.0247
SC	GL	-	12	14	3	1.00E-09	-0.0006
SC	GL	-	12	14	0	1.00E-09	-16.4770
SC	GL	-	12	14	1	1.00E-09	0.2445
SC	GL	-	12	14	2	1.00E-09	0.0223
SC	GL	-	12	14	3	1.00E-09	-0.0006
SC	GL	-	12	14	4	1.00E-09	0.0003
SC	GL	-	12	14	5	1.00E-09	0.0000

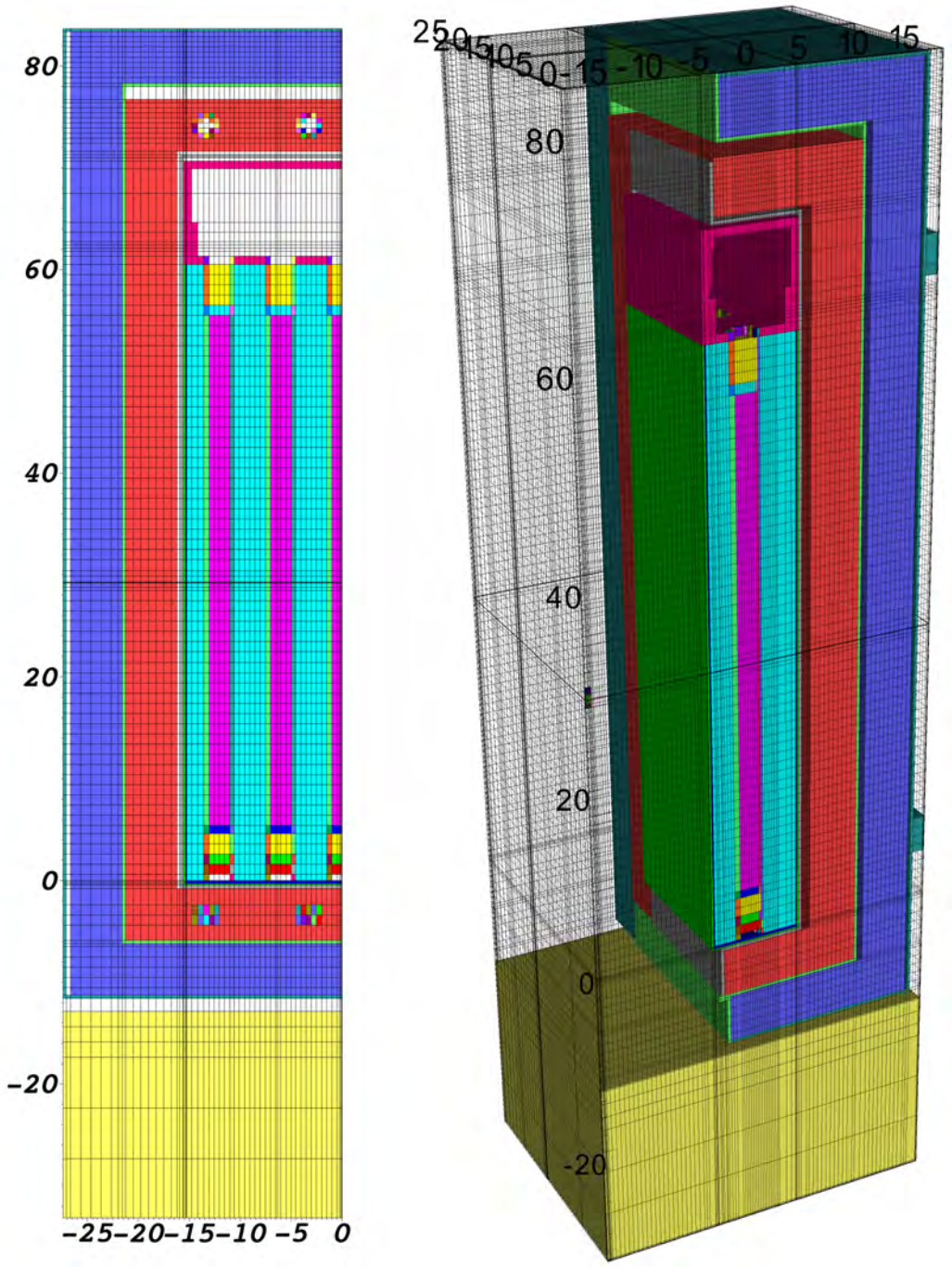

Figure 20: Spatial mesh generated via SCALE's Maverick input sequence.

Next, Figure 21, Figure 22, and Figure 23 show the top five largest magnitude relative sensitivities of response

$$R \equiv \left\langle N\sigma^{^3He}_{(n,p)}\left(\vec{r},E\right),\phi\left(\vec{r},E\right)\right\rangle = \left\langle \Sigma^{^3He}_{(n,p)}\left(\vec{r},E\right),\phi\left(\vec{r},E\right)\right\rangle, \tag{38}$$

where

$$\langle f,g\rangle \equiv \int_{V_{active}} d^3\vec{r}\int_0^\infty dEfg, \tag{39}$$

and

$$\phi\left(\vec{r},E\right) \equiv \int_{4\pi} d\mathbf{\Omega}\mathbf{\Omega}\psi\left(\vec{r},\mathbf{\Omega},E\right), \tag{40}$$

with V_{active} as the volume associated with the active region of the five helium-3 detectors. Each helium-3 tube has an active length of $50.8\,cm$ and an inner radius of $1.190625\,cm$, the total active volume is $1131.185\,cm^3$.

Associated with each sensitivity figure are the corresponding microscopic cross sections plotted on a secondary axis for reference. The most notable change from 16 to 61 cm is the increase in the absolute magnitude of the sensitivity of the response with respect to cadmium-113 (n,γ) reaction type within the cadmium sheath around the *bare detector assembly*. For the particular (predominantly fast) source spectrums of FTC-CF-004 and FTC-CF-053, the cadmium front cover yields very little change in response and response sensitivity.

Shown in Table 15 and Table 16, are the top 60 combined relative sensitivities from all three simulations. Each is ranked by its absolute value

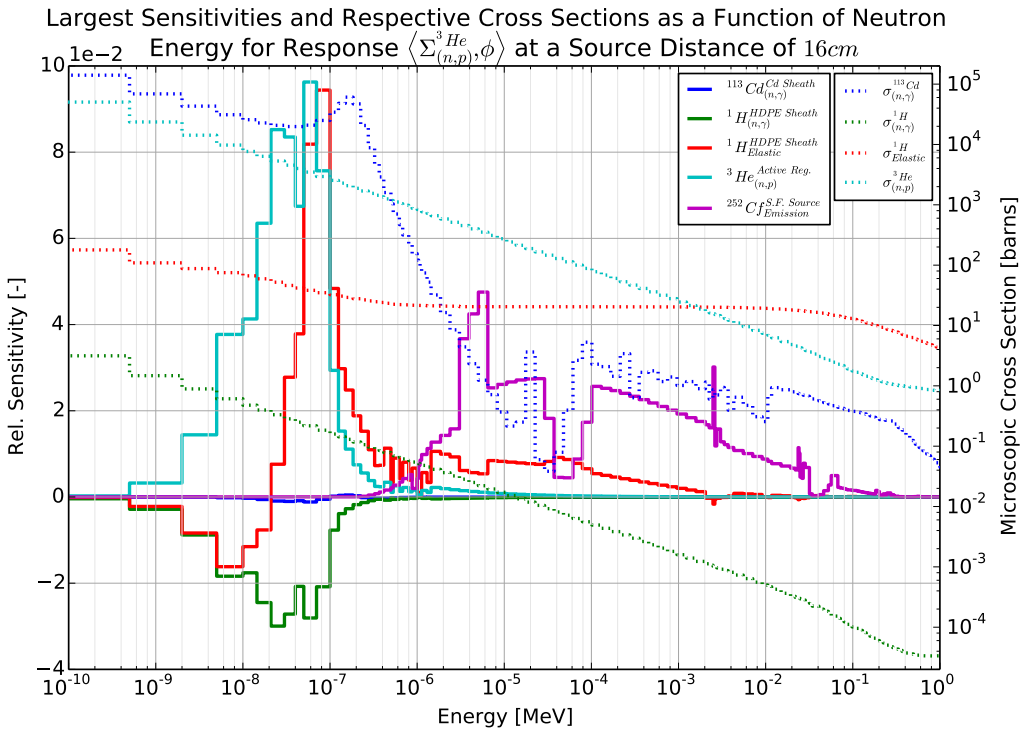

Figure 21: Largest by integrated magnitude relative microscopic cross section sensitivities with neutron source FTC-CF-004 a distance of 16.125 cm away from the central helium-3 tube as a function of neutron energy. These are paired with their respective cross sections for reference.

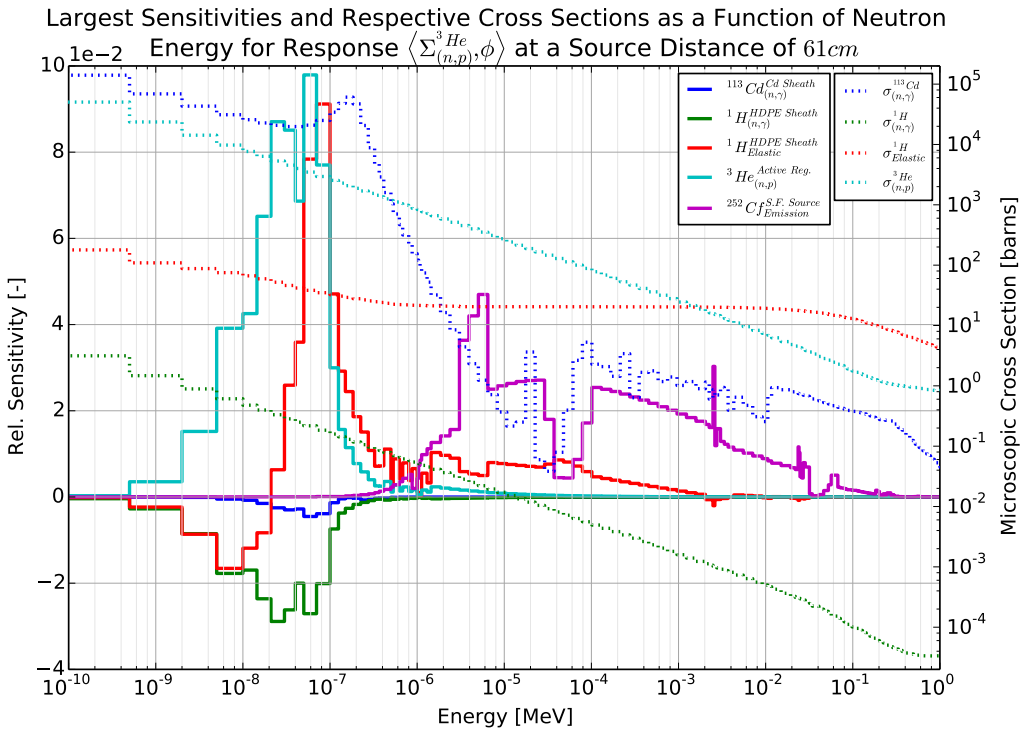

Figure 22: Largest by integrated magnitude relative microscopic cross section sensitivities with neutron source FTC-CF-004 a distance of 61.125 cm away from the central helium-3 tube as a function of neutron energy. These are paired with their respective cross sections for reference.

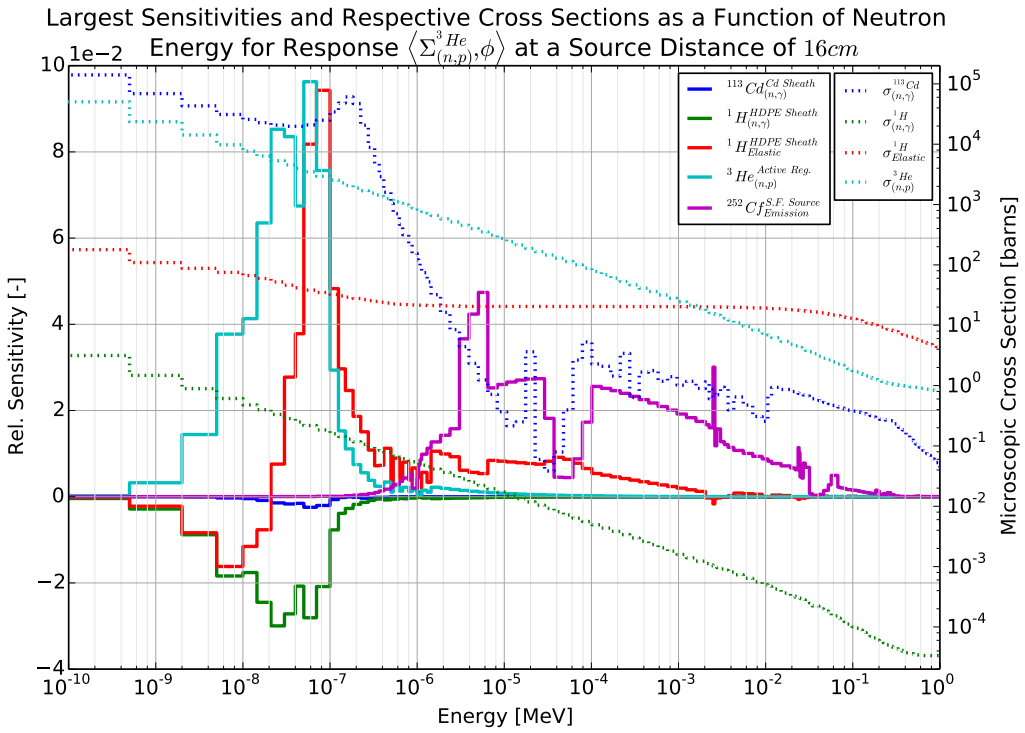

Figure 23: Largest by integrated magnitude relative microscopic cross section sensitivities with neutron source FTC-CF-004 at a distance of 16.125 cm away from the central helium-3 tube with 0.15875 cm thick cadmium front cover as a function of neutron energy. These are paired with their respective cross sections for reference.

and each is designated by the source distance and whether or not the cadmium cover was present. Relative sensitivities range from just over 1.0 for the californium-252 spontaneous fission rate to just under 6E-5 for the cadmium-113 elastic scatter cross section for the 16 cm no cover simulation.

Lastly, the generated sensitivity information was combined with cross section covariance data to propagate the uncertainty contribution from the cross section information to the response value. This process is achieved via

$$\boldsymbol{C_{rc}} \equiv \boldsymbol{S}\boldsymbol{C_{\alpha}}\boldsymbol{S}^{T}, \tag{41}$$

where $\boldsymbol{C_{rc}}$ is the output response covariance matrix, $\boldsymbol{S} = \left(S_1^r \dots S_{\boldsymbol{N}_\alpha}^r\right)^T$ is a $\boldsymbol{N}_\alpha \times 1$ dimension vector of relative sensitivities, and $\boldsymbol{C_{\alpha}}$ is an $\boldsymbol{N}_\alpha \times \boldsymbol{N}_\alpha$ dimension matrix of relative cross section covariances. The covariances are obtained from SCALE's 44 group covariance library (revision 5) and transformed onto the 200 group energy mesh. In this particular work, the one response, R, yields a 1×1 dimension $\boldsymbol{C_{rc}}$, i.e. one scalar response variance. The overall percent standard deviation, i.e.

$$\frac{\sqrt{\boldsymbol{C_{rc}}}}{R} \times 100$$

was found to be 0.3664% of the response value.

To understand the contributions of each individual material, isotope and reaction type to the overall response uncertainty, the sensitivity vector, $\boldsymbol{S}$,

Table 15: Largest magnitude microscopic cross section sensitivities integrated over energy group for response $\left\langle \Sigma^{^3He}_{(n,p)}, \phi \right\rangle$ for distances 16 and 61 cm, with and without the cadmium front cover.

Distance + Cd Cover	Material	Nuclide	Rxn.	Value (-)
61 cm No Cov	Source	Cf-252	S.F.	1.000075E+00
16 cm No Cov	Source	Cf-252	S.F.	1.000013E+00
16 cm Cover	Source	Cf-252	S.F.	1.000008E+00
61 cm No Cov	Act. Fill Gas	He-3	(n,p)	6.975793E-01
16 cm Cover	Act. Fill Gas	He-3	(n,p)	6.798563E-01
16 cm No Cov	Act. Fill Gas	He-3	(n,p)	6.798367E-01
16 cm Cover	HDPE Sheath	H-1	El.	5.981877E-01
16 cm No Cov	HDPE Sheath	H-1	El.	5.959725E-01
61 cm No Cov	HDPE Sheath	H-1	El.	5.570021E-01
16 cm No Cov	HDPE Sheath	H-1	(n,γ)	-2.257094E-01
16 cm Cover	HDPE Sheath	H-1	(n,γ)	-2.256494E-01
61 cm No Cov	HDPE Sheath	H-1	(n,γ)	-2.176688E-01
61 cm No Cov	HDPE In. Crdle	H-1	El.	-2.486313E-02
61 cm No Cov	Cd Sheath	Cd-113	(n,γ)	-2.404090E-02
61 cm No Cov	Concrete	H-1	El.	1.466112E-02
16 cm No Cov	Cd Sheath	Cd-113	(n,γ)	-1.287175E-02
61 cm No Cov	Inact. Fill Gas	He-3	(n,p)	-8.230846E-03
16 cm Cover	Cd Sheath	Cd-113	(n,γ)	-6.598353E-03
61 cm No Cov	HDPE Sheath	C	El.	-5.636768E-03
61 cm No Cov	HDPE In. Crdle	H-1	(n,γ)	-5.279760E-03
16 cm No Cov	HDPE Sheath	C	El.	-4.428016E-03
16 cm Cover	HDPE Sheath	C	El.	-4.401700E-03
16 cm No Cov	HDPE In. Crdle	H-1	El.	3.264912E-03
16 cm Cover	HDPE In. Crdle	H-1	El.	3.262812E-03
16 cm No Cov	Inact. Fill Gas	He-3	(n,p)	-2.250142E-03
16 cm Cover	Inact. Fill Gas	He-3	(n,p)	-2.246392E-03
61 cm No Cov	Concrete	O-16	El.	1.910412E-03
16 cm Cover	HDPE In. Crdle	H-1	(n,γ)	-1.822845E-03
16 cm No Cov	HDPE In. Crdle	H-1	(n,γ)	-1.820148E-03
16 cm No Cov	Concrete	H-1	El.	1.284364E-03

Table 16: Largest magnitude microscopic cross section sensitivities integrated over energy group for response $\left\langle \Sigma^{^3He}_{(n,p)}, \phi \right\rangle$ for distances 16 and 61 cm, with and without the cadmium front cover (continued).

Distance + Cd Cover	**Material**	**Nuclide**	**Rxn.**	**Value (-)**
16 cm Cover	Concrete	H-1	El.	1.066591E-03
16 cm Cover	HDPE In. Crdle	C	El.	1.019100E-03
16 cm No Cov	HDPE In. Crdle	C	El.	1.016441E-03
61 cm No Cov	Concrete	C	El.	9.064406E-04
61 cm No Cov	HDPE Out Crdle	H-1	(n,γ)	-8.442705E-04
61 cm No Cov	HDPE Out Crdle	H-1	El.	-7.992698E-04
16 cm No Cov	HDPE Out Crdle	H-1	El.	5.409009E-04
16 cm Cover	HDPE Out Crdle	H-1	El.	5.357247E-04
61 cm No Cov	HDPE In. Crdle	C	El.	5.113292E-04
61 cm No Cov	Air	N-14	El.	-4.762717E-04
61 cm No Cov	Concrete	H-1	(n,γ)	-4.281808E-04
16 cm Cover	Al Sheath	Al-27	El.	-3.663768E-04
16 cm No Cov	He-3 Al Tube	Al-27	(n,γ)	-3.380107E-04
16 cm Cover	He-3 Al Tube	Al-27	(n,γ)	-3.379881E-04
61 cm No Cov	He-3 Al Tube	Al-27	(n,γ)	-3.217216E-04
61 cm No Cov	Al Sheath	Al-27	El.	-2.851055E-04
16 cm No Cov	Al Sheath	Al-27	El.	-2.579803E-04
61 cm No Cov	Concrete	Si-28	El.	2.167939E-04
16 cm No Cov	HDPE Out Crdle	H-1	(n,γ)	-2.160516E-04
16 cm Cover	HDPE Out Crdle	H-1	(n,γ)	-2.139809E-04
16 cm No Cov	HDPE Sheath	C	(n,γ)	-2.025254E-04
16 cm Cover	HDPE Sheath	C	(n,γ)	-2.024716E-04
16 cm Cover	Cd Sheath	Cd-114	El.	-1.992028E-04
16 cm Cover	Cd Sheath	Cd-112	El.	-1.578123E-04
16 cm No Cov	Concrete	O-16	El.	1.521616E-04
16 cm Cover	Concrete	O-16	El.	1.445626E-04
16 cm Cover	Cd Sheath	Cd-111	El.	-8.830421E-05
16 cm No Cov	Al In. Crdle	Al-27	El.	8.078568E-05
16 cm No Cov	Concrete	C	El.	7.220300E-05
16 cm No Cov	Cd Sheath	Cd-113	El.	5.960251E-05

can be distributed along the diagonal of an identity matrix

$$diag\left(\boldsymbol{S}\right) \equiv \begin{pmatrix} S_1^r & 0 & 0 \\ 0 & \ddots & 0 \\ 0 & 0 & S_{\boldsymbol{N}_\alpha}^r \end{pmatrix}, \tag{42}$$

and then used as

$$diag\left(\boldsymbol{S}\right) \boldsymbol{C_\alpha} diag\left(\boldsymbol{S}\right). \tag{43}$$

This block-wise multiplication produces a $\boldsymbol{N}_\alpha \times \boldsymbol{N}_\alpha$ matrix where each element contains the uncertainty contribution from its corresponding material, isotope and reaction type. Figure 24 plots the top contributing uncertainties in an illustrative way so as to highlight the overall magnitude of the individual uncertainty contributions as well as the magnitude of the corresponding relative sensitivities involved.

The helium-3 (n, p) reaction cross section is responsible for over 90% of the overall response uncertainty due to cross section uncertainty. Hydrogen-1's (n, γ) and elastic cross sections follow suit at roughly 8.8 and 2.4%. Table 17 lists the top 25 contributing constituents to response uncertainty. Note that off-diagonal terms will come in symmetric pairs.

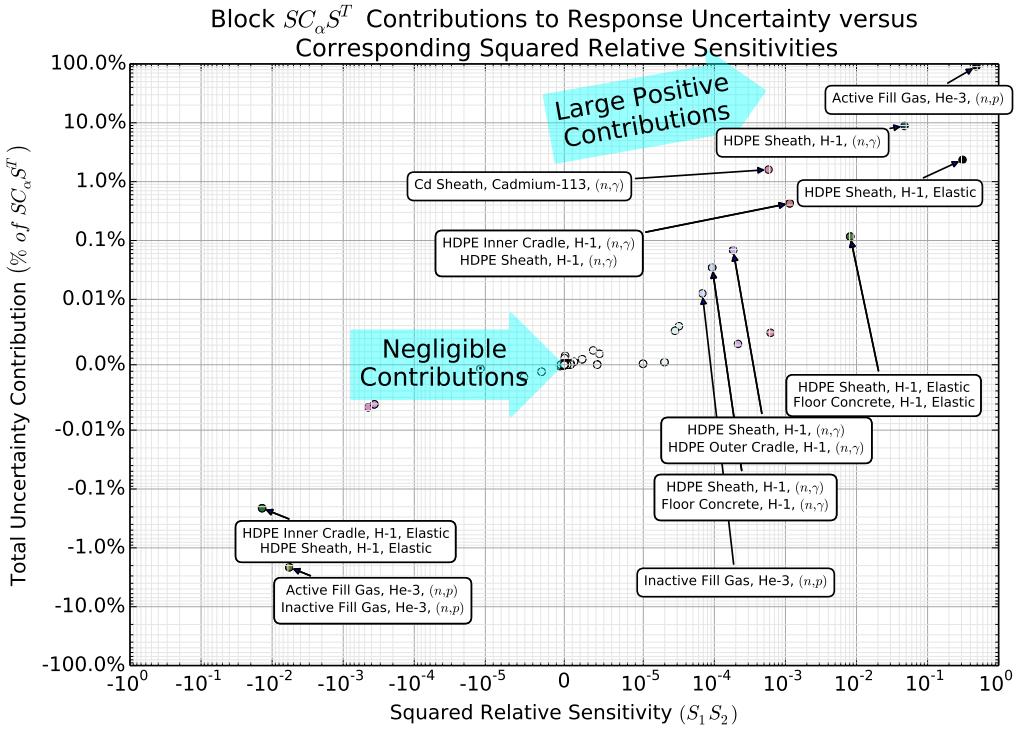

Figure 24: Largest contributors to uncertainty in the response due to uncertainties in microscopic cross sections. Each point defines two constituents whose relative sensitivities and parameter covariance submatrix are multiplied. Total response uncertainty contribution (percent standard deviation of response value) from cross section uncertainties is 0.3664%. The uncertainty contribution shown above is a percentage of this standard deviation.

Table 17: Largest contributors to uncertainty in the response due to uncertainties in microscopic cross sections. Each row defines the two constituents whose relative sensitivities and parameter covariance submatrix are multiplied. Total response uncertainty contribution (percent standard deviation of response value) from cross section uncertainties is 0.3664%. The uncertainty contribution shown below is a percentage of this standard deviation.

Constituent 1	**Constituent 2**	**Squared Sensitivities**	**% Uncertainty Contrib.**
Active Fill Gas, He-3, (n,p)	Active Fill Gas, He-3, (n,p)	4.866168E-01	90.61756
HDPE Sheath, H-1, (n,γ)	HDPE Sheath, H-1, (n,γ)	4.737970E-02	8.82229
HDPE Sheath, H-1, El.	HDPE Sheath, H-1, El.	3.102513E-01	2.35062
Active Fill Gas, He-3, (n,p)	Inactive Fill Gas, He-3, (n,p)	-5.741667E-03	-2.13842
Inactive Fill Gas, He-3, (n,p)	Active Fill Gas, He-3, (n,p)	-5.741667E-03	-2.13842
Cd Sheath, Cd-113, (n,γ)	Cd Sheath, Cd-113, (n,γ)	5.779647E-04	1.60104
HDPE Inner Crdle, H-1, (n,γ)	HDPE Sheath, H-1, (n,γ)	1.149239E-03	0.42793
HDPE Sheath, H-1, (n,γ)	HDPE Inner Crdle, H-1, (n,γ)	1.149239E-03	0.42793
HDPE Inner Crdle, H-1, El.	HDPE Sheath, H-1, El.	-1.384882E-02	-0.21196
HDPE Sheath, H-1, El.	HDPE Inner Crdle, H-1, El.	-1.384882E-02	-0.21196
HDPE Sheath, H-1, El.	Floor Concrete, H-1, El.	8.166275E-03	0.11676
Floor Concrete, H-1, El.	HDPE Sheath, H-1, El.	8.166275E-03	0.11676
HDPE Sheath, H-1, (n,γ)	HDPE Outer Crdle, H-1, (n,γ)	1.837713E-04	0.06843
HDPE Outer Crdle, H-1, (n,γ)	HDPE Sheath, H-1, (n,γ)	1.837713E-04	0.06843
HDPE Sheath, H-1, (n,γ)	Floor Concrete, H-1, (n,γ)	9.320160E-05	0.03469
Floor Concrete, H-1, (n,γ)	HDPE Sheath, H-1, (n,γ)	9.320160E-05	0.03469
Inactive Fill Gas, He-3, (n,p)	Inactive Fill Gas, He-3, (n,p)	6.774682E-05	0.01262
HDPE Outer Crdle, H-1, El.	HDPE Sheath, H-1, El.	-4.451949E-04	-0.00650
HDPE Sheath, H-1, El.	HDPE Outer Crdle, H-1, El.	-4.451949E-04	-0.00650
Floor Concrete, H-1, El.	HDPE Inner Crdle, H-1, El.	-3.645214E-04	-0.00605
HDPE Inner Crdle, H-1, El.	Floor Concrete, H-1, El.	-3.645214E-04	-0.00605
HDPE Sheath, C, El.	HDPE Sheath, C, El.	3.177315E-05	0.00589
HDPE Inner Crdle, H-1, (n,γ)	HDPE Inner Crdle, H-1, (n,γ)	2.787586E-05	0.00519
HDPE Inner Crdle, H-1, El.	HDPE Inner Crdle, H-1, El.	6.181755E-04	0.00489
Floor Concrete, H-1, El.	Floor Concrete, H-1, El.	2.149485E-04	0.00318

IV Overall Results Comparison

Comparison between the MCNP DRF and full simulations versus experimental measurements are presented. For both sets of simulations, uncertainties pertaining to the stochastic nature of the MCNP results, response uncertainties introduced due to uncertainties in input cross section information, and uncertainty due to the californium source emission rates are addressed.

Table 18 and Table 19 represent the computed count rates of the DRF and full simulations compared directly to experimentally measured count rates which are displayed in Figure 25 and Figure 26 respectively. Uncertainty information about experimental uncertainty (Exp. Unc.), stochastic uncertainty (Sto.), response uncertainty due to cross section data (XS), source emission rate uncertainty (Src.), and the total combination of stochastic, cross section data, and source emission uncertainties (Sim. Total) are given in Table 20 and Table 21 and also displayed as error bars in Figure 25 and Figure 26.

The DRF approximation simulations add a noticeable positive bias on the order of 1% as compared to the full simulations. Both simulation sets fall within the 1σ total uncertainty ranges. The largest contributor to uncertainty is the source emission rate with an uncertainty of 2.4% of 157755 neutrons per second. Next, at roughly an order of magnitude smaller, is the uncertainty due to cross section data uncertainty which was estimated at 0.3664% of the response value. Then, enough histories within MCNP were

used to minimize the stochastic uncertainty to the order of the experimental count rate uncertainty; roughly on the order of 0.25% depending on the source distance away from the detector.

Overall, this validation exercise serves as a sound base for which to test inverse algorithm methodologies while attempting to locate and identify nuclear holdup via passive neutron assay techniques. If plans to more accurately bound the source emission data are sucessful, then this would serve to narrow the overall uncertainties within this work. One other possibility that may be worth pursuing would be to recreate the experimental Mannhart californium-252 fission spectrum for use with the MCNP DRF and full simulation runs. This could potentially bring the simulated response values even closer to the experimentally measured values.

Appendices A, B, and C give detailed information for the detector used and inputs for the MCNP, SCALE, and Denovo codes used to generate the simulated output dislpayed throughout this work.

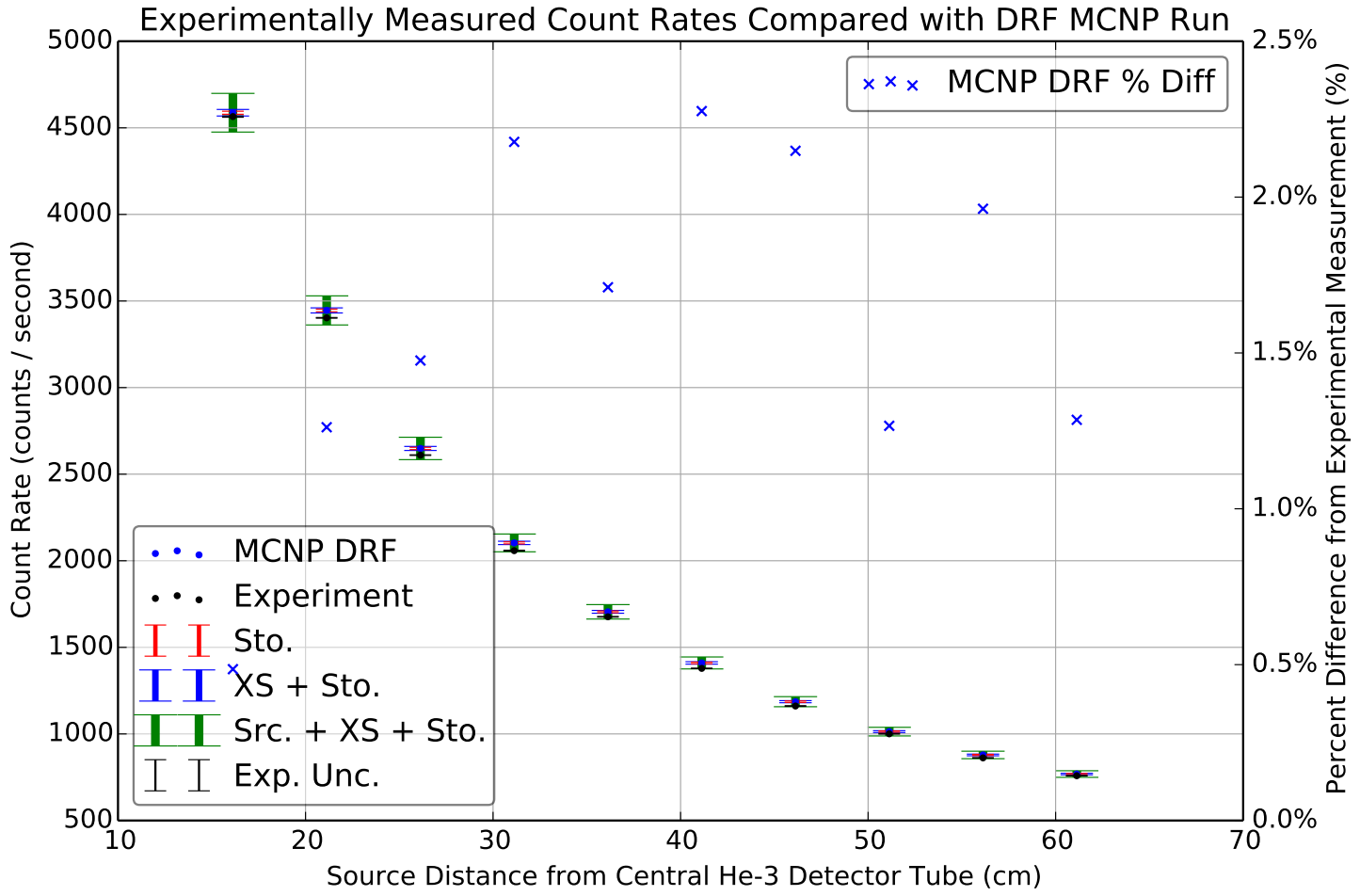

Figure 25: Comparison of the MCNP DRF simulations versus experiment. Response values and their associated uncertainties are displayed.

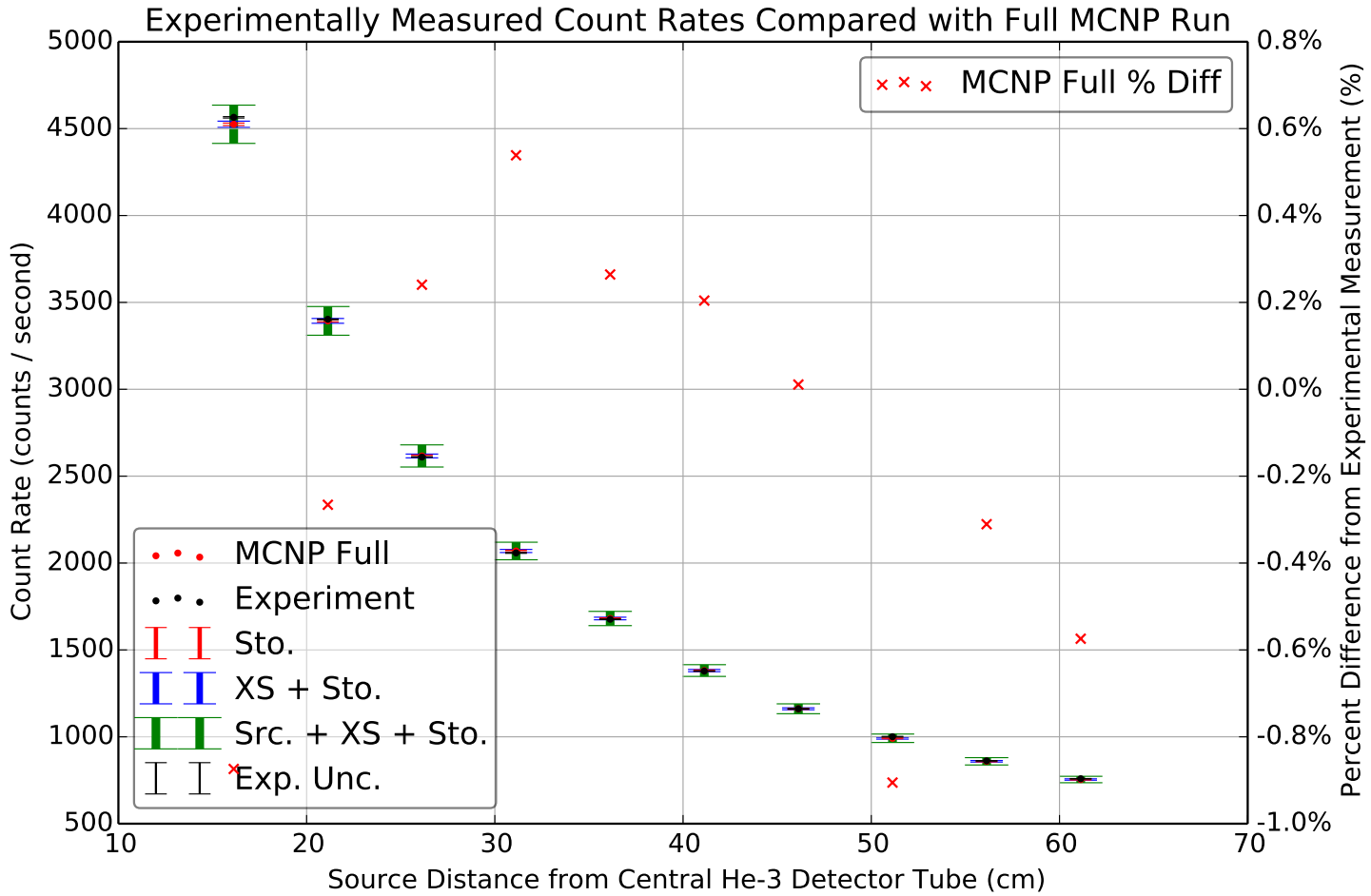

Figure 26: Comparison of the MCNP full simulations versus experiment. Response values and their associated uncertainties are displayed.

Table 18: Comparison of detector response between simulated MCNP DRF run and experimental measurements.

Distance from Detector (cm)	Experimental Count Rate (c/s)	Simulated Count Rate (c/s)	Percent Difference (%)
16	4565.001	4587.164	0.4855
21	3402.641	3445.572	1.2617
26	2610.021	2648.537	1.4757
31	2058.254	2103.065	2.1771
36	1676.399	1705.077	1.7107
41	1378.492	1409.865	2.2759
46	1161.146	1186.093	2.1485
51	1000.609	1013.279	1.2662
56	861.684	878.595	1.9625
61	758.584	768.335	1.2855

Table 19: Comparison of detector response between simulated MCNP Full run and experimental measurements.

Distance from Detector (cm)	Experimental Count Rate (c/s)	Simulated Count Rate (c/s)	Percent Difference (%)
16	4565.001	4525.103	-0.8740
21	3402.641	3393.595	-0.2659
26	2610.021	2616.302	0.2407
31	2058.254	2069.340	0.5386
36	1676.399	1680.829	0.2643
41	1378.492	1381.307	0.2042
46	1161.146	1161.272	0.0109
51	1000.609	991.550	-0.9053
56	861.684	859.007	-0.3106
61	758.584	754.228	-0.5742

Table 20: Comparison of absolute detector response uncertainties between MCNP DRF run and experimental measurements.

Distance from Detector (cm)	**Exp. Unc. (c/s)**	**Sto. (c/s)**	**XS (c/s)**	**Src. (c/s)**	**Sim. Total (c/s)**
16	3.973	8.779	16.807	110.092	111.713
21	2.025	7.534	12.625	82.694	83.990
26	1.846	6.529	9.704	63.565	64.632
31	2.419	5.827	7.706	50.474	51.390
36	1.936	5.160	6.247	40.922	41.716
41	1.151	4.637	5.166	33.837	34.542
46	1.997	4.225	4.346	28.466	29.104
51	1.780	3.914	3.713	24.319	24.910
56	1.521	3.627	3.219	21.086	21.637
61	1.372	3.370	2.815	18.440	18.956

Table 21: Comparison of absolute detector response uncertainties between MCNP Full run and experimental measurements.

Distance from Detector (cm)	**Exp. Unc. (c/s)**	**Sto. (c/s)**	**XS (c/s)**	**Src. (c/s)**	**Sim. Total (c/s)**
16	3.973	6.966	16.580	108.602	110.081
21	2.025	5.991	12.434	81.446	82.607
26	1.846	5.273	9.586	62.791	63.737
31	2.419	4.697	7.582	49.664	50.459
36	1.936	4.235	6.159	40.340	41.026
41	1.151	3.818	5.061	33.151	33.752
46	1.997	3.503	4.255	27.871	28.410
51	1.780	3.251	3.633	23.797	24.291
56	1.521	3.031	3.147	20.616	21.074
61	1.372	2.835	2.763	18.101	18.529

References

[1] Bill Harker, Merlyn Krick, W Geist, and J Longo. INCC Software Users Manual. *Los Alamos National Laboratory document LA-UR-99-1291*, 1998.

[2] Californium Source Information. `http://www.frontier-cf252.com/californium.html#model10`. Accessed: 2015-01-04.

[3] S. Croft and D. Henzlova. Determining Cf-252 Source Strength by Absolute Passive Neutron Correlation Counting. *Nuclear Instruments and Methods in Physics Research Section A*, 714:5–12, 2013.

[4] Forrest B Brown, RF Barrett, TE Booth, JS Bull, LJ Cox, RA Forster, TJ Goorley, RD Mosteller, SE Post, RE Prael, et al. MCNP Version 5. *Trans. Am. Nucl. Soc*, 87(273):02–3935, 2002.

[5] Denise B Pelowitz. MCNP6 User's Manual, Version 1. Technical report, Los Alamos National Laboratory, Report LA-CP-13-00634, Revision 0,(May 2013), 2013.

[6] W Mannhart. Evaluation of the Cf-252 fission neutron spectrum between 0 MeV and 20 MeV. In *Proc*, page 158, 1987.

[7] Timothy E. Valentine. MCNP-DSP Users Manual. *ORNL/TM-13334 R2, Oak Ridge National Lab*, 2001.

[8] RJ McConn Jr, Christopher J Gesh, Richard T Pagh, Robert A Rucker, and Robert Williams III. Compendium of Material Composition Data for Radiation Transport Modeling. *PNNL-15870 Rev*, 1, 2011.

[9] Richard Evans, John Mattingly, and Dan Cacuci. Sensitivity Analysis and Data Assimilation in A Subcritical Plutonium Metal Benchmark. *Nuclear Science and Engineering*, 176(3):325–338, 2014.

[10] D.G. Cacuci. *Sensitivity and Uncertainty Analysis: Theory*, volume 1. CRC Press, 2003.

[11] Oak Ridge National Laboratory. *Scale: A Comprehensive Modeling and Simulation Suite for Nuclear Safety Analysis and Design, ORNL/TM-2005/39, Version 6.1*, 2011. Available from Radiation Safety Information Computational Center at Oak Ridge National Laboratory as CCC-785.

A Detector CAD Model

Detector measurements were taken at ORNL during the measurement campaign. The detector was disassembled for each piece to be individually measured. The following figures contained within Appendix A are a close approximation to the detector measurements. Approximations were used when geometry translation to implicit equations were prohibitive. Specific approximations include the hand truck scoop, shown in Figure 42, the internals of the junction box, shown in Figure 31, and various bolt or screw holes that may appear in the CAD drawings but are absent from the actual input deck.

The CAD drawings represent measurements in millimeters and each of the numbered surfaces is used within the MCNP input deck template. Origin labels designate the locate origin chosen for input within the MCNP input deck. If necessary, a piece was then translated and/or rotated to the appropriate global coordinate in MCNP. The drawings in this appendix are no longer drawn to the scale represented in the title blocks.

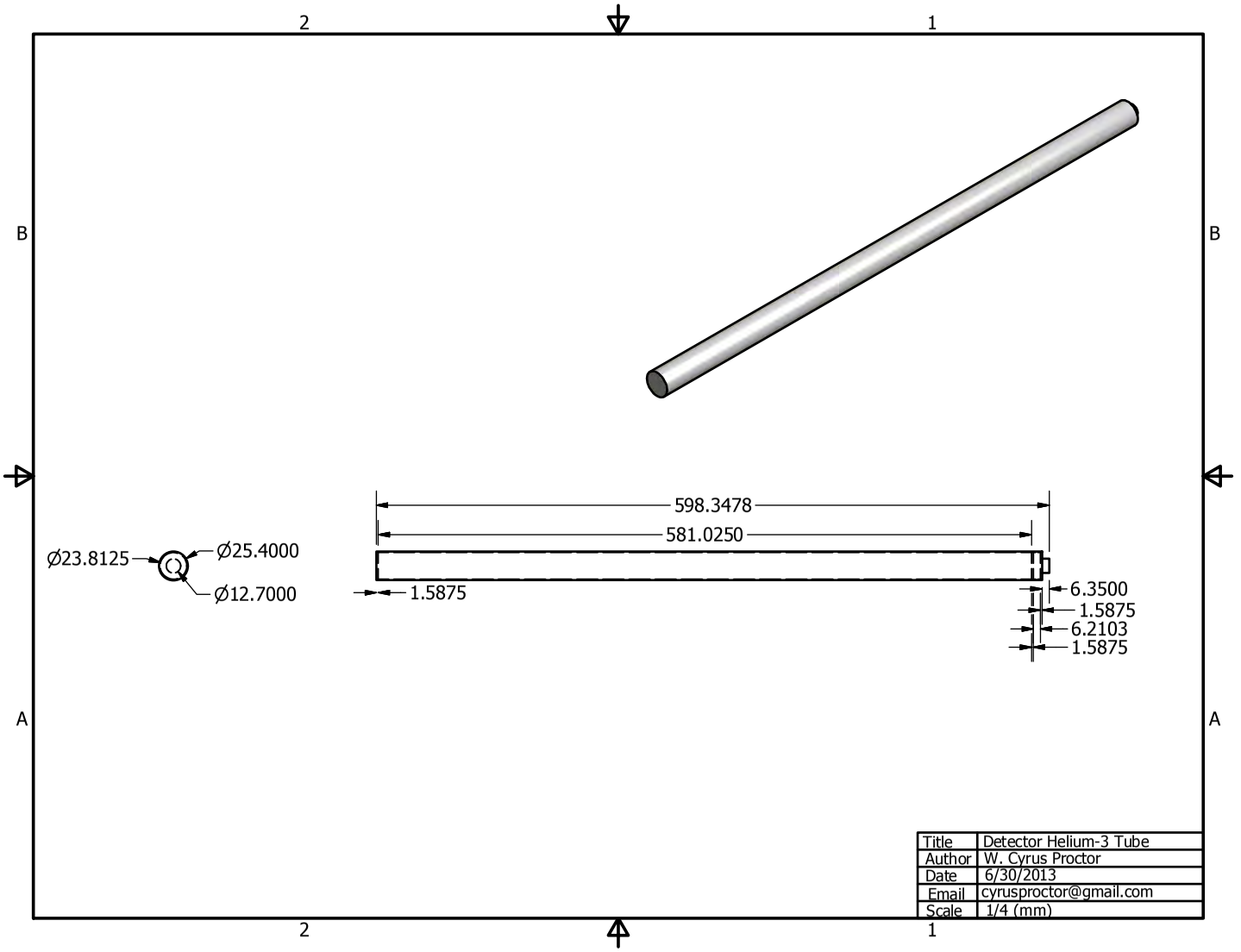

Figure 27: Detector He-3 tube contained within the *bare detector assembly*.

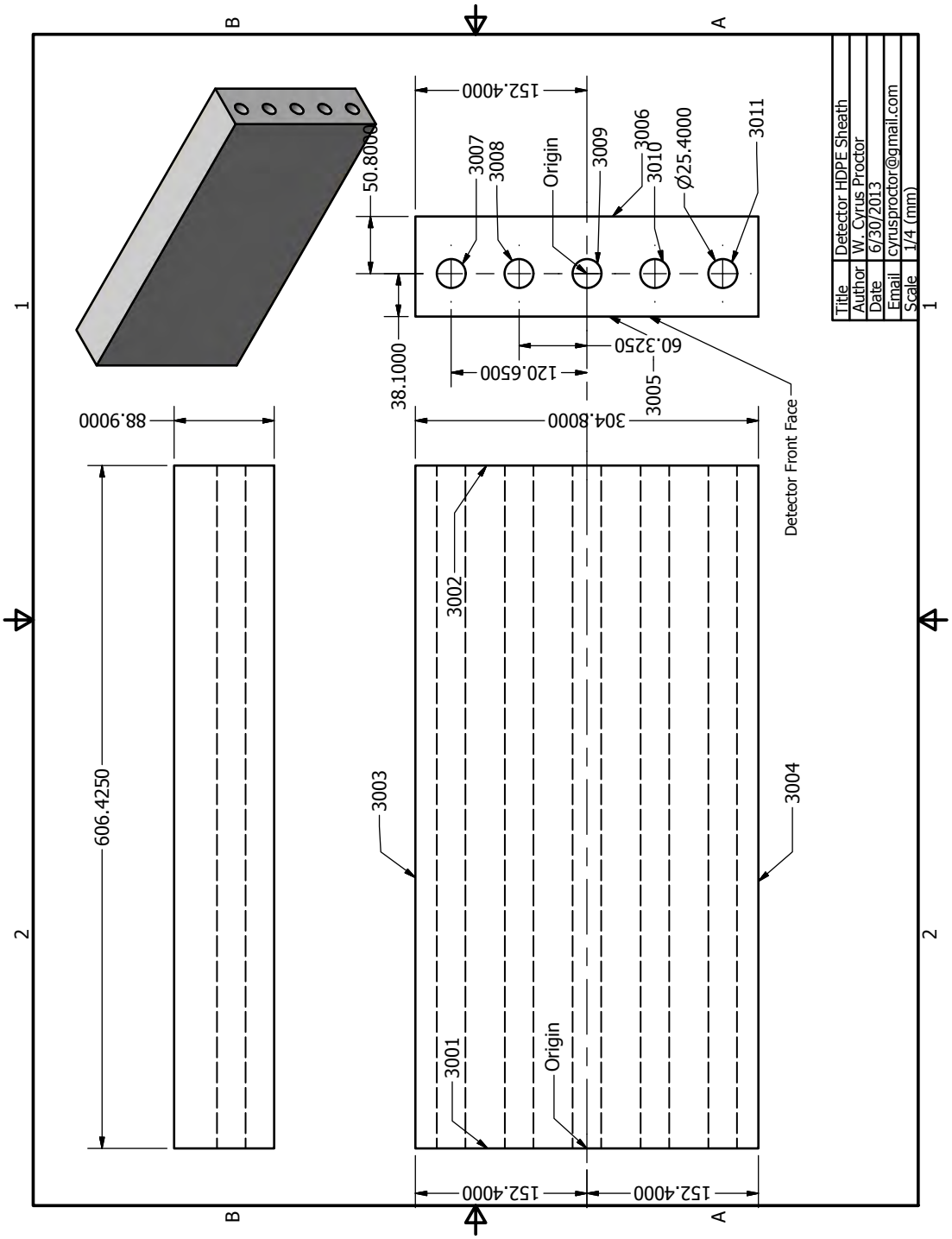

Figure 28: Detector HDPE sheath contained within the *bare detector assembly*.

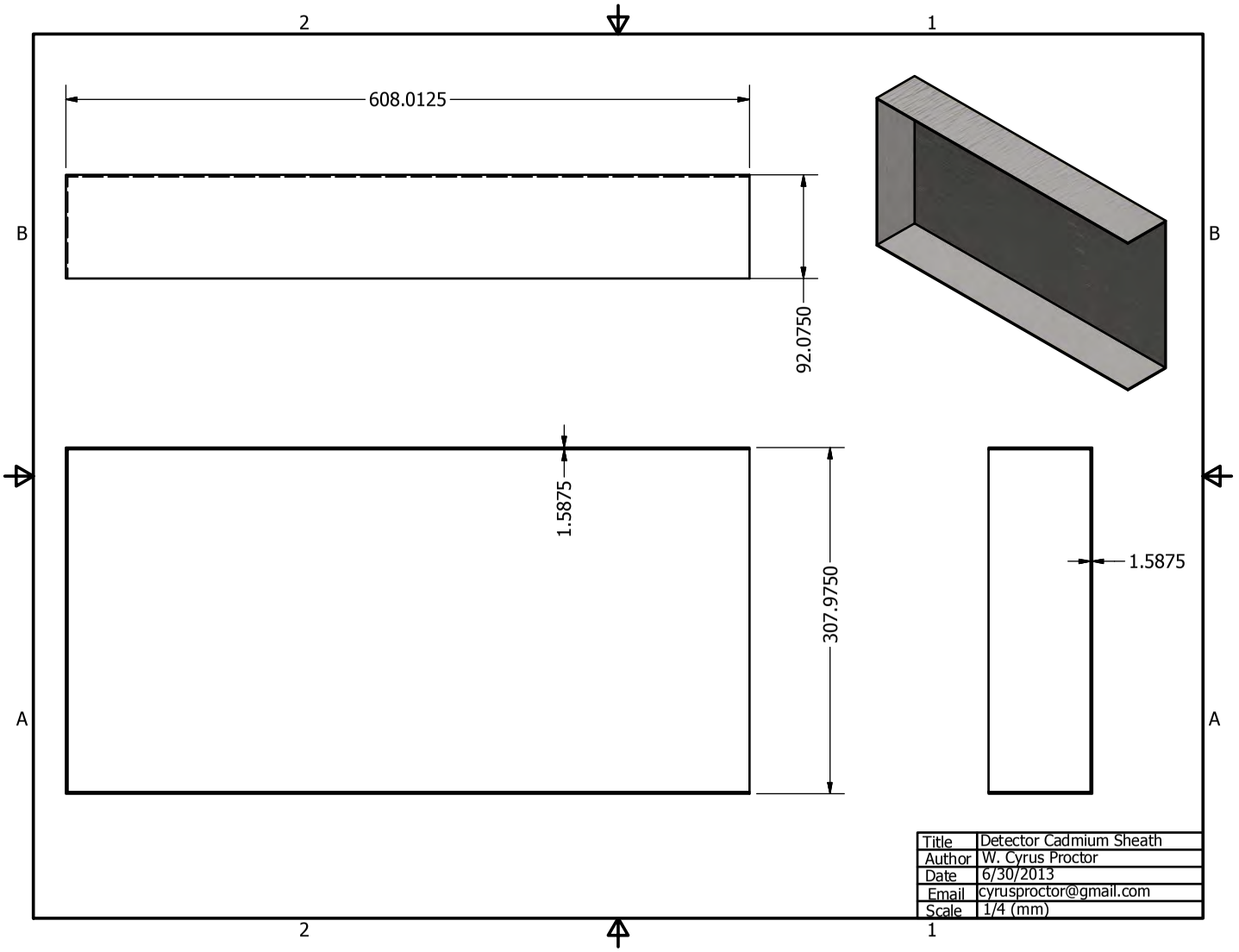

Figure 29: Detector cadmium sheath contained within the *bare detector assembly*.

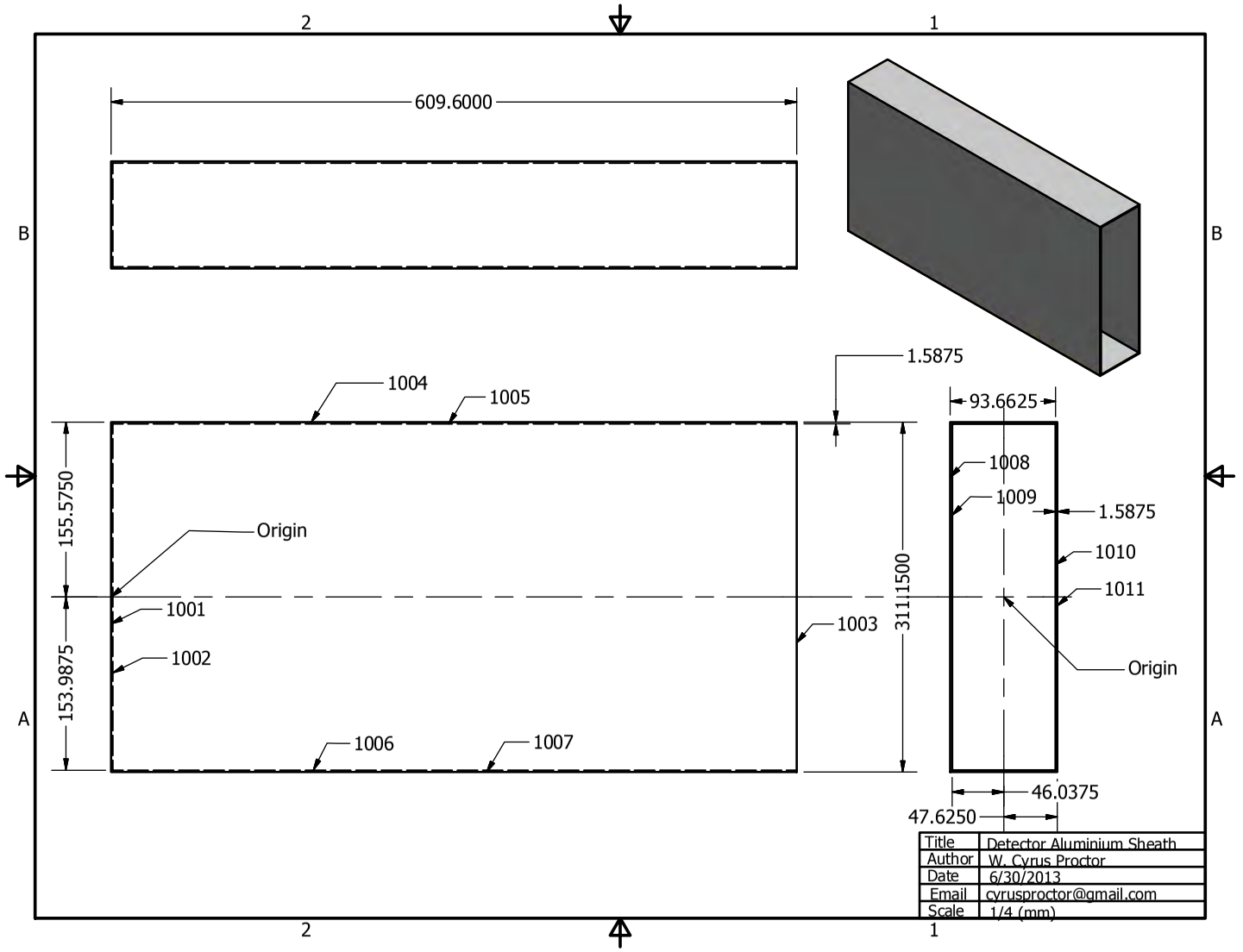

Figure 30: Detector aluminum sheath contained within the *bare detector assembly*.

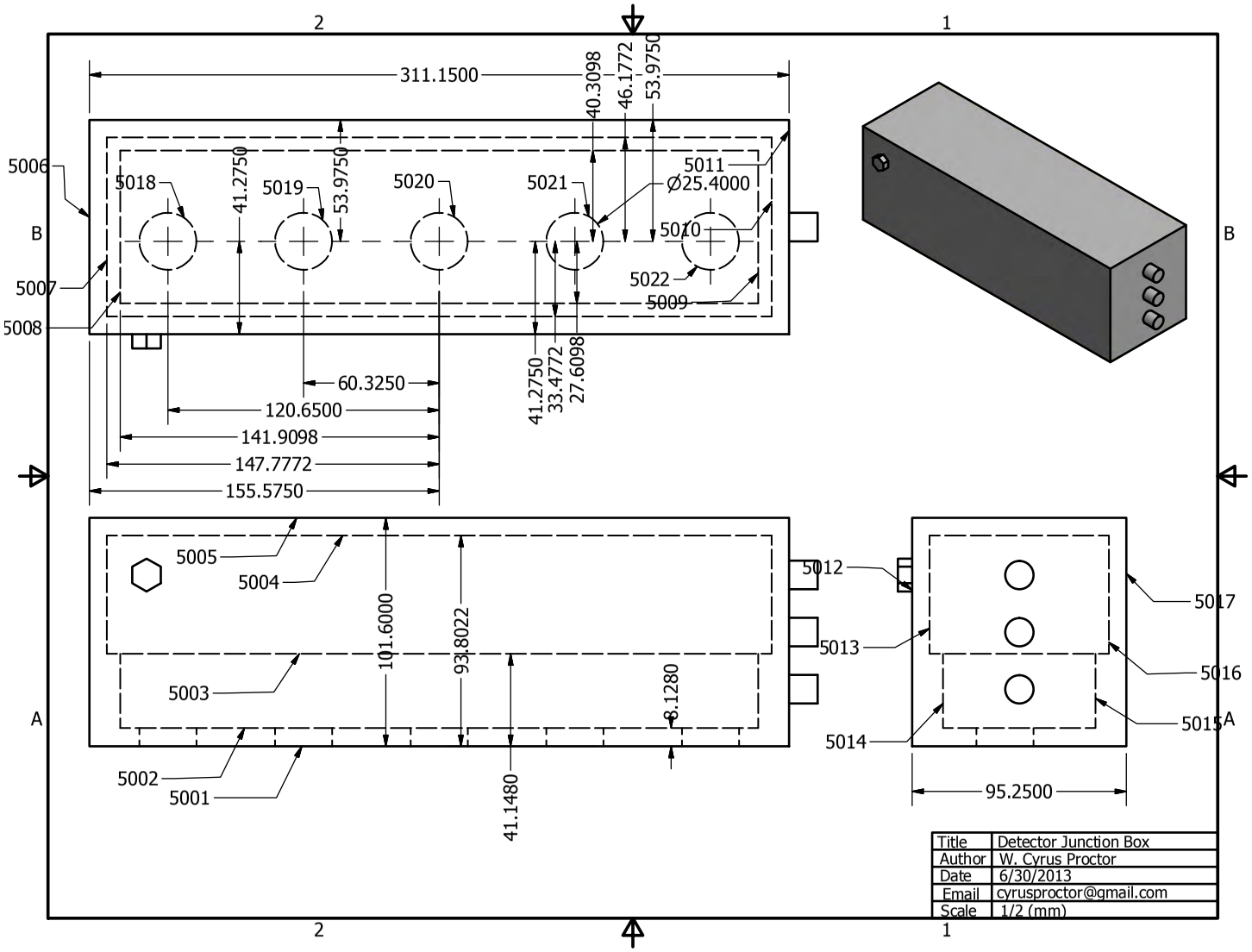

Figure 31: Detector junction box contained within the *bare detector assembly*. Internals were not modeled.

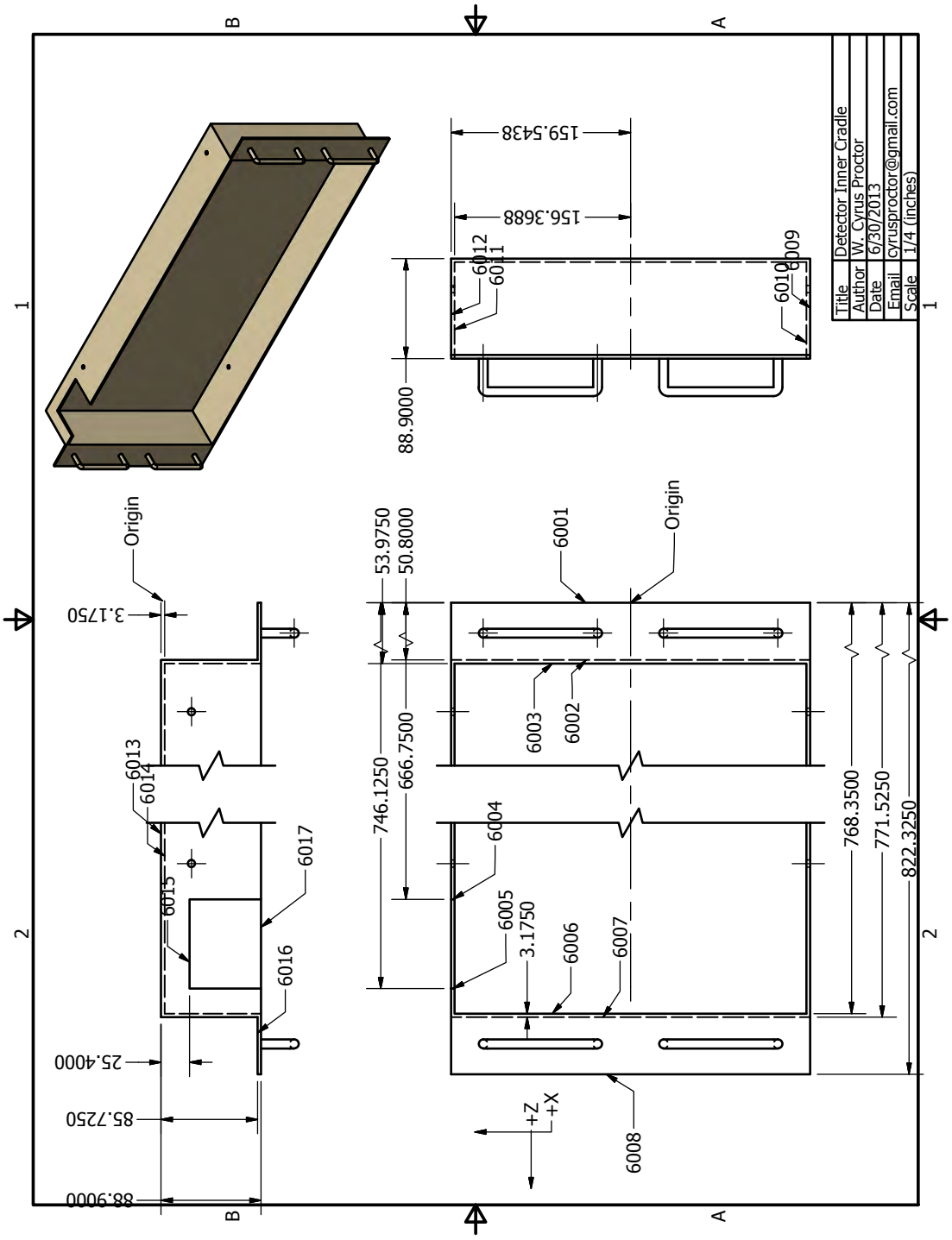

Figure 32: Inner cradle contained within the *inner housing assembly*.

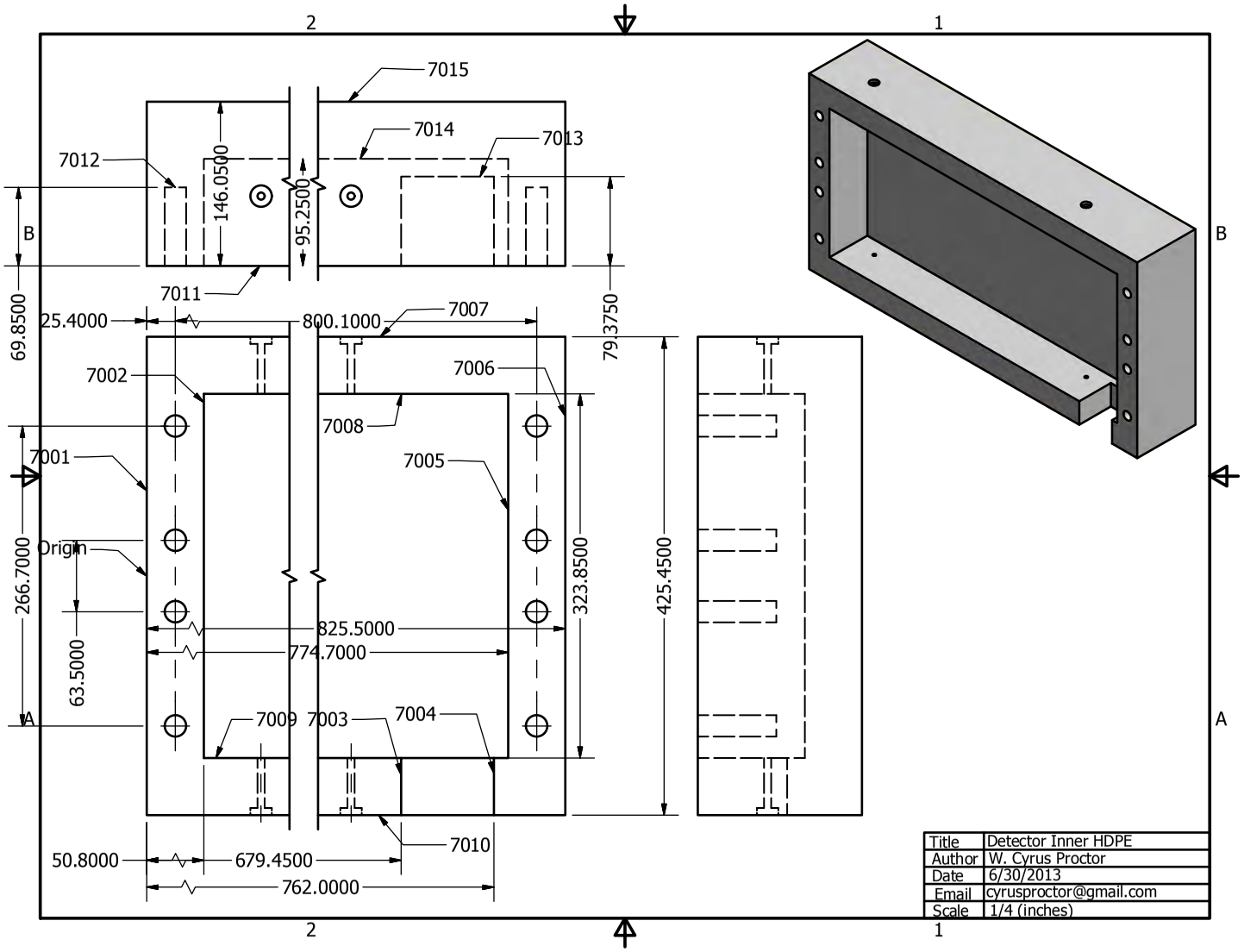

Figure 33: Inner HDPE housing contained within the *inner housing assembly*.

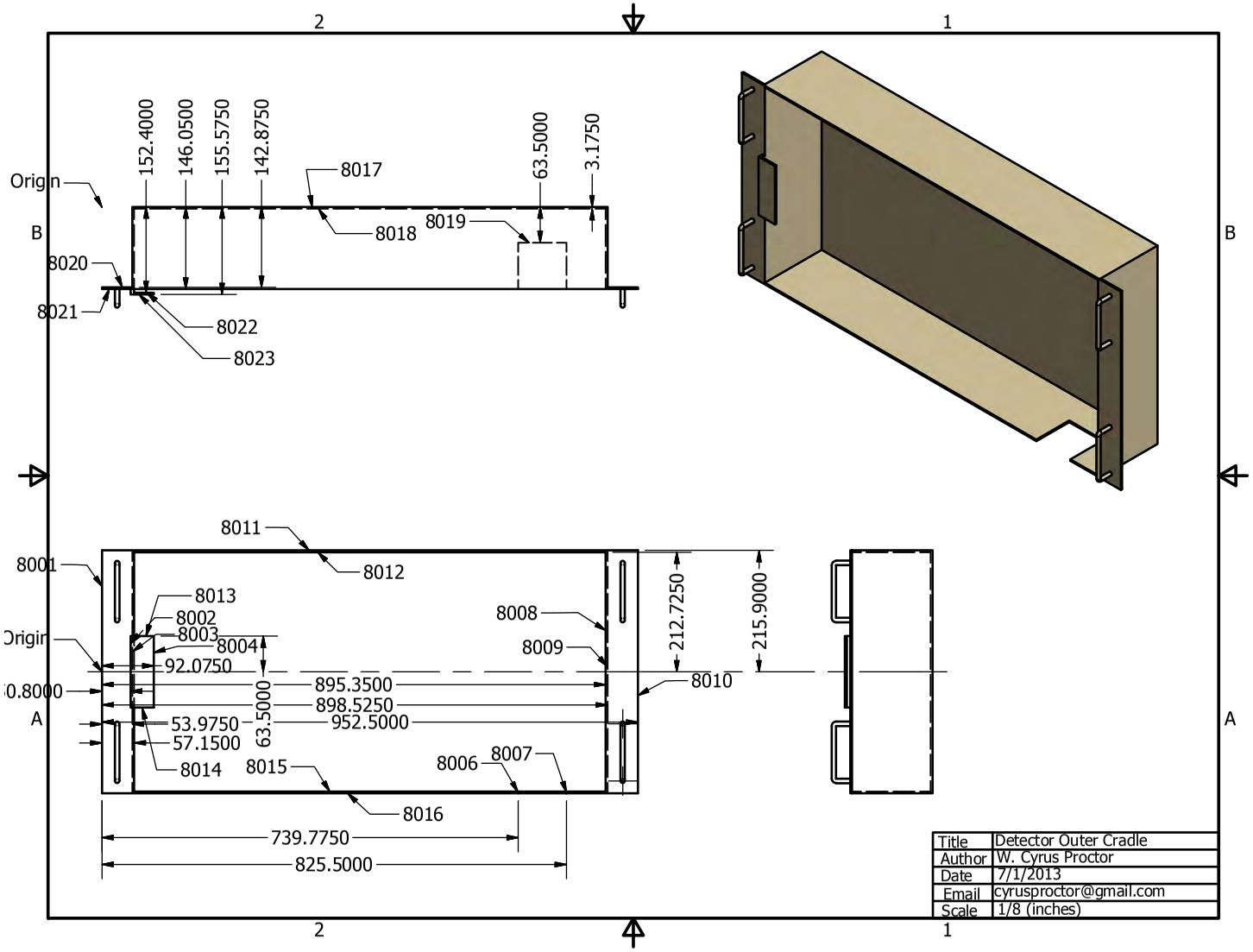

Figure 34: Outer cradle contained within the *outer housing assembly*.

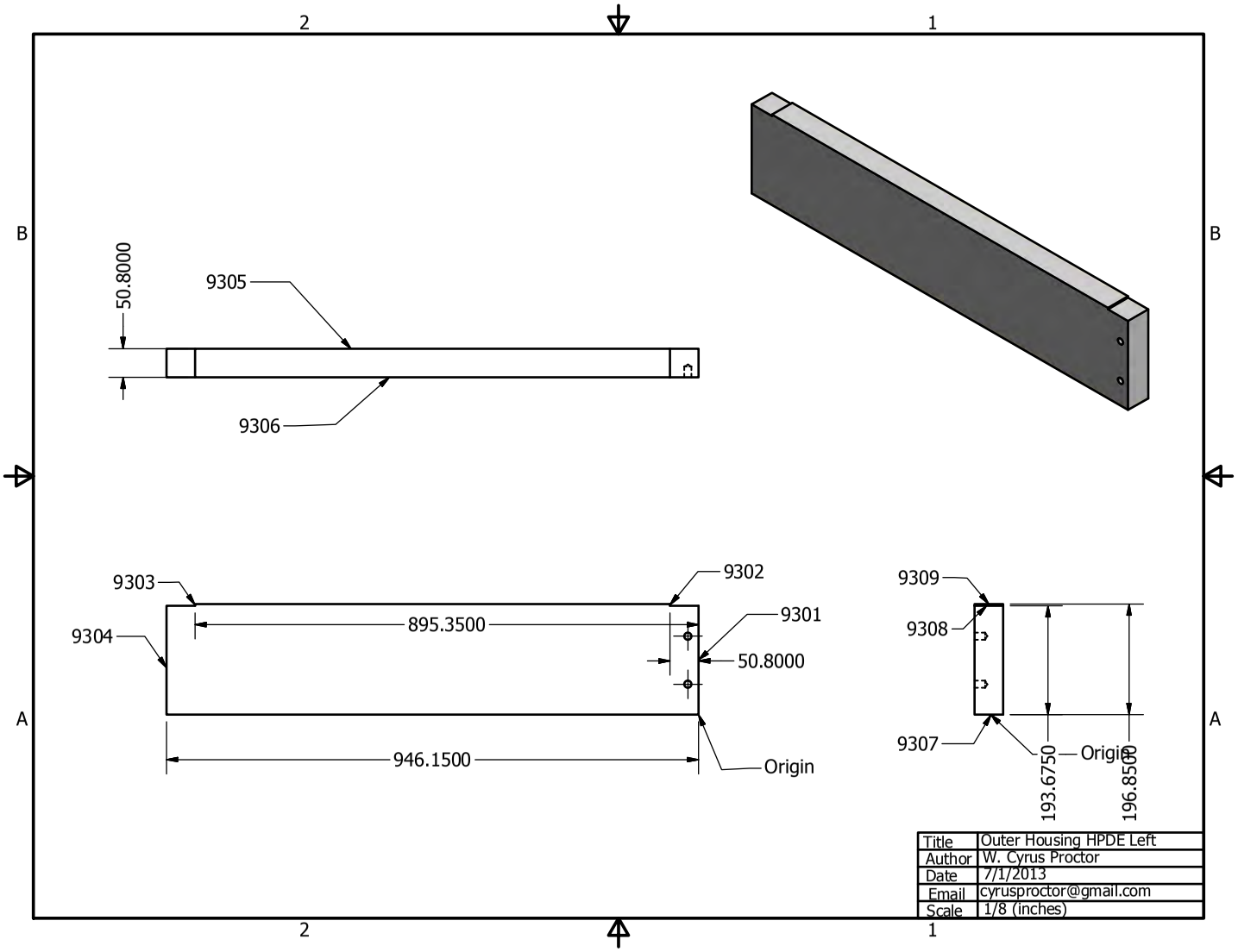

Figure 35: Left piece of outer HDPE housing contained within the *outer housing assembly*.

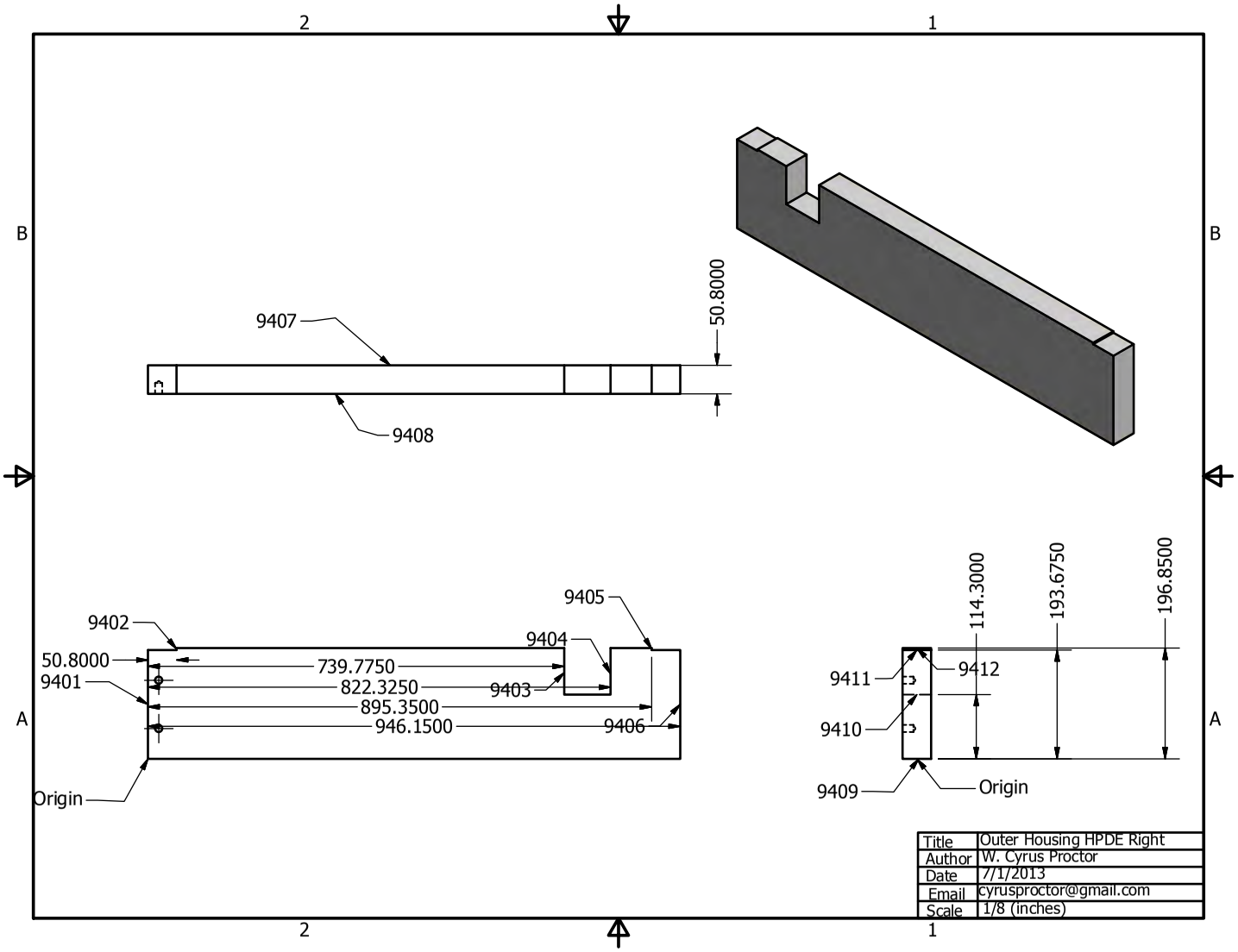

Figure 36: Right piece of outer HDPE housing contained within the *outer housing assembly*.

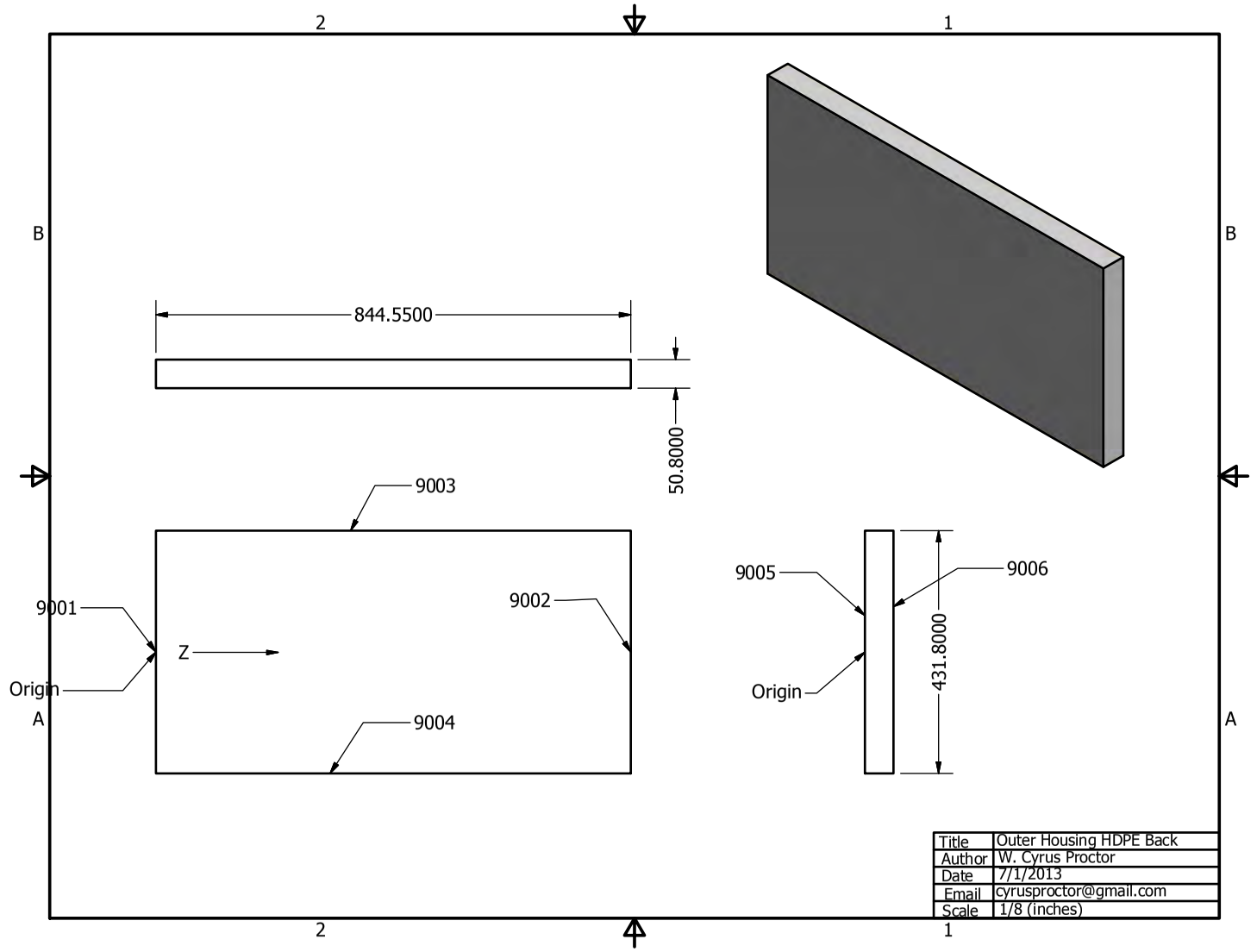

Figure 37: Back piece of outer HDPE housing contained within the *outer housing assembly*.

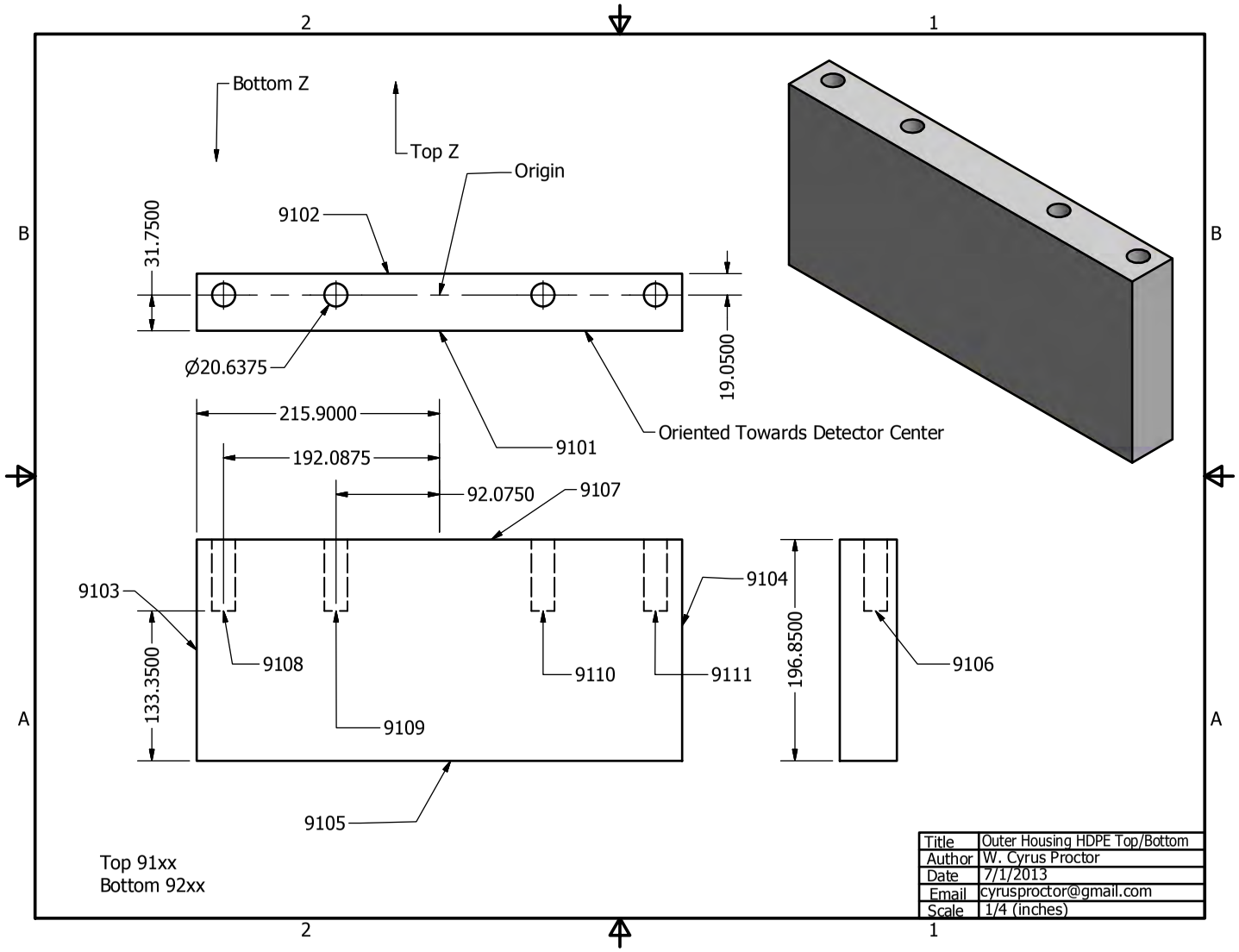

Figure 38: Top and bottom piece of outer HDPE housing contained within the *outer housing assembly*.

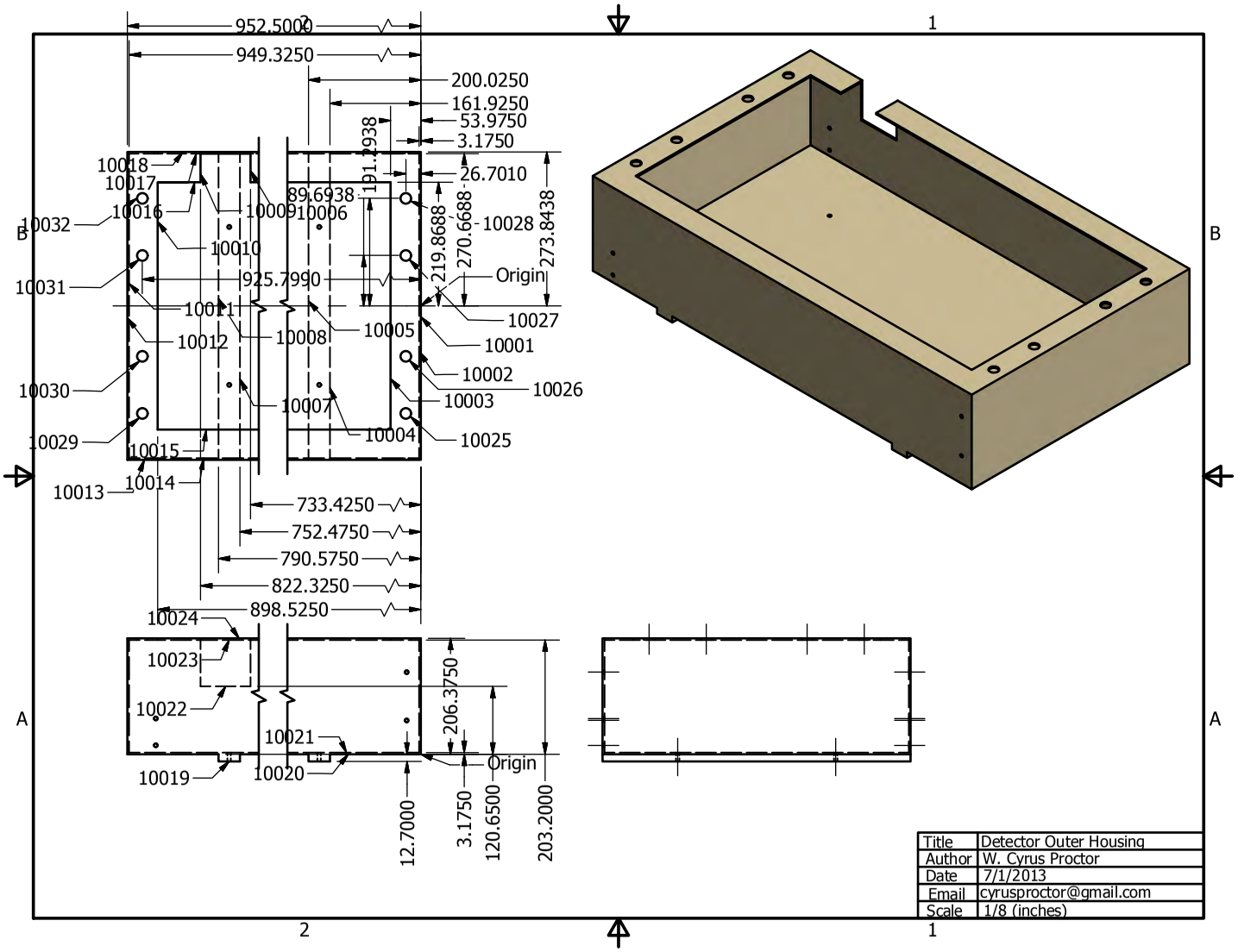

Figure 39: Outer housing contained within the *outer housing assembly*.

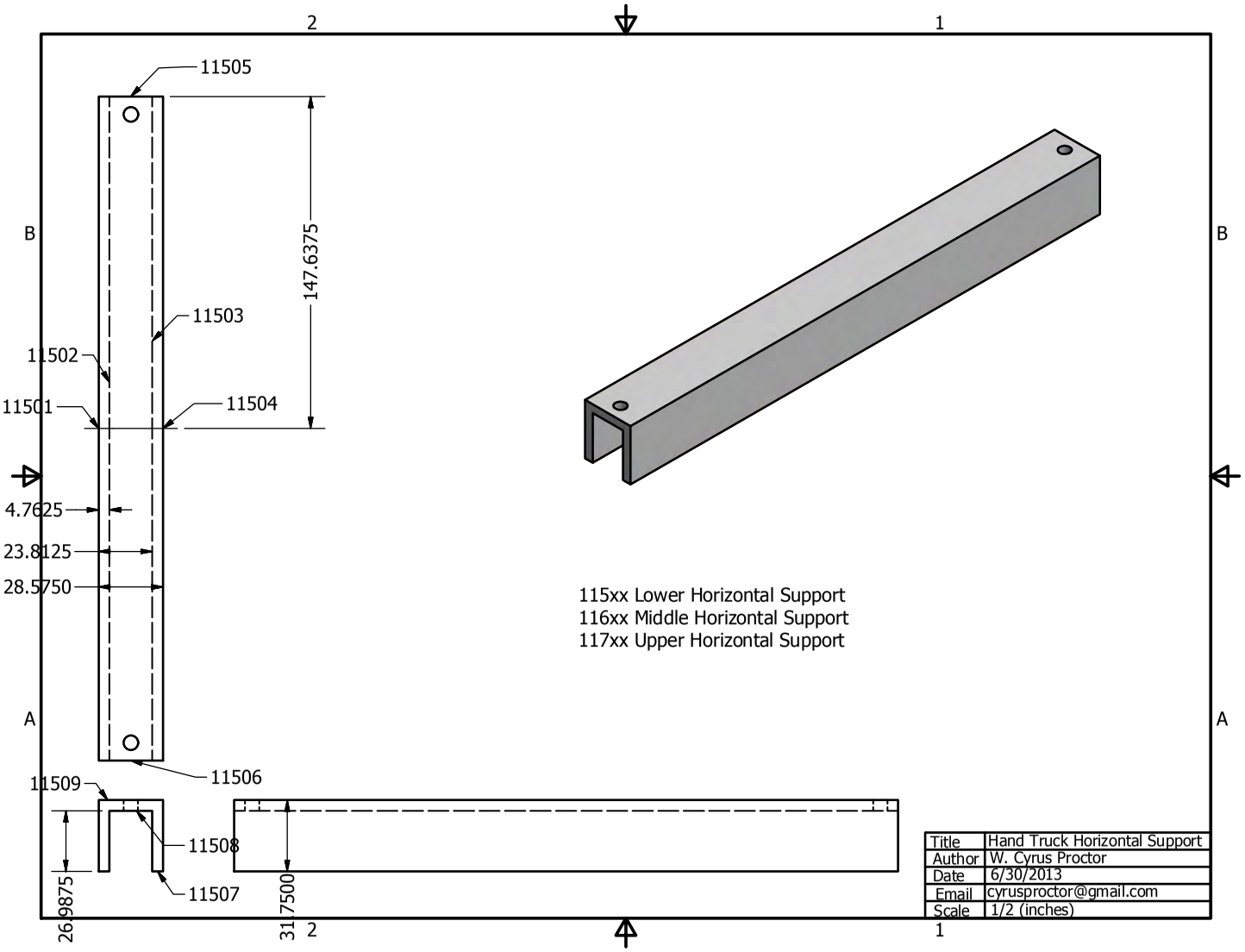

Figure 40: Hand truck horizontal support bar (three total) contained within the *outer housing assembly*.

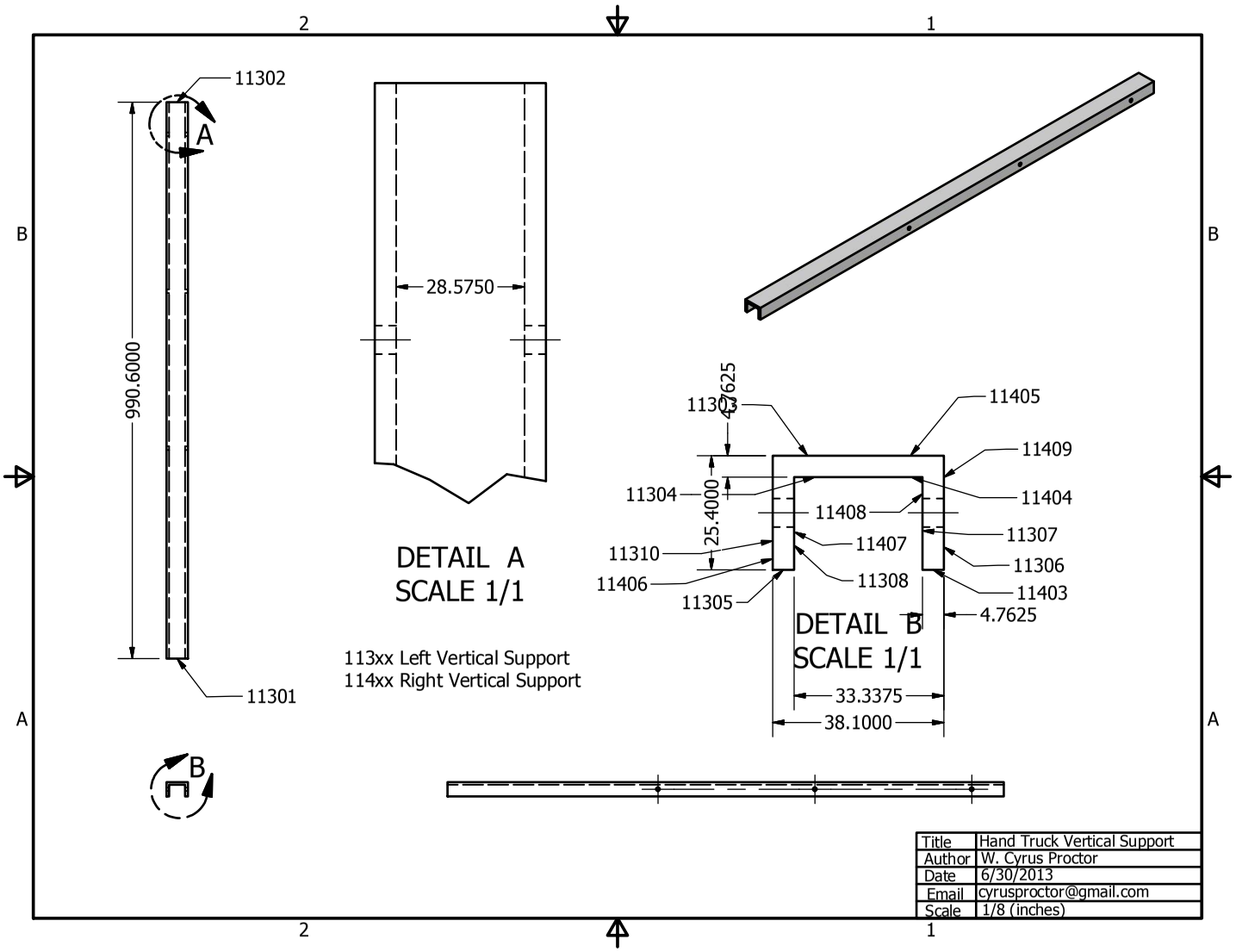

Figure 41: Hand truck vertical support bar (two total) contained within the *outer housing assembly*.

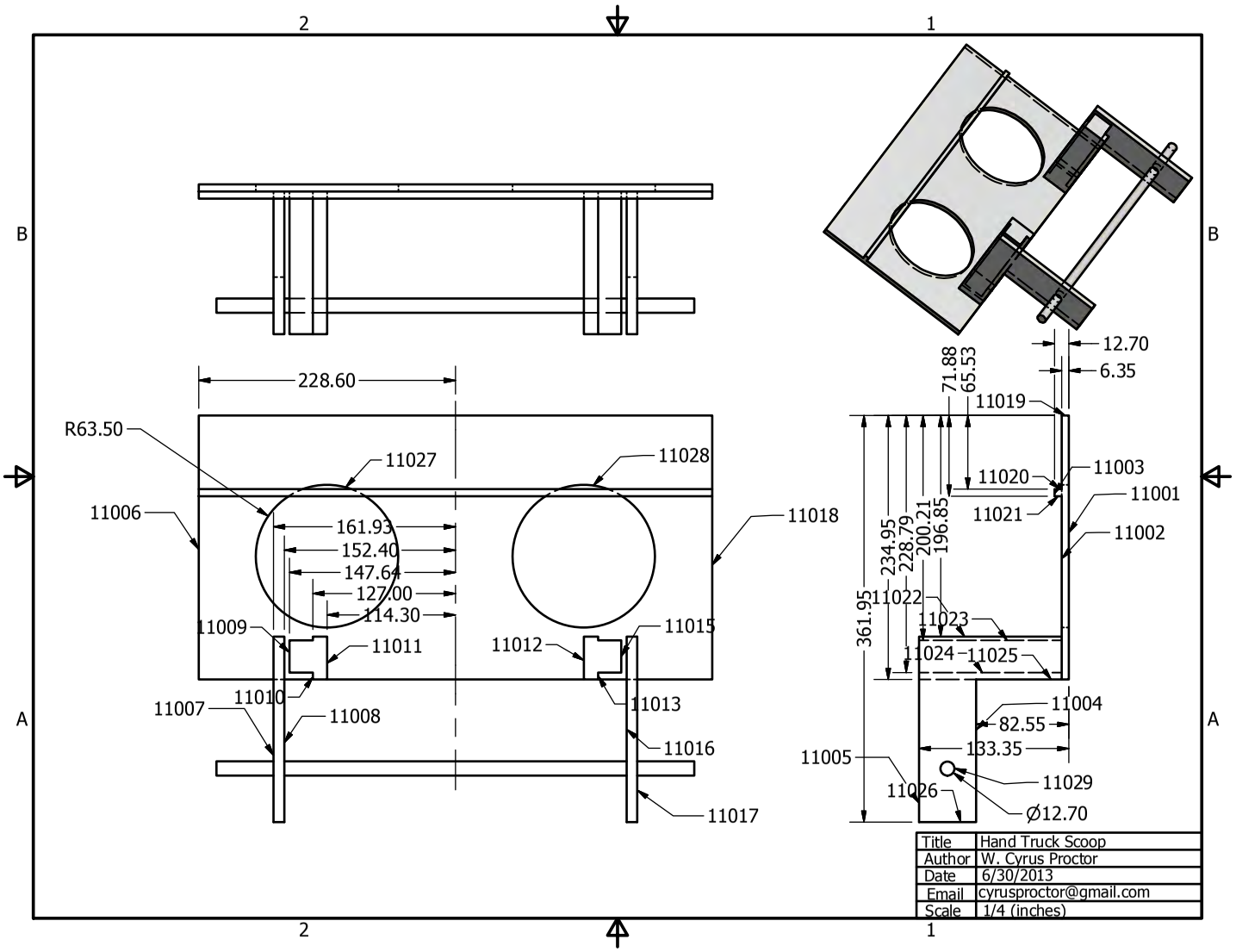

Figure 42: Hand truck scoop contained within the *outer housing assembly*. Geometry simplified for MCNP.

B MCNP Template and Run Scripts

The following Python scripts and input templates give all the necessary tools to run a sample sensitivity analysis similar to the results in Table 13. "run_all.py" takes three command-line arguments. "run_all.py" will read in information from "energy.list", "sample_perturbations.list", and "upright_spatial_setup_FTC-CF-004.mcnp.inp.template".
Using "spawn_mcnp_child.py", "run_all.py" will manage all jobs based on the total number of CPU's its given until all MCNP runs are complete. "sample_post_process.py" will read the directory names given in "sample_dir.list" and mine relevant tally data in each of the runs to produce several comma separated value files.

Also, "fission_spectrum.txt" was used to generate the comparison fission spectrums in Maple17 used in Figure 14.

```
#!/usr/bin/env python

# W. Cyrus Proctor

import os
import sys
import numpy as np
import math

from spawn_mcnp_child import spawn_mcnp_children

def run_mcnp_jobs():

  # Takes three arguments
  # 1.) Which file prefix to run
  # 2.) Number of processes per file to use
  # 3.) Total number of processes to use at once

  file_prefix         = sys.argv[1]
  processes_per_file  = int(sys.argv[2])
  total_num_processes = int(sys.argv[3])

  print "File Prefix:",file_prefix
  print "Processes per File:",processes_per_file
  print "Total Number of Processes:",total_num_processes

  if total_num_processes % processes_per_file !=0:
    print "WARNING: you will have idle processes!"

  # Current working directory
  cwd = os.getcwd()

  template_filename = "upright_spatial_setup_FTC-CF-004.mcnp.inp.template"
  pert_filename     = "sample_perturbations.list"

  generate_mcnp_perturbation_decks(file_prefix,cwd,template_filename,pert_filename)
  #generate_mcnp_rotation_decks(file_prefix,cwd,template_filename,rot_filename)
  # exit(0)

  run_list = list()
  # Cycle through all directories
  for root, dirs, files in os.walk(cwd):
    # Cycle through all files
    for filename in files:
      # Find only files that match the file_prefix and end with ".inp"
      if filename.startswith(file_prefix) and filename.endswith(".inp"):
        file_path       = root
        input_filename  = filename
        output_filename = filename[:-4]+".out"
        restart_filename = filename[:-4]+".runtp"
        run_list.append(tuple((file_path,input_filename,output_filename,\
            restart_filename)))
```

```
  for combo in run_list:
    print combo

  spawn_mcnp_children(total_num_processes,processes_per_file,run_list)


def generate_mcnp_perturbation_decks(file_prefix,cwd,template_filename,pert_filename):
  with open(pert_filename) as f:
    while True:
      line = f.readline()
      if not line: break
      if line[0] == '#':
        if line.find('sdist') != -1:
          sdist_list = f.readline().split()
        if line.find('sorient') != -1:
          sorient_list = f.readline().split()
        if line.find('smat') != -1:
          smat_list = f.readline().split()
        if line.find('sden') != -1:
          sden_list = f.readline().split()
        if line.find('scoord') != -1:
          scoord_list = f.readline().split()
        if line.find('pden') != -1:
          pden_list = f.readline().split()
        if line.find('fgden') != -1:
          fgden_list = f.readline().split()
        if line.find('fe') != -1:
          fe_list = f.readline().split()
        if line.find('fden') != -1:
          fden_list = f.readline().split()

  template = open(template_filename,'r').read()

  count = 1

  # Default Indices
  isorient_default = 1             # 0 degrees
  ismat_default    = 0             # 304L SS
  isden_default    = ismat_default # 8.0 g/cc
  iscoord_default  = 2             # 0 cm off-center
  ipden_default    = 0             # 0.95 g/cc
  ifgden_default   = 0             # 0.0020628254 g/cc
  ife_default      = 0             # Concrete material 14
  ifden_default     = ife_default  # 2.35 g/cc

  for isdist,sdist in enumerate(sdist_list):
    isorient = isorient_default
    ismat    = ismat_default
    isden    = isden_default
    iscoord  = iscoord_default
    ipden    = ipden_default
    ifgden   = ifgden_default
    ife      = ife_default
    ifden    = ifden_default

    sorient = sorient_list[isorient_default]
    smat    = smat_list[ismat_default]
    sden    = sden_list[isden_default]
    scoord  = scoord_list[iscoord_default]
    pden    = pden_list[ipden_default]
    fgden   = fgden_list[ifgden_default]
    fe      = fe_list[ife_default]
    fden    = fden_list[ifden_default]

    for isorient,sorient in enumerate(sorient_list):
      count = create_template(count,cwd,file_prefix,isdist,isorient,ismat,isden,iscoord,\
        ipden,ifgden,ife,ifden,template,sdist,sorient,smat,sden,scoord,pden,\
        fgden,fe,fden)
    isorient = isorient_default
    sorient  = sorient_list[isorient_default]

    for ismat,smat in enumerate(smat_list):
      count = create_template(count,cwd,file_prefix,isdist,isorient,ismat,isden,iscoord,\
        ipden,ifgden,ife,ifden,template,sdist,sorient,smat,sden,scoord,pden,\
        fgden,fe,fden)
    ismat   = ismat_default
    isden   = isden_default
    smat    = smat_list[ismat_default]
    sden    = sden_list[isden_default]

    for iscoord,scoord in enumerate(scoord_list):
      count = create_template(count,cwd,file_prefix,isdist,isorient,ismat,isden,iscoord,\
        ipden,ifgden,ife,ifden,template,sdist,sorient,smat,sden,scoord,pden,\
        fgden,fe,fden)
    iscoord = iscoord_default
    scoord  = scoord_list[iscoord_default]

    for ipden,pden in enumerate(pden_list):
      count = create_template(count,cwd,file_prefix,isdist,isorient,ismat,isden,iscoord,\
        ipden,ifgden,ife,ifden,template,sdist,sorient,smat,sden,scoord,pden,\
        fgden,fe,fden)
    ipden   = ipden_default
    pden    = pden_list[ipden_default]

    for ifgden,fgden in enumerate(fgden_list):
      count = create_template(count,cwd,file_prefix,isdist,isorient,ismat,isden,iscoord,\
        ipden,ifgden,ife,ifden,template,sdist,sorient,smat,sden,scoord,pden,\
        fgden,fe,fden)
    ifgden  = ifgden_default
    fgden   = fgden_list[ifgden_default]

    for ife,fe in enumerate(fe_list):
      count = create_template(count,cwd,file_prefix,isdist,isorient,ismat,isden,iscoord,\
        ipden,ifgden,ife,ifden,template,sdist,sorient,smat,sden,scoord,pden,\
        fgden,fe,fden)
    ife     = ife_default
    ifden   = ifden_default
    fe      = fe_list[ife_default]
    fden    = fden_list[ifden_default]


def create_template(count,cwd,file_prefix,isdist,isorient,ismat,isden,iscoord,\
  ipden,ifgden,ife,ifden,template,sdist,sorient,smat,sden,scoord,pden,\
  fgden,fe,fden):
  dir_name = str(isdist) + "_" + str(isorient) + "_" + str(ismat) +\
    "_" + str(iscoord) + "_" + str(ipden) + "_" + str(ifgden) +\
    "_" + str(ife)
  working_template = generate_input_deck(template,sdist,sorient,\
    smat,sden,scoord,pden,fgden,fe,fden)
  dir_path = cwd + "/" + dir_name
  if not os.path.exists(dir_path):
    os.makedirs(dir_path)
  os.chdir(dir_path)
  open(file_prefix + "upright_spatial_setup_FTC-CF-004_" + dir_name + ".inp","w").write(working_template)
  print str(count) + " Wrote out " + file_prefix + "upright_spatial_setup_FTC-CF-004_" + dir_name + ".inp in directory: " + dir_path
  os.chdir(cwd)
  count = count + 1

  return count


def generate_input_deck(template,sdist,sorient,smat,sden,scoord,\
  pden,fgden,fe,fden):
  t = template
```

```
  t = t.replace("<smat>",smat)
  if float(sden) != 0:
    t = t.replace("<sden>",sden)
  else:
    t = t.replace("<sden>","")
  t = t.replace("<pden>",pden)
  t = t.replace("<fgden>",fgden)
  t = t.replace("<fe>",fe)
  if float(fe) != 0:
    t = t.replace("<fden>",fden)
  else:
    t = t.replace("<fden>","")

  # Nominal Source Coordinates
  sxnom = 0.0
  synom = float(sdist)
  sznom = 29.21

  # Perturbed Source Coordinates
  sxpert = sxnom + float(scoord)
  sypert = synom + float(scoord)
  szpert = sznom + float(scoord)

  t = t.replace("<sxdist>",str(sxpert))
  t = t.replace("<sydist>",str(sypert))
  t = t.replace("<szdist>",str(szpert))

  transform_list = x_rotation_transform(float(sorient))
  t = t.replace("<sorient>",'\n'.join(map(str,transform_list)))

  return t


def generate_mcnp_rotation_decks(file_prefix,cwd,template_filename,rot_filename):
  rotation_list = np.loadtxt(rot_filename)
  template = open(template_filename,'r').read()
  for rot in rotation_list:
    transform_list = x_rotation_transform(rot)
    working_template = template
    working_template = working_template.replace("<<<rotation>>>",'\n'.join(map(str,transform_list)))
    dir_name = str(abs(int(rot)))
    if rot < 0:
      dir_name = "neg_" + dir_name
    elif rot > 0:
      dir_name = "pos_" + dir_name
    dir_path = cwd + "/" + dir_name
    if not os.path.exists(dir_path):
      os.makedirs(dir_path)
    os.chdir(dir_path)
    open(file_prefix + "upright_spatial_setup_FTC-CF-004_" + dir_name + ".inp","w").write(working_template)
    print "Wrote out " + file_prefix + "upright_spatial_setup_FTC-CF-004_" + dir_name + ".inp in directory: " + dir_path
    os.chdir(cwd)

def x_rotation_transform(deg):
    return [1,0,0,0,math.cos(deg*(math.pi/180)),\
    -math.sin(deg*(math.pi/180)),0,math.sin(deg*(math.pi/180)),\
    math.cos(deg*(math.pi/180))]


if __name__ == "__main__":
  run_mcnp_jobs()
```

fig/mcnp/run_all.py

```
#!/usr/bin/env python

# W. Cyrus Proctor

import sys
import subprocess
import os

def spawn_mcnp_children(total_num_processes,processes_per_file,run_list):

  # Find initial working directory
  iwd = os.getcwd()

  child_list      = list()
  restart_list    = list()
  is_running_list = list()
  process_pool    = 0

  while True:
    if total_num_processes - process_pool >= processes_per_file:
      # Add another child
      child,file_path,restart_filename = add_child(run_list,processes_per_file)
      if child:
        child_list.append(child)
  restart_list.append(file_path + "/" + restart_filename)
        is_running_list.append(1)
        process_pool += processes_per_file
    # Cycle through all children
    for i,a_child in enumerate(child_list):
      # See if this child has already completed
      if is_running_list[i] == 1:
        # Poll child for completion
        if a_child.poll() != None:
          print "\n\nChild",a_child.pid,"is complete!"
          print "********** Output **********"
          print a_child.communicate()[0],
          print "******** End Output ********"
          is_running_list[i] = 0
          process_pool -= processes_per_file
      else:
        # Remove runtp files for size
  try:
          os.remove(restart_list[i])
        except OSError:
          pass
    # Last One
    try:
      os.remove(restart_list[i])
    except OSError:
      pass


    if process_pool == 0 and not run_list:
      print "All Runs Complete!"
      break


  # Change back to initial working directory
  os.chdir(iwd)
  print "Done!"


def add_child(run_list,processes_per_file):
  if run_list:
```

```
    file_path,input_filename,output_filename,restart_filename = run_list.pop(0)
  else:
    return None,None,None
  print "\n\nMoving to:",file_path
  os.chdir(file_path)
  child = spawn_mcnp_child(input_filename,output_filename,restart_filename,\
      processes_per_file)
  print "Started Child Process:",child.pid
  print "  In Directory:",file_path
  print "  Input File:",input_filename
  print "  Output File:",output_filename
  print "  Binary Restart File:",restart_filename
  print "  Number of Tasks:",processes_per_file
  return child,file_path,restart_filename


def spawn_mcnp_child(input_filename,output_filename,restart_filename,\
    num_shared_processes):
  child = subprocess.Popen('mcnp5' + ' i=' + input_filename +\
        ' o=' + output_filename + ' r=' + restart_filename + ' TASKS ' +\
       str(num_shared_processes) + ' 2>&1',\
       shell=True, stdout = subprocess.PIPE)

  return child

"""
# Test Routine
def spawn_mcnp_child(input_filename,output_filename,num_shared_processes):
  child = subprocess.Popen('sleep 10 && ls -1'+\
        ' 2>&1', shell=True, stdout = subprocess.PIPE)

  return child
"""
```

fig/mcnp/spawn_mcnp_child.py

```
#!/usr/bin/env python
# W. Cyrus Proctor

import os
import numpy as np

# Change for Windows or Unix
slash = "\\"

# Define all perturbations
sdist_dict   = {0:-16.1275}
sorient_dict = {0:-90, 1:0}
smat_dict    = {0:400}
sden_dict    = {0:-8.00}
scoord_dict  = {0:-5, 2:0, 4:5}
pden_dict    = {0:-0.95, 2:-1.045}
fgden_dict   = {0:-0.0020628254, 2:-0.00226910794}
fe_dict      = {0:14}
fden_dict    = {0:-2.35}

def read_in_data(prefix,dir_filename,energy_filename,):

  energy = np.loadtxt(energy_filename)

  cwd = os.getcwd()
  dir_list = open(dir_filename).read().split('\n')
  dir_list = dir_list[:-1]

  default_rr_dict       = dict()
  default_rr_error_dict = dict()
  default_rr_sum_dict   = dict()
  rr_dict          = dict()
  rr_error_dict    = dict()
  rr_diff_dict     = dict()
  rr_diff_sum_dict = dict()

  for isdist in sdist_dict:
    default_dir = str(isdist) + "_1_0_2_0_0_0"
    out_filename = prefix + default_dir + ".out"
    os.chdir(cwd + slash + default_dir)
    print cwd + slash + default_dir
    rr_array,rr_error_array = read_tally(out_filename)
    default_rr_dict[isdist] = rr_array
    default_rr_error_dict[isdist] = rr_error_array
    default_rr_sum_dict[isdist] = np.sum(rr_array)
    os.chdir(cwd)

  for isdist in sdist_dict:
    for isorient in sorient_dict:
      for ismat in smat_dict:
        for iscoord in scoord_dict:
          for ipden in pden_dict:
            for ifgden in fgden_dict:
              for ife in fe_dict:
                dir = str(isdist)    + "_" + \
                      str(isorient) + "_" + \
                      str(ismat)    + "_" + \
                      str(iscoord)  + "_" + \
                      str(ipden)    + "_" + \
                      str(ifgden)   + "_" + \
                      str(ife)
                out_filename = prefix + dir + ".out"
                if os.path.exists(cwd + slash + dir):
                  os.chdir(cwd + slash + dir)
                  print cwd + slash + dir
                  rr_array,rr_error_array = read_tally(out_filename)
                  rr_dict[dir] = rr_array
                  rr_error_dict[dir] = rr_error_array
                  rr_diff_dict[dir] = 100.0 * np.divide(rr_array-default_rr_dict[isdist],default_rr_dict[isdist])
                  rr_diff_sum_dict[dir] = 100.0 * np.divide(np.sum(rr_array)-default_rr_sum_dict[isdist],default_rr_sum_dict[isdist])
                  os.chdir(cwd)

  return energy,rr_dict,rr_error_dict,rr_diff_dict,rr_diff_sum_dict


def translate(key):

  key_list = key.split('_')
  isdist   = int(key_list[0])
  isorient = int(key_list[1])
  ismat    = int(key_list[2])
  isden    = int(key_list[2]) # should match ismat
  iscoord  = int(key_list[3])
  ipden    = int(key_list[4])
  ifgden   = int(key_list[5])
  ife      = int(key_list[6])
  ifden    = int(key_list[6]) # should match ife

  trans = str(sdist_dict[isdist])     + " " + \
          str(sorient_dict[isorient]) + " " + \
          str(smat_dict[ismat])       + " " + \
          str(sden_dict[isden])       + " " + \
```

```
          str(scoord_dict[iscoord])   + " " + \
          str(pden_dict[ipden])       + " " + \
          str(fgden_dict[ifgden])     + " " + \
          str(fe_dict[ife])           + " " + \
          str(fden_dict[ifden])
  return trans


def read_tally(output_filename):
    with open(output_filename,"r") as f:
        while True:
            line = f.readline()
            if not line: break
            if line.find("cell:         total") != -1:
                rr_array       = np.array([])
                rr_error_array  = np.array([])
                f.readline()
                while True:
                    line = f.readline()
                    if line.find("total") != -1:
                        break
                    line = line.split()
                    rr_array       = np.append(rr_array,float(line[1]))
                    rr_error_array = np.append(rr_error_array,float(line[2]))

                return  rr_array,rr_error_array


def write_data(filename,energy,rr_dict,rr_error_dict,rr_diff_dict,rr_diff_sum_dict):
  length = 20
  precision = length - 7

  rr_data          = energy.reshape(len(energy),1)
  rr_error_data    = energy.reshape(len(energy),1)
  rr_diff_data     = energy.reshape(len(energy),1)
  rr_diff_sum_data = np.array([[0.0]])
  master_label = "Energy,".rjust(length-2)
  for key in rr_dict.keys():
    master_label       += key + ",".rjust(length+1)
    rr_data             = np.hstack((rr_data,rr_dict[key].reshape(len(energy),1)))
    rr_error_data       = np.hstack((rr_error_data,rr_error_dict[key].reshape(len(energy),1)))
    rr_diff_data        = np.hstack((rr_diff_data,rr_diff_dict[key].reshape(len(energy),1)))
    rr_diff_sum_data    = np.hstack((rr_diff_sum_data,rr_diff_sum_dict[key].reshape(1,1)))

  np.savetxt(filename + "_rr" + ".csv",rr_data,header = master_label, fmt = '%' + str(length) + '.' + str(precision) + 'e',delimiter=",")
  np.savetxt(filename + "_rr_error" + ".csv",rr_error_data,header = master_label, fmt = '%' + str(length) + '.' + str(precision) + 'e',delimiter=",")
  np.savetxt(filename + "_rr_diff" + ".csv",rr_diff_data,header = master_label, fmt = '%' + str(length) + '.' + str(precision) + 'e',delimiter=",")
  np.savetxt(filename + "_rr_diff_sum" + ".csv",rr_diff_sum_data,header = master_label, fmt = '%' + str(length) + '.' + str(precision) + 'e',delimiter="
      ,")


def main():
  energy,rr_dict,rr_error_dict,rr_diff_dict,rr_diff_sum_dict = \
    read_in_data("01upright_spatial_setup_FTC-CF-004_","sample_dir.list","energy.list")
  write_data("2014-06-13_data_master",energy,rr_dict,rr_error_dict,rr_diff_dict,rr_diff_sum_dict)


if __name__ == "__main__":
    main()
```

fig/mcnp/sample_post_process.py

```
1.00000E-11
2.00000E-11
3.00000E-11
4.00000E-11
5.00000E-11
6.00000E-11
7.00000E-11
8.00000E-11
9.00000E-11
1.00000E-10
2.00000E-10
3.00000E-10
4.00000E-10
5.00000E-10
6.00000E-10
7.00000E-10
8.00000E-10
9.00000E-10
1.00000E-09
2.00000E-09
3.00000E-09
4.00000E-09
5.00000E-09
6.00000E-09
7.00000E-09
8.00000E-09
9.00000E-09
1.00000E-08
2.00000E-08
3.00000E-08
4.00000E-08
5.00000E-08
6.00000E-08
7.00000E-08
8.00000E-08
9.00000E-08
1.00000E-07
2.00000E-07
3.00000E-07
4.00000E-07
5.00000E-07
6.00000E-07
7.00000E-07
8.00000E-07
9.00000E-07
1.00000E-06
2.00000E-06
3.00000E-06
4.00000E-06
5.00000E-06
6.00000E-06
7.00000E-06
8.00000E-06
9.00000E-06
1.00000E-05
2.00000E-05
3.00000E-05
4.00000E-05
5.00000E-05
6.00000E-05
7.00000E-05
8.00000E-05
9.00000E-05
1.00000E-04
2.00000E-04
3.00000E-04
```

```
4.00000E-04
5.00000E-04
6.00000E-04
7.00000E-04
8.00000E-04
9.00000E-04
1.00000E-03
2.00000E-03
3.00000E-03
4.00000E-03
5.00000E-03
6.00000E-03
7.00000E-03
8.00000E-03
9.00000E-03
1.00000E-02
2.00000E-02
3.00000E-02
4.00000E-02
5.00000E-02
6.00000E-02
7.00000E-02
8.00000E-02
9.00000E-02
1.00000E-01
2.00000E-01
3.00000E-01
4.00000E-01
5.00000E-01
6.00000E-01
7.00000E-01
8.00000E-01
9.00000E-01
1.00000E+00
2.00000E+00
3.00000E+00
4.00000E+00
5.00000E+00
6.00000E+00
7.00000E+00
8.00000E+00
9.00000E+00
1.00000E+01
1.10000E+01
1.20000E+01
1.30000E+01
1.40000E+01
1.50000E+01
1.60000E+01
1.70000E+01
1.80000E+01
1.90000E+01
2.00000E+01
```

fig/mcnp/energy.list

```
# sdist
-16.1275
# sorient
-90 0
# smat
400
# sden
-8.00
# scoord
-5 0 5
# pden
-0.95 -1.045
# fgden
-0.0020628254 -0.00226910794
# fe
14
# fden
-2.35
```

fig/mcnp/sample_perturbations.list

```
0_0_0_2_0_0_0
0_1_0_0_0_0_0
0_1_0_1_0_0_0
0_1_0_2_0_0_0
0_1_0_2_0_1_0
0_1_0_2_1_0_0
```

fig/mcnp/sample_dir.list

```
ORNL He-3 Slab Neutron Detector Template -- Upright
C
C     Created by: W. Cyrus Proctor
C     Created on Wednesday April 16, 2014 15:18:18
C     Modified on June 11, 2014 09:50:14
C
C ------------------------------------------------------------------------------
C Cell Cards ------------------------------------------------------------------
C ------------------------------------------------------------------------------
C ++++++++++++++++++++
C Californium Source +
C ++++++++++++++++++++
1         100       -15.10000 -1                                    imp:n=1 $ Cf-252 Sphere
2         200       -0.001205 (-8 -3 6 (11 :-7 :8 )1 ):(8 -3 11 )   imp:n=1 $ Capsule Inner Chamber
3         <smat>    <sden> -10 -4  5 (3:8:-6) (11:-3:10) (-8:10:3)  imp:n=1 $ Capsule Wall  -- with 304L SS density
4         <smat>    <sden> -9  -11 7                                imp:n=1 $ Capsule Cork  -- with 304L SS density
C ++++++++++++++++++
C Aluminium Sheath +
C ++++++++++++++++++
1001      1         -2.698900 +1001 -1002 +1004 -1007 +1008 -1011   imp:n=1 $ Aluminium Sheath Bottom
1002      1         -2.698900 +1002 -1003 +1004 -1005 +1008 -1011   imp:n=1 $ Aluminium Sheath Negative X
1003      1         -2.698900 +1002 -1003 +1006 -1007 +1008 -1011   imp:n=1 $ Aluminium Sheath Positive X
1004      1         -2.698900 +1002 -1003 +1005 -1006 +1008 -1009   imp:n=1 $ Aluminium Sheath Negative Y
1005      1         -2.698900 +1002 -1003 +1005 -1006 +1010 -1011   imp:n=1 $ Aluminium Sheath Positive Y
C +++++++++++++++++
C Cadmium Sheath +
C +++++++++++++++++
```

```
2001     2        -8.650000 +2001 -2002 +2004 -2007 +2008 -2010          imp:n=1 $ Cadmium Sheath Bottom
2002     2        -8.650000 +2002 -2003 +2004 -2005 +2008 -2010          imp:n=1 $ Cadmium Sheath Negative X
2003     2        -8.650000 +2002 -2003 +2006 -2007 +2008 -2010          imp:n=1 $ Cadmium Sheath Positive X
2004     2        -8.650000 +2002 -2003 +2005 -2006 +2009 -2010          imp:n=1 $ Cadmium Sheath Positive Y
C +++++++++++++++
C HDPE Sheath +
C +++++++++++++++
3001     3        <pden>    +3001 -3002 +3003 -3004 +3005 -3006
                            +3007 +3008 +3009 +3010 +3011                imp:n=1 $ HDPE Sheath
C +++++++++++++++
C He-3 Tube #1 +
C +++++++++++++++
4101     4        <fgden> +4102 -4103 -4107                              imp:n=1 $ He-3 Tube #1 He-3 Lower Insensitive Region
4102     4        <fgden> +4103 -4104 -4107                              imp:n=1 $ He-3 Tube #1 He-3 Active Region
4103     4        <fgden> +4104 -4105 -4107                              imp:n=1 $ He-3 Tube #1 He-3 Upper Insensitive Region
4104     5        -2.698900       (+4101 -4102 -4108):
                                  (+4101 -4105 +4107 -4108):
                                  (+4105 -4106 -4108)                    imp:n=1 $ He-3 Tube #1 Tube wall
C +++++++++++++++
C He-3 Tube #2 +
C +++++++++++++++
4201     4        <fgden> +4202 -4203 -4207                              imp:n=1 $ He-3 Tube #2 He-3 Lower Insensitive Region
4202     4        <fgden> +4203 -4204 -4207                              imp:n=1 $ He-3 Tube #2 He-3 Active Region
4203     4        <fgden> +4204 -4205 -4207                              imp:n=1 $ He-3 Tube #2 He-3 Upper Insensitive Region
4204     5        -2.698900    (+4201 -4202 -4208):
                               (+4201 -4205 +4207 -4208):
                               (+4205 -4206 -4208)                       imp:n=1 $ He-3 Tube #2 Tube wall
C +++++++++++++++
C He-3 Tube #3 +
C +++++++++++++++
4301     4        <fgden> +4302 -4303 -4307                              imp:n=1 $ He-3 Tube #3 He-3 Lower Insensitive Region
4302     4        <fgden> +4303 -4304 -4307                              imp:n=1 $ He-3 Tube #3 He-3 Active Region
4303     4        <fgden> +4304 -4305 -4307                              imp:n=1 $ He-3 Tube #3 He-3 Upper Insensitive Region
4304     5        -2.698900    (+4301 -4302 -4308):
                               (+4301 -4305 +4307 -4308):
                               (+4305 -4306 -4308)                       imp:n=1 $ He-3 Tube #3 Tube wall
C +++++++++++++++
C He-3 Tube #4 +
C +++++++++++++++
4401     4        <fgden> +4402 -4403 -4407                              imp:n=1 $ He-3 Tube #4 He-3 Lower Insensitive Region
4402     4        <fgden> +4403 -4404 -4407                              imp:n=1 $ He-3 Tube #4 He-3 Active Region
4403     4        <fgden> +4404 -4405 -4407                              imp:n=1 $ He-3 Tube #4 He-3 Upper Insensitive Region
4404     5        -2.698900    (+4401 -4402 -4408):
                               (+4401 -4405 +4407 -4408):
                               (+4405 -4406 -4408)                       imp:n=1 $ He-3 Tube #4 Tube wall
C +++++++++++++++
C He-3 Tube #5 +
C +++++++++++++++
4501     4        <fgden> +4502 -4503 -4507                              imp:n=1 $ He-3 Tube #5 He-3 Lower Insensitive Region
4502     4        <fgden> +4503 -4504 -4507                              imp:n=1 $ He-3 Tube #5 He-3 Active Region
4503     4        <fgden> +4504 -4505 -4507                              imp:n=1 $ He-3 Tube #5 He-3 Upper Insensitive Region
4504     5        -2.698900    (+4501 -4502 -4508):
                               (+4501 -4505 +4507 -4508):
                               (+4505 -4506 -4508)                       imp:n=1 $ He-3 Tube #5 Tube wall
C +++++++++++++++
C Junction Box +
C +++++++++++++++
5001     6        -2.698900 +5001 -5002 +5006 -5011 +5012 -5017
                            +5018 +5019 +5020 +5021 +5022                imp:n=1 $ Junction Box Bottom
5002     6        -2.698900 (+5002 -5003 +5006 -5011 +5012 -5017)
                            #(+5002 -5003 +5008 -5009 +5014 -5015)       imp:n=1 $ Junction Box Lower Section
5003     6        -2.698900 (+5003 -5004 +5006 -5011 +5012 -5017)
                            #(+5003 -5004 +5007 -5010 +5013 -5016)       imp:n=1 $ Junction Box Upper Section
5004     6        -2.698900 +5004 -5005 +5006 -5011 +5012 -5017          imp:n=1 $ Junction Box Top
C +++++++++++++++
C Inner Cradle +
C +++++++++++++++
6001     7        -2.698900 +6001 -6002 +6009 -6012 -6016 +6017          imp:n=1 $ Inner Cradle Bottom Flap
6002     7        -2.698900 (+6002 -6007 +6009 -6012 -6013 +6017)
                            #(+6003 -6006 +6010 -6011 -6014 +6017)
                            #(+6004 -6005 +6011 -6012 -6015 +6017)       imp:n=1 $ Inner Cradle
6003     7        -2.698900 +6007 -6008 +6009 -6012 -6016 +6017          imp:n=1 $ Inner Cradle Top Flap
C ++++++++++++++++++
C Inner Cradle HDPE +
C ++++++++++++++++++
7001     8       <pden>   +7001 -7006 +7007 -7010 +7011 -7015
                            #(-7016 +7011 -7012)
                            #(-7017 +7011 -7012)
                            #(-7018 +7011 -7012)
                            #(-7019 +7011 -7012)
                            #(-7020 +7011 -7012)
                            #(-7021 +7011 -7012)
                            #(-7022 +7011 -7012)
                            #(-7023 +7011 -7012)
                            #(+7002 -7005 +7008 -7009 +7011 -7014)
                            #(+7003 -7004 +7009 -7010 +7011 -7013)       imp:n=1 $ Inner Cradle HDPE
C +++++++++++++++
C Outer Cradle +
C +++++++++++++++
8001     9        -2.698900 +8001 -8003 +8011 -8016 -8020 +8021          imp:n=1 $ Outer Cradle Bottom Flap
8002     9        -2.698900 (+8003 -8009 +8011 -8016 -8017 +8021)
                            #(+8004 -8008 +8012 -8015 -8018 +8021)
                            #(+8006 -8007 +8015 -8016 -8019 +8021)       imp:n=1 $ Outer Cradle
8003     9        -2.698900 +8009 -8010 +8011 -8016 -8020 +8021          imp:n=1 $ Outer Cradle Top Flap
8004     9        -2.698900 (+8002 -8004 +8013 -8014 -8021 +8023):
                            (+8004 -8005 +8013 -8014 -8022 +8023)       imp:n=1 $ Outer Cradle Bottom Lip
C ++++++++++++++++++
C Outer Cradle HDPE +
C ++++++++++++++++++
9001     10       <pden> +9001 -9002 +9003 -9004 -9005 +9006             imp:n=1 $ Outer Cradle HDPE Back
9002     10       <pden> +9101 -9102 +9103 -9104 -9105 +9107
                            #(-9108 -9106 +9107)
                            #(-9109 -9106 +9107)
                            #(-9110 -9106 +9107)
                            #(-9111 -9106 +9107)                         imp:n=1 $ Outer Cradle HDPE Top
9003     10       <pden> +9201 -9202 +9203 -9204 -9205 +9207
                            #(-9208 -9206 +9207)
                            #(-9209 -9206 +9207)
                            #(-9210 -9206 +9207)
                            #(-9211 -9206 +9207)                         imp:n=1 $ Outer Cradle HDPE Bottom
9004     10       <pden> (+9301 -9304 +9305 -9306 -9307 +9308):
                            (+9302 -9303 +9305 -9306 -9308 +9309)        imp:n=1 $ Outer Cradle HDPE Left
9005     10       <pden> ((+9401 -9406 +9407 -9408 -9409 +9411):
                            (+9402 -9405 +9407 -9408 -9411 +9412))
                            #(+9403 -9404 +9407 -9408 -9410 +9412)       imp:n=1 $ Outer Cradle HDPE Right
C +++++++++++++++
C Outer Housing +
C +++++++++++++++
10001    11       -2.698900 (+10001 -10012 +10013 -10018 -10020 +10024
                            #(+10002 -10011 +10014 -10017 -10021 +10023)
                            #(+10003 -10010 +10015 -10016 -10023 +10024)
                            #(+10006 -10009 +10016 -10018 -10022 +10024)
                            #(-10025 -10023 +10024)
                            #(-10026 -10023 +10024)
                            #(-10027 -10023 +10024)
                            #(-10028 -10023 +10024)
                            #(-10029 -10023 +10024)
                            #(-10030 -10023 +10024)
                            #(-10031 -10023 +10024)
                            #(-10032 -10023 +10024)):
                            (+10004 -10005 +10013 -10018 -10019 +10020):
                            (+10007 -10008 +10013 -10018 -10019 +10020)  imp:n=1 $ Outer Housing
C ++++++++++++
C Hand Truck +
C ++++++++++++
```

```
11001    12       -2.698900 (+11001 -11002 +11006 -11017 +11018 -11024
                            #(-11026 +11001 -11002)
                            #(-11027 +11001 -11002)):
                            (+11002 -11003 +11006 -11017 +11019 -11020):
                            (+11001 -11005 +11007 -11008 +11022 -11024):
                            (+11004 -11005 +11007 -11008 +11024 -11025):
                            (+11001 -11005 +11015 -11016 +11022 -11024):
                            (+11004 -11005 +11015 -11016 +11024 -11025):
                            (-11028 +11006 -11017):
                            (+11001 -11005 +11009 -11010 +11022 -11023):
                            (+11001 -11005 +11010 -11011 +11021 -11024):
                            (+11001 -11005 +11012 -11013 +11021 -11024):
                            (+11001 -11005 +11013 -11014 +11022 -11023) imp:n=1 $ Hand Truck Scoop
11002    12       -2.698900 +11101 -11102 +11103 -11104                 imp:n=1 $ Hand Truck Left Wheel
11003    12       -2.698900 +11201 -11202 +11203 -11204                 imp:n=1 $ Hand Truck Right Wheel
11004    12       -2.698900 (+11301 -11302 +11303 -11304 +11306 -11309):
                            (+11301 -11302 +11304 -11305 +11306 -11307):
                            (+11301 -11302 +11304 -11305 +11308 -11309) imp:n=1 $ Hand Truck Left Vertical Support
11005    12       -2.698900 (+11401 -11402 +11404 -11405 +11406 -11409):
                            (+11401 -11402 +11403 -11404 +11406 -11407):
                            (+11401 -11402 +11403 -11404 +11408 -11409) imp:n=1 $ Hand Truck Right Vertical Support
11006    12       -2.698900 (+11501 -11504 +11505 -11506 +11508 -11509):
                            (+11501 -11502 +11505 -11506 +11507 -11508):
                            (+11503 -11504 +11505 -11506 +11507 -11508) imp:n=1 $ Hand Truck Lower Horizontal Support
11007    12       -2.698900 (+11601 -11604 +11605 -11606 +11608 -11609):
                            (+11601 -11602 +11605 -11606 +11607 -11608):
                            (+11603 -11604 +11605 -11606 +11607 -11608) imp:n=1 $ Hand Truck Middle Horizontal Support
11008    12       -2.698900 (+11701 -11704 +11705 -11706 +11708 -11709):
                            (+11701 -11702 +11705 -11706 +11707 -11708):
                            (+11703 -11704 +11705 -11706 +11707 -11708) imp:n=1 $ Hand Truck Upper Horizontal Support
11009    12       -2.698900 (+11801 +11803 -11804 +11805 -11806):
                            (+11802 +11803 -11804 +11807 -11808)        imp:n=1 $ Hand Truck Handle
C +++++++
C Floor +
C +++++++
12001    <fe>     <fden> +12001 -12002 +12003 -12004 +12005 -12006      imp:n=1 $ Floor
C ++++++++++++++++++++++
C Detector Bounding Box +
C ++++++++++++++++++++++
13001    13       -0.001205 #1001 #1002 #1003 #1004 #1005
                            #2001 #2002 #2003 #2004
                            #3001
                            #4101 #4102 #4103 #4104
                            #4201 #4202 #4203 #4204
                            #4301 #4302 #4303 #4304
                            #4401 #4402 #4403 #4404
                            #4501 #4502 #4503 #4504
                            #5001 #5002 #5003 #5004
                            #6001 #6002 #6003
                            #7001
                            #8001 #8002 #8003 #8004
                            #9001 #9002 #9003 #9004 #9005
                            #10001
                           (+13001 -13002 +13003 -13004 +13005 -13006) imp:n=1  $ Air
C +++++
C Air +
C +++++
25001    13       -0.001205 #1 #2 #3 #4
                            #11001 #11002 #11003 #11004 #11005 #11006
                            #11007 #11008 #11009
                            #12001
                            #(+13001 -13002 +13003 -13004 +13005 -13006)
                            -50000                                      imp:n=1  $ Air
25002    0                  +50000                                      imp:n=0  $ Outside

C
C ---------------------------------------------------------------------------
C Surface Cards ---------------------------------------------------------------
C ---------------------------------------------------------------------------
C
50000    so        500
C ++++++++++++++++++
C Californium Source +
C ++++++++++++++++++++
1        1         so        1.6817774274e-005                               $ Source
3        1         cz        0.19558                                         $ Cylinder -- Capsule Inner Radius
4        1         cz        0.27686                                         $ Cylinder -- Capsule Outer Radius
5        1         pz       -0.8009                                          $ Capsule Outside Radius Bottom
6        1         pz       -0.6104                                          $ Capsule Inside Radius Bottom
7        1         pz        0.6104                                          $ Capsule Bottom of Cork
8        1         pz        0.7866                                          $ Capsule Inside Radius Top
9        1         pz        1.0041                                          $ Capsule Top of Cork
10       1         pz        1.1803                                          $ Capsule Outside Radius Top
11       1         kz       -1.089220919         0.01085267467       0       $ Cone -- Cork
C ++++++++++++++++++
C Aluminium Sheath +
C ++++++++++++++++++
1001     10        pz        0.000000
1002     10        pz        0.158750
1003     10        pz        60.96000
1004     10        px       -15.55750
1005     10        px       -15.39875
1006     10        px        15.39875
1007     10        px        15.55750
1008     10        py       -4.762500
1009     10        py       -4.603750
1010     10        py        4.603750
1011     10        py        4.762500
C +++++++++++++++++
C Cadmium Sheath +
C +++++++++++++++++
2001     20        pz        0.000000
2002     20        pz        0.158750
2003     20        pz        60.80125
2004     20        px       -15.39875
2005     20        px       -15.24000
2006     20        px        15.24000
2007     20        px        15.39875
2008     20        py       -4.603750
2009     20        py        4.445000
2010     20        py        4.603750
C ++++++++++++++
C HDPE Sheath +
C ++++++++++++++
3001     30        pz        0.0000001 $ Shifted
3002     30        pz        60.642499
3003     30        px       -15.239999
3004     30        px        15.239999
3005     30        py       -3.8099999
3006     30        py        5.0799999
3007     30        c/z      -12.06500  0.000000  1.270000
3008     30        c/z      -6.032500  0.000000  1.270000
3009     30        c/z       0.000000  0.000000  1.270000
3010     30        c/z       6.032500  0.000000  1.270000
3011     30        c/z       12.06500  0.000000  1.270000
C ++++++++++++++
C He-3 Tube #1 +
C ++++++++++++++
4101     40        pz        0.000000
4102     40        pz        0.158750
4103     40        pz        3.810000
4104     40        pz        54.61000
4105     40        pz        58.89625
4106     40        pz        59.05500
4107     40        c/z      -12.06500  0.000000  1.190625
```

```
4108     40        c/z      -12.06500  0.000000  1.27000
C +++++++++++++++
C He-3 Tube #2 +
C +++++++++++++++
4201     40        pz        0.000000
4202     40        pz        0.158750
4203     40        pz        3.810000
4204     40        pz        54.61000
4205     40        pz        58.89625
4206     40        pz        59.05500
4207     40        c/z      -6.032500  0.000000  1.190625
4208     40        c/z      -6.032500  0.000000  1.27000
C +++++++++++++++
C He-3 Tube #3 +
C +++++++++++++++
4301     40        pz        0.000000
4302     40        pz        0.158750
4303     40        pz        3.810000
4304     40        pz        54.61000
4305     40        pz        58.89625
4306     40        pz        59.05500
4307     40        c/z       0.000000  0.000000  1.190625
4308     40        c/z       0.000000  0.000000  1.27000
C +++++++++++++++
C He-3 Tube #4 +
C +++++++++++++++
4401     40        pz        0.000000
4402     40        pz        0.158750
4403     40        pz        3.810000
4404     40        pz        54.61000
4405     40        pz        58.89625
4406     40        pz        59.05500
4407     40        c/z       6.032500  0.000000  1.190625
4408     40        c/z       6.032500  0.000000  1.27000
C +++++++++++++++
C He-3 Tube #5 +
C +++++++++++++++
4501     40        pz        0.000000
4502     40        pz        0.158750
4503     40        pz        3.810000
4504     40        pz        54.61000
4505     40        pz        58.89625
4506     40        pz        59.05500
4507     40        c/z       12.06500  0.000000  1.190625
4508     40        c/z       12.06500  0.000000  1.27000
C +++++++++++++++
C Junction Box +
C +++++++++++++++
5001     50        pz        0.000000
5002     50        pz        0.812800
5003     50        pz        4.114800
5004     50        pz        9.380220
5005     50        pz        10.16000
5006     50        px       -15.55750
5007     50        px       -14.77772
5008     50        px       -14.19098
5009     50        px        14.19098
5010     50        px        14.77772
5011     50        px        15.55750
5012     50        py       -4.127500
5013     50        py       -3.347720
5014     50        py       -2.760980
5015     50        py        4.030980
5016     50        py        4.617720
5017     50        py        5.397500
5018     50        c/z      -12.65000  0.000000  1.27000
5019     50        c/z      -6.032500  0.000000  1.27000
5020     50        c/z       0.000000  0.000000  1.27000
5021     50        c/z       6.032500  0.000000  1.27000
5022     50        c/z       12.65000  0.000000  1.27000
C +++++++++++++++
C Inner Cradle +
C +++++++++++++++
6001     60        pz        0.000000
6002     60        pz        5.080000
6003     60        pz        5.397500
6004     60        pz        66.67500
6005     60        pz        74.61250
6006     60        pz        76.83500
6007     60        pz        77.15250
6008     60        pz        82.23250
6009     60        px       -15.95438
6010     60        px       -15.63688
6011     60        px        15.63688
6012     60        px        15.95438
6013     60        py        0.000000
6014     60        py       -0.317500
6015     60        py       -2.540000
6016     60        py       -8.572500
6017     60        py       -8.890000
C ++++++++++++++++++
C Inner Cradle HDPE +
C ++++++++++++++++++
7001     70        pz        0.000000
7002     70        pz        5.080000
7003     70        pz        67.94500
7004     70        pz        76.20000
7005     70        pz        77.47000
7006     70        pz        82.55000
7007     70        px       -21.27250
7008     70        px       -16.19250
7009     70        px        16.19250
7010     70        px        21.27250
7011     70        py        0.000000
7012     70        py        6.985000
7013     70        py        7.937500
7014     70        py        9.525000
7015     70        py        14.60500
7016     70        c/y      -13.33500  2.540000  0.952500
7017     70        c/y      -3.175000  2.540000  0.952500
7018     70        c/y       3.175000  2.540000  0.952500
7019     70        c/y       13.33500  2.540000  0.952500
7020     70        c/y      -13.33500  80.01000  0.952500
7021     70        c/y      -3.175000  80.01000  0.952500
7022     70        c/y       3.175000  80.01000  0.952500
7023     70        c/y       13.33500  80.01000  0.952500
C +++++++++++++++
C Outer Cradle +
C +++++++++++++++
8001     80        pz        0.000000
8002     80        pz        5.080000
8003     80        pz        5.397500
8004     80        pz        5.715000
8005     80        pz        9.207500
8006     80        pz        73.97750
8007     80        pz        82.55000
8008     80        pz        89.53500
8009     80        pz        89.85250
8010     80        pz        95.25000
8011     80        px       -21.59000
8012     80        px       -21.27250
8013     80        px       -6.350000
8014     80        px        6.350000
8015     80        px        21.27250
8016     80        px        21.59000
```

```
8017     80        py        0.000000
8018     80        py       -0.317500
8019     80        py       -6.350000
8020     80        py       -14.28750
8021     80        py       -14.60500
8022     80        py       -15.24000
8023     80        py       -15.55750
C ++++++++++++++++++
C Outer Cradle HDPE +
C ++++++++++++++++++
C Back Piece
9001     90        pz        0.000000
9002     90        pz        84.45500
9003     90        px       -21.59000
9004     90        px        21.59000
9005     90        py        0.000000
9006     90        py       -5.080000
C Top Piece
9101     90        pz        84.45500
9102     90        pz        89.53500
9103     90        px       -21.59000
9104     90        px        21.59000
9105     90        py        0.000000
9106     90        py       -13.33500
9107     90        py       -19.68500
9108     90        c/y      -19.20875  87.63000  1.031875
9109     90        c/y      -9.207500  87.63000  1.031875
9110     90        c/y       9.207500  87.63000  1.031875
9111     90        c/y       19.20875  87.63000  1.031875
C Bottom Piece
9201     90        pz       -5.080000
9202     90        pz        0.000000
9203     90        px       -21.59000
9204     90        px        21.59000
9205     90        py        0.000000
9206     90        py       -13.33500
9207     90        py       -19.68500
9208     90        c/y      -19.20875 -3.175000  1.031875
9209     90        c/y      -9.207500 -3.175000  1.031875
9210     90        c/y       9.207500 -3.175000  1.031875
9211     90        c/y       19.20875 -3.175000  1.031875
C Left Piece
9301     90        pz       -5.080000
9302     90        pz        0.000000
9303     90        pz        84.45500
9304     90        pz        89.53500
9305     90        px       -26.67000
9306     90        px       -21.59000
9307     90        py        0.000000
9308     90        py       -19.36750
9309     90        py       -19.68500
C Right Piece
9401     90        pz       -5.080000
9402     90        pz        0.000000
9403     90        pz        68.89750
9404     90        pz        77.15250
9405     90        pz        84.45500
9406     90        pz        89.53500
9407     90        px        21.59000
9408     90        px        26.67000
9409     90        py        0.000000
9410     90        py       -11.43000
9411     90        py       -19.36750
9412     90        py       -19.68500
C ++++++++++++++++
C Outer Housing +
C ++++++++++++++++
10001    100       pz        0.000000
10002    100       pz        0.317500
10003    100       pz        5.397500
10004    100       pz        16.19250
10005    100       pz        20.00250
10006    100       pz        73.34250
10007    100       pz        75.24750
10008    100       pz        79.05750
10009    100       pz        82.23250
10010    100       pz        89.85250
10011    100       pz        94.93250
10012    100       pz        95.25000
10013    100       px       -27.38438
10014    100       px       -27.06688
10015    100       px       -21.98688
10016    100       px        21.98688
10017    100       px        27.06688
10018    100       px        27.38438
10019    100       py        1.270000
10020    100       py        0.000000
10021    100       py       -0.317500
10022    100       py       -12.06500
10023    100       py       -20.32000
10024    100       py       -20.63750
10025    100       c/y      -19.12938  2.670100  0.952500
10026    100       c/y      -8.969380  2.670100  0.952500
10027    100       c/y       8.969380  2.670100  0.952500
10028    100       c/y       19.12938  2.670100  0.952500
10029    100       c/y      -19.12938  92.57990  0.952500
10030    100       c/y      -8.969380  92.57990  0.952500
10031    100       c/y       8.969380  92.57990  0.952500
10032    100       c/y       19.12938  92.57990  0.952500
C ++++++++++++
C Hand Truck +
C ++++++++++++
C Scoop
11001    110       pz        0.000000
11002    110       pz        0.635000
11003    110       pz        1.270000
11004    110       pz        8.255000
11005    110       pz        13.33500
11006    110       px       -22.86000
11007    110       px       -16.19250
11008    110       px       -15.24000
11009    110       px       -14.76375
11010    110       px       -12.70000
11011    110       px       -11.43000
11012    110       px        11.43000
11013    110       px        12.70000
11014    110       px        14.76375
11015    110       px        15.24000
11016    110       px        16.19250
11017    110       px        22.86000
11018    110       py        0.000000
11019    110       py        6.553320
11020    110       py        7.188320
11021    110       py        19.68500
11022    110       py        20.02121
11023    110       py        22.87871
11024    110       py        23.49500
11025    110       py        36.19500
11026    110       c/z      -11.43000  12.53300  6.350000
11027    110       c/z       11.43000  12.53300  6.350000
11028    110       c/x       31.43250  10.79500  0.635000
C Left Wheel
11101    110       c/x       31.43250  10.79500  0.635000
11102    110       c/x       31.43250  10.79500  10.16000
11103    110       px       -21.00000
```

```
11104    110       px       -16.55500
C Right Wheel
11201    110       c/x       31.43250  10.79500  0.635000
11202    110       c/x       31.43250  10.79500  10.16000
11203    110       px        16.55500
11204    110       px        21.00000
C Left Vertical Support
11301    110       pz         0.635000
11302    110       pz         99.12350
11303    110       px       -15.24000
11304    110       px       -14.76375
11305    110       px       -12.70000
11306    110       py         19.54496
11307    110       py         20.02121
11308    110       py         22.87871
11309    110       py         23.35496
C Right Vertical Support
11401    110       pz         0.635000
11402    110       pz         99.12350
11403    110       px         12.70000
11404    110       px         14.76375
11405    110       px         15.24000
11406    110       py         19.54496
11407    110       py         20.02121
11408    110       py         22.87871
11409    110       py         23.35496
C Lower Horizontal Support
11501    110       pz         36.67125
11502    110       pz         37.14750
11503    110       pz         39.05250
11504    110       pz         39.52875
11505    110       px       -14.76375
11506    110       px         14.76375
11507    110       py         20.02121
11508    110       py         22.40246
11509    110       py         22.87871
C Middle Horizontal Support
11601    110       pz         64.61125
11602    110       pz         65.08750
11603    110       pz         66.99250
11604    110       pz         67.46875
11605    110       px       -14.76375
11606    110       px         14.76375
11607    110       py         20.02121
11608    110       py         22.40246
11609    110       py         22.87871
C Upper Horizontal Support
11701    110       pz         92.55125
11702    110       pz         93.02745
11703    110       pz         94.93250
11704    110       pz         95.40875
11705    110       px       -14.76375
11706    110       px         14.76375
11707    110       py         20.02121
11708    110       py         22.40246
11709    110       py         22.87871
C Handle
11801    110       pz         95.40875
11802    110       pz         99.12350
11803    110       py         20.02121
11804    110       py         23.49500
11805    110       c/y        0.000000  95.40875  11.19120
11806    110       c/y        0.000000  95.40875  11.66880
11807    110       c/y        0.000000  99.12350  12.70000
11808    110       c/y        0.000000  99.12350  15.24000
C +++++++
C Floor +
C +++++++
12001    120       pz         0.000000
12002    120       pz         20.32000
12003    120       px      -150.00000
12004    120       px       150.00000
12005    120       py      -150.00000
12006    120       py       150.00000
C ++++++++++++++++++++++++
C Detector Bounding Box +
C ++++++++++++++++++++++++
13001    130       pz        -0.0000001 $ Shifted Bounding Box 1e-7 outwards to be unique surfaces for tallys
13002    130       pz         95.250001
13003    130       px       -27.384381
13004    130       px        27.384381
13005    130       py        -0.0000001
13006    130       py         23.812501

C ccccccccccccccccc
C Transformations C
C ccccccccccccccccc
# tr1
<sxdist>
<sydist>
<szdist>
<sorient>
tr10     0.0       0.63500  -0.476250
tr20     0.0       0.63500  -0.317500
tr30     0.0       0.00000  -0.158750
tr40     0.0       0.00000   1.428750
tr50     0.0       0.00000   60.48375
tr60     0.0       5.71500  -5.873750
tr70     0.0      -2.85750  -5.873750
tr80     0.0       12.0650  -11.58875
tr90     0.0       17.7800  -6.191250
tr100    0.0       18.4150  -11.58875
tr110    0.0       0.140042 -12.858751
tr120    0.0       0.00000  -33.178751
tr130    0.0      -4.12750  -11.58875
C ccccccccccccccccc
C Material Input C
C ccccccccccccccccc
m1       13027           1.0                                                    $ Aluminium Sheath
m2       48000           1.0                                                    $ Cadmium Sheath
m3        1001           0.666662
          6000           0.333338
mt3      poly.60t                                                               $ HDPE Sheath
m4        1001          -0.008125016100
          2003          -0.243122473900
          6000          -0.024204598210
         18000          -0.724547911700                                        $ He-3 4 atm with P-10 quench 1 atm
m5       13027           1.0                                                    $ He-3 Aluminum Tube
m6       13027           1.0                                                    $ Junction Box Aluminum
m7       13027           1.0                                                    $ Inner Cradle Aluminum
m8        1001           0.666662
          6000           0.333338
mt8      poly.60t                                                               $ Inner Cradle HDPE
m9       13027           1.0                                                    $ Outer Cradle Aluminum
m10       1001           0.666662
          6000           0.333338
mt10     poly.60t                                                               $ Outer Cradle HDPE
m11      13027           1.0                                                    $ Outer Housing Aluminum
m12      13027           1.0                                                    $ Hand Truck Aluminum
m13       6000          -0.000124
          7014          -0.755268
          8016          -0.231781
         18000          -0.012827                                              $ Air (Dry, Near Sea Level)
m14       1001          -0.008485
          6000          -0.050064
```

```
          8016          -0.473483
         12000          -0.024183
         13027          -0.036063
         14000          -0.1451
         16000          -0.00297
         19000          -0.001697
         20000          -0.246924
         26000          -0.011031                                        $ Ordinary Concrete NBS 03
m100     98252           1.0                                             $ Californium-252
m200      6000          -0.000124                                        $ Air (Dry, Near Sea Level) -- from PNNL
          7014          -0.755268
          8016          -0.231781
         18000          -0.012827
m400      6000          -0.0003                                          $SS-304,SS-304L (with ENDF-VI) -- from Vised
         14028          -0.004594
         14029          -0.000241
         14030          -0.000165
         15031          -0.000225
         16032          -0.000142
         16033          -1e-006
         16034          -7e-006
         24050          -0.00793
         24052          -0.159031
         24053          -0.018378
         24054          -0.004661
         25055          -0.01
         26054          -0.039996
         26056          -0.644764
         26057          -0.015026
         26058          -0.002039
         28058          -0.06234
         28060          -0.024654
         28061          -0.001085
         28062          -0.003504
         28064          -0.000917
m500      8016          -0.001197                                        $Zircaloy-2
         24000          -0.000997
         26000          -0.000997
         28000          -0.000499
         40000          -0.982348
         50000          -0.013962
c ccccccccccccccccccc
C Source Definition C
c ccccccccccccccccccc
sdef pos=<sxdist> <sydist> <szdist> SUR=0     ERG=D1    CEL=1     RAD=D2
SP1      -3         1.18      1.03419                                  $ Watt Fission Spectrum with Coeffs a & b for Cf-252 (MCNP6)
SI2       0         1.681774274e-005                                   $ Sampling Radius from R1 to R2
SP2      -21        2                                                  $ Power law p(x) = x^A <-- Specify A
#  E0
   1.00E-11
   2.00E-11
   3.00E-11
   4.00E-11
   5.00E-11
   6.00E-11
   7.00E-11
   8.00E-11
   9.00E-11
   1.00E-10
   2.00E-10
   3.00E-10
   4.00E-10
   5.00E-10
   6.00E-10
   7.00E-10
   8.00E-10
   9.00E-10
   1.00E-09
   2.00E-09
   3.00E-09
   4.00E-09
   5.00E-09
   6.00E-09
   7.00E-09
   8.00E-09
   9.00E-09
   1.00E-08
   2.00E-08
   3.00E-08
   4.00E-08
   5.00E-08
   6.00E-08
   7.00E-08
   8.00E-08
   9.00E-08
   1.00E-07
   2.00E-07
   3.00E-07
   4.00E-07
   5.00E-07
   6.00E-07
   7.00E-07
   8.00E-07
   9.00E-07
   1.00E-06
   2.00E-06
   3.00E-06
   4.00E-06
   5.00E-06
   6.00E-06
   7.00E-06
   8.00E-06
   9.00E-06
   1.00E-05
   2.00E-05
   3.00E-05
   4.00E-05
   5.00E-05
   6.00E-05
   7.00E-05
   8.00E-05
   9.00E-05
   1.00E-04
   2.00E-04
   3.00E-04
   4.00E-04
   5.00E-04
   6.00E-04
   7.00E-04
   8.00E-04
   9.00E-04
   1.00E-03
   2.00E-03
   3.00E-03
   4.00E-03
   5.00E-03
   6.00E-03
   7.00E-03
   8.00E-03
   9.00E-03
   1.00E-02
   2.00E-02
   3.00E-02
   4.00E-02
   5.00E-02
```

```
   6.00E-02
   7.00E-02
   8.00E-02
   9.00E-02
   1.00E-01
   2.00E-01
   3.00E-01
   4.00E-01
   5.00E-01
   6.00E-01
   7.00E-01
   8.00E-01
   9.00E-01
   1.00E+00
   2.00E+00
   3.00E+00
   4.00E+00
   5.00E+00
   6.00E+00
   7.00E+00
   8.00E+00
   9.00E+00
   1.00E+01
   1.10E+01
   1.20E+01
   1.30E+01
   1.40E+01
   1.50E+01
   1.60E+01
   1.70E+01
   1.80E+01
   1.90E+01
   2.00E+01
C CCCCCCCCC
C Tallies C
C CCCCCCCCC
C Detector Front Surface
f11:n 13005
fc11  front
C ft11  scx 1
c11   0 1
fq11  e c
C Detector Back Surface
f21:n 13006
fc21  back
C ft21  scx 1
c21   0 1
fq21  e c
C Detector Left Surface
f31:n 13003
fc31  left
C ft31  scx 1
c31   0 1
fq31  e c
C Detector Right Surface
f41:n 13004
fc41  right
C ft41  scx 1
c41   0 1
fq41  e c
C Detector Bottom Surface
f51:n 13001
fc51  bottom
C ft51  scx 1
c51   0 1
fq51  e c
C Detector Top Surface
f61:n 13002
fc61  top
C ft61  scx 1
c61   0 1
fq61  e c
C Inner Detector Front Surface
f71:n 3005
fc71  front
C ft71  scx 1
c71   0 1
fq71  e c
C Inner Detector Back Surface
f81:n 3006
fc81  back
C ft81  scx 1
c81   0 1
fq81  e c
C Inner Detector Left Surface
f91:n 3003
fc91  left
C ft91  scx 1
c91   0 1
fq91  e c
C Inner Detector Right Surface
f101:n 3004
fc101  right
C ft101  scx 1
c101   0 1
fq101  e c
C Inner Detector Bottom Surface
f111:n 3001
fc111  bottom
C ft111  scx 1
c111   0 1
fq111  e c
C Inner Detector Top Surface
f121:n 3002
fc121  top
C ft121  scx 1
c121   0 1
fq121  e c
C He-3 Tubes (Active Regions) Reaction Rates
f4:n 4102 4202 4302 4402 4502 t
fc4  (n,p) Reaction Rate
fm4  -1 4 (103)
C ft4  scx 1
fq4  e f
C CCCCCCCCCCC
C Data Cards C
C CCCCCCCCCCC
mode  n
nps 1e2
C nps   1e9
rand  gen=2
C print
```

fig/mcnp/upright_spatial_setup_FTC–CF–004.mcnp.inp.template

```
> # W. Cyrus Proctor
> # 01/15/2014
> # Updated 06/13/2014
```

```
> # Updated 11/30/2014

> # Generates the fission spectrum in SCALE 200-Group format for Denovo. Using
> Mannhart fit.

> # Now includes a fit from modified Maxwellian from Mannhart's experiments
> # Nucl. Sci. Eng., 91, 114 (1985) as well as a comparison from MCNP6 and 5.

> # Calculates area under watt spectrum of Cf-252. Bins are used in
> # MCNP simulations as well as the a and b parameters. With no alteration
> # (point source in vacuum) a source distribution should match this one.


restart
with(plots)
Digits := 30
> # MCNP 5 Cf-252 Spontaneous Fission Watt Spectrum Parameters
a := 1.025
b := 2.926
> # MCNP 6 Cf-252 Spontaneous Fission Watt Spectrum Parameters
a6 := 1.18
b6 := 1.03419
> # Mannhart Experimental
> # Nuclear Temperate for Cf-252 (MeV)
T := 1.42
> # Mannhart Maxwellian correction factor for Cf-252
R := proc (E) options operator, arrow; piecewise(E <= 5,
.955+0.707e-1*E+(-1)*0.444e-1*E^2+0.1998e-1*E^3+(-1)*0.457e-2*E^4+0.368e-3*E^5,
5 < E, 1.16+(-1)*0.432e-1*E+0.185e-2*E^2+(-1)*0.316e-4*E^3) end proc

> # MCNP 5 PDF
f := proc (E) options operator, arrow; exp(-E/a)*sinh(sqrt(b*E)) end proc
> # MCNP 6 PDF
f6 := proc (E) options operator, arrow; exp(-E/a6)*sinh(sqrt(b6*E)) end proc
> # Prompt neutron energy spectrum with Mannhart correction for Cf-252
N := proc (E) options operator, arrow;
2*R(E)*sqrt(E)*exp(-E/T)/(sqrt(Pi)*T^(3/2)) end proc

> # MCNP 5 Normalization Constant
C := evalf(1/(int(f(E), E = 0 .. 20)))
> # MCNP 6 Normalization Constant
C6 := evalf(1/(int(f6(E), E = 0 .. 20)))
> # Mannhart Normalization Constant
Cm := evalf(1/(int(N(E), E = 0 .. 20)))


> # Expected Values
> # MCNP 5
EC := evalf((int(E*f(E), E = 0 .. 20))/(int(f(E), E = 0 .. 20)))
> # MCNP 6
EC6 := evalf((int(E*f6(E), E = 0 .. 20))/(int(f6(E), E = 0 .. 20)))
> # Mannhart
ECm := evalf((int(E*N(E), E = 0 .. 20))/(int(N(E), E = 0 .. 20)))

> # Variance
> # MCNP 5
VC := evalf((int((E-EC)^2*f(E), E = 0 .. 20))/(int(f(E), E = 0 .. 20)))
> # MCNP 6
VC6 := evalf((int((E-EC6)^2*f6(E), E = 0 .. 20))/(int(f6(E), E = 0 .. 20)))
> # Mannhart
VCm := evalf((int((E-ECm)^2*N(E), E = 0 .. 20))/(int(N(E), E = 0 .. 20)))
> # Energy Grid [1E-5,20 MeV] Copied from Excel with 200 bins
EE := Vector(201, {(1) = 0.10000e-10, (2) = 0.50000e-9, (3) = 0.20000e-8, (4) =
0.50000e-8, (5) = 0.10000e-7, (6) = 0.14500e-7, (7) = 0.21000e-7, (8) =
0.30000e-7, (9) = 0.40000e-7, (10) = 0.50000e-7, (11) = 0.70000e-7, (12) =
0.10000e-6, (13) = 0.12500e-6, (14) = 0.15000e-6, (15) = 0.18400e-6, (16) =
0.22500e-6, (17) = 0.27500e-6, (18) = 0.32500e-6, (19) = 0.36680e26, (20) =
0.41399e-6, (21) = 0.50000e-6, (22) = 0.53158e-6, (23) = 0.62506e-6, (24) =
0.68256e-6, (25) = 0.80000e-6, (26) = 0.87643e-6, (27) = 0.10000e-5, (28) =
0.10400e-5, (29) = 0.10800e-5, (30) = 0.11253e-5, (31) = 0.13000e-5, (32) =
0.14450e-5, (33) = 0.18554e-5, (34) = 0.23824e-5, (35) = 0.30590e-5, (36) =
0.39279e-5, (37) = 0.50435e-5, (38) = 0.64760e-5, (39) = 0.83153e-5, (40) =
0.10677e-4, (41) = 0.13710e-4, (42) = 0.17604e-4, (43) = 0.22603e-4, (44) =
0.29023e-4, (45) = 0.37266e-4, (46) = 0.47851e-4, (47) = 0.61442e-4, (48) =
0.78893e-4, (49) = 0.10130e-3, (50) = 0.13007e-3, (51) = 0.16702e-3, (52) =
0.21445e-3, (53) = 0.27536e-3, (54) = 0.35357e-3, (55) = 0.45400e-3, (56) =
0.58295e-3, (57) = 0.74852e-3, (58) = 0.96112e-3, (59) = 0.12341e-2, (60) =
0.15846e-2, (61) = 0.20347e-2, (62) = 0.22487e-2, (63) = 0.24852e-2, (64) =
0.26126e-2, (65) = 0.27465e-2, (66) = 0.30354e-2, (67) = 0.33546e-2, (68) =
0.37074e-2, (69) = 0.43074e-2, (70) = 0.55308e-2, (71) = 0.71017e-2, (72) =
0.91188e-2, (73) = 0.10595e-1, (74) = 0.11709e-1, (75) = 0.15034e-1, (76) =
0.19305e-1, (77) = 0.21875e-1, (78) = 0.23579e-1, (79) = 0.24176e-1, (80) =
0.24788e-1, (81) = 0.26058e-1, (82) = 0.27000e-1, (83) = 0.28501e-1, (84) =
0.31828e-1, (85) = 0.34307e-1, (86) = 0.40868e-1, (87) = 0.46309e-1, (88) =
0.52475e-1, (89) = 0.56562e-1, (90) = 0.67379e-1, (91) = 0.71998e-1, (92) =
0.79499e-1, (93) = 0.82503e-1, (94) = 0.86517e-1, (95) = 0.98037e-1, (96) =
.11109, (97) = .11679, (98) = .12277, (99) = .12907, (100) = .13569, (101) =
.14264, (102) = .14996, (103) = .15764, (104) = .16573, (105) = .17422, (106) =
.18316, (107) = .19255, (108) = .20242, (109) = .21280, (110) = .22371, (111) =
.23518, (112) = .24724, (113) = .27324, (114) = .28725, (115) = .29452, (116) =
.29721, (117) = .29849, (118) = .30197, (119) = .33373, (120) = .36883, (121) =
.38774, (122) = .40762, (123) = .45049, (124) = .49787, (125) = .52340, (126) =
.55023, (127) = .57844, (128) = .60810, (129) = .63928, (130) = .67206, (131) =
.70651, (132) = .74274, (133) = .78082, (134) = .82085, (135) = .86294, (136) =
.90718, (137) = .96164, (138) = 1.0026, (139) = 1.1080, (140) = 1.1648, (141) =
1.2246, (142) = 1.2874, (143) = 1.3534, (144) = 1.4227, (145) = 1.4957, (146) =
1.5724, (147) = 1.6530, (148) = 1.7377, (149) = 1.8268, (150) = 1.9205, (151) =
2.0190, (152) = 2.1225, (153) = 2.2313, (154) = 2.3069, (155) = 2.3457, (156) =
2.3653, (157) = 2.3852, (158) = 2.4660, (159) = 2.5924, (160) = 2.7253, (161) =
2.8651, (162) = 3.0119, (163) = 3.1664, (164) = 3.3287, (165) = 3.6788, (166) =
4.0657, (167) = 4.4933, (168) = 4.7237, (169) = 4.9659, (170) = 5.2205, (171) =
5.4881, (172) = 5.7695, (173) = 6.0653, (174) = 6.3763, (175) = 6.5924, (176) =
6.7032, (177) = 7.0469, (178) = 7.4082, (179) = 7.7880, (180) = 8.1873, (181) =
8.6071, (182) = 9.0484, (183) = 9.5123, (184) = 10.000, (185) = 10.513, (186) =
11.052, (187) = 11.618, (188) = 12.214, (189) = 12.523, (190) = 12.840, (191) =
13.499, (192) = 13.840, (193) = 14.191, (194) = 14.550, (195) = 14.918, (196) =
15.683, (197) = 16.487, (198) = 16.905, (199) = 17.332, (200) = 19.640, (201) =
20.000})
interface(displayprecision = 30)
> # Uncomment to produce Integrals of PDFs
> # MCNP 5 Integral of PDF
for i to 200 do printf("%40.30f ", evalf(int(C*f(E), E = EE[i] .. EE[i+1]))) end
do
> # MCNP 6 Integral of PDF
for i to 200 do printf("%40.30f ", evalf(int(C6*f6(E), E = EE[i] .. EE[i+1])))
end do
> # Mannhart Integral of PDF
for i to 200 do printf("%40.30f ", evalf(int(Cm*N(E), E = EE[i] .. EE[i+1])))
end do
```

fig/mcnp/fission_spectrum.txt

C SCALE and Denovo Inputs

Denovo runs were started firstly by creating a SCALE input for MAVRIC. Materials were input using information from Table 6 and Table 7. Each detector component was given a unique material number, even if the actual material was the same composition as material in other components. By having unique material numbers for each component, this allows Denovo to track separate sensitivities that are not only a function of composition but also position and/or geometry within the problem. KENO VI geometry specifications were used when manually converting the MCNP input to SCALE. Mesh generation occured within the SCALE input deck.

MAVRIC was run in input mode to generate a shielded ampx cross section library for use in Denovo. The input was run twice with two separate versions of SCALE. Once, with SCALE6.1, to generate the ampx file and ice file. Agian, with a snapshot of a development version of SCALE dated 2012-05-22. This version contains a set of material mixer routines for volume averaging that tends to work well for Denovo and is preferred over the SCALE6.1 version. The development version would generate the matertial mixing file and binary xkba input file read in by Denovo. A covariance library for cross section uncertainty information was also obtained from the SCALE6.1 version.

With the necessary SCALE files generated, pykba input decks were set up to complete the forward, adjoint and sensitivity computations. Cross

sections and mesh information were read in from the SCALE files while run specific information, boundary conditions, Pn order, quadrature, tolerance, etc., were input in the pykba input files. Each file was then run in sequence to generate the corresponding sensitivities.

```
=mavric parm=(nodose,forinput)
Upright w/ FTC-CF-004
V7-200N47G
read comp
Al       1       6.023709E-02    END
Cd       2       4.633948E-02    END
C        3       4.078643E-02    END
H        3       8.157286E-02    END
He-3     4       1.001373E-04    END
C        4       2.503433E-06    END
H        4       1.001373E-05    END
Ar       4       2.253089E-05    END
He-3     5       1.001373E-04    END
C        5       2.503433E-06    END
H        5       1.001373E-05    END
Ar       5       2.253089E-05    END
Al       6       6.023709E-02    END
Al       7       6.023709E-02    END
Al       8       6.023709E-02    END
C        9       4.078643E-02    END
H        9       8.157286E-02    END
Al       10      6.023709E-02    END
C        11      4.078643E-02    END
H        11      8.157286E-02    END
Al       12      6.023709E-02    END
C        13      7.491768E-09    END
N        13      3.912866E-05    END
O        13      1.051248E-05    END
Ar       13      2.330027E-07    END
H-1      14      1.191457E-02    END
C        14      5.898872E-03    END
O-16     14      4.189230E-02    END
Mg       14      1.408077E-03    END
Al-27    14      1.891502E-03    END
Si       14      7.311340E-03    END
S        14      1.310802E-04    END
K        14      6.142366E-05    END
Ca       14      8.719047E-03    END
Fe       14      2.795390E-04    END
C        15      1.203336E-04    END
Si-28    15      7.910881E-04    END
Si-29    15      4.006868E-05    END
Si-30    15      2.652018E-05    END
P-31     15      3.499632E-05    END
S-32     15      2.139693E-05    END
S-33     15      1.461153E-07    END
S-34     15      9.928043E-07    END
Cr-50    15      7.649022E-04    END
Cr-52    15      1.475059E-02    END
Cr-53    15      1.672410E-03    END
Cr-54    15      4.163044E-04    END
Mn-55    15      8.769213E-04    END
Fe-54    15      3.572256E-03    END
Fe-56    15      5.553304E-02    END
Fe-57    15      1.271437E-03    END
Fe-58    15      1.695598E-04    END
Ni-58    15      5.183905E-03    END
Ni-60    15      1.981852E-03    END
Ni-61    15      8.578767E-05    END
Ni-62    15      2.725891E-04    END
Ni-64    15      6.910545E-05    END
Cf-252   16      3.607278E-02    END
end comp
read geometry
'unit              1
'com="He-3 Tube"
'cylinder           10        1.190625  58.89625  54.61000
'cylinder           20        1.190625  54.61000  3.810000
'cylinder           30        1.190625  3.810000  0.158750
'cylinder           40        1.270000  59.05500  0.000000
'cylinder           70        1.270000  60.64250  0.000000
'cylinder           70        1.270000  59.05500  0.000000
'media              5         1         10
'media              4         1         20
'media              5         1         30
'media              6         1         40 -10 -20 -30
'media              0         1         70 -40
'boundary           70
unit               1
com="He-3 Tube"
cylinder           10        1.270000  60.64250  0.000000
cylinder           20        1.190625  60.48375  56.19750
cylinder           30        1.190625  56.19750  5.397500
cylinder           40        1.190625  5.397500  1.746250
cylinder           50        1.270000  1.587500  0.000000
media              6         1         10 -20 -30 -40 -50
media              5         1         20
media              4         1         30
media              5         1         40
media              13        1         50
boundary           10
unit               2
com="HDPE Sheath"
cuboid             10        15.24000 -15.24000  5.080000 -3.810000  60.64250  0.000000
cylinder           20        1.270000  60.64250  0.000000  origin    x=-12.06500  y=0.0  z=0.0
cylinder           30        1.270000  60.64250  0.000000  origin    x=-6.032500  y=0.0  z=0.0
cylinder           40        1.270000  60.64250  0.000000  origin    x=0.0        y=0.0  z=0.0
cylinder           50        1.270000  60.64250  0.000000  origin    x=6.032500   y=0.0  z=0.0
cylinder           60        1.270000  60.64250  0.000000  origin    x=12.06500   y=0.0  z=0.0
hole               1         origin    x=-12.06500  y=0.0  z=0
hole               1         origin    x=-6.032500  y=0.0  z=0
hole               1         origin    x=0.0        y=0.0  z=0
hole               1         origin    x=6.032500   y=0.0  z=0
hole               1         origin    x=12.06500   y=0.0  z=0
media              3         1         10 -20 -30 -40 -50 -60
media              0         1         20 30 40 50 60
boundary           10
unit               3
com="Cadmium Sheath"
cuboid             10        15.39875 -15.39875  4.603750 -4.603750   60.80125  0.000000  origin    x=0.0     y=0.63500 z=-0.317500
```

```
cuboid             20        15.24000 -15.24000 -4.445000 -4.603750   60.80125  0.158750  origin    x=0.0     y=0.63500 z=-0.317500
hole               2         origin    x=0.0     y=0.0     z=0.0
'media              2          1          10
media              2         1         10 -20
media              13        1         20
boundary           10
unit               4
com="Aluminum Sheath"
cuboid             10        15.55750 -15.55750  4.762500 -4.762500  60.96000  0.000000  origin    x=0.0     y=0.63500 z=-0.476250
hole               3         origin    x=0.0     y=0.0     z=0.0
media              1         1         10
boundary           10
unit               5
com="Junction Box"
cuboid             10        15.55750 -15.55750  5.397500 -4.127500  10.16000  0.000000  origin    x=0.0     y=0.0     z=60.48375
cuboid             20        14.19098 -14.19098  4.030980 -2.760980  4.114800  0.812800  origin    x=0.0     y=0.0     z=60.48375
cuboid             30        14.77772 -14.77772  4.617720 -3.347720  9.380220  4.114800  origin    x=0.0     y=0.0     z=60.48375
cylinder           40        1.27000   0.812800  0.000000  origin    x=-12.06500  y=0.0  z=60.48375
cylinder           50        1.27000   0.812800  0.000000  origin    x=-6.032500  y=0.0  z=60.48375
cylinder           60        1.27000   0.812800  0.000000  origin    x=0.0        y=0.0  z=60.48375
cylinder           70        1.27000   0.812800  0.000000  origin    x=6.032500   y=0.0  z=60.48375
cylinder           80        1.27000   0.812800  0.000000  origin    x=12.06500   y=0.0  z=60.48375
media              7         1         10 -20 -30 -40 -50 -60 -70 -80
media              13        1         20
media              13        1         30
media              13        1         40
media              13        1         50
media              13        1         60
media              13        1         70
media              13        1         80
boundary           10
'unit               6
'com="Inner Cradle"
'cuboid              10         15.95438 -15.95438  0.000000 -10.89000  82.23250  0.000000  origin     x=0.0     y=5.71500 z=-5.873750
'cuboid              20         15.95438 -15.95438  0.000000 -8.890000  77.15250  5.080000  origin     x=0.0     y=5.71500 z=-5.873750
'cuboid              30         15.63688 -15.63688 -0.317500 -8.890000  76.83500  5.397500  origin     x=0.0     y=5.71500 z=-5.873750
'cuboid              40         15.95438 -15.95438 -8.572500 -8.890000  82.23250  77.15250  origin     x=0.0     y=5.71500 z=-5.873750
'cuboid              50         15.95438 -15.95438 -8.572500 -8.890000  5.080000  0.000000  origin     x=0.0     y=5.71500 z=-5.873750
'cuboid              60         15.95438  15.63688 -2.540000 -8.890000  74.61250  66.67500  origin     x=0.0     y=5.71500 z=-5.873750
'media               13         1          10 -20 -40 -50
'media               8          1          20 -30 -60
'media               13         1          30
'media               8          1          40
'media               8          1          50
'media               13         1          60
'hole                4          origin     x=0.0     y=0.0     z=0.0
'hole                5          origin     x=0.0     y=0.0     z=0.0
'boundary            10
unit               6
com="Inner Cradle"
cuboid             10        15.95438 -15.95438  0.000000 -10.89000  77.15250  5.080000  origin    x=0.0     y=5.71500 z=-5.873750
cuboid             20        15.95438 -15.95438  0.000000 -8.890000  77.15250  5.080000  origin    x=0.0     y=5.71500 z=-5.873750
cuboid             30        15.63688 -15.63688 -0.317500 -8.890000  76.83500  5.397500  origin    x=0.0     y=5.71500 z=-5.873750
'cuboid             40         15.95438 -15.95438 -8.572500 -8.890000  82.23250  77.15250  origin     x=0.0     y=5.71500 z=-5.873750
'cuboid             50         15.95438 -15.95438 -8.572500 -8.890000  5.080000  0.000000  origin     x=0.0     y=5.71500 z=-5.873750
cuboid             60        15.95438  15.63688 -2.540000 -8.890000  74.61250  66.67500  origin    x=0.0     y=5.71500 z=-5.873750
media              13        1         10 -20
media              8         1         20 -30 -60
media              13        1         30
'media              8          1          40
'media              8          1          50
media              13        1         60
hole               4         origin    x=0.0     y=0.0     z=0.0
hole               5         origin    x=0.0     y=0.0     z=0.0
boundary           10
unit               7
com="Inner Cradle HDPE"
cuboid             5         21.27250 -21.27250  14.60500 -2.000000  82.55000  0.000000  origin    x=0.0     y=-2.85750 z=-5.873750
cuboid             10        21.27250 -21.27250  14.60500  0.000000  82.55000  0.000000  origin    x=0.0     y=-2.85750 z=-5.873750
cuboid             20        16.19250 -16.19250  9.525000  0.000000  77.47000  5.080000  origin    x=0.0     y=-2.85750 z=-5.873750
cuboid             30        21.27250  16.19250  7.937500  0.000000  76.20000  67.94500  origin    x=0.0     y=-2.85750 z=-5.873750
cuboid             140       15.95438 -15.95438  0.000000 -0.317500  82.23250  77.15250  origin    x=0.0     y=-2.85750 z=-5.873750
cuboid             150       15.95438 -15.95438  0.000000 -0.317500  5.080000  0.000000  origin    x=0.0     y=-2.85750 z=-5.873750
ycylinder          40        0.952500  6.985000  0.000000  origin    x=-13.33500 y=-2.85750 z=-3.33375
ycylinder          50        0.952500  6.985000  0.000000  origin    x=-3.175000 y=-2.85750 z=-3.33375
ycylinder          60        0.952500  6.985000  0.000000  origin    x=3.175000  y=-2.85750 z=-3.33375
ycylinder          70        0.952500  6.985000  0.000000  origin    x=13.33500  y=-2.85750 z=-3.33375
ycylinder          80        0.952500  6.985000  0.000000  origin    x=-13.33500 y=-2.85750 z=74.13625
ycylinder          90        0.952500  6.985000  0.000000  origin    x=-3.175000 y=-2.85750 z=74.13625
ycylinder          100       0.952500  6.985000  0.000000  origin    x=3.175000  y=-2.85750 z=74.13625
ycylinder          110       0.952500  6.985000  0.000000  origin    x=13.33500  y=-2.85750 z=74.13625
media              13        1         5  -10 -140 -150
media              9         1         10 -20 -30 -40 -50 -60 -70 -80 -90 -100 -110
media              13        1         20
media              13        1         30
media              13        1         40
media              13        1         50
media              13        1         60
media              13        1         70
media              13        1         80
media              13        1         90
media              13        1         100
media              13        1         110
media              8         1         140
media              8         1         150
hole               6         origin    x=0.0     y=0.0     z=0.0
boundary           5         origin    x=0.0     y=0.0     z=0.0
unit               8
com="Outer Cradle"
cuboid             10        21.59000 -21.59000  0.000000 -17.55750  95.25000  0.000000  origin    x=0.0     y=12.0650 z=-11.58875
cuboid             20        21.59000 -21.59000  0.000000 -14.60500  89.85250  5.397500  origin    x=0.0     y=12.0650 z=-11.58875
cuboid             30        21.27250 -21.27250 -0.317500 -14.60500  89.53500  5.715000  origin    x=0.0     y=12.0650 z=-11.58875
cuboid             40        21.59000 -21.59000 -14.28750 -14.60500  95.25000  89.85250  origin    x=0.0     y=12.0650 z=-11.58875
cuboid             50        21.59000 -21.59000 -14.28750 -14.60500  5.397500  0.000000  origin    x=0.0     y=12.0650 z=-11.58875
cuboid             60        21.59000  21.27250 -6.350000 -14.60500  82.55000  73.97750  origin    x=0.0     y=12.0650 z=-11.58875
cuboid             70        6.350000 -6.350000 -15.24000 -15.55750  9.207500  5.080000  origin    x=0.0     y=12.0650 z=-11.58875
cuboid             80        6.350000 -6.350000 -14.60500 -15.24000  5.715000  5.080000  origin    x=0.0     y=12.0650 z=-11.58875
cuboid             90        21.59000 -21.59000  0.000000 -14.28750  5.397500  0.317500  origin    x=0.0     y=12.0650 z=-11.58875
cuboid             100       21.59000 -21.59000  0.000000 -14.28750  94.93250  89.85250  origin    x=0.0     y=12.0650 z=-11.58875
cuboid             110       21.59000 -21.59000  0.000000 -14.28750  0.317500  0.000000  origin    x=0.0     y=12.0650 z=-11.58875
cuboid             120       21.59000 -21.59000  0.000000 -14.28750  95.25000  94.93250  origin    x=0.0     y=12.0650 z=-11.58875
media              13        1         10 -20 -40 -50 -70 -80 -90 -100 -110 -120
media              10        1         20 -30 -60
media              13        1         30
media              10        1         40
media              10        1         50
media              13        1         60
media              10        1         70
media              10        1         80
media              11        1         90
media              11        1         100
media              12        1         110
media              12        1         120
hole               7         origin    x=0.0     y=0.0     z=0.0
boundary           10
unit               9
com="Outer Housing HDPE Back"
cuboid             10        21.59000 -21.59000  0.000000 -5.080000  84.45500  0.000000  origin    x=0.0     y=17.7800 z=-6.191250
media              11        1         10
boundary           10
unit               10
com="Outer Housing HDPE Top"
cuboid             10        21.59000 -21.59000  0.000000 -5.715000  89.53500  84.45500  origin    x=0.0     y=17.7800 z=-6.191250
media              11        1         10
boundary           10
```

```
unit              11
com="Outer Housing HDPE Bottom"
cuboid            10        21.59000 -21.59000  0.000000 -5.715000  0.000000   -5.080000  origin    x=0.0     y=17.7800 z=-6.191250
media             11        1         10
boundary          10
unit              12
com="Outer Housing HDPE Left"
cuboid            10       -21.59000 -26.67000  0.000000 -19.68500  89.53500 -5.080000  origin    x=0.0     y=17.7800 z=-6.191250
cuboid            20       -21.59000 -26.67000  0.000000 -19.36750  89.53500 -5.080000  origin    x=0.0     y=17.7800 z=-6.191250
cuboid            30       -21.59000 -26.67000 -19.36750 -19.68500  84.45500  0.000000  origin    x=0.0     y=17.7800 z=-6.191250
media             13        1         10 -20 -30
media             11        1         20
media             11        1         30
boundary          10
unit              13
com="Outer Housing HDPE Right"
cuboid            10        26.67000  21.59000  0.000000 -19.68500  89.53500 -5.080000  origin    x=0.0     y=17.7800 z=-6.191250
cuboid            20        26.67000  21.59000  0.000000 -19.36750  89.53500 -5.080000  origin    x=0.0     y=17.7800 z=-6.191250
cuboid            30        26.67000  21.59000 -19.36750 -19.68500  84.45500  0.000000  origin    x=0.0     y=17.7800 z=-6.191250
cuboid            40        26.67000  21.59000 -11.43000 -19.68500  77.15250  68.89750  origin    x=0.0     y=17.7800 z=-6.191250
media             13        1         10 -20 -30
media             11        1         20 -40
media             11        1         30 -40
media             13        1         40
boundary          10
unit              14
com="Outer Housing"
cuboid            10        27.38438 -27.38438  1.270000 -22.63750  95.25000  0.000000  origin    x=0.0     y=18.4150 z=-11.58875
cuboid            20        27.38438 -27.38438  0.000000 -20.63750  95.25000  0.000000  origin    x=0.0     y=18.4150 z=-11.58875
cuboid            30        27.06688 -27.06688 -0.317500 -20.32000  94.93250  0.317500  origin    x=0.0     y=18.4150 z=-11.58875
cuboid            40        21.98688 -21.98688 -20.32000 -20.63750  89.85250  5.397500  origin    x=0.0     y=18.4150 z=-11.58875
cuboid            50        27.38438  27.06688 -20.32000 -12.06500  82.23250  73.34250  origin    x=0.0     y=18.4150 z=-11.58875
cuboid            60        27.38438  21.98688 -20.32000 -20.63750  82.23250  73.34250  origin    x=0.0     y=18.4150 z=-11.58875
cuboid            70        27.38438 -27.38438  1.270000  0.000000  79.05750  75.24750  origin    x=0.0     y=18.4150 z=-11.58875
cuboid            80        27.38438 -27.38438  1.270000  0.000000  20.00250  16.19250  origin    x=0.0     y=18.4150 z=-11.58875
ycylinder         90        0.952500 -20.32000 -20.63750  origin    x=-19.12938 y=18.4150 z=-8.91865
ycylinder         100       0.952500 -20.32000 -20.63750  origin    x=-8.969380 y=18.4150 z=-8.91865
ycylinder         110       0.952500 -20.32000 -20.63750  origin    x=8.969380  y=18.4150 z=-8.91865
ycylinder         120       0.952500 -20.32000 -20.63750  origin    x=19.12938  y=18.4150 z=-8.91865
ycylinder         130       0.952500 -20.32000 -20.63750  origin    x=-19.12938 y=18.4150 z=80.99115
ycylinder         140       0.952500 -20.32000 -20.63750  origin    x=-8.969380 y=18.4150 z=80.99115
ycylinder         150       0.952500 -20.32000 -20.63750  origin    x=8.969380  y=18.4150 z=80.99115
ycylinder         160       0.952500 -20.32000 -20.63750  origin    x=19.12938  y=18.4150 z=80.99115
media             13        1         10 -20 -70 -80
media             12        1         20 -30 -40 -50 -60 -90 -100 -110 -120 -130 -140 -150 -160
media             13        1         30
media             13        1         40
media             13        1         50
media             13        1         60
media             12        1         70
media             12        1         80
media             13        1         90
media             13        1        100
media             13        1        110
media             13        1        120
media             13        1        130
media             13        1        140
media             13        1        150
media             13        1        160
hole              8         origin    x=0.0     y=0.0     z=0.0
hole              9         origin    x=0.0     y=0.0     z=0.0
hole              10        origin    x=0.0     y=0.0     z=0.0
hole              11        origin    x=0.0     y=0.0     z=0.0
hole              12        origin    x=0.0     y=0.0     z=0.0
hole              13        origin    x=0.0     y=0.0     z=0.0
boundary          10
unit              15
com="Floor"
cuboid            10        150.0000 -150.0000 150.0000 -150.00000  20.32000  0.000000  origin    x=0.0     y=0.00000 z=-33.178751
media             14        1         10
boundary          10
unit              16
com="Model 10 Californium Source"
cuboid            10        0.27686  -0.27686   0.27686  -0.27686   1.1803   -0.8009
zcylinder         20        0.27686   1.1803   -0.8009
zcylinder         30        0.19558   1.1803   -0.6104
zcylinder         40        0.19558   1.0041    0.6104
cuboid            50        0.05 -0.05  0.05 -0.05  0.05 -0.05
'sphere            50        1.681774274e-005
media             13        1         10 -20
media             15        1         20 -30
media             13        1         30 -40 -50
media             15        1         40
media             16        1         50
boundary          10
unit              17
cuboid            10       -200       200      -200       200       200.0    -200.0
cuboid            20       -150       150      -150       150       150.0    -150.0
media             0         1         10 -20
media             13        1         20
hole              14        origin    x=0.0     y=0.0     z=0.0
hole              15        origin    x=0.0     y=0.0     z=0.0
' Y-Position from -16 to -61
' a2=0 Vertical; a2=90 Horizontal facing away; a2=-90 Horizontal facing towards
hole              16        origin    x=0.0     y=-16.1275 z=29.21     rotate    a1=0.0    a2=0.0    a3=0.0
boundary          10
global unit       999
cuboid            10        200      -200       200      -200       200      -200
media             0         1         10
hole              17        origin    x=0       y=0       z=0       rotate    a1=-90      a2=-90      a3=90
boundary          10
end geometry
read definitions
gridGeometry 1
zplanes
27.384380
27.066880
26.670000
25.670000
24.670000
23.670000
22.670000
21.986880
21.590000
21.272500
20.522500
19.772500
19.022500
18.272500
17.522500
16.772500
16.192500
15.954380
15.636880
15.557500
15.398750
15.319375
15.240000
14.777720
14.190980
13.589000
13.081000
12.573000
12.065000
11.557000
```

```
11.049000
10.604500
10.096500
9.588500
9.080500
8.572500
8.064500
7.556500
7.048500
6.540500
6.350000
6.032500
5.524500
5.016500
4.572000
4.064000
3.556000
3.048000
2.540000
2.032000
1.524000
1.016000
0.508000
0.276860
0.138430
0.050000
0.000000 end
yplanes
19.685000
18.415000
18.097500
17.780000
17.280000
16.780000
16.280000
15.780000
15.280000
14.780000
14.280000
13.780000
13.280000
12.700000
12.065000
11.747500
11.167500
10.667500
10.167500
9.667500
9.167500
8.667500
8.167500
7.667500
7.167500
6.667500
6.350000
5.715000
5.397500
5.238750
5.159375
5.080000
4.617720
4.030980
3.175000
3.000000
2.750000
2.500000
2.250000
2.000000
1.750000
1.500000
1.250000
1.000000
0.750000
0.500000
0.250000
0.000000
-0.250000
-0.500000
-0.750000
-1.000000
-1.587500
-1.905000
-2.222500
-2.540000
-2.760980
-2.857500
-3.175000
-3.347720
-3.492500
-3.810000
-3.889375
-3.968750
-4.127500
-4.222500
-4.857500
-5.175000
-5.492500
-5.992500
-6.492500
-6.992500
-7.492500
-7.992500
-8.492500
-8.992500
-9.492500
-9.992500
-10.492500
-10.992500
-11.492500
-11.992500
-12.492500
-12.992500
-13.492500
-13.992500
-14.492500
-14.992500
-15.492500
-15.850640
-15.989070
-16.077500
-16.127500
-16.177500
-16.265930
-16.404360 end
xplanes
83.661250
83.343750
82.843750
82.343750
81.843750
81.343750
80.843750
80.343750
79.843750
79.343750
```

```
78.843750
78.263750
77.946250
76.676250
76.358750
75.858750
75.358750
74.858750
74.358750
73.858750
73.358750
72.858750
72.358750
71.596250
71.278750
70.961250
70.643750
69.863970
67.468750
64.598550
63.658750
62.706250
62.388750
62.071250
61.753750
61.296550
60.483750
59.483750
58.483750
57.483750
56.483750
55.483750
54.483750
53.483750
52.483750
51.483750
50.483750
49.483750
48.483750
47.483750
46.483750
45.483750
44.483750
43.483750
42.483750
41.483750
40.483750
39.483750
38.483750
37.483750
36.483750
35.483750
34.483750
33.483750
32.483750
31.483750
30.390300
29.825150
29.260000
29.210000
29.160000
28.784550
28.409100
27.409100
26.409100
25.409100
24.409100
23.409100
22.409100
21.409100
20.409100
19.409100
18.409100
17.409100
16.409100
15.409100
14.409100
13.409100
12.409100
11.409100
10.409100
9.409100
8.413750
7.413750
6.413750
5.413750
4.603750
3.603750
2.603750
1.603750
0.603750
0.000000
-0.158750
-0.317500
-0.476250
-0.793750
-2.381250
-3.381250
-4.381250
-5.873750
-6.191250
-6.508750
-7.508750
-8.508750
-9.508750
-10.508750
-11.271250
-11.588750
-12.858751
-14.358751
-15.858751
-17.358751
-22.358751
-27.358751
-33.178751 end
end gridGeometry
end definitions
read sources
   src 1
    strength=100
    neutrons
    sphere 0.0 origin x=20.0 y=0.0 z=1.0
   end src
end sources
read importanceMap
    gridGeometryid=1
    mmsubcells=1
    mmtolerance=0.0001
end importanceMap
end data
end
=shell
echo $TMPDIR
cp ${TMPDIR}/i_ice ${RTNDIR}/ice
cp ${TMPDIR}/ft42f001 ${RTNDIR}/xs42.ampx
```

```
cp ${TMPDIR}/xkba_b.inp ${RTNDIR}/xkba_b.inp
end
'zlinear 10 0.0 -150.0
```

fig/denovo/neup_scale.inp

```
#!/usr/bin/env python

# File automagically generated on Sun, 30 Nov 2014 13:18:56
# Copywrite (C) 2013 W. Cyrus Proctor & R. Todd Evans

import sys
import sc as denovo
import numpy as np

# Begin by initializing the MPI environment
denovo.initialize(sys.argv)

reader = denovo.Mavric_Binary_Input("xkba_b.inp")
db = denovo.DB("pykba")
reader.read_db(db)

# Specify the number of x-, y- and z- blocks plus number of energy sets for the solves
# based on the number of processes (nodes).Choices seen here are default and are free to change.
if denovo.nodes() == 1:
    db.insert("num_blocks_i", 1)
    db.insert("num_blocks_j", 1)
    db.insert("num_sets", 1)
elif denovo.nodes() == 2:
    db.insert("num_blocks_i", 2)
    db.insert("num_blocks_j", 1)
    db.insert("num_sets", 1)
elif denovo.nodes()== 4:
    db.insert("num_blocks_i", 2)
    db.insert("num_blocks_j", 2)
    db.insert("num_sets", 1)
elif denovo.nodes() == 8:
    db.insert("num_blocks_i", 2)
    db.insert("num_blocks_j", 2)
    db.insert("num_sets",2)
elif denovo.nodes() == 64:
    db.insert("num_blocks_i", 8)
    db.insert("num_blocks_j", 8)
    db.insert("num_sets",1)
else:
  print "ERROR: Set number of CPUs does not match default blocks * sets"
  exit(-1)

db.insert("problem_name","neup")
db.insert("eigen_solver","arnoldi")
db.insert("eq_set","1")

# Multi-group structure options
db.insert("num_groups",200)
db.insert("Pn_order",1)
db.insert("downscatter",0,1)
db.insert("partition_upscatter",1,1)
db.insert("transport_correction","none")

# Within-group solver options
db.insert("tolerance",1.0E-9)
db.insert("max_itr", 500)
db.insert("aztec_diag", 0)
db.insert("aztec_output", 0)

# Quadrature options
if denovo.node() != 0:
  db.add_db("quadrature_db", "quad_options")
db.insert("quadrature_db","quad_type","glproduct")
db.insert("quadrature_db", "polars_octant",12)
db.insert("quadrature_db", "azimuthals_octant",14)
db.insert("quadrature_db","adjoint",0,1)
db.insert("quadrature_db","Pn_order",1)

# boundary conditions
db.insert("boundary", "reflect")
db.add_db("boundary_db","reflect")
db.insert("boundary_db","reflect",[0, 0, 0, 0, 1, 0],1)

# output options
db.add_db("silo_db","silo_options")
db.insert("silo_db","silo_out_unknowns",1,1)
db.insert("silo_db","silo_out_moments",1,1)
#db.insert("silo_db","silo_out_keff",1,1)
db.insert("silo_db","silo_output","forward")

#db.insert("problem_type","EIGENVALUE")
db.insert("problem_type","FIXED_SOURCE")
db.insert("mg_solver","krylov")
db.add_db("upscatter_db", "upscatter");
db.insert("upscatter_db", "max_itr", 1000)
db.insert("upscatter_db", "tolerance", 1.0E-9)
db.insert("upscatter_db", "aztec_output", 1)
db.insert("upscatter_db", "aztec_kspace", 5)
db.insert("upscatter_db", "max_itr", 500)
db.insert("keff",1.0)
db.insert("add_fission_left",1,1)
# Add GPT database
db.add_db("gpt_db","gpt_options")
db.insert("gpt_db","source_data","source")

# Make manager, material, and angles
manager = denovo.Manager()
mat     = denovo.Mat()
source = denovo.Zero_Source()
angles  = denovo.Angles()

# partition the problem
manager.partition(db, mat, angles)

# get mapping and mesh objects
mapp    = manager.get_map()
indexer = manager.get_indexer()
mesh    = manager.get_mesh()

# global and local cell numbers
Gx = indexer.num_global(denovo.X)
Gy = indexer.num_global(denovo.Y)
Gz = mesh.num_cells_dim(denovo.Z)
Nx = mesh.num_cells_dim(denovo.X)
Ny = mesh.num_cells_dim(denovo.Y)
Nz = mesh.num_cells_dim(denovo.Z)

if denovo.node() == 0:
  print ">>> Partitioned global mesh with %i x %i x %i cells" % (Gx, Gy, Gz)

# Read in material IDs
matids = denovo.Vec_Int(mapp.num_global(),0)
```

```
for k in xrange(Gz):
   ids = denovo.Vec_Int(Gx*Gy,0)
   reader.read_ids(ids,k)
   for cell in xrange(Gx*Gy):
      matids[cell+k*Gx*Gy]=ids[cell]
reader.close()
denovo.barrier()
denovo.gsum_Vec_Int(matids)

# Read in the ampx microscopic cross section file and number density file
ampx = denovo.AMPX_Micro()
# ampx.read_AMPX(xs file,density file)
ampx.read_AMPX("xs42.ampx","ice")
# get the ampx ids
ampxids = ampx.ampx_ids()
mat.build(db,mapp)
mat.set_num(17)
# assign the vacuum
mat.assign_zero(0)
# here we convert ampx ids into material ids.
# then we read from the ampx class into the material class.
# the XS_DB class is under the material class Mat
C = int(1e6)
for aid in ampxids:
   mid = aid/C
   nid = aid - mid*C
   # mat.assign_ampx(material id,nuclide id,ampx id,ampx class, density file)
   mat.assign_ampx(mid,nid,aid,ampx,"ice")


# we can dump this to a SILO file for later use if desired
if denovo.node()==0: mat.write_SILO("XS_200")

# Build macroscopic xs's from micro for each materials
for mid in xrange(mat.num_mat()):
   mat.build_macro_mat(mid)

######## Cross sections are completely defined at this point
if denovo.node()==0:
   print "finished reading from input file"
# here we build the mixing table (materials are spatially homogenized)
table = denovo.Mixing_Table()
table.read("scale.mmt")
mixer = denovo.Macro_Mixer(mat)
mixer.read_table(table)
mixer.mix_with_global_ids(matids,mat)

# Output the geometry SILO file
silo = denovo.SILO()
silo.open("geometry")
silo.close()

# Assign source data
source_data = denovo.Source_Data(mat.num_groups());

# Mannhart 27-group PDF
if mat.num_groups() == 27:
   spectrum = np.array([ 4.246206E-13, 1.781829E-12, 2.541090E-12, 8.680554E-12, \
                         3.189175E-11, 3.335569E-11, 3.443406E-11, 1.907337E-10, \
                         1.207906E-10, 8.226006E-11, 1.225102E-10, 4.437715E-10, \
                         1.198695E-09, 1.254263E-08, 5.157869E-08, 3.665315E-07, \
                         5.542462E-06, 6.495629E-05, 7.073864E-04, 1.429646E-02, \
                         7.959341E-02, 1.657301E-01, 1.629723E-01, 1.105391E-01, \
                         2.306726E-01, 2.082133E-01, 2.720441E-02 ])

# Unexpected group structure
else:
   print "ERROR: forward.py: Expecting 27 energy group structure!"
   exit(-1)

source_mid = 16
source_nid = str(98252)
for g in xrange(mat.num_groups()):
    source_data.set(source_mid,source_nid,'S.F.',g,spectrum[g])
print source_data.get(source_mid)

# Assign response data
response_data = denovo.Source_Data(mat.num_groups());
MT = str(103) #'(n,p)'
MID = 4
NID = str(2003) #'He^3'
for g in xrange(mat.num_groups()):
    response_data.set(MID,NID,MT,g,
                      mat.rho(MID,int(NID))*mat.total(MID,int(NID),int(MT),g))


# here we partition, setup and solve
manager.partition_energy(mat,angles)

# Display the contents of the database on screen
db.output()

manager.setup(source_data)
manager.verify()
manager.solve(angles)
#eig = denovo.Eigenproblem()
#keff = eig.eigenvalue()

manager.output()
manager.compute_response("forward",response_data)
manager.clear()
if denovo.node() == 0:
   print "Homogeneous Run Complete"
manager.close()
denovo.finalize()
```

fig/denovo/forward.py

```
#!/usr/bin/env python

# File automagically generated on Sun, 30 Nov 2014 13:18:56
# Copywrite (C) 2013 W. Cyrus Proctor & R. Todd Evans

import sys
import sc as denovo
import numpy as np

# Begin by initializing the MPI environment
denovo.initialize(sys.argv)

reader = denovo.Mavric_Binary_Input("xkba_b.inp")
db = denovo.DB("pykba")
reader.read_db(db)
```

```
# Specify the number of x-, y- and z- blocks plus number of energy sets for the solves
# based on the number of processes (nodes).Choices seen here are default and are free to change.
if denovo.nodes() == 1:
    db.insert("num_blocks_i", 1)
    db.insert("num_blocks_j", 1)
    db.insert("num_sets", 1)
elif denovo.nodes() == 2:
    db.insert("num_blocks_i", 2)
    db.insert("num_blocks_j", 1)
    db.insert("num_sets", 1)
elif denovo.nodes()== 4:
    db.insert("num_blocks_i", 2)
    db.insert("num_blocks_j", 2)
    db.insert("num_sets", 1)
elif denovo.nodes() == 8:
    db.insert("num_blocks_i", 2)
    db.insert("num_blocks_j", 2)
    db.insert("num_sets",2)
elif denovo.nodes() == 64:
    db.insert("num_blocks_i", 8)
    db.insert("num_blocks_j", 8)
    db.insert("num_sets",1)
else:
  print "ERROR: Set number of CPUs does not match default blocks * sets"
  exit(-1)

db.insert("problem_name","neup")
db.insert("eigen_solver","arnoldi")
db.insert("eq_set","1")

# Multi-group structure options
db.insert("num_groups",200)
db.insert("Pn_order",1)
db.insert("downscatter",0,1)
db.insert("partition_upscatter",1,1)
db.insert("transport_correction","none")

# Within-group solver options
db.insert("tolerance",1.0E-9)
db.insert("max_itr", 500)
db.insert("aztec_diag", 0)
db.insert("aztec_output", 0)

# Quadrature options
if denovo.node() != 0:
  db.add_db("quadrature_db", "quad_options")
db.insert("quadrature_db","quad_type","glproduct")
db.insert("quadrature_db", "polars_octant",12)
db.insert("quadrature_db", "azimuthals_octant",14)
db.insert("quadrature_db","adjoint",1,1)
db.insert("quadrature_db","Pn_order",1)

# boundary conditions
db.insert("boundary", "reflect")
db.add_db("boundary_db","reflect")
db.insert("boundary_db","reflect",[0, 0, 0, 0, 1, 0],1)

# output options
db.add_db("silo_db","silo_options")
db.insert("silo_db","silo_out_unknowns",1,1)
db.insert("silo_db","silo_out_moments",1,1)
#db.insert("silo_db","silo_out_keff",1,1)
db.insert("silo_db","silo_output","adjoint")

#db.insert("problem_type","EIGENVALUE")
db.insert("problem_type","FIXED_SOURCE")
db.insert("mg_solver","krylov")
db.add_db("upscatter_db", "upscatter");
db.insert("upscatter_db", "max_itr", 1000)
db.insert("upscatter_db", "tolerance", 1.0E-9)
db.insert("upscatter_db", "aztec_output", 1)
db.insert("upscatter_db", "aztec_kspace", 5)
db.insert("upscatter_db", "max_itr", 500)
db.insert("keff",1.0)
db.insert("add_fission_left",1,1)
# Add GPT database
db.add_db("gpt_db","gpt_options")
db.insert("gpt_db","source_data","source")

# Make manager, material, and angles
manager = denovo.Manager()
mat     = denovo.Mat()
source = denovo.Zero_Source()
angles  = denovo.Angles()

# partition the problem
manager.partition(db, mat, angles)

# get mapping and mesh objects
mapp    = manager.get_map()
indexer = manager.get_indexer()
mesh    = manager.get_mesh()

# global and local cell numbers
Gx = indexer.num_global(denovo.X)
Gy = indexer.num_global(denovo.Y)
Gz = mesh.num_cells_dim(denovo.Z)
Nx = mesh.num_cells_dim(denovo.X)
Ny = mesh.num_cells_dim(denovo.Y)
Nz = mesh.num_cells_dim(denovo.Z)

if denovo.node() == 0:
  print ">>> Partitioned global mesh with %i x %i x %i cells" % (Gx, Gy, Gz)

# Read in material IDs
matids = denovo.Vec_Int(mapp.num_global(),0)
for k in xrange(Gz):
  ids = denovo.Vec_Int(Gx*Gy,0)
  reader.read_ids(ids,k)
  for cell in xrange(Gx*Gy):
    matids[cell+k*Gx*Gy]=ids[cell]
reader.close()
denovo.barrier()
denovo.gsum_Vec_Int(matids)

# Read in the ampx microscopic cross section file and number density file
ampx = denovo.AMPX_Micro()
# ampx.read_AMPX(xs file,density file)
ampx.read_AMPX("xs42.ampx","ice")
# get the ampx ids
ampxids = ampx.ampx_ids()
mat.build(db,mapp)
mat.set_num(17)
# assign the vacuum
mat.assign_zero(0)
# here we convert ampx ids into material ids.
# then we read from the ampx class into the material class.
# the XS_DB class is under the material class Mat
C = int(1e6)
for aid in ampxids:
  mid = aid/C
  nid = aid - mid*C
  # mat.assign_ampx(material id,nuclide id,ampx id,ampx class, density file)
  mat.assign_ampx(mid,nid,aid,ampx,"ice")
```

```
# we can dump this to a SILO file for later use if desired
if denovo.node()==0: mat.write_SILO("XS_27")

# Build macroscopic xs's from micro for each materials
for mid in xrange(mat.num_mat()):
  mat.build_macro_mat(mid)

######## Cross sections are completely defined at this point
if denovo.node()==0:
  print "finished reading from input file"
# here we build the mixing table (materials are spatially homogenized)
table = denovo.Mixing_Table()
table.read("scale.mmt")
mixer = denovo.Macro_Mixer(mat)
mixer.read_table(table)
mixer.mix_with_global_ids(matids,mat)

# Output the geometry SILO file
silo = denovo.SILO()
silo.open("geometry")
silo.close()


# Assign source data
source_data = denovo.Source_Data(mat.num_groups());

# Mannhart 27-group PDF
if mat.num_groups() == 27:
  spectrum = np.array([ 4.246206E-13, 1.781829E-12, 2.541090E-12, 8.680554E-12, \
                        3.189175E-11, 3.335569E-11, 3.443406E-11, 1.907337E-10, \
                        1.207906E-10, 8.226006E-11, 1.225102E-10, 4.437715E-10, \
                        1.198695E-09, 1.254263E-08, 5.157869E-08, 3.665315E-07, \
                        5.542462E-06, 6.495629E-05, 7.073864E-04, 1.429646E-02, \
                        7.959341E-02, 1.657301E-01, 1.629723E-01, 1.105391E-01, \
                        2.306726E-01, 2.082133E-01, 2.720441E-02 ])

# Unexpected group structure
else:
  print "ERROR: forward.py: Expecting 27 energy group structure!"
  exit(-1)



source_mid = 16
source_nid = str(98252)
for g in xrange(mat.num_groups()):
    source_data.set(source_mid,source_nid,'S.F.',g,spectrum[g])
print source_data.get(source_mid)

# Assign response data
response_data = denovo.Source_Data(mat.num_groups());
MT = str(103) #'(n,p)'
MID = 4
NID = str(2003) #'He^3'
for g in xrange(mat.num_groups()):
    response_data.set(MID,NID,MT,g,
                      mat.rho(MID,int(NID))*mat.total(MID,int(NID),int(MT),g))


# here we partition, setup and solve
manager.partition_energy(mat,angles)

# Display the contents of the database on screen
db.output()

manager.setup(response_data)
manager.verify()
manager.solve(angles)

manager.output()
manager.compute_response("adjoint",source_data)
manager.clear()
if denovo.node() == 0:
  print "Homogeneous Run Complete"
manager.close()
denovo.finalize()
```

fig/denovo/adjoint.py

```
#!/usr/bin/env python

# File automagically generated on Sun, 30 Nov 2014 19:41:49
# Copywrite (C) 2013 W. Cyrus Proctor & R. Todd Evans

import sys
import sc as denovo
import numpy as np

# Begin by initializing the MPI environment
denovo.initialize(sys.argv)

reader = denovo.Mavric_Binary_Input("xkba_b.inp")
db = denovo.DB("pykba")
reader.read_db(db)

# Specify the number of x-, y- and z- blocks plus number of energy sets for the solves
# based on the number of processes (nodes).Choices seen here are default and are free to change.
if denovo.nodes() == 1:
    db.insert("num_blocks_i", 1)
    db.insert("num_blocks_j", 1)
    db.insert("num_sets", 1)
elif denovo.nodes() == 2:
    db.insert("num_blocks_i", 2)
    db.insert("num_blocks_j", 1)
    db.insert("num_sets", 1)
elif denovo.nodes()== 4:
    db.insert("num_blocks_i", 2)
    db.insert("num_blocks_j", 2)
    db.insert("num_sets", 1)
elif denovo.nodes() == 8:
    db.insert("num_blocks_i", 2)
    db.insert("num_blocks_j", 2)
    db.insert("num_sets",2)
elif denovo.nodes() == 64:
    db.insert("num_blocks_i", 8)
    db.insert("num_blocks_j", 8)
    db.insert("num_sets",1)
else:
  print "ERROR: Set number of CPUs does not match default blocks * sets"
  exit(-1)

db.insert("problem_name","neup")
db.insert("eigen_solver","arnoldi")
```

```
db.insert("eq_set","1")

# Multi-group structure options
db.insert("num_groups",200)
db.insert("Pn_order",1)
db.insert("downscatter",0,1)
db.insert("partition_upscatter",1,1)
db.insert("transport_correction","none")

# Multi-group Eigenvalue solver options
db.add_db("eigenvalue_db","eigenvalue_options")
db.insert("eigenvalue_db","diagnostic_level", 2)
db.insert("eigenvalue_db","k_tolerance",1.0E-9)
db.insert("eigenvalue_db","L2_tolerance",1.0E-9)
db.insert("eigenvalue_db","energy_dep_ev",1,1)

# Within-group solver options
db.insert("tolerance",1.0E-9)
db.insert("max_itr", 500)
db.insert("aztec_diag", 0)
db.insert("aztec_output", 0)

# Quadrature options
if denovo.node() != 0:
  db.add_db("quadrature_db", "quad_options")
db.insert("quadrature_db","quad_type","glproduct")
db.insert("quadrature_db", "polars_octant",12)
db.insert("quadrature_db", "azimuthals_octant",14)
db.insert("quadrature_db","adjoint",1,1)
db.insert("quadrature_db","Pn_order",1)

# boundary conditions
db.insert("boundary", "reflect")
db.add_db("boundary_db","reflect")
db.insert("boundary_db","reflect",[0, 0, 0, 0, 1, 0],1)

# output options
db.add_db("silo_db","silo_options")
db.insert("silo_db","silo_out_unknowns",1,1)
db.insert("silo_db","silo_out_moments",1,1)
db.insert("silo_db","silo_out_keff",1,1)
db.insert("silo_db","silo_output","adjoint")

db.insert("problem_type","SENSITIVITY")
db.add_db("gpt_db","gpt_options")
db.insert("gpt_db","forward_input","forward")
db.insert("forward_input","forward")
db.insert("gpt_db","adjoint_input","adjoint")
db.insert("gpt_db","text_suq_file","sensitivity")
db.insert("gpt_db","silo_suq_file","sensitivity")

# Make manager, material, and angles
manager = denovo.Manager()
mat     = denovo.Mat()
source = denovo.General_Source()
angles  = denovo.Angles()

# partition the problem
manager.partition(db, mat, angles)

# get mapping and mesh objects
mapp    = manager.get_map()
indexer = manager.get_indexer()
mesh    = manager.get_mesh()

# global and local cell numbers
Gx = indexer.num_global(denovo.X)
Gy = indexer.num_global(denovo.Y)
Gz = mesh.num_cells_dim(denovo.Z)
Nx = mesh.num_cells_dim(denovo.X)
Ny = mesh.num_cells_dim(denovo.Y)
Nz = mesh.num_cells_dim(denovo.Z)

if denovo.node() == 0:
  print ">>> Partitioned global mesh with %i x %i x %i cells" % (Gx, Gy, Gz)

# Read in material IDs
matids = denovo.Vec_Int(mapp.num_global(),0)
for k in xrange(Gz):
  ids = denovo.Vec_Int(Gx*Gy,0)
  reader.read_ids(ids,k)
  for cell in xrange(Gx*Gy):
    matids[cell+k*Gx*Gy]=ids[cell]
reader.close()
denovo.barrier()
denovo.gsum_Vec_Int(matids)

# Read in the ampx microscopic cross section file and number density file
ampx = denovo.AMPX_Micro()
# ampx.read_AMPX(xs file,density file)
ampx.read_AMPX("xs42.ampx","ice")
# get the ampx ids
ampxids = ampx.ampx_ids()
mat.build(db,mapp)
mat.set_num(17)
# assign the vacuum
mat.assign_zero(0)
# here we convert ampx ids into material ids.
# then we read from the ampx class into the material class.
# the XS_DB class is under the material class Mat
C = int(1e6)
for aid in ampxids:
  mid = aid/C
  nid = aid - mid*C
  # mat.assign_ampx(material id,nuclide id,ampx id,ampx class, density file)
  mat.assign_ampx(mid,nid,aid,ampx,"ice")


# we can dump this to a SILO file for later use if desired
if denovo.node()==0: mat.write_SILO("XS_27")

# Build macroscopic xs's from micro for each materials
for mid in xrange(mat.num_mat()):
  mat.build_macro_mat(mid)

######## Cross sections are completely defined at this point
if denovo.node()==0:
  print "finished reading from input file"
# here we build the mixing table (materials are spatially homogenized)
table = denovo.Mixing_Table()
table.read("scale.mmt")
mixer = denovo.Macro_Mixer(mat)
mixer.read_table(table)
mixer.mix_with_global_ids(matids,mat)

# Assign source data
source_data = denovo.Source_Data(mat.num_groups());

# Mannhart 27-group PDF
if mat.num_groups() == 27:
  spectrum = np.array([ 4.246206E-13, 1.781829E-12, 2.541090E-12, 8.680554E-12, \
                        3.189175E-11, 3.335569E-11, 3.443406E-11, 1.907337E-10, \
                        1.207906E-10, 8.226006E-11, 1.225102E-10, 4.437715E-10, \
                        1.198695E-09, 1.254263E-08, 5.157869E-08, 3.665315E-07, \
                        5.542462E-06, 6.495629E-05, 7.073864E-04, 1.429646E-02, \
```

```
                        7.959341E-02, 1.657301E-01, 1.629723E-01, 1.105391E-01, \
                        2.306726E-01, 2.082133E-01, 2.720441E-02 ])

# Unexpected group structure
else:
  print "ERROR: forward.py: Expecting 27 energy group structure!"
  exit(-1)


source_mid = 16
source_nid = str(98252)
for g in xrange(mat.num_groups()):
    source_data.set(source_mid,source_nid,'S.F.',g,spectrum[g])
print source_data.get(source_mid)

# Assign response data
response_data = denovo.Source_Data(mat.num_groups());
MT = str(103) #'(n,p)'
MID = 4
NID = str(2003) #'He^3'
for g in xrange(mat.num_groups()):
    response_data.set(MID,NID,MT,g,
                      mat.rho(MID,int(NID))*mat.total(MID,int(NID),int(MT),g))


# here we partition, setup and solve
manager.partition_energy(mat,angles)

# Display the contents of the database on screen
db.output()

###### Compute the sensitivities
if denovo.node()==0: print "Start sensitivity coefficients"
manager.sc_coeff(mat,response_data,source_data)
manager.close()
denovo.finalize()
```

fig/denovo/sensitivity.py

4.5. Task E: Implement data integration and inverse methods

These methods build on recent advances in probabilistic inverse problems and data assimilation methods. Using sensitivities from the radiation transport simulator, the deterministic moments-based data assimilation method is computationally efficient, where the largest work is expended into the inversion of a small-to-medium covariance matrix. A Newton-type non-linear optimization method was employed here. Furthermore, we had anticipated the need to be a bound-constrained optimization method, so that unphysical solutions are precluded. The requirement for constrained optimization eliminates many optimization libraries as candidates for deployment in this module, but some libraries do provide this functionality. Monte Carlo methods for sampling the solution PDF were also examined, especially if the holdup problem solution PDF is found to have multiple local maxima. The University of South Carolina was responsible for completing this task.

The accomplishment of this task was reported in: Dan G. Cacuci and Madalina C. Badea, *MULTI-PRED: A Software Module for Reducing Uncertainties in Predicted Results through Data Assimilation, Model Calibration and Validation – MULTI-PRED User's Manual Version* 1, University of South Carolina, November 2016. This document is replicated on the following pages.

MULTI-PRED: A Software Module for Reducing Uncertainties in Predicted Results through Data Assimilation, Model Calibration and Validation
MULTI-PRED User's Manual Version 1

November 2016

Dan G. Cacuci and Madalina C. Badea

University of South Carolina
Department of Mechanical Engineering,
300 Main Street, Columbia, SC 29208, USA
badea@cec.sc.edu

Table of Contents

1 Fundamentals of Predictive Modeling

The MULTI-PRED module embodies the time-dependent predictive modeling methodology of Cacuci and Ionescu-Bujor [Ca2010a], which considers a time-dependent generic physical system comprises N_α^ν model parameters and N_r^ν distinct responses, respectively, at every time node $\nu = 1,2,\ldots,N_t$. Hence, at every time node ν, the (column) vector $\boldsymbol{\alpha}^\nu$ of J_α^ν system parameters, and the (column) vector $\boldsymbol{r}^\nu$ of J_r^ν measured responses can be represented in component form as

$$\boldsymbol{\alpha}^\nu = \left\{\alpha_n^\nu \,|\, n = 1,\ldots N_\alpha^\nu\right\}, \quad \boldsymbol{r}^\nu = \left\{r_i^\nu \,|\, i = 1,\ldots,N_r^\nu\right\}, \ \nu = 1,\ldots,N_t \tag{1.1}$$

At any time node ν, the system parameters are considered to be variates with mean values $\left(\boldsymbol{\alpha}^0\right)^\nu$. Furthermore, the correlations between two parameters α_i^ν and α_j^μ, at two time nodes μ and ν, have the general form

$$c_{\alpha,ij}^{\nu\mu} \equiv \left\langle \left[\alpha_i^\nu - \left(\alpha_i^\nu\right)^0\right]\left[\alpha_j^\mu - \left(\alpha_j^\mu\right)^0\right]\right\rangle \tag{1.2}$$

The above covariances constitute the elements of symmetric covariance matrices of the form

$$\boldsymbol{C}_\alpha^{\mu\nu} \equiv \left\langle \left(\boldsymbol{\alpha} - \boldsymbol{\alpha}^0\right)^\mu \left[\left(\boldsymbol{\alpha} - \boldsymbol{\alpha}^0\right)^\nu\right]^\dagger \right\rangle = \left(\boldsymbol{C}_\alpha^{\mu\nu}\right)^\dagger = \boldsymbol{C}_\alpha^{\nu\mu} = \left(\boldsymbol{C}_\alpha^{\nu\mu}\right)^\dagger \tag{1.3}$$

Similarly, the measured responses are characterized by mean values $(\boldsymbol{r}_m)^\nu$ at a time node ν, and by symmetric covariance matrices between two time nodes μ and ν defined as

$$\boldsymbol{C}_m^{\mu\nu} \equiv \left\langle (\boldsymbol{r} - \boldsymbol{r}_m)^\mu \left[(\boldsymbol{r} - \boldsymbol{r}_m)^\nu\right]^\dagger \right\rangle = \left(\boldsymbol{C}_m^{\mu\nu}\right)^\dagger = \boldsymbol{C}_m^{\nu\mu} = \left(\boldsymbol{C}_m^{\nu\mu}\right)^\dagger \tag{1.4}$$

In the most general case, the measured responses may be correlated to the parameters through symmetric response-parameter uncertainty matrices of the form

$$\boldsymbol{C}_{r\alpha}^{\mu\nu} \equiv \left\langle \left(\boldsymbol{r}-\boldsymbol{r}_m\right)^{\mu}\left[\left(\boldsymbol{\alpha}-\boldsymbol{\alpha}^0\right)^{\nu}\right]^{\dagger}\right\rangle = \left(\boldsymbol{C}_{r\alpha}^{\mu\nu}\right)^{\dagger} = \boldsymbol{C}_{r\alpha}^{\nu\mu} = \left(\boldsymbol{C}_{r\alpha}^{\nu\mu}\right)^{\dagger} \tag{1.5}$$

Note that the matrices $\boldsymbol{C}_{r\alpha}^{\mu\nu}$ are not bona-fide variance-covariance matrices, in that they are not necessarily square positive matrices (often, they are rectangular), and the elements on their respective main diagonals (if they happen to be square) are also covariances (or correlations) rather that variances.

At any given time node ν, a response r_i^{ν} can be a function of not only the system parameters at time node ν, but also of the system parameters at all previous time nodes μ, $1 \le \mu \le \nu$; this means that $\boldsymbol{r}^{\nu} = \boldsymbol{R}^{\nu}\left(\boldsymbol{p}^{\nu}\right)$, where the vector $\boldsymbol{p}^{\nu} \equiv \left(\boldsymbol{\alpha}^1,\ldots,\boldsymbol{\alpha}^{\mu},\ldots,\boldsymbol{\alpha}^{\nu}\right)$ has been introduced for notational convenience. In general, the response computed using the model depends nonlinearly and implicitly (in an analytically intractable form) on the model parameters. Furthermore, the uncertainties in parameters and modeling induce uncertainties in the computed responses, and can be computed either by means of statistical methods (for relatively simple models with few parameters) or deterministically, by using the propagation of moments (errors) method, as described by [Ca2003]. In this method, the computed response is linearized via a functional Taylor-series expansion around the nominal values, $\boldsymbol{p}_0^{\nu} \equiv \left(\left(\boldsymbol{\alpha}^0\right)^1,\ldots,\left(\boldsymbol{\alpha}^0\right)^{\mu},\ldots,\left(\boldsymbol{\alpha}^0\right)^{\nu}\right)$, of the parameters $\boldsymbol{p}^{\nu}$, as follows:

$$\boldsymbol{r}^{\nu} = \boldsymbol{R}^{\nu}\left(\boldsymbol{p}^{\nu}\right) = \boldsymbol{R}^{\nu}\left(\boldsymbol{p}_0^{\nu}\right) + \sum_{\mu=1}^{\nu} \boldsymbol{S}^{\nu\mu}\left(\boldsymbol{p}_0^{\mu}\right)\left[\boldsymbol{\alpha}^{\mu} - \left(\boldsymbol{\alpha}^0\right)^{\mu}\right] + \ldots,\ \nu = 1,\ldots,N_t, \tag{1.6}$$

where $\boldsymbol{R}^{\nu}\left(\boldsymbol{p}_0^{\nu}\right)$ denotes the vector of computed responses at a time node ν, at the nominal parameter values $\boldsymbol{p}_0^{\nu}$, while $\boldsymbol{S}^{\nu\mu}\left(\boldsymbol{p}_0^{\mu}\right)$, $1 \le \mu \le \nu$, represents the $\left(J_r^{\nu} \times J_{\alpha}^{\mu}\right)$-dimensional matrix containing the first Gateaux-derivatives of the computed responses with respect to the parameters, defined as

$$\boldsymbol{S}^{\nu\mu}\left(\boldsymbol{p}_0^{\mu}\right)\equiv\begin{pmatrix} s_{11}^{\nu\mu} & \cdots & s_{1N}^{\nu\mu} \\ \vdots & s_{in}^{\nu\mu} & \vdots \\ s_{I1}^{\nu\mu} & \cdots & s_{IN}^{\nu\mu} \end{pmatrix}\equiv\begin{pmatrix} \dfrac{\partial R_1^{\nu}\left(\boldsymbol{p}_0^{\mu}\right)}{\partial\alpha_1^{\mu}} & \cdots & \dfrac{\partial R_1^{\nu}\left(\boldsymbol{p}_0^{\mu}\right)}{\partial\alpha_N^{\mu}} \\ \vdots & \dfrac{\partial R_i^{\nu}}{\partial\alpha_n^{\mu}} & \vdots \\ \dfrac{\partial R_I^{\nu}\left(\boldsymbol{p}_0^{\mu}\right)}{\partial\alpha_1^{\mu}} & \cdots & \dfrac{\partial R_I^{\nu}\left(\boldsymbol{p}_0^{\mu}\right)}{\partial\alpha_N^{\mu}} \end{pmatrix},1\le\mu\le\nu \tag{1.7}$$

Since the response $\boldsymbol{R}^{\nu}\left(\boldsymbol{p}_0^{\nu}\right)$ at time node ν can depend only on parameters $\left(\boldsymbol{\alpha}^0\right)^{\mu}$ which appear up to the current time node ν, it follows that $\boldsymbol{S}^{\nu\mu}=\boldsymbol{0}$ when $\mu>\nu$, and hence non-zero terms in the expansion shown in (1.6) can only occur in the range $1\le\mu\le\nu$. It is important to note that discretization parameters are also included among the components of $\boldsymbol{\alpha}$, and the sensitivities of responses to such discretization parameters can be computed as described in [Ca2003].

By introducing the block matrix

$$\boldsymbol{S}\equiv\begin{pmatrix} \boldsymbol{S}^{11} & \cdots & \boldsymbol{0} \\ \vdots & \ddots & \vdots \\ \boldsymbol{S}^{N_t1} & \cdots & \boldsymbol{S}^{N_tN_t} \end{pmatrix}, \tag{1.8}$$

and the (block) column vectors

$$\boldsymbol{\alpha}\equiv\left(\boldsymbol{\alpha}^1,\ldots,\boldsymbol{\alpha}^{\mu},\ldots,\boldsymbol{\alpha}^{N_t}\right), \tag{1.9}$$

$$\boldsymbol{r}\equiv\left(\boldsymbol{r}^1,\ldots,\boldsymbol{r}^{\mu},\ldots,\boldsymbol{r}^{N_t}\right), \tag{1.10}$$

$$\boldsymbol{R}\left(\boldsymbol{\alpha}^0\right)\equiv\left(\boldsymbol{R}^1,\ldots,\boldsymbol{R}^{\mu},\ldots,\boldsymbol{R}^{N_t}\right), \tag{1.11}$$

the system shown in (1.6) can be written in the form

$$\boldsymbol{r}=\boldsymbol{R}\left(\boldsymbol{\alpha}^0\right)+\boldsymbol{S}\left(\boldsymbol{\alpha}-\boldsymbol{\alpha}^0\right)+\textit{higher order terms} \tag{1.12}$$

Applying the propagation of errors method to (1.12), which involves the formal integration of the over the unknown joint distributions of the parameters $\boldsymbol{\alpha}$, yields the following expressions for the expectation value, $\langle \boldsymbol{r} \rangle$, of the response $\boldsymbol{r}$, and the corresponding covariance matrix, $\boldsymbol{C}_{rc}\left(\boldsymbol{\alpha}^0\right)$, of the computed responses, i.e.,

$$\langle \boldsymbol{r} \rangle = \boldsymbol{R}\left(\boldsymbol{\alpha}^0\right), \tag{1.13}$$

and

$$\boldsymbol{C}_{rc}\left(\boldsymbol{\alpha}^0\right) \equiv \left\langle \delta \boldsymbol{r} \delta \boldsymbol{r}^\dagger \right\rangle = \left[\boldsymbol{S}\left(\boldsymbol{\alpha}^0\right)\right] \left\langle \delta \boldsymbol{\alpha} \delta \boldsymbol{\alpha}^\dagger \right\rangle \left[\boldsymbol{S}\left(\boldsymbol{\alpha}^0\right)\right]^\dagger = \left[\boldsymbol{S}\left(\boldsymbol{\alpha}^0\right)\right] \boldsymbol{C}_\alpha \left[\boldsymbol{S}\left(\boldsymbol{\alpha}^0\right)\right]^\dagger . \tag{1.14}$$

The covariance matrix of the computed responses, $\boldsymbol{C}_{rc}$, has the symmetric structure

$$\boldsymbol{C}_{rc} \equiv \begin{pmatrix} \boldsymbol{C}_{rc}^{11} & \cdots & \boldsymbol{C}_{rc}^{1N_t} \\ \vdots & \ddots & \vdots \\ \boldsymbol{C}_{rc}^{N_t 1} & \cdots & \boldsymbol{C}_{rc}^{N_t N_t} \end{pmatrix},$$

with components defined as

$$\boldsymbol{C}_{rc}^{\nu\mu} = \sum_{\eta=1}^{\nu} \sum_{\rho=1}^{\mu} \boldsymbol{S}^{\nu\eta} \boldsymbol{C}_\alpha^{\eta\rho} \left(\boldsymbol{S}^{\mu\rho}\right)^\dagger = \left(\boldsymbol{C}_{rc}^{\mu\nu}\right)^\dagger ; \quad \nu, \mu = 1, ..., N_t . \tag{1.15}$$

As indicated by (1.13), the expectation value of the computed responses for linearized models in which the numerical errors are neglected is given by the value of the response computed at the nominal parameter-values.

According to the maximum entropy algorithm described in [Ca2010a], to the computational and experimental information described in (1.1) through (1.15) indicates that the most objective probability distribution for this information is a multivariate Gaussian of the form

$$p(z|\boldsymbol{C})d(z)=\frac{exp\left[-\frac{1}{2}Q(z)\right]}{det(2\pi\boldsymbol{C})^{1/2}}d(z)\,,\ Q(z)\equiv z^{\dagger}\,\boldsymbol{C}^{-1}z\,,-\infty<z_j<\infty \tag{1.16}$$

where:

$$z\equiv\begin{pmatrix}\boldsymbol{\alpha}-\boldsymbol{\alpha}^0\\ \boldsymbol{r}-\boldsymbol{r}_m\end{pmatrix},\boldsymbol{\alpha}^0\triangleq\left(\left(\boldsymbol{\alpha}^0\right)^1,\ldots,\left(\boldsymbol{\alpha}^0\right)^{\mu},\ldots,\left(\boldsymbol{\alpha}^0\right)^{N_t}\right), \tag{1.17}$$

$$\boldsymbol{C}\equiv\begin{pmatrix}\boldsymbol{C}_{\alpha} & \boldsymbol{C}_{\alpha r}\\ \boldsymbol{C}_{r\alpha} & \boldsymbol{C}_{m}\end{pmatrix}, \tag{1.18}$$

with

$$\boldsymbol{C}_{\alpha}=\begin{pmatrix}\boldsymbol{C}_{\alpha}^{11} & \boldsymbol{C}_{\alpha}^{12} & \ldots & \ldots\\ \boldsymbol{C}_{\alpha}^{21} & \boldsymbol{C}_{\alpha}^{22} & \ldots & \ldots\\ \ldots & \ldots & \ldots & \ldots\\ \ldots & \ldots & \ldots & \boldsymbol{C}_{\alpha}^{N_tN_t}\end{pmatrix},\boldsymbol{C}_{\alpha r}=\begin{pmatrix}\boldsymbol{C}_{\alpha r}^{11} & \boldsymbol{C}_{\alpha r}^{12} & \ldots & \ldots\\ \boldsymbol{C}_{\alpha r}^{21} & \boldsymbol{C}_{\alpha r}^{22} & \ldots & \ldots\\ \ldots & \ldots & \ldots & \ldots\\ \ldots & \ldots & \ldots & \boldsymbol{C}_{\alpha r}^{N_tN_t}\end{pmatrix}\ \text{and}$$

$$\boldsymbol{C}_{m}=\begin{pmatrix}\boldsymbol{C}_{m}^{11} & \boldsymbol{C}_{m}^{12} & \ldots & \ldots\\ \boldsymbol{C}_{m}^{21} & \boldsymbol{C}_{m}^{22} & \ldots & \ldots\\ \ldots & \ldots & \ldots & \ldots\\ \ldots & \ldots & \ldots & \boldsymbol{C}_{m}^{N_tN_t}\end{pmatrix}.$$

The posterior information, which is contained in (1.16) and (1.12), can now be condensed into a recommended best-estimate value $\left(z^{be}\right)^{\nu}$ at a time node ν for the parameters $\boldsymbol{\alpha}^{\nu}$ and responses $\boldsymbol{r}^{\nu}$, together with corresponding best-estimate recommended uncertainties for these quantities. If a loss function is given, decision theory indicates how these best-estimate quantities are to be computed. If no specific loss function is provided, the recommended best-estimate updated posterior mean vector $\left(z^{be}\right)^{\nu}$ and its respective best-estimate posterior covariance matrix are usually evaluated by assuming "quadratic loss". In such a case, the bulk of the contribution to the distribution $p(z|\boldsymbol{C})$ in (1.16) is extracted by computing it at the point in phase space where the respective exponent attains its minimum, subject to (1.12). Subsequent computations are facilitated by recasting (1.12) in the form

$$\boldsymbol{Z}\left(\boldsymbol{\alpha}^0\right)z+\boldsymbol{d}=\boldsymbol{0}\,,\quad \boldsymbol{d}\equiv\boldsymbol{R}\left(\boldsymbol{\alpha}^0\right)-\boldsymbol{r}_m\,, \tag{1.19}$$

where $\boldsymbol{r}_m\equiv\left(\boldsymbol{r}_m^1,\ldots,\boldsymbol{r}_m^\mu,\ldots,\boldsymbol{r}_m^{N_t}\right)$ is the vector comprising all of the experimentally measured responses, $\boldsymbol{d}\equiv\boldsymbol{R}\left(\boldsymbol{\alpha}^0\right)-\boldsymbol{r}_m$ is a vector of "deviations" reflecting the discrepancies between the nominal computations and the nominally measured responses, while $\boldsymbol{Z}$ denotes the partitioned matrix

$$\boldsymbol{Z}\equiv\left(\boldsymbol{S}\quad\boldsymbol{U}\right);\quad \boldsymbol{U}\equiv\begin{pmatrix}-\boldsymbol{I}^{11} & \cdots & \boldsymbol{0}\\ \vdots & \ddots & \vdots\\ \boldsymbol{0} & \cdots & -\boldsymbol{I}^{N_tN_t}\end{pmatrix}, \tag{1.20}$$

where $\boldsymbol{I}^{\nu\nu},\nu=1,\ldots,N_t$, denotes the identity matrix of corresponding dimensions.

Computing the stationary point of $Q(z)$ subject to (1.19) poses a constrained minimization problem which can be solved by introducing Lagrange multipliers, $\boldsymbol{\lambda}$, to construct the augmented Lagrangian functional $P(z,\boldsymbol{\lambda})$ defined as

$$P\left(z,\boldsymbol{\lambda}\right)\equiv Q\left(z\right)+2\boldsymbol{\lambda}^\dagger\left[\boldsymbol{Z}\left(\boldsymbol{\alpha}^0\right)z+\boldsymbol{d}\right]=min,\ at\ z=z^{be}\equiv\begin{pmatrix}\boldsymbol{\alpha}^{be}-\boldsymbol{\alpha}^0\\ \boldsymbol{r}^{be}-\boldsymbol{r}_m\end{pmatrix}. \tag{1.21}$$

where $\boldsymbol{\lambda}=\left(\boldsymbol{\lambda}^1,\ldots,\boldsymbol{\lambda}^\nu,\ldots,\boldsymbol{\lambda}^{N_t}\right)$ denotes the corresponding vector of Lagrange multipliers. In the above expression, the superscript "be" denotes "best-estimated values", and the factor "2" was introduced for convenience in front of $\boldsymbol{\lambda}$ in order to simplify the subsequent algebraic derivations. The point z^{be} where the functional $P(z,\boldsymbol{\lambda})$ attains its extremum (minimum) is defined implicitly through the conditions

$$\nabla_z P\left(z,\boldsymbol{\lambda}\right)=\boldsymbol{0},\quad \nabla_{\boldsymbol{\lambda}} P\left(z,\boldsymbol{\lambda}\right)=\boldsymbol{0},\quad at\ z=z^{be}\,. \tag{1.22}$$

The solution to the above constrained minimization problem leads to the following final results for the predictive best-estimate parameters, responses, and their corresponding reduced uncertainties (covariance matrices) are as follows:

1. The best-estimate predicted nominal values for the calibrated (adjusted) parameters:

$$\boldsymbol{\alpha}^{be} = \boldsymbol{\alpha}^0 + \left(\boldsymbol{C}_{\alpha r} - \boldsymbol{C}_{\alpha} \left[\boldsymbol{S}\left(\boldsymbol{\alpha}^0\right) \right]^{\dagger} \right) \left[\boldsymbol{C}_d \left(\boldsymbol{\alpha}^0\right) \right]^{-1} \boldsymbol{d} \,. \tag{1.23}$$

In component form, the above expression for the calibrated best-estimate parameter values becomes

$$\left(\boldsymbol{\alpha}^{be}\right)^{\nu} = \left(\boldsymbol{\alpha}^0\right)^{\nu} + \sum_{\mu=1}^{N_t} \left\{ \left[\boldsymbol{C}_{\alpha r}^{\nu\mu} - \sum_{\rho=1}^{\mu} \boldsymbol{C}_{\alpha}^{\nu\rho} \left(\boldsymbol{S}^{\dagger} \right)^{\mu\rho} \right] \left[\sum_{\eta=1}^{N_t} \boldsymbol{K}_d^{\mu\eta} \boldsymbol{d}^{\eta} \right] \right\}, \quad \nu = 1,\ldots,N_t \,, \tag{1.24}$$

where $\boldsymbol{K}_d^{\nu\eta}$ denotes the corresponding (ν,η)-element of the block-matrix $\boldsymbol{C}_d^{-1}$, with the block-matrix $\boldsymbol{C}_d\left(\boldsymbol{\alpha}^0\right)$ defined as follows:

$$\begin{aligned} \boldsymbol{C}_d \left(\boldsymbol{\alpha}^0\right) \equiv \left\langle \boldsymbol{d}\boldsymbol{d}^{\dagger} \right\rangle &= \left\langle \left(\delta\boldsymbol{r} - \boldsymbol{S}\left(\boldsymbol{\alpha}^0\right) \delta\boldsymbol{\alpha} \right) \left(\delta\boldsymbol{r}^{\dagger} - \delta\boldsymbol{\alpha}^{\dagger} \left[\boldsymbol{S}\left(\boldsymbol{\alpha}^0\right) \right]^{\dagger} \right) \right\rangle \\ &= \boldsymbol{C}_{rc}\left(\boldsymbol{\alpha}^0\right) - \boldsymbol{C}_{r\alpha} \left[\boldsymbol{S}\left(\boldsymbol{\alpha}^0\right) \right]^{\dagger} - \left[\boldsymbol{S}\left(\boldsymbol{\alpha}^0\right) \right] \boldsymbol{C}_{\alpha r} + \boldsymbol{C}_m . \end{aligned} \tag{1.25}$$

In component form, the matrix $\boldsymbol{C}_d$ is expressed as

$$\begin{aligned} \boldsymbol{C}_d \equiv \begin{pmatrix} \boldsymbol{C}_d^{11} & \cdots & \boldsymbol{C}_d^{1N_t} \\ \vdots & \ddots & \vdots \\ \boldsymbol{C}_d^{N_t 1} & \cdots & \boldsymbol{C}_d^{N_t N_t} \end{pmatrix} &= \begin{pmatrix} \boldsymbol{C}_{rc}^{11} + \boldsymbol{C}_m^{11} & \cdots & \boldsymbol{C}_{rc}^{1N_t} + \boldsymbol{C}_m^{1N_t} \\ \vdots & \ddots & \vdots \\ \boldsymbol{C}_{rc}^{N_t 1} + \boldsymbol{C}_m^{N_t 1} & \cdots & \boldsymbol{C}_{rc}^{N_t N_t} + \boldsymbol{C}_m^{N_t N_t} \end{pmatrix} \\ - \begin{pmatrix} \boldsymbol{C}_{r\alpha}^{11} \left(\boldsymbol{S}^{\dagger} \right)^{11} + \boldsymbol{S}^{11} \boldsymbol{C}_{\alpha r}^{11} & \cdots & \boldsymbol{S}^{11} \boldsymbol{C}_{\alpha r}^{1N_t} + \sum_{\rho=1}^{N_t} \boldsymbol{C}_{r\alpha}^{1\rho} \left(\boldsymbol{S}^{\dagger} \right)^{N_t \rho} \\ \vdots & \ddots & \vdots \\ \boldsymbol{C}_{r\alpha}^{N_t 1} \left(\boldsymbol{S}^{\dagger} \right)^{11} + \sum_{\rho=1}^{N_t} \boldsymbol{S}^{N_t \rho} \boldsymbol{C}_{\alpha r}^{\rho 1} & \cdots & \sum_{\rho=1}^{N_t} \left[\boldsymbol{C}_{r\alpha}^{N_t \rho} \left(\boldsymbol{S}^{\dagger} \right)^{N_t \rho} + \boldsymbol{S}^{N_t \rho} \boldsymbol{C}_{\alpha r}^{\rho N_t} \right] \end{pmatrix} . \end{aligned} \tag{1.26}$$

2. The best-estimate predicted nominal values for the calibrated (adjusted) responses:

$$\boldsymbol{r}\left(\boldsymbol{\alpha}^{be}\right) = \boldsymbol{r}_m + \left(\boldsymbol{C}_m - \boldsymbol{C}_{r\alpha} \left[\boldsymbol{S}\left(\boldsymbol{\alpha}^0\right) \right]^{\dagger} \right) \left[\boldsymbol{C}_d \left(\boldsymbol{\alpha}^0\right) \right]^{-1} \boldsymbol{d} \,. \tag{1.27}$$

At a specific time node ν, each component $\left(\boldsymbol{r}^{be}\right)^{\nu}$ of $\boldsymbol{r}\left(\boldsymbol{\alpha}^{be}\right)$ has the explicit form

$$\left(\boldsymbol{r}^{be}\right)^{\nu}=\left(\boldsymbol{r}_{m}\right)^{\nu}+\sum_{\mu=1}^{N_t}\left\{\left[\boldsymbol{C}_{m}^{\nu\mu}-\sum_{\rho=1}^{\mu}\boldsymbol{C}_{r\alpha}^{\nu\rho}\left(\boldsymbol{S}^{\dagger}\right)^{\mu\rho}\right]\left[\sum_{\eta=1}^{N_t}\boldsymbol{K}_{d}^{\mu\eta}\boldsymbol{d}^{\eta}\right]\right\},\quad \nu=1,\ldots,N_t\,. \tag{1.28}$$

3. The expressions for the best-estimate predicted covariances $\boldsymbol{C}_{\alpha}^{be}$ and $\boldsymbol{C}_{r}^{be}$, corresponding to the best-estimate parameters $\boldsymbol{\alpha}^{be}$ and responses $\boldsymbol{r}\left(\boldsymbol{\alpha}^{be}\right)$, together with the predicted best-estimate parameter-response covariance matrix $\boldsymbol{C}_{\alpha r}^{be}$:

$$\begin{aligned}\boldsymbol{C}_{\alpha}^{be}&\equiv\left\langle\left(\boldsymbol{\alpha}-\boldsymbol{\alpha}^{be}\right)\left(\boldsymbol{\alpha}-\boldsymbol{\alpha}^{be}\right)^{\dagger}\right\rangle\\&=\boldsymbol{C}_{\alpha}-\left[\boldsymbol{C}_{\alpha d}\left(\boldsymbol{\alpha}^{0}\right)\right]\left[\boldsymbol{C}_{d}\left(\boldsymbol{\alpha}^{0}\right)\right]^{-1}\left[\boldsymbol{C}_{\alpha d}\left(\boldsymbol{\alpha}^{0}\right)\right]^{\dagger},\end{aligned} \tag{1.29}$$

$$\begin{aligned}\boldsymbol{C}_{r}^{be}&\equiv\left\langle\left(\boldsymbol{r}-\boldsymbol{r}\left(\boldsymbol{\alpha}^{be}\right)\right)\left(\boldsymbol{r}-\boldsymbol{r}\left(\boldsymbol{\alpha}^{be}\right)\right)^{\dagger}\right\rangle\\&=\boldsymbol{C}_{m}-\left[\boldsymbol{C}_{rd}\left(\boldsymbol{\alpha}^{0}\right)\right]\left[\boldsymbol{C}_{d}\left(\boldsymbol{\alpha}^{0}\right)\right]^{-1}\left[\boldsymbol{C}_{rd}\left(\boldsymbol{\alpha}^{0}\right)\right]^{\dagger},\end{aligned} \tag{1.30}$$

$$\begin{aligned}\boldsymbol{C}_{r\alpha}^{be}=\boldsymbol{C}_{\alpha r}^{be}&\equiv\left\langle\left(\boldsymbol{\alpha}-\boldsymbol{\alpha}^{be}\right)\left(\boldsymbol{r}-\boldsymbol{r}\left(\boldsymbol{\alpha}^{be}\right)\right)^{\dagger}\right\rangle\\&=\boldsymbol{C}_{r\alpha}-\left[\boldsymbol{C}_{rd}\left(\boldsymbol{\alpha}^{0}\right)\right]\left[\boldsymbol{C}_{d}\left(\boldsymbol{\alpha}^{0}\right)\right]^{-1}\left[\boldsymbol{C}_{\alpha d}\left(\boldsymbol{\alpha}^{0}\right)\right]^{\dagger},\end{aligned} \tag{1.31}$$

where

$$\boldsymbol{C}_{rd}\left(\boldsymbol{\alpha}^{0}\right)\equiv\left\langle\left(\boldsymbol{r}-\boldsymbol{r}_{m}\right)\boldsymbol{d}^{\dagger}\right\rangle=\left(\boldsymbol{C}_{m}-\boldsymbol{C}_{r\alpha}\left[\boldsymbol{S}\left(\boldsymbol{\alpha}^{0}\right)\right]^{\dagger}\right), \tag{1.32}$$

and

$$\boldsymbol{C}_{\alpha d}\left(\boldsymbol{\alpha}^{0}\right)\equiv\left\langle\left(\boldsymbol{\alpha}-\boldsymbol{\alpha}^{0}\right)\boldsymbol{d}^{\dagger}\right\rangle=\left(\boldsymbol{C}_{\alpha r}-\boldsymbol{C}_{\alpha}\left[\boldsymbol{S}\left(\boldsymbol{\alpha}^{0}\right)\right]^{\dagger}\right). \tag{1.33}$$

For completeness, the block-matrix components, which correlate two (distinct or not) time-nodes, of the above calibrated best-estimate covariance matrices are given below:

$$\left(\boldsymbol{C}_{\alpha}^{be}\right)^{\nu\mu} = \boldsymbol{C}_{\alpha}^{\nu\mu} - \sum_{\eta=1}^{N_t}\sum_{\rho=1}^{N_t}\left[\boldsymbol{C}_{\alpha r}^{\nu\rho} - \sum_{\pi=1}^{\rho}\boldsymbol{C}_{\alpha}^{\nu\pi}\left(\boldsymbol{S}^{\dagger}\right)^{\rho\pi}\right]\boldsymbol{K}_{d}^{\rho\eta}\left[\boldsymbol{C}_{r\alpha}^{\eta\mu} - \sum_{\pi=1}^{\eta}\boldsymbol{S}^{\eta\pi}\boldsymbol{C}_{\alpha}^{\pi\mu}\right], \tag{1.34}$$

$$\left(\boldsymbol{C}_{r}^{be}\right)^{\nu\mu} = \boldsymbol{C}_{m}^{\nu\mu} - \sum_{\eta=1}^{N_t}\sum_{\rho=1}^{N_t}\left[\boldsymbol{C}_{m}^{\nu\rho} - \sum_{\pi=1}^{\rho}\boldsymbol{C}_{r\alpha}^{\nu\pi}\left(\boldsymbol{S}^{\dagger}\right)^{\rho\pi}\right]\boldsymbol{K}_{d}^{\rho\eta}\left[\boldsymbol{C}_{m}^{\eta\mu} - \sum_{\pi=1}^{\eta}\boldsymbol{S}^{\eta\pi}\boldsymbol{C}_{\alpha r}^{\pi\mu}\right], \tag{1.35}$$

$$\left(\boldsymbol{C}_{r\alpha}^{be}\right)^{\nu\mu} = \boldsymbol{C}_{r\alpha}^{\nu\mu} - \sum_{\eta=1}^{N_t}\sum_{\rho=1}^{N_t}\left[\boldsymbol{C}_{m}^{\nu\rho} - \sum_{\pi=1}^{\rho}\boldsymbol{C}_{r\alpha}^{\nu\pi}\left(\boldsymbol{S}^{\dagger}\right)^{\rho\pi}\right]\boldsymbol{K}_{d}^{\rho\eta}\left[\boldsymbol{C}_{\alpha r}^{\eta\mu} - \sum_{\pi=1}^{\eta}\boldsymbol{S}^{\eta\pi}\boldsymbol{C}_{\alpha}^{\pi\mu}\right]. \tag{1.36}$$

Note in Eq. (1.29) that a symmetric positive matrix is subtracted from the initial parameter covariance matrix $\boldsymbol{C}_{\alpha}$; hence, in this sense, the best-estimate predicted parameter uncertainty matrix $\boldsymbol{C}_{\alpha}^{be}$ has been reduced by the calibration (adjustment) procedure, through the introduction of new information from experiments. Similarly, a symmetric positive matrix is subtracted in (1.30) from the initial covariance matrix $\boldsymbol{C}_{m}$ of the experimental-responses; hence, the best-estimate predicted response covariance matrix $\boldsymbol{C}_{r}^{be}$ has been improved (reduced) through the introduction of new experimental information. Furthermore, (1.31) indicates that the calibration (adjustment) procedure will introduce correlations between the calibrated (adjusted) parameters and responses even if the parameters and response were initially uncorrelated, since $\boldsymbol{C}_{r\alpha}^{be} \neq 0$ even if $\boldsymbol{C}_{r\alpha} = 0$, i.e.,

$$\boldsymbol{C}_{r\alpha}^{be} = \boldsymbol{C}_{m}\left[\boldsymbol{C}_{\mathrm{rc}}\left(\boldsymbol{\alpha}^{0}\right) + \boldsymbol{C}_{m}\right]^{-1}\left[\boldsymbol{S}\left(\boldsymbol{\alpha}^{0}\right)\right]\boldsymbol{C}_{\alpha}, \text{ when } \boldsymbol{C}_{r\alpha} = 0. \tag{1.37}$$

As the above expression indicates, the adjustment (calibration) modifies the correlations among the parameters through couplings introduced by the sensitivities of the participating responses. In the calibration procedure, the sensitivities play the role of weighting functions for propagating the initial parameter-covariances and experimental-response covariances to the adjusted best-estimate predicted quantities. Thus, as indicated by Eqs. (1.29) through (1.31), the incorporation of additional (experimental) information in the adjustment (calibration) process reduces the variances of the adjusted parameters and responses while also modifying their correlations.

Note that Eq. (1.30) expresses the best-estimate response covariance matrix $\boldsymbol{C}_{r}^{be}$ in terms of the initial covariance matrix $\boldsymbol{C}_{m}$ of the experimental-responses. Alternatively, it is of interest to derive the expression of the computed best-estimate response covariance matrix, $\boldsymbol{C}_{\mathrm{rc}}^{be}$,

directly from the model (the subscript "rc", denotes "computed response", to distinguish it from the covariance $\boldsymbol{C}_r^{be}$, which is obtained directly from the calibration/adjustment process). The starting point for computing $\boldsymbol{C}_{rc}^{be}$ is the linearization of the model, similar to that shown in Eq. (1.12), but around $\boldsymbol{\alpha}^{be}$ instead of $\boldsymbol{\alpha}^0$, i.e.

$$\boldsymbol{r} = \boldsymbol{R}\left(\boldsymbol{\alpha}^{be}\right) + \boldsymbol{S}\left(\boldsymbol{\alpha}^{be}\right)\left(\boldsymbol{\alpha} - \boldsymbol{\alpha}^{be}\right) + \textit{higher order terms}\,. \tag{1.38}$$

It follows from Eq. (1.38) that

$$\begin{aligned}
\boldsymbol{C}_{rc}^{be} &= \left\langle \left(\boldsymbol{r} - \boldsymbol{R}\left(\boldsymbol{\alpha}^{be}\right)\right)\left(\boldsymbol{r} - \boldsymbol{R}\left(\boldsymbol{\alpha}^{be}\right)\right)^{\dagger} \right\rangle \triangleq \left[\boldsymbol{S}\left(\boldsymbol{\alpha}^{be}\right)\right]\left\langle \left(\boldsymbol{\alpha} - \boldsymbol{\alpha}^{be}\right)\left(\boldsymbol{\alpha} - \boldsymbol{\alpha}^{be}\right)^{\dagger} \right\rangle \left[\boldsymbol{S}\left(\boldsymbol{\alpha}^{be}\right)\right]^{\dagger} \\
&= \left[\boldsymbol{S}\left(\boldsymbol{\alpha}^{be}\right)\right]\boldsymbol{C}_{\alpha}^{be}\left[\boldsymbol{S}\left(\boldsymbol{\alpha}^{be}\right)\right]^{\dagger} \\
&= \left[\boldsymbol{S}\left(\boldsymbol{\alpha}^{be}\right)\right]\left[\boldsymbol{C}_{\alpha} - \left(\boldsymbol{C}_{\alpha r} - \boldsymbol{C}_{\alpha}\left[\boldsymbol{S}\left(\boldsymbol{\alpha}^{0}\right)\right]^{\dagger}\right)\left[\boldsymbol{C}_d\left(\boldsymbol{\alpha}^{0}\right)\right]^{-1}\left(\boldsymbol{C}_{\alpha r} - \left[\boldsymbol{S}\left(\boldsymbol{\alpha}^{0}\right)\right]\boldsymbol{C}_{\alpha}\right)\right]\left[\boldsymbol{S}\left(\boldsymbol{\alpha}^{be}\right)\right]^{\dagger}
\end{aligned} \tag{1.39}$$

Comparing Eq. (1.39) to Eq. (1.30) reveals that, in general, $\boldsymbol{C}_{rc}^{be} \neq \boldsymbol{C}_r^{be}$ since $\boldsymbol{S}\left(\boldsymbol{\alpha}^{be}\right) \neq \boldsymbol{S}\left(\boldsymbol{\alpha}^{0}\right)$. Nevertheless, when the model is "perfect" (i.e., free of higher-order numerical errors) and exactly linear, then the sensitivity matrix $\boldsymbol{S}$ is independent of the parameter values $\boldsymbol{\alpha}$, i.e.,

$$\boldsymbol{S}\left(\boldsymbol{\alpha}^{be}\right) = \boldsymbol{S}\left(\boldsymbol{\alpha}^{0}\right) = \boldsymbol{S}\,, \text{ for "perfect" and linear models,} \tag{1.40}$$

Using (1.40) in (1.39) reduces the later expression to

$$\begin{aligned}
\boldsymbol{C}_{rc}^{be} &= \boldsymbol{S}\left[\boldsymbol{C}_{\alpha} - \left(\boldsymbol{C}_{\alpha r} - \boldsymbol{C}_{\alpha}\boldsymbol{S}^{\dagger}\right)\boldsymbol{C}_d^{-1}\left(\boldsymbol{C}_{\alpha r} - \boldsymbol{S}\boldsymbol{C}_{\alpha}\right)\right]\boldsymbol{S}^{\dagger} \\
&= \boldsymbol{C}_{rc} - \left(\boldsymbol{C}_{rc} - \boldsymbol{S}\boldsymbol{C}_{\alpha r}\right)\left[\boldsymbol{C}_{rc} + \boldsymbol{C}_e - \boldsymbol{C}_{r\alpha}\boldsymbol{S}^{\dagger} - \boldsymbol{S}\boldsymbol{C}_{\alpha r}\right]^{-1}\left(\boldsymbol{C}_{rc} - \boldsymbol{C}_{\alpha r}\boldsymbol{S}^{\dagger}\right) \\
&= \boldsymbol{C}_r^{be}, \quad \textbf{\textit{for "perfect" linear models.}}
\end{aligned} \tag{1.41}$$

It is important to note that the computation of the best estimate parameter and response values, together with their corresponding best-estimate uncertainties --see Eqs. (1.23), (1.27), (1.29), (1.30) and (1.31) -- require the inversion of a single matrix, namely the matrix $\boldsymbol{C}_d\left(\boldsymbol{\alpha}^{0}\right)$ defined in Eq. (1.26). This is usually advantageous in practice, since the order of the matrix

$\boldsymbol{C}_d\left(\boldsymbol{\alpha}^0\right)$ is given by the number of measured (or computed responses), which is most often considerably smaller that the number of model parameters under consideration.

On the other hand, when the number of parameter exceeds the number of responses, it is possible to derive alternative expressions for the best-estimate calibrated parameters and their corresponding best-estimate covariances, by performing all derivations in the "parameter space" rather than in "response space". This entails using Eq. (1.12) to eliminate the response (variables) $\boldsymbol{r}$ at the outset, and carrying out the minimization procedure solely for the parameters (variables) $\boldsymbol{\alpha}$. Equivalently, as shown by [Ca2010a], the Sherman-Morrison-Woodbury extension can be employed to obtain the alternative expression

$$\begin{aligned} \boldsymbol{C}_d^{-1} &\equiv \left(\boldsymbol{C}_{rc} - \boldsymbol{C}_{r\alpha}\boldsymbol{S}^\dagger - \boldsymbol{S}\boldsymbol{C}_{\alpha r} + \boldsymbol{C}_m\right)^{-1} \\ &= \boldsymbol{A}^{-1} - \boldsymbol{A}^{-1}\boldsymbol{S}\left(\boldsymbol{C}_\alpha^{-1} + \boldsymbol{S}^\dagger\boldsymbol{A}^{-1}\boldsymbol{S}\right)^{-1}\boldsymbol{S}^\dagger\boldsymbol{A}^{-1}; \\ \boldsymbol{A} &\equiv \boldsymbol{C}_m - \boldsymbol{C}_{r\alpha}\boldsymbol{S}^\dagger - \boldsymbol{S}\boldsymbol{C}_{\alpha r}. \end{aligned} \tag{1.42}$$

The above expression provides the bridge between the "response-space" and "parameter-space" formulations. This expression also highlights the fact that the response-space formulation requires a single inversion of a square symmetric matrix (namely, the matrix $\boldsymbol{C}_d$) of the same dimensions as the number of responses. In contradistinction, the "parameter space" formulation requires the inversion of three symmetric matrices, two of which have dimensions equal to the number of parameters and one of dimensions equal to the number of responses. Hence, from a computational standpoint, the "response-space" formulations should be used whenever possible.

In view of Eq. (1.26), it is essential to note that the inverse matrix, $\boldsymbol{C}_d^{-1}$, incorporates simultaneously all of the available information about the system parameters and responses, at all time nodes [i.e., $\nu = 1,2,...,N_t$]. Specifically, at any time node ν, $\boldsymbol{C}_d^{-1}$ incorporates information not only from time nodes prior in time to ν (i.e., information regarding the "past" and "present" states of the system) but also from time nodes posterior in time to ν (i.e., information about the "future" states of the system). Through the matrix $\boldsymbol{C}_d^{-1}$, at any specified time node ν, the calibrated best-estimates parameters $\left(\boldsymbol{\alpha}^{be}\right)^\nu$ and responses $\boldsymbol{r}\left(\boldsymbol{\alpha}^{be}\right) \triangleq \boldsymbol{r}^{be}$, together with the corresponding calibrated best-estimate covariance matrices $\left(\boldsymbol{C}_\alpha^{be}\right)^{\nu\mu}$, $\left(\boldsymbol{C}_r^{be}\right)^{\nu\mu}$,

and $\left(\boldsymbol{C}_{\alpha r}^{be}\right)^{\nu\mu}$ will also incorporate automatically all of the available information about the system parameters and responses at all time nodes [i.e., $\nu = 1,2,...,N_t$].

In this respect, the methodology presented in this section is conceptually related to the "foresight" aspects encountered in decision analysis. It is also important to note that, in practice, the application of the methodology developed in this section involves two distinct computational stages. A complete sensitivity data base (i.e., sensitivities $s_{ni}^{\nu\mu}$ at all times nodes $\nu, \mu = 1,\ldots,N_t$) needs to be generated "off-line" prior to performing the "data assimilation" and "model calibration" (or data adjustment) stages. All sensitivities are subsequently combined with appropriate covariance matrices to compute calibrated best-estimate responses, parameters, and best-estimate covariance matrices.

Because of the "foresight" and "off-line" characteristics, the methodology presented in this Section can be called the "off-line with foresight" data assimilation and adjustment (model calibration) methodology, underscoring that all sensitivities are generated separately, prior to performing the uncertainty analysis, and that foresight characteristics are included in the calibration procedure. Since the incorporation of foresight effects involves the inversion of the matrix $\boldsymbol{C}_d$, this methodology is best suited for problems involving relatively few time nodes. For large-scale highly nonlinear problems involving many time nodes, the matrix $\boldsymbol{C}_d$ becomes very large, requiring large amounts of computer storage; the inversion of $\boldsymbol{C}_d$ may become prohibitively expensive in such cases. These difficulties can be reduced at the expense of using less than the complete information available at any specific time node. For example, even in time-dependent problems in which the entire time history is known (e.g., transient behavior of reactor systems), one may nevertheless choose to use only information up to the current time index, and disregard the information about "future" system states.

On the other hand, in dynamical problems such as climate or weather prediction, in which the time variable advances continuously and states beyond the current time are not known, information about future states cannot be reliably accounted for anyway. Thus, the most common way of reducing the dimensionality of the data assimilation and model calibration problem is to disregard information about future states and limit the amount of information assimilated about "past states". Data assimilation and model calibration procedure using such a limited amount of information can be performed either off-line or on-line, assimilating the new data as the time index advances.

The simplest case of dynamic data assimilation and model calibration is when these operations are performed by using information on-line from only two successive time-steps. In this particular case, the expressions given by Eqs. (1.24), (1.28), (1.34), (1.35) and (1.36) for the best-estimate predicted calibrated quantities reduce to the following explicit formulas:

The components $\left(\boldsymbol{\alpha}^{be}\right)^{k}$, representing the calibrated best-estimates for the system parameters at time node k, can be written in a particular form of Eq. (1.24), as follows:

$$\begin{aligned}&\left(\boldsymbol{\alpha}^{be}\right)^{k}=\left(\boldsymbol{\alpha}^{0}\right)^{k}\\&+\sum_{\mu=k-1}^{k}\left\{\left[\boldsymbol{C}_{\alpha r}^{k\mu}-\sum_{\rho=k-1}^{\mu}\boldsymbol{C}_{\alpha}^{k\rho}\left(\boldsymbol{S}^{\dagger}\right)^{\mu\rho}\right]\left[\sum_{\eta=k-1}^{k}\boldsymbol{K}_{d}^{\mu\eta}\boldsymbol{d}^{\eta}\right]\right\},\quad k=1,2,...,N_{t}.\end{aligned}\tag{1.43}$$

The vector $\left(\boldsymbol{r}^{be}\right)^{k}$, representing the best-estimates predicted values for the system parameters at a time node k, take on the following particular form of Eq. (1.28):

$$\begin{aligned}&\left(\boldsymbol{r}^{be}\right)^{k}=\left(\boldsymbol{r}_{m}\right)^{k}\\&+\sum_{\mu=k-1}^{k}\left\{\left[\boldsymbol{C}_{m}^{k\mu}-\sum_{\rho=k-1}^{\mu}\boldsymbol{C}_{r\alpha}^{k\rho}\left(\boldsymbol{S}^{\dagger}\right)^{\mu\rho}\right]\left[\sum_{\eta=k-1}^{k}\boldsymbol{K}_{d}^{\mu\eta}\boldsymbol{d}^{\eta}\right]\right\},\quad k=1,2,...,N_{t}.\end{aligned}\tag{1.44}$$

The components $\left(\boldsymbol{C}_{\alpha}^{be}\right)^{\nu\mu}$, $(\nu,\mu=k-1,k)$, of the calibrated best-estimate covariance matrix, $\boldsymbol{C}_{\alpha}^{be}$, for the calibrated best-estimates system parameters is obtained by particularizing Eq. (1.34) to two consecutive time nodes $(k-1,k)$, $k=1,2,...,N_{t}$, leading to

$$\begin{aligned}&\left(\boldsymbol{C}_{\alpha}^{be}\right)^{\nu\mu}=\boldsymbol{C}_{\alpha}^{\nu\mu}-\sum_{\eta=k-1}^{k}\sum_{\rho=k-1}^{k}\left[\boldsymbol{C}_{\alpha r}^{\nu\rho}-\sum_{\pi=k-1}^{\rho}\boldsymbol{C}_{\alpha}^{\nu\pi}\left(\boldsymbol{S}^{\dagger}\right)^{\rho\pi}\right]\boldsymbol{K}_{d}^{\rho\eta}\left[\boldsymbol{C}_{r\alpha}^{\eta\mu}-\sum_{\pi=k-1}^{\eta}\boldsymbol{S}^{\eta\pi}\boldsymbol{C}_{\alpha}^{\pi\mu}\right],\\&for\quad \nu=k-1,k;\quad and\quad \mu=k-1,k;\quad k=1,2,...,N_{t}.\end{aligned}\tag{1.45}$$

4. The components $\left(\boldsymbol{C}_{r}^{be}\right)^{\nu\mu}$, $(\nu,\mu=k-1,k)$, of the calibrated best-estimate covariance matrix $\boldsymbol{C}_{r}^{be}$, for the best-estimate responses takes on the following particular form of Eq. (1.35):

$$\left(\boldsymbol{C}_r^{be}\right)^{\nu\mu} = \boldsymbol{C}_m^{\nu\mu} - \sum_{\eta=k-1}^{k}\sum_{\rho=k-1}^{k}\left[\boldsymbol{C}_m^{\nu\rho} - \sum_{\pi=k-1}^{\rho}\boldsymbol{C}_{r\alpha}^{\nu\pi}\left(\boldsymbol{S}^{\dagger}\right)^{\rho\pi}\right]\boldsymbol{K}_d^{\rho\eta}\left[\boldsymbol{C}_m^{\eta\mu} - \sum_{\pi=k-1}^{\eta}\boldsymbol{S}^{\eta\pi}\boldsymbol{C}_{\alpha r}^{\pi\mu}\right], \tag{1.46}$$
$$for \quad \nu = k-1,k; \quad and \quad \mu = k-1,k; \quad k = 1,2,...,N_t.$$

5. The components $\left(\boldsymbol{C}_{\alpha r}^{be}\right)^{\nu\mu}$, $(\nu,\mu = k-1,k)$, of the best-estimate response-parameter covariance matrix $\boldsymbol{C}_{\alpha r}^{be}$ take on the following form:

$$\left(\boldsymbol{C}_{r\alpha}^{be}\right)^{\nu\mu} = \boldsymbol{C}_{r\alpha}^{\nu\mu} - \sum_{\eta=k-1}^{k}\sum_{\rho=k-1}^{k}\left[\boldsymbol{C}_m^{\nu\rho} - \sum_{\pi=k-1}^{\rho}\boldsymbol{C}_{r\alpha}^{\nu\pi}\left(\boldsymbol{S}^{\dagger}\right)^{\rho\pi}\right]\boldsymbol{K}_d^{\rho\eta}\left[\boldsymbol{C}_{r\alpha}^{\eta\mu} - \sum_{\pi=k-1}^{\eta}\boldsymbol{S}^{\eta\pi}\boldsymbol{C}_{\alpha}^{\pi\mu}\right] \tag{1.47}$$
$$for \quad \nu = k-1,k; \quad and \quad \mu = k-1,k; \quad k = 1,2,...,N_t.$$

For each time node, $k = 1,2,...,N_t$, the quantities $\boldsymbol{K}_d^{\nu\eta}$ which appear in Eq. (1.43) through (1.47) have the following expressions:

$$\begin{aligned}\boldsymbol{K}_d^{k-1,k-1} &= \left[\boldsymbol{C}_d^{k-1,k-1} - \boldsymbol{C}_d^{k-1,k}\left(\boldsymbol{C}_d^{k,k}\right)^{-1}\boldsymbol{C}_d^{k,k-1}\right]^{-1} \\ &= \left(\boldsymbol{C}_d^{k-1,k-1}\right)^{-1} + \left(\boldsymbol{C}_d^{k-1,k-1}\right)^{-1}\boldsymbol{C}_d^{k-1,k}\boldsymbol{K}_d^{k,k}\boldsymbol{C}_d^{k,k-1}\left(\boldsymbol{C}_d^{k-1,k-1}\right)^{-1}\end{aligned} \tag{1.48}$$

$$\begin{aligned}\boldsymbol{K}_d^{k-1,k} &= -\left(\boldsymbol{C}_d^{k-1,k-1}\right)^{-1}\boldsymbol{C}_d^{k-1,k}\left[\boldsymbol{C}_d^{k,k} - \boldsymbol{C}_d^{k,k-1}\left(\boldsymbol{C}_d^{k-1,k-1}\right)^{-1}\boldsymbol{C}_d^{k-1,k}\right]^{-1} \\ &= -\left(\boldsymbol{C}_d^{k-1,k-1}\right)^{-1}\boldsymbol{C}_d^{k-1,k}\boldsymbol{K}_d^{k,k}\end{aligned} \tag{1.49}$$

$$\begin{aligned}\boldsymbol{K}_d^{k,k} &= \left[\boldsymbol{C}_d^{k,k} - \boldsymbol{C}_d^{k,k-1}\left(\boldsymbol{C}_d^{k-1,k-1}\right)^{-1}\boldsymbol{C}_d^{k-1,k}\right]^{-1} \\ &= \left(\boldsymbol{C}_d^{k,k}\right)^{-1} + \left(\boldsymbol{C}_d^{k,k}\right)^{-1}\boldsymbol{C}_d^{k,k-1}\boldsymbol{K}_d^{k-1,k-1}\boldsymbol{C}_d^{k-1,k}\left(\boldsymbol{C}_d^{k,k}\right)^{-1}\end{aligned} \tag{1.50}$$

$$\begin{aligned}\boldsymbol{K}_d^{k,k-1} &= -\left(\boldsymbol{C}_d^{k,k}\right)^{-1}\boldsymbol{C}_d^{k,k-1}\left[\boldsymbol{C}_d^{k-1,k-1} - \boldsymbol{C}_d^{k-1,k}\left(\boldsymbol{C}_d^{k,k}\right)^{-1}\boldsymbol{C}_d^{k,k-1}\right]^{-1} \\ &= -\left(\boldsymbol{C}_d^{k,k}\right)^{-1}\boldsymbol{C}_d^{k,k-1}\boldsymbol{K}_d^{k-1,k-1}\end{aligned} \tag{1.51}$$

For time-independent problems, the (time-dependent) results derived in Eqs. (1.43) through (1.47) reduce to expressions that are formally identical to Eqs. (1.23), (1.27), (1.29), (1.30) and (1.31). Hence, the later expressions can be used directly to obtain the best-estimate predicted values for parameters, responses, and their respective covariances. Recall that modeling errors can be treated in a manner similar to parameter uncertainties, by including the

discretization intervals among the components of the vector $\boldsymbol{\alpha}$ of model parameters, as detailed in [Ca2003].

Finally, it is important to emphasize that the explicit formulas presented in this Section are based on the linearized relationship between responses and parameters that customarily underlies the "propagation of moments" method, i.e., Eq. (1.12), without considering nonlinearities explicitly. Nevertheless, this limitation is not as severe as it may appear at first glance, since nonlinear relations between computed responses and model parameters can be treated by considering Eq. (1.12) iteratively, starting with the known nominal values of the quantities involved. The first iteration (in such an iterative procedure) would yield all of the major explicit results derived in Eqs. (1.23), (1.27), (1.29), (1.30) and (1.31).The subsequent iteration would the results of Eqs. (1.23), (1.27), (1.29), (1.30) and (1.31) as the "prior information" in a second application of these formulas, and compute the new ("second-iteration") best-estimate quantities by using once again these formulas. This iterative procedure would be continued until the best-estimated values would converge within a small, user-specified, convergence criterion. The actual application of the model calibration (adjustment) algorithms –see Eqs. (1.23), (1.27), (1.29), (1.30) and (1.31), to a physical system is straightforward, in principle, although it can become computationally very demanding in terms of data handling and computational speed requirements.

The minimum value, $Q_{min} \equiv Q\left(z^{be}\right)$, of $Q(z)$ takes on the following expression:

$$Q_{min} \equiv Q\left(z^{be}\right) = \boldsymbol{d}^{\dagger}\left[\boldsymbol{C}_d\left(\boldsymbol{\alpha}^0\right)\right]^{-1}\boldsymbol{d}\ ,\ \boldsymbol{d} \equiv \boldsymbol{R}\left(\boldsymbol{\alpha}^0\right) - \boldsymbol{r}_m\ . \tag{1.52}$$

As the above expression indicates, $Q_{min} \equiv Q\left(z^{be}\right)$ represents the square of the length of the vector $\boldsymbol{d}$, measuring (in the corresponding metric) the deviations between the experimental and nominally computed responses, and can be evaluated directly from the given data (i.e., given parameters and responses, together with their original uncertainties) after having inverted the deviation-vector uncertainty matrix $\boldsymbol{C}_d\left(\boldsymbol{\alpha}^0\right)$. It is also very important to note that $Q_{min} \equiv Q\left(z^{be}\right)$ is independent of calibrating (or adjusting) the original data. As the dimension of $\boldsymbol{d}$ indicates, the number of degrees of freedom characteristic of the calibration under consideration is equal to the number of experimental responses. In the extreme case of

absence of experimental responses, no actual calibration takes place since $\boldsymbol{d} = \boldsymbol{R}\left(\boldsymbol{\alpha}^0\right)$, so that the best-estimate parameter values are just the original nominal values, i.e., $\left(\boldsymbol{\alpha}^{be}\right)^k = \left(\boldsymbol{\alpha}^0\right)^k$; an actual adjustment occurs only when at least one experimental response is included.

Replacing Eq. (1.52) in Eq. (1.16) shows that the bulk of the contribution to the joint posterior probability distribution, which comes from the point $z = z^{be}$, takes on the form of the following multivariate Gaussian distribution:

$$\begin{aligned} p\left(z^{be}\,|\boldsymbol{C}\right) &\equiv exp\left[-\frac{1}{2}Q\left(z^{be}\right)\right] \\ &= exp\left\{-\frac{1}{2}\left[\boldsymbol{r}_m - \boldsymbol{R}\left(\boldsymbol{\alpha}^0\right)\right]^{\dagger}\left[\boldsymbol{C}_d\left(\boldsymbol{\alpha}^0\right)\right]^{-1}\left[\boldsymbol{r}_m - \boldsymbol{R}\left(\boldsymbol{\alpha}^0\right)\right]\right\}. \end{aligned} \tag{1.53}$$

The above relation indicates that experimental responses can be considered as random variables approximately described by a multivariate Gaussian distribution with means located at the nominal values of the computed responses, and with a covariance matrix $\boldsymbol{C}_d\left(\boldsymbol{\alpha}^0\right)$. In turn, the random variable $Q_{min} \equiv Q\left(z^{be}\right)$ obeys a χ^2-distribution with n degrees of freedom, where n denotes the total number of experimental responses considered in the calibration (adjustment) procedure. Since $Q_{min} \equiv Q\left(z^{be}\right)$ is the "χ^2 of the calibration (adjustment) at hand", it can be used as an indicator of the agreement between the computed and experimental responses, measuring essentially the consistency of the experimental responses with the model parameters. For model calibration (adjustment), it is important to assess if: (i) the response and data measurements are free of gross errors (blunders such as wrong settings, mistaken readings, etc), and (ii) the measurements are consistent with the assumptions regarding the respective means, variances, and covariances. As has been noted there, when the distance between any two nominal response values, $\left|R_i^0 - R_j^0\right|$, is smaller or at least not much larger than the sum of the corresponding uncertainties, say $\sigma_i + \sigma_j$, the data is considered to be consistent or to agree "within error bars". However, if the distances $\left|R_i^0 - R_j^0\right|$ are larger than $\left(\sigma_j + \sigma_k\right)$, the data are considered to be inconsistent or discrepant. Inconsistencies can be caused by unrecognized or ill-corrected experimental effects (e.g., background, dead time of the counting electronics, instrumental resolution, sample impurities, calibration errors, etc,).

Note that the probability that two equally precise measurements yield a separation greater than $\sigma_i + \sigma_j = 2\sigma$ is very small, namely $erfc(1) \approx 0.157$ for Gaussian sampling distributions with standard deviation σ. Thus, although there is a nonzero probability that genuinely discrepant data do occur, it is much more likely that apparently discrepant experiments actually indicate the presence of unrecognized errors, an issue addressed in the work of [Ca2010b].

2 Illustrative Examples

Two models have been considered as examples for the time-independent (Paragraph 2.1) and time-dependent (Paragraph 2.2) use of the MULTI-PRED module.

2.1 A Simple Time-Independent Neutron Diffusion Model

More details of this model (a steady-state neutron diffusion problem) may be accessed in the reference [Ca2014].

Consider the diffusion of monoenergetic neutrons due to distributed sources of strength S $\text{neutrons}/\text{cm}^3 \cdot \text{s}$ within a slab of material of extrapolated thickness $2a$. The linear neutron diffusion equation that models mathematically this problem is

$$D\frac{d^2\varphi}{dx^2} - \Sigma_a\varphi + S = 0\,, \quad x \in (-a,a)\,, \tag{2.1}$$

where $\varphi(x)$ is the neutron flux, D is the diffusion coefficient, Σ_a is the macroscopic absorption cross section, and S is the distributed source term. Note that, in view of the problem's symmetry, the origin $x = 0$ has been conveniently chosen at the middle (center) of the slab. The boundary conditions for Eq. (3.1) are that the neutron flux must vanish at the extrapolated distance, i.e.,

$$\varphi(\pm a) = 0\,. \tag{2.2}$$

A typical response R for the neutron diffusion problem modeled by Eqs. (2.1) and (2.2) would be the reading of a detector placed within the slab, for example, at a distance b from the slab's midline at $x = 0$. Such a response is given by the reaction rate

$$R(\boldsymbol{e}) \equiv \Sigma_d\varphi(b)\,, \tag{2.3}$$

where Σ_d represents the detector's equivalent reaction cross section. The system parameters for this problem are thus the positive constants Σ_a, D, S, and Σ_d, which will be considered to be the components of the vector $\boldsymbol{\alpha}$ of system parameters, defined as

$$\boldsymbol{\alpha} \equiv \left(\Sigma_a, D, S, \Sigma_d\right). \tag{2.4}$$

Consider that the components of $\boldsymbol{\alpha} \equiv \left(\Sigma_a, D, S, \Sigma_d\right)$ are imprecisely (e.g., experimentally) determined quantities, with mean nominal values $\boldsymbol{\alpha}^0 = \left(\Sigma_a^0, D^0, S^0, \Sigma_d^0\right)$ and standard deviations $\boldsymbol{h}_\alpha \triangleq \left(\delta\Sigma_a, \delta D, \delta S, \delta\Sigma_d\right)$, respectively. The vector $\boldsymbol{e}(x)$ appearing in the functional dependence of R in Eq. (2.3) denotes the concatenation of $\varphi(x)$ with $\boldsymbol{\alpha}$, defined as

$$\boldsymbol{e} \equiv \left(\varphi, \boldsymbol{\alpha}\right). \tag{2.5}$$

The nominal value $\varphi^0(x)$ of the flux is determined by solving Eqs. (2.1) and (2.2) for the nominal parameter values $\boldsymbol{\alpha}^0 = \left(\Sigma_a^0, D^0, S^0, \Sigma_d^0\right)$, to obtain

$$\varphi^0(x) = \frac{S^0}{\Sigma_a^0}\left(1 - \frac{\cosh xk}{\cosh ak}\right), \quad k \equiv \sqrt{\Sigma_a^0 / D^0}\,, \tag{2.6}$$

where $k \equiv \sqrt{\Sigma_a^0 / D^0}$ is the nominal value of the reciprocal diffusion length for our illustrative example. Inserting Eq. (2.6) together with the nominal value Σ_d^0 into Eq. (2.3) gives the nominal response

$$R\left(\boldsymbol{e}^0\right) = \frac{S^0 \Sigma_d^0}{\Sigma_a^0}\left(1 - \frac{\cosh bk}{\cosh ak}\right), \quad \boldsymbol{e}^0 \equiv \left(\varphi^0, \boldsymbol{\alpha}^0\right). \tag{2.7}$$

Note that even though Eq. (2.1) is linear in φ, the solution $\varphi(x)$ depends nonlinearly on $\boldsymbol{\alpha}$, as evidenced by Eq. (2.6). The same is true of the response $R(\boldsymbol{e})$. Even though $R(\boldsymbol{e})$ is linear separately in φ and in $\boldsymbol{\alpha}$, as shown in Eq. (2.3), R is not simultaneously linear in φ and $\boldsymbol{\alpha}$, which leads to a nonlinear dependence of $R(\boldsymbol{e})$ on $\boldsymbol{\alpha}$. This fact is confirmed by the explicit expression of $R(\boldsymbol{e})$ given in Eq. (2.7).

The sensitivities of the system response to the system parameters have been computed efficiently using the Adjoint Sensitivity Analysis Procedure (ASAP), for details see [Ca2014]. The expressions of the partial sensitivities of $R(\boldsymbol{e})$ to the various parameters have been obtained as:

$$\frac{\partial R}{\partial S} = \frac{\Sigma_d^0}{\Sigma_a^0}\left(1 - \frac{\cosh bk}{\cosh ak}\right), \tag{2.8}$$

$$\frac{\partial R}{\partial \Sigma_d} = \frac{S^0}{\Sigma_a^0}\left(1 - \frac{\cosh bk}{\cosh ak}\right), \tag{2.9}$$

$$\frac{\partial R}{\partial \Sigma_a} = -\frac{S^0\Sigma_d^0}{\left(\Sigma_a^0\right)^2}\left(1 - \frac{\cosh bk}{\cosh ak}\right) + \frac{1}{2\sqrt{D^0\Sigma_a^0}}\frac{S^0\Sigma_d^0}{\Sigma_a^0}\frac{a\sinh ak\cosh bk - b\sinh bk\cosh ak}{\left(\cosh ak\right)^2}, \tag{2.10}$$

$$\frac{\partial R}{\partial D} = -\frac{1}{2}\sqrt{\frac{\Sigma_a^0}{D^0}}\frac{S^0\Sigma_d^0}{D^0\Sigma_a^0}\frac{a\sinh ak\cosh bk - b\sinh bk\cosh ak}{\left(\cosh ak\right)^2}. \tag{2.11}$$

To illustrate with numerical values the application of these formulas, consider that the slab of extrapolated thickness a consists of water with material properties having the following nominal values: $\Sigma_a^0 = 0.0197\,cm^{-1}$, $D^0 = 0.16\ cm$, containing distributed neutron sources emitting nominally $S^0 = 10^7\,neutrons\cdot cm^{-3}\cdot s^{-1}$. For the sake of argument, consider that all of these parameters are uncorrelated and have the following relative standard deviations: $\Delta\Sigma_a^0/\Sigma_a^0 = 5\%$, $\Delta D^0/D^0 = 5\%$, $\Delta S^0/S^0 = 15\%$.

Furthermore, consider that measurements are performed with an infinitely thin detector immersed at different locations, $x = b$, in the water slab, having an indium-like nominal

detector cross section $\Sigma_d^0 = 7.438 cm^{-1}$, uncorrelated to the other parameters, with a standard deviation $\Delta\Sigma_d^0 / \Sigma_d^0 = 10\%$. Collecting this information (and omitting, for simplicity, the respective units), it follows that the covariance matrix for the model parameters is

$$\boldsymbol{C}_\alpha = \begin{pmatrix} \left(9.85\times10^{-4}\right)^2 & 0 & 0 & 0 \\ 0 & \left(8.0\times10^{-3}\right)^2 & 0 & 0 \\ 0 & 0 & \left(1.5\times10^{6}\right)^2 & 0 \\ 0 & 0 & 0 & \left(7.44\times10^{-1}\right)^2 \end{pmatrix}. \tag{2.12}$$

To illustrate the effects of several consistent measurements, and also to test that symmetric measurements (with respect to the vertical plane through the origin) do preserve the solution's symmetry, we consider four consistent ($\chi^2 = 1.21$) measurements, taken at the symmetric locations $10 cm, -10 cm, \ -40 cm, 40 cm$, and having the following values and relative standard deviations (abbreviated as "rsd"):

$$r_1^m \triangleq r\left(meas.at \ \ 10 cm\right) = 3.40\times10^9 n\cdot cm^{-3}\cdot sec^{-1};\ rsd\left(r_1^m\right) = 5\%; \tag{2.13}$$

$$r_2^m \triangleq r\left(meas.at \ -10 cm\right) = 3.59\times10^9 n\cdot cm^{-3}\cdot sec^{-1};\ rsd\left(r_2^m\right) = 6\%; \tag{2.14}$$

$$r_3^m \triangleq r\left(meas.at \ -40 cm\right) = 3.77\times10^9 n\cdot cm^{-3}\cdot sec^{-1};\ rsd\left(r_3^m\right) = 5\%; \tag{2.15}$$

$$r_4^m \triangleq r\left(meas.at \ \ 40 cm\right) = 3.74\times10^9 n\cdot cm^{-3}\cdot sec^{-1};\ rsd\left(r_4^m\right) = 5\%; \tag{2.16}$$

Thus, the covariance matrix of the measured responses is

$$\boldsymbol{C}_m = \begin{pmatrix} \left(1.7\times10^{8}\right)^2 & 0 & 0 & 0 \\ 0 & \left(2.15\times10^{8}\right)^2 & 0 & 0 \\ 0 & 0 & \left(1.89\times10^{8}\right)^2 & 0 \\ 0 & 0 & 0 & \left(1.87\times10^{8}\right)^2 \end{pmatrix} \tag{2.17}$$

The nominal values of the computed responses at the above locations are as follows:

$$r_1\left(comp.\ at\ \ 10\,cm\right)=3.77\times10^{9}\,n\cdot cm^{-3}\cdot sec^{-1};\tag{2.18}$$

$$r_2\left(comp.\ at\ \ -10\,cm\right)=3.77\times10^{9}\,n\cdot cm^{-3}\cdot sec^{-1};\tag{2.19}$$

$$r_3\left(comp.\ \ at\ \ -40\,cm\right)=3.66\times10^{9}\,n\cdot cm^{-3}\cdot sec^{-1};\tag{2.20}$$

$$r_4\left(comp.\ \ at\ \ 40\,cm\right)=3.66\times10^{9}\,n\cdot cm^{-3}\cdot sec^{-1};\tag{2.21}$$

As expected, the above computed responses confirm the problem's symmetry. The matrices S and S_{rel}, with $\Delta\alpha_j \triangleq std.\,dev.\left(\alpha_j\right)$, containing the nominal values of the absolute and relative sensitivities, respectively, are:

$$\boldsymbol{S}\triangleq\left(\frac{\partial R_i}{\partial\alpha_j}\right)=\begin{pmatrix}-1.92\times10^{11} & -1.33\times10^{9} & 3.78\times10^{2} & 5.08\times10^{8}\\ -1.92\times10^{11} & -1.33\times10^{5} & 3.78\times10^{2} & 5.08\times10^{8}\\ -1.76\times10^{11} & -1.24\times10^{5} & 3.66\times10^{2} & 4.92\times10^{8}\\ -1.76\times10^{11} & -1.24\times10^{9} & 3.66\times10^{2} & 4.92\times10^{8}\end{pmatrix},\tag{2.22}$$

$$\boldsymbol{S}_{rel}\triangleq\left(\frac{\partial R_i}{\partial\alpha_j}\frac{\Delta\alpha_j}{R_i}\right)=\begin{pmatrix}-0.99999 & -5.41\times10^{-6} & 1.00 & 1.00\\ -0.99999 & -5.64\times10^{-6} & 1.00 & 1.00\\ -9.46\times10^{-1} & -5.64\times10^{-2} & 1.00 & 1.00\\ -9.46\times10^{-1} & -5.41\times10^{-2} & 1.00 & 1.00\end{pmatrix}.\tag{2.23}$$

Using the above sensitivities together with the covariance matrix shown in Eq. (2.12) yields the following value for the covariance matrix of the computed responses:

$$\boldsymbol{C}_{rc}=\boldsymbol{S}\boldsymbol{C}_{\alpha}\boldsymbol{S}^{\dagger}=\begin{pmatrix}4.99\times10^{17} & 4.99\times10^{17} & 4.82\times10^{17} & 4.82\times10^{17}\\ 4.99\times10^{17} & 4.99\times10^{17} & 4.82\times10^{17} & 4.82\times10^{17}\\ 4.82\times10^{17} & 4.82\times10^{17} & 4.66\times10^{17} & 4.66\times10^{17}\\ 4.82\times10^{17} & 4.82\times10^{17} & 4.66\times10^{17} & 4.66\times10^{17}\end{pmatrix}\tag{2.24}$$

Note that the particular values (essentially either unity or zero) of the components of the sensitivity matrix lead to a fully correlated covariance matrix for the four computed responses.

Applying the data assimilation and adjustment procedure to the above information leads to the following best estimate parameter values, relative standard deviations (abbreviated as "rsd"), and covariances:

$$\Sigma_a^{be} = 0.0198\,cm^{-1},\ rsd\left(\Sigma_a^{be}\right) = 4.79\%; \tag{2.25}$$

$$D^{be} = 0.1591\ cm,\ rsd\left(D^{be}\right) = 5.00\%; \tag{2.26}$$

$$S^{be} = 9.85\times10^{6}\,n\cdot cm^{-3}\cdot s^{-1},\ rsd\left(S^{be}\right) = 9.21\%; \tag{2.27}$$

$$\Sigma_d^{be} = 7.388\,cm^{-1},\ \ rsd\left(\Sigma_d^{be}\right) = 8.53\%; \tag{2.28}$$

$$\begin{aligned} \boldsymbol{C}_{\alpha}^{be} = & \begin{pmatrix} 9.50\times10^{-4} & 0 & 0 & 0 \\ 0 & 7.99\times10^{-3} & 0 & 0 \\ 0 & 0 & 9.08\times10^{5} & 0 \\ 0 & 0 & 0 & 6.30\times10^{-1} \end{pmatrix} \\ & \times \begin{pmatrix} 1.0 & -8.89\times10^{-4} & 3.51\times10^{-1} & 1.67\times10^{-1} \\ -8.89\times10^{-4} & 1.0 & 1.02\times10^{-2} & 4.84\times10^{-3} \\ 3.51\times10^{-1} & 1.02\times10^{-2} & 1.0 & -8.24\times10^{-1} \\ 1.67\times10^{-1} & 4.84\times10^{-3} & -8.24\times10^{-1} & 1.0 \end{pmatrix} \\ & \times \begin{pmatrix} 9.50\times10^{-4} & 0 & 0 & 0 \\ 0 & 7.99\times10^{-3} & 0 & 0 \\ 0 & 0 & 9.08\times10^{5} & 0 \\ 0 & 0 & 0 & 6.30\times10^{-1} \end{pmatrix}, \end{aligned} \tag{2.29}$$

Here are the best estimate response values, relative standard deviations (abbreviated as "rsd"), and covariances:

$$at\ \left(10\,cm\right):\ r_1^{be} = 3.66\times10^{9}\,n\cdot cm^{-3}\cdot sec^{-1};\ rsd\left(r_1^{be}\right) = 2.59\%; \tag{2.30}$$

$$at\ (-10\,cm):\ r_2^{be} = 3.66\times10^9\, n\cdot cm^{-3}\cdot sec^{-1};\ rsd\left(r_2^{be}\right) = 2.59\%; \tag{2.31}$$

$$at\ (-40\,cm):\ r_3^{be} = 3.56\times10^9\, n\cdot cm^{-3}\cdot sec^{-1};\ rsd\left(r_3^{be}\right) = 2.58\%; \tag{2.32}$$

$$at\ (40\,cm):\ r_4^{be} = 3.56\times10^9\, n\cdot cm^{-3}\cdot sec^{-1};\ rsd\left(r_4^{be}\right) = 2.58\%; \tag{2.33}$$

$$\boldsymbol{C}_r^{be} = \begin{pmatrix} 9.04\times10^{15} & 9.04\times10^{15} & 8.64\times10^{15} & 8.64\times10^{15} \\ 9.04\times10^{15} & 9.04\times10^{15} & 8.64\times10^{15} & 8.64\times10^{15} \\ 8.64\times10^{15} & 8.64\times10^{15} & 8.45\times10^{15} & 8.45\times10^{15} \\ 8.64\times10^{15} & 8.64\times10^{15} & 8.45\times10^{15} & 8.45\times10^{15} \end{pmatrix} \tag{2.34}$$

Predicted response-parameter correlation matrix:

$$\boldsymbol{C}_{r\alpha}^{be} = \begin{pmatrix} -7.81\times10^{3} & 3.89\times10^{4} & 1.38\times10^{13} & 4.57\times10^{6} \\ -7.81\times10^{3} & 3.89\times10^{4} & 1.38\times10^{13} & 4.57\times10^{6} \\ 1.50\times10^{3} & -4.13\times10^{4} & 1.64\times10^{13} & 5.41\times10^{6} \\ 1.50\times10^{3} & -4.13\times10^{4} & 1.64\times10^{13} & 5.41\times10^{6} \end{pmatrix}. \tag{2.35}$$

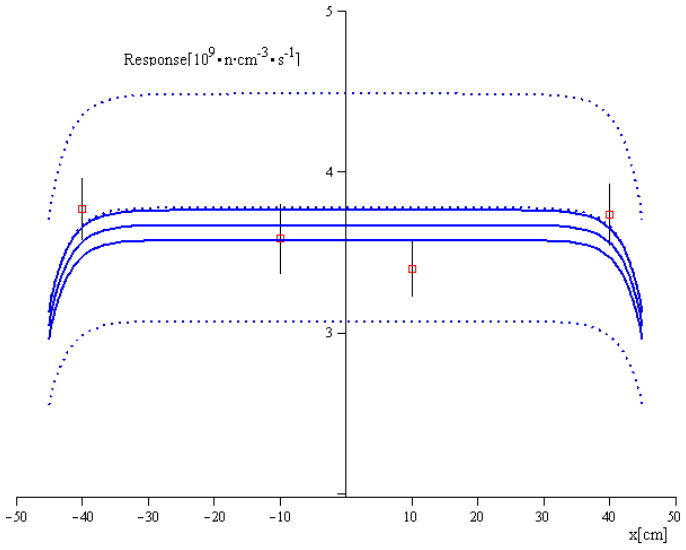

Figure 2.1.1: Four precise consistent precise measurements ($\chi^2 = 1.21$)

Figure 2.1.1 shows the spatial variation of the original nominal computed values and standard deviations (depicted using solid lines) together with the best estimate response values and corresponding standard deviations (depicted using broken lines). The value of $\chi^2 = 1.21$ indicates a very good consistency among the four measurements.

2.2 Time-Dependent A Spent Fuel Dissolver Model

The "dissolver" is a mechanical and chemical module that produces feed stock for the chemical separation processes employed in the "head end" segment of an aqueous nuclear fuel reprocessing facility. The specific dissolver model considered in this work was originally developed by Lewis and Weber [Le1980], and has been selected due to its applicability to material separations and its potential role in diversion activities associated with proliferation and international safeguards. The equations that model the time dependent start-up conditions for the dissolver are presented in this section . The dissolver model comprises sixteen time-dependent state functions and 635 model parameters related to the model's equation of state and inflow conditions. In particular, the most important response for the dissolver model is the time-dependent nitric acid in the compartment furthest away from the inlet, because this is the location where Lewis and Weber [Le1980] reported measurements (unique in the open literature) at 307 time instances, t_i, $i = 1,...,I = 307$, over a period of 10.5 hours.

The predictive modeling formalism presented in Section 1 is subsequently used to combine the computational results with the experimental information measured in the compartment furthest from the inlet, and then predict optimal values and uncertainties throughout the dissolver. The numerical results presented in this section show that, even though the experimental data pertains solely to the compartment furthest from the inlet (where the data was measured), the predictive modeling procedure actually improves the predictions and reduces the predicted uncertainties not only in the compartment in which the data was actually measured, but throughout the entire dissolver including the compartment furthest from the measurements. This is because the predictive modeling methodology combines and transmits information simultaneously over the entire phase-space, comprising all time steps and spatial locations. Further details are provided in References [Ca2015, Pe2015a, Pe2015b, Pe2015c, Ca2016] .

The spent nuclear fuel dissolver model considered in this work is schematically depicted in Figure 2.2.1. The dissolver start-up conditions involve a non-ideal mixture of nitric acid and water at ambient conditions.

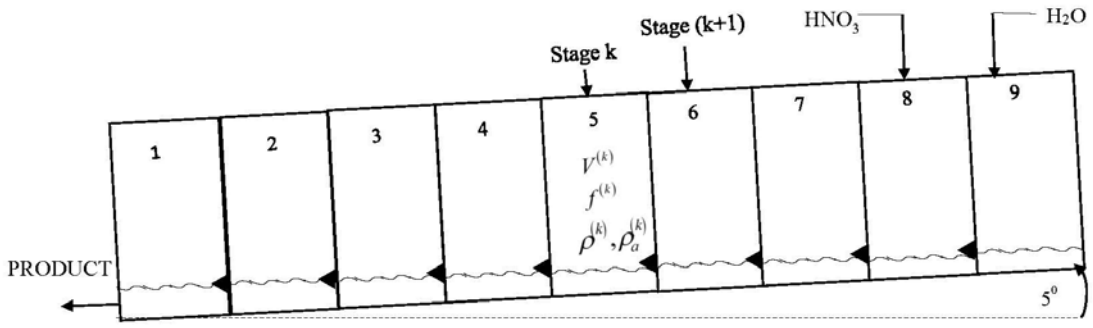

Figure 2.2.1: Liquid flow diagram for the compartmented rotary dissolver (after Lewis and Weber [Le 1980])

The liquid flows through the dissolver's eight compartments, labeled using the superscript *k*, $k = 1,...,8$, from compartment #8 towards compartment #1. Compartment 9 is used for rinsing, and is not relevant to this work. The equation modeling the time and spatial variation of the physical and chemical processes occurring within the dissolver's start-up were originally developed by Weber and Lewis [Le1980] and subsequently modified by Peltz and Cacuci [Pe2015b], to obtain the following system of first-order nonlinear ordinary differential equations:

$$V^{(k)}(t)\frac{d}{dt}\left[\rho_a^{(k)}\right]+\left[\rho_a^{(k)}(t)-\rho_a^{(k+1)}(t)\right]C\left[V^{(k+1)}(t)\right]=0,\ k=1,...,7,\ 0<t\le t_f,$$

$$V^{(8)}(t)\frac{d}{dt}\left[\rho_a^{(8)}\right]+\rho_a^{(8)}(t)\,f^{(in)}(t)=\rho_a^{in}(t)\,f^{(in)}(t),\ 0<t\le t_f.$$

$$\frac{d}{dt}\left[V^{(k)}(t)\right]=-C\left[V^{(k)}(t)\right]+C\left[V^{(k+1)}(t)\right],\ k=1,...,7,\ 0<t\le t_f,$$

$$\frac{d}{dt}\left[V^{(8)}(t)\right]=-C\left[V^{(8)}(t)\right]+f^{(in)}(t),\ 0<t\le t_f.$$

where

$$C\left(V^{(k)}\right)=\begin{cases}\left(\dfrac{V^{(k)}-V_0}{G}\right)^p\ [\ell/h], & \text{if } V^{(k)}(t)-V_0>0,\ k=1,...,8,\\ 0, & \text{otherwise.}\end{cases}$$

The quantities appearing in the above equations are defined as follows: (i) $V^{(k)}(t)$ denotes the volume of the liquid phase, in units of liters $[\ell]$; (ii) $\rho_a^{(k)}(t)$ denotes the volumetric mass concentration of nitric acid of the liquid phase, in units of $[g/\ell]$; (iii) $\rho_a^{(in)}(t)$ denotes the inlet nitric mass concentration; (iv) $f^{(in)}(t)$ denotes the inflow volumetric flow rate; (iv) the scalar quantities G, V_0 and p are experimentally determined parameters, with nominal (mean) values and estimated relative standard deviations presented in Table 2.2.1.

The initial conditions for above equations are as follows:

$$\rho_a^{(k)}(0) = 0.0, \;\; V^{(k)}(0) = V_0^{(k)}, \quad k = 1,...,8.$$

The compatibility condition for a fully developed initial flow implies that $\frac{d}{dt}V^{(k)}(0) = 0,\ k = 1,...,8$; in turn, this condition implies that

$$V_0^{(k)} \equiv G\left[f^{(in)}(0)\right]^{1/p} + V_0, \quad k = 1,...,8.$$

The equation of state for the dissolver model is

$$\rho^{(k)}(t) = 63a\rho_a^{(k)}(t) + b, \;\; k = 1,...,8.$$

where $\rho^{(k)}(t)$ denotes the volumetric mass density of the liquid phase, in units of gram/liter $[g/\ell]$, and where a and b are experimentally determined scalar parameters with nominal (mean) values and estimated relative standard deviations presented in Table 2.2.1.

The time-dependent nominal value of the inflow volumetric flow rate, $f^{(in)}(t)$, is obtained from the following expression:

$$f^{(in)}(t) = \dot{m}^{(in)}(t) \big/ \rho^{(k)}(t) = \dot{m}^{(in)}(t)\left[63a\rho_a^{(in)}(t) + b\right]^{-1},$$

where $\dot{m}^{(in)}(t)$ denotes the liquid solution mass rate inflow in units of gram/hour $[g/h]$. In particular, the initial nominal value of $f^{(in)}(t)$ is $f^{(in)}(0) = 36.79\times10^3/1001.2$ at $t = 0$. The

time-dependent variations of the inlet mass flow rate of solution, $\dot{m}^{(in)}(t)$, and inlet nitric mass concentration, $\rho_a^{(in)}(t)$, are presented in Figures 2.2.2 and 2.2.3, respectively. The estimated relative standard deviations of $\rho_a^{(in)}(t)$ and $\dot{m}^{(in)}(t)$ are presented in Table 2.2.1.

Table 2.2.1: Nominal (mean) values and corresponding standard deviations for model parameters.

Parameter	$\rho_a^{(in)}(t)$	$\dot{m}^{(in)}(t)$	a	b	V_0	p	G
Nominal value	See Fig. 2	See Fig. 3	0.48916	1001.2 $[g/\ell]$	4.8 $[\ell]$	2.7	0.201941 $[\ell]$
Standard deviation	20%	10%	10%	10%	10%	10%	10%

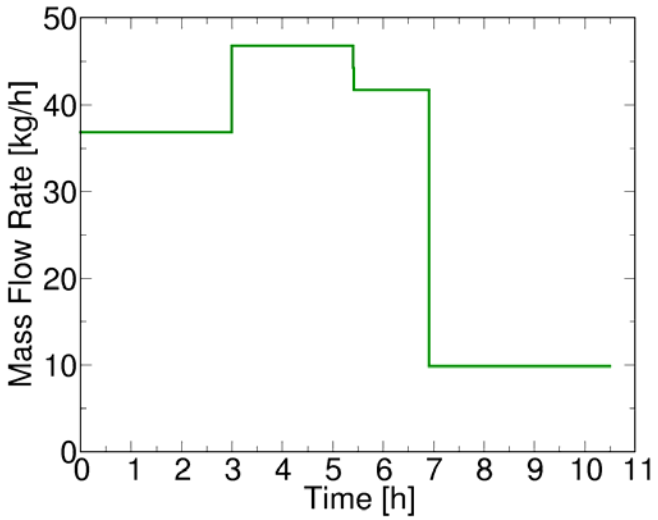

Figure 2.2.2: Time variation of the inlet mass flow rate of solution, $\dot{m}^{(in)}(t)/1000\,[\mathrm{kg/h}]$.

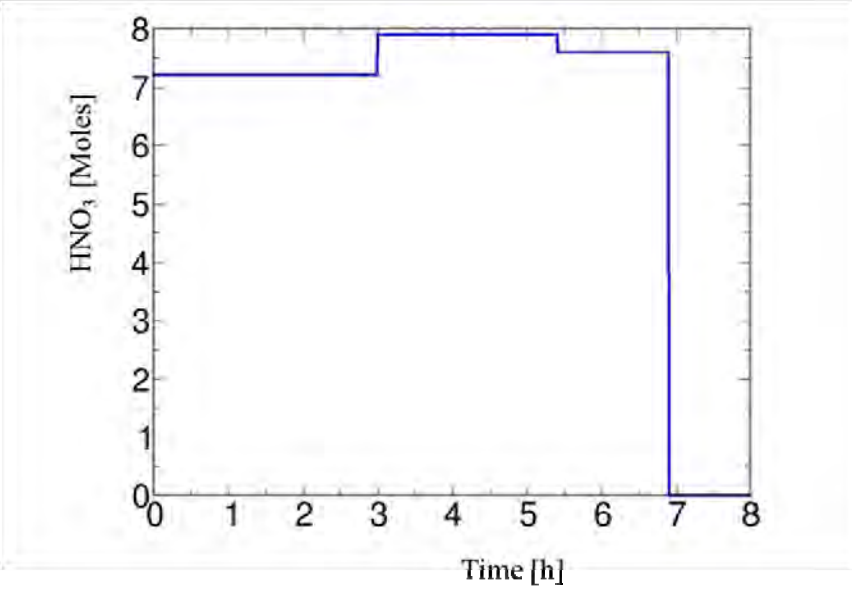

Figure2.2.3: Time variation of the inlet nitric acid mass concentration, $\rho_a^{(in)}(t)/63$ [moles].

The dissolver model comprises sixteen state variables $\left[\rho_a^{(1)}(t),...,\rho_a^{(8)}(t),V^{(1)}(t),...,V^{(8)}(t)\right]$ as well as 635 model parameters $\left[\rho_a^{(in)}(t_1),...,\rho_a^{(in)}(t_{307}),\dot{m}^{(in)}(t_1),...,\dot{m}^{(in)}(t_{307}),\rho_a^{(1)}(0),...,\rho_a^{(8)}(0),V^{(1)}(0),...,V^{(8)}(0),a,b,V_0,p,G\right]$.

At any time instance, ν, the system parameters are considered to be uncorrelated variates, denoted as $\boldsymbol{\alpha}^{\nu}=\left\{\alpha_n^{\nu}\,|n=1,...N_{\alpha}^{\nu}\right\}$, with mean values, denoted as $\left(\boldsymbol{\alpha}^0\right)^{\nu}$, and standard deviations as given in Table 2.2.1. Solving the equations presented in the foregoing at the nominal values for the model's parameters yields the time-dependent evolutions of the computed nominal values of the nitric acid concentrations in all of the compartments. In particular, the computed nominal values for $\rho_{a,nom}^{(1)}(t)$, $\rho_{a,nom}^{(4)}$, and $\rho_{a,nom}^{(7)}$, of the time-dependent acid concentrations in compartments #1 (furthest from the dissolver's inlet), #4 (in the dissolver's middle section), and #7 (closest to the dissolver's inlet), respectively, are depicted in Figure 2.2.4. The time evolutions of these concentrations are similar to each other, albeit time-delayed, as expected, and also resemble the time variation, depicted in Figure 2.2.3, of the inlet nitric acid mass concentration, $\rho_a^{(in)}(t)$.

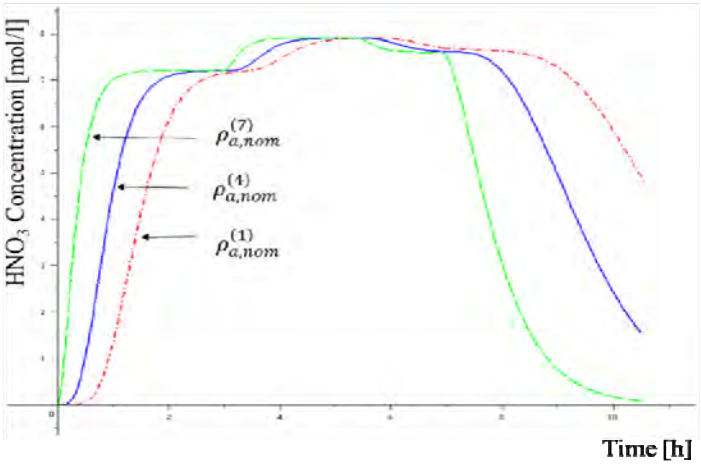

Figure 2.2.4: Time-evolution of the nominal values of the computed nitric acid concentrations $\rho_{a,nom}^{(1)}$, $\rho_{a,nom}^{(4)}$, $\rho_{a,nom}^{(7)}$, in compartments #1, #4, and #7, respectively.

The nitric acid concentration in compartment 1, $\rho_a^{(1)}(t)$, was measured by Lewis and Weber [Le1980] at 307 time instances, t_i, $i = 1,...,I = 307$, over a period of 10.5 hours. The nominal values of these measurements are denoted as $\rho_{a,meas}^{(1)}(t_i)$, and are depicted using blue circles in Figure 2.2.5. Notably, these experimental results are unique in the open literature for a rotary dissolver. The relative standard deviation of each of these measurements has been estimated to be 5%. Figures 2.2.5 also depicts the time-evolution of the normalized nominal values of the computed nitric acid concentration in compartment #1, $\rho_{a,nom}^{(1)}$, which is obtained by solving the dissolver equations using the nominal values for the model's parameters. The agreement between the nominal values of the computed and experimentally measured nitric concentration in compartment #1 is remarkable.

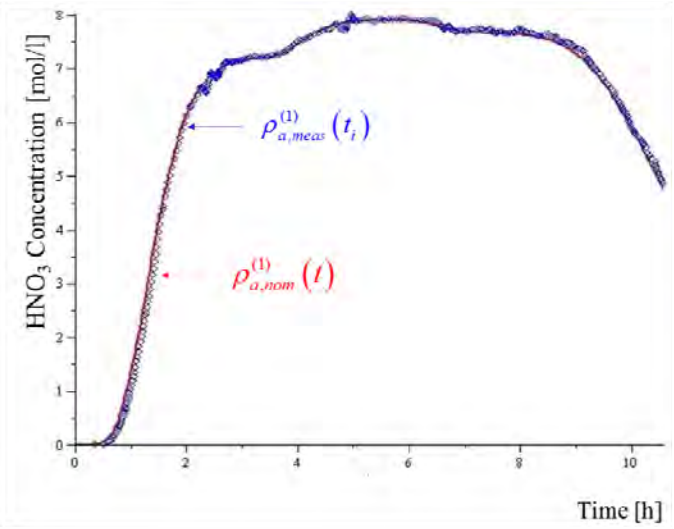

Figure 2.2.5: Red graph: time-evolution of the nominal values of the computed response of the nitric acid concentration, $\rho^{(1)}_{a,nom}(t)$. Blue circles: experimentally measured nominal values, $\rho^{(1)}_{a,meas}(t_i)$, of the nitric acid concentration, at time instances t_i, $i = 1,...,I = 307$ (Lewis and Weber [Le1980]).

Numerical Results

The optimally predicted "best-estimate" nominal values for the model parameters result from applying Eq. (1.24), and the reduced predicted covariances ("uncertainties") accompanying these predicted nominal values are computed using Eq. (1.34). Table 2.2.2 and Figures 2.2.6 through 2.2.9 present the results of applying these equations for the scalar model parameters involved in the equation of state.

Table 2.2.2: Initial and Predicted Nominal Values and Standard Deviations for the Scalar Model Parameters

Scalar Parameters	Nominal Values	Predicted Values	Nominal Relative Standard Deviation	Predicted Relative Standard Deviation
#1: a	0.48916	0.50621	10%	7.67834%
#2: b	$1001.2\left[g/\ell\right]$	$948.7\left[g/\ell\right]$	10%	4.54535%

#3: V_0	$4.8[\ell]$	$5.123[\ell]$	10%	4.97098%
#4: G	$0.20194[\ell]$	$0.20591[\ell]$	10%	9.82085%
#5: p	2.7	2.61256	10%	9.44417%

As Table 2.2.2 indicates, the uncertainties for these parameters are reduced from initially 10% to values as low as 4.5%. The uncertainty reduction is proportional to the sensitivity of the responses (i.e., acid concentrations) to the respective parameters. The predicted optimal values were also calibrated accordingly, as shown in Table 2.2.2, differing from their original nominal values.

Figure 2.2.6 displays the initial correlation matrix for the scalar parameters listed in Table 2.2.2, which are uncorrelated, having a relative standard deviation of 10%. The numbers on the vertical axis are in units of $(\%)^2$, so the numbers shown are to be multiplied by 10^{-4}, while the numbers on the two horizontal axes correspond to the parameter numbering in Table 2.2.2. The results after having applied Eq. (1.34) are displayed in Figure 2.2.7, which shows the predicted correlation matrix for the scalar parameters listed in Table 2.2.2. It is seen that the application of the predictive modeling methodology induces non-zero correlations among several of the parameters notably between parameters #4 and #5 (*G* and *p*) and, to a lesser extent, between parameters #2 and #3 (*b* and V_0). The diagonal values in Figure 2.2.7 are the predicted variances, i.e., the squares of the values shown in the last column of Table 2.2.1

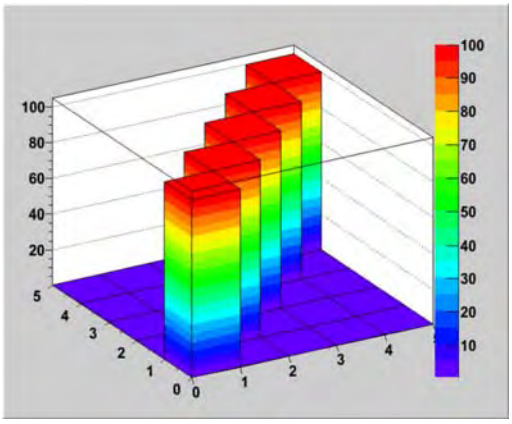

Figure 2.2.6: Initial correlation matrix for the scalar parameters listed in Table 2.2.2.

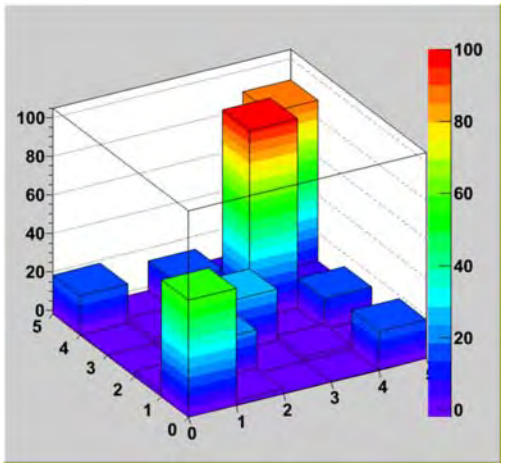

Figure 2.2.7: Predicted correlation matrix, $\left(\boldsymbol{C}_{\alpha}^{be}\right)^{\nu\mu}$, for the scalar parameters listed in Table 2.2.2.

The results of applying Eqs. (1.24) and (1.34) for the time dependent inlet acid concentration, $\rho_a^{(in)}(t)$, are depicted in Figures 2.2.8 and 2.2.9, respectively. The time-dependent calibration of the nominal value $\rho_a^{(in)}(t)$ is relatively small, and so is the reduction in the corresponding time-dependent standard deviation, from the initial value of $\sigma\left[\rho_a^{(in)}(t)\right] = 20\%$.

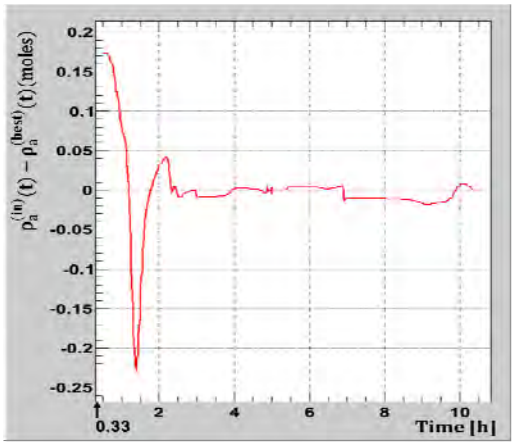

Figure 2.2.8: Time-dependent behavior of the difference between the nominal value, $\rho_a^{(in)}(t)$, and the optimally predicted "best estimate" value, $\rho_a^{(best)}(t)$, for the inlet acid concentration.

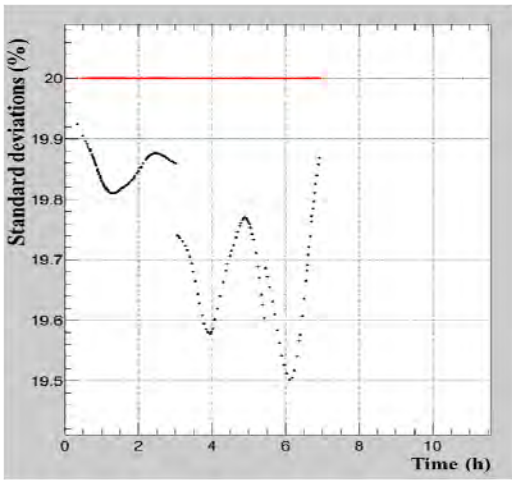

Figure 2.2.9: Time-dependent behavior of the original relative standard deviation $\sigma\left[\rho_a^{(in)}(t)\right]=20\%$ (in red) and the optimally predicted "best estimate" relative standard deviation $\sigma\left[\rho_a^{(best)}(t)\right]$ (in black), for the inlet acid concentration.

The results of applying Eqs. (1.24) and (1.34) to the time dependent mass flow rate, $\dot{m}^{(in)}(t)$, are depicted in Figure 2.2.10 and 2.2.11, respectively. The time-dependent calibration of the nominal value $\dot{m}^{(in)}(t)$ is also relatively small, and so is the reduction in the corresponding time-dependent standard deviation, from the initial value of $\sigma\left[\dot{m}^{(in)}(t)\right]=10\%$.

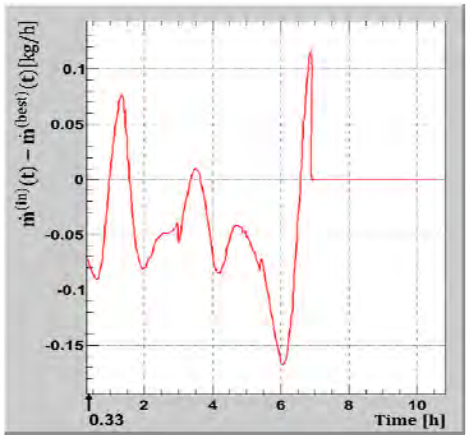

Figure 2.2.10: Time-dependent behavior of the difference between the nominal value, $\dot{m}^{(in)}(t)$, and the optimally predicted "best estimate" value, $\dot{m}^{(best)}(t)$, for the inlet mass flow rate.

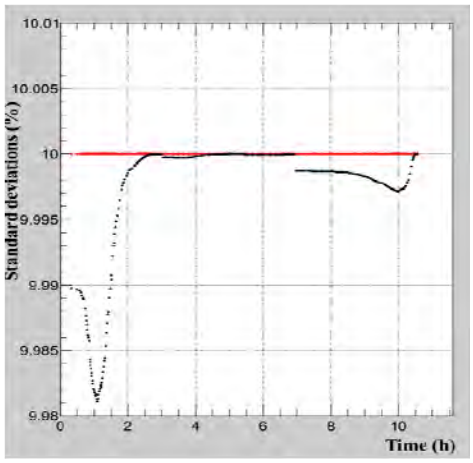

Figure 2.2.11: Time-dependent behavior of original relative standard deviation, $\sigma\left[\dot{m}^{(in)}(t)\right]=10\%$, and the optimally predicted "best estimate" $\sigma\left[\dot{m}^{(best)}(t)\right]$, for the inlet mass flow rate.

The predicted best estimate nominal values for the nitric acid concentration responses are obtained using Eq. (1.28). Figure 2.2.12 presents the computed, experimental, and best estimate predicted nominal values for the nitric acid concentration in compartment #1. All of these values are in close agreement with one another.

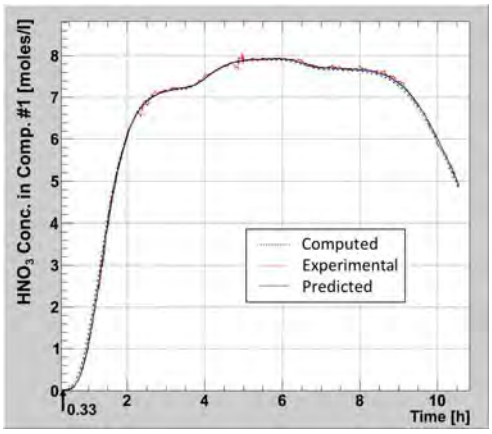

Figure 2.2.12: Computed, experimental, and best estimate predicted nominal values for the nitric acid concentration in compartment #1.

The full covariance matrix of the computed acid concentration in compartment #1, which arises due to uncertainties in the model parameters and is obtained using Eq. (1.15), is depicted in Figure 2.2.13. As can be noted from this figure, the computed responses in the early stages of the transient, between time instances 5 - 75, are strongly (up to -0.86

[moles/l]^2) anti-correlated in time with the responses computed towards the end of the transient, between time instances 266-307. At other time instances, the responses are weakly correlated, except for the responses between time instances 5-60, which are strongly (up to 0.86 [moles/l]^2) correlated to each other, and again at the end of the transient, between time instances 260-307, when they again become strongly correlated. Variances of 0.86 [moles/l]^2, as noticed at the end of the transient, correspond to relative standard deviations of about 20%.

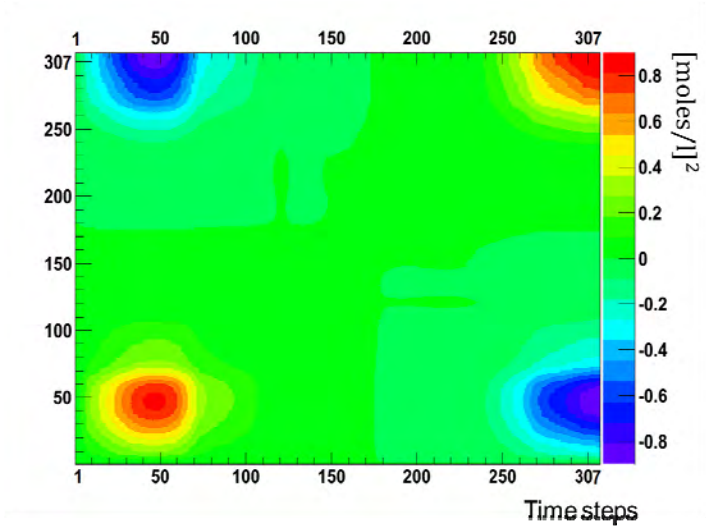

Figure 2.2.13: Time-dependent *computed* correlation matrix (arising from parameter uncertainties), $\boldsymbol{C}_{rc}^{\nu\mu}$, for the nitric acid concentration in compartment #1.

The predicted best estimate response correlations are obtained by using Eq. (1.35) and are depicted in Figure 2.2.14. As indicated in this figure, all best-estimate correlations, including the predicted standard deviations, are significantly reduced and rendered uniform. The corresponding (+/-) one-standard deviations are plotted in Figure 2.2.15, which depicts the behavior in time of the measured response standard deviation (5%), the computed response standard deviation [i.e., the diagonal elements of Eq. (1.15) stemming from uncertainties in the model parameters], and the best-estimate predicted response standard deviation obtained using Eq. (1.35). It is evident from Figure 2.2.15 that the "predicted best-estimate" response standard deviation is smaller than either the "measured" standard deviation or the "computed" one, for the entire time-interval under consideration.

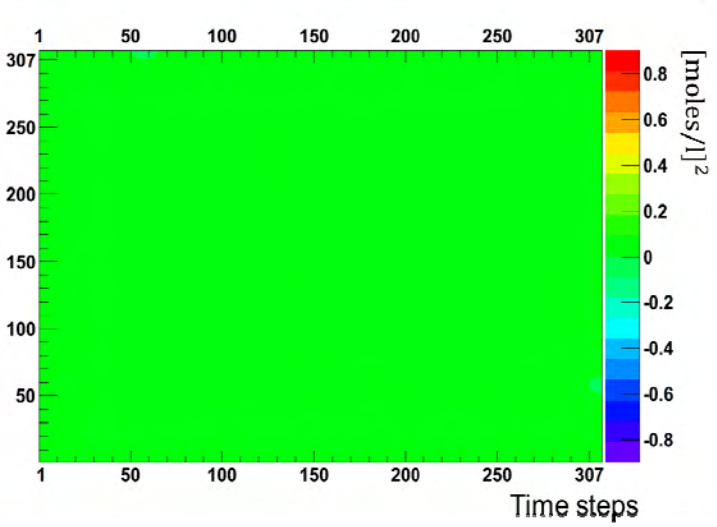

Figure 2.2.14: Time-dependent *best-estimate predicted* correlation matrix, $\left(\boldsymbol{C}_r^{be}\right)^{\nu\mu}$, for the nitric acid concentration in compartment #1.

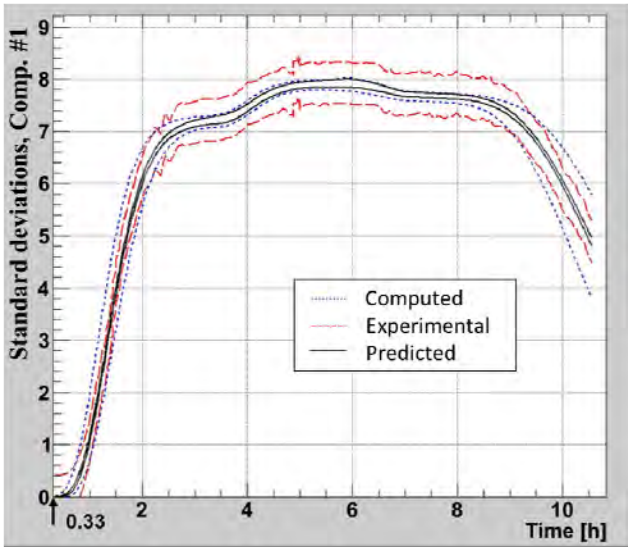

Figure 2.2.15: Computed, experimental, and best estimate predicted (+/-) *absolute* standard deviations for the nitric acid concentration in compartment #1.

Even though no measurements were performed in the dissolver compartments 2 through 8, the nominal values of the "best-estimate" responses, $\left(\boldsymbol{r}^{be}\right)^{\nu}$, in these compartments can be computed by using the calibrated best estimate parameter values $\left(\boldsymbol{\alpha}^{be}\right)^{\nu}$. In this vein, the best-

estimate predicted parameter values for all 635 model parameters (as presented in Table 2.2.2 and depicted Figures 2.2.8 and 2.2.10) together with their reduced predicted uncertainties (as presented in Table 2.2.2 and depicted Figures 2.2.9 and 2.2.11) were used to re-compute the nominal values of the best-estimate responses, $\left(\boldsymbol{r}^{be}\right)^{\nu}$. It turned out that these best-estimate responses were very close to the originally computed nominal values. In addition, the best-estimate predicted uncertainties in the best-estimate computed responses can be obtained by using the "propagation of errors" formula given Eq. (1.15), but using the best estimated parameter values and their corresponding best-estimate standard deviations, i.e.,

$$\left(\boldsymbol{C}_r^{be}\right)^{\nu\mu} = \sum_{\eta=1}^{\nu}\sum_{\rho=1}^{\mu}\left[\boldsymbol{S}^{\nu\eta}\right]^{be}\left[\boldsymbol{C}_{\alpha}^{\eta\rho}\right]^{be}\left[\left(\boldsymbol{S}^{\mu\rho}\right)^{\dagger}\right]^{be}; \quad \nu,\mu = 1,...,N_t. \qquad \text{(A)}$$

As will be shown below, the computation of the best-estimate uncertainties using Eq. (A) for the compartments in which no measurement were performed indeed underwent reductions, in all compartments, by comparison to the originally computed uncertainties. Typical results will be presented in the figures below, for compartment #4 (in the middle of the dissolver) and for compartment #7; the uncertainty reductions in the other compartments are not reproduced here because they can be obtained by interpolating linearly between the results presented for compartments #1, #4, and #7.

The original covariance matrix of the computed acid concentration in compartment #4, obtained using Eq. (1.15), is depicted in Figure 2.2.16. As can be noted from this figure, the computed responses in the early stages of the transient, between time instances 5 - 30, are anti-correlated in time with the responses computed towards the end of the transient, between time instances 266-307. The anti-correlations for the acid concentration in compartment #4 are similar to the time-dependent response anti-correlations in compartment #1. The acid concentration responses in compartment #4 are less strongly correlated at other time instances, except for the responses between the initial stages of the transient (time instances 1-50) and again at the end of the transient (time instances 260-307), when they are positively correlated,

with variances reaching as high as 0.6 [moles/l]^2. This value corresponds to an absolute standard deviation of 0.77 [moles/l], which in turn corresponds to a relative standard deviation of over 50% --which is rather large compute uncertainty in this response (i.e., the acid concentration in compartment #4). Overall, the time-correlations for the acid concentration in compartment #4 are similar to the time-dependent response correlations in compartment #1, but stronger, in relative terms.

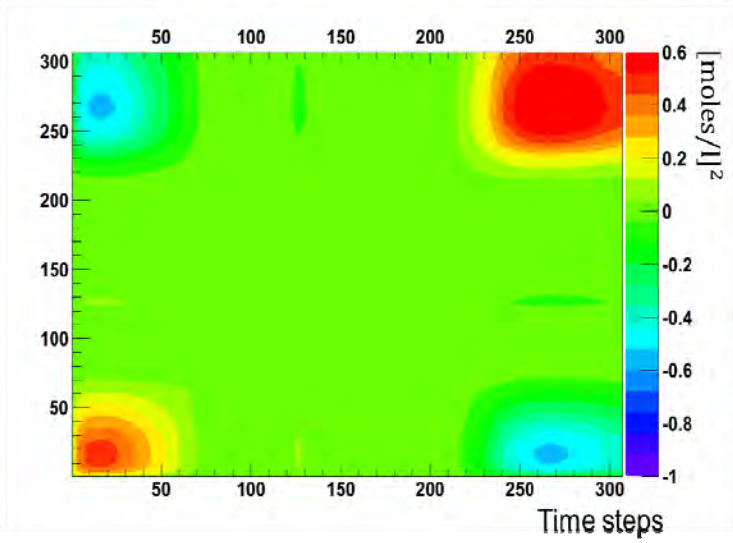

Figure 2.2.16: Time-dependent *computed* correlation matrix (arising from parameter uncertainties), $\boldsymbol{C}_{rc}^{\nu\mu}$, for the nitric acid concentration in compartment #4.

The predicted best estimate response correlations obtained by using Eq. (A) are depicted in Figure 2.2.17. As indicated in this figure, all best-estimate correlations, including the predicted standard deviations, are drastically reduced and rendered much more uniform. The corresponding (+/-) one-standard deviations are plotted in Figure 2.2.18, which depicts the behavior in time of the computed response standard deviation [i.e., the diagonal elements of Eq. (1.15) stemming from uncertainties in the model parameters] and the best-estimate predicted response standard deviation obtained using Eq. (1.35). It is evident from Figure 2.2.16 that the "predicted best-estimate" response standard deviation is considerably smaller than the "computed" one, for the entire time-interval under consideration.

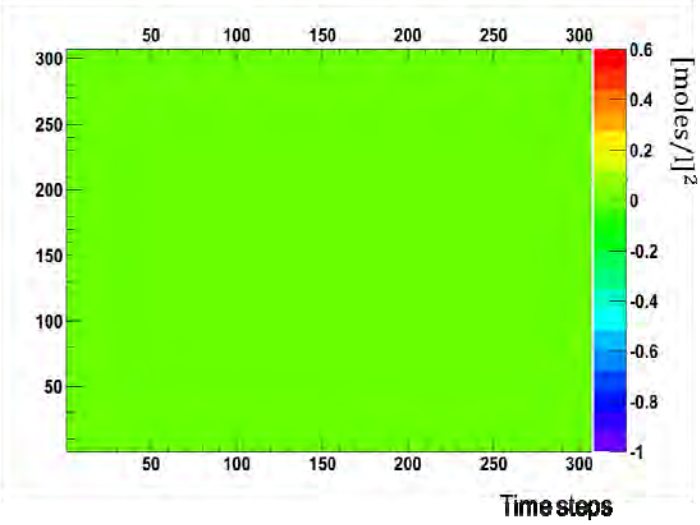

Figure 2.2.17: Time-dependent *best-estimate predicted* correlation matrix, $\left(\boldsymbol{C}_r^{be}\right)^{\nu\mu}$, for the nitric acid concentration in compartment #4.

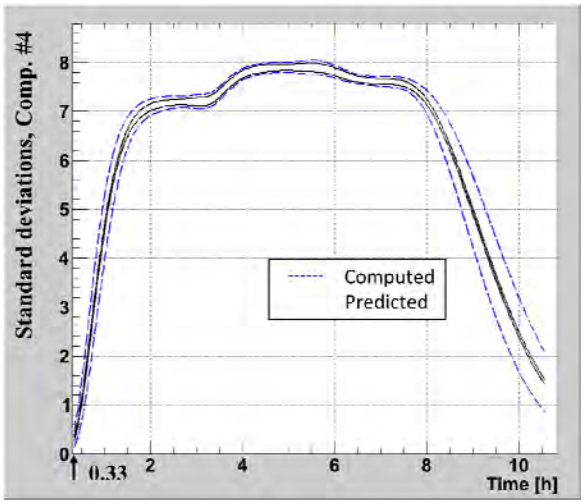

Figure 2.2.18: Computed and best estimate predicted *absolute* standard deviations (+/-) for the nitric acid concentration in compartment #4.

The original covariance matrix of the computed acid concentration in compartment #7, obtained using Eq. (1.15), is depicted in Figure 2.2.19, which displays an "island of anti-correlated responses between time instances 1-10 and responses at instances 220-260, as well as an "island" of positively correlated acid concentrations among the time instances 220-260. Although the absolute values of the overall uncertainties are smaller in this compartment, by comparison to the other compartments, their relative values are actually larger than in the other compartments. For example, the largest variance of the acid concentration in

compartment being 0.2 $[moles/l]^2$, which occurs during the time instances 220-240; this variance corresponds to a relative standard deviation of 90%, as can be deduced from Figure 2.2.21. The predicted best estimate response correlations obtained by using Eq. (A) are depicted in Figure 2.2.20. As indicated in this figure, all best-estimate correlations, including the predicted standard deviations, are drastically reduced and rendered much more uniform. The corresponding (+/-) one-standard deviations are plotted in Figure 2.2.21, which depicts the behavior in time of the computed response standard deviation [i.e., the diagonal elements of Eq. (1.15) stemming from uncertainties in the model parameters] and the best-estimate predicted response standard deviation obtained using Eq. (A). It is evident from Figure 2.2.21 that the "predicted best-estimate" response standard deviation for the acid concentration in compartment #7 is considerably smaller than the "computed" one, over the entire time-interval under consideration.

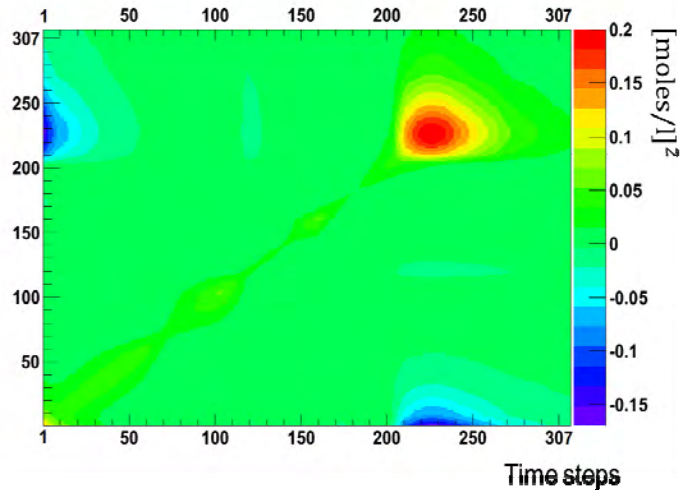

Figure 2.2.19: Time-dependent *computed* correlation matrix (arising from parameter uncertainties), $\boldsymbol{C}_{rc}^{\nu\mu}$, for the nitric acid concentration in compartment #7.

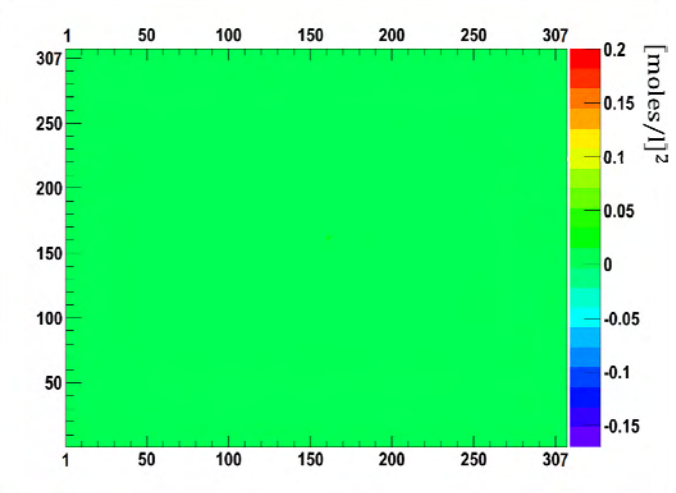

Figure 2.2.20: Time-dependent *best-estimate predicted* correlation matrix, $\left(\boldsymbol{C}_r^{be}\right)^{\nu\mu}$, for the nitric acid concentration in compartment #7.

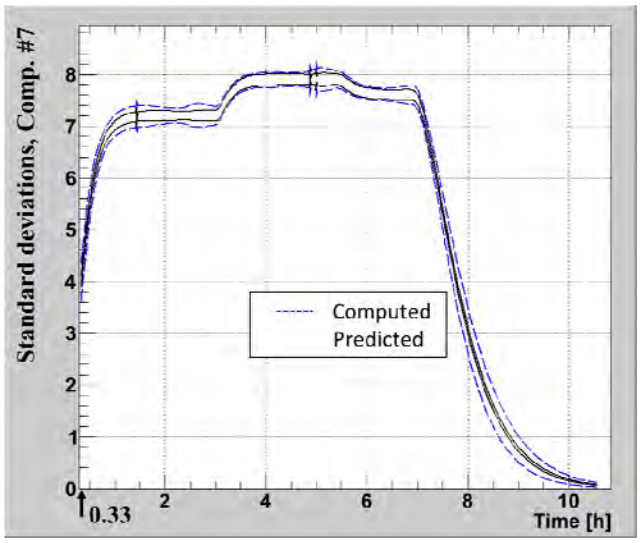

Figure 2.2.21: Computed (blue graph) and best estimate predicted (black graph) *absolute* standard deviations (+/-) for the nitric acid concentration in compartment #7.

The results presented in the forgoing highlight the very beneficial effects of the comprehensive framework of the predictive modeling methodology of Cacuci and Ionescu-Bujor [Ca2010a,b], which considers the entire phase-space of parameters and responses simultaneously over the entire time interval of interest. In particular, this unique feature made it possible to "spread out" the positive effects of having performed measurements in one region of the dissolver (in this case, in compartment #1) to reduce significantly the predicted

uncertainties in the acid concentration not only in the compartment where measurements were performed but also in all of the other compartments, where measurements were lacking. Further results are presented in [Ca2015], [Ca2016], [Pe2015a], [Pe2015b] and [Pe2015c].

3 MULTI-PRED Module

The module MULTI-PRED is a computational implementation of the time-dependent mathematical formalism of Cacuci and Ionescu-Bujor **[Ca2010a]**.

All routines are written as C++ scripts running under the CERN Platform ROOT (https://root.cern.ch/) compatible with both Linux/Unix and Windows operating systems.

The developed software has the following tree-structure of the directories:

1) MULTI-PRED/**example**/**KERNEL** *directory* containing the ***kernel*** of the MULTI-PRED module; the *kernel* is *invariant* on its time-*independent* or time-*dependent* use; this is an *intrinsic property* of the mathematical formalism of Cacuci and Ionescu-Bujor **[Ca2010a]**.

2) MULTI-PRED/**example**/**INPfiles** *directory* containing the (ASCII format) initial/raw *input files*

3) MULTI-PRED/**example** /**vorKERNEL** *directory* containing the script vorMULTI-PRED.C which transforms the initial/raw input files into compatible format for the MULTI-PRED kernel.

4) MULTI-PRED/**example** /**nachKERNEL** *directory* containing the scripts for extracting and displaying the results of the MULTI-PRED module.

"**example**" means "**diffusion**" or "**dissolver**".

3.1 Kernel

The following relations from the work **[Ca2010a]** have been selected for implementation in the kernel of the MULTI-PRED module.

Covariances of the computed responses:

$$\begin{aligned} \boldsymbol{C}_{rc}\left(\boldsymbol{\alpha}^0\right) \equiv \left\langle \delta\boldsymbol{r}\delta\boldsymbol{r}^\dagger \right\rangle = \left[\boldsymbol{S}\left(\boldsymbol{\alpha}^0\right)\right]\left\langle \delta\boldsymbol{\alpha}\delta\boldsymbol{\alpha}^\dagger \right\rangle \left[\boldsymbol{S}\left(\boldsymbol{\alpha}^0\right)\right]^\dagger = \\ \left[\boldsymbol{S}\left(\boldsymbol{\alpha}^0\right)\right]\boldsymbol{C}_\alpha \left[\boldsymbol{S}\left(\boldsymbol{\alpha}^0\right)\right]^\dagger \end{aligned} \tag{3.1}$$

Discrepancy between the nominal computations and the nominally measured responses:

$$\boldsymbol{d} \equiv \boldsymbol{R}\left(\boldsymbol{\alpha}^0\right) - \boldsymbol{r}_m \tag{3.2}$$

The calibrated best-estimate parameter values:

$$\boldsymbol{\alpha}^{be} = \boldsymbol{\alpha}^0 + \left(\boldsymbol{C}_{\alpha r} - \boldsymbol{C}_\alpha \left[\boldsymbol{S}\left(\boldsymbol{\alpha}^0\right)\right]^\dagger\right)\left[\boldsymbol{C}_d\left(\boldsymbol{\alpha}^0\right)\right]^{-1}\boldsymbol{d} \tag{3.3}$$

with:

$$\begin{aligned} \boldsymbol{C}_d\left(\boldsymbol{\alpha}^0\right) \equiv \left\langle \boldsymbol{d}\boldsymbol{d}^\dagger \right\rangle = \left\langle \left(\delta\boldsymbol{r} - \boldsymbol{S}\left(\boldsymbol{\alpha}^0\right)\delta\boldsymbol{\alpha}\right)\left(\delta\boldsymbol{r}^\dagger - \delta\boldsymbol{\alpha}^\dagger\left[\boldsymbol{S}\left(\boldsymbol{\alpha}^0\right)\right]^\dagger\right)\right\rangle \\ = \boldsymbol{C}_{rc}\left(\boldsymbol{\alpha}^0\right) - \boldsymbol{C}_{r\alpha}\left[\boldsymbol{S}\left(\boldsymbol{\alpha}^0\right)\right]^\dagger - \left[\boldsymbol{S}\left(\boldsymbol{\alpha}^0\right)\right]\boldsymbol{C}_{\alpha r} + \boldsymbol{C}_m . \end{aligned} \tag{3.4}$$

The best-estimate predicted nominal values for the calibrated (adjusted) responses:

$$\boldsymbol{r}\left(\boldsymbol{\alpha}^{be}\right) = \boldsymbol{r}_m + \left(\boldsymbol{C}_m - \boldsymbol{C}_{r\alpha}\left[\boldsymbol{S}\left(\boldsymbol{\alpha}^0\right)\right]^\dagger\right)\left[\boldsymbol{C}_d\left(\boldsymbol{\alpha}^0\right)\right]^{-1}\boldsymbol{d} . \tag{3.5}$$

Best-estimate predicted covariances corresponding to the best-estimate parameters:

$$\begin{aligned} \boldsymbol{C}_\alpha^{be} \equiv \left\langle \left(\boldsymbol{\alpha} - \boldsymbol{\alpha}^{be}\right)\left(\boldsymbol{\alpha} - \boldsymbol{\alpha}^{be}\right)^\dagger \right\rangle \\ = \boldsymbol{C}_\alpha - \left[\boldsymbol{C}_{\alpha d}\left(\boldsymbol{\alpha}^0\right)\right]\left[\boldsymbol{C}_d\left(\boldsymbol{\alpha}^0\right)\right]^{-1}\left[\boldsymbol{C}_{\alpha d}\left(\boldsymbol{\alpha}^0\right)\right]^\dagger , \end{aligned} \tag{3.6}$$

Best-estimate predicted covariances corresponding to the best-estimate responses:

$$\begin{aligned} \boldsymbol{C}_r^{be} &\equiv \left\langle \left(\boldsymbol{r}-\boldsymbol{r}\left(\boldsymbol{\alpha}^{be}\right)\right)\left(\boldsymbol{r}-\boldsymbol{r}\left(\boldsymbol{\alpha}^{be}\right)\right)^{\dagger} \right\rangle \\ &= \boldsymbol{C}_m - \left[\boldsymbol{C}_{rd}\left(\boldsymbol{\alpha}^0\right)\right]\left[\boldsymbol{C}_d\left(\boldsymbol{\alpha}^0\right)\right]^{-1}\left[\boldsymbol{C}_{rd}\left(\boldsymbol{\alpha}^0\right)\right]^{\dagger}, \end{aligned} \tag{3.7}$$

Predicted best-estimate parameter-response covariances:

$$\boldsymbol{C}_{r\alpha}^{be} = \boldsymbol{C}_{r\alpha} - \left[\boldsymbol{C}_{rd}\left(\boldsymbol{\alpha}^0\right)\right]\left[\boldsymbol{C}_d\left(\boldsymbol{\alpha}^0\right)\right]^{-1}\left[\boldsymbol{C}_{\alpha d}\left(\boldsymbol{\alpha}^0\right)\right]^{\dagger}, \tag{3.8}$$

where

$$\boldsymbol{C}_{rd}\left(\boldsymbol{\alpha}^0\right) \equiv \left\langle \left(\boldsymbol{r}-\boldsymbol{r}_m\right)\boldsymbol{d}^{\dagger} \right\rangle = \left(\boldsymbol{C}_m - \boldsymbol{C}_{r\alpha}\left[\boldsymbol{S}\left(\boldsymbol{\alpha}^0\right)\right]^{\dagger}\right), \tag{3.9}$$

and

$$\boldsymbol{C}_{\alpha d}\left(\boldsymbol{\alpha}^0\right) \equiv \left\langle \left(\boldsymbol{\alpha}-\boldsymbol{\alpha}^0\right)\boldsymbol{d}^{\dagger} \right\rangle = \left(\boldsymbol{C}_{\alpha r} - \boldsymbol{C}_{\alpha}\left[\boldsymbol{S}\left(\boldsymbol{\alpha}^0\right)\right]^{\dagger}\right). \tag{3.10}$$

The formulas above (Eqs. 3.1-10) correspond to Eqs. 30, 35, 39, 41, 43, 45-49 from **[Ca2010a]**, respectively.

For computational reasons, Eqs. 3.1-10 have been organized as follows:

Notations:

$$A \equiv \boldsymbol{C}_M - \boldsymbol{C}_{r\alpha}\boldsymbol{S}^T \tag{3.11}$$

$$B \equiv -\boldsymbol{C}_{r\alpha}^T + \boldsymbol{C}_{\alpha}\boldsymbol{S}^T \tag{3.12}$$

and then:

$$\boldsymbol{d} = \boldsymbol{r} - \boldsymbol{m} \tag{3.13}$$

$$\boldsymbol{C}_r = \boldsymbol{S}\boldsymbol{C}_{\alpha}\boldsymbol{S}^T \tag{3.14}$$

$$\boldsymbol{C}_d = \boldsymbol{A} + \boldsymbol{S}\boldsymbol{B} \tag{3.15}$$

$$\boldsymbol{\alpha}^{BE} = \boldsymbol{\alpha} - \boldsymbol{B}\boldsymbol{C}_d^{-1}\boldsymbol{d} \tag{3.16}$$

$$\boldsymbol{C}_{\alpha}^{BE} = \boldsymbol{C}_{\alpha} - \boldsymbol{B}\boldsymbol{C}_d^{-1}\boldsymbol{B}^T \tag{3.17}$$

$$\boldsymbol{r}^{BE} = \boldsymbol{m} + \boldsymbol{A}\boldsymbol{C}_d^{-1}\boldsymbol{d} \tag{3.18}$$

$$\boldsymbol{C}_r^{BE} = \boldsymbol{C}_m - \boldsymbol{A}\boldsymbol{C}_d^{-1}\boldsymbol{A}^T \tag{3.19}$$

$$\boldsymbol{C}_{r\alpha}^{BE} = \boldsymbol{C}_{r\alpha} - \boldsymbol{A}\boldsymbol{C}_d^{-1}\boldsymbol{B}^T \tag{3.20}$$

Additionally, the consistency indicator:

$$\chi^2 = \boldsymbol{d}^T \boldsymbol{C}_d^{-1}\boldsymbol{d} \tag{3.21}$$

Here are the block-matrix structures of the ***basic input*** elements ($\boldsymbol{\alpha}, \boldsymbol{r}, \boldsymbol{m}, \boldsymbol{C}_{\alpha}, \boldsymbol{C}_{m}, \boldsymbol{C}_{r\alpha}, \boldsymbol{S}$) in the equations 3.11-21:

i) Nominal system parameters, computed responses, and measured responses:

$$\alpha = \begin{pmatrix} \alpha_1^1 \\ \alpha_2^1 \\ . \\ \alpha_{N_\alpha}^1 \\ . \\ . \\ \alpha_1^\mu \\ \alpha_2^\mu \\ . \\ \alpha_{N_\alpha}^\mu \\ . \\ . \\ \alpha_1^{N_t} \\ \alpha_2^{N_t} \\ . \\ \alpha_{N_\alpha}^{N_t} \end{pmatrix} \qquad r = \begin{pmatrix} r_1^1 \\ r_2^1 \\ . \\ r_{N_r}^1 \\ . \\ . \\ r_1^\mu \\ r_2^\mu \\ . \\ r_{N_r}^\mu \\ . \\ . \\ r_1^{N_t} \\ r_2^{N_t} \\ . \\ r_{N_r}^{N_t} \end{pmatrix} \qquad m = \begin{pmatrix} m_1^1 \\ m_2^1 \\ . \\ m_{N_r}^1 \\ . \\ . \\ m_1^\mu \\ m_2^\mu \\ . \\ m_{N_r}^\mu \\ . \\ . \\ m_1^{N_t} \\ m_2^{N_t} \\ . \\ m_{N_r}^{N_t} \end{pmatrix}$$

$$\begin{aligned} N_t &= number\ of\ time\ nodes \\ N_\alpha &= number\ of\ sistem\ parameters \\ N_r &= number\ of\ sistem\ responses \end{aligned} \qquad (3.22)$$

Observation: $\boldsymbol{\alpha}^{BE}$ has the same structure as $\boldsymbol{\alpha}$; $\boldsymbol{r}^{BE}$ has the same structure as $\boldsymbol{r}$.

ii) Nominal correlations between system parameters:

$$C_\alpha = \begin{pmatrix} C_\alpha^{11} & C_\alpha^{12} & . & . & C_\alpha^{1\nu} & . & . & C_\alpha^{1N_t} \\ C_\alpha^{21} & C_\alpha^{22} & . & . & C_\alpha^{2\nu} & . & . & C_\alpha^{2N_t} \\ . & . & . & . & . & . & . & . \\ . & . & . & . & . & . & . & . \\ C_\alpha^{\mu 1} & C_\alpha^{\mu 2} & . & . & C_\alpha^{\mu\nu} & . & . & C_\alpha^{\mu N_t} \\ . & . & . & . & . & . & . & . \\ . & . & . & . & . & . & . & . \\ C_\alpha^{N_t 1} & C_\alpha^{N_t 2} & . & . & C_\alpha^{N_t \nu} & . & . & C_\alpha^{N_t N_t} \end{pmatrix} \qquad (3.23)$$

The matrices ($\mathbf{C}_\alpha^{11}, \mathbf{C}_\alpha^{22}, ..., \mathbf{C}_\alpha^{N_t N_t}$) on the diagonal of the block-matrix structure $\mathbf{C}_\alpha$ contain the correlations between system parameters at the *same* time node ($1, 2, ..., N_t$). The off-diagonal matrices contain correlations between system parameters at *different* time nodes.

This is the structure of a matrix of the type $\mathbf{C}_\alpha^{\mu\nu}$:

$$C_{\alpha}^{\mu\nu} = \begin{pmatrix} C_{\alpha,11}^{\mu\nu} & C_{\alpha,12}^{\mu\nu} & . & . & C_{\alpha,1j}^{\mu\nu} & . & . & C_{\alpha,1N_\alpha}^{\mu\nu} \\ C_{\alpha,21}^{\mu\nu} & C_{\alpha,22}^{\mu\nu} & . & . & C_{\alpha,2j}^{\mu\nu} & . & . & C_{\alpha,2N_\alpha}^{\mu\nu} \\ . & . & . & . & . & . & . & . \\ . & . & . & . & . & . & . & . \\ C_{\alpha,i1}^{\mu\nu} & C_{\alpha,i2}^{\mu\nu} & . & . & C_{\alpha,ij}^{\mu\nu} & . & . & C_{\alpha,iN_\alpha}^{\mu\nu} \\ . & . & . & . & . & . & . & . \\ . & . & . & . & . & . & . & . \\ C_{\alpha,N_\alpha 1}^{\mu\nu} & C_{\alpha,N_\alpha 2}^{\mu\nu} & . & . & C_{\alpha,N_\alpha j}^{\mu\nu} & . & . & C_{\alpha,N_\alpha N_\alpha}^{\mu\nu} \end{pmatrix} \tag{3.24}$$

where N_α is the number of system parameters (static and transient).

The elements in the matrix above are (finally!) numbers. For example:

$$\mathbf{C}_{\alpha,ij}^{\mu\nu} = \left\langle \Delta\boldsymbol{\alpha}_i^{\mu} \Delta\boldsymbol{\alpha}_j^{\nu} \right\rangle = \left\langle \Delta\boldsymbol{\alpha}_j^{\nu} \Delta\boldsymbol{\alpha}_i^{\mu} \right\rangle = \mathbf{C}_{\alpha,ji}^{\nu\mu} \tag{3.25}$$

is the correlation between response i at time node μ and the response j at time node ν.

Therefore:

$$\mathbf{C}_{\alpha}^{\mu\nu} = \left(\mathbf{C}_{\alpha}^{\nu\mu}\right)^T, \forall \mu,\nu \le N_t \tag{3.26}$$

Observation: $\boldsymbol{C}_{\alpha}^{BE}$ has the same structure as $\boldsymbol{C}_{\alpha}$.

iii) correlations of the measured responses:

$$C_m = \begin{pmatrix} C_m^{11} & C_m^{12} & . & . & C_m^{1\nu} & . & . & C_m^{1N_t} \\ C_m^{21} & C_m^{22} & . & . & C_m^{2\nu} & . & . & C_m^{2N_t} \\ . & . & . & . & . & . & . & . \\ . & . & . & . & . & . & . & . \\ C_m^{\mu 1} & C_m^{\mu 2} & . & . & C_m^{\mu\nu} & . & . & C_m^{\mu N_t} \\ . & . & . & . & . & . & . & . \\ . & . & . & . & . & . & . & . \\ C_m^{N_t 1} & C_m^{N_t 2} & . & . & C_m^{N_t\nu} & . & . & C_m^{N_t N_t} \end{pmatrix} \tag{3.27}$$

The matrices on the diagonal ($\mathbf{C}_m^{11}, \mathbf{C}_m^{22}, ..., \mathbf{C}_m^{N_t N_t}$) contain the correlations between measured responses at the *same* time node ($1, 2, ..., N_t$). The off-diagonal matrices contain correlations between measured responses at *different* time nodes.

This is the structure of a matrix of the type $\mathbf{C}_m^{\mu\nu}$ in the block matrix $\mathbf{C}_m$:

$$C_m^{\mu\nu} = \begin{pmatrix} C_{m,11}^{\mu\nu} & C_{m,12}^{\mu\nu} & . & . & C_{m,1j}^{\mu\nu} & . & . & C_{m,1N_r}^{\mu\nu} \\ C_{m,21}^{\mu\nu} & C_{m,22}^{\mu\nu} & . & . & C_{m,2j}^{\mu\nu} & . & . & C_{m,2N_r}^{\mu\nu} \\ . & . & . & . & . & . & . & . \\ . & . & . & . & . & . & . & . \\ C_{m,i1}^{\mu\nu} & C_{m,i2}^{\mu\nu} & . & . & C_{m,ij}^{\mu\nu} & . & . & C_{m,iN_r}^{\mu\nu} \\ . & . & . & . & . & . & . & . \\ . & . & . & . & . & . & . & . \\ C_{m,N_r1}^{\mu\nu} & C_{m,N_r2}^{\mu\nu} & . & . & C_{m,N_rj}^{\mu\nu} & . & . & C_{m,N_rN_r}^{\mu\nu} \end{pmatrix} \tag{3.28}$$

where N_r is the number of (TRANSIENT) responses.

The elements in the matrix above are numbers. For example:

$$\mathbf{C}_{m,ij}^{\mu\nu} = \left\langle \Delta\mathbf{m}_i^{\mu} \Delta\mathbf{m}_j^{\nu} \right\rangle = \left\langle \Delta\mathbf{m}_j^{\nu} \Delta\mathbf{m}_i^{\mu} \right\rangle = \mathbf{C}_{m,ji}^{\nu\mu} \tag{3.29}$$

is the correlation between response i at time node μ and the response j at time node ν.

$$\text{Therefore: } \mathbf{C}_m^{\mu\nu} = \left(\mathbf{C}_m^{\nu\mu}\right)^T, \forall \mu,\nu \le N_t \tag{3.30}$$

Observation: $\boldsymbol{C}_r$ and $\boldsymbol{C}_r^{BE}$ have the same structure as $\boldsymbol{C}_m$.

iv) correlations of the measured responses with system parameters

$$C_{r\alpha} = \begin{pmatrix} C_{r\alpha}^{11} & C_{r\alpha}^{12} & . & . & C_{r\alpha}^{1\nu} & . & . & C_{r\alpha}^{1N_t} \\ C_{r\alpha}^{21} & C_{r\alpha}^{22} & . & . & C_{r\alpha}^{2\nu} & . & . & C_{r\alpha}^{2N_t} \\ . & . & . & . & . & . & . & . \\ . & . & . & . & . & . & . & . \\ C_{r\alpha}^{\mu 1} & C_{r\alpha}^{\mu 2} & . & . & C_{r\alpha}^{\mu\nu} & . & . & C_{r\alpha}^{\mu N_t} \\ . & . & . & . & . & . & . & . \\ . & . & . & . & . & . & . & . \\ C_{r\alpha}^{N_t 1} & C_{r\alpha}^{N_t 2} & . & . & C_{r\alpha}^{N_t\nu} & . & . & C_{r\alpha}^{N_tN_t} \end{pmatrix} \tag{3.31}$$

The matrices on the diagonal ($\mathbf{C}_{r\alpha}^{11}, \mathbf{C}_{r\alpha}^{22}, ..., \mathbf{C}_{r\alpha}^{N_tN_t}$) contain the correlations between measured responses and system parameters at the *same* time node ($1, 2, ..., N_t$). The off-diagonal matrices contain correlations between measured responses and system parameters at *different* time nodes.

This is the structure of a matrix of the type $\mathbf{C}_{r\alpha}^{\mu\nu}$:

$$C_{r\alpha}^{\mu\nu} = \begin{pmatrix} C_{r\alpha,11}^{\mu\nu} & C_{r\alpha,12}^{\mu\nu} & . & . & C_{r\alpha,1j}^{\mu\nu} & . & . & C_{r\alpha,1N_\alpha}^{\mu\nu} \\ C_{r\alpha,21}^{\mu\nu} & C_{r\alpha,22}^{\mu\nu} & . & . & C_{r\alpha,2j}^{\mu\nu} & . & . & C_{r\alpha,2N_\alpha}^{\mu\nu} \\ . & . & . & . & . & . & . & . \\ . & . & . & . & . & . & . & . \\ C_{r\alpha,i1}^{\mu\nu} & C_{r\alpha,i2}^{\mu\nu} & . & . & C_{r\alpha,ij}^{\mu\nu} & . & . & C_{r\alpha,iN_\alpha}^{\mu\nu} \\ . & . & . & . & . & . & . & . \\ . & . & . & . & . & . & . & . \\ C_{r\alpha,N_r1}^{\mu\nu} & C_{r\alpha,N_r2}^{\mu\nu} & . & . & C_{r\alpha,N_rj}^{\mu\nu} & . & . & C_{r\alpha,N_rN_\alpha}^{\mu\nu} \end{pmatrix} \tag{3.32}$$

Where N_α is the number of system parameters (static and transient) and N_r is the number of system responses.

The elements in the matrix above are numbers. For example:

$$\mathbf{C}_{r\alpha,ij}^{\mu\nu} = \left\langle \Delta\mathbf{m}_i^\mu \Delta\boldsymbol{\alpha}_j^\nu \right\rangle = \left\langle \Delta\boldsymbol{\alpha}_j^\nu \Delta\mathbf{m}_i^\mu \right\rangle = \mathbf{C}_{r\alpha,ji}^{\nu\mu} \tag{3.33}$$

is the correlation between the measured response i at time node μ and the parameter j at time node ν.

Observation: $\boldsymbol{C}_{r\alpha}^{BE}$ has the same structure as $\boldsymbol{C}_{r\alpha}$.

v) sensitivities of the system responses to the system parameters

$$S = \begin{pmatrix} S^{11} & 0 & . & . & 0 & . & . & 0 \\ S^{21} & S^{22} & 0 & . & 0 & . & . & 0 \\ . & . & . & . & . & . & . & . \\ . & . & . & . & . & . & . & . \\ S^{\mu 1} & S^{\mu 2} & . & . & S^{\mu\nu} & . & S^{\mu\mu} . & . \\ . & . & . & . & . & . & . & . \\ . & . & . & . & . & . & . & 0 \\ S^{N_t 1} & S^{N_t 2} & . & . & S^{N_t\nu} & . & S^{N_t\mu} . & . \; S^{N_tN_t} \end{pmatrix}, \; \nu \le \mu \le N_t \tag{3.34}$$

This is a block-matrix structure. The structure of a matrix of the type $\mathbf{S}^{\mu\nu}$:

$$S^{\mu\nu} = \begin{pmatrix} \frac{\partial r_1^\mu}{\partial \alpha_1^\nu} & \frac{\partial r_1^\mu}{\partial \alpha_2^\nu} & . & \frac{\partial r_1^\mu}{\partial \alpha_{N_\alpha}^\nu} \\ \frac{\partial r_2^\mu}{\partial \alpha_1^\nu} & \frac{\partial r_2^\mu}{\partial \alpha_2^\nu} & . & \frac{\partial r_2^\mu}{\partial \alpha_{N_\alpha}^\nu} \\ . & . & \frac{\partial r_i^\mu}{\partial \alpha_j^\nu} & . \\ \frac{\partial r_{N_r}^\mu}{\partial \alpha_1^\nu} & \frac{\partial r_{N_r}^\mu}{\partial \alpha_2^\nu} & . & \frac{\partial r_{N_r}^\mu}{\partial \alpha_{N_\alpha}^\nu} \end{pmatrix} \tag{3.35}$$

where N_r is the number of responses and N_α the number of system parameters.

An element in the matrix above, with the general form:

$$\mathbf{S}_{ij}^{\mu\nu} = \frac{\partial \mathbf{r}_i^\mu}{\partial \boldsymbol{\alpha}_j^\nu} \tag{3.36}$$

is the sensitivity of response i at time node μ to the parameter j at time node ν.

The MULTI-PRED kernel computation can be launched with the ROOT command:

root -l bestpred.C

in the directory:

MULTI-PRED/**example**/**KERNEL**

under Linux/Unix operating systems.

In Windows, the script **bestpred.C** is launched by a simple **double click** (the first launch may need an explicit "Open With" ROOT preinstalled software).

Table 3.1: Input and output files (matrices) for the MULTI-PRED kernel

Input matrix	Input file	Output matrix	Output file
α	a.abs	α^{BE}	aBE.out
C_α	ca.abs	C_α^{BE}	caBE.out
r	r.abs	r^{BE}	rBE.out
m	m.abs		
C_m	cm.abs	C_m^{BE}	cmBE.out
$C_{r\alpha}$	car.abs	$C_{r\alpha}^{BE}$	carBE.out
S	s.abs	C_r	CR.out
		χ^2	chi2.out

The *prerequisite* input files (**a.abs, ca.abs, …, s.abs**) for the MULTI-PRED kernel are listed on the left (yellow) side of the **Table 3.1**. Let us recall their contents:

a.abs	nominal parameters
c**a.abs**	nominal parameter correlations
m.abs	measured response(s)
r.abs	nominal computed response(s)
cm.abs	correlations for measured response(s)
s.abs	sensitivities of the response(s) to all parameters (static and transient)
car.abs	initial correlations between parameters and response(s)

They ***must*** exist in the directory MULTI-PRED/**example**/**vorKERNEL** (see also the Paragraph 3.2) before launching the MULTI-PRED kernel. The prerequisite input files (**a.abs, ca.abs, …, s.abs**) contain the corresponding block-matrices from the first column of Table 3.1 (with block-matrix structures given by the Eqs. 3.22-3.35), written in **sparse format**:

1) first row:

nr nc nz

where:

nr (integer) – number of rows

nc (integer) – number of columns

nz (integer) – number of non-zero elements / number of following lines in the file

2) nz rows of the type:

ir ic w

where:

ir (integer) – global row coordinate in the corresponding block-matrix

ic (integer) – global column coordinate in the corresponding block-matrix

w (float) – numerical value of the element with the global coordinates (ir,ic) in the block-matrix

Remark: The prerequisite input files (**a.abs, ca.abs, …, s.abs**) **are created semi-automatically** (see next Paragraph!).

3.2 *Input data and their preparation*

The raw input data have to be delivered by the user, respecting some simple formatting.

The following steps (**1-3**) have to be ***strictly*** followed by the user:

STEP 1) Edit and fill the TXT file:

MULTI-PRED/**example**/**vorKERNEL**/**dimensions.txt**

which is a header file (to contain the *steering data* of the chosen model) for the C++ script:

MULTI-PRED/**example**/**vorKERNEL**/**vorbestpred.C (to be NEVER changed!)**

Examples:

A) dimension.txt-file in the case of the "**Diffusion Model"** (Paragraph 2.1):

```
**********************************************************************
//number of responses
4
//number of time nodes
1
//number of static parameters
4
//number of transient parameters
0
//Only standard deviations for nominal sistem parameters? 0-NO; 1-
YES absolut; 2-YES relativ
2
//Only standard deviations for measured responses? 0-NO; 1-YES
absolut; 2-YES relativ
2
//Initial correlations between parameters and responses? 0-NO; 1-YES
0
**********************************************************************
```

B) dimension.txt-file in the case of the "**Dissolver Model**" (Paragraph 2.2):

```
**********************************************************************
//number of responses
1
//number of time nodes
307
//number of static parameters
5
//number of transient parameters
2
```

```
//Only standard deviations for nominal sistem parameters? 0-NO; 1-
YES absolut; 2-YES relativ
2
//Only standard deviations for measured responses? 0-NO; 1-YES
absolut; 2-YES relativ
1
//Initial correlations between parameters and responses? 0-NO; 1-YES
0
--------------------------------------------------------------------------
```

IMPORTANT!!:

The file **vorbestest.C** will create the sparse matrices:

a.abs	nominal parameters
m.abs	measured response
r.abs	nominal computed response
s.abs	sensitivities of the response to all parameters (static and transient)

directly (according to the steering data), making use of the raw input data (already) existing in the directory MULTI-PRED/**example**/**INPfiles**.

Any of the next 3 files (sparse matrices with structures according to Eqs. 3.23, 3.27 and 3.31) have to be provided by the user (and automatically no more touched by **vorbestpred.C**) in the case that the steering file **dimensions.txt** is asking for ("**green**" options in the 2 examples before):

ca.abs	nominal parameter correlations
cm.abs	correlations for measured response
car.abs	initial correlations between parameters and responses

As an example, let us consider the following logical ramifications in the (final part of) steering file **dimensions.txt**:

```
**************************************************************************
  //Only standard deviations for nominal sistem parameters? 0-NO; 1-YES absolut; 2-YES relativ
  0
  //Only standard deviations for measured responses? 0-NO; 1-YES absolut; 2-YES relativ
  0
  //Initial correlations between parameters and responses? 0-NO; 1-YES
  0
**************************************************************************
```

This logical configuration will lead to:

the sparse matrix **car.abs** (initial correlations between responses and parameters) will be still automatically provided by the script **vorbestpred.C**; it will contain in fact only one line of 3 integers:

nr nc 0, i.e.:

nr – number of rows

nc – number of columns

0 non-zero elements (in sparse format).

ca.abs and **cm.abs** have to be provided by the user.

STEP 2) The user has to create the following ASCII format input files (containing the raw input data) in the directory MULTI-PRED/**example**/**INPfiles**:

experimental.txt	the experimental response(s)
NOM.txt	the nominal response(s)
paramSTAT.txt	the nominal values of the *static* system parameters
paramTRANSI.txt	the nominal values of the *transient* system parameters
sensiSTAT.txt	sensitivities to the *static* parameters
sensiTRANSI.txt	sensitivities to the *transient* parameters
respSIGMA.txt	standard deviations for experimental response(s)
paramSIGMA.txt	nominal standard deviations for parameters

Here are the structures of these files (**A** refers to "Diffusion Model" and **B** means "Dissolver Model"):

experimental.txt

It contains two columns:

1st column - time nodes (but it may contain only a time node counter);

2nd column – the experimental values of the response(s)

The iteration tree looks like:

LOOP for the number of responses (A=4 or B=1)

    LOOP for time nodes (A=1 or B=307)

Model **A**: 4 x 1 lines.

Model **B**: 307 x 1 lines.

NOM.txt

It has the *same* structure as experimental.txt!

paramSTAT.txt

It contains only one column with the nominal values of the static parameters.

The iteration tree looks like:

LOOP for the number of static parameters (A=4 or B=5)

Model **A**: 4 lines.

Model **B**: 5 lines.

paramTRANSI.txt

This is a file needed only for Model B.

It contains two columns:

1st column - time nodes (but it may contain only a time node counter);

2nd column – the nominal values of the transient parameters

The iteration tree looks like:

LOOP for the number of transient parameters (B=2)

    LOOP for time nodes (B=307)

Model **B**: 2 x 307 lines.

sensiSTAT.txt

It contains two columns:

1st column: time nodes (but it may contain only a time node counter);

2nd column: sensitivity values

The iteration tree looks like:

LOOP for the number of responses (A=4 or B=1)

    LOOP for the number of static parameters (A=4 or B=5)

        LOOP for time nodes (A=1 or B=307)

Model **A**: 4 x 4 x 1 lines.

Model **B**: 1 x 5 x 307 lines.

sensiTRANSI.txt

This is a file needed only for Model B.

It contains two columns:

1st column: time nodes (but it may contain only a time node counter);

2nd column: sensitivity values

The iteration tree looks like:

LOOP for the number of responses (B=1)

LOOP for the number of transient boundary conditions (B=2)

LOOP for perturbation nodes (B=307)

LOOP for time nodes (B=307)

Model **B**: 1 x 2 x 307 x 307 lines!

The zeros before perturbation nodes (because of causality reasons) are formally kept in the file structure for safety reasons. Anyhow, these zeros will be not transferred towards the sparse matrices as they will contain only the non-zero elements and their matrix coordinates (row number and column number).

respSIGMA.txt

It contains one column with standard deviations (absolute or relative, according to the logical option in the steering file **dimensions.txt**) of the response(s).

The iteration tree looks like:

LOOP for the number of responses (A=4 or B=1)

LOOP for time nodes (A=1 or B=307)

Model **A**: 4 lines.

Model **B**: 307 lines.

paramSIGMA.txt

It contains one column with standard deviations (absolute or relative, according to the logical option in the steering file **dimensions.txt**) of the system parameters

The iteration tree looks like:

LOOP for the number of all parameters (static and transient) (A=4 or B=7)

Model **A**: 4 lines.

Model **B**: 7 lines.

STEP 3) The user has to run the C++ script

MULTI-PRED/**example**/**vorKERNEL**/**vorbestpred.C** C++ script for reading the input files from MULTI-PRED/**example**/**INPfiles** and generating the sparse matrices a.abs, ca.abs, m.abs, r.abs, cm.abs, s.abs, car.abs (ASCII files containing in sparse matrix format the required data structure for the BEST-EST module)

Remark: As user, never modify the file **vorbestpred.C**!

3.3 Output data

The output data obtained by running the BEST-EST procedure are contained in the directory:

MULTI-PRED/**example**/**KERNEL**

All files to be found in this directory are explained in the Table 3.2:

Table 3.2: Output files (matrices) for the MULTI-PRED kernel

Matrix	File	Output matrix	Output file
α	a.inp	α^{BE}	aBE.out
C_α	ca.inp	C_α^{BE}	caBE.out
r	r.inp	r^{BE}	rBE.out
m	m.inp		
C_m	cm.inp	C_m^{BE}	cmBE.out
$C_{r\alpha}$	car.inp	$C_{r\alpha}^{BE}$	carBE.out
S	s.inp	C_r	CR.out
		χ^2	chi2.out

The *prerequisite* input files (**a.abs, ca.abs, …, s.abs**) for the MULTI-PRED kernel are listed on the left (yellow) side of the **Table 3.1**, in Paragraph 3.2. The same information with the same format is formally written/practically cloned (as safety measure) by the kernel in the files (**a.inp, ca.inp, …, s.inp**), see the left (yellow) side of the **Table 3.2**. Let us recall their contents:

a.inp nominal parameters (same as a.abs)

ca.inp	nominal parameter correlations (same as ca.abs)
m.inp	measured response(s) (same as m.abs)
r.inp	nominal computed response(s) (same as r.abs)
cm.inp	correlations for measured response(s) (same as cm.abs)
s.inp	sensitivities of the response(s) to all parameters (static and transient) (same as s.abs)
car.inp	initial correlations between parameters and response(s) (same as car.abs)

The (real) output of the kernel is written in the files on the right (blue) side of the **Table 3.2**. Here are their contents:

aBE.out	best-estimate parameters (same structure as a.abs)
caBE.out	best-estimate parameter correlations (same structure as ca.abs)
rBE.out	best-estimate response(s) (same structure as r.abs)
cmBE.out	best estimate correlations for response(s) (same structure as cm.abs)
carBE.out	best-estimate correlations between parameters and response(s) (same structure as car.abs)
CR.out	initial correlations between computed response(s) (same structure as cm.abs)
chi2.out	value of the consistency indicator χ^2

The data contained in these files from Table 3.2 (***.inp** and ***.out)** plus the steering data from the file (already existing, used for the data preparation)
MULTI-PRED/**example**/**vorKERNEL**/**dimensions.txt**
are sufficient for displaying the results of the MULTI-PRED procedure.

3.4 Display results

The results of the MULTI-PRED procedure, as well as their comparison with the a-priori data, are displayed by semi-automatic C++ scripts. Here are the scripts with their descriptions:

Script and Figure	Function
paramMOnom.C (see Fig. **3.1**)	- plot nominal correlations of the static parameters - create the file paramMOnomBest.out (it contains a one-to-one comparison of the nominal an best-estimate static parameters with their relative standard deviations)
paramMObest.C (see Fig. **3.2**)	- plot best-estimate correlations of the static parameters - create the file paramMOnomBest.out (the same content as above)
corRESPnom.C (see Fig. **3.3**)	plot initial correlations between computed responses
corRESPbest.C (see Fig. **3.4**)	plot best-estimate correlations between responses
RESPsimexpbest.C (see Fig. **3.5**)	plot computed, experimental and best-estimate responses
sigonlyRESPsimexpbest.C (see Fig. **3.6**)	plot (±) one standard deviation bands for computed, experimental and best-estimate responses
paramBCexpbest.C (see Fig. **3.7**)	plot experimental and best-estimate transient boundary conditions
sigrelparamBCexpbest.C (see Fig. **3.8**)	plot experimental and best-estimate relative standard deviations (in percent) of the transient boundary conditions

These scripts are semi-automatic in the sense they ask the user (after launching) for some preferred options.

The interactions possible with these scripts are exposed in the next panels.

Script: **paramMOnom.C**	
Action: plot nominal correlations of the static parameters	
Launching command: root -l paramMOnom.C	
Produced figure: Fig. 3.1	
Dissolver Model	**Diffusion Model**
root -l paramMOnom.C root [0] Processing paramMOnom.C... Number of responses: 1 Number of time nodes: 307 Number of model parameters: 5 Number of transient parameters: 2 What kind of best-estimate relative standard deviations? 1 = relative to nominal values 2 = relative to best-estimate values 1 Set a minimum and a maximum for the histogram? 1 = Yes! 2 = No! 2 root [1]	root -l paramMOnom.C root [0] Processing paramMOnom.C... Number of responses: 4 Number of time nodes: 1 Number of model parameters: 4 Number of transient parameters: 0 What kind of best-estimate relative standard deviations? 1 = relative to nominal values 2 = relative to best-estimate values 2 Set a minimum and a maximum for the histogram? 1 = Yes! 2 = No! 2 root [1]

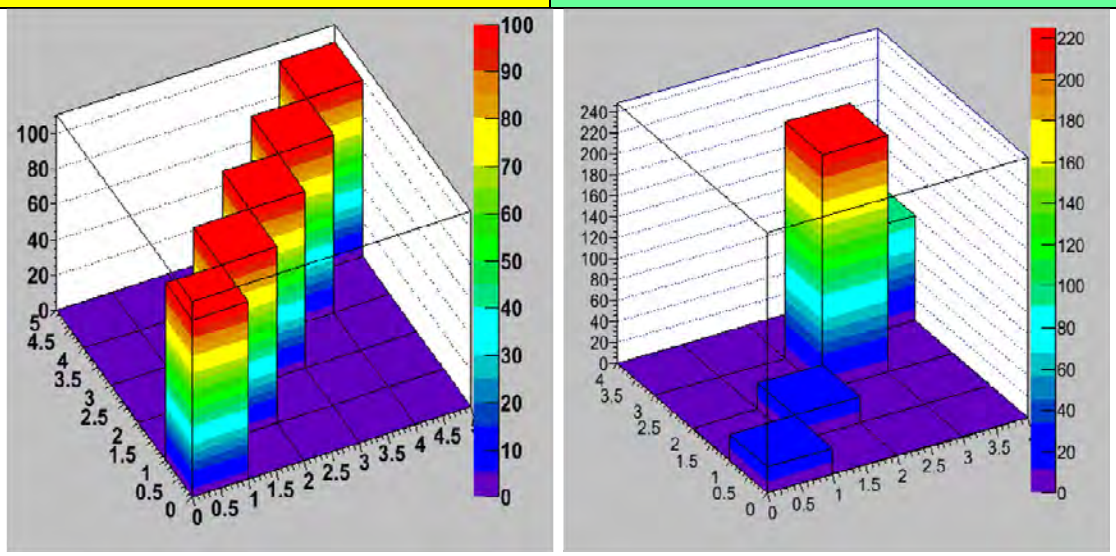

Figure 3.1: Nominal static parameters correlations. Left: Dissolver Model. Right: Diffusion Model.

Some observations:

1) All scripts are applicable to both type of results (time-independent or time-dependent); some user feed-back may be required during running.

2) The user (required) feed-back is displayed in red in all panels.

3) Sometimes it appears the question:

```
What kind of best-estimate relative standard deviations?
1 = relative to nominal values
2 = relative to best-estimate values
```

Because the best-estimate nominal values can be sometimes smaller than the a-priori values, the a-priori values may be chosen as normalizations for the best-estimate relative standard deviations (option 1); in such a case the best-estimate relative standard deviations will be always smaller than the a-priori relative standard deviations.

4) By selecting on the tool-bar of any plot the option **File->Save** the following picture format may be selected: ps, eps, pdf, gif, jpg, png. The corresponding file will keep the name of the script producing it, with the extension ps, eps and so on.

5) The scripts of the type **paramMOnom.C** and **paramMObest.C** are delivering also a text file **paramMOnomBest.out** which contains a one-to-one comparison of the nominal and best-estimate static parameters with their relative standard deviations.

Here is the content of this file in the case of the diffusion model:

```
paramMO No.     NOM        sigNOM %       BEST            sigBEST %

1             0.0197      +-5            0.019841811     +-4.7893643
2             0.16        +-5.0000005    0.15911883      +-5.0203853
3           10000000     +-15.000001     9847789         +-9.2185526
4          7.4380002      +-10           7.3876824       +-8.5332766
```

6) Under Windows operating system the launching command for all scripts is **Double Click**.

Script: **paramMObest.C**	
Action: plot best-estimate correlations of the static parameters	
Launching command: root -l paramMObest.C	
Produced figure: Fig. 3.2	
Dissolver Model	**Diffusion Model**
root -l paramMObest.C root [0] Processing paramMObest.C... Number of responses: 1 Number of time nodes: 307 Number of model parameters: 5 Number of transient parameters: 2 What kind of best-estimate relative standard deviations? 1 = relative to nominal values 2 = relative to best-estimate values 2 Set a minimum and a maximum for the histogram? 1 = Yes! 2 = No! 2 root [1]	root -l paramMObest.C root [0] Processing paramMObest.C... Number of responses: 4 Number of time nodes: 1 Number of model parameters: 4 Number of transient parameters: 0 What kind of best-estimate relative standard deviations? 1 = relative to nominal values 2 = relative to best-estimate values 2 Set a minimum and a maximum for the histogram? 1 = Yes! 2 = No! 2 root [1]

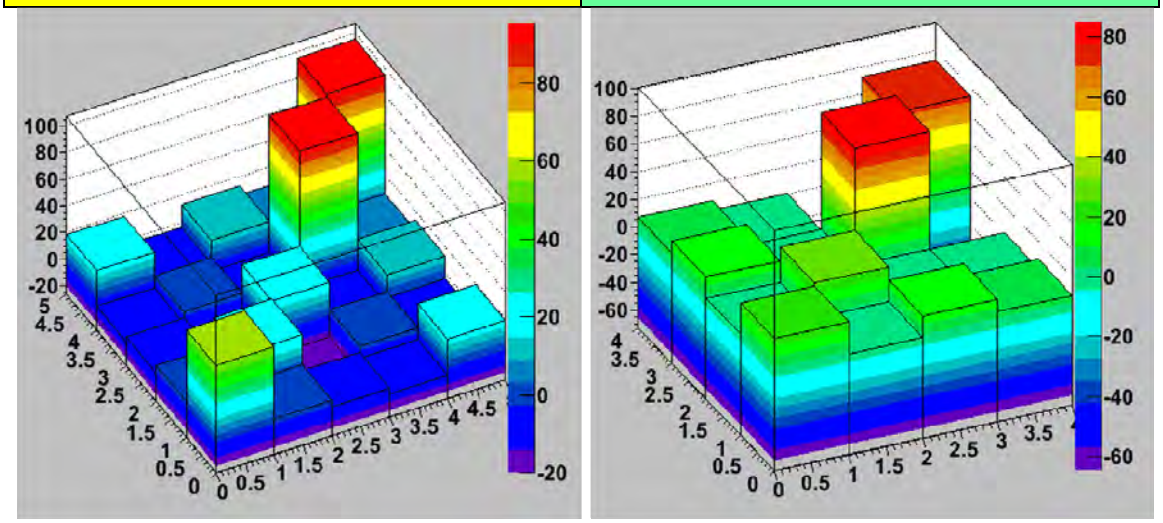

Figure 3.2: Best-estimate static parameters correlations. Left: Dissolver Model. Right: Diffusion Model.

Script: **corRESPnom.C**

Action: plot initial correlations between computed responses

Launching command: root -l corRESPnom.C

Produced figure: Fig. 3.3

Dissolver Model

```
root -l corRESPnom.C
root [0]
Processing corRESPnom.C...
Number of responses: 1
Number of time nodes: 307
Number of model parameters: 5
Number of transient parameters: 2
What kind of response?
1 = static
2 = transient
2
Which response to be plotted?
 Enter an integer between 1 and
1.
1
Set a minimum and a maximum for
the histogram?
1 = Yes!
2 = No!
1
Provide the minimum!
0.0
Provide the maximum!
0.35
root [1]
```

Diffusion Model

```
root -l corRESPnom.C
root [0]
Processing corRESPnom.C...
Number of responses: 4
Number of time nodes: 1
Number of model parameters: 4
Number of transient parameters: 0
What kind of response?
1 = static
2 = transient
1
Set a minimum and a maximum for
the histogram?
1 = Yes!
2 = No!
2
root [1]
```

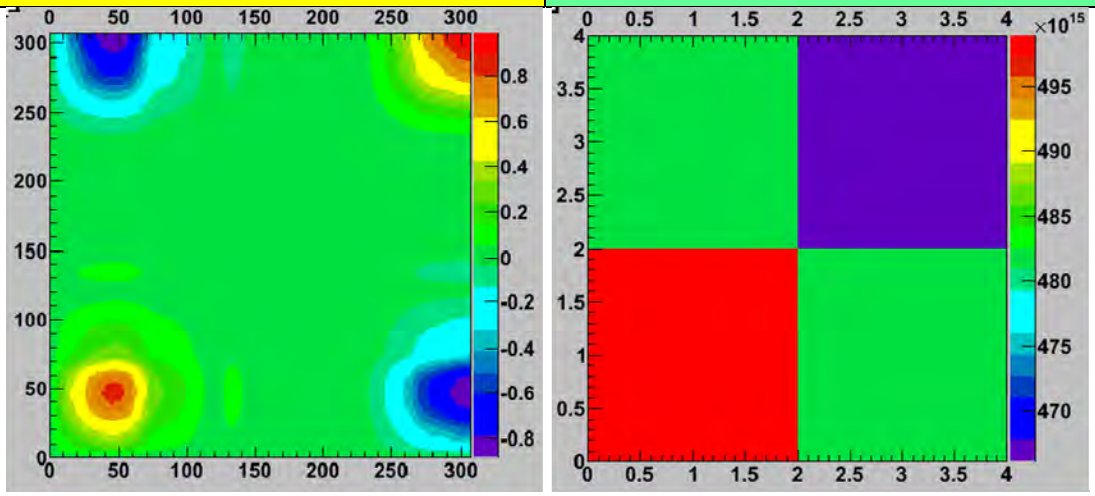

Figure 3.3: Initial correlations between computed responses. Left: Dissolver Model. Right: Diffusion Model.

Script: **corRESPbest.C**	
Action: plot best-estimate correlations between computed responses	
Launching command: root -l corRESPbest.C	
Produced figure: Fig. 3.4	
Dissolver Model	**Diffusion Model**

```
root -l corRESPbest.C
root [0]
Processing corRESPbest.C...
Number of responses: 1
Number of time nodes: 307
Number of model parameters: 5
Number of transient parameters: 2
What kind of response?
1 = static
2 = transient
2
Which response to be plotted?
 Enter an integer between 1 and
1.
1
Set a minimum and a maximum for
the histogram?
1 = Yes!
2 = No!
2
root [1]
```

```
root -l corRESPbest.C
root [0]
Processing paramMObest.C...
Number of responses: 4
Number of time nodes: 1
Number of model parameters: 4
Number of transient parameters: 0
What kind of best-estimate
relative standard deviations?
1 = relative to nominal values
2 = relative to best-estimate
values
2
Set a minimum and a maximum for
the histogram?
1 = Yes!
2 = No!
2
root [1]
```

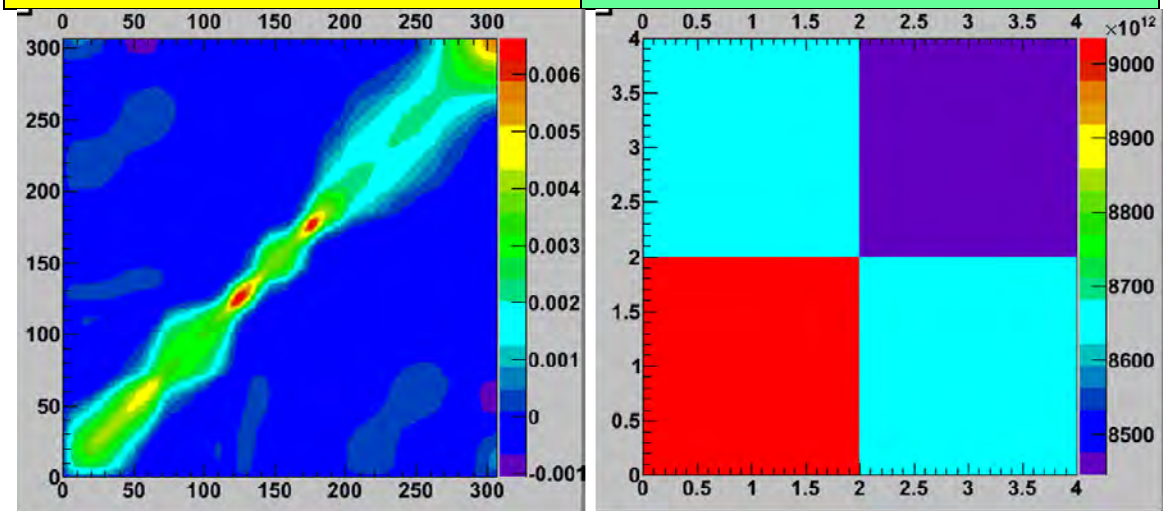

Figure 3.4: Best-estimate correlations of the responses. Left: Dissolver Model. Right: Diffusion Model.

Script: **RESPsimexpbest.C**	
Action: plot computed, experimental and best-estimate responses	
Launching command: root -l RESPsimexpbest.C	
Produced figure: Fig. 3.5	
Dissolver Model	**Diffusion Model**
root -l RESPsimexpbest.C root [0] Processing RESPsimexpbest.C... Number of responses: 1 Number of time nodes: 307 Number of model parameters: 5 Number of transient parameters: 2 transient response Which response to be plotted? Enter an integer between 1 and 1. 1 Set a minimum and a maximum for the histogram? 1 = Yes! 2 = No! 2 root [1]	root -l RESPsimexpbest.C root [0] Processing RESPsimexpbest.C... Number of responses: 4 Number of time nodes: 1 Number of model parameters: 4 Number of transient parameters: 0 static response Set a minimum and a maximum for the histogram? 1 = Yes! 2 = No! 2 root [1]

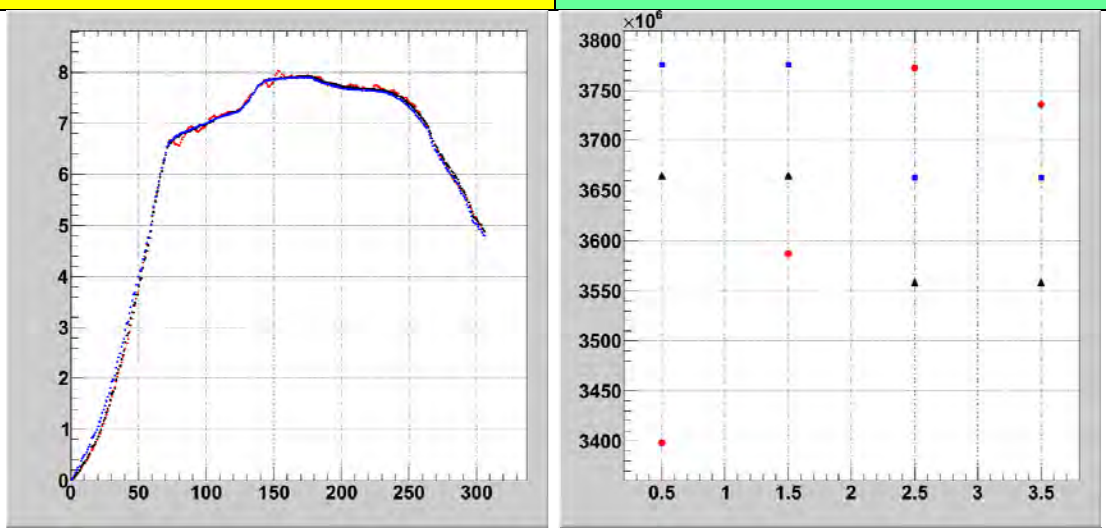

Figure 3.5: Computed (blue), experimental (red) and best-estimate response (black). Left: Dissolver Model. Right: Diffusion Model

Script: **sigonlyRESPsimexpbest.C**	
Action: plot (±) one standard deviation bands for computed, experimental and best-estimate responses	
Launching command: root -l sigonlyRESPsimexpbest.C	
Produced figure: Fig. 3.6	
Dissolver Model	**Diffusion Model**
root -l sigonlyRESPsimexpbest.C root [0] Processing sigonlyRESPsimexpbest.C... Number of responses: 1 Number of time nodes: 307 Number of model parameters: 5 Number of transient parameters: 2 transient response Which response to be plotted? Enter an integer between 1 and 1. 1 Set a minimum and a maximum for the histogram? 1 = Yes! 2 = No! 2 root [1]	root -l sigonlyRESPsimexpbest.C root [0] Processing sigonlyRESPsimexpbest.C... Number of responses: 4 Number of time nodes: 1 Number of model parameters: 4 Number of transient parameters: 0 static response Set a minimum and a maximum for the histogram? 1 = Yes! 2 = No! 1 Provide the minimum! 2500000000 Provide the maximum! 5000000000 root [1]

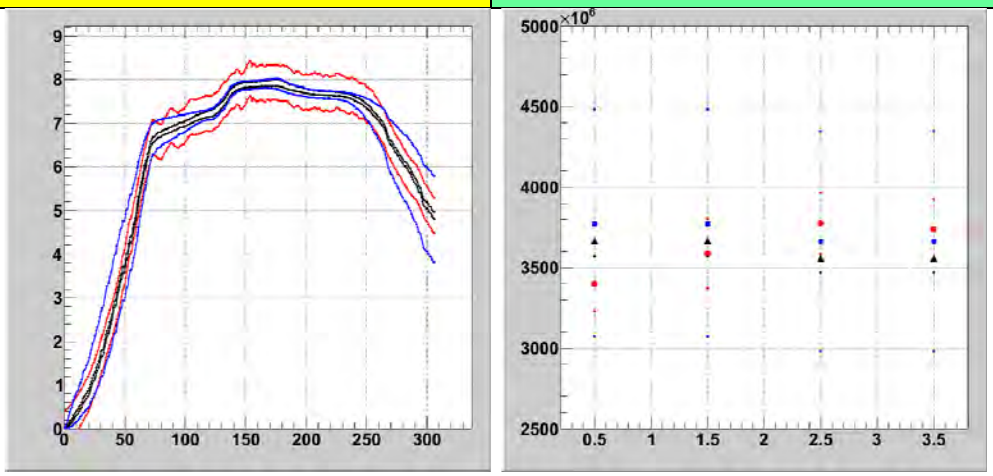

Figure 3.6: Upper- and lower bands indicate (±) one standard deviation about the respective mean response values depicted in Figure 4.5. Left: Dissolver Model. Right: Diffusion Model.

Script: **paramBCexpbest.C**	
Action: plot experimental and best-estimate transient boundary conditions	
Launching command: root -l paramBCexpbest.C	
Produced figure: Fig. 3.7	
Dissolver Model	**Diffusion Model**
root -l paramBCexpbest.C root [0] Processing paramBCexpbest.C... Number of responses: 1 Number of time nodes: 307 Number of model parameters: 5 Number of transient parameters: 2 Which boundary conditions have to be plotted? Integer allowed between 1 and 2. 1 Set a minimum and a maximum for the histogram? 1 = Yes! 2 = No! 2 root [1]	NOT applicable!

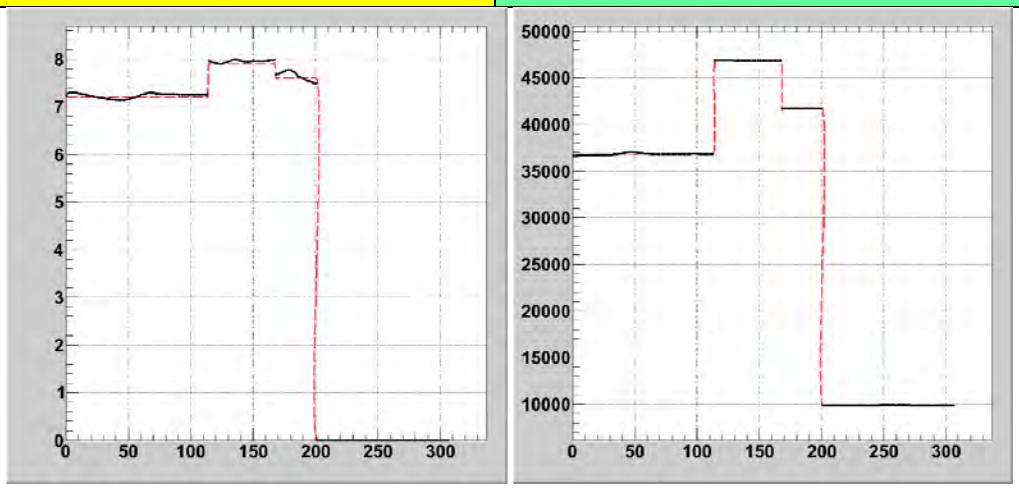

Figure 3.7: Dissolver Model: Experimental (red) and best-estimate (black) transient boundary conditions. Left: inlet nitric acid mass concentration. Right: inlet mass flow rate.

Script: **sigrelparamBCexpbest.C**	
Action: plot experimental and best-estimate relative standard deviations (in percent) of the transient boundary conditions	
Launching command: root -l sigrelparamBCexpbest.C	
Produced figure: Fig. 3.8	
Dissolver Model	**Diffusion Model**
root -l sigrelparamBCexpbest.C root [0] Processing sigrelparamBCexpbest.C... Number of responses: 1 Number of time nodes: 307 Number of model parameters: 5 Number of transient parameters: 2 What kind of best-estimate relative standard deviations? 1 = relative to nominal values 2 = relative to best-estimate values 1 Which boundary conditions have to be plotted? Integer allowed between 1 and 5. 1 Set a minimum and a maximum for the histogram? 1 = Yes! 2 = No! 1 Provide the minimum 9.98 Provide the maximum 10.01 root [1]	NOT applicable!

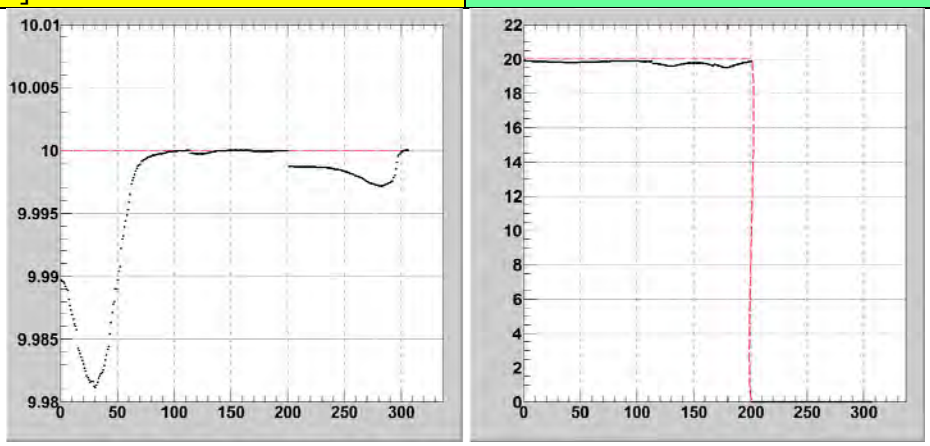

Figure 3.8: Dissolver Model: Experimental (red) and best-estimate (black) relative standard deviations (in percent) of the transient boundary conditions. Left: inlet mass flow rate. Right: inlet nitric acid mass concentration.

References

[Le1980] B. E. Lewis and F. E. Weber, "A Mathematical Model for Liquid Flow Transients in a Rotary Dissolver", ORNL/TM-7490, Oak Ridge National Laboratory (1980).

[Ca2003] Cacuci, D.G.: *Sensitivity and Uncertainty Analysis. Theory*. Volume I, Chapman & Hall / CRC, 2003.

[Ca2010a] D. G. Cacuci and M. Ionescu-Bujor, Model calibration and best-estimate prediction through experimental data assimilation: I. Mathematical framework, Nucl. Sci. Eng., 165 (2010) 18-44.

[Ca2010b] D.G. Cacuci and M. Ionescu-Bujor, Sensitivity and Uncertainty Analysis, Data Assimilation and Predictive Best-Estimate Model Calibration, Chapter 17 in Vol.3, pp 1913 – 2051, *Handbook of Nuclear Engineering*, D. G. Cacuci, Editor, ISBN: 978-0-387-98150-5, Springer New York / Berlin, 2010.

[Ca2015] Dan G. Cacuci, James J. Peltz, Aurelian F. Badea, and Madalina C. Badea, "Spent Fuel Dissolver Predictive Modeling: I. Application of the Adjoint Sensitivity Analysis Methodology for Nonlinear Systems with Operator-Type Responses," *Trans. Am. Nucl. Soc.*, Track 14894, Washington, DC, 2015.

[Pe2015a] James J. Peltz, Aurelian F. Badea, Madalina C. Badea, and Dan G. Cacuci, "Spent Fuel Dissolver Predictive Modeling: II. Uncertainty Reduction via Experimental Data Assimilation", *Trans. Am. Nucl. Soc*., Track 14895, Washington, DC, 2015.

[Pe2015b] James J. Peltz and Dan G. Cacuci "Predictive Modeling Applied to a Paradigm Spent Fuel Dissolver Model: I. Adjoint Sensitivity Analysis," *Nucl. Sci. Eng., accepted,* December 2015.

[Pe2015c] James J. Peltz, Dan G. Cacuci, Aurelian F. Badea, and Madalina C. Badea, "Predictive Modeling Applied to a Paradigm Spent Fuel Dissolver Model: II. Uncertainty Quantification and Reduction," *Nucl. Sci. Eng., accepted,* December 2015.

[Ca2016] Dan G. Cacuci, Aurelian F. Badea, Madalina C. Badea, and James J. Peltz, , "Efficient Computation of Operator-Type Response Sensitivities for Uncertainty Quantification and Predictive Modeling: Illustrative Application to a Spent Nuclear Fuel Dissolver Model," *Appl. Math & Comp*., *submitted*, December 3, 2015

[Ca2014] Cacuci, D.G. and Badea, M.C.: *Predictive modelling of coupled multi-physics systems: II. Illustrative application to reactor physics*, Annals of Nuclear Energy, 70, pp. 279-291, 2014.

[ROOT] https://root.cern.ch

4.6. Task F: Perform high-quality holdup measurements

To test the DIMP method, some holdup detector measurements are necessary. It is crucial that the pipe, box, or duct geometry be known precisely, as well as any other significant surroundings. Also, the uncertainties in the detector response should be well documented. In order to ensure the quality of the measurements and uncertainties, and to enable replication in case of identifying discrepancies between the measured and computed results we conducted our own set of holdup experiments. This was done in collaboration with ORNL where our partner operates a state-of-the-art holdup lab whose staff supervised a graduate student conducting these experiments and helped trouble-shoot observed discrepancies when they arose. NC State University and ORNL were responsible for completing this task.

The accomplishment of this task was reported in: Noel Benjamin Nelson, *Validation and Uncertainty Quantification of the Data Integration with Modeled Predictions (DIMP) Inverse Radiation Transport Model for Holdup Measurements*, Doctoral Proposal, NC State University, 2016. This document is replicated on the following pages.

© Copyright 2016 by Noel Benjamin Nelson

All Rights Reserved

Validation and Uncertainty Quantification of the Data Integration with Modeled Predictions (DIMP) Inverse Radiation Transport Model For Holdup Measurements

by
Noel Benjamin Nelson

A dissertation submitted to the Graduate Faculty of
North Carolina State University
in partial fulfillment of the
requirements for the Degree of
Doctor of Philosophy

Nuclear Engineering

Raleigh, North Carolina

2016

APPROVED BY:

Robin Gardner	John Mattingly
Ralph Smith	Louise Worrall

Yousry Azmy
Chair of Advisory Committee

DEDICATION

In memory of my dearest and loving mother, Deanna Nelson.

BIOGRAPHY

The author was born in a small town in Oregon called John Day, to parents R. Bryan and Deanna Nelson as the youngest of two children. He graduated from Grant Union High School as the Valedictorian in 2008. He continued his studies at Oregon State University (OSU) for four years in Nuclear Engineering.

At OSU he worked diligently beside his studies as a cook for the university dormitory kitchens and as an undergraduate researcher for the chemistry department. In his chemistry research, he observed the effects of electric voltage, frequency, and amperage on the polymer brush growth of hemoglobin for use in the manufacture of prosthetics. He graduated Summa Cum Laude from Oregon State with an Honors B.S. in nuclear engineering in the summer of 2012.

He continued his graduate studies at North Carolina State University under the direction of Dr. Yousry Azmy. His research includes inverse holdup source characterization methods, and detector response validation and uncertainty quantification.

ACKNOWLEDGEMENTS

We thank the Nuclear Energy Universities Program (NEUP) for its financial support of the initial project, and the Consortium of Nonproliferation Enabling Capabilities (CNEC) for its continued financial support.

TABLE OF CONTENTS

LIST OF TABLES

LIST OF FIGURES

CHAPTER

1

INTRODUCTION

1.1 Research Motivation and Goals

The goal of this work is to validate the Data Integration with Modeled Predictions (DIMP) inverse particle transport method for solving the special nuclear material (SNM) holdup problem. Holdup problems arise when radioactive material becomes trapped in processing equipment at nuclear fuel processing facilities. Examples of processing equipment can include but are not limited to pipes, ducts and filters, glove boxes, and valves. [1] SNM holdup is of interest to the nuclear fuel industry for many reasons. These reasons include: criticality safety, maintaining accurate SNM inventory and nuclear safeguards regime, and radiation worker safety.

Criticality safety is important for fairly obvious reasons. If enough nuclear material buildup occurs over time in a section of equipment, it can present a criticality risk. Even if the holdup deposit geometry is not at risk of becoming critical, accumulation of radioactive materials can pose a radiation hazard to facility employees who may become exposed to the resulting radiation field while working in the vicinity of the heldup material. Finally, SNM is important to track for economic purposes and to ensure transparency. All fissile nuclear material must be accounted for within reasonable margins to verify that it is exclusively used for the peaceful purposes of the facility's operations under applicable international safeguard protocols and treaties.

Therefore, holdup sources are important to quantify in total material mass, isotopic composition, as well as distribution and location. There are several models to choose from in order to solve the holdup problem. The most common model used in industry is called the Generalized Geometry Holdup (GGH) model. [1] The GGH model is based on a set of core assumptions. All sources in the model must be approximated as a point, line, or area source. The source type is chosen based on the measurements and judgements of a holdup survey crew. They use handheld field detectors (often simple Geiger counters) to measure the approximate distribution of the source in a piece of equipment. After determining the relative size, shape, and location of a source, measurement points are determined and another survey crew will take spectral measurements of the source with gamma-ray detectors (generally NaI or CDTe). The GGH model is then employed based on one of the three GGH source distributions using background correction models and a self-attenuation factor to calculate the approximate amount of radiation source material present in grams. [1] This model can have a high degree of uncertainty and requires a large amount of measured data and application of user judgement.

The DIMP method, in contrast, seeks a more automated system by posing the holdup configuration as an inverse problem. Initial survey crews would not be required, and few assumptions are necessary to predict source distribution, size, strength, and location within equipment. DIMP uses an adjoint particle transport model to calculate an importance map for a grid of detectors in the target geometric configuration utilizing as-built information of dimensions and material composition of the facility's structure. Deterministic transport codes are capable of modeling such configurations with a varying degree of fidelity of the models to achieve a desirable computational precision. Together, the computed flux and detector response function can be used to predict detector responses from a given source distribution. Alternatively, and more efficiently in the present case, folding the importance function with a given source distribution yields an estimate of the detector response where the importance function is the adjoint flux computed with an adjoint source set to that detector's response function. DIMP calculates the optimal source distribution(s), location(s), and strength(s) that best match calculated responses to experimental responses with no presumptions of the source shape and minimal obvious restrictions on its physical location, e.g. a source cannot be hanging in the air in the middle of a room.

Currently, the DIMP model has been validated for a Cs-137 point source and a Co-60 line source. [2] It performed well with low error that was mostly attributed to the weakness of the available sources (older button sources). [2] This work intends to expand upon the model and previous research with realistic holdup experiments using strong Uranium sources measured with a field holdup NaI detector, and compare the results to the Holdup Measurement System (HMS-4), a GGH model. [3] Four experimental holdup measurement campaigns were performed in this work

including a Cs-137 point source, a highly enriched Uranium (HEU) disk source, an HEU line source in a pipe, and a set of HEU area sources in a duct.

1.2 Preliminary Work & Results

The initial work performed thus far, includes two numerical convergence studies performed with synthetic detector responses computed with simulated Cs-137 and Co-60 point sources and the first holdup source validation exercise conducted with experimental responses measured from a Cs-137 calibration source. The synthetic convergence studies demonstrated the ability of DIMP to converge as additional detection points were added. DIMP performed well above 5 detection points and reached a reasonaby accurate spatial distribution for the Cs-137 point source alone. A definite convergence was not quite achieved for the Cs-137 point source and Co-60 line of point sources simulated together. While most of the Co-60 sources were resolved (especially the stronger ones), all five were never mapped. DIMP eventually appeared to diverge after 21 detector points, and it was surmised that this was due to the build up in total response error overcoming the information supplied by the new detection information. Additionaly, another convergence study was performed to access the functionality of DIMP with purely uncollimated detector responses. The study produced promising results for the Cs-137 point source case with synthetic responses if the true source distribution was used as the initial guess. Otherwise, DIMP became stuck in local minima, so a new set initial guess values for the source parameter vector, α will have to be used for future work with purely uncollimated responses.

The validation exercise used experimental measurements taken by the 1"x2" NaI ORNL field holdup detector of a Cs-137 point source held by a ring stand to validate against responses generated by DIMP's predicted sources. These measurements required a collimator correction factor to calibrate DIMP according to the complex collimator geometry of the field holdup detector. DIMP performed well with only two minor issues, and produced the correct source distribution in space with 80% of the true source activity. The two issues that will require further attention include two possible outlier measurement points that did not match the value projected by the MCNP calculated colimator correction factor, and that the run under the standard initial guess caused DIMP to become stuck in a local minima. Future work with the new detector configuration will require recalibration of the initial guess.

1.3 Planned Work for PhD

This proposal seeks to outline a set of tasks planned for completion as part of this project. The planned work covers three areas. The first is completion of DIMP's validation against the experimental measurements using well quantified holdup-like SNM sources taken at Oak Ridge National Laboratories (ORNL) and comparing the results against HMS-4. These measurements include detector responses of an HEU disk source, an HEU line source in a large round duct, and area sources in an L-duct in addition to various sources in a large round duct. The second task involves improving the point DRF to account for the special collimation geometry of the ORNL field holdup detector. The final task will cover the investigation of a new peak DRF to improve DIMP's performance over the current point DRF. Additionally refinement of the preliminary work completed so far and summarized above will continue as needed.

1.4 Proposal Outline

The second chapter of this Proposal will discuss relevant background information, such as inverse methodology and details of the DIMP system in the context of the available literature. The third chapter covers the preliminary numerical convergence results of DIMP. The fourth chapter will describe the experimental setup of the SNM holdup measurements. The fifth chapter discusses the preliminary experimental results of the first experimental validation conducted with a Cs-137 point source. The final chapter will outline future work intended to bring the project to the desirable state of completion.

CHAPTER

2

REVIEW OF THE LITERATURE

2.1 Inverse Problems

Inverse problems are often more complex than their counterparts, the forward problem. In the forward problem, an effect is predicted from an imposed cause. For example, in the typical forward radiation transport problem, a source with an initial state and parameters (e.g. radiation source distribution in space and angle, and its energy spectrum, etc.) are known and the state of the system at other points in space and time (e.g. radiation flux, temperature, dose, etc.) are unknown. A forward model is used to calculate the solution at those points from the known source and properties of the problem domain (e.g. dimensions, material composition, nuclear data, etc.).

An inverse problem, in contrast, poses the reverse question. The cause(s) are sought from a set of measured effects, or a model is identified to connect a set of input causes to output effects . Information at various points in space and time called "measurements" are considered known, but the source state or the domain configuration that produces them is treated as unknown. An inverse model is used to calculate a possible solution state of the system from the measurements. This is where the difficulty of inverse problems arises. The existence and uniqueness of an inverse solution is typically not certain, and solutions can be very unstable depending on the quality of the measurements.

One way to approach the difficulty of inverse problems is to find solutions with probabilistic methods. While the solution that best fits the measurement data is not always the true solution, the chance that it is the true solution should increase with increasing amount of measured data. This idea is formalized via Bayes' theorem [4]:

$$p(hypothesis|data,I) \propto p(data|hypothesis,I)p(hypothesis|I), \tag{2.1}$$

where $data$ is the experimentally measured data (e.g. detector responses), the $hypothesis$ is the unknowns of the system (source parameters in this work), and I is all the additional knowledge of the system (system geometry, detector efficiency, detector response functions, etc.). The three probability density functions (PDFs) appearing in Eq. 2.1, namely $p(hypothesis|data,I)$, $p(data|hypothesis,I)$, and $p(hypothesis|I)$ are the posterior, likelihood, and prior respectively. The prior is the conditional probability that the hypothesis occurs based only on information I. The likelihood represents the probability of measurement data occurring based on a given configuration of the unknown data (hypothesis) and the information in I. This is proportional to the posterior, or the probability of the given $hypothesis$ (source configuration) being true based on the information I and the measurement $data$.

In order to solve an inverse problem, the likelihood function is maximized thereby minimizing the error between the experimentally measured data and the results predicted by the model from an input configuration of the source parameters. The most probable source parameter values are determined by nonlinear least squares estimation. Ideally, the source configuration that produces the minimum error between the measured data and the predicted data is close to the true solution (if the measurement and model errors are sufficiently small).

2.2 NDA and GGH

Nuclear fuel holdup is an application of the unknown radiation source inverse problem. The typical holdup configuration comprises material containing sources of radiation that have accumulated potentially for decades as radioactive deposits in nuclear fuel processing equipment at facilities. These deposits need to be located and their mass quantified for criticality safety, radiation safety, inventory, and nonproliferation purposes. One method of achieving this goal is destructive analysis (DA). DA involves taking the piece of equipment apart or dislodging the radioactive deposit chemically by dissolution to physically examine the source. Naturally, DA is often costly and disruptive to ordinary fuel processing operations. Therefore, it is often more appealing to perform nondestructive analysis or NDA.

NDA methods seek to gather information about the fuel deposit (or radiation source) without physically or chemically altering it or the structure containing it. This is normally accomplished through the interpretation of information obtained from radiation detector response spectra. Several models have been developed for interpreting radiation measurements and solving general inverse radiation problems including: the Monte Carlo Library Least-squares method for determining elemental composition of a target material by active source interrogation [5], a Levenberg-Marquardt nonlinear optimization of the radiation transport model for determining nuclear metal thicknesses [6], and the GGH model [1] commonly used in the nuclear fuel processing industry to quantify holdup sources.

The base model used for performance comparison of the DIMP methodology developed in this work is the GGH model, a standardized industry approach. GGH is often used in industry because of its ease of implementation and acceptable accuracy for relatively simple calculations. However, it requires a fair amount of active user interface and time, as the method requires an initial source search survey. Then after planning a case by case measurement scheme depending on the type of source discovered, the attention of a measurement crew is required to execute the measurements with portable field radiation detectors.

GGH requires a specific set of assumptions and conditions in order to accurately predict holdup source characteristics. The system based on the GGH model used in this work for direct comparison is called the Holdup Measurement System (HMS-4) [3]. HMS-4 relies on a survey crew to scan for sources inside equipment, and when found, determine their approximate spatial distribution. After the survey, measurement points are chosen based on the approximate source distribution, local area geometry, and model assumptions. Then these measurements are used to calculate the approximate mass of radioactive material contained within the holdup source.

The four core assumptions of GGH are as follows: first, the radiation detector used for measurements is shielded on the back and sides. Second, a cylindrical collimator is attached to the front of the crystal to restrict the field of view of the detector to a known solid angle. Third, the detector is properly placed such that each holdup source can be generalized to a point source, uniform line source, or uniform area source. Fourth, the distance between the detector and holdup source is known. Several correction factors are used along with these assumptions to calculate the total mass of the holdup deposit. [1]

In order to comply well with the third assumption, many measurements locations are determined by the detector's field of view. For example, in order to measure a point source the source distribution must hold 5% or less of the detector's field of view (based on the solid angle between source and detector). A line source must cross the entire view of the detector but remain thin. An area source must occupy 95% or more of the detector's field of view. [1] Some of the measurement locations

chosen in this work followed these constraints in order to serve as HMS-4 measurement points and potentially serving the purposes of response measurements for our new approach, DIMP, as well.

2.3 DIMP methodology

DIMP is a more general inverse problem solution method that requires no correction factors and that does not limit the spatial distribution of the source to a preconceived set of options. Instead, it maximizes agreement between the measurement vector $\vec{r}_m$ (responses) and the modeled responses, $\vec{r}_p$, predicted by a configuration of the model parameters, $\vec{\alpha}$

$$\vec{r}_m = R\vec{\alpha} \tag{2.2}$$

where R is the mapping operator from the model parameter input space to the response space. The solution of this problem is linear for radiation transport and has a closed form solution for the posterior means and covariances. Cacuci's Best Estimate method based on Bayesian inference is used to find the posterior solution mean and uncertainty. [7]

2.3.1 Radiation Transport

First, the model used in the inverse framework will be described in detail followed by specification of the source parameters contained in $\vec{\alpha}$, and a few notes on the measurements $\vec{r}_m$. The model for the radiation transport problem is based on the time independent linear Boltzmann Transport equation for neutral particles in non-multiplying media. [8]

$$\hat{\Omega}\cdot\vec{\nabla}\psi(\vec{x},E,\hat{\Omega})+\sigma(\vec{x},E)\psi(\vec{x},E,\hat{\Omega})=\int dE'\int d\hat{\Omega}'\sigma_s(\vec{x};E',\hat{\Omega}'\rightarrow E,\hat{\Omega})\psi(\vec{x},E',\hat{\Omega}')+q(\vec{x},E,\hat{\Omega})\,, \tag{2.3}$$

where $\psi(\vec{x},E,\hat{\Omega})$ is the angular flux of particles $[particles/cm^2\text{-}s]$ defined over the spatial domain

$x\in V\,,\ \hat{\Omega}\in 4\pi\,,\ E\in(0,\infty)\,,$

and with explicit boundary conditions

$\psi(\vec{x},E,\hat{\Omega})=\psi_0(\vec{x},E,\hat{\Omega})$ for $\vec{x}\in\partial V$ and $\hat{\Omega}\cdot\hat{n}<0$.

$\hat{\Omega}$ is the unit directional vector along which particles are traveling, $\hat{n}$ is the unit vector normal to the boundary surface ∂V at the point $\vec{x}$, and $\sigma(\vec{x},E)$ the total particle interaction macroscopic

cross-section [$c\,m^{-1}$]. Also, $\sigma_s(\vec{x};E',\hat{\Omega}' \rightarrow E,\hat{\Omega})$ is the macroscopic scattering cross-section of particles from one direction ($\hat{\Omega}'$) and energy (E') to the direction and energy range $d\hat{\Omega}'$, dE' about the direction and energy of interest ($\hat{\Omega}, E$), and $q(\vec{x},E,\hat{\Omega})$ is the external source of radiation particles in the configuration of interest [in $particles/cm^3\text{-}s$]. In DIMP the geometric configuration and material composition of all objects in the problem domain are considered known, hence the cross sections are retrieved and calculated for nuclide mixtures by MAVRIC [12]. Next, it is useful to define the scalar flux $\phi(\vec{x},E)$ as

$$\phi(\vec{x},E) = \int_{4\pi} d\hat{\Omega}\psi(\vec{x},E,\hat{\Omega})\,. \tag{2.4}$$

Reaction rates are key components to many radiation problems, such as dose and fission rates. In this case, the reaction rate definition can be used to define a detector response, r, as

$$r(E') = \int_0^\infty dE \int_V d\vec{x}\sigma_d(\vec{x},E',E)\phi(\vec{x},E)\,, \tag{2.5}$$

where $\sigma_d(\vec{x},E',E)$ is the detector response function (DRF). There are several ways to model and define DRFs, and this will be explored further in the full dissertation. In Eq. 2.5, $\sigma_d(\vec{x},E',E)$ is the probability per unit path length that a particle at $\vec{x}$ incident with energy E registers a response in the detector's channel dedicated to energy E'. With this definition in mind, one could use the inverse of the forward transport equation, Eq. 2.3 as the mapping function for the inverse problem. However, direct inverses are often numerically unstable and computationally expensive. Equation 2.5 requires a solution of the transport equation for every potential source distribution in order to determine the corresponding $\phi(\vec{x},E)$ then compute r and compare it to the measured values. Alternatively, the problem can be reformulated using the adjoint of the transport equation [2]. The adjoint identity can be stated as

$$\langle Ap,h\rangle = \langle p,A^\dagger h\rangle, \tag{2.6}$$

where $\langle,\rangle$ denotes an inner product, A is an operator, p and h are any pair of functions in the domain of A, and $A^\dagger$ is the adjoint operator. Furthermore, in this application we define the inner product as follows

$$\langle p,h\rangle = \int_{4\pi} d\hat{\Omega}\int_0^\infty dE\int_V dV\,p(\vec{x},E,\hat{\Omega})h(\vec{x},E,\hat{\Omega})\,. \tag{2.7}$$

Now, consider the fixed source linear transport equation in operator form

$$L\psi = q, \tag{2.8}$$

where L is the transport operator (for all angular fluxes, ψ), and q is the external source. Next, take the inner product of Eq. 2.8 with the adjoint angular flux $\psi^\dagger$

$$\langle L\psi, \psi^\dagger \rangle = \langle q, \psi^\dagger \rangle \,. \tag{2.9}$$

Applying the adjoint identity (Eq. 2.6) to the above equation yields [9]

$$\langle L\psi, \zeta \rangle = \langle \psi, L^\dagger \zeta \rangle + P[\psi, \zeta] \,, \tag{2.10}$$

where ζ is an arbitrary function ($\zeta = \psi^\dagger$ in our case) and $P[\psi,\zeta]$ is the bilinear concomitant, evaluated on the external surface of volume V,

$$P[\psi,\zeta] = \int_{4\pi} d\hat{\Omega} \int_0^\infty dE \int_{\partial V} dS \hat{\Omega}\cdot\hat{n}\psi(\vec{x},E,\hat{\Omega})\zeta(\vec{x},E,\hat{\Omega}) \,. \tag{2.11}$$

Substituting Eq. 2.10 into Eq. 2.9 yields

$$\langle \psi, L^\dagger \psi^\dagger \rangle = \langle q, \psi^\dagger \rangle - P[\psi, \psi^\dagger] \,. \tag{2.12}$$

Next we set the adjoint source to the detector response function, DRF, namely $q^\dagger = \sigma_d$, implying

$$L^\dagger \psi^\dagger = \sigma_d \,. \tag{2.13}$$

Substituting this relationship into Eq. 2.12 yields

$$\langle \psi, \sigma_d \rangle = \langle q, \psi^\dagger \rangle - P[\psi, \psi^\dagger]. \tag{2.14}$$

Now, applying the following vacuum boundary conditions

$$\psi(\vec{x},E,\hat{\Omega}) = 0 \,;\; for \;\; \vec{x} \in \partial V \;\; and \;\; \hat{\Omega}\cdot\hat{n} < 0, \tag{2.15}$$

$$\psi^\dagger(\vec{x},E,\hat{\Omega}) = 0 \;\; for \;\; \vec{x} \in \partial V \;\; and \;\; \hat{\Omega}\cdot\hat{n} > 0, \tag{2.16}$$

will cause the bilinear concomitant term to vanish thus producing

$$\langle \psi, \sigma_d \rangle = \langle q, \psi^\dagger \rangle. \tag{2.17}$$

Finally, recalling the reaction rate Eq. 2.5 and substituting it in Eq. 2.17 leads to

$$\vec{r}_p(E) = \int_0^\infty dE \int_V dV \phi^\dagger(\vec{x}, E) q(\vec{x}, E) \tag{2.18}$$

where $\phi^\dagger(\vec{x}, E)$ is the adjoint scalar flux, or importance, and $\vec{r}_p(E)$ is the predicted response. The advantage of the formulation in Eq. 2.18 over the one in Eq. 2.5 is the computationally inexpensive evaluation of the former once $\phi^\dagger$ is known for a set of detectors. During the search for optimal source distribution Eq. 2.18 comprises an inner product of the precomputed adjoint fluxes and a guess of the source distribution. In contrast, Eq. 2.5 requires a full forward transport solution for every attempted source distribution. The set of discretized importance values are calculated by the discrete ordinates package DENOVO [12], and folded with the predicted source distribution ($q(\vec{x}, E)$) during the search for the best match between the resulting responses and the measurement responses $\vec{r}_m$. The optimal source distribution is found through an optimization process that if successfully converged, yields $\vec{r}_p(E) \cong \vec{r}_m(E)$, and in this case we call the corresponding $q(\vec{x}, E)$ a solution to the inverse problem.

Currently, only the peak responses are compared for both predicted and measured responses. A full response comparison was attempted in previous work [2] including the continuum and peak responses, but the continuum response was very difficult to calculate. Accurate representation of the continuum response requires a fairly sophisticated DRF. Some research has been invested in the area of DRFs for unshielded detectors [10], but more development of the DRF is required to apply it to collimated detector responses as shown in Ref. [11].

2.3.2 Nonlinear Optimization

In order to optimize the predicted source distribution, the posterior probability is maximized by minimizing the residual ($Q(\vec{z})$) of the difference vector ($\vec{z}$) which contains the absolute differences in the model parameters from the initial guess and those between the measured and predicted responses. The optimization method implemented in this work is the gradient based Quasi-Newton method with the best estimate covariance as described in Ref. [7]. The method works by minimizing $Q(\vec{z})$ according to nonlinear least squares using the following Newton update step for the k^{th} iteration

$$\vec{\alpha}_{k+1} = \vec{\alpha}_k - \lambda_k \left(\nabla_\alpha^2 Q(\vec{z}_k) \right)^{-1} \vec{\nabla}_\alpha Q(\vec{z}_k). \tag{2.19}$$

where $\lambda_k \in [0, 1]$ is the line search parameter which controls the search step size. α_k is the source spatial distribution written in vector form (model parameters) for all peak energies at iteration k,

and α_0 is the priori or initial guess. The gradient of Q is

$$\vec{\nabla}_\alpha Q(\vec{z}) = C_\alpha^{-1}\vec{z}_\alpha + S^T C_m^{-1}\vec{z}_r \tag{2.20}$$

where C_α, C_m, and S are the source distribution and measurement covariance matrices, and the collective matrix of adjoint sensitivies ($\phi^\dagger(E)$), respectively as defined in Ref. [9]. Under the Gauss-Newton approximation, the Hessian is defined as

$$\nabla_\alpha^2 Q(\vec{z}) \approx C_\alpha^{-1} + S^T C_m^{-1} S \tag{2.21}$$

where the inverses of the covariance matrices are replaced by the appropriate linear systems of equations (consult Ref. [9]) and solved for efficiently using standard linear methods (e.g. Gaussian Partial Pivoting). Finally, the functional of the difference vector, $Q(\vec{z})$ is then defined as

$$Q(\vec{z}) = \vec{z}^T C^{-1}\vec{z}, \tag{2.22}$$

and the inverse of the covariance, C^{-1}, is

$$C^{-1} = \begin{bmatrix} C_\alpha^{-1} & 0 \\ 0 & C_m^{-1} \end{bmatrix}. \tag{2.23}$$

The difference vector, $\vec{z}$ is

$$\vec{z} \equiv \begin{bmatrix} \vec{\alpha} - \vec{\alpha}^0 \\ \vec{r}_p - \vec{r}_m \end{bmatrix} = \begin{bmatrix} \vec{z}_\alpha \\ \vec{z}_r \end{bmatrix} \tag{2.24}$$

where $\vec{r}_p$ is the response calculated with the attempted source distribution and $\vec{r}_m$ is the measured response.

2.4 DIMP Structure and Outline

DIMP is a system of modules assembled from various existing, production-level computer codes where the system-level control is implemented in a Python command structure. The input to DIMP comprises all prior information such as system object dimensions, material composition and corresponding radiation interaction cross-sections, source energy information, etc., that the DIMP system overlays in a 3-D adjoint photon transport model to calculate response information for comparison with measured responses. Finally, the optimization algorithm calculates the best estimate of the source distribution from the minimization of the response error.

A general outline of DIMP's procedure is shown in Figure 2.1

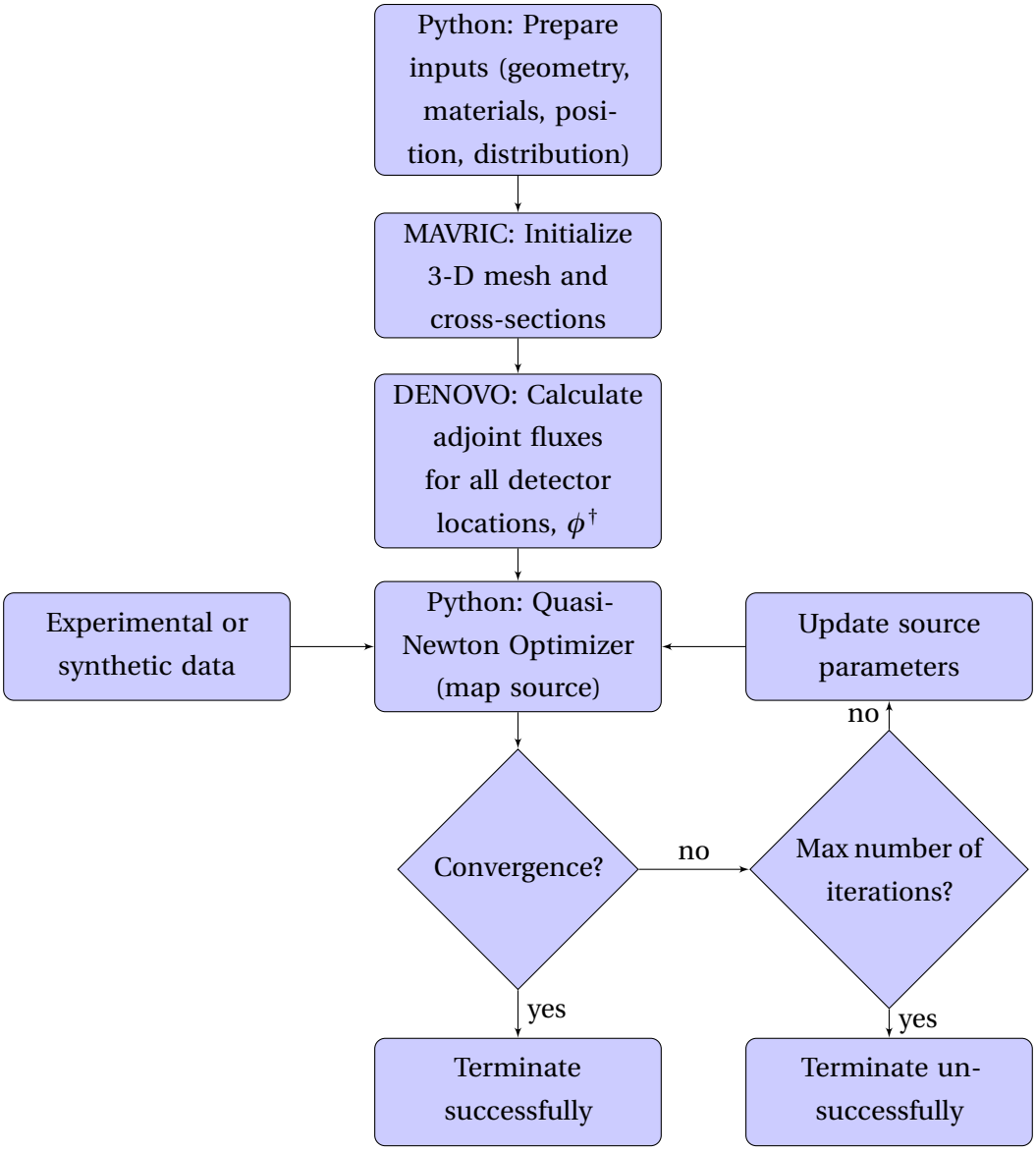

Figure 2.1 DIMP Algorithm Flowchart

First, numerous model parameters such as detector specifications, object dimensions, material compositions, and locations, and expected source energy peak ranges are initialized as inputs by Python for use by MAVRIC. MAVRIC calculates cross-sections for all materials appearing in the problem configuration after retrieving the basic elemental cross-sections from the Evaluated Nuclear Data Files (ENDF) tables. Next, MAVRIC initializes the 3-D mesh for the adjoint transport problem and passes this information along with the cross-sections to DENOVO. DENOVO calculates

the importances or adjoint fluxes, $\phi^{\dagger}(E)$ in each computational cell across the entire mesh. The importances from DENOVO are then folded with an iterate of the source parameters vector, α, yielding the set of detector responses that correspond to that particular source distribution. These are passed to the Python based gradient optimizer program.

The Quasi-Newton optimizer compares the predicted responses from DENOVO's adjoint flux to the measured responses. Measured responses are normally taken by field detector measurements, but in this proof-of-principle stage and in support of debugging activities we exercised the option of calculating synthetic responses by MCNP tallies, except in Chapter 5 where we utilize measured detector responses. With each iterative step, the optimizer attempts to reduce the difference between the predicted and measured responses by nonlinear least squares operations, until a local minimum in the error is found. The source distribution that has the least error is called the best estimate source distribution and is considered the solution of the inverse problem in a PDF sense. The distribution that minimizes the sum of the errors squared has the inverse property of maximizing the likelihood distribution from the original Bayes equation, Eq. 2.1. The source distribution that maximizes the likelihood distribution has the highest probability of matching the true source distribution. Note, there is no guarantee that this distribution is the global minimum; however, a good initial guess will often yield a result that is sufficiently close to the global minimum.

CHAPTER

3

NUMERICAL CONVERGENCE STUDY

In order to prepare for quantifying the uncertainty introduced by changing many variables in the realistic holdup experiments conducted for the purpose of validating the DIMP methodology, numerical convergence studies were performed. In this study, a previous source configuration benchmarked in Ref. [2] (a Cs-137 point source and five Co-60 point sources arranged along a straight line) was simulated using synthetic MCNP detector responses and the results used to verify DIMP's convergence to the known source distributions while varying selected features or parameters. The choice to employ synthetic responses as opposed to experimentally measured responses is dictated by the large number of cases needed to test the desired dependencies. Also, the ability to repeat certain "experiments" either exactly or with tweaks to the setup, to facilitate debugging a certain feature of the code or limitations of the model demand such simulated measurement environments. Convergence of DIMP was measured by the accuracy of the predicted source's position, strength, and spatial distribution compared with the true source used in generating the synthetic responses. An additional measure of DIMP convergence is provided by the level of agreement of the predicted and synthetic responses as quantified by the reduced chi-squared. To test the convergence behavior, DIMP source maps over the spatial extent of the room were computed as a sequence of increasing number of detectors starting with one detector all the way up to 24 detector points. DIMP showed stable convergence towards the true point source configuration with a minimum of 5 detectors to

resolve a reasonable approximation of the true source configuration.

The original study that employed this setup [2] involved synthetic and experimental measurements of calibration radioisotope sources placed in room 2144 in Burlington Engineering Laboratories at North Carolina State University. A stack of Cs-137 sources was placed in the corner on the floor and a string of five Co-60 sources were placed in a straight line on a counter in the middle of the room. The first source was meant to represent a point source and the second approximates a line source. See Ref. [9] for a detailed description and photos of the room, placement of the radiation sources, and the experimental setup.

In the original work, source maps predicted by the optimization of detector responses would often yield configurations with multiple source cells even for a single point source in the true source setup. This is because DIMP makes no prior assumptions about the spatial distribution of a source (unlike other methods such as GGH), and bases its source predictions solely on prior information (room geometry, energy of source peaks, etc.) and measured responses. So, it is quite likely in a given DIMP source map mesh that many cells will have non-zero values due, among other reasons to noise in the measrued (or synthetic) responses and numerical errors in the computational model. Therefore, a cut-off criterion is normally chosen to exclude from the solution to the inverse problem sources that are too small in magnitude.

3.1 Convergence of DIMP for a Mono-energetic Point Source

The first test involves only a simulated Cs-137 point source considered in the original setup [2]. Synthetic responses of a varying number of detectors were computed with MCNP using the true source strength and location, then these responses were fed into DIMP to predict the optimal source distribution. The resulting DIMP-predicted source distribution is then compared to the the true source distribution used in MCNP as the number of detection points was increased from three to nine. DENOVO solves the inverse problem using a deterministic discrete ordinates particle transport method, whereas MCNP uses a stochastic particle transport model, so in the sense described in Ref. [9] this presents an "inverse misdemeanor" not an "inverse crime". The two codes produce non-identical numerical errors that prevent the exact true source distribution from being predicted by DIMP. Each detector point's set of simulated responses comprised one unshielded measurement and six directional measurements along positive and negative coordinate axes in three dimensions. The results of this convergence study are displayed in Table 3.1. The true location of the Cs-137 point source is (440, 5, 1) cm, and its true strength is 107.685 kBq.

Table 3.1 Spatial distribution of the Cs-137 point source computed with DIMP from synthetic responses as a function of increasing number of detectors. Only cells with source strength larger than 1% of the true source strength are listed.

3 Det.	x (cm) Δx (cells)	y (cm) Δy (cells)	z (cm) Δz (cells)	Δd (cm)	q (Bq)	$\frac{q}{q_{true}}$ (%)	$\chi^2_R/det.$
	391.16 -5	50.04 6	3.31 0	66.47	4.02E4	37.33	3.919E5
	410.46 -3	58.17 7	3.31 0	60.86	2.05E4	19.06	
	72.64 -38	171.96 21	-6.22 -2	403.58	1.30E3	1.21	
4 Det.							
	410.46 -3	25.65 3	3.31 0	36.11	5.91E4	54.90	3.391E5
	444.37 1	41.91 5	3.31 0	37.24	2.34E4	21.71	
	439.42 0	253.24 31	173.40 22	302.23	2.43E3	2.26	
5 Det.							
	439.42 0	2.67 0	3.31 0	3.33	8.77E4	81.48	72.34
	439.42 0	17.53 2	3.31 0	12.75	1.98E4	18.42	
6 Det.							
	444.37 1	2.67 0	3.31 0	5.47	9.80E4	91.01	69.17
	444.37 1	17.53 2	3.31 0	13.47	1.33E4	12.32	

Table 3.1 Convergence data cont.

7 Det.	x (cm) Δx (cells)	y (cm) Δy (cells)	z (cm) Δz (cells)	Δd (cm)	q (Bq)	$\frac{q}{q_{true}}$ (%)	$\chi^2_R/det.$
	439.42 0 439.42 0	9.40 1 2.67 0	3.31 0 3.31 0	5.00 3.33	5.51E4 5.21E4	51.12 48.35	20.74
8 Det.							
	439.42 0 439.42 0	9.40 1 2.67 0	3.31 0 3.31 0	5.00 3.33	5.51E4 5.21E4	51.13 48.35	18.73
9 Det.							
	439.42 0 439.42 0	9.40 1 2.67 0	3.31 0 3.31 0	5.00 3.33	5.59E4 5.11E4	51.88 47.49	17.78

The table shows the coordinates and strength of each individual cell where the predicted source strength exceeded 1% of the true source's strength, along with the distance from its true location (Δd) to the mesh cell center and its strength relative to that of the true strength used in generating the synthetic responses. The x,y,z coordinates listed for each cell correspond to the coordinates of that cell's center point, and the $\Delta x,\Delta y,\Delta z$ indicates the difference of the cell's x,y,z mesh index from the corresponding mesh index of the cell that contains the true point source, respectively. Also shown in Table 3.1 is the reduced chi-squared value per detector of the detector responses computed from the predicted source configuration computed via

$$\chi^2_R = \frac{1}{\nu}\sum_{i=1}^{n}\frac{(r_{m,i}-r_{p,i})^2}{\sigma_i^2} \tag{3.1}$$

where $\nu = n-p$ is the degree of freedom or the difference between the number of measurements, n, and the number of parameters, p. σ_i^2 is the variance (Poisson or MCNP variance) in the measurements, $r_{m,i}$, and $r_{p,i}$ are the modeled responses. The reduced chi-squared is normalized per detector in order to screen out the expected modeling error between DENOVO adjoint-based responses and

MCNP responses that accumulate with each additional detector. As evidenced by the large error in the predicted source locations, weak strengths, and the resulting very large chi-squared-per-detector values, DIMP does not perform adequately with fewer than 5 detectors for this source configuration. With so few detectors, the code places the source near to one of the detectors. From 5 detection points upwards to 9 detectors, DIMP converges on a 50/50 split between two very probable source cells in the corner near to where the true source is in fact located. While it does not converge to a single cell that contains the true source, it remains stable and converges to the true source cell and its neighbor as a consequence of inconsistent numerical errors in the MCNP and DENOVO models of the radiation transport process.

3.2 Convergence of DIMP for Poly-energetic Multiple Point Sources

The second DIMP convergence test involves the full original source setup with the Cs-137 point source in the corner and the five Co-60 point sources along the center of the southern wall. Again, purely synthetic measurements generated with MCNP were used as detector responses where the number of detection points was increased from 3 to 24 points total, each comprising one bare detector and six directional responses as described earlier. The results of the second convergence study are shown in Table 3.2. The true location and strength of the Cs-137 point source remains the same as stated in Sec. 3.1, while the true location of the Co-60 line source is centered at approximately (120, 9.525, 90.17) cm. The individual x coordinates of the five point sources that compose the line source are x=96.52, 107.95, 119.38, 130.175, and 143.764 cm, and their strengths are 0.525, 2.218, 5.767, 31.793, and 3.845 kBq respectively. Note, DIMP treats the two coincident photons from Co-60 as independent sources with no correlation in their spatial location. Therefore, each Co source cell mapped by DIMP from one of these two energies may or may not coincide with source cells from the other energy.

Table 3.2 Spatial distribution of the Cs-137 point source and the Co-60 line source computed with DIMP from synthetic responses as a function of increasing number of detectors. Δd is measured from the strongest point source on the Co-60 line at x=130.175 cm.

Energy (MeV)	x (cm) Δx (cells)	y (cm) Δy (cells)	z (cm) Δz (cells)	Δd (cm)	q (Bq)	$\frac{q(E)}{q_{true(E)}}$ (%)	$\chi^2_R/det.$
3 Detectors							
1.332	82.30 -5	17.53 1	207.62 15	127.08	3.00E4	135.96	2.634E4
1.173	72.64 -6	17.53 1	190.51 13	115.94	2.81E4	127.42	
0.662	381.51 -6	66.29 8	3.31 0	84.76	2.70E4	25.12	
0.662	391.16 -5	66.29 8	3.31 0	78.41	2.34E4	21.72	
0.662	72.64 -38	171.96 21	-6.22 -2	403.58	1.80E3	1.67	
4 Detectors							
1.332	82.30 -5	17.53 1	92.90 1	48.62	2.00E4	90.40	774.1
1.173	91.95 -4	17.53 1	113.53 4	45.51	2.10E4	95.34	
0.662	400.81 -4	58.17 -2	3.31 0	66.09	4.39E4	40.78	
0.662	381.51 -6	50.04 6	3.31 0	73.86	1.44E4	13.40	
0.662	458.72 3	261.37 32	139.19 18	291.84	4.04E3	3.76	

Table 3.2 Convergence data cont.

Energy (MeV)	x (cm) Δx (cells)	y (cm) Δy (cells)	z (cm) Δz (cells)	Δd (cm)	q (Bq)	$\frac{q(E)}{q_{true(E)}}$ (%)	$\chi^2_R/det.$
5 Detectors							
1.332	120.90 -1	17.53 1	92.90 1	12.55	1.37E4	62.06	29.84
1.332	149.86 2	17.53 1	92.90 1	21.42	6.95E3	31.48	
1.173	130.56 0	17.53 1	92.90 1	8.46	2.09E4	94.72	
0.662	439.42 0	2.67 0	3.31 0	3.33	5.59E4	51.94	
0.662	439.42 0	9.40 1	3.31 0	5.00	4.73E4	43.90	
0.662	439.42 0	2.67 0	10.13 1	9.44	4.14E3	3.85	
6 Detectors							
1.332	120.90 -1	9.40 0	92.90 1	9.67	1.88E4	85.14	69.73
1.332	169.16 4	9.40 0	92.90 1	39.08	2.73E3	12.36	
1.173	120.90 -1	17.53 1	92.90 1	12.55	1.71E4	77.42	
1.173	169.16 4	2.67 -1	92.90 1	39.68	3.78E3	17.14	
0.662	444.37 1	2.67 0	3.31 0	5.47	9.32E4	86.58	
0.662	439.42 0	17.53 2	3.31 0	12.75	1.64E4	15.21	

Table 3.2 Convergence data cont.

Energy (MeV)	x (cm) Δx (cells)	y (cm) Δy (cells)	z (cm) Δz (cells)	Δd (cm)	q (Bq)	$\frac{q(E)}{q_{true(E)}}$ (%)	$\chi^2_R/det.$
7 Detectors							
1.332	130.56 0	9.40 0	92.90 1	2.76	1.10E4	49.74	47.39
1.332	130.56 1	17.53 1	97.18 2	10.64	1.06E4	48.00	
1.173	130.56 0	9.40 0	92.90 1	2.76	1.31E4	59.42	
1.173	130.56 0	17.53 1	92.90 1	8.46	8.39E3	38.02	
0.662	439.42 0	2.67 0	3.31 0	3.33	1.05E5	97.22	
0.662	439.42 0	33.78 4	10.13 1	30.20	4.99E3	4.64	
8 Detectors							
1.332	130.56 0	17.53 1	92.90 1	8.46	9.17E3	41.54	93.56
1.332	140.21 1	17.53 1	92.90 1	13.12	7.33E3	33.22	
1.173	140.21 1	9.40 0	97.18 2	12.24	1.34E4	60.78	
1.173	120.90 -1	17.53 1	92.90 1	12.55	6.63E3	30.04	
0.662	439.42 0	9.40 1	3.31 0	5.00	5.63E4	52.31	
0.662	439.42 0	2.67 0	3.31 0	3.33	5.03E4	46.70	

Table 3.2 Convergence data cont.

Energy (MeV)	x (cm) Δx (cells)	y (cm) Δy (cells)	z (cm) Δz (cells)	Δd (cm)	q (Bq)	$\frac{q(E)}{q_{true(E)}}$ (%)	$\chi^2_R/det.$
9 Detectors							
1.332	130.56 0	9.40 0	97.18 2	7.02	1.84E4	83.40	75.84
1.332	140.21 1	9.40 0	92.90 1	10.40	2.40E3	10.86	
1.332	159.51 3	-1.40 -2	97.18 2	32.08	1.39E3	6.32	
1.173	140.21 1	-1.40 -2	97.18 2	16.40	3.04E4	137.72	
1.173	169.16 4	-6.86 -3	97.18 2	42.87	8.81E2	4.00	
0.662	449.20 2	17.53 2	3.31 0	15.71	7.52E4	69.83	
0.662	439.42 0	2.67 0	3.31 0	3.33	6.57E4	60.97	

Table 3.2 Convergence data cont.

Energy (MeV)	x (cm) Δx (cells)	y (cm) Δy (cells)	z (cm) Δz (cells)	Δd (cm)	q (Bq)	$\frac{q(E)}{q_{true(E)}}$ (%)	$\chi^2_R/det.$
12 Detectors							
1.332	140.21 1	9.40 0	92.90 1	10.40	1.08E4	48.90	43.91
1.332	111.25 -2	17.53 1	97.18 2	21.71	8.60E3	38.94	
1.332	130.56 0	17.53 1	104.98 3	16.83	8.64E2	3.92	
1.332	130.56 0	17.53 1	87.87 0	8.33	8.42E2	3.82	
1.332	169.16 4	-1.40 -2	97.18 2	41.09	7.72E2	3.50	
1.173	130.56 0	9.40 0	92.90 1	2.76	1.80E4	81.70	
1.173	120.90 -1	9.40 0	92.90 1	9.67	3.02E3	13.68	
1.173	111.25 -2	17.53 1	104.98 3	25.32	1.13E3	5.14	
1.173	159.51 3	17.53 1	92.90 1	30.53	4.76E2	2.16	
0.662	439.42 0	2.67 0	3.31 0	3.33	9.32E4	86.55	
0.662	439.42 0	25.65 3	3.31 0	20.79	1.07E4	9.89	
0.662	439.42 0	9.40 1	10.13 1	10.15	3.98E3	3.69	

Table 3.2 Convergence data cont.

Energy (MeV)	x (cm) Δx (cells)	y (cm) Δy (cells)	z (cm) Δz (cells)	Δd (cm)	q (Bq)	$\frac{q(E)}{q_{true(E)}}$ (%)	$\chi^2_R/det.$
15 Detectors							
1.332	140.21 1	9.40 0	92.90 1	10.40	9.96E3	22.56	64.60
1.332	111.25 -2	17.53 1	92.90 1	20.73	8.46E3	38.32	
1.332	130.56 0	17.53 1	92.90 1	8.46	1.74E3	7.90	
1.332	140.21 1	17.53 1	104.98 3	19.59	7.37E2	3.34	
1.173	130.56 0	17.53 1	92.90 1	8.46	7.99E3	36.20	
1.173	140.21 1	2.67 -1	92.90 1	12.46	7.84E3	35.52	
1.173	101.60 -3	17.53 1	97.18 2	30.49	4.85E3	22.00	
1.173	140.21 1	17.53 1	104.98 3	19.59	6.28E2	2.84	
0.662	439.42 0	9.40 1	3.31 0	5.00	7.96E4	73.88	
0.662	444.37 1	2.67 0	3.31 0	5.47	2.65E4	24.64	

Table 3.2 Convergence data cont.

Energy (MeV)	x (cm) Δx (cells)	y (cm) Δy (cells)	z (cm) Δz (cells)	Δd (cm)	q (Bq)	$\frac{q(E)}{q_{true(E)}}$ (%)	$\chi^2_R/det.$
18 Detectors							
1.332	140.21 1	9.40 0	92.90 1	10.40	1.15E4	52.16	37.00
1.332	120.90 -1	17.53 1	92.90 1	12.55	6.75E3	30.56	
1.332	91.95 -4	17.53 1	104.98 3	41.77	2.09E3	9.48	
1.332	120.90 -1	17.53 1	79.31 -1	16.36	1.11E3	5.02	
1.173	130.56 0	9.40 0	92.90 1	2.76	2.14E4	97.12	
1.173	91.95 -4	17.53 1	104.98 3	41.77	1.33E3	6.02	
0.662	439.42 0	9.40 1	3.31 0	5.00	5.76E4	53.50	
0.662	439.42 0	2.67 0	3.31 0	3.33	4.91E4	45.56	

Table 3.2 Convergence data cont.

Energy (MeV)	x (cm) Δx (cells)	y (cm) Δy (cells)	z (cm) Δz (cells)	Δd (cm)	q (Bq)	$\frac{q(E)}{q_{true(E)}}$ (%)	$\chi^2_R/det.$
21 Detectors							
1.332	140.21 1	9.40 0	92.90 1	10.40	1.13E4	51.24	37.97
1.332	120.90 -1	9.40 0	92.90 1	9.67	9.81E3	44.46	
1.332	91.95 -4	17.53 1	70.76 -2	43.61	1.10E3	4.98	
1.173	140.21 1	9.40 0	92.90 1	10.40	7.60E3	34.44	
1.173	130.56 0	9.40 0	92.90 1	2.76	7.01E3	31.76	
1.173	120.90 -1	9.40 0	92.90 1	9.67	6.95E3	31.48	
1.173	91.95 -4	17.53 1	70.76 1	43.61	7.81E2	3.54	
0.662	439.42 0	2.67 0	3.31 0	3.33	9.34E4	86.70	
0.662	439.42 0	25.65 3	3.31 0	20.79	1.38E4	12.86	

Table 3.2 Convergence data cont.

Energy (MeV)	x (cm) Δx (cells)	y (cm) Δy (cells)	z (cm) Δz (cells)	Δd (cm)	q (Bq)	$\frac{q(E)}{q_{true(E)}}$ (%)	$\chi^2_R/det.$
24 Detectors							
1.332	111.25 -2	17.53 1	87.87 0	20.67	6.14E3	27.84	299.1
1.332	120.90 -1	9.40 0	92.90 1	9.67	5.08E3	23.02	
1.332	149.86 2	17.53 1	87.87 0	21.37	3.10E3	14.04	
1.332	149.86 2	17.53 1	92.90 1	21.42	2.33E3	10.54	
1.332	111.25 -2	17.53 1	79.31 -1	23.24	1.32E3	6.00	
1.332	120.90 -1	17.53 1	104.98 3	19.21	1.16E3	5.26	
1.173	140.21 1	17.53 1	92.90 1	13.12	7.71E3	34.92	
1.173	111.25 0	17.53 1	87.87 0	20.67	4.94E3	22.36	
1.173	82.30 -5	17.53 1	79.31 -1	49.74	2.10E3	9.50	
1.173	149.86 2	17.53 1	87.87 0	21.37	2.07E3	9.36	
1.173	120.90 -1	17.53 1	104.98 3	19.21	8.21E2	3.72	
0.662	439.42 0	2.67 0	3.31 0	3.33	8.67E4	80.51	
0.662	439.42 0	17.53 2	3.31 0	12.75	1.66E4	15.45	
0.662	439.42 0	25.65 3	10.13 1	22.59	3.64E3	3.38	

The tables show similar types of information as the previous convergence study, but reveal a more interesting feature. Again, DIMP does not converge with fewer than 5 detectors for this source configuration comprising a six-point distribution with three distinct energies. From 5-7 detectors the point source is well resolved, merely wavering between two configurations: a 50/50 split of the source with the correct cell and a neighboring cell and most of the source strength (>70%) concentrated in one of these two cells. The Co-60 line source however, is only resolved as one- or two-cell sources. The predicted Co-60 point sources match approximately in total strength and location with the stronger sources on the true line source.

From 8-21 detectors, more points on the predicted Co-60 line source are resolved. However, DIMP never maps all five source points of the true Co-60 line source, and typically smears the locations of the stronger points on the line between the correct cell and a neighbor. Unfortunately, at 24 detectors, DIMP begins to diverge by predicting source points beyond the boundaries of the true Co-60 line source. The new detector information creates more source configurations than it eliminates as the total error between the transport model and the synthetic responses increases with the addition of each new detector. This failure will be investigated further in the near future.

3.2.1 Convergence of DIMP Using Uncollimated Responses Only

Verifying the necessity and contribution of directional responses to the performance of DIMP's source prediction is of high interest for future work. Collimated detectors require more complex DRFs in order to calculate full response spectra [11], so it would be easier and more efficient to run DIMP with only unshielded detection points. In order to determine DIMP's dependence on directional responses, a convergence study was conducted with only unshielded responses. This numerical simulation involved only the Cs-137 point source, as reported in Section 3.1. Purely synthetic measurements generated with MCNP were used as unshielded detector responses where the number of detection points was increased from 3 to 42 points total, in order to provide an equivalent number of data points to the base six detection points case with seven responses per detection point. The results of this convergence study are shown in Table 3.2.1.

Table 3.3 Spatial distribution of the Cs-137 point source computed with DIMP from synthetic responses as a function of a selected number of detectors using only unshielded responses. Only cells with source strength larger than 1% of the true source strength are listed.

3 Det.	x (cm) Δx (cells)	y (cm) Δy (cells)	z (cm) Δz (cells)	Δd (cm)	q (Bq)	$\frac{q}{q_{true}}$ (%)	$\chi^2_R/det.$
	391.16	220.73	97.18	241.19	6.11E3	5.67	2.777E-2
	-5	27	13				
7 Det.							
	400.81	245.11	92.90	260.07	1.92E4	17.87	2.87E-2
	-4	30	12				
	198.12	-6.86	92.90	259.02	8.47E3	7.87	
	-25	-2	12				
	410.46	50.04	14.41	55.50	6.51E3	6.04	
	-3	6	2				
	400.81	236.98	97.18	254.17	1.81E3	1.68	
	-4	29	13				
15 Det.							
	400.81	74.42	3.31	79.75	1.88E4	17.50	31.11
	-4	9	0				
	246.38	17.53	147.74	243.27	6.53E3	6.06	
	-20	2	19				
	217.42	131.32	14.41	256.27	3.68E3	3.41	
	-23	16	2				
	391.16	228.85	87.87	245.03	2.91E3	2.71	
	-5	28	11				
	400.81	220.73	122.08	250.47	2.01E3	1.86	
	-4	27	16				
	420.12	58.17	27.99	62.85	1.53E3	1.42	
	-2	7	4				

Table 3.3 Convergence data cont.

30 Det.	x (cm) Δx (cells)	y (cm) Δy (cells)	z (cm) Δz (cells)	Δd (cm)	q (Bq)	$\frac{q}{q_{true}}$ (%)	$\chi^2_R/det.$
	410.46	25.65	3.31	36.11	1.57E4	14.54	2.82
	-3	3	0				
	420.12	115.06	181.96	212.73	1.29E4	11.98	
	-2	14	23				
	400.81	17.53	3.31	41.21	1.22E4	11.37	
	-4	2	0				
	420.46	131.32	3.31	129.75	6.54E3	6.07	
	-2	16	0				
	284.99	9.40	181.96	238.31	4.24E3	3.94	
	-16	1	23				
	159.51	66.29	14.41	287.42	1.86E3	1.72	
	-29	8	2				
	246.38	171.96	14.41	256.01	1.82E3	1.69	
	-20	21	2				

Table 3.3 Convergence data cont.

42 Det.	x (cm) Δx (cells)	y (cm) Δy (cells)	z (cm) Δz (cells)	Δd (cm)	q (Bq)	$\frac{q}{q_{true}}$ (%)	$\chi^2_R/det.$
	429.77	33.78	45.10	53.65	1.85E4	17.18	6.37
	-1	4	6				
	400.81	17.53	3.31	41.21	1.08E4	10.0	
	-4	2	0				
	371.86	2.67	3.31	68.22	8.78E3	8.16	
	-7	0	0				
	333.25	9.40	190.51	217.55	6.76E3	6.28	
	-11	1	24				
	439.42	66.29	10.13	61.97	4.90E3	4.55	
	0	8	1				
	381.51	147.57	3.31	154.12	4.59E3	4.26	
	-6	18	0				
	429.77	33.78	3.31	30.63	3.26E3	3.02	
	-1	4	0				
	140.21	-1.40	3.31	299.87	3.21E3	2.99	
	-31	-1	0				
	227.08	163.83	-0.97	265.65	2.63E3	2.44	
	-22	20	-1				
	420.46	115.06	156.30	191.38	2.09E3	1.94	
	-2	14	20				

Unfortunately, DIMP did not perform well leading to the conjecture that directional responses are indeed necessary and integral to the accuracy of DIMP's source prediction. In all of the simulations, the Cs-137 point source was predicted broadly distributed throughout the mesh with the closest cells (not always the highest activity cells) being at least 5 cells away from the true source cell. None of the sources were above 18% of the true source strength, and the reduced chi-squared values were lower or comparable to DIMP's predictions with directional responses (Table 3.1). Usually, when DIMP predicts an incorrect source distribution, it places weak sources near prominent detector points. The possibility of DIMP being stuck in a local minimum was also investigated by using the true source distribution as an initial guess. DIMP predicted the solution in the true source cell with

95% or above of the true source strength for each case with a reduced chi-squared value closer to one, so many of the cases reported in Table may have only shown a local minimum. The reduced chi-squared was also greatly improved for searches with greater than 14 detection points. Therefore, it seems the initial guess and alpha vector parameters for the unshielded responses source search must be fairly different from those of the combined directional and unshielded response source search. Once the correct alpha vector range for unshielded responses is found, further investigation with the full Cs-137 and Co-60 source search will continue in order to better test DIMP's performance with unshielded responses for more complex source configurations.

3.2.2 Limitations of the DIMP algorithm and Assumptions for synthetic responses

While in the process of testing the convergence properties of DIMP for the original test case, two limitations of the model and model assumptions were discovered. These limitations include the alignment of sources and detection points in plane with one another and close proximity of a source to a detector. The issue arises from an assumption (involving the lead brick collimator model) made in the computation of MCNP directional responses as synthetic measurements which causes significant disagreement with the predicted responses from DENOVO under the prescribed conditions. DENOVO calculates the adjoint flux, and consequently we compute the detector response from the adjoint flux and the source configuration at the center of the detector coordinates, whereas MCNP calculates responses at the face of the brick about five centimeters off of the detector face along the axis in the intended measurement direction. This difference between the MCNP and DENOVO models that was originally designed to simplify computation of the synthetic directional responses caused the two abovementioned limitations that produced discrepancies between the responses computed with the two models as elaborated below.

3.2.2.1 In-plane Sources and Detectors

The first limitation was discovered after poor convergence was observed for an earlier 12 detector simulation where 6 detection points were kept the same as the previous work [2], and 6 new, distinct points were chosen within the room enclosure in cells whose material assignment is air but without preference of specific locations or alignment with other mesh or room features. The resulting poorly converged results are shown in Table 3.4.

Table 3.4 Spatial distribution of the Cs-137 point source and the Co-60 line source computed with DIMP from synthetic responses of 12 detectors that include three coplanar detectors with sources.

Energy (MeV)	x (cm) Δx (cells)	y (cm) Δy (cells)	z (cm) Δz (cells)	Δd (cm)	q (Bq)	$\frac{q(E)}{q_{true(E)}}$ (%)	$\chi^2_R/det.$
1.332	140.21 1	17.53 1	97.18 2	14.62	3.87E3	8.76	1551
1.173	140.21 0	17.53 1	97.18 0	14.62	1.488E3	3.34	
1.173	130.56 3	17.53 1	97.18 3	10.64	1.33E3	3.02	
0.662	391.16 -5	41.91 5	-0.97 -1	61.25	7.56E3	7.02	
0.662	439.42 0	98.81 12	19.44 0	95.60	3.05E3	2.84	

Clearly, DIMP did not converge well for this early 12 detector case as evidenced by the poor agreement of strength and location with the true source and also by the large reduced chi-squared value especially in comparison with the 12 detector case shown in Table 3.2 where none of the detection points suffered the poor placement conditions under investigation in this section. This discrepancy was very puzzling considering the good agreement reported previously [2] with six detectors that are a subset of the 12 detectors employed to generate the results reported in Table 3.4. Convergent behavior of DIMP would have improved the agreement between the true and predicted source distribution with increasing number of detection points. All of the predicted source cells are excessively weak in strength and placed away from the walls at least a few cells closer to the detectors. While the Co-60 prediction was only a few cells off in location from the center of the true line source, it spans cells in the z direction instead of the x direction. The Cs-137 predicted point source is more than a few cells off from the corner of the room where the true source was located. Furthermore, the large value of the reduced chi-square per detector indicated a significant disagreement between predicted responses and the measured responses especially in view of the much smaller value of 69.73 achieved with the first six detectors [2]. Figure 3.1 compares the synthetic responses computed by MCNP with those predicted by the inner product of the true source configuration with DENOVO's adjoint fluxes. The logarithmic scale shows the overall differences in responses, while the linear scale emphasizes those in the higher intensity Co-60 responses.

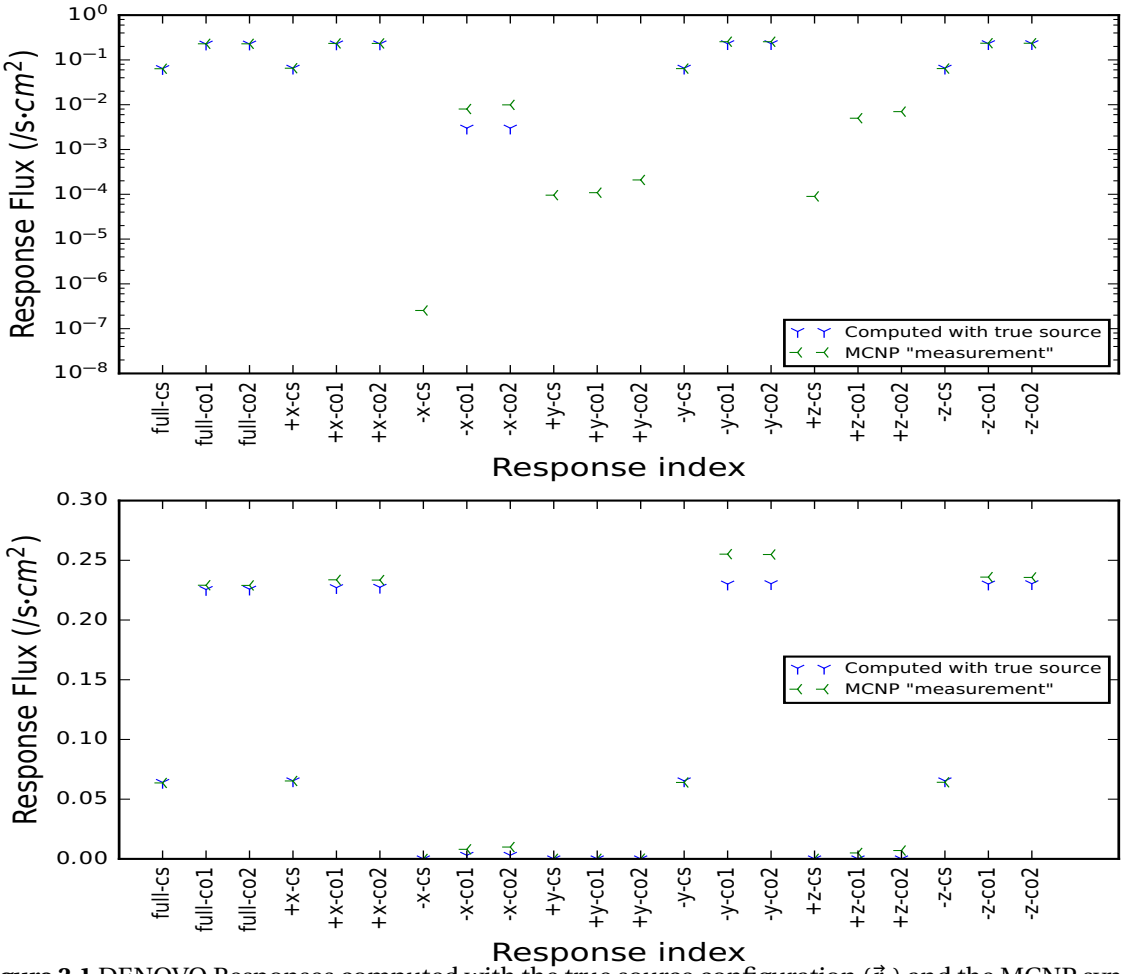

Figure 3.1 DENOVO Responses computed with the true source configuration ($\vec{r}_t$) and the MCNP synthetic responses ($\vec{r}_m$) for a detector that is in-plane with a source, and located at x=101.6 cm, y=88.9 cm, z=114.3 cm on logarithmic (above) and linear (below) scales. The horizontal axis indicates the type of response (collimated or uncollimated), the response's energy, and the axis of alignment if it is a collimated response.

Upon comparison of the two sets of responses, significant differences were observed in all of the responses except for the unshielded or "full" responses. Again, the true Co-60 line source is located at approximately x=96.5-143.8 cm, y=9.5 cm, and z=90.2 cm.

Since the full responses agreed rather well, this pointed to the lead block collimator as the reason for the discrepancy. In DENOVO, the detector response is computed at a single cell, namely the cell containing the coordinates of the centerpoint of the detector's face, and a point DRF

function determines the level of attenuation for the flux at that point by the collimator. Some of the differences can be attributed to when the DRF in the DENOVO adjoint transport calculations causes an uncollided flux to be zero, while a nonzero heavily attenuated flux is computed by MCNP. In MCNP, the lead block's center point is chosen to be the original center point of the detector face and the tally is moved approximately five centimeters along the detector's measurement axis to the corresponding face of the lead block for each directional response tally (refer to sketch in Fig. 3.2.

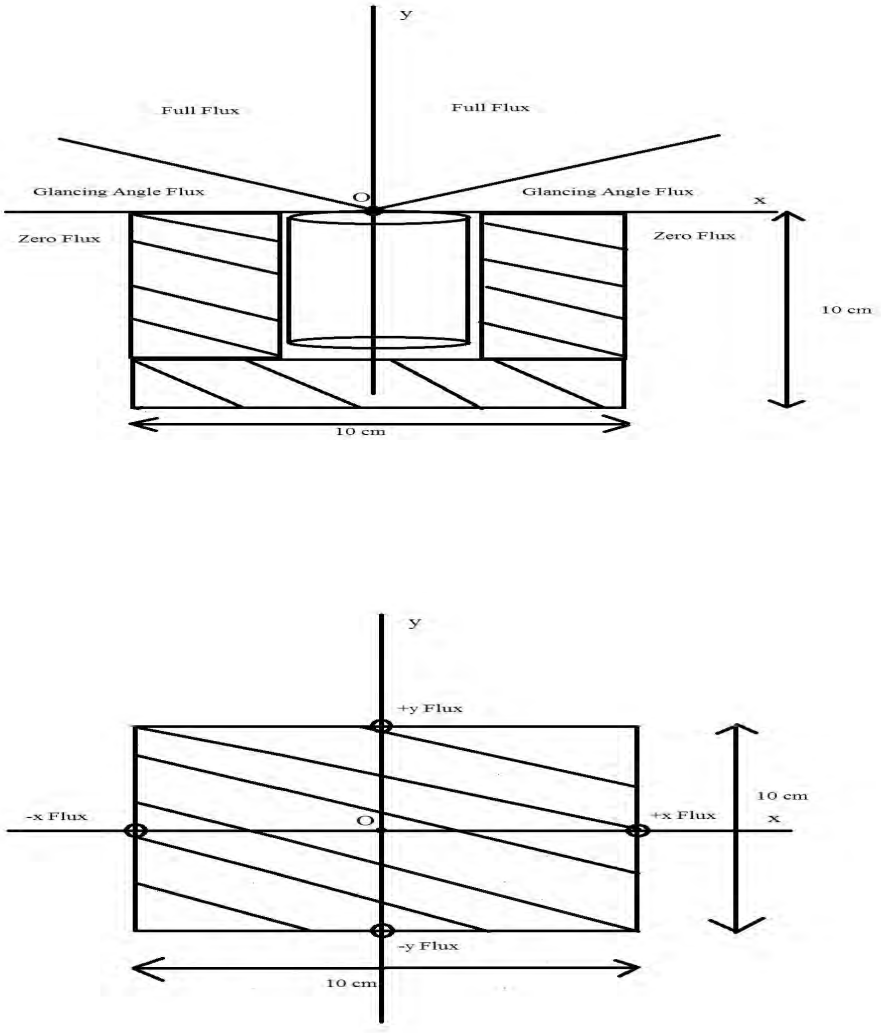

Figure 3.2 Representation of the synthetic response calculation for DENOVO (above) and MCNP (below) for an arbitrary detection point.

As seen above, the origin is shifted from the original coordinates in DENOVO by five centimeters for each directional response. In MCNP, the whole setup is replaced with a single 10 cm^3 lead cube, and the tally is shifted by five centimeters from the original origin to the face of the lead cube for the directional response of interest. This changes the angle of incidence as well as the distance between source and detector slightly from the original geometry at the detector's face coordinates. When detector and source are co-planar, this can affect the synthetic response greatly, causing false positive or negative responses for point sources and noticeable variation in intensity for line sources. To resolve this discrepancy in the MCNP model, future synthetic collimated responses will be generated separately on a direction by direction basis (further separation may be required to prevent the tally interference effects mentioned above).

3.2.2.2 Proximity Between Sources and Detectors

A similar discrepancy in the responses was observed when all of the in-plane detectors were moved a necessary distance out of alignment with source cells, and yet, the source map was only slightly improved. The DIMP predicted source distribution provided measures of agreement with the true source for this 12 detector arrangement that had no coplanar sources and detectors that are displayed in Table 3.5.

Table 3.5 Spatial distribution of the Cs-137 point source and the Co-60 line source computed with DIMP from synthetic responses of 12 detectors with some detectors and sources in close proximity.

Energy (MeV)	x (cm) Δx (cells)	y (cm) Δy (cells)	z (cm) Δz (cells)	Δd (cm)	q (Bq)	$\frac{q(E)}{q_{true(E)}}$ (%)	$\chi^2_R/det.$
1.332	140.21 1	17.53 1	87.87 0	13.04	6.34E3	28.72	109.3
1.332	149.86 2	9.40 0	87.87 0	19.82	5.98E3	27.10	
1.332	149.86 2	17.53 1	79.31 -1	23.86	5.16E2	2.34	
1.173	140.21 1	17.53 1	87.87 0	13.04	6.49E3	29.42	
1.173	149.86 2	9.40 0	87.87 0	19.82	6.29E3	28.48	
0.662	439.42 0	2.67 0	3.31 0	3.33	9.63E4	89.46	
0.662	439.42 0	17.53 2	3.31 0	12.75	1.29E4	12.02	

In this case, DIMP's prediction is much improved, but the results were still worse than the 6 detector case reported earlier [2]. The reduced chi-squared per detector is nearly double the six detector value, and the predicted Co-60 source only reached half of its true strength. Again, comparison of the synthetic and predicted responses reveal a few discrepancies as seen for one such detector that was placed too close to the source (within 35 cm or about nine cells) in Figure 3.3 for all seven directions. The detector is closest in proximity to the true location of the Cs-137 point source (x=440 cm, y=5 cm, z=1cm).

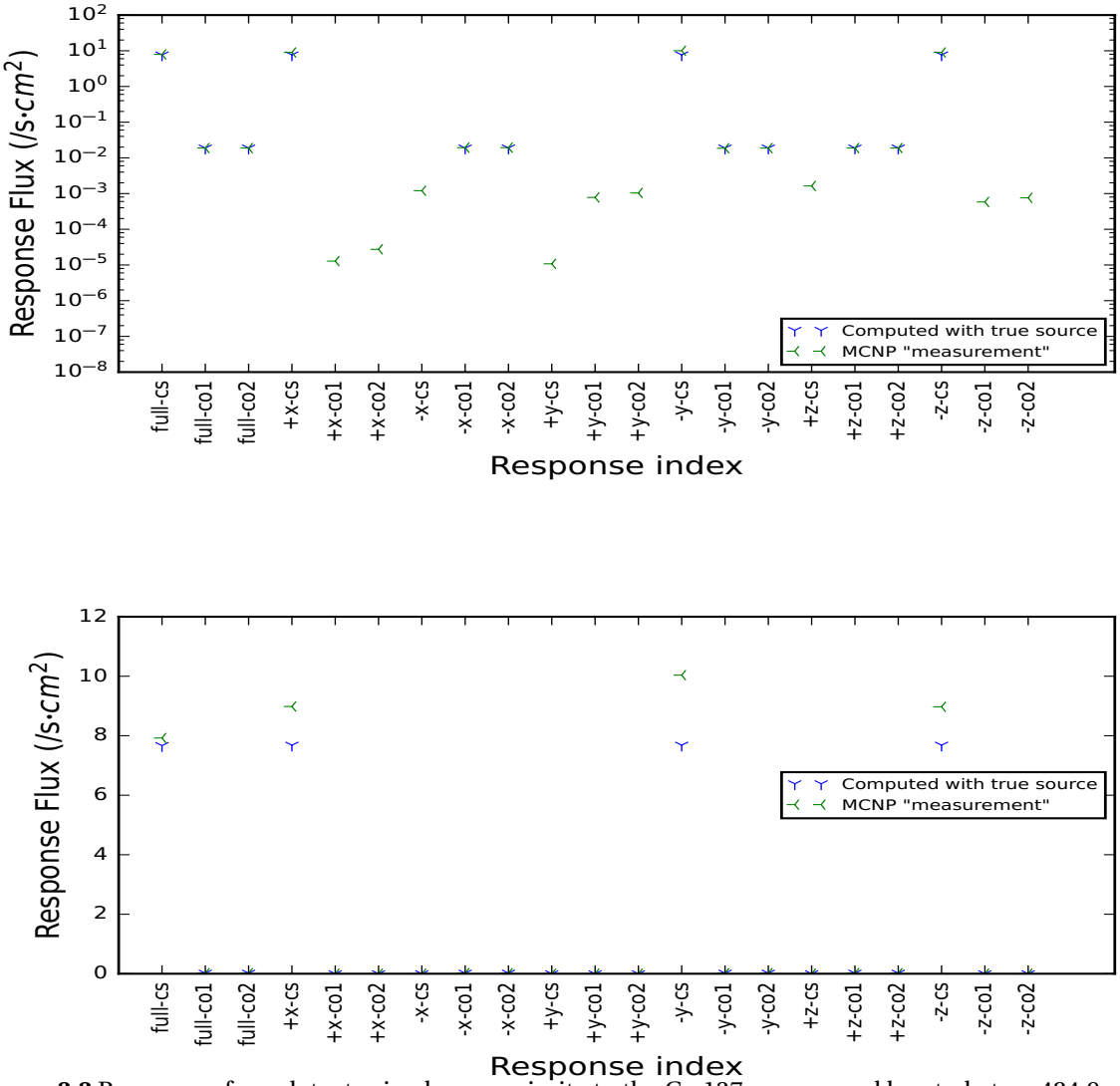

Figure 3.3 Responses for a detector in close proximity to the Cs-137 source, and located at x=424.9 cm, y=30.0 cm, z=16.0 cm on logarithmic (top) and linear (bottom) scales.

Oddly, even the unshielded responses show a slight discrepancy between the synthetic and true response values this time. The linear scale of Fig. 3.3 highlights this and illustrates the differences in the large magnitude Cs-137 responses. There is still a problem with the MCNP $+x$, $-y$, and $-z$ directional responses, since a directional response should never significantly exceed the unshielded response in magnitude as is the case for the $-y$-cs value. Here too, the cause for the discrepancy is the MCNP lead block face tally assumption. While the angular collimation based attenuation

may remain small, the geometric attenuation differences incurred by moving the detection point 5 cm closer to the source can be significant on a relative scale when the detector-source separation distance is of comparable length.

CHAPTER

4

HOLDUP EXPERIMENTAL SETUP

Four measurement experimental campaigns were conducted at the International Safeguards laboratory at ORNL using a calibration button point source, an HEU disk calibration source, a set of HEU line sources tied together within a small round duct structure, and a case with multiple HEU sources and fixtures. Each measurement campagin was designed to test and validate source prediction results calculated by the DIMP code system in a specific configuration relevant to the validation of the fundamental methodology or the holdup application. Each campaign's measured results except for the first one were also compared to the current holdup model used in practice at ORNL, HMS-4 (Holdup Measurement System). This chapter will discuss the experimental setup including source location, structure, dimensions and composition, and detector location choice rationale.

The activities and active source dimensions of the calibration source are included with all of the sources used in the measurement campaign in a consolidated table (Table 4.1). Note that only the active volume of these sources was simulated in DIMP and not their containers, since attenuation was deemed to be negligible with one exception, the HEU disk, which was encased in a 0.159cm thick stainless steel casing instead of the typical plastic and cardboard casings.

Table 4.1 Dimensions and activities of all sources used for experimental measurements conducted in the International Safeguards laboratory at ORNL.

Point/Disk Sources						
Source	Active Radius (cm)	Thickness (cm)	Activity (μCi)	Manufactured	Measured	Activity Measured (μCi)
Cs-137*	0.25	0.318	5.01	9/28/2005	5/14/2015	4.04 ± 0.61
HEU Disk	2.381	0.0701	23.5	12/5/2004	5/19/2015	23.5 ± 0.24
Line Sources						
Source	Active Line (cm)	Diameter (cm)	Activity (μCi)	Manufactured	Measured	Activity Measured (μCi)
HEU Rod 1	28.5	0.5	3.335	5/2004	5/27/2015	3.335 ± 0.003
HEU Rod 2	28.5	0.5	3.357	5/2004	5/27/2015	3.357 ± 0.003
HEU Rod 3	28.5	0.5	3.285	5/2004	5/27/2015	3.285 ± 0.003
HEU Rod 4	28.5	0.5	3.257	5/2004	5/27/2015	3.257 ± 0.003
HEU Rod 5	28.5	0.5	3.372	5/2004	5/27/2015	3.372 ± 0.003
HEU Rod 6	28.5	0.5	3.214	5/2004	5/27/2015	3.214 ± 0.003
Area Sources						
Source	Active Area (cm)	Thickness (cm)	Activity (μCi)	Manufactured	Measured	Activity Measured (μCi)
HEU Card 1	1058	0.1	23.99	5/2004	6/29/2015	23.99 ± 0.022
HEU Card 2	1058	0.1	24.01	5/2004	6/29/2015	23.99 ± 0.022
HEU Card 3	1058	0.1	28.01	5/2004	6/29/2015	23.99 ± 0.022
HEU Card 4	1058	0.1	24.13	5/2004	6/29/2015	23.99 ± 0.022

*Note: The calibration sources used in this work were created by Eckert and Ziegler, and the active source dimensions (active radius, A.R., and thickness) used in the MCNP model were taken from the Type D disc model in the catalog. Furthermore, according to the supplier "Sources are manufactured with contained activity (Act.) values of ±15% of the requested activity value unless otherwise noted in the catalog." [13]

The HEU source record maintained at ORNL reports each source's mass. The uncertainties in the activity were calculated from the mass measurement uncertainty to be about 0.1 %. The emission energies and relative intensities of the gamma-rays of interest for each source used are listed in Table 4.2.

Table 4.2 Gamma ray energies and relative intensities with their uncertainties listed in parentheses, of all sources measured were taken from Brookhaven National Laboratory's Nudat2.6 database. [14] Unlisted uncertainties in Ref. [14] were assumed to be one in the last digit.

Source	Peak No.	Energy (keV)	Relative Intensity (%)
Am-241	1	59.5409(1)	35.9(4)
U-235	1	105.0(1)	2.00(3)*
U-235	2	109.0(1)	2.16(13)*
U-235	3	143.76(2)	10.96(14)
U-235	4	163.356(3)	5.08(6)
U-235	5	185.715(5)	57.0(6)
U-235	6	202.12(1)	1.080(23)
U-235	7	205.316(10)	5.02(6)
Ba-133	1	80.9979(11)	35.6(3)*
Ba-133	2	356.0129(7)	62.05(1)
Cs-137	1	661.657(3)	85.10(20)
Co-60	1	1173.228(3)	99.85(3)
Co-60	2	1332.492(4)	99.9825(6)

*Note: gamma-rays from the same source that were within 1 keV of each other were assigned their average energy and their intensities summed together.

4.1 Unshielded Cs-137 Button

The first measurement involved only one Cs-137 point source (calibration button source) held above the origin in the selected coordinate system for the computational models by a clamp on a ring stand. This simple experiment was performed to confirm previous results presented by Hykes [2]. It was surmised that some of the inconsistency in the previous results could be attributed to weakness of the employed sources. Although the Cs-137 button source is only slightly stronger than the source used by Hykes, it will make a good initial source configuration for the calibration of DIMP to the ORNL field detector.

In order to minimize the influence of gamma ray scattering by various objects in the lab a 5m x 5m floor space was marked with tape and cleared of all objects deemed non-essential for the experimental measurement. For the vast majority of the measurement time, this remained true. Occasionally, a chair or stool was moved within the measurement boundaries to hold the MCA, or a staff member might have walked through the marked zone inadvertently. However, the effect of these infractions on the precision of the measured response is considered negligible as no foreign object (including the chair carrying the MCA) remained in the field of view of the detector for any significant length of the measurement time.

The equipment deployed in conducting the experiment included two ring stands, a 2"x1" NaI detector, and a Cs-137 calibration source. The stands each had a pole approximately 1.5m tall and a diameter of 2cm and a rectangular base (0.27m x 0.16m). The list of coordinate locations of the center-point of the face of the detector for each detector measurement and the source location are shown in Table 4.3.

Table 4.3 Coordinate locations of the center point of the detector face for each measurement of the Cs-137 point source. The origin is located on the floor at the very center of the cleared square. The uncertainty in each measurement coordinate is 1 mm.

Measurement #	Location (cm)	Total Distance	Detector Orientation
Source	(0,0,87)	0	
1	(51,140,87)	149.0	$-y$
2	(120,32,77)	124.6	$-x$
3	(100,-20,96)	102.4	$-x$
4	(10,-74,81)	74.9	$+y$
5	(-5,-60,93)	60.5	$+y$
6	(-50,0,97)	51.0	$+x$
7	(-40,16,84)	43.2	$+x$
8	(-7,20,89)	21.3	$-y$
9	(3,10,87)	10.4	$-y$
10	(2,0.3,87)	2.02	$-x$

4.2 HEU Disc

The next validation experiment involved measuring a larger HEU source that could either be treated as an area source (multiple cells in a block) or a single cell source depending on mesh resolution. This source again was held above the origin of the measurement area by a clamp on a ring stand. This allowed for measuring a more relevant radiation source to holdup and calibrating DIMP to HEU sources without significantly increasing the complexity of the source geometry. The detector measurement coordinates and the coordinates of the center of the HEU disk source are shown in Table 4.4. A photograph of the experimental setup is presented in Fig. 4.1.

Figure 4.1 Photograph of the HEU Disk source measurement experimental setup.

Table 4.4 Coordinate locations of the detector face for each measurement of the HEU Disk source. The uncertainty in each measurement coordinate is 1 mm.

Measurement #	Location (cm)	Total Distance to	Detector Orientation
Source	(0,0,91)	0	
1	(100,-20,100)	102.4	$-x$
2	(16,-40,88)	43.2	$+y$
3	(5,-50,95)	50.4	$+y$
4	(-60,-5,97)	60.5	$+x$
5	(-74,10,85)	74.9	$+x$
6	(-7,20,93)	21.3	$-y$
7	(3,10,91)	10.4	$-y$
8	(2,0.3,91)	2.02	$-x$
9	(40,0,91)	40.0	$-x$
10	(6,-1,91)	6.08	$-x$

4.3 HEU Line Source in the Small Round Duct

The next set of experiments involved the arrangement of various HEU sources chosen from Table 4.1 within three steel fixtures to simulate realistic holdup in a facility environment. The three fixtures were: a small round duct, an L-duct, and a pipe array. The coordinate locations and the dimensions of the fixtures and their respective carts are displayed in Table 4.5. Each cart is a metal dolley with wheels and steel strut supports to hold the fixture in place. Detailed drawings of the small round duct and the L-duct are included in Figs. 4.2 and 4.3. The pipe array is not included because it was never filled with a source.

Table 4.5 Coordinate locations and dimensions of the holdup equipment structures.

Fixture	Dim. 1 (cm)	Dim. 2 (cm)	Dim. 3 (cm)	Dim. 4	Obj. Center Loc. (cm)
SRD Cart	x=57	y=122	z=2.54	Th.≈0.25	(0,0,8)
L-duct Cart	x=122	y=57	z=2.54	Th.≈0.25	(140,140.5,8.27)*
Pipe Ar. Cart	x=122	7=57	z=2.54	Th.≈0.25	(-131,-152.5,8.27)
SRD	L=189	R_{out}=7.5		Th.≈0.45	(0,-1,123.5)
L-duct	x=175	y=38	z=91/76/61	Th.≈0.5	(118,141,106.5/99/91.5)
Pipe Array	L=130	R_{out}=2		Th.≈0.55	(-129,-152.5,95)

*Note: The height dimensions are variable along three sections of the L-duct.

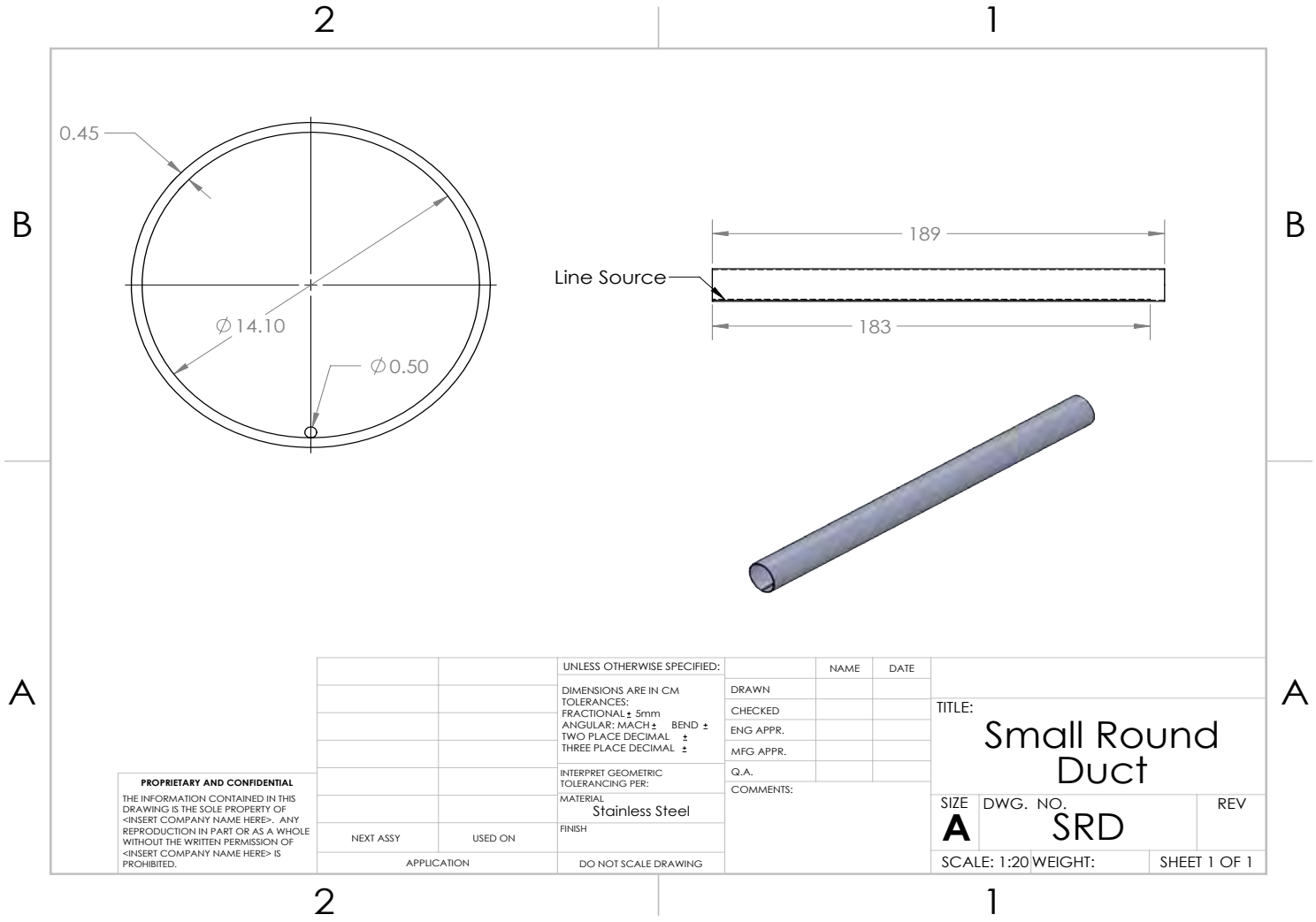

Figure 4.2 Drawing of the small round duct fixture with the appropriate dimensions.

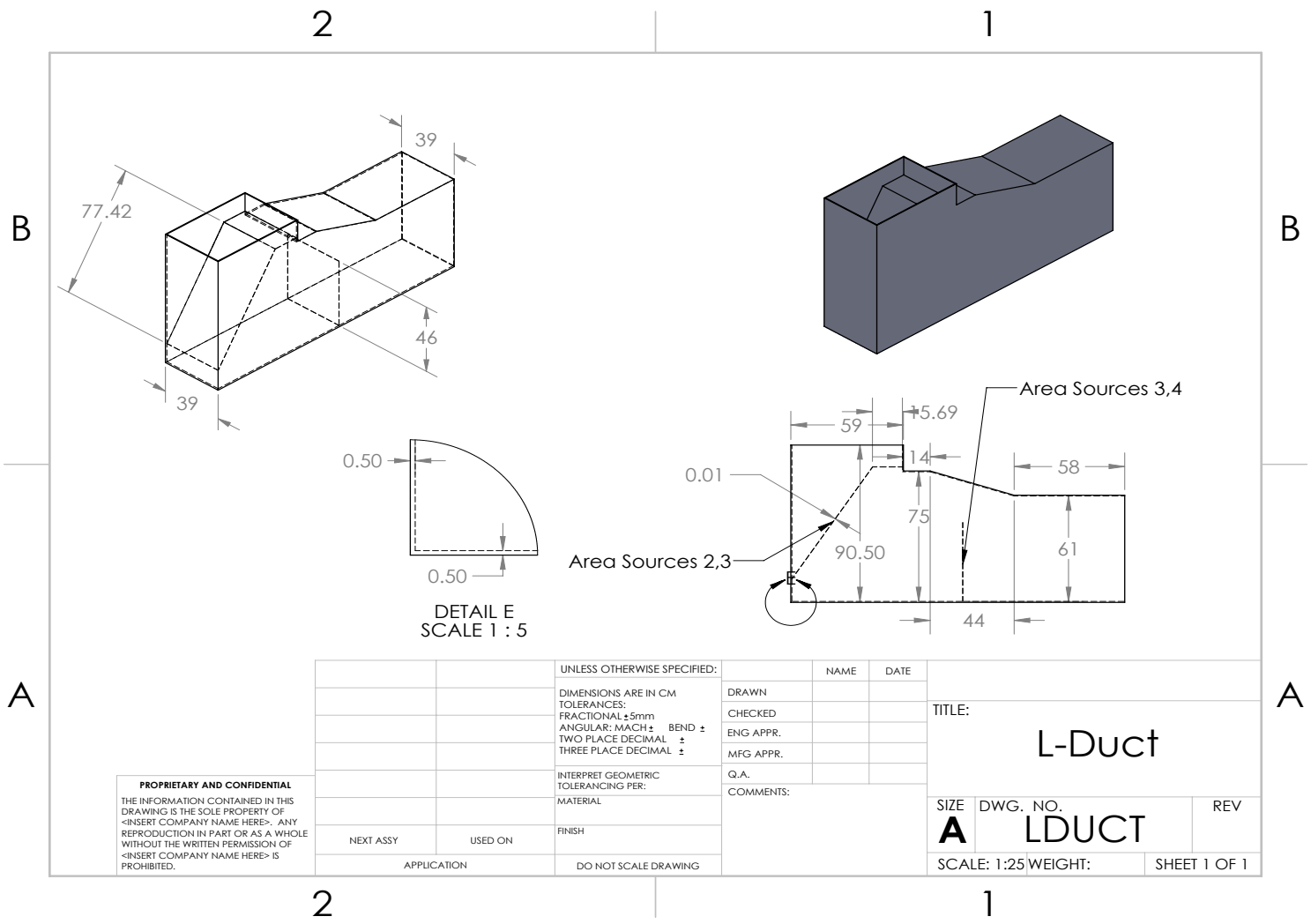

Figure 4.3 Drawing of the L-duct fixture with the appropriate dimensions.

For the first case, the small round duct was loaded with a set of six line sources taped end to end across the majority of the length of the pipe (the source did not span the last six centimeters of the southern end of the pipe). The pipe was enclosed on both ends with steel end caps. The coordinate locations for each detector measurement and the center of the line source are displayed in Table 4.6. A photograph of the general experimental setup is included for perspective in Fig. 4.4

Table 4.6 Coordinate locations of the detector face for each measurement of the line sources in the small round duct. The uncertainty in each measurement coordinate is 1 mm.

Measurement #	Location (cm)	Total Distance to Midpoint of the Source	Detector Orientation
Source	(0,1.5,116.5)	0	
1	(36,-74.2,115)	36	$-x$
2	(36,-43,115)	36	$-x$
3	(36,-12.8,115)	36	$-x$
4	(36,17.8,115)	36	$-x$
5	(36,48.5,115)	36	$-x$
6	(36,79.2,115)	36	$-x$
7	(-10,-50,120)	10.6	$+x$
8	(-20-,-25,112)	20.5	$+x$
9	(-50,10,107)	50.9	$+x$
10	(-60,40,123)	60.4	$+x$
11	(0,114,117)	20.5	$-y$
12	(0,-104,119)	13.7	$+y$
13	(0,1.5, 81)	35.5	$+z$

Figure 4.4 Photograph of the general holdup-like source measurement experimental setup.

4.4 HEU Line Source in the Small Round Duct & HEU Area Sources in the L-Duct

For the final case, the small round duct was left loaded with the same source as in the previous case, and then the L-duct was loaded with four rectangular area sources (also known as "card" sources). The first two were taped together vertically across the diameter of the duct at the eastern section. The other two card sources were taped diagonally across a filter in L section at the western end. This geometry was chosen as a difficult geometry for traditional holdup measurements. The coordinate locations of the center of each card source and those of the detector measurements are shown in Table 4.7.

Table 4.7 Coordinate locations of the detector face for each measurement of the line sources in the small round duct and the area sources in the L-duct. The uncertainty in each measurement coordinate is 1 mm.

Measurement #	Location (cm)	Total Distance to Source Center	Detector Orientation
Source 1	(0,1.5,116.5)	0	
Source 2	(46.5,141.5,83.28)	0	
Source 3	(78.28,141,123.5)	0	
Source 4	(120.5,133.5,86.4)	0	
Source 5	(121,148.5,86.4)	0	
1	(36,-74.2,115)	36	$-x$
2	(36,-43,115)	36	$-x$
3	(36,-12.8,115)	36	$-x$
4	(36,17.8,115)	36	$-x$
5	(36,48.5,115)	36	$-x$
6	(36,79.2,115)	36	$-x$
7	(-10,-50,120)	10.6	$+x$
8	(-20-,-25,112)	20.5	$+x$
9	(-50,10,107)	50.9	$+x$
10	(-60,40,123)	60.4	$+x$
11	(0,114,117)	20.5	$-y$
12	(0,-104,119)	13.7	$+y$
13	(36,27.8,116.5)	113	$+y$
14	(36, 79.2,116.5)	62	$+y$
15	(22.5,141,83.3)	24	$+x$
16	(30.5,141,123.5)	47.8	$+x$
17	(116.8,184.1,84.4)	35.9	$-y$
18	(108,230,92.4)	82.6	$-y$
19	(122.8,97.9,90.4)	38.8	$+y$
20	(135.8,32,80.4)	102.7	$+y$
21	(78.3,180,123.5)	39	$-y$
22	(126,210,86.4)	61.7	$-y$
23	(62.3,62,83)	80.6	$+y$
24	(80,22,94.9)	122.4	$+y$
25	(215.5,141,86.4)	94.8	$-x$

4.5 Simulation Experimental Geometry

The base simulation geometry for all experiments includes a main void cell on top of a floor cell composed of a standard tile and concrete mixture across a 5m x 5m square area. The cells are contained between −2.5 m on the west boundary to +2.5 m on the east boundary. The same is true for −2.5 m from the south boundary and ending at +2.5m at the north boundary. The origin is in the center, just above the upper floor surface boundary. The z axis is defined from −10 cm (the underside of the floor) to 3 m above the floor. For DENOVO, each cell (e.g. floor, steel fixtures, ring stand, etc.) is simulated with parallelepipeds to approximate all of the necessary surfaces in Cartesian geometry since DENOVO does not permit curved surfaces. However, curved surfaces were employed in the synthetic response simulations to model the detector and the geometric arrangement executed by MCNP.

Though the physical geometry of the detector is simulated in MCNP, it is not simulated in DENOVO. Instead, the response values are taken at the center face of the detector after multiplying the adjoint source by a point DRF factor to approximate the effects of the shielding and collimator. The current point DRF formulation used by DIMP is described in Ref. [9]. Further details of the DRF and material geometry will be formalized in the dissertation (the full laboratory room specs. are being obtained from ORNL and the DRF is being updated for the new detector).

4.6 Experimental Measurement Equipment

The field equipment used to take measurements for all experimental campaigns included a detector with a preamplifier and a multichannel analyzer with full pulse processing integration. Both pieces of equipment were essential for HMS-4 and DIMP holdup measurements.

The detector was a 1 inch diameter by 2 inches height right cylinder EFC Model 1X2P collimated NaI scintillation detector. This is a standard field detector for HMS-4 measurements. [3] The detector is well shielded with lead except on the front face where the collimator aperture allows radiation into the detector from a limited extent of directions, i.e. fixed solid angle. Hence, the detector has approximately a 23 degree in-axial-plane angle of vision from the axis normal to its circular front face.

The MCA is a GBS Elektronik GmbH MCA-166 Rossendorf model [15] that has a self-contained set of pulse processing equipment. The MCA receives a preamplified signal directly from the detector through a coaxial cable, which it amplifies and counts across a spectrum of energies. The number

of counts is divided into channels (proportional to energy) and sent directly to the computer for recording and post-processing.

*Note: Detector fell once. No significant changes in the spectra were seen. Channel (energy) calibration drift was observed before and after the event (no apparent correlation).

CHAPTER

5

PRELIMINARY EXPERIMENTAL VALIDATION RESULTS

DIMP performed fairly well for the first ORNL experiment involving the Cs-137 point source after some adjustments. Under the standard initial guess ($\alpha = 10^{-4}$, the baseline static low source cell probability), DIMP failed to predict any source cells with magnitude larger than 1% of the true source strength, however using the true source configuration as the initial guess yielded a very good result alluding to DIMP becoming trapped in a local minimum during the first source search. The usual initial guess is chosen with a flat low source probability in every mesh cell allowing feedback with the measured responses to increase the source probability in the appropriate cells. Also, a correction factor had to be applied to the measured responses to account for the effects observed as a result of the special collimator geometry for ORNL's 1" x 2" NaI field holdup detector that were not featured in the previous detector design used in Ref [2] and utilized in the synthetic data presented in previous chapters of this work. Furthermore, two measurement points had higher than expected flux values, so further investigation will be made to determine if they are statistical outliers or further adjustments to the detector model should be made.

5.1 Development of the Collimation Correction Factor

The detector used in [2] was a 2" x 2" NaI detector, collimated by the placement of lead bricks (as in Fig. 3.2) above and to the sides of the detector to produce a forward facing hemisphere FOV. The 1" x 2" NaI field holdup detector provided by ORNL to conduct the measurement campaigns has a much more sophisticated collimator that narrows the FOV to roughly 23 degrees and partially obscures the crystal face as shown in Fig. 5.1 below.

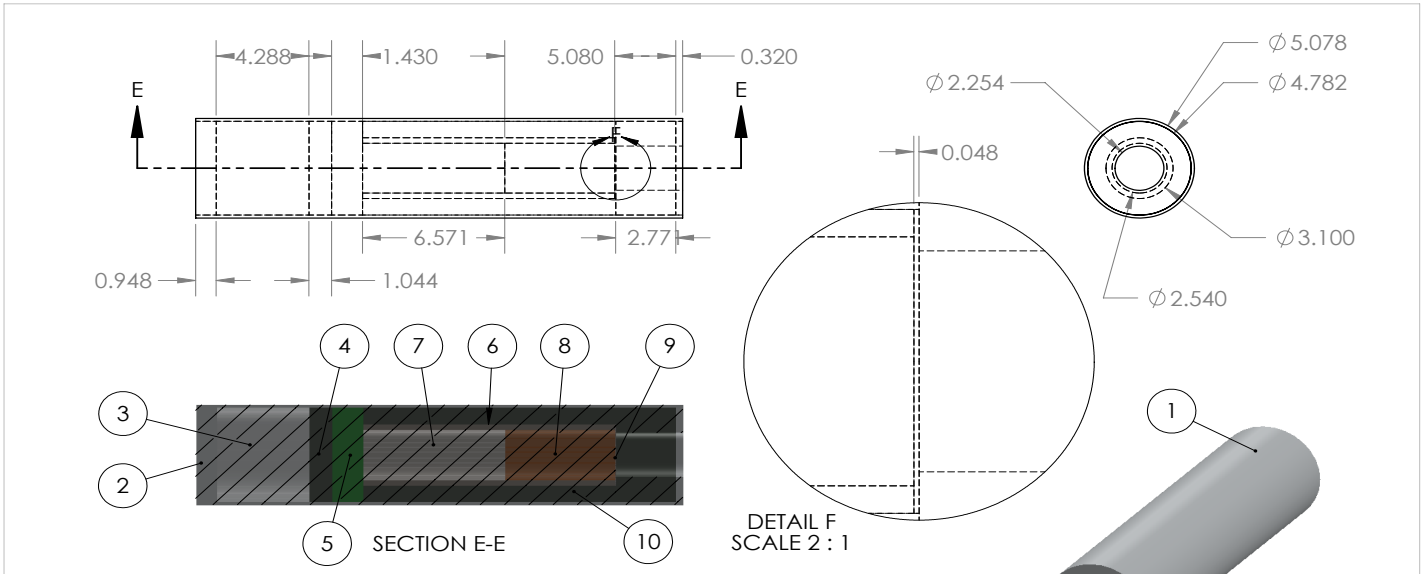

ITEM NO.	PART	Material
1	Case	Aluminum
2	Plug	Aluminum
3	Electronic Housing	Void
4	Rear Shield	Lead
5	Polymer plate	Plastic
6	Steel Enclosure	Stainless Steel
7	PMT	Void
8	Crystal	NaI
9	Tin Shield	Tin
10	Collimator	Lead
11	Collimator Front	Lead
12	Front Cap	Aluminum

UNLESS OTHERWISE SPECIFIED:
DIMENSIONS ARE IN CENTIMETERS
TOLERANCES: 0.001
FRACTIONAL ±
ANGULAR: MACH ± BEND ±
TWO PLACE DECIMAL ±
THREE PLACE DECIMAL ±
INTERPRET GEOMETRIC TOLERANCING PER:
MATERIAL
FINISH
DO NOT SCALE DRAWING

	NAME	DATE
DRAWN	NBN	8/22/14
CHECKED		
ENG APPR.		
MFG APPR.		
Q.A.		
COMMENTS:		

TITLE: ORNL 1x2" NaI Detector

SIZE A | DWG. NO. NAIDET | REV

SCALE: 1:2.5 | WEIGHT: | SHEET 1 OF 1

Figure 5.1 Schematic of the 1" x 2" NaI field holdup detector.

The front of the lead collimator touches the crystal face and covers about 12% the face reducing the detector's solid angle FOV. Since the previous configuration [2] did not suffer such a reduction in solid angle, DIMP requires a collimation correction factor to adjust the detector efficiency for the effect of this collimation on the directional responses. The reduction in solid angle is illustrated by Fig. 5.2

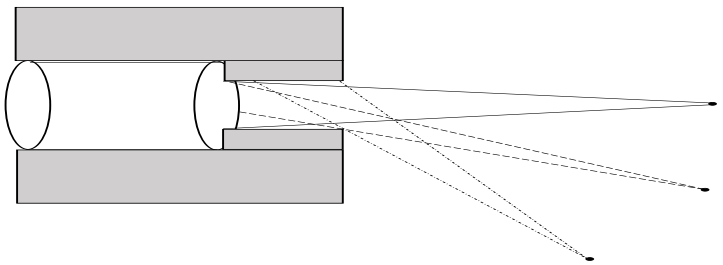

Figure 5.2 Sketch of the detector collimator shadowing effect on the detector crystal (reducing the effective solid angle).

A fairly simple way to compute such a factor, is to simulate the detector with and without the collimator geometry (just the detector crystal) in MCNP and compare the results to the analytical solid angle calculations. Using the ratio of the two fluxes (with and without the collimator) as the collimation correction factor, the measured responses can be corrected by this factor to better match the responses predicted by the true source distribution folded with DENOVO adjoint fluxes. Thus, the collimation correction factor ($S_{col}(\vec{r},E)$) can be calculated as follows

$$S_{col}(\vec{r},E)=\frac{\phi^{syn}_{col}(\vec{r},E)}{\phi^{syn}_{unc}(\vec{r},E)} \tag{5.1}$$

where $\phi^{syn}_{col}(\vec{r},E)$ and $\phi^{syn}_{unc}(\vec{r},E)$ are the collimated and uncollimated synthetic responses calculated

from the true source configuration in MCNP. Dividing the measured responses by $S_{col}(\vec{r}, E)$ will produce an approximate value of the response that would have been measured with a 2 pi FOV detector that is assumed in the current version of DIMP. A more appropriate way to account for the collimator's effect is to determine a directionally dependent DRF.
The correction factor was used to adjust each of the measured responses from the Cs-137 point source campagin before initializing DIMP's source search algorithm. The experiment involved ten detection points measured within the experimental area in a spiral pattern around the 4 μ Ci point source held by a clamp on the ring stand (similar to the HEU setup in Fig. 4.1). The distance between the source and detection points ranged from 0.02-1.25 m as discussed in the previous chapter, and the coordinates of the true Cs-137 point source are (0,0,87) cm.

Consider the DIMP predicted source map shown in Figure 5.3.

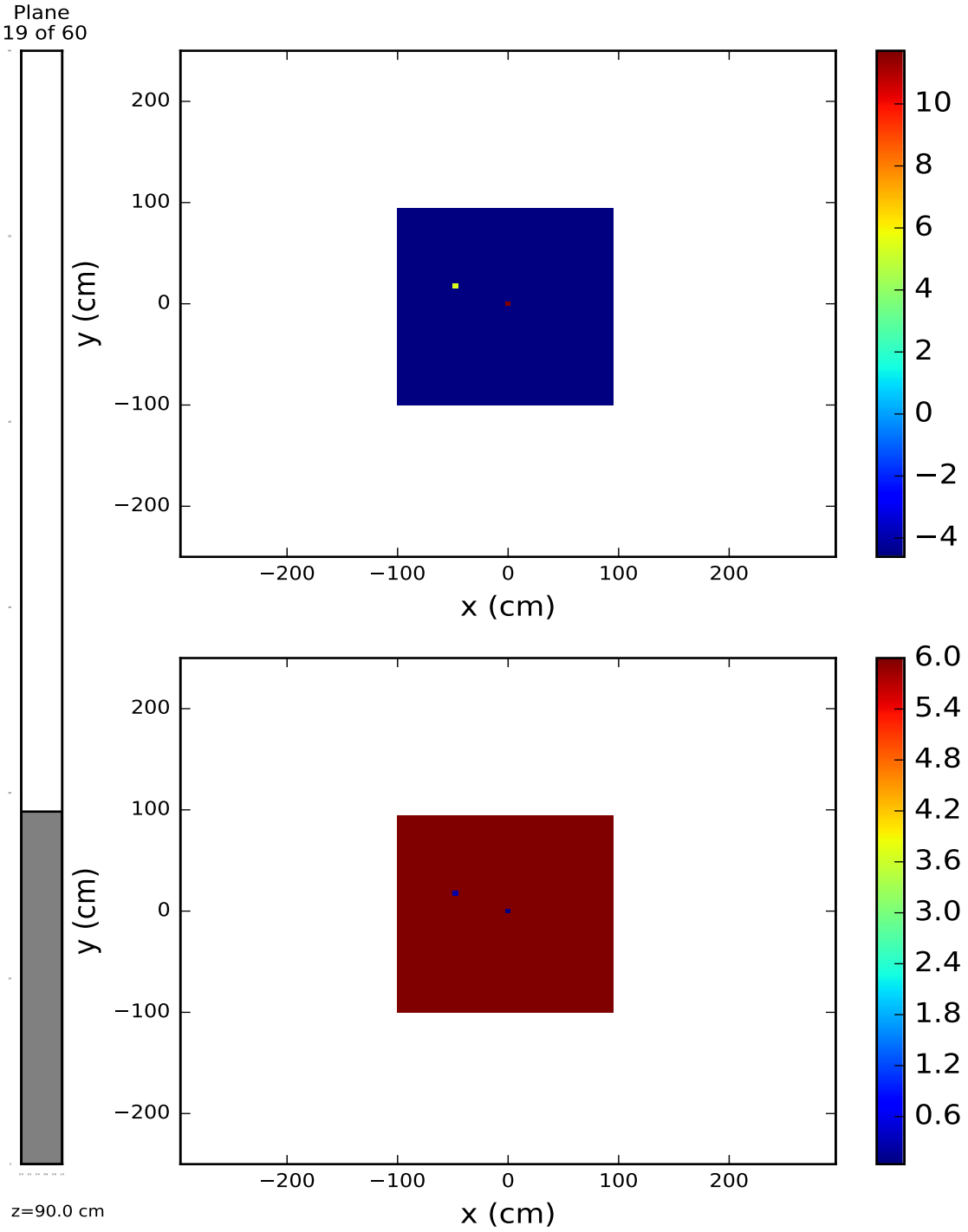

Figure 5.3 DIMP predicted source map (above) for a 5m x 5m square space (reduced to a 2m x 2m search area) with a Cs-137 point source suspended by clamps on a ring stand, and the corresponding uncertainty (below).

As seen above, DIMP performed well predicting the source in the correct cell (0,0,90) with 80% of the true source activity with fairly low uncertainty. Only 80% of the true source strength was obtained because the corrected measured responses still had a margin of error when compared with those calculated by DENOVO. This is a promising result for the first of four experimental measurements, but there are two issues with this result. The first, is that as in [2] the source search had to be narrowed to a lower number of mesh cells in order to find a good source configuration. Otherwise, the gradient source search algorithm often becomes stuck in local minima and predicts weak distributed sources. The second is that two detection point fluxes did not match up with MCNP synthetic fluxes, so for the time being they were adjusted to the synthetic values artificially. Further investigation will determine a physical justification for those values if possible. They may be removed as outliers, since both points were measured fairly close to the source.

CHAPTER

6

PLAN OF WORK

The full extent of the work intended for the PhD dissertation includes validation of the data from the 3 other experimental campaigns, developing a DRF factor to account for the collimation geometry of the detector, and exploring the use of peak detector response functions from the original Master's work to improve response accuracy. Each area of work is valuable to the development of the DIMP methodology and its application to the holdup problem and more generally future inverse radiation transport research.

Each experimental campaign provides more information about the capabilities and limitations of DIMP. The first campaign (the Cs-137 point source) provided a working base data set similar to previous results. Only the geometry was significantly changed to allow for easy calibration of the model. The second campaign (the HEU disk source) maintained the same geometry as the first, but used a source that was more typical for holdup to finalize the calibration of DIMP for SNM. The third campaign (HEU in the large round duct) provides the first realistic simulation of a field holdup deposit in steel piece of equipment, by placing a set of line sources across the bottom of a pipe. The final campaign tests the most difficult situation by providing a case with multiple sources with difficult geometry in two pieces of equipment. The final test was designed to challenge both the HMS-4 and DIMP systems and reveal their capabilities and relative strengths and weaknesses.

After considering the DIMP system without directional detectors, there appears to be some promise for using detection without collimation. DIMP performed well for the Cs-137 point source from the Burlington simulation case under an ideal initial guess and a sufficient number of detectors to narrow the solution set. However, this work was only carried out for the simplest case. DIMP's uncollimated responses only configuration will have to be verified for a more complex source distribution to be certain of its potential for future application. This requires the development of better guesses for the initial source distribution or more robust search procedures that improve the probability of DIMP's optimizer locating the global minimum rather than getting stuck in local minima, such as an adaptive program that identifies equipment structures and limits the source search to mesh cells contained within those structures. Another alternative is to replace the gradient based optimization subroutine with one that is less prone to becoming stuck in local minima.

While conducting the work that yielded the preliminary results, it quickly became clear that a new DRF would have to be developed for the 1"x2" NaI field holdup detector. Overestimation of the measured responses by the responses predicted with the true source configuration lead to the conjecture that the former detector DRF based on a full hemisphere field of view was no longer sufficient to account for the new detector collimator geometry. The previously used detector experimental setup consisted of an unshielded 2"x2" detector that was covered with improvised lead shielding (a set of lead bricks) [2]. The setup restricted the detectors FOV to the forward 2π hemisphere. The former detector had only a hemispherical collimator, whereas the field holdup detector has a more complex and restrictive collimator. The field detector has a collimator which restricts the FOV to a narrower cone (23 degrees from center of face to the normal axis) of the forward unit sphere. This not only restricts the solid angle of the detector, but reduces the area of the front surface of the detector crystal which can be intersected by uncollided rays of radiation. A preliminary collimation factor has been calculated with MCNP to verify the extent of this effect on the uncollided photon flux, but further refinement may be necessary. Again, the new detector configuration will also require a suitable initial source guess range in DIMP that can function for all of the experimental campaign measurements.

Furthermore, DRF improvement is also being sought by using Gardner's model [10] to improve the calculation of peak responses. Our previous investigation [11] sought to modify the DRF model in order to improve DIMP's collided flux algorithms for full response simulation. Utilizing the full response in DIMP would have improved the counting efficiency thereby reducing counting times to achieve the same statistical confidence level in the measured responses. Unfortunately, there were too many limitations in the Compton continuum responses predicted by the DRF for shielded

and collimated detectors to warrant implementation of the full DRF in the DIMP formalism. The peak responses predicted by Gardner's DRF model still compared well with those measured with the field detector, so a filtered peak DRF could be implemented in the uncollided flux algorithms of DIMP. Further investigation will be conducted to determine if the peak DRF from Gardner's model significantly improves the performance of DIMP.

REFERENCES

[1] T. D. Reilly, "Nondestructive Assay of Holdup," *Passive Nondestructive Assay of Nuclear Materials 2007 Addendum*, Washington D.C.: Los Alamos National Laboratory, 2007.

[2] J. M. Hykes and Y. Azmy, "Radiation Source Mapping with Bayesian Inverse Methods," *Nuclear Science and Engineering*, vol. 179, pp 1-17, 2015.

[3] S. E. Smith, et al., "Holdup Measurement System 4 (HMS4)-Automation & Improved Accuracy," BWXT Y-12 report Y/DK-2190, ORTEC, 2004. [Online]. Available: `http://www.ortec-online.com`. [Accessed 16 August 2016].

[4] A. Tarantola, *Inverse Problem Theory and Methods for Model Parameter estimation*, Philadelphia: Society for Industrial and Applied Mathematics, 2005.

[5] F. Li, et al., "Implementation of the Monte Carlo-Library Least-Squares Approach to Energy Dispersive X-Ray Fluorescence Analysis," *International Centre for Diffraction Data*, vol. 1097, issue 2, pp 227-235, 2008.

[6] J. Mattingly and D. Mitchell, "A Framework for the Solution of Inverse Radiation Transport Problems," *IEEE Transactions on Nuclear Science*, vol. 57, issue 6, pp 3734-3743, 2010.

[7] D. G. Cacuci and M. Jonescu-Bujor, "Sensitivity and Uncertainty Analysis, Data Assimilation, and Predictive Best-Estimate Model Calibration," *Handbook of Nuclear Engineering*, New York: Springer, 2010.

[8] E. E. Lewis and W. F. Miller Jr., *Computational methods of neutron transport*, La Grange Park, IL: American Nuclear Society, 1993.

[9] J. Hykes, "Radiation Source Mapping with Bayesian Inverse Methods," PhD Thesis, North Carolina State University, 2012.

[10] R. P. Gardner and A. Sood, "A Monte Carlo simulation approach for generating NaI detector response functions (DRFs) that accounts for non-linearity and variable flat continua," *Nuclear Instruments and Methods in Physics Research B*, vol. 213, pp. 87-99, 2004.

[11] N. Nelson, "Validation and Uncertainty Quantification of a 1x2" NaI Collimated Detector Using Detector Response Functions Created by g03," MS Thesis, North Carolina State University, 2014.

[12] *Scale: A Comprehensive Modeling and Simulation Suite for Nuclear Safety Analysis and Design*, ORNL/TM-2005/39, Version 6.1, June 2011. Available from Radiation Safety Information Computational Center at Oak Ridge National Laboratory as CCC-785.

[13] Eckert & Ziegler Isotope Products, "Eckert & Ziegler Reference & Calibration Sources: Product Information," Valencia, CA, 2007.

[14] National Nuclear Data Center, ”Nudat2.6: Decay Radiation Search,” Brookhaven National Laboratory, 2013. [Online]. Available: `http://www.nndc.bnl.gov/nudat2/indx_dec.jsp`. [Accessed 14 June 2015].

[15] GBS Elektronik GmbH, "MCA 166-USB: Multi channel analyzer with USB interface," GroBerkmannsdorf, Germany, 2008.

4.7. Task G: Validate DIMP method against measured and manufactured data

This project was designed to culminate in a test of the DIMP methodology on holdup problems. A few representative configurations were to be tested, e.g. pipe, duct, and box sources. To demonstrate the viability of the DIMP method, the mass of the nuclides of interest and its uncertainty were to be estimated for the selected configurations, using gamma responses. In early stages of this task, the problems were solved using manufactured responses (i.e. computed by a tool such as MCNP). In the latter stages of the project, the data driving DIMP were to come from actual measurements at the holdup laboratory cited in Task F. While we started on this task, progress has been limited so far, but work on it will continue even after this project concluded. NC State University was responsible for completing this task, in consultation and with support from ORNL.

The accomplishment of this task was reported in: Noel Nelson, Yousry Azmy, "Numerical Convergence and Validation of the DIMP Inverse Particle Transport Model," accepted for publication in the proceedings of *M&C 2017 - International Conference on Mathematics & Computational Methods Applied to Nuclear Science & Engineering*, Jeju, Korea, April 16-20, 2017, on USB (2017). This document is replicated on the following pages.

Numerical Convergence and Validation of the DIMP Inverse Particle Transport Model

Noel Nelson,* Yousry Azmy,*

* *North Carolina State University, Box 7909, Raleigh, NC 27695*
nnelson@ncsu.edu, yyazmy@ncsu.edu

INTRODUCTION

The goal of this work is to validate the Data Integration with Modeled Predictions (DIMP) inverse particle transport method for solving the special nuclear material (SNM) holdup problem. Holdup problems arise when radioactive material (with a known emission spectrum) becomes trapped in processing equipment at nuclear fuel processing facilities. Examples of processing equipment can include but are not limited to pipes, ducts and filters, glove boxes, and valves. [1] SNM holdup is of interest to the nuclear fuel industry for many reasons. These reasons include: criticality safety, maintaining accurate SNM inventory and nuclear safeguards regime, and radiation worker safety.

Therefore, holdup sources are important to quantify in total material mass as well as distribution and location. The DIMP method offers a well automated system that poses the holdup configuration as an inverse problem. Initial survey crews would not be required, and few assumptions are necessary to predict source distribution, strength, and location within equipment. DIMP uses an adjoint particle transport model to calculate an importance map for a grid of detectors in the target geometric configuration utilizing as-built information of dimensions and material composition of the facility's structure. Deterministic transport codes are capable of modeling such configurations with a varying degree of fidelity of the models to achieve the desired computational accuracy. Together, the computed flux and detector response functions can be used to predict detector responses from a given source distribution. Alternatively, and more efficiently in the present case, folding the importance function with a given source distribution yields an estimate of the detector response where the importance function is the adjoint flux computed with an adjoint source set to that detector's response function. DIMP calculates the optimal source distribution(s), location(s), and strength(s) that best matches calculated responses to experimental responses with no presumptions of the source shape and minimal obvious restrictions on its physical location, e.g. a source cannot be hanging in the air in the middle of a room.

Currently, the DIMP model has been validated for a Cs-137 point source and a Co-60 line source. It performed well with low error that was mostly attributed to the weakness of the available sources (older button sources). [2] This work intends to expand upon the model and previous research with realistic holdup experiments using strong Uranium sources measured with a field holdup NaI detector, and compare the results to the Holdup Measurement System (HMS-4), a Generalized Geometry Holdup (GGH) model. Four experimental holdup measurement campaigns were performed in this work including a Cs-137 point source, a highly enriched Uranium (HEU) disk source, an HEU line source in a pipe, and a set of HEU area sources in a duct.

THEORY: DIMP FORMALISM

Inverse problems are often very complex and ill-conditioned. For such problems, information at various points in space and time denoted "measurements" are considered known, but the source state or its spatial configuration is treated as unknown. An inverse model is used to calculate a possible solution state of the system from the measurements. This is where the difficulty of inverse problems arises. The existence and uniqueness of an inverse solution is typically not certain, and solutions can be very unstable depending on the quality of the measurements.

One way to address the difficulty of inverse problems is to find solutions with probabilistic methods. While the solution that best fits the measurement data is not always the true solution, the chance that it is the true solution should increase with increasing amount of measured data. This idea is formalized via Bayes' theorem [3]:

$$p(hypothesis|data, I) \propto p(data|hypothesis, I)p(hypothesis|I), \tag{1}$$

where *data* is the experimentally measured data (e.g. detector responses), the *hypothesis* is the unknowns of the system (source parameters in this work), and I is all the additional knowledge of the system (system geometry, detector efficiency, detector response functions, etc.). The three probability density functions (PDFs) above $p(hypothesis|data, I)$, $p(data|hypothesis, I)$, and $p(hypothesis|I)$ are the posterior, likelihood, and prior respectively. The prior is the conditional probability that the hypothesis occurs based only on information I. The likelihood represents the probability of measurement data occurring based on a given configuration of the unknown data (hypothesis) and the information in I. This is proportional to the posterior, or the probability of the given *hypothesis* (source configuration) being true based on the information I and the measurement *data*.

In order to solve an inverse problem, the likelihood function is maximized thereby minimizing the error between the experimentally measured data and the synthetic responses (results predicted by the model from an input configuration of the source parameters). DIMP maximizes agreement between the measurement vector $\boldsymbol{r}_m$ (responses) and the modeled responses, $\boldsymbol{r}_p$, predicted by a configuration of the model parameters, $\boldsymbol{\alpha}$

$$\boldsymbol{r}_m = R\boldsymbol{\alpha} \tag{2}$$

where R is the mapping operator from the model parameter input space to the response space. The solution of this problem is linear for radiation transport and has a closed form solution for the posterior means and covariances. Cacuci's Best Estimate method based on Bayesian inference is used to find the posterior solution mean and uncertainty. [4]

Radiation Transport

First, the model used in the inverse framework will be described in detail followed by specification of the source parameters contained in $\boldsymbol{\alpha}$, and a few notes on the measurements $\boldsymbol{r}_m$. The model for the radiation transport problem is based on the time independent linear Boltzmann Transport equation for neutral particles in non-multiplying media. [5]

$$\hat{\Omega} \cdot \boldsymbol{\nabla}\psi(\boldsymbol{x}, E, \hat{\Omega}) + \sigma(\boldsymbol{x}, E)\psi(\boldsymbol{x}, E, \hat{\Omega}) = \int dE' \int d\hat{\Omega}'\sigma_s(\boldsymbol{x}; E', \hat{\Omega}' \rightarrow E, \hat{\Omega})\psi(\boldsymbol{x}, E', \hat{\Omega}') + q(\boldsymbol{x}, E, \hat{\Omega}) \,, \tag{3}$$

where $\psi(\boldsymbol{x}, E, \hat{\Omega})$ is the angular flux of particles $[particles/cm^2\text{-}s]$ defined over the spatial domain

$$x \in V \,, \quad \hat{\Omega} \in 4\pi \,, \quad E \in (0, \infty) \,,$$

and with explicit boundary conditions

$$\psi(\boldsymbol{x}, E, \hat{\Omega}) = \psi_0(\boldsymbol{x}, E, \hat{\Omega}) \quad \text{for } \boldsymbol{x} \in \partial V \text{ and } \hat{\Omega} \cdot \hat{n} < 0 \,.$$

$\hat{\Omega}$ is the unit directional vector along which particles are traveling, $\hat{n}$ is the unit vector normal to the boundary surface ∂V at the point $\boldsymbol{x}$, and $\sigma(\boldsymbol{x}, E)$ the total particle interaction macroscopic cross-section $[cm^{-1}]$. Also, $\sigma_s(\boldsymbol{x}; E', \hat{\Omega}' \rightarrow E, \hat{\Omega})$ is the macroscopic scattering cross-section of particles from one direction ($\hat{\Omega}'$) and energy (E') in the direction and energy range of $d\hat{\Omega}'$, dE' about the direction and energy of interest ($\hat{\Omega}, E$), and $q(\boldsymbol{x}, E, \hat{\Omega})$ is the external source of radiation particles in the configuration of interest [in $particles/cm^3\text{-}s$]. In DIMP the geometric configuration and material composition of all objects in the problem domain are considered known, hence the cross sections are retrieved and calculated for nuclide mixtures by MAVRIC [6]. Next, it is useful to define the scalar flux $\phi(\boldsymbol{x}, E)$ as

$$\phi(\boldsymbol{x}, E) = \int_{4\pi} d\hat{\Omega}\psi(\boldsymbol{x}, E, \hat{\Omega}) \,. \tag{4}$$

Reaction rates are key components to many radiation problems, such as dose and fission rates. In this case, the reaction rate definition can be used to define a detector response, r, as

$$r(E') = \int_0^\infty dE \int_V d\boldsymbol{x}\sigma_d(\boldsymbol{x}, E', E)\phi(\boldsymbol{x}, E) \,, \tag{5}$$

where $\sigma_d(\boldsymbol{x}, E', E)$ is the detector response function (DRF). There are several ways to model and define DRFs, and this is currently under active consideration. In Eq. 5, $\sigma_d(\boldsymbol{x}, E', E)$ is the probability per unit path length that a particle at $\boldsymbol{x}$ incident with energy E registers a response in the detector's channel dedicated to energy E'. With this definition in mind, one could use the inverse of the forward transport equation, Eq. 3 as the mapping function for the inverse problem. However, direct inverses are often numerically unstable and computationally expensive. Equation 5 requires a solution of the transport equation for every potential source distribution in order to determine the corresponding $\phi(\boldsymbol{x}, E)$ then compute r and compare it to the measured values. Alternatively, the problem can be reformulated using the adjoint of the transport equation [2]. The adjoint identity can be stated as

$$\langle Ap, h\rangle = \langle p, A^\dagger h\rangle, \tag{6}$$

where $\langle , \rangle$ denotes an inner product, A is an operator, p and h are any pair of functions in the domain of A, and $A^\dagger$ is the adjoint operator. Furthermore, in this application we define the inner product as follows

$$\langle p, h\rangle = \int_{4\pi} d\hat{\Omega} \int_0^\infty dE \int_V dV p(\boldsymbol{x}, E, \hat{\Omega})h(\boldsymbol{x}, E, \hat{\Omega}) \,. \tag{7}$$

Now, consider the fixed source linear transport equation in operator form

$$L\psi = q, \tag{8}$$

where L is the transport operator (for all angular fluxes, ψ), and q is the external source. Next, take the inner product of Eq. 8 with the adjoint angular flux $\psi^\dagger$

$$\langle L\psi, \psi^\dagger\rangle = \langle q, \psi^\dagger\rangle \,. \tag{9}$$

Applying the adjoint identity (Eq. 6) to the above equation yields [7]

$$\langle L\psi, \zeta\rangle = \langle \psi, L^\dagger\zeta\rangle + P[\psi, \zeta] \,, \tag{10}$$

where ζ is an arbitrary function ($\zeta = \psi^\dagger$ in our case) and $P[\psi, \zeta]$ is the bilinear concomitant, evaluated on the external surface of volume V,

$$P[\psi, \zeta] = \int_{4\pi} d\hat{\Omega} \int_0^\infty dE \int_{\partial V} dS\, \hat{\Omega} \cdot \hat{n}\psi(\boldsymbol{x}, E, \hat{\Omega})\zeta(\boldsymbol{x}, E, \hat{\Omega}) \,. \tag{11}$$

Substituting Eq. 10 into Eq. 9 yields

$$\langle \psi, L^\dagger\psi^\dagger\rangle = \langle q, \psi^\dagger\rangle - P[\psi, \psi^\dagger] \,. \tag{12}$$

Next we set the adjoint source to the detector response function, DRF, namely $q^\dagger = \sigma_d$, implying

$$L^\dagger\psi^\dagger = \sigma_d \,. \tag{13}$$

Substituting this relationship into Eq. 12 yields

$$\langle \psi, \sigma_d\rangle = \langle q, \psi^\dagger\rangle - P[\psi, \psi^\dagger]. \tag{14}$$

Now, applying the following vacuum boundary conditions

$$\psi(\boldsymbol{x}, E, \hat{\Omega}) = 0 \,; \; for \;\; \boldsymbol{x} \in \partial V \;\; and \;\; \hat{\Omega} \cdot \hat{n} < 0, \tag{15}$$

$$\psi^\dagger(\boldsymbol{x}, E, \hat{\Omega}) = 0 \;\; for \;\; \boldsymbol{x} \in \partial V \;\; and \;\; \hat{\Omega} \cdot \hat{n} > 0, \tag{16}$$

will cause the bilinear concomitant term to vanish thus producing

$$\langle \psi, \sigma_d\rangle = \langle q, \psi^\dagger\rangle. \tag{17}$$

Finally, recalling the reaction rate Eq. 5 and substituting it in Eq. 17 leads to

$$\boldsymbol{r}_p(E) = \int_0^\infty dE \int_V dV\phi^\dagger(\boldsymbol{x}, E)q(\boldsymbol{x}, E) \tag{18}$$

where $\phi^{\dagger}(\boldsymbol{x}, E)$ is the adjoint scalar flux, or importance, and $\boldsymbol{r}_p(E)$ is the predicted response. The advantage of the formulation in Eq. 18 over the one in Eq. 5 is the computationally inexpensive evaluation of the former once $\phi^{\dagger}$ is known for a set of detectors. During the search for optimal source distribution Eq. 18 comprises an inner product of the precomputed adjoint fluxes and a guess of the source distribution. In contrast, Eq. 5 requires a full forward transport solution for every attempted source distribution. The set of discretized importance values are calculated by the discrete ordinates package DENOVO [6] using S_n=8 and 23 groups, and they are folded with the predicted source distribution ($q(\boldsymbol{x}, E)$) during the search for the best match between the resulting responses and the measurement responses $\boldsymbol{r}_m$. The cross-sections for DENOVO are generated by MAVRIC (part of ORNL's SCALE package) from the Evaluated Nuclear Data Files (200n-47g ENDF/B-VII.0) libraries. The optimal source distribution is found through an optimization process that if successfully converged, yields $\boldsymbol{r}_p(E) \cong \boldsymbol{r}_m(E)$, and in this case we call the corresponding $q(\boldsymbol{x}, E)$ a solution to the inverse problem.

Currently, only the peak responses are compared for both predicted and measured responses. A full response comparison was attempted in previous work [2] including the continuum and peak responses, but the continuum response was very difficult to calculate. Accurate representation of the continuum response requires a fairly sophisticated DRF. Some research has been invested in the area of DRFs for unshielded detectors [8], but more development of the DRF is required to apply it to collimated detector responses as shown in Ref. [9].

Nonlinear Optimization

In order to optimize the predicted source distribution, the posterior probability is maximized by minimizing the residual ($Q(z)$) of the difference vector (z) which contains the absolute differences in the model parameters from the initial guess and those between the measured and predicted responses. The optimization method implemented in this work is the gradient based Quasi-Newton method with the best estimate covariance as described in Ref. [4]. The method works by minimizing $Q(z)$ according to nonlinear least squares using the following Newton update step for the k^{th} iteration

$$\boldsymbol{\alpha}_{k+1} = \boldsymbol{\alpha}_k - \lambda_k \left(\nabla^2_{\alpha} Q(z_k) \right)^{-1} \nabla_{\alpha} Q(z_k). \tag{19}$$

where $\lambda_k \in [0, 1]$ is the line search parameter which controls the search step size. α_k is the source spatial distribution written in vector form (model parameters) for all peak energies at iteration k, and α_0 is the priori or initial guess. The gradient of Q is

$$\nabla_{\alpha} Q(z) = C_{\alpha}^{-1} z_{\alpha} + S^T C_m^{-1} z_r \tag{20}$$

where C_{α}, C_m, and S are the source distribution and measurement covariance matrices, and the collective matrix of adjoint sensitivities ($\phi^{\dagger}(E)$), respectively as defined in Ref. [7]. Under the Gauss-Newton approximation, the Hessian is defined as

$$\nabla^2_{\alpha} Q(z) \approx C_{\alpha}^{-1} + S^T C_m^{-1} S \tag{21}$$

where the inverses of the covariance matrices are replaced by the appropriate linear systems of equations (consult Ref. [7]) and solved for efficiently using standard linear methods (e.g. Gaussian Partial Pivoting). Finally, the functional of the difference vector, $Q(z)$ is then defined as

$$Q(z) = z^T C^{-1} z, \tag{22}$$

and the inverse of the covariance, C^{-1}, is

$$C^{-1} = \begin{bmatrix} C_{\alpha}^{-1} & 0 \\ 0 & C_m^{-1} \end{bmatrix}. \tag{23}$$

The difference vector, z is

$$z \equiv \begin{bmatrix} \boldsymbol{\alpha} - \boldsymbol{\alpha}^0 \\ \boldsymbol{r}_p - \boldsymbol{r}_m \end{bmatrix} = \begin{bmatrix} z_{\alpha} \\ z_r \end{bmatrix} \tag{24}$$

where $\boldsymbol{r}_p$ is the response calculated with the attempted source distribution and $\boldsymbol{r}_m$ is the measured response.

RESULTS AND ANALYSIS

Several simulations of radiation sources in various geometries have been performed with DIMP. To confirm the stability of the DIMP method, several simulations of a source configuration was performed using synthetic responses while increasing the number of detection points per simulation to verify if DIMP converges to the true solution.

Preliminary Convergence Studies

A preliminary convergence study was performed involving only the Cs-137 point source using 3 to 9 detection points. DIMP converged and performed well for that case resolving the source to the cell with the true coordinate location and a neighboring cell and determining the source strength within 0.7% of its true value. These small errors in the DIMP solution are to be expected due to the different computational models applied to the computation of detector responses (Monte Carlo) and the adjoint responses (Discrete Ordinates) but are representative of measurement errors. Another numerical study was performed with synthetic responses for the Cs-137 and Co-60 sources using only unshielded detector responses and another using only directional responses. DIMP performed adequately with directional responses, but failed to resolve the unknown source using only unshielded responses due to the optimizer becoming trapped in local minima. If an initial guess close to the true source configuration was supplied, the global minimum was found by DIMP producing the correct answer with a greatly reduced chi-squared value. This suggests that the DIMP gradient based optimizer only supplied a local minima under the original initial guess supplied. Adaptive meshing and alternative optimization methods are being explored for DIMP to avoid this issue.

DIMP Convergence with Multiple Sources

The convergence test involves the original source setup used in Ref. [2] depicting a Cs-137 point source and five Co-60 point sources located at two separate locations in a room at

NC State University. The basic source layout is shown in Fig. 1.

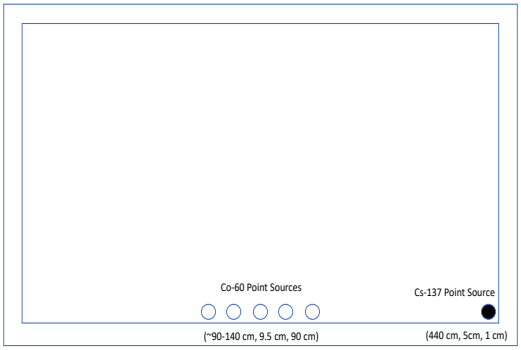

Fig. 1. Rough layout schematic of the simulation geometry of Burlington 2144 at NC State University.

Initial results indicated that DIMP seemed to diverge beyond 21 detection points for this case. This anomaly has been further investigated, and the reason for the divergence was poor detector response agreement between one of DENOVO's predicted responses and the MCNP synthetic response. This response was overlooked because it was a detection point, coplanar (in xy) with one of the Co-60 point sources originally chosen in the Hykes experiment Ref. [2]. The DIMP DRF produced a false positive and negative result in the z-directional predicted responses from DENOVO for that point. Upon replacement of the detection point with a low error detection point, DIMP converged with fairly stable results.

For the purposes of this convergence study only synthetic measurements generated with MCNP were used as detector responses where the number of detection points was increased from 3 to 24 points total. Each detection point consists of 7 measurements: an unshielded detector response and six collimated directional detector responses along the coordinate axes (e.g. +x, -x, etc.). [2] The results of the convergence study are shown in Figures 2-6. The true location and strength of the Cs-137 point source is (440, 5, 1) cm, and the corresponding strength is 107.685 kBq. The true location of the Co-60 line source is centered at approximately (120, 9.525, 90.17) cm. The individual x coordinates of the five point sources that compose the line source are x=96.52, 107.95, 119.38, 130.175, and 143.764 cm, and their strengths are 0.525, 2.218, 5.767, 31.793, and 3.845 kBq respectively. Note, DIMP treats the two coincident photons from Co-60 as independent sources with no correlation in space. Therefore, each Co source cell mapped by DIMP from one energy can be in the same cell or a different cell from the ones of the other energy.

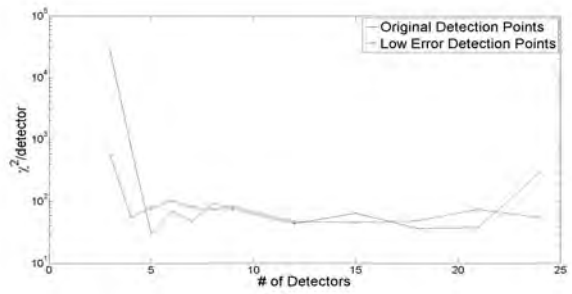

Fig. 2. Comparison of the reduced chi-squared per detector as a function of an increasing number of detection points for the original 24 detectors and a low-error detector responses set.

The reduced chi-squared is normalized per detector in order to screen out the expected modeling error between DENOVO adjoint based responses and MCNP responses that accumulate with the addition of each detector. As evidenced by the large error in the predicted source locations, weak strengths, and the resulting very large chi-squared-per-detector values, DIMP does not perform adequately with fewer than 5 detectors for this source configuration. With so few detectors, the code places the source near to one of the detectors. DIMP does not converge with fewer than 5 detectors for this source configuration comprising a six-point distribution with three distinct energies. Beyond seven detectors, the low-error detection points curve decreases gradually and flattens off suggesting convergence, instead of the unstable divergence of the old set. Each source configuration consisted of activities (in Bq) calculated across a 52x53x54 mesh employed in the DENOVO model of the room's configuration where the predicted source strength exceeded 1% of the source's known true strength along with its strength relative to that of the true strength used in generating the synthetic responses (Figs. 3 and 4) and the distance from its true location (Δd) to the mesh cell center (as shown in Figs 5 and 6). The x,y,z coordinates listed for each cell correspond to the coordinates of that cell's center point, and the Δx,Δy,Δz indicates the difference of the cell's x,y,z mesh index from the mesh index of the cell that contains the true point source.

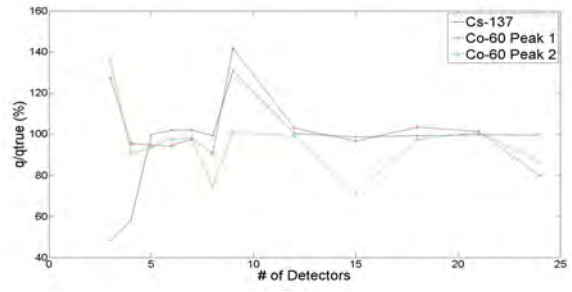

Fig. 3. Total predicted source strength across all cells above 1% relative to the total true source strength as a function of increasing detection points using the original 24 detection points.

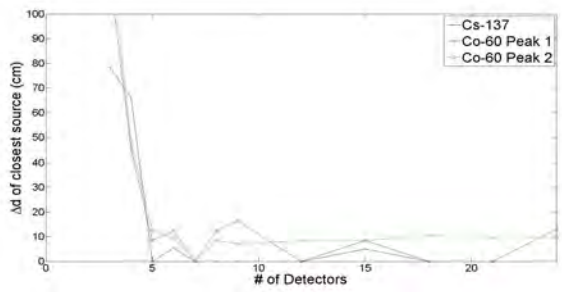

Fig. 4. Total predicted source strength across all cells above 1% relative to the total true source strength as a function of increasing detection points using the low-error detection points.

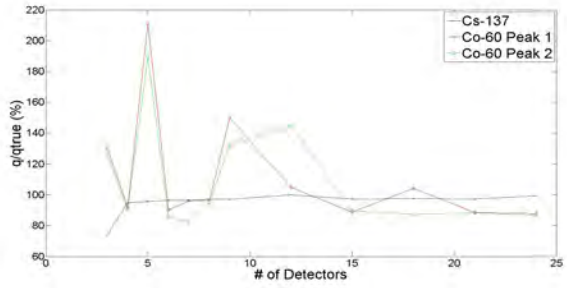

Fig. 5. Distance between the predicted source cell and the true source cell (Δd) as a function of increasing detection points using the original 24 detection points. Note: the location of the closest cell of the predicted set is compared to the strongest Co-60 point source location.

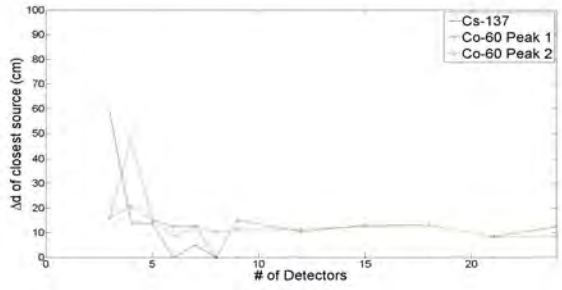

Fig. 6. Distance between the predicted source cell and the true source cell (Δd) as a function of increasing detection points using the low-error detection points. Note: the location of the closest cell of the predicted set is compared to the strongest Co-60 point source location.

Similar gradually decreasing and fairly flat curves can be observed for the low-error sets of the relative source strength and distance graphs. From 5-7 detectors the Cs-137 point source is well resolved, merely wavering between two configurations: a 50/50 split of the source with the correct cell and a neighboring cell and most of the source strength (>70%) concentrated in one of these two cells. The Co-60 line source however, is only resolved as one- or two-cell sources. The predicted Co-60 point sources match approximately in total strength and location with the stronger sources on the true line source. From 8-24 detectors, 2-3 of the point sources in the predicted Co-60 line source are resolved. However, DIMP never maps all five source points of the true Co-60 line source, and typically smears the locations of the stronger points on the line between the correct cell and a neighbor. This is reasonable because two of the sources are less than 10% of the strongest Co-60 point source. Overall, DIMP performed well once the discrepant detection point was removed from the synthetic-measurement set. Such model discrepancies between DENOVO predicted responses and MCNP synthetic responses are correlated to current limitations in DIMP. The DIMP DRF does not perform well if the detector cell is in-plane with the source cell (including the neighboring cells). In this type of situation, DIMP has a tendency to create false positive or false negative responses for the appropriate directional responses. Adjustments to the current directional DRF are being investigated to relax this limitation.

Experimental Results

Four measurement experimental campaigns were conducted at the International Safeguards laboratory at Oak Ridge National Laboratories (ORNL) using a calibration button point source, an HEU disk calibration source, a set of HEU line sources tied together within a small round duct structure, and a case with multiple HEU sources and fixtures. Each measurement campagin was designed to test and validate source prediction results calculated by the DIMP code system in a specific configuration relevant to the validation of the fundamental methodology for the holdup application. Each campaign's measured results except for the first one will be compared to the current holdup model used in practice at ORNL, HMS-4 (Holdup Measurement System). This section will discuss the experimental setup including source location, structure, dimensions and composition, and detector location choice rationale.

Experimental Setup

The activities and active source dimensions of the calibration source are available upon request from the International Safeguards group at Oak Ridge National Laboratories. Note that only the active volume of these sources was simulated in DIMP and not their containers, since attenuation was deemed to be negligible with one exception, the HEU disk, which was encased in thin layer of stainless steel casing instead of the typical plastic and cardboard casings.

The HEU source record maintained at ORNL reports each source's mass. The uncertainties in the activity were calculated from the mass measurement uncertainty to be about 0.1 %. The emission energies and relative intensities of the gamma-rays of interest for each source used are listed in Table I.

TABLE I. Gamma ray energies and relative intensities with their uncertainties listed in parentheses, of all sources measured were taken from Brookhaven National Laboratory's Nudat2.6 database. [10] Unlisted uncertainties in Ref. [10] were assumed to be one in the last digit. *Note: gamma-rays from the same source that were within 1 keV of each other were assigned their average energy and their intensities summed together.

Source	Peak Number	Energy (keV)	Relative Intensity ($)
Am-241	1	59.5409(1)	35.9(4)
U-235	1	105.0(1)	2.00(3)*
U-235	2	109.0(1)	2.16(13)*
U-235	3	143.76(2)	10.96(14)
U-235	4	163.356(3)	5.08(6)
U-235	5	185.715(5)	57.0(6)
U-235	6	202.12(1)	1.080(23)
U-235	7	205.316(10)	5.02(6)
Ba-133	1	80.9979(11)	35.6(3)*
Ba-133	2	356.0129(7)	62.05(1)
Cs-137	1	661.657(3)	85.10(20)
Co-60	1	1173.228(3)	99.85(3)
Co-60	2	1332.492(4)	99.9825(6)

Unshielded Cs-137 Button

The first measurement involved only one Cs-137 point source (calibration button source) held above the origin in the selected coordinate system for the computational models by a clamp on a ring stand. This simple experiment was performed to confirm previous results presented by Hykes [2]. It was surmised that some of the inconsistency in the previous results could be attributed to weakness of the employed sources. Although the Cs-137 button source is only slightly stronger than the source used by Hykes, it will make a good initial source configuration for the calibration of DIMP to the ORNL field detector.

In order to minimize the influence of gamma ray scattering by various objects in the lab a 5m x 5m floor space was marked with tape and cleared of all objects deemed non-essential for the experimental measurement. For the vast majority of the measurement time, this remained true. Occasionally, a chair or stool was moved within the measurement boundaries to hold the MCA, or a staff member might have walked through the marked zone inadvertently. However, the effect of these infractions on the precision of the measured response is considered negligible as no foreign object (including the chair carrying the MCA) remained in the field of view of the detector for any significant length of the measurement time.

The equipment deployed in conducting the experiment included two ring stands, a 2"x1" NaI detector, and a Cs-137 calibration source. The stands each had a pole approximately 1.5m tall and a diameter of 2cm and a rectangular base (0.27m x 0.16m). The list of coordinate locations of the center-point of the face of the detector for each detector measurement and the source location are shown in Table II.

TABLE II. Coordinate locations of the center point of the detector face for each measurement of the Cs-137 point source. The origin is located on the floor at the very center of the cleared square. The uncertainty in each measurement coordinate is 1 mm.

Measurement #	Location (cm)	Total Distance	Detector Orientation
Source	(0,0,87)	0	
1	(51,140,87)	149.0	$-y$
2	(120,32,77)	124.6	$-x$
3	(100,-20,96)	102.4	$-x$
4	(10,-74,81)	74.9	$+y$
5	(-5,-60,93)	60.5	$+y$
6	(-50,0,97)	51.0	$+x$
7	(-40,16,84)	43.2	$+x$
8	(-7,20,89)	21.3	$-y$
9	(3,10,87)	10.4	$-y$
10	(2,0.3,87)	2.02	$-x$

The next validation experiment involved measuring a larger HEU source that could either be treated as an area source (multiple cells in a block) or a single cell source depending on mesh resolution. This source again was held above the origin of the measurement area by a clamp on a ring stand. This allowed for measuring a more relevant radiation source to holdup and calibrating DIMP to HEU sources without significantly increasing the complexity of the source geometry. The detector measurement coordinates and the coordinates of the center of the HEU disk source are shown in Table III. A photograph of the experimental setup is presented in Fig. 7.

Fig. 7. Photograph of the HEU Disk source measurement experimental setup.

TABLE III. Coordinate locations of the detector face for each measurement of the HEU Disk source. The uncertainty in each measurement coordinate is 1 mm.

Measurement #	Location (cm)	Total Distance	Detector Orientation
Source	(0,0,91)	0	
1	(100,-20,100)	102.4	$-x$
2	(16,-40,88)	43.2	$+y$
3	(5,-50,95)	50.4	$+y$
4	(-60,-5,97)	60.5	$+x$
5	(-74,10,85)	74.9	$+x$
6	(-7,20,93)	21.3	$-y$
7	(3,10,91)	10.4	$-y$
8	(2,0.3,91)	2.02	$-x$
9	(40,0,91)	40.0	$-x$
10	(6,-1,91)	6.08	$-x$

The next set of experiments involved the arrangement of various HEU sources within three steel fixtures to simulate realistic holdup in a facility environment. The three fixtures were: a small round duct, an L-duct, and a pipe array. Each cart is a metal dolley with wheels and steel strut supports to hold the fixture in place. The pipe array is not included because it was never filled with a source. The HEU measurements will be included in future publications once the validation analysis is completed.

A photograph of the general experimental setup is included for perspective in Fig. 8

Fig. 8. Photograph of the general holdup-like source measurement experimental setup.

Simulation Experimental Geometry

The base simulation geometry for all experiments includes a main void region on top of a floor region composed of a standard tile and concrete mixture across a 5m x 5m square area. The cells are contained between −2.5 m on the west boundary to +2.5 m on the east boundary. The same is true for −2.5 m from the south boundary and ending at +2.5m at the north boundary. The origin is in the center, just above the upper floor surface boundary. The z axis is defined from −10 cm (the underside of the floor) to 3 m above the floor. For DENOVO, each cell (e.g. floor, steel fixtures, ring stand, etc.) is simulated with parallelepipeds to approximate all of the necessary surfaces in Cartesian geometry since DENOVO does not permit curved surfaces. However, curved surfaces were employed in the synthetic response simulations to model the detector and the geometric arrangement executed by MCNP.

Though the physical geometry of the detector is simulated in MCNP, it is not simulated in DENOVO. Instead, the response values are taken at the center face of the detector after multiplying the adjoint source by a point DRF factor to approximate the effects of the shielding and collimator. The current point DRF formulation used by DIMP is described in Ref. [7].

Experimental Measurement Equipment

The field equipment used to take measurements for all experimental campaigns included a detector with a preamplifier and a multichannel analyzer with full pulse processing integration. Both pieces of equipment were essential for HMS-4 and DIMP holdup measurements.

The detector was a 1 inch diameter by 2 inches height right cylinder EFC Model 1X2P collimated NaI scintillation detector. This is a standard field detector for HMS-4 measurements. [11] The detector is well shielded with lead except on the front face where the collimator aperture allows radiation into the detector from a limited extent of directions, i.e. fixed solid angle. Hence, the detector has approximately a 23 degree in-axial-plane angle of vision from the axis normal to its circular front face.

The MCA is a GBS Elektronik GmbH MCA-166 Rossendorf model [12] that has a self-contained set of pulse processing equipment. The MCA receives a preamplified signal directly from the detector through a coaxial cable, which it amplifies and counts across a spectrum of energies. The number of counts is divided into channels (proportional to energy) and sent directly to the computer for recording and post-processing.

Cs-137 Point Source

DIMP performed fairly well for the first validation exercise using ORNL experimental measurements involving the Cs-137 point source after some adjustments. Under the standard initial guess ($\alpha = 10^{-4}$, the baseline static low source cell probability), DIMP failed to predict any source cells with magnitude larger than 1% of the true source strength, however using the true source configuration as the initial guess yielded a very good result alluding to DIMP becoming trapped in a local minimum during the first source search. The usual initial guess is chosen with a flat low source probability in every mesh cell allowing feedback with the measured responses to increase the source probability in the appropriate cells. Also, a correction factor had to be applied to the measured responses to account for the effects observed as a result of the special

collimator geometry for ORNL's 1" x 2" NaI field holdup detector that were not featured in the previous detector design used in Ref [2] and utilized in the synthetic data presented in previous sections of this paper. Furthermore, two measurement points had higher than expected flux values, so further investigation is currently underway to determine if they are statistical outliers or further adjustments to the detector model need be made.

Development of the Collimation Correction Factor

The detector used in [2] was a 2" x 2" NaI detector, collimated by the placement of lead bricks above and to the sides of the detector to produce a forward facing hemisphere field of view (FOV). The 1" x 2" NaI field holdup detector provided by ORNL to conduct the measurement campaigns has a much more sophisticated collimator that narrows the FOV to roughly 23 degrees and partially obscures the crystal face. The front of the lead collimator touches the crystal face and covers about 12% the face reducing the detector's solid angle FOV. Since the previous configuration [2] did not suffer such a reduction in solid angle, DIMP requires a collimation correction factor to adjust the detector efficiency for the effect of this collimation on the directional responses. The source-location dependent reduction in solid angle is illustrated by Fig. 9

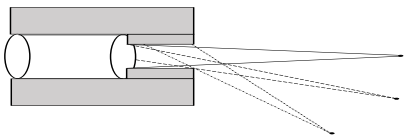

Fig. 9. Sketch of the detector collimator shadowing effect on the detector crystal (reducing the effective solid angle).

A fairly simple way to compute such a factor, is to simulate the detector with and without the collimator geometry (just the detector crystal) in MCNP and compare the results to the analytical solid angle calculations. Using the ratio of the two fluxes (with and without the collimator) as the collimation correction factor, the measured responses can be corrected by this factor to better match the responses predicted by the true source distribution folded with DENOVO adjoint fluxes. Thus, the collimation correction factor ($S_{col}(\boldsymbol{r}, E)$) can be calculated as follows

$$S_{col}(\boldsymbol{r}, E) = \frac{\phi^{syn}_{col}(\boldsymbol{r}, E)}{\phi^{syn}_{unc}(\boldsymbol{r}, E)} \tag{25}$$

where $\phi^{syn}_{col}(\boldsymbol{r}, E)$ and $\phi^{syn}_{unc}(\boldsymbol{r}, E)$ are the collimated and uncollimated synthetic responses calculated from the true source configuration in MCNP. Dividing the measured responses by $S_{col}(\boldsymbol{r}, E)$ will produce an approximate value of the response that would have been measured with a $2\,\pi$ FOV detector that is assumed in the current version of DIMP. A more rigorous way to account for the collimator's effect is to determine a directionally dependent DRF.

The correction factor was used to adjust each of the measured responses from the Cs-137 point source campagin before initializing DIMP's source search algorithm. The experiment involved ten detection points measured within the experimental area in a spiral pattern around the 4 μ Ci point source held by a clamp on the ring stand (similar to the HEU setup in Fig. 7). The distance between the source and detection points ranged from 0.02-1.25 m as discussed in the previous section, and the coordinates of the true Cs-137 point source are (0,0,87) cm.

Consider the DIMP predicted source map shown in Figure 10 of the Appendix. As in this source-strength map, DIMP performed well predicting the source in the correct cell (0,0,90) with 80% of the true source activity with fairly low uncertainty. Only 80% of the true source strength was obtained because the FOV-corrected measured responses still had a margin of error when compared with those calculated by DENOVO. This is a promising result for the first of four experimental measurements, but there are two issues with this result. The first, is that as in [2] the source search had to be narrowed to a lower number of mesh cells in order to find a good source configuration. Specifically, instead of allowing the point source to occupy any number of cells within the full volume of air in the problem configuration (100 x 100 x 61 cells) we limit the region where the source can be located to 40 x 40 x 30. Otherwise, the gradient source search algorithm often becomes stuck in local minima and predicts weak distributed sources with larger values of the reduced chi-squared. The second is that two detection point fluxes did not match up with MCNP synthetic fluxes, so for the time being they were adjusted to the synthetic values artificially. Further investigation will determine a physical explanation for those discrepant values if possible. They may be removed as outliers, since both points were measured fairly close to the source.

CONCLUSIONS

DIMP is a reliable inverse radiation transport solver that has proven stable for point and line radiation sources configurations. Although, DIMP does not resolve the entire line source with full accuracy, it still approximates the strong point sources in the line well. DIMP maps the source within a few cells of its true location and generally predicts the correct source strength when using more than 5 detection points.

DIMP performed fairly well for the first validation exercise concerning the Cs-137 point source suspended by a clamp stand once a detector collimation factor was applied to the measured responses and the spatial domain for the source search was reduced by 90% (a full order of magnitude). Without the domain reduction, DIMP's optimizer often failed to predict the correct source because it became stuck in local minima that were less optimal than the true source specification as quantified by the corresponding reduced chi-squared values. With the success of the reduced search, it can be concluded that future DIMP optimization searches should be attempted with either an alternate optimizer that does not easily become trapped in local minima or an adaptive mesh algorithm applied to reduce the search spatial domain to only logically accept-

able source cells (in equipment, not floors, walls, random air cells, etc.).

DIMP is expected to perform well for the remaining validation exercises. DIMP will also be verified against SNM masses predicted by ORNL's HMS-4 system. The validation will consist of three additional measurements conducted over experimental campaigns involving two single source cases and one multi-source case in various geometries. Two of the campaigns were meant to simulate holdup-like sources in a realistic facility geometry (e.g. sources in pipes and ducts), while the others were used for calibration of the DIMP system.

ACKNOWLEDGMENTS

The authors of this work would like to acknowledge support from the U.S. Department of Energy Nuclear Energy University Programs under contract 127981. This material is based upon work by the authors (NBN, YYA) supported in part by the Department of Energy National Nuclear Security Administration under Award Number(s) DE-NA0002576. The authors would also like to acknowledge Dr. Louise Worrall and the International Safeguards and Security Technology group at Oak Ridge National Laboratory for their assistance with the experimental data collection presented in this paper.

REFERENCES

1. "Nondestructive Assay of Holdup," *Passive Nondestructive Assay of Nuclear Materials 2007 Addendum*, T. D. Reilly, Washington D.C.: Los Alamos National Laboratory, 2007.
2. J. M. Hykes and Y. Azmy, "Radiation Source Mapping with Bayesian Inverse Methods," *Nuclear Science and Engineering*, vol. 179, pp 1-17, 2015.
3. A. Tarantola, *Inverse Problem Theory and Methods for Model Parameter estimation*, Philadelphia: Society for Industrial and Applied Mathematics, 2005.
4. D. G. Cacuci and M. Jonescu-Bujor, "Sensitivity and Uncertainty Analysis, Data Assimilation, and Predictive Best-Estimate Model Calibration," *Handbook of Nuclear Engineering*, New York: Springer, 2010.
5. E. E. Lewis and W. F. Miller Jr., *Computational methods of neutron transport*, La Grange Park, IL: American Nuclear Society, 1993.
6. *Scale: A Comprehensive Modeling and Simulation Suite for Nuclear Safety Analysis and Design*, ORNL/TM-2005/39, Version 6.1, June 2011. Available from Radiation Safety Information Computational Center at Oak Ridge National Laboratory as CCC-785.
7. J. Hykes, "Radiation Source Mapping with Bayesian Inverse Methods," PhD Thesis, North Carolina State University, 2012.
8. R. P. Gardner and A. Sood, "A Monte Carlo simulation approach for generating NaI detector response functions (DRFs) that accounts for non-linearity and variable flat continua," *Nuclear Instruments and Methods in Physics Research B*, vol. 213, pp. 87-99, 2004.
9. N. Nelson, "Validation and Uncertainty Quantification of a 1x2" NaI Collimated Detector Using Detector Response Functions Created by g03," MS Thesis, North Carolina State University, 2014.
10. National Nuclear Data Center, "Nudat2.6: Decay Radiation Search," Brookhaven National Laboratory, 2013. [Online]. Available: `http://www.nndc.bnl.gov/nudat2/indx_dec.jsp`. [Accessed 14 June 2015].
11. S. E. Smith, et al., "Holdup Measurement System 4 (HMS4)-Automation & Improved Accuracy," BWXT Y-12 report Y/DK-2190, ORTEC, 2004. [Online]. Available: `http://www.ortec-online.com`. [Accessed 16 August 2016].
12. GBS Elektronik GmbH, "MCA 166-USB: Multi channel analyzer with USB interface," GroBerkmannsdorf, Germany, 2008.

APPENDIX

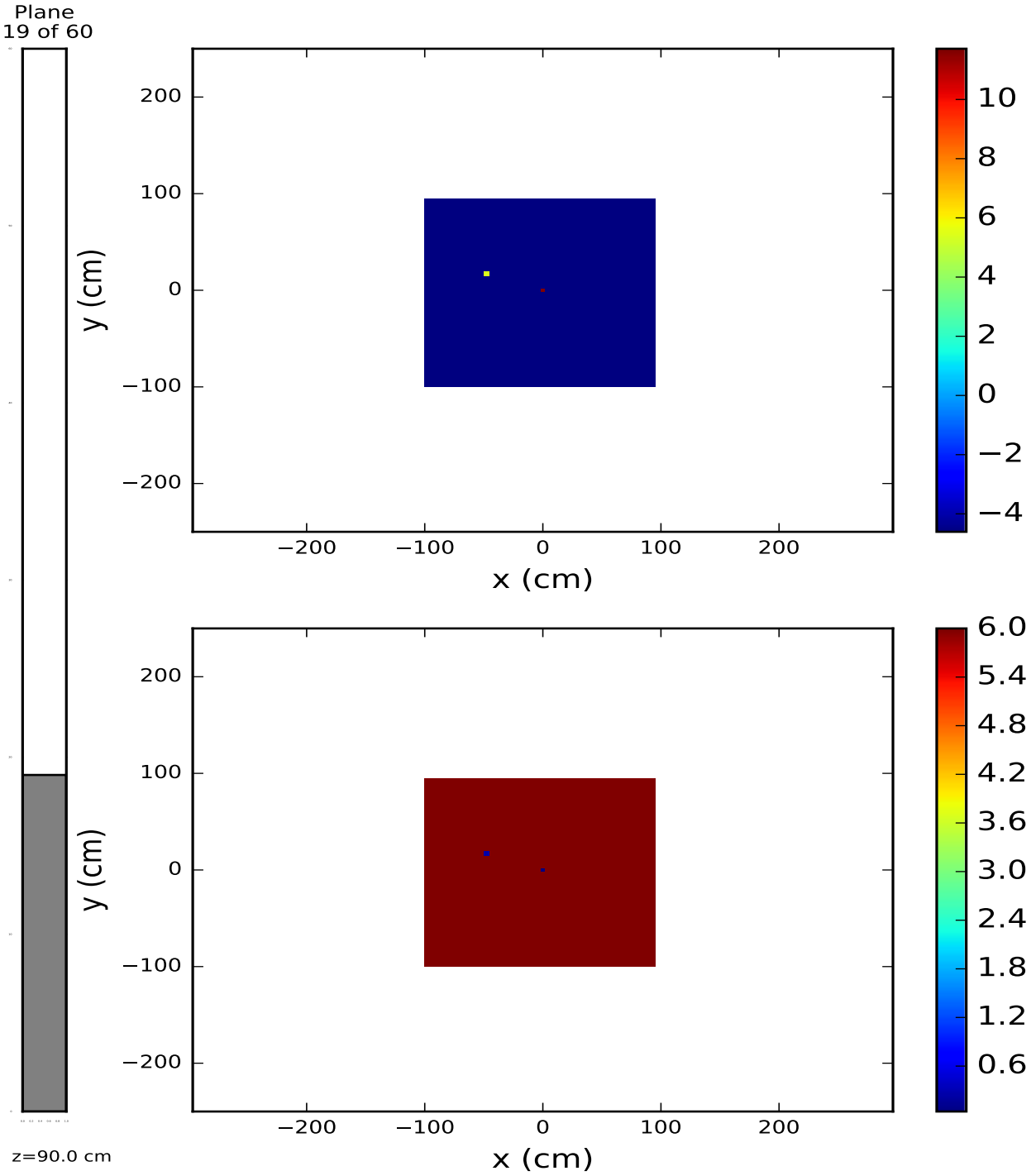

Fig. 10. DIMP predicted source map (above) for a 5m x 5m square space (reduced to a 2m x 2m search area) with a Cs-137 point source suspended by clamps on a ring stand, and the corresponding uncertainty (below).